15th Numerical Towing Tank Symposium

7-9 October 2012

Cortona/Italy

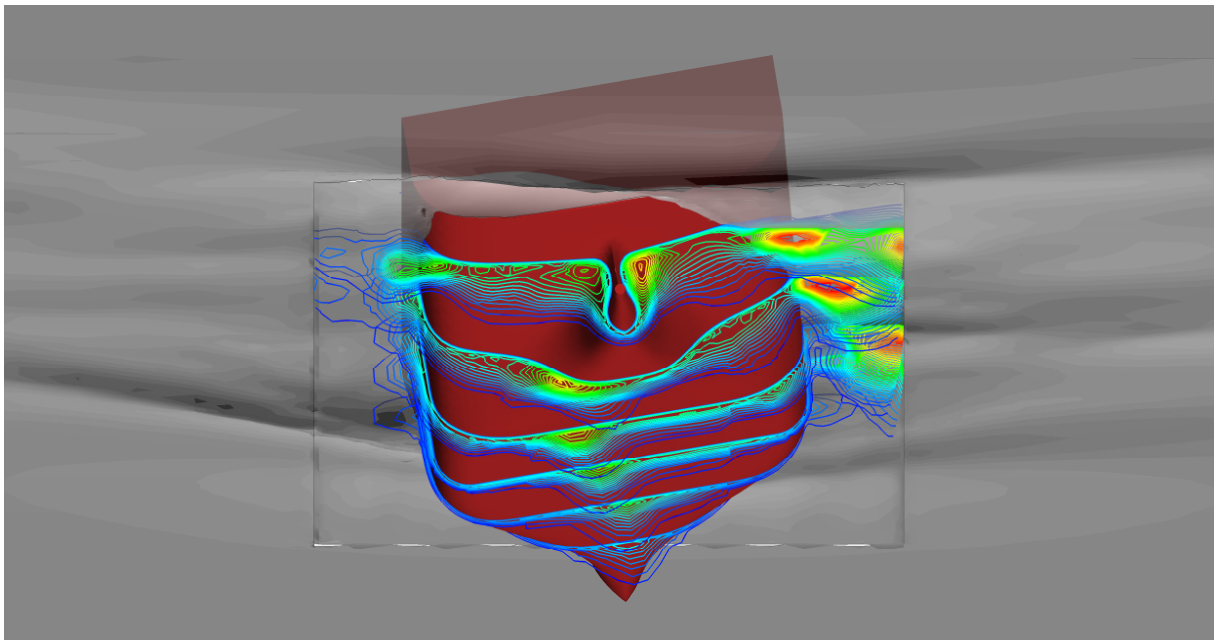

Volker Bertram, Emilio Campana (Ed.)

The Italian Ship Model Basin
INSEAN

TuTech
TUHH Technologie GmbH

Sponsored by

CD-Adapco
www.cd-adapco.com

Germanischer Lloyd
www.gl-group.org

Table of Contents

Database Fed Body Force Propulsor
Jens Höpken, Ould el Moctar

Design of retrofit devices using CFD, validated with wind tunnel tests
Marion C. James, Stephen R. Turnock, Dominic A. Hudson

Evaluation of RANS turbulence models for the flow around an axisymmetric streamlined body
Mattias Johansson, Mattias Liefvendahl

Real-time computation of interactive waves using the GPU
Martijn de Jong, Auke van der Ploeg, Auke Ditzel, Kees Vuik

Implementation of Anisotropic Mesh Refinement in OpenFOAM
J. Karlsson, A. Feymark, C. Eskilsson

A Study of CFD Modelling Variations for Numerical Underwater Noise Prediction
Paula Kellett, Osman Turan, Atilla Incecik

About the Effect of Discretisation Schemes on the Results of Numerical Calculations of Ship Flow
Lutz Kleinsorge, Robert Bronsart, Katja Hartig

Wave Reconstruction for Deterministic Prediction of Nonlinear Wave-field
Hiroshi Kobayashi, Claudio Lugni

Influence of Roughened Propeller Tip Surface on Tip Vortex Structures
Christian Krüger, Nikolai Kornev, Mathias Paschen, Christian Semlow

OpenFOAM Simulation of Regular Wave and Wave Load on Cylinder
Linghan Li, Mingyi Tan, James Blake

Simulation of inflow turbulence noise
Thomas P. Lloyd, Mathieu Gruber, Stephen R. Turnock, Victor F. Humphrey

Introducing Non-condensable Gas in Unsteady Sheet Cavitation Modelling
Nai-Xian Lu, Göran Bark, Rickard Bensow

The influence of phase difference and pitch axis position on the performance of heaving and pitching hydrofoils
J. Mattheijssens, J.-P. Marcel, W. Bosschaerts, D. Lefeber

Simulation of Extreme Motion of Floating Bodies Using Overlapping Grids
Milovan Perić, Eberhard Schreck

Numerical modelling and error estimation of the flow behind marine propellers
Robert Pfannenschmidt, Lars Greitsch, Martin Greve

Using CFD to Assess Fluid Structure Interaction in a Moonpool
Alessio Pistidda, Harald Ottens

Influence of drift angle on rudder – propeller interaction

Charles Badoe[*], Alexander Phillips[*], and Stephen R Turnock[*]

[*]Fluid-Structure Interaction Research Group, School of Engineering Sciences, University of Southampton,
Highfield, Southampton SO17 1BJ, UK

Corresponding author's email: cb3e09@soton.ac.uk

1. Introduction

The importance of a rudder cannot be understated; although relatively small, the hydrodynamic forces and moments developed on it are essential in the assessment of the manoeuvring characteristics of a ship. When a rudder angle is applied, a ship develops a drift angle which decreases the effective inflow angle to the rudder. Additionally, the effect of the hull and propeller upstream of the rudder straightens the flow, this increases the effective inflow to the rudder. Flow straightening effect as a result of the propeller and hull is important in the development of rudder forces and their role in manoeuvring and course keeping.

The primary aim of this paper is to increase the knowledge on flow straightening influence of the propeller and hull on the effective angle of drift at the stern of a ship. Preliminary investigations compared with wind tunnel experiments carried out by Molland and Turnock [1, 2] using a modified Wageningen B4.40 propeller and Rudder No.2 are presented. Two separate investigations were considered.

1. A propeller – rudder combination in straight line flow (with no applied drift angle) was conducted to understand the interaction effect. This study employed a body force propeller model.

2. Three centre-boards with relatively small thickness and with three different lengths placed upstream of the propeller–rudder combination were proposed for investigation based on the finding in (1) to understand the effect of an upstream plate on flow straightening. This study is still under investigation. Real propeller geometry is employed with the aim of establishing the use of the arbitrary mesh interface (AMI) in the current version of OpenFOAM [3].

2. Theoretical approach

An open source CFD code Open FOAM (Open Field Operation and Manipulation) [3] was used for the investigation. It solves the Reynolds Averaged Navier Stokes (RANS) equations using a cell-centered finite-volume method. The RANS equations can be written in the form:

$$\frac{\partial \overline{U_i}}{\partial x_i} = 0 \qquad (1)$$

$$\rho \frac{\partial \overline{U_i}}{\partial t} + \rho \frac{\partial \overline{U_i U_j}}{\partial x_j} = -\frac{\partial P}{\partial x_i} + \frac{\partial}{\partial x_j}\left\{ \mu \left(\frac{\partial \overline{U_i}}{\partial x_j} + \frac{\partial \overline{U_j}}{\partial x_i} \right) \right\} - \rho \frac{\partial \overline{u'_i u'_j}}{\partial x_j} + f_i \qquad (2)$$

The Reynolds stress ($\rho\overline{u'_i u'_j}$) was modelled to close the governing equation by employing a Shear Stress Transport (SST) eddy viscosity turbulence model. The SST k-ω model was developed by Menter [4] to effectively blend the robust and accurate formulation of the k-ω model in the near-wall region with the free-stream independence of the k-ε model in the far field. Previous investigations using this model has shown to be better at replicating flows involving separation, which is an important issue in the analysis of ship flow, where separation always occurs in the region of ship stern [5] .

3. Propeller modeling

3.1 Actuator disk implementation in OpenFOAM

The momentum equations include a bodyforce term f_{b_i}, used to model the effects of a propeller without modeling the real propeller. There are numerous approaches for calculating f_{b_i} including simple prescribed distributions, which recover the total thrust T and torque Q, to more sophisticated

methods which use a propeller performance code in an interactive way with the RANS solver to capture propeller rudder interaction and to distribute f_{b_i} according to the actual blade loading [6]. To implement the bodyforce model in OpenFOAM an actuator disk region is defined where the rotor (propeller) is accounted for by adding momentum (volume force) to the fluid [7]. The radial distribution of forces, with components f_{b_x} (axial), f_{b_r}(radial) = 0 and f_{b_θ}(tangential), is based on non-iterative calculation of Hough and Ordway [8] circulation distribution with optimum type from Goldstein [9] and without any loading at the root and tip:

$$f_{b_x} = A_x r^* \sqrt{1 - r^*} \quad (3)$$

$$f_{b_\theta} = A_\theta \frac{r^* \sqrt{1 - r^*}}{r^*(1 - r'_h) + r'_h} \quad (4)$$

Equations (3) & (4) represent body forces per unit volume normalized by U^2/L where U is the reference velocity; L is a reference length, and ρ the fluid density. Coefficients are expressed as:

$$r^* = \frac{r^* - r'_h}{1 - r'_h}, r'_h = \frac{R_H}{R_P}, r^* = \frac{r}{R_P} \quad (5)$$

$$r = \sqrt{(y - Y_{PC})^2 + (z - Z_{PC})^2} \quad (6)$$

$$A_x = \frac{C_T}{\Delta} \frac{105}{16(4+3r'_h)(1-r'_h)} \quad (7)$$

$$A_x = \frac{K_Q}{\Delta J^2} \frac{105}{\pi(4+3r'_h)(1-r'_h)} \quad (8)$$

$$C_T = \frac{2T}{\rho U^2 \pi {R_P}^2} \quad (9)$$

where C_T and K_Q are the thrust and torque coefficients, J is the advance coefficient, n is the number of rotations per second (rps), R_P is the propeller radius, R_H is the hub radius, Δ is the mean chord length projected into the xz plane (or actuator disk thickness), and Y_{PC} and Z_{PC} define the propeller center coordinates. As derived, these forces are defined over an "actuator cylinder" with volume defined by R_P,R_H, and Δ.

3.2 Arbitrary mesh interface (AMI) in OpenFOAM

The arbitrary mesh interface for non-conformal patches is a technique that allows simulation across disconnected, but adjacent mesh domains. The domain can either be moving relative to one another or stationary. AMI implementation is based on the Farrell and Maddison [10] algorithm. It is integrated into boundary patch classes within OpenFOAM and is available for un-matched/non-conformal cyclic patch pairs; sliding interfaces, e.g. for rotating machinery.

4. Experimental data

The experimental data used for this investigation was obtained through wind tunnel test performed by Molland and Turnock [1,2] at the University of Southampton 3.5x 2.5m RJ Mitchell Wind Tunnel. The experimental set-up is shown in Figures 1 and 2. Figure 1 is the set-up for propeller – rudder combination (zero drift). It comprises of a 1m span and 1.5m aspect ratio rudder based on NACA 0020 aerofoil section and a 0.8m diameter propeller based on Wageningen B4.40 series. Figure 2 is the set-up of the rudder – propeller combination with centre boards for investigating the effect of an upstream plate on flow straightening. Details of the propeller, rudder and centre-boards dimensions can be found in [1,2].

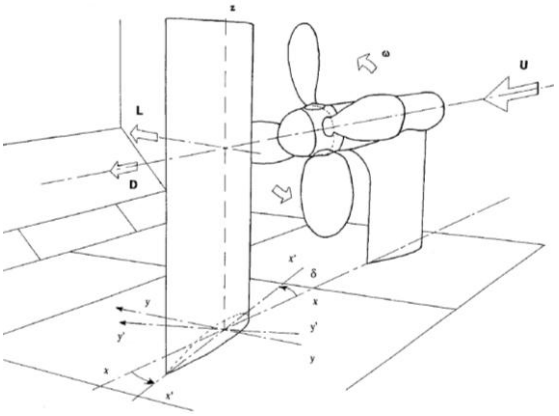

Fig. 1.0: Rudder –propeller configuration [2]

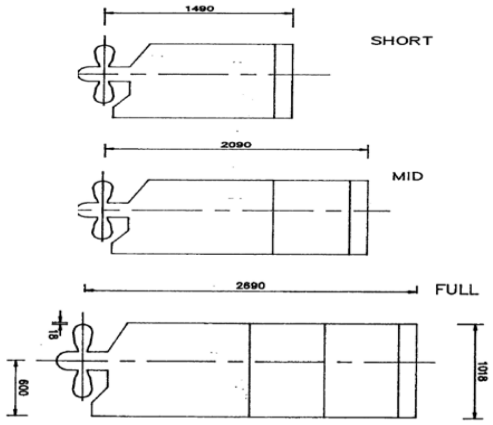

Fig. 2.0: Dimensions of three-centreboard configurations [2]

5. Rudder-propeller combination (zero drift).

5.1 Numerical model

The solver settings and simulation parameters can be found in table 5-1.

Mesh	
Type of mesh	Unstructured (Hexahedral)
No. of elements	Approximately 2.5M
y^+ on rudder	30 - 60
Boundary Domain Physics	
Inlet	Freestream velocity 10m/s
Outlet	Zero gradient
Tunnel floor/side walls	Slip
Tunnel roof	Slip
Rudder	Zero gradient
Domain physics/Turbulence model	Incompressible/SimpleFom k-ω SST Turbulence Model. Automatic wall function
Solver settings	
solver	GAMG
smoother	Gauss Seidel
Grad (U) Scheme	Gauss linear
Div (U)	Gauss linear UpwindV
Coupling	SIMPLE
Convergence criteria	P 1e-7, U 1e-8, k 1e-8, omega 1e-8

Table 5-1: Numerical Settings [6,7,1]

5.2 Mesh Technique

An unstructured hexahedral grid created using SnappyHexMesh utility within OpenFOAM was used for the geometry. An initial coarse block mesh was created defining the size of the domain after which specific areas of interest within the domain were then specified for refinement in progressive layers. The total number of grid points was around 2.5 million. It should be noted that the relatively initial coarse mesh was assumed to be good enough for producing data for a qualitative comparison with experimental data in the code development phase. Boundary layer elements were grown around the rudder surface mesh.

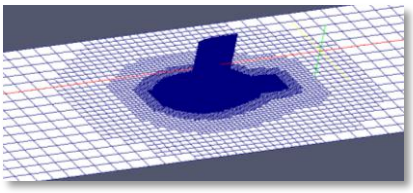

Fig 3.0: Tunnel floor and rudder Mesh

6. Results and Discussions

The propeller-rudder combination using rudder No.2 was simulated at zero drift angle for the standard set of flow conditions. Pressure distributions were plotted for several rudder angles, and for a wind speed of 10m/s and Reynolds number of 0.4 x 10^6. The propeller was fixed at X/D =0.39 and operates at an advance coefficient of J = 0.35. As regards the propeller model it was important that the cells belonging to the actuator disk region were identified properly and that the momentum source terms added to only those cells in order not to increase further the numerical errors. Results are presented both for field and integral quantities.

6.1 Lift and Drag data

Figure 4.0 compares the lift and drag coefficients from the rudder behind a propeller in straight flow (zero drift) and an earlier investigation conducted for the same rudder in free-stream with experimental data from Molland and Turnock [1]. By comparison of the calculations with experiment it is seen that there is a considerable increase in lift when a rudder is placed behind a propeller. This is because the inflow velocity to the rudder is greater as (a result of the propeller accelerating the flow) compared to free-stream rudder. Generally lift increases as propeller loading increases. Results show good agreement at low angles of attack, where the flow is fully attached, but slightly deteriorates at the angle of attack in increases. However the results are within 10% of mean experimental value. The computed drag is predicted higher than found in the free-stream rudder. For the rudder behind a propeller the drag coefficient showed good agreement with experiment for rudder angles up to ten degrees whilst drag is over-predicted for rudder angle in excess of ten degrees. This could be due to several factors; first the wall boundary layer at the rudder root was neglected, this might also have contributed to the difference observed in the lift plot. Secondly the over prediction might also be due to frictional drag computation (laminar-turbulent transition). The boundary layer flow might not have been fully turbulent prior to generation of the data (for the rudder behind the propeller). The problem has been addressed by Hoffman *et al* [11] who carried out investigations

on "the Influence of Freestream Turbulence on Turbulent Boundary Layers with Mild Adverse Pressure Gradients". They concluded that transition is a very sensitive flow phenomenon and, as such, can be strongly affected by experimental conditions (in particular, the level of freestream turbulence); CFD computations tend to overestimate the drag force [12].

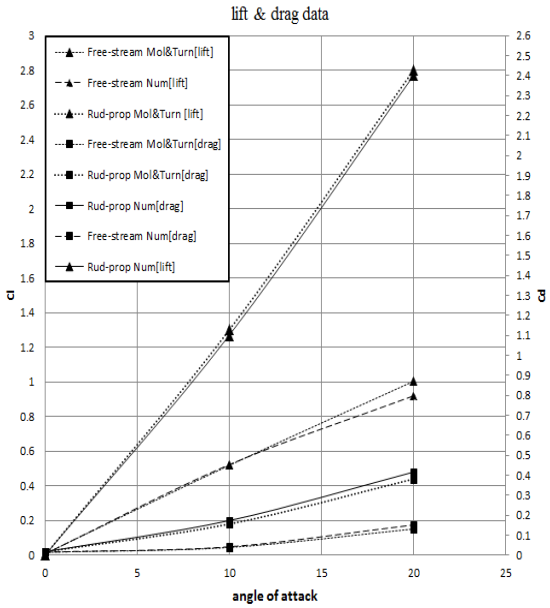

Fig 4.0: Force data for Rudder No.2 Free-stream (w/o propeller) and with propeller J=0.35

6.2 Velocity distribution at the rudder

In order to fully understand the influence of the propeller on the flow downstream of the rudder before the application of a drift angle, axial velocity components were studied at various locations along the rudder. Propeller effects on the rudder can be observed on all the plots because of regions of high axial velocity at the side of the rudder in the slipstream. Close to the leading edge at a distance of x =0.1m acceleration of the fluid was rapid at the suction side. At different stations farther downstream x = 0.75m through to the wake region x = 1.1m the development of the tip vortices can be observed. This is due to the difference in pressure between the suction and pressure side, and the pressure difference together with the rotation of the flow causes high velocity regions to move to the tip and upward to the root of the suction and pressure side.

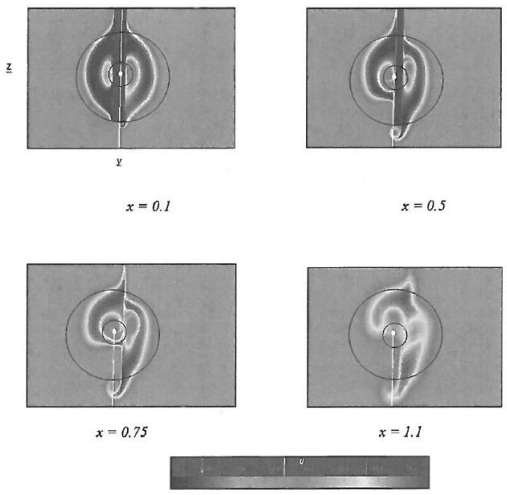

Fig 5.0: Axial velocity component at various x locations; $\delta = 9.6^{o}$

6.3 Rudder surface pressure distribution

Pressure distribution around a rudder is an important parameter, both in terms of hydrodynamic characteristics (because it determines the lift and drag coefficients of the rudder) and in terms of boundary-layer behaviour (because the pressure gradient affects development of both laminar and turbulent boundary layers. The computed pressure distribution represented by the local pressure coefficient C_P is given in the equation below

$$C_{P} = \frac{p - p_{\infty}}{0.5\rho U_{\infty}^{2}} \qquad (10)$$

where $p - p_{\infty}$ is the local pressure ρ is the density and U is the free stream velocity. Figure 6.0 presents the pressure distribution on the rudder surfaces as a result of the action of the propeller. High velocity regions observed were due to the swirl in the slipstream hitting the lower regions in the pressure and suction side. The introduction of the propeller generates high pressure peaks both positive and negative which causes an increase in lift coefficient. Figure 7.0 also shows the plot of pressure distribution at eight spanwise locations of the rudder from the root to the tip. These plots were created to investigate the performance of the propeller code used. Agreement was good in areas close to the tip Figs (7.0.g &7.0.h). The slight difference observed was as a result of the tip vortex, which introduces some unsteadiness which could not be captured by the solver. At mid chord (7.0d, 7.0.e &7.0.f), areas close to the hub, pressure distributions were under predicted. This is due to the fact that the propeller code does not take into

account the effect of the hub hence flow effect as a result of the hub could not be adequately captured. Flow effects for Fig (7.0.a) were not adequately captured, this was due to the fact that the floor boundary layer was neglected hence the interaction between the floor and the root could not be modeled. Also body force was not smoothly distributed around the entire actuator disk region which will introduce some discrepancies between numerical and experimental results as also suggested by [13].

7. Conclusions and future work

Results of the present work have shown how CFD can be applied to gain valuable insight into the physics of forces associated with the rudder when vessel is at an angle of drift. Comparisons between calculated and measured hydrodynamic forces and moments showed that the CFD results for both rudder and propeller can be predicted within 10% of measured data. In general the magnitude of drift angle depends on advance ratio. When rudders are placed behind a propeller, lift force increases with increasing propeller loading.

Effect of drift is to shift the forces associated with the rudder but not to change them totally. Based on these findings, the current investigation underway into flow straightening with the centreboards will be carried out in oblique flow to simulate drift angle. Exact set-up (as test 1) will be used i.e. (constant wind speed, Reynolds number and rudder-propeller separation) but this time employing the use of AMI to a real propeller geometry. Test will be conducted for a range of drift angles (-15^o; $+7.5^o$; -7.5^o and $+15^o$) and advances ratios. Through these tests further insight into the performance of a rudder (through lift, drag and sideforce plots) and propeller (plot of difference between actual and open water propeller thrust against rudder incidence) will be obtained. The main challenge highlighted by the findings (in test 1) is appropriate mesh design. The mesh could have been redistributed in order to resolve the slipstream flow better and allow smoother distribution of body force. Future investigation will focus on improving the mesh to accurately capture flow features.

Acknowledgements

The research presented in this paper has been financially supported by Shell Shipping UK. Mr Badoe would like to express his gratitude for their support.

References

[1] A. F. Molland and S. R. Turnock. Wind tunnel investigation of the influence of propeller loading on ship rudder performance. Technical report, Ship Science Report No. 46, 1991

[2] A.F. Molland and S.R. Turnock. Wind tunnel tests on the effect of a ship hull on rudder-propeller performance at different drift angles. Technical report, University of Southampton Ship Science Report No. 76, May 1995.

[3] Open FOAM User Guide, Version 1.6, and 24th July 2009

[4] Menter, F R. (1994) Two-Equation Eddy-Viscosity Turbulence Models for Engineering Applications [J]. AIAA Journal, 32(8):1598-1605

[5] Larsson, L. and Baba, E. (1996). Ship resistance and flow computations. Advances in marine hydrodynamics. Ohkusu 9ed), Comp. Mech. Publ., pp.1-75.

[6] E.G. Paterson, R.V. Wilson, and F. Stern. (2003).General purpose parallel unsteady RANS ship hydrodynamic code CFDSHIP-IOWA. Technical report, Iowa Institute of Hydraulic Research, The University of Iowa.

[7] Svenning, E. (2010).Implementation of Actuator Disk in OpenFOAM.

[8] Hough, G. and Ordway, D. (1964) “The Generalized Actuator Disk,” Technical Report TARTR 6401, Therm Advanced Research, Inc.

[9] Goldstein, S. (1929) "On the Vortex Theory of Screw Propellers", Proc. of the Royal Society (A) 123, 440.

[10] P. E. Farrell and J. R. Maddison, Conservative interpolation between volume meshes by local Galerkin projection. Comput. Methods Appl. Mech Engrg 200:89 (2011).

[11] Hoffman, J. A., Kassir, S. M., and Larwood, S. M., “The Influence of Freestream Turbulence on

Turbulent Boundary Layers with Mild Adverse Pressure Gradients," NASA CR 177520, 1989.

[12] Clauser, F. H., "Turbulent Boundary Layers in Adverse Pressure Gradients," Journal of the Aeronautical Sciences, Vol. 21, No. 2, 1954, pp. 91–108

[13] Simonsen, C. (2000) Propeller – Rudder interaction by RANS PhD thesis, University of Denmark.

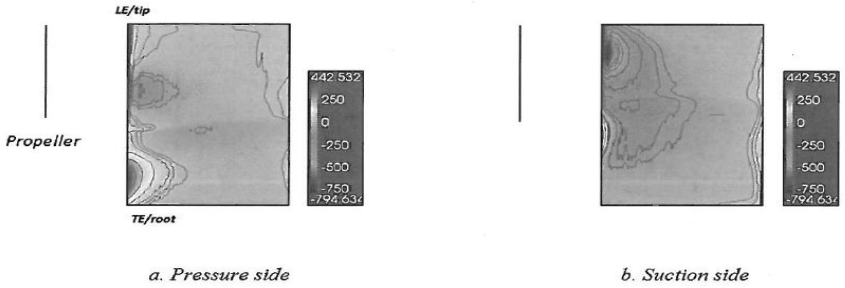

Fig 6.0: Pressure distribution on rudder surface $\delta = 9.6^{o}$

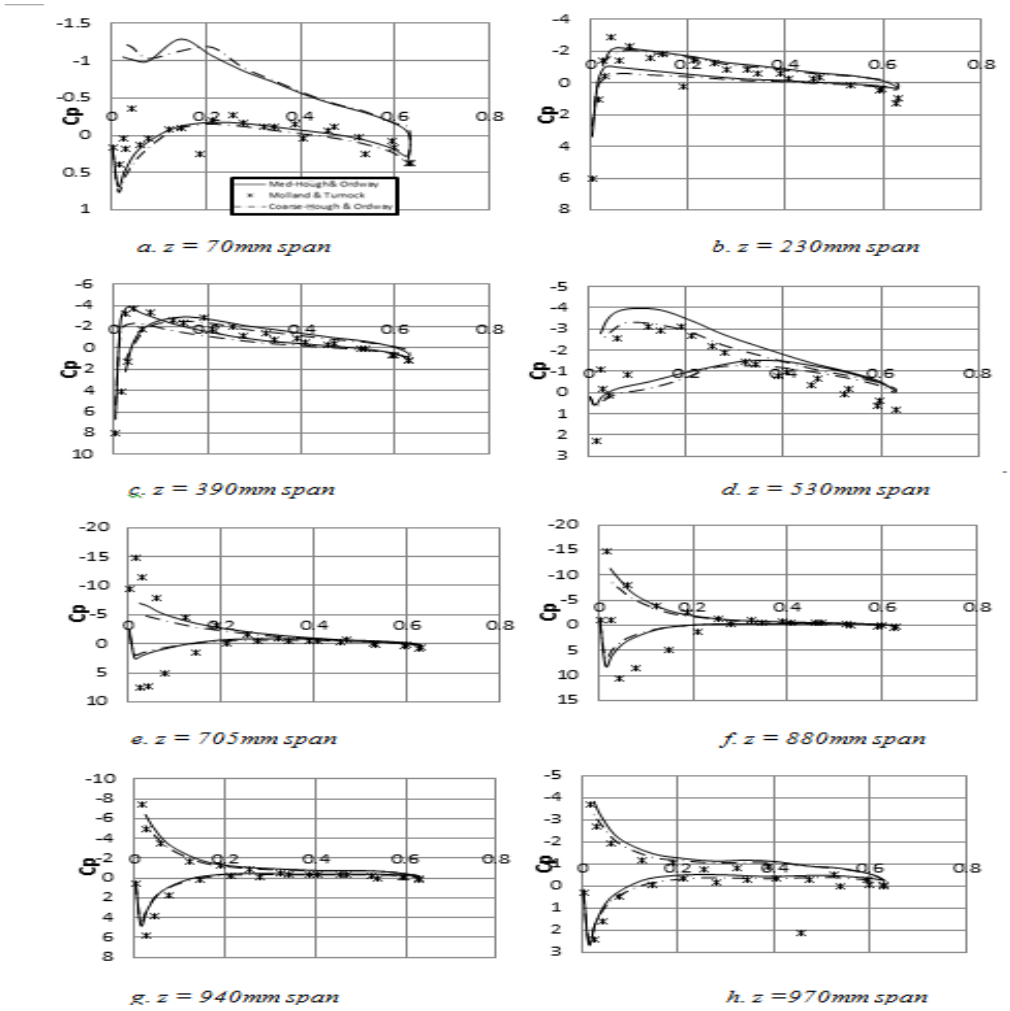

Fig 7.0: Numerical and experimental Cp plot, J =0.35 $\delta = 9.6^{o}$

On novel simulation methods for complex flows in maritime applications

Henry Bandringa, h.j.bandringa@rug.nl
Roel Verstappen, r.w.c.p.verstappen@rug.nl
Fred Wubs, f.w.wubs@rug.nl
Christiaan Klaij, c.klaij@marin.nl
Auke van der Ploeg, a.v.d.ploeg@marin.nl

1 Introduction

Turbulent flows in maritime applications usually contain a wide range of length and time scales, especially for high Reynolds numbers. Therefore, it is not feasible to solve such flows with direct numerical simulation. To reduce CPU-times, a model is proposed. Verstappen *et al.* proposed an LES model based on regularization. The regularization model filters the convective terms in the Navier-Stokes equations without adding any artificial dissipation. The spatial discretization preserves the energy too [9]. This is quite important, since artificial dissipation can interfere with the subtle interplay between inertia and dissipation of the flow. In Fig. 1, an example of the regularization model is displayed. It shows that the regularization model captures the boundary layer, with far less grid points than DNS. A novel aspect of our research will be

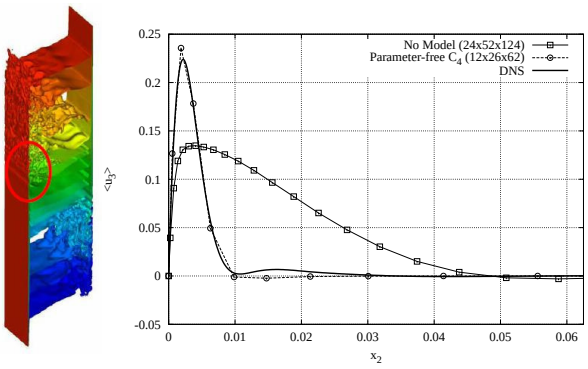

Figure 1: Differentially heated cavity (left); DNS with Raleigh number is $10^{11}(\sim \mathrm{Re} = 10^4)$. *Results on a stretched Cartesian grid obtained from joint work between RuG and Barcelona-Tech [7]. Average velocity profile at horizontal mid-height plane (right), where the wall-normal coordinate is displayed against the velocity. DNS needs* $5.0 \cdot 10^8$ *grid points to resolve the boundary layer, whereas symmetry preserving discretization without regularization needs* $1.5 \cdot 10^5$ *grid points. With a regularization model, only* $1.9 \cdot 10^4$ *grid points are needed to capture the boundary layer. So a very strong reduction of the required number of nodes has been achieved.*

to implement the regularization model on *unstructured* grids. On these grids, we hope to get similar behavior as for *structured* grids shown in Fig. 1 and many others [6–9]. The symmetry preserving discretization and regularization model are being implemented in MARIN's in-house CFD solver ReFRESCO. Furthermore, we expect that the new discretization and modelling techniques allow LES computations on a coarser mesh/larger time step while maintaining the same accuracy, resulting in a reduced computation time.

In ReFRESCO, the incompressible Navier-Stokes equations are discretized with a finite volume approach. The discrete variables are defined at the cell centers (co-located) on unstructured grids. An implicit time integration is used. The linearized systems of equations are solved with flexible GMRES (FGMRES), using SIMPLER as preconditioner [1].

The incompressible Navier-Stokes equation, given in conservative form, for velocity component ϕ is

$$\frac{\partial}{\partial t}\int_\Omega \rho\phi \mathrm{d}\Omega + \int_\Gamma \rho\phi(\mathbf{u}\cdot\mathbf{n})\mathrm{d}\Gamma + \int_\Gamma p\mathbf{n}\mathrm{d}\Gamma - \int_\Gamma (\mu\nabla\phi)\cdot\mathbf{n}\mathrm{d}\Gamma = 0, \qquad \int_\Gamma \mathbf{u}\cdot\mathbf{n}\ \mathrm{d}\Gamma = 0,$$

where Ω is any part of the fluid domain, $\Gamma = \partial\Omega$, ρ the density of the fluid, $\mathbf{u}$ the velocity vector. The dynamic viscosity is given by μ, p is the pressure.

The discretized form of the incompressible Navier-Stokes equations becomes

$$\mathcal{M}\frac{d\mathbf{u}_h}{dt} + \mathcal{C}(\mathbf{u}_h)\mathbf{u}_h + \mathcal{G}p_h - \mathcal{V}\mathbf{u}_h = 0, \quad \mathcal{D}\mathbf{u}_h = 0,$$

where the diagonal mass matrix $\mathcal{M}$ is built from the volume of the fluid cells, $\mathbf{u}_h$ is the discrete velocity vector, $\mathcal{C}(\mathbf{u}_h)$ represents the discretization of the convective fluxes, $\mathcal{G}p_h$ is the discrete integrated pressure gradient, p_h is the discrete pressure, $\mathcal{V}$ represents the diffusive term and finally the discrete integrated divergence is denoted as $\mathcal{D}\mathbf{u}_h$.

A spatial and temporal discretization of the Navier-Stokes equations preserves the underlying symmetries if [9] the following holds.

1. $\mathcal{C}(\mathbf{u}_h) = -\mathcal{C}^T(\mathbf{u}_h)$. This can be achieved by using a central scheme with interpolation factors one-half, so no artificial damping is introduced.
2. The relation $\mathcal{D} = -\mathcal{G}^T$ is satisfied.
3. An approach to avoid spurious pressure oscillations is employed, without artificial damping. The current approach in ReFRESCO is to employ the pressure weighted interpolation

(PWI) method [2], which solves the pressure decoupling problem, but also introduces artificial dissipation [4]. Hence, the current method does not satisfy this requirement.

4. The time-derivative is discretized using a skew-symmetric operator. This can be accomplished by employing a second-order implicit midpoint rule, for instance. We will only use this method for the two-dimensional test case.

Symmetry preserving discretization preserves the discrete kinetic energy. Therefore, our objective for this paper is to investigate how the discretization influences the total discrete kinetic energy for a two- and three-dimensional test case, by varying different aspects of the (standard) discretization. Therefore, we study the results obtained with the following methods.

Standard QUICK without limiters is applied to discretize convection. Linear extrapolation is used to determine the value at the boundary. The time derivatives are discretized using a second-order backward differencing formula (BDF2). To circumvent the spurious pressure oscillations, PWI is employed.

Variant 1 QUICK is replaced by a central scheme with interpolation factors one-half, linear extrapolation by constant extrapolation. The rest is left unchanged. A co-located grid, has only values at the cell centers. The pressure at the boundary, for instance, is determined by an extrapolation from the cell center towards the boundary. The relation $\mathcal{D} = -\mathcal{G}^T$ implies that constant extrapolation must be used instead of linear extrapolation.

Variant 2 The PWI is halved and the rest of the discretization is identical to the standard discretization.

2 Numerical experiments

2.1 2D Manufactured solution

The first test case will be a two-dimensional manufactured solution for the Navier-Stokes equations

$$
\begin{aligned}
u &= -\cos(\pi x)\sin(\pi y)\left(0.2 + e^{-0.11t}\right) \\
v &= \sin(\pi x)\cos(\pi y)\left(0.2 + e^{-0.11t}\right) \\
p &= -\tfrac{1}{4}\left[\cos(2\pi x) + \cos(2\pi y)\right]\left(0.2 + e^{-0.11t}\right),
\end{aligned}
$$

which is referred to as (modified) Taylor vortex. Here a source term is added to the Navier-Stokes equations such that the Taylor vortex becomes an exact solution. For this case, a uniform 32×32 Cartesian grid is employed, on the domain $[0, 2]^2$. At all boundaries, the exact velocities are prescribed. Because there are no boundary conditions for the pressure, the pressure level is not fixed, so after each time step, the average pressure level is set to zero. The standard discretization will be compared with the symmetry preserving discretization, where for this particular case the PWI can be turned off, without triggering spurious pressure oscillations. Fig. 2 illustrates the influence of artificial dissipation on the total discrete kinetic energy. The error in the kinetic energy is larger for the standard discretization, especially on a coarser grid. This example illustrates that the symmetry preserving discretization lacks artificial dissipation. The mesh Péclet number and mesh CFL number are determined by $\mathrm{Pe}_{h_x} = \frac{u_{\mathrm{ref}} h_x}{\mu}$ and $\mathrm{CFL}_h = \frac{u_{\mathrm{ref}} \Delta t}{h_x} + \frac{v_{\mathrm{ref}} \Delta t}{h_y}$, respectively.

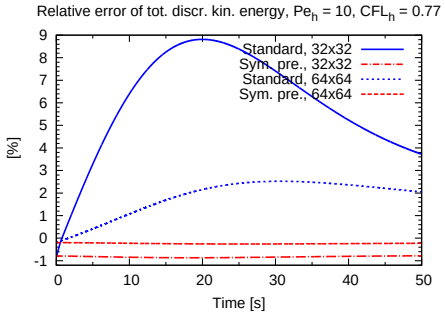

Figure 2: Relative error of total discrete kinetic energy for the standard discretization and symmetry preserving discretization on two uniform Cartesian grids.

2.2 3D Square cylinder

In this section, we test aspects of the symmetry preserving discretization with the help of the flow past a square cylinder $\mathrm{Re} = \frac{\rho u_{\mathrm{ref}} D}{\mu} = 500$, where D denotes the width of the square cylinder. Here, the PWI cannot be turned off, since that will result in spurious pressure oscillations. Therefore, symmetry preserving discretization cannot be tested yet. Alternatively, a null-space filter can be applied to suppress pressure oscillations. This approach does not add artificial dissipation [4]. In this subsection, we focus on how aspect 1, 2 and 3, as mentioned in section 1, will affect the total discrete kinetic energy. In the previous test case, we considered uniform Cartesian meshes. Now, in order to capture the boundary layer, the mesh has to be stretched.

2.2.1 Description square cylinder

All geometrical lengths are normalized with D. The domain size is plotted in Fig. 3. The blockage parameter corresponding to this setup is given by $\beta = 5.0\%$. The boundary conditions for the square cylinder are as follows. At the inlet, a uniform flow was prescribed ($\frac{u}{u_{\mathrm{ref}}} = 1$, $\frac{v}{u_{\mathrm{ref}}} = 0$, $\frac{w}{u_{\mathrm{ref}}} = 0$). At the outlet $p = 0$ and $\partial \mathbf{u}/\partial n = 0$. No-slip boundary conditions are prescribed at the square cylinder. At the sides, located at $9.5D$ from the cylinder,

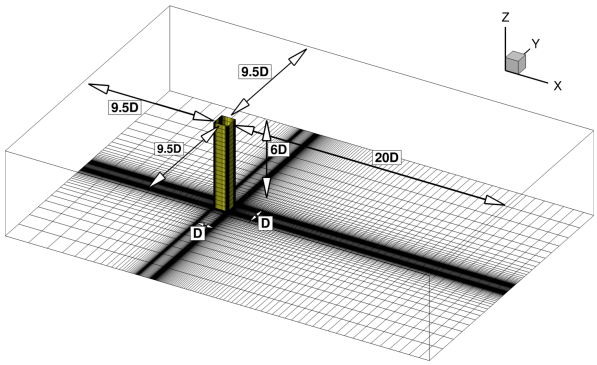

Figure 3: 3D coarse Cartesian mesh used for computation of the flow around a square cylinder.

free-slip is imposed whereas at the top (z_{max}) and bottom (z_{min}), a symmetry boundary condition is prescribed.

We want to test symmetry-preserving discretization without using corrections for eccentricity and non-orthogonality. Therefore stretched Cartesian grids are used for the numerical experiments, although other types of grids are more appropriate for the square cylinder. The distance between the square cylinder and the nearest grid cell, defined as δ, is $D/200$ everywhere for the fine mesh and $D/100$ for the coarse mesh. The grid is stretched, using a hyperbolic tangent function, from δ towards the walls, except for the span-wise direction where it is kept uniform. Also the grid is stretched towards the corners of the square cylinder. The fine mesh has $(60+60+180)\times(60+60+60)\times 40$ grid cells. For the coarse mesh the number of grid cells is halved in each direction. The dimensionless time steps are

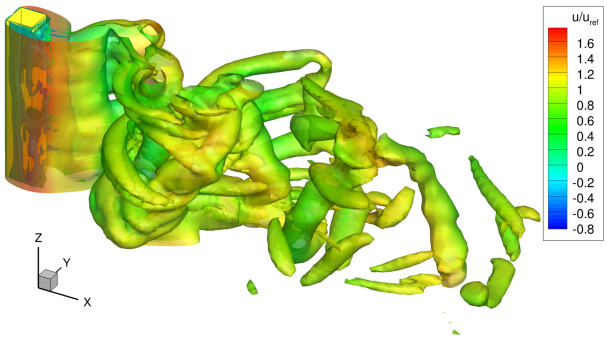

Figure 4: A snapshot of the velocity u/u_{ref}, obtained from standard discretization on a 3D fine Cartesian mesh.

$\frac{u_{\mathrm{ref}}\Delta t}{D} = 1/8$, and $1/16$ for the grid with $\delta = 1/100$ and $\frac{u_{\mathrm{ref}}\Delta t}{D} = 1/16$ for the fine mesh. The dimensionless wall distance (y^+) on the fine mesh is 0.95. The coarse mesh has a y^+ of 1.6. An impression of the turbulent structures on the fine mesh, is shown in Fig. 4.

Our test setup is similar to that of Sohankar *et al.* [5]. The main difference is that our domain is a bit larger in the streamwise and cross wise direction. Consequently, Sohankar *et al.* have a blockage parameter $\beta = 5.6\%$. In the span-wise direction we have the same size, but we do not apply periodic boundary conditions in the span-wise direction and convective Sommerfeld boundary condition at the outflow.

2.2.2 Setup numerical experiment

We aim to investigate which part of the discretization contributes the most to the artificial dissipation. We start with the standard discretization in ReFRESCO. Thereafter we change the discretization of convection and the extrapolation towards the boundary (Variant 1). Finally, we reduce the influence of PWI by halving it (Variant 2).

All test cases on the coarse mesh use the same initial condition, which was computed with the standard discretization at a point in time when the vortex shedding was well developed. At the fine mesh, the simulation started from a fluid in rest. To avoid any startup effects, we have based the statistical analysis on the time interval from 75 till 200.

The relative convergence tolerance for the residuals, is set to 10^{-6} (measured in ∞-norm).

2.2.3 Drag and lift coefficient, Strouhal number

As usual, the lift and drag coefficients are nondimensionalized as follows $\mathrm{C}_D = \frac{F_x}{\frac{1}{2}\rho u_{ref}^2 LD}$ and $\mathrm{C}_L = \frac{F_y}{\frac{1}{2}\rho u_{ref}^2 LD}$, where F_x is the total force in the x-direction, consisting of the shear stress and the pressure acting in the x-direction. Here, LD is the frontal area of the square cylinder. The total force in the y-directions is given by F_y, which consists of the normal stress and the pressure acting in the y-direction. The dimensionless Strouhal number is defined as $\mathrm{St} = \frac{\mathrm{f}_S D}{u_{\mathrm{ref}}}$, where f_S is the frequency corresponding to the drag or the lift coefficient. The Strouhal numbers were determined from the spectra of the lift (and drag).

2.2.4 Numerical results

Since the grids are stretched, the mesh Péclet number varies in the computational domain. The smallest mesh Péclet numbers for the 3D coarse grid and 3D fine grid are $\mathrm{Pe}_h = 16.67$ and $\mathrm{Pe}_h = 8.33$, respectively. With these mesh Péclet numbers, it is possible that variant 1 (central discretization for convection) gives rise to numerical noise. This occurs for both meshes. Further down in the wake field (Fig. 5(b)) numerical noise is present, because the time step does not allow sufficient dissipation

of the small length scales that are present in the solution produced by variant 1. The lift coefficient for variant 1 (Fig. 8(b)) seems to have an extra frequency compared to Fig. 8(a) and Fig. 8(c). This also holds for the drag coefficient. But, the magnitude spectrum of the drag and lift coefficient (Fig. 6) shows no extra peaks compared to the results of standard discretization (Fig. 6) or variant 2 (Fig. 7). So, despite this behavior, there is no clear indication that the numerical noise affects the Strouhal number.

The wake field (Fig. 5(a)) for the standard discretization shows a much smoother pattern. Since, the only difference is that artificial dissipation of the QUICK scheme, we may conclude that artificial dissipation is very active for this particular test case in which there is only a narrow band of refinement around the square cylinder.

Also observe that the width of the wake field at the outlet is much wider in variant 1 (Fig. 5(b)) than in the standard discretization (Fig. 5(a)). Moreover, the structures appear to be bigger.

Since the mesh Péclet number for the 3D fine grid is still larger than 2, we cannot be absolutely sure, that the obtained results are correct. Therefore, a grid should be employed, such that $\mathrm{Pe}_h \leq 2$, resulting in an enormous amount of grids cells. Note that the symmetry-preserving discretization does not necessary have to satisfy this mesh Péclet condition, to obtain correct results [3]. In practice, satisfying the mesh Péclet condition $\mathrm{Pe}_h \leq 2$ may not be feasible. The regularization model, which remains to be implemented, is expected to relax this restriction.

Table 1: 3D coarse grid.

Discr.	$\frac{u_{\mathrm{ref}}\Delta t}{D}$	C_D	C_L	St_{C_D}	St_{C_L}
Standard	1/8	1.980	-0.000	0.256	0.128
Standard	1/16	1.983	-0.043	0.256	0.128
Variant 1	1/8	1.943	-0.028	0.235	0.118
Variant 1	1/16	1.947	0.016	0.240	0.120
Variant 2	1/8	1.978	-0.010	0.256	0.128
Variant 2	1/16	1.985	-0.023	0.256	0.128

Table 2: 3D fine grid.

Discr.	$\frac{u_{\mathrm{ref}}\Delta t}{D}$	C_D	C_L	St_{C_D}	St_{C_L}
Standard	1/16	1.947	-0.032	0.264	0.128
Variant 1	1/16	1.923	-0.037	0.264	0.128
Variant 2	1/16	1.950	0.032	0.262	0.131

From Table 1 and 2, it is clear that the influence of the time step on the drag and lift coefficient and Strouhal number is almost negligible compared to the influence of the grid density, irrespective of the choice of discretization. For the fine mesh, the grid is refined twice in every direction. Therefore, we halved the time step, and chose $\frac{u_{\mathrm{ref}}\Delta t}{D} = 1/16$ for the fine mesh.

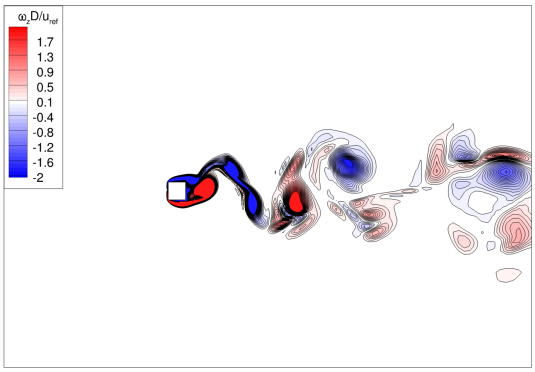

(a) Standard.

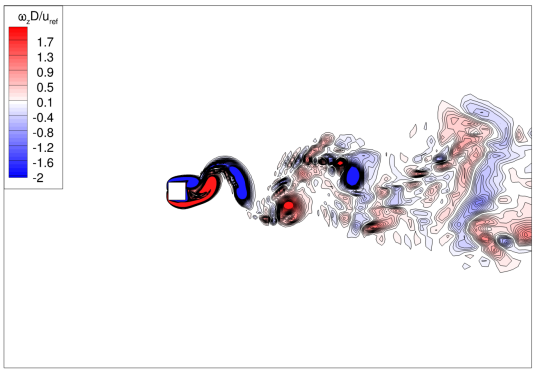

(b) Variant 1.

Figure 5: The dimensionless vorticity in z-direction, $\omega_z D/u_{\mathrm{ref}}$ at time 200 on 3D fine grid.

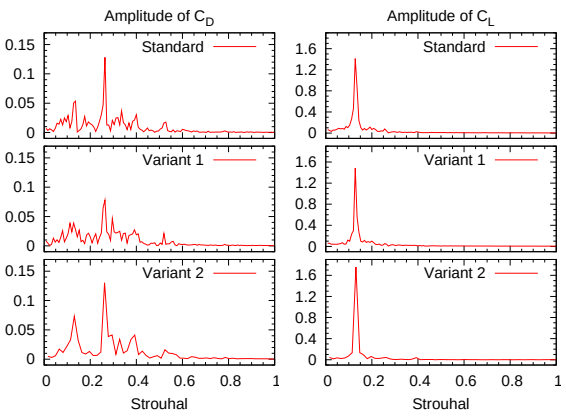

(a) Amplitude of C_D. (b) Amplitude of C_L.

Figure 6: Magnitude spectra of C_D and C_L, Re = 500, time step $\frac{u_{\mathrm{ref}}\Delta t}{D} = 1/16$. 3D fine grid.

Comparing the drag and lift coefficient on the two grids, displayed in Table 1 and 2, we can conclude that the Strouhal number for the standard discretization remains almost the same. However, the drag coefficient is still changing. Note that the grid influence for the C_D is larger for the standard discretization than for variant 1, 1.8% versus 1.2%. Since the value of the drag coefficient is still grid dependent, we have to refine the grid at least once

more, to obtain a grid independent drag coefficient.

From Table 1 and 2 it is also clear that variant 2 provides almost similar results compared to the standard discretization.

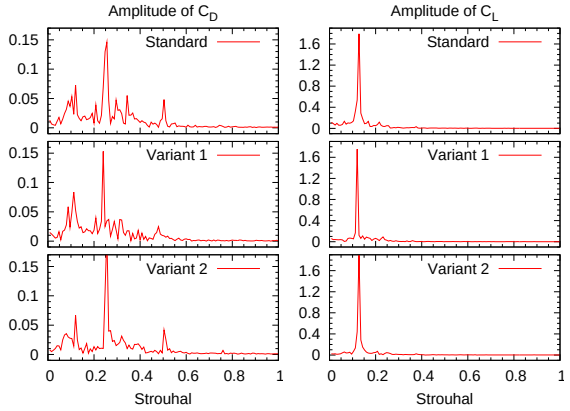

(a) Amplitude of C_D. (b) Amplitude of C_L.

Figure 7: Magnitude spectra of C_D and C_L, Re $= 500$, *time step* $\frac{u_{\text{ref}}\Delta t}{D} = 1/16$. *3D coarse grid.*

Table 3: Sohankar et al. *results [5].*

Mesh	$\frac{u_{\text{ref}}\Delta t}{D}$	C_D	St_{C_L}
$169 \times 121 \times 25$	$1/40$	1.87	0.126
$209 \times 129 \times 41$	$1/40$	1.84	0.127
$209 \times 129 \times 41$	$1/80$	1.84	0.122

Since our blockage parameter is a bit smaller than Sohankars *et al.* [5], one would expect that the value of the drag coefficient is smaller in our case compared to Sohankar *et al.* situation. This is not the case, however. Although there is a clear downward trend in the drag coefficient, the values are still too large compared to the values in Table 3. Still, variant 1 provides a C_D, closer to Sohankars results, than the standard discretization or variant 2. On the fine mesh, the C_D of variant 1 deviates 4.5% from Sohankars C_D whereas the C_D of standard discretization and variant 2 deviates 5.8% and 6.0%. The Strouhal numbers, however, are close to the results obtained by Sohankar *et al.*.

2.2.5 Total kinetic energy

The question was which parts of the discretization influences the kinetic energy by introducing artificial dissipation. From Fig. 9 and Fig. 10, it is observed that QUICK discretization for convection changes the total discrete kinetic energy slightly, compared to the results for variant 1. It seems that artificial dissipation leads to a decrease of the total discrete kinetic energy, which is to be expected. Also PWI is observed to affect the energy, see Fig. 10 and Fig. 9. Showing similar results compared to the standard discretization.

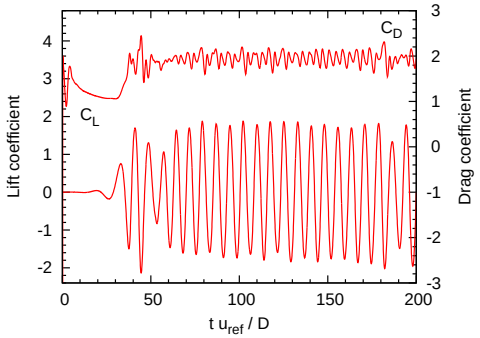

(a) Standard.

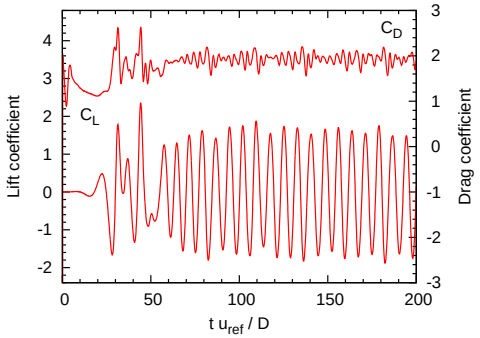

(b) Variant 1.

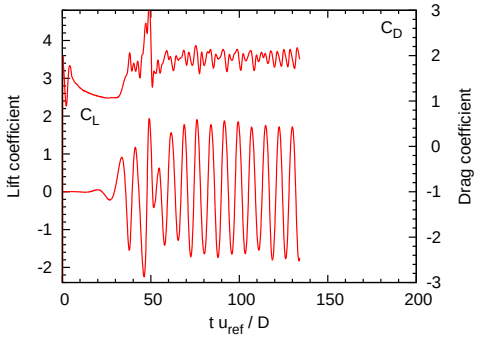

(c) Variant 2.

Figure 8: Lift and drag coefficient, Re $= 500$, *time step* $\frac{u_{\text{ref}}\Delta t}{D} = 1/16$. *3D fine grid.*

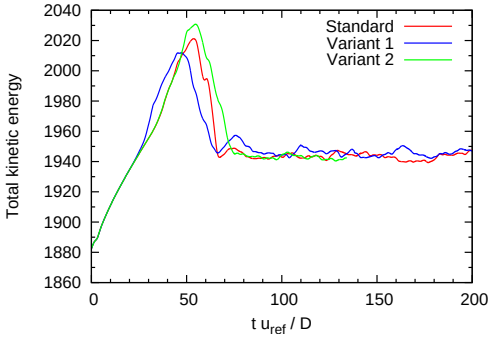

Figure 9: Total discrete kinetic energy, Re $= 500$, *time step* $\frac{u_{\text{ref}}\Delta t}{D} = 1/16$. *3D fine grid.*

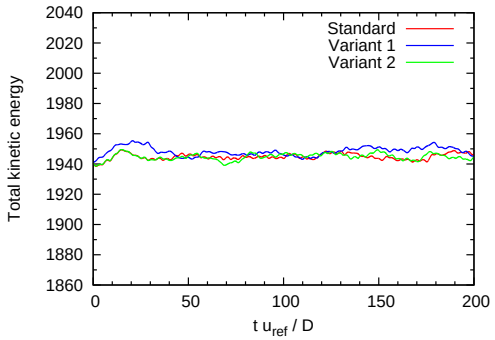

Figure 10: Total discrete kinetic energy, Re = 500, *time step* $\frac{u_{\text{ref}}\Delta t}{D} = 1/16$. *3D coarse grid.*

3 Conclusions and discussions

Symmetry preserving discretization looks promising for the 2D manufactured solution test case. The relative error of total kinetic energy is much smaller compared to the standard discretization. But for the 3D square cylinder, we cannot draw this conclusion yet. Because not all the required aspects (needed for symmetry preserving discretization) have been tested. When variant 1 was tested, numerical noise was observed for both meshes, since the mesh Péclet number was larger than 2. But the drag and lift coefficient and Strouhal number were not affected by this behavior. The influence of the PWI (variant 2) on the drag and Strouhal number is hardly noticeable. The results are almost identical to the results obtained by standard discretization. The drag coefficient is still grid dependent. Despite this, variant 1 provides a C_D closer to Sohankars [5] results than standard discretization or variant 2. For now, it seems that QUICK and also PWI influences the total discrete kinetic energy, but more research is needed.

4 Future work

Since the discretizations does not yet meet the mesh Péclet number condition, it would be recommendable to refine the grid. But then an enormous amount of grid cells are needed. To relax this criteria, a regularization model (LES) [6–8] will be implemented in the near future. This model preserves the symmetry and conservation properties. The pressure at the boundary, for instance, is obtained by constant extrapolation, which is only first-order accurate. Therefore, we have to modify this extrapolation to second-order accuracy, without violating $\mathcal{D} = -\mathcal{G}^T$. Another important aspect is the method to avoid the pressure oscillations. The method, currently used in ReFRESCO (PWI) does not conserve energy. We will investigate the so-called null-space filtering [4], which does not introduce artificial dissipation. So far, we only focused on structured meshes. In the near future, we will test symmetry preserving discretization on unstructured meshes. And also implement a regularization model on these type of meshes. For square cylinder with Re = 500, we only had Sohankars results as reference data. Therefore, we will in the near future compute the flow around the square cylinder with Re = 22000. Since for this particular case there is much more experimental and numerical data available.

Acknowledgement

The research reported in this paper is part of the project 'High-Quality Simulation of Complex Flows in Maritime Applications', which is part of the maritime innovation project (MIP) funded by Agentschap NL. This support is gratefully acknowledged.

References

[1] C.M. Klaij and C. Vuik. SIMPLE-type preconditioners for cell-centered, colocated finite volume discretization of incompressible Reynolds-averaged NavierStokes equations. *Int. J. Numer. Meth. Fluids*, 2012. doi:10.1002/fld.3686.

[2] T.F. Miller and F.W. Schmidt. Use of a pressure-weighted interpolation method for the solution of the incompressible Navier-Stokes equations on a nonstaggered grid system. *Numerical Heat Transfer*, 14(2):213–233, 1988. doi:10.1080/10407788808913641.

[3] I. Rodriguez, R. Borell, O. Lehmkuhl, C.D. Perez-Segarra, and A. Oliva. Direct numerical simulation of the flow over a sphere at Re = 3700. *J. Fluid Mech.*, 679:263–287, 2011. doi:10.1017/jfm.2011.136.

[4] Shashank, J.L. Larsson, and G. Iaccarino. A co-located incompressible Navier-Stokes solver with exact mass, momentum and kinetic energy conservation in the inviscid limit. *Journal of Computational Physics*, 229(12):4425–4430, 2010. doi:10.1016/j.jcp.2010.03.010.

[5] A. Sohankar, C. Norberg, and L. Davidson. Simulation of three-dimensional flow around a square cylinder at moderate Reynolds numbers. *Physics of Fluids*, 11(2):288–306, 1999. doi:10.1063/1.869879.

[6] F.X. Trias and R.W.C.P. Verstappen. On the construction of discrete filters for symmetry-preserving regularization models. *Computers & Fluids*, 40(1):139–148, 2011. doi:10.1016/j.compfluid.2010.08.015.

[7] F.X. Trias, R.W.C.P. Verstappen, A. Gorobets, M. Soria, and A. Oliva. Parameter-free symmetry-preserving regularization modelling of turbulent differentially heated cavity. *Computers & Fluids*, 39(10):1815–1831, 2010. doi:10.1016/j.compfluid.2010.06.016.

[8] R.W.C.P. Verstappen. On restraining the production of small scales of motion in a turbulent channel flow. *Computers & Fluids*, 37(7):887–897, 2008. doi:10.1016/j.compfluid.2007.01.013.

[9] R.W.C.P. Verstappen and A.E.P. Veldman. Symmetry-preserving discretization of turbulent flow. *Journal of Computational Physics*, 187(1):343–368, 2003. doi:10.1016/S0021-9991(03)00126-8.

Flip through in a sloshing tank: a hydroelastic study.

Andrea Bardazzi, Claudio Lugni
CNR-INSEAN Italian Ship Model Basin, Via di Vallerano 139, Rome/Italy
a.bardazzi@insean.it, c.lugni@insean.it

The transportation of liquefied natural gas (LNG) by ships container still leaves open many questions regarding the safety of such operations. The need to maintain low temperature inside the tank, in order to keep the gas in the liquid state, means that the side walls, designed to obtain a good thermal insulation as well as an adequate mechanical property, are not capable to supporting the necessary devices, such as the rings bufflets installed in oil tankers, for the damping of the sloshing phenomena.
The inner corrugated surface of the tank is the only way to reduce the sloshing phenomena and, sometimes, it is not sufficient. Expecially in conditions of partial filling of the tank, there may be violent impacts between the waves propagating inside the tank and walls. This events could be particularly localized in space and time, and can compromise the integrity of the structure. In fact, when the time scales of the impacts are comparable to the highest natural periods of vibration of the structure, hydroelastic effects may occur increasing the stress for the structure. Depending on the local characteristic of the wave front in the instants preceding the impact, different events may characterize the flow evolution: if the angle between the fluid and the wall is small, a single air bubble is entrapped during the impact, when the angle is greater, flip-through events or flat-impact can occur.
The object of this work concerns about the study of the hydroelastic interaction that may occur during a flip-through impact against an elastic vertical plate collocated in a 2D sloshing tank with shallow water condition. To evaluate the effects of hydroelasticity, the same impact has been generated both on rigid and elastic plate.
The measure of the hydrodynamic pressure is not a good indicator for the real stress of the structure bacause its highly stochastic behaviour and the possibility of hydroelastic effects appear. For this reasons, in the elastic tests, the plate deformation has been measured with the strain gauges, while, in the tests on rigid wall, the hydrodynamic pressure has been measured.
The model properties (fig.1), as the tank dimension and the mechanical characteristics of the elastic plate, has been obtained by scaling the prototype tank (type Mark III) with respect to the geometrical and Froude scales. For a more accurate scaling of the mechanical properties of the elastic plate, it is necessary take in account also the structural scaling. Satisfy both, structural and Froude scale, require particular conditions difficult to be verified. The scale factor considered for these experiments is $\lambda = L_p/L_m = 33$, where L_p and L_m indicate the length of prototype and the model.
Several natural modes of a generic panel of Mark III tank, with a frequency range of 100-500 Hz, play important roles in the panel's dynamic evolution[4]. However, because the lower modes are associated with the corrugated steel plate of a Mark III panel, only the lowest frequency is considered in the present study.
Due to the particular configuration of the model, the impact phenomenon and the flow can be considered 2D and as a consequence, the dynamic behaviour of the plate's vertical centreline can be modelled by the Euler beam theory. When the elastic plate is partially or fully wet an added-mass term has been taken into account in the formula for the evaluation of the wet natural frequency. This term of added-mass is found as solution of the sloshing problem for the surge motion. Its analytical expression for the linearized problem is described by Faltinsen & Timoka (pp.536)[4].

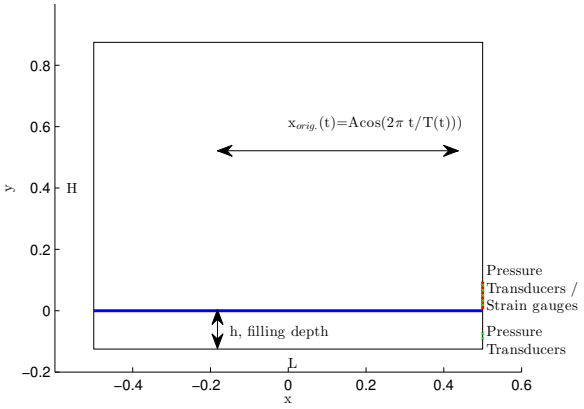

Figure 1: Sketch of the tank model. The red line is the elastic(rigid) plate, the green cross indicate the position of the strain-gauges and the pressure transducer, the blue line is the still water level. $x_{orig}(t)$ is the motion imposed at the tank.

Experimental set-up

The model of the tank used in the experiments is the same used in experiments reported in Lugni *et al.*[1, 2, 3]. It is made in plexiglass and it is reinforced with an aluminium armature which also allows tests in depressurized conditions. With a length and height of 1 m and with a width of 0.1 m, the tank ensure, in the middle vertical plane, the condition of two-dimensionality for the flow and for the wave impacts.

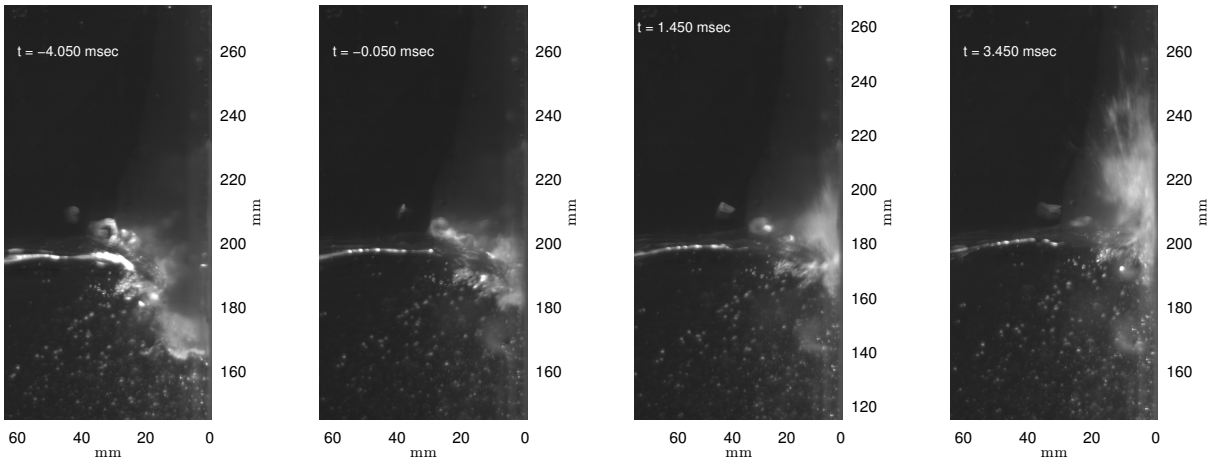

Figure 2: Flip-through evolution.

The elastic plate is made of aluminium and its length and thickness are respectively 0.09 m and 2.5 mm and it has the lowest natural wet frequency of 620 Hz. It is fixed in a extremely rigid stainless steel wall of the tank, at a distance of 13 cm from the bottom of the tank. The plate has been clamped to the steel frame in correspondence of superior and inferior ends, while the lateral ends are free to move. To measure the plate's strain, nine strain gauges have been installed on the outer face of the plate, five along the vertical centreline, the other four along the horizontal one.

The position chosen for the panel is derived by previous wave-impact experiments[1, 2, 3] in rigid sloshing-tank. Those tests highlighted how the impact phenomena occur at height of $17 - 18$

cm and this justify the choice to place the centre of the plate at 17.5 cm above the bottom of the tank.
The rigid plate, that replaces the elastic one in the tank during the rigid tests, is made by aluminium but it is 2 cm thick. Its lower natural frequency is about 8 kHz and this allow to consider the plate as rigid. Five pressure transducers have been installed on the rigid plate in the same position of the strain-guages for the elastic one. Other two pressure transducers were collocated below the elastic/rigid plate at a distance of 3 and 5 cm from the bottom of the tank. The movimentation system is managed by the hexapod system by "MISTRAL", which force the tank to move with a surge sinusoidal motion $x(t) = A\cos(2\pi t/T(t))$. The amplitude imposed for the flip-through event is $A/L = 0.30$ and the period's initial ramp $T(t)$ is:

$$T(t) = T_1 \exp{(t/T_a)^2} + T_0(1 - \exp{(t/T_a)^2} \tag{1}$$

where $T_1 = 4$ sec, $T_0 = 0.05$ sec. Two accelerometer, collocated on the vertical rigid wall and on the hexapod, have been used to verify the rigidity of the wall as well as the global motion of the tank. The signals of the transducer were recorded through an acquisition system with a sampling rate of 20 kHz. A digital fast-cam, with a frame rate of 5 kHz, has been used for recording the flow in proximity of the impact area, while two slower digital cam, with a frame rate of 100 Hz, have been used for a global view of the sloshing motion.

Discussion of the results

This section shows the results of the impact tests and the comparison between the elastic and rigid case. Figure 2 shows the evolution of a flip-through event against the tank wall. This particular event, first defined flip-through by Prof. Peregrine[5], can occur when a breaking wave approaches to a vertical wall. It is characterized by 3 main stages: wave advancement, focusing and flip-through stage. In the first one (first panel fig. 2), the wave moves against the wall while the through quickly rises up along the wall. In the second stage (second panel fig. 2), the wave front and the through move toward each other, giving a strong vertical acceleration of the flow. In the last stage (third and fourth panels fig. 2), the flow turns suddenly around the focusing point originating an energetic vertical jet.

When the impact occurs against the rigid wall, figure 3, the load acting on the wall is typically impulsive, the peak of pressure is characterized by a rise time of about 1.0 msec and by a spatial distribution of few centimeters. No oscillations have been observed because in this kind of events no air is entrapped in the flow.

When the same impact occurs against the elastic wall, the kinematic evolution of the flow is similar to the rigid one but there is a strong difference in the dynamics evolution. The four frames in fig 4 show the kinematic evolution of the flow. In each frame is present the beam displacement (red line on the right), below are plotted the normalized stress in the middle of the beam (left) and the hydrodynamic pressure recorded from the sensor 2, located below the plate (right). All the plots and the images are time synchronized.

During the advancement stage the hydrodynamic load is not so elevate and the beam's deformation is quite null. The maximum peak of stress occurs during the focusing stage, just before the flip-through stage. Also the hydrodynamic pressure, in this stage, reaches its maximum value. After the impulsive load, the beam dynamic is characterized by a typical damped free-oscillation. During the free-oscillation stage there is a strong interaction between the structure and the fluid field, this is demostrated by the presence of an oscillatory component in the pressure signal as consequence of the beam motion. The two signals, stress and pressure, are characterized by the same main frequency and by a phase shift, while there is not phase shift between the pressure

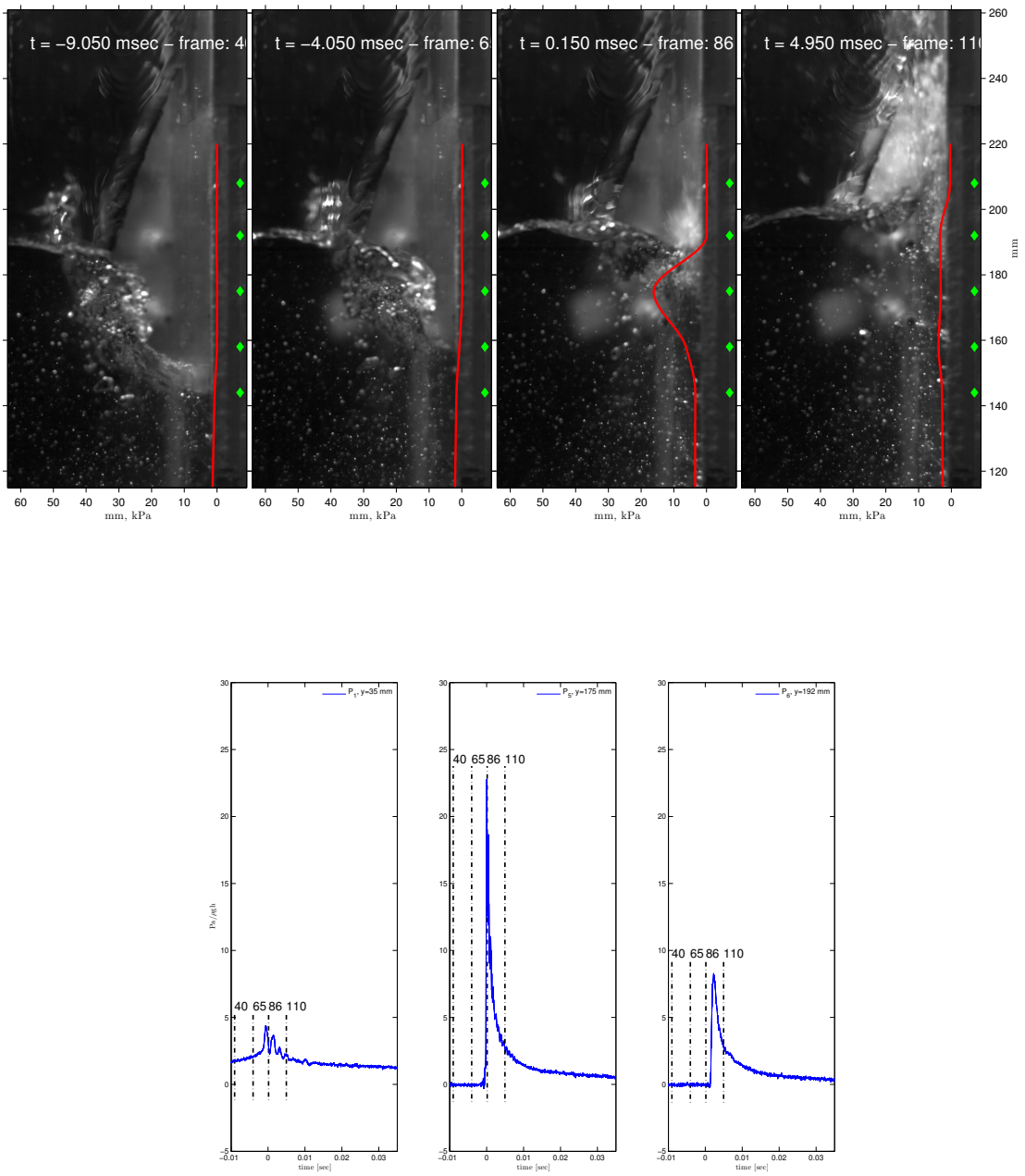

Figure 3: Flip-through evolution against a rigid wall. The plots show the pressure distribution in three different point of the wall. The curve in the camera image is the interpolation of the pressure recorded by the sensors (green diamonds).

and the beam acceleration ($\ddot{w} \propto \ddot{\sigma}$). This means that the oscillatory component in the pressure field depends on the beam acceleration. The hydroelastic interaction interests also the first peak of pressure, increasing the value with respect to the rigid test (frame 120 fig.3,4).

The natural frequency that characterizes the beam motion is not constant but depends by the instantaneous wetted length of the beam that modifies the added-mass contribute. In order to estimate the instantaneous frequency of the recorded data the Empirical Mode Decomposition (EMD) and the Hilbert transform are used. The top panel in figure 5 shows the two principal intrinsic mode function extracted with EMD, while in the bottom panel is plotted their instantaneous frequency. Always in the same panel, the blue dash line is the instantaneous

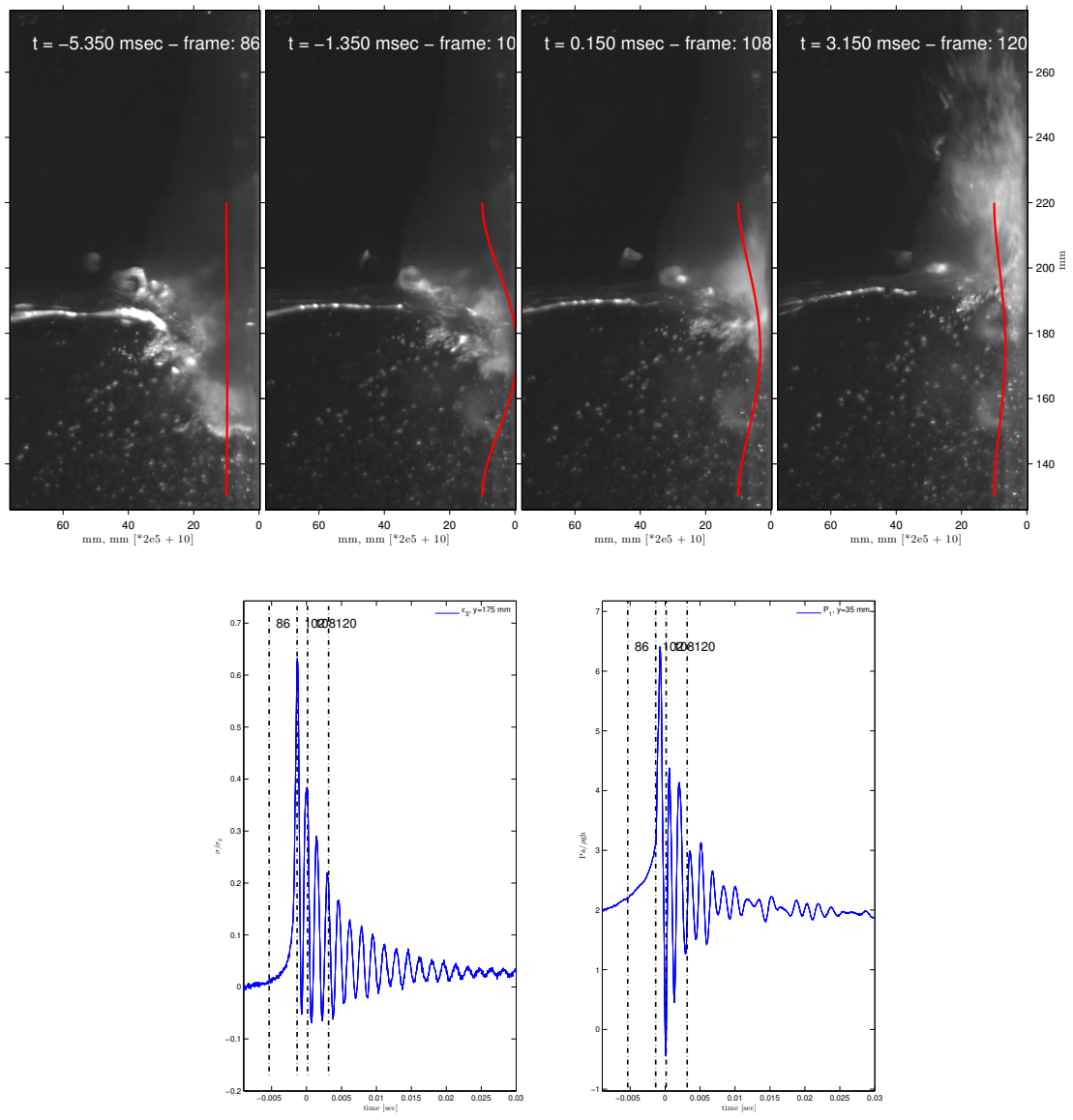

Figure 4: Flip-through event against the elastic wall. The four frames shows the time evolution of the impact and the plate displacement synchronized in time (red line), below are plotted the plate stress (left panel) and the hydrodynamic pressure (right panel).

frequency and it has been calculated using the mathematical model (Euler beam+added mass). The wetted length of the beam, necessary to calculate the frequency,has been extrapolated from the experimental images. The agreement between sperimental and analytical data confirms the validity of the model used for the prediction of the wet natural frequency.

Conclusions

The object of this research activity is the investigation about the role of hydroelasticity during a wave impact against an elastic plate inserted in a rigid wall of a sloshing tank: the flip-through impact had been considered. Through Froude scaling, the geometrical dimensions and the

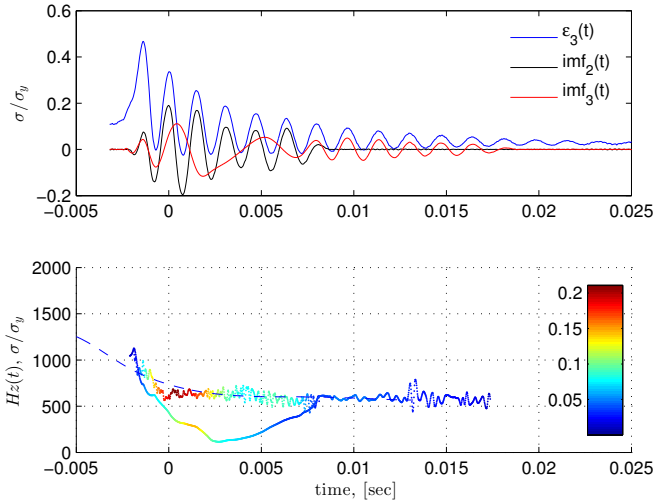

Figure 5: The top panel shows the most relevant IMFs that reconstruct the oscillatory component of the signal, obtained with the EMD. The bottom panel shows the instantaneous frequencies of the signal obtained with the Hilber transform (scatter plot) and the instantaneous first wet natural frequency obtained with the mathematical model(dash line).

mechanical characteristics of a panel of Mark III type tank have been defined. Strain gauges and pressure transducers have been used to measure the deformations of the elastic wall and the hydrodynamic pressure. To evaluate the effect of the hydroelasticity, the same phenomenon has been reproduced both on rigid and elastic wall. Although the overall kinematical evolution of the impact is quite similar, strong differences have been observed from the dynamical point of view between elastic and rigid case. A free-oscillation behaviour after the maximum peaks, characterizes the evolution of the stress along the wall. The hydroelastic interaction deeply modifies the pressure field with respect the fully rigid case, by originating a oscillatory component and increasing the maximum pressure peak. This behaviour should imply that a quasi-static model can strongly underestimate the real load.

References

[1] Lugni, C.,Brocchini, M. and Flatinsen, O. M., "Wave impact loads: The role of the flip-through", *Phys. Fluids*, 18, 122101, 2006.

[2] Lugni, C., Miozzi, M., Brocchini, M. and Flatinsen, O. M., "Evolution of the air cavity during a depressurized wave impact. I. The kinematic flow field", *Phys. Fluids*, 22, 056101, 2010.

[3] Lugni, C., Miozzi, M., Brocchini, M. and Flatinsen, O. M., "Evolution of the air cavity during a depressurized wave impact. II. The dynamic field", *Phys. Fluids*, 22, 056102, 2010.

[4] Faltinsen, O. M. and Timokha A. N., "*Sloshing*", Cambridge University Press, Cambridge,2009.

[5] Peregrine, D.H., "Water-Wave Impact on walls", *Ann.Rev.of Fluid Mech*,2003,35,23-43

[6] N. E. Huang *et al.*, "The empirical mode decomposition and the Hilber spectrum for non-stationary time series analysis", *Proc. R. Soc. London*, Ser. A 454, 903, 1998

Computational Tools for Propeller Cavitation Analysis

Rickard E. Bensow, Göran Bark, Nai-Xian Lu, Claes Eskilsson, and Florian Vesting

Dept. of Shipping and Marine Technology
Chalmers University of Technology, 412 96 Gothenburg, Sweden
E-mail: {rickard.bensow, bark, naixian.lu, claes.eskilsson, florian.vesting}@chalmers.se

In recent years, there's been an increased interest in high efficiency ship propulsion. The two main paths to achieve this are to (a) utilize interaction effects between propeller, hull and rudder in a system design, possibly including modifications such as ducts, stators, or vortex generators, and (b) allow for a higher loaded blade with smaller blade area, which then leads to more cavitation on the propeller.

The fast development in CFD in the last decade has made option (a) more and more feasible as these devices needs careful design for full scale conditions, possible only through CFD. Ship hull computations in self-propelled conditions, using either a hybrid RANS/potential flow solver or a full RANS approach, is a standard feature in many commercial and in-house software today. At smp'11 [1], several studies were presented on the effect of modifiers using these techniques. The next step in this development is to use these tools in an automated optimization as is done for propeller or rudder in e.g. Han et al. [2] or Vesting and Bensow [3].

When it comes to assessing cavitation effects in propeller design, necessary to explore option (b), potential flow codes represent a quick and fairly reliable tool to determine the main influence of cavitation on thrust and efficiency around the design point. This includes to some extent also pressure pulses of the lowest harmonics. However, more detailed effects of cavitation, such as high frequency or broadband noise or erosion, are not possible to assess with any computational tool today. Recent results using LES [4][5] or Euler methods [6][7] indicate that these methods are capable of capturing much of the cavitation dynamics, but we cannot expect high fidelity predictions of all aspects of cavitation nuisance in reasonable computational time in the near (or any) future. Moreover, experiments can only provide an incomplete picture to assist the designer. Experience and knowledge are still necessary components for a successful design.

This paper will discuss some possibilities to combine the tools described above, based on recent years of research at Chalmers on propeller cavitation and computational tools in propulsor analysis. We believe the combination will in the future open up to assess both option (a) and (b) simultaneously through:

- Improved design knowledge and guidelines on assessing cavitation nuisance, based on improved understanding of cavitation physics gained through detailed studies of experiments and LES results,
- The application of these guidelines to cavitation predictions of a flow solution in order to assess the risk of e.g. erosion, and
- Including this assessment in an automated optimization procedure using simulations of a self propelled ship.

We remark that this is a review of work done at Chalmers, and the references reflect this restriction; a complete review would include a broader list of authors.

Starting with the first bullet, we have worked for several years on identifying and describing the hydrodynamics that influence the erosiveness of cavitation and how well these flow features can be represented by different computational tools. The EroCav handbook [8] holds the foundation for the description developed, based on the focusing of energy from the global cavity into the micro cavity and its collapse. This description has since then been refined and reworked in several steps, through the mechanisms of the creation of the focusing

cavities, e.g. [9] and Figure 1, to a detailed analysis of the behaviour at the collapse and even beyond that through the character of the rebound, e.g. [10][11] and Figure 2; the most comprehensive summary is the recent keynote of Bark and Bensow [11].

When it comes to the predictive capability of computational tools, this is still a matter of sailing in partly uncharted waters. As our method for erosion analysis is based on the hydrodynamic behaviour of the flow, we have started the exploration based on the, in our view, most feasible simulation approach still containing enough of the dynamics of the flow to assess the necessary hydrodynamics: incompressible LES. Different RANS approaches, of course requiring less computational effort, do not from a theoretical point of view contain enough of the dynamics to capture the phenomena to look for, and compressibility, taking acoustic interaction into account, is overwhelmingly costly to consider for marine applications. Never the less, work is in progress to extend our studies in both these directions, mapping how neglecting compressibility can affect the results using compressible LES and RANS [7], as well as identifying the limitations imposed by using a RANS approach [5][13].

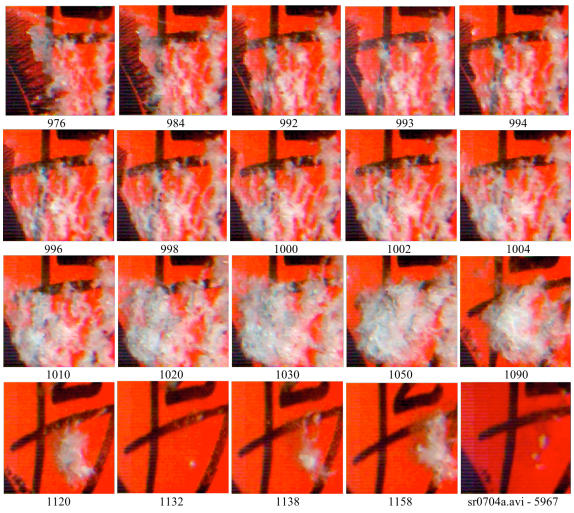

Figure 1 Decomposition of main cloud during an upstream moving collapse generating secondary cavitation on propeller P1477. Leading edge to the left; from SSPA cavitation tunnel. [9]

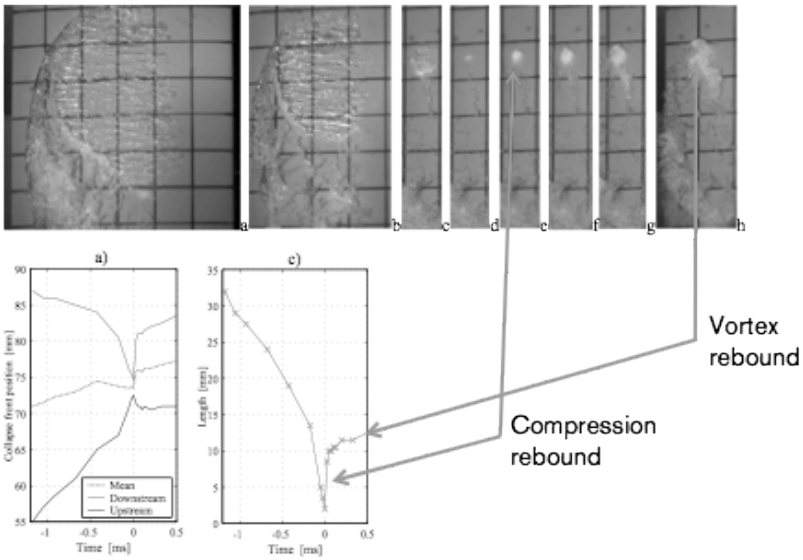

Figure 2 Generalized rebound. Rather symmetric collapse of a sheet on a foil in unsteady inflow from right. Plots of upstream and downstream collapse fronts and streamwise length of cavity. Experiment in the SSPA cavitation tunnel. [10]

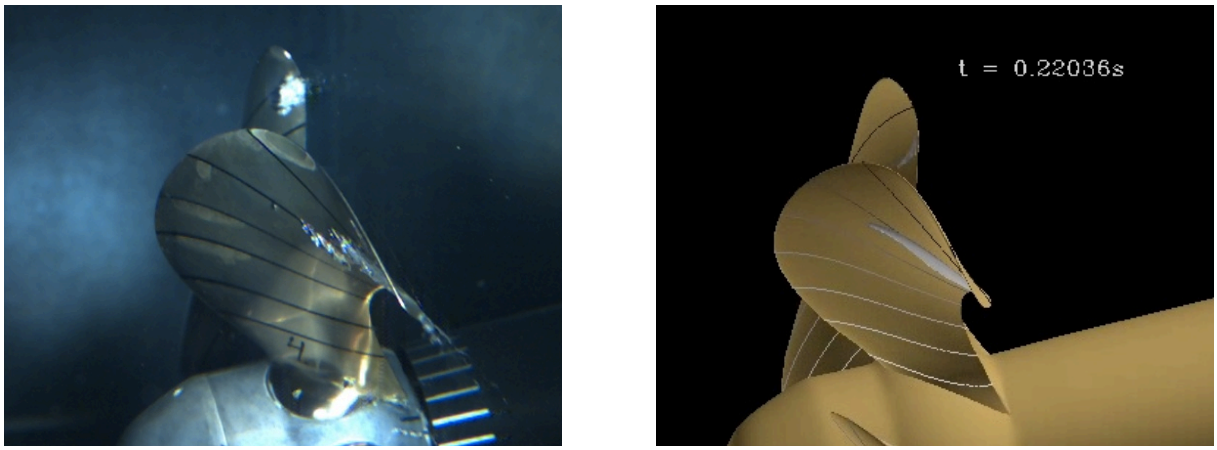

Figure 3 Cavitation behaviour on a high skew yacht propeller, from experiments and LES.[13]

Summarising our findings regarding the capabilities of incompressible LES, we have in a series of publications systematically demonstrated that LES can capture many of the main mechanisms controlling the behaviour of cavitation, at least qualitatively, making it plausible that reasonable noise and erosion assessments will become possible. This relates to shedding behaviour [5][15], upstream moving collapses [16], leading edge desinence [4][5], cavity – leading edge/tip vortex interaction [4], and vortex rebounds [10]. To fully validate the tools, better sets of experimental data would be needed; a daunting task to fund and perform. The main feature that is eluding is the dynamics of the tip vortex, both a cavitating one and one yet to cavitate. This is directly related to the difficulties in correctly computing a vortex, already in non-cavitating conditions.

So far, the presented material rely on high fidelity analysis, both through experiments and simulations, that are not feasible to perform within the normal tight time frame available to a propeller designer, at least not in design iterations. The knowledge gained can however be put to use through design philosophies on controlling the cavitation by the pressure distribution on the blade and by identifying risky behaviour that can be identified using more approximate tools, such as RANS or even potential flow methods. Regarding noise prediction, these tools can be expected to give reasonable prediction of the first few harmonics of the blade passing frequency, with RANS giving primarily a higher reliability rather than a wider noise spectrum. Recent work by Li and Terwisga [17] indicate even some possibilities to predict erosion using RANS, although the possibility to capture enough cavitation dynamics in RANS is still to be proved. Moreover, for automated optimisation even RANS is too costly and the tools are still limited to potential flow methods. In Vesting [17], some simple constraints are developed based on rudimentary knowledge of the causes of cavitation nuisance. Two examples are given in Figure 4: (A) a long and thick cavity at the tip indicates a noisy cavity and probably strong tip vortex cavitation, and (B) a convex closure line of the sheet cavity indicates risk for substantial shedding of the sheet with risk for both erosion and noise. Leading edge desinence is another behaviour that can be considered risky and is possible to capture at this approximation level. This is still work in progress, and both the design philosophies as well as the reliability of design tools to analyse propeller needs much further testing and verification through the high-fidelity CFD we're developing; experimental test of a range of propellers to verify an optimisation is just too costly.

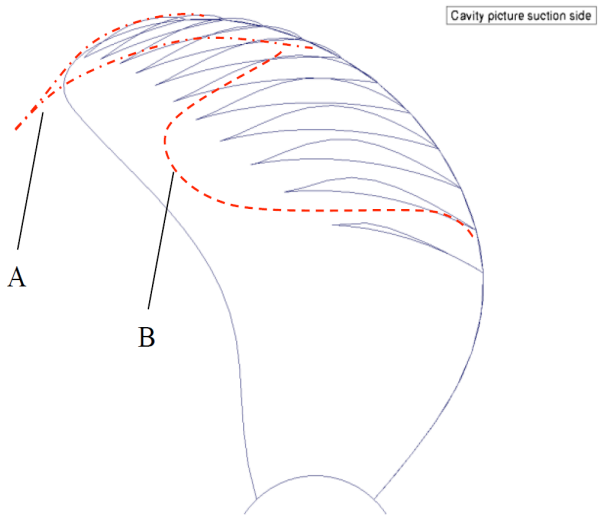

Figure 4 Cavity extent as predicted by a Vortex-Lattice method, where A and B indicate cavity shapes that are unwanted from a noise and erosion point of view.

Finally, when it comes to performing automated optimisation of the propulsor installation, it is clear that a mix of methods with varying fidelity must be used. For the final design, or a few candidates, one might want to perform experiments, complemented by LES (which will be feasible in a few years), but in design iterations this is not possible. Even a full RANS, resolving both the hull and the propulsor system (thus including flow improving devices etc.) will for a long time be too costly when hundreds of variants need to be tested in a genetic optimisation. A hybrid RANS/potential flow approach is possible today in the time frame of a research study, as is demonstrated in [3], but the two weeks this took is still too much for a design office, especially considering that the optimisation was not yet fully converged. Potential flow methods in a fixed wake flow are thus the only realistic method to consider for the majority of computations. However, to reach good convergence in the optimisation algorithms, it even seems preferable to use surrogate methods where the variants are computed from a very fast approximation of the design space; this is discussed in the recent work of Vesting [18]. The response surface, or corresponding approximation method, can then be constructed based on information from both fixed wake and propeller hull computations, by hybrid RANS/BEM or even full RANS, perhaps with inspiration from approaches using variable fidelity, see e.g. [19].

As the tools discussed above complement each other, we believe all will have a role for many years to come. Even though RANS computations can be realised faster and faster, the reliability in an optimisation will be greatly increased when evaluating many variants allowing for extensive use still of potential flow methods. Well resolved RANS and LES will be more and more used for analysing the final design candidates, complementing experiments with an excellent data set facilitating the understanding of possible problems and thus also giving the foundation for knowing which design changes are necessary to resolve them.

Acknowledgements

The research discussed here has been funded by Rolls-Royce Marine, through the University Technology Centre at Chalmers, EU projects STREAMLINE (FP7), VIRTUE (FP6), and HTA (JRP6), and to some extent with input also from EROCAV (FP5). Computations have been performed on HPC resources of C3SE, Chalmers Centre for Computational Science and Engineering.

References

[1] Abdel-Maksoud, M, ed., Proceedings of *2nd Int. Symposium on Marine Propulsors*, Hamburg, Germany, 2011.

[2] Han, K.-J., Larsson, L., and Regnström, B., "Numerical optimization of the propeller behind a ship hull at full scale," *26th Symposium on Naval Hydrodynamics*, Italy, 2006.

[3] Vesting, F., and Bensow, R.E., "Propeller Optimisation considering Sheet Cavitation in Hull Interaction," *2nd Int. Symposium on Marine Propulsors*, Hamburg, Germany, 2011.

[4] Bensow, R.E., and Bark, G., "Implicit LES predictions of the cavitating flow on a propeller," *J. Fluids Eng. Trans. ASME*, **132**(4), 2010.

[5] Bensow, R.E., "Simulation of the unsteady cavitation on the the Delft Twist11 foil using RANS, DES and LES," *Workshop of 2nd Int. Symposium on Marine Propulsors*, Hamburg, Germany, 2011.

[6] Schmidt, S.J., Thalhamer, M., Schnerr, G.H., "Inertia Controlled Instability and Small Scale Structures of Sheet and Cloud Cavitation," *7th Int. Symposium on Cavitation CAV2009*, Ann Arbor, MI, USA, 2009.

[7] Eskilsson, C., and Bensow, R.E., "A Compressible Model for Cavitating Flow: Comparison between Euler, RANS and LES Simulations," *29th Symposium on Naval Hydrodynamics*, Gothenburg, Sweden, 2012.

[8] Bark, G., Berchiche N., and Grekula, M., "Application of principles for observation and analysis of eroding cavitation, EROCAV observation handbook," Ed. 3.1, Chalmers University of Technology, Sweden, 2004.

[9] Bark, G., Grekula, M., Berchiche, N., and Bensow, R.E., "On Some Physics to Consider in Numerical Simulation of Erosive Cavitation," *7th Int. Symposium on Cavitation CAV2009*, Ann Arbor, MI, USA, 2009.

[10] Bark G., Grekula M., and Lu, N.-X., "Analysis of Erosive Cavitation by High Speed Video Records," *2nd Int. Conference on Advanced Model Measurement Technology for the EU Maritime Industry*, Newcastle, UK, 2011.

[11] Grekula, M., and Bark, G., "Analysis of high- speed video data for assessment of the risk of cavitation erosion," *1st Int. Conference on Advanced Model Measurement Technology for EU Maritime Industry,* Nantes, France, 2009. Also included in [16].

[12] Bark, G., and Bensow, R.E., "Hydrodynamic Mechanisms Controlling Cavitation Erosion," *29th Symposium on Naval Hydrodynamics*, Gothenburg, Sweden, 2012.

[13] Lu, N.-X., Svennberg, U., Bark, G., and Bensow, R.E., "Numerical Simulations of the Cavitating Flow on a Marine Propeller," *8th Int. Symposium on Cavitation CAV2012,* Singapore, 2012.

[14] Lu, N.-X., Bensow, R.E., and Bark, G., "LES of Unsteady Cavitation on the Delft Twisted Foil," *J. Hydrodynamics, Ser. B*, **22**(5), 2010.

[15] Lu, N.-X., "Large Eddy Simulation of Cavitation on Hydrofoils," Licentiate Thesis, Chalmers University of Technology, Sweden, 2010.

[16] Bensow, R.E., "Capturing Secondary Cavitation A Step Towards Numerical Assessment of Cavitation Nuisance," *Ship Technology Research* **58**(2), 2011.

[17] Li, Z. and Terwisga, T.v., "On the capability of a RANS method to assess the cavitation erosion risk on a hydrofoil," *8th Int. Symposium on Cavitation,* Singapore, 2012.

[18] Vesting, F., "Methods for Constrained Optimisation of Propellers," Licentiate Thesis, Chalmers University of Technology, Sweden, 2012.

[19] Calcagni, D., Salvatore, F., Bernardini, G., and Miozzi, M., "Automated Marine Propeller Design Combining Hydrodynamics Models and Neural Networks," *1st Int. Symposium on Fishing Vessel Energy Efficiency E-Fishing*, Vigo, Spain, 2011.

[20] Grekula, M., "Cavitation Mechanisms Related to Erosion; Studies on Kaplan Turbines, Foils and Propellers," PhD thesis, Chalmers University of Technology, Sweden, 2010.

CFD Simulations for Offshore Industry Applications

Volker Bertram (FutureShip), Hamburg/Germany, volker.bertram@GL-group.com
RV Ahilan (GL Noble Denton), London/UK, rv.ahilan@GL-group.com

We apply our methods and expertise for ship flows increasingly to a wider range of applications, particularly so to problems arising in the offshore industry. The following will illustrate the variety of problems encountered and how modern CFD simulations are employed to analyse problems and guide us towards solutions. The focus lies here on RANSE methods, which have supplemented "classical" hydrodynamic approaches (Green function methods, semi-empirical approaches like the Morison formula, etc) increasingly over the past years. Most of the examples shown here were computed using Comet and Star CCM+ of cd-adapco.

Foremost, we may think of using CFD analyses for load predictions, supplying detailed input for structural analyses. Long-term spectral distributions of wave loads (as needed for fatigue analyses) are based on linear seakeeping methods (and potential theory). However, for extreme loads, CFD has become the standard tool, sometimes alone, sometimes in combination with potential flow methods:

- Extreme wave scenarios, including freak waves, using free-surface RANSE solvers, Fig.1, e.g. *El Moctar et al. (2007).*
- Impact loads, using free-surface RANSE solvers. Impact loads appear for slamming and sloshing analyses, Fig.2, *Peric et al. (2007).* Mostly, these simulations assume weak fluid-structure interaction, i.e. the fluid dynamic simulation specifies the loads for the structural finite-element analyses (FEA), but the deformation is not considered for the CFD (computational fluid dynamics) simulation. However, strong fluid-structure interaction considering also the effect of the structural response on the fluid dynamics is feasible, *Oberhagemann et al. (2008), El Moctar et al. (2011).*
- As a special case, ice loads may be considered. Here, simulations of offshore structures in brash ice consider e.g. the loads for dynamic positioning of drill ships, *Wang and Derradji-Aouat (2011).*LS-DYNA, a finite-element code usually used for ship-ship collision analyses can be applied for these simulations.

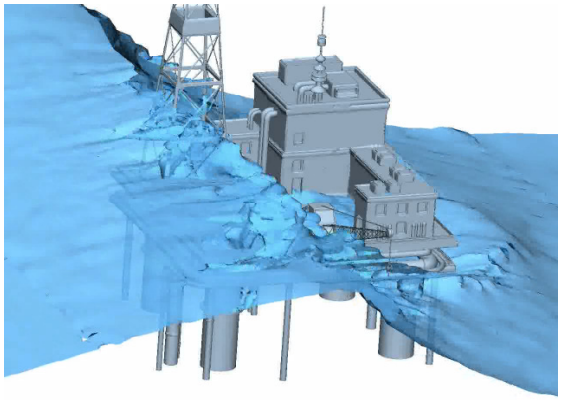

Fig.1: Simulation of platform in extreme waves

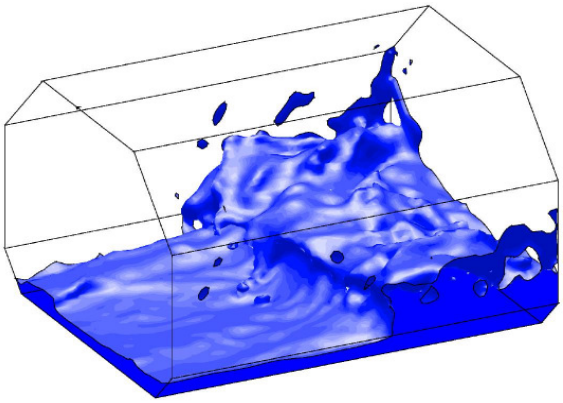

Fig.2: Sloshing simulation using free-surface CFD

Also, operational procedures may be guided based on simulations. This concerns in particular accident response procedures. Progress in simulation techniques and computer hardware have led to a multitude of applications that were previously not possible at all or previously approximated by more expensive and/or less accurate model tests, e.g.:

- Towing of damaged structures
  After an accident, damaged ships or offshore structures often must be towed to repair sites. Typically, the initial accident will impair the strength of the structure, but may also affect re-

sidual freeboard and stability. This must be considered for the towing. CFD simulations for towed systems manoeuvring in waves represent the state-of-the-art approach for the hydrodynamic issues, Fig.3.

- Oil spills
  Multi-phase flows, i.e. flows with several fluids of differing density and viscosity, can be simulated by all major commercial CFD codes. For oil spills, oil and water are considered, sometimes also air (when waves or sloshing plays a role). *Vasconcellos and Alho (2012)* give a typical application for an oil spill in an FPSO, Fig.4.
- Gas dispersion
  From a simulation point of view, gas dispersion is very similar to fluid dispersion. The same techniques and software can be applied, albeit with different density and viscosity. In addition, for gas (including smoke) dispersion, thermal processes and thermal buoyancy play usually a significant role and must be reflected in the simulation model. Such simulations may concern external flows, Fig.5, typically near crew quarters or helidecks on platforms, or internal flows in closed working or living areas, Fig.6. They may also cover extreme temperatures or speeds, including supersonic, explosive leaks, Fig.7.

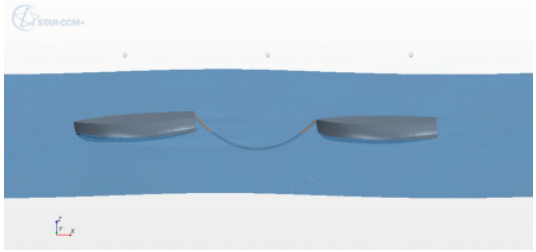

Fig.3: Tug-tow system in waves
[Milovan Peric (cd-adapco) in pers. comm.]

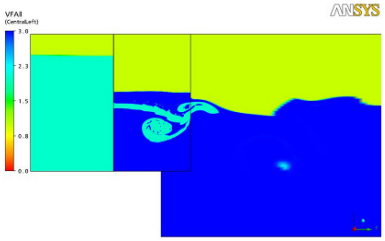

Fig.4: Oil spill simulation, *Vasconcellos and Alho (2012)*

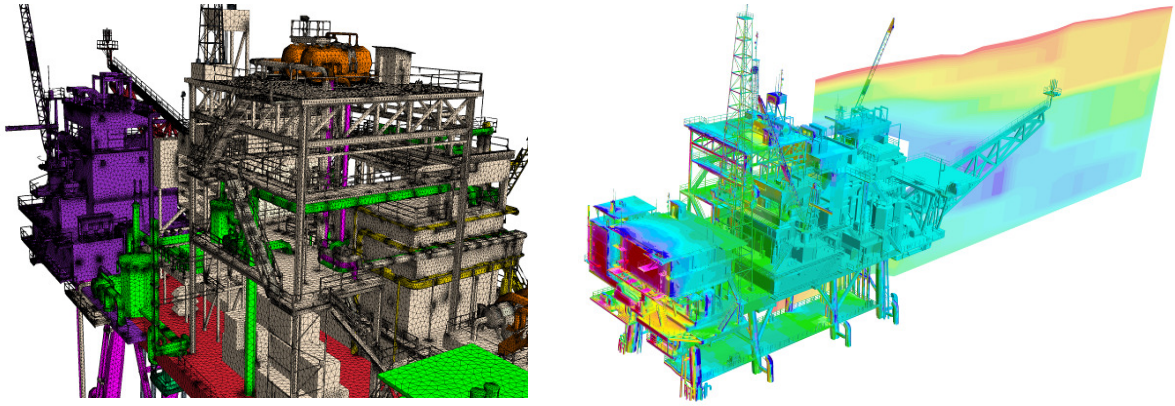

Fig.5: Mesh for offshore superstructure and CFD simulated flow around it, *Peric and Bertram (2011)*

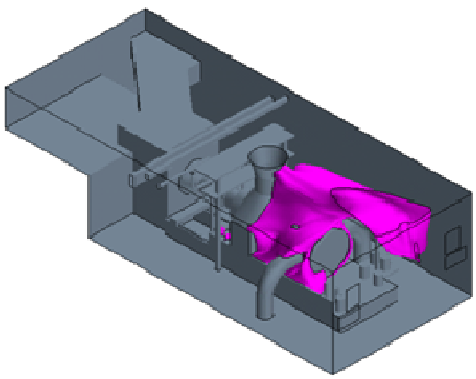

Fig.6: Gas dispersion in closed working areas after (potential) leak

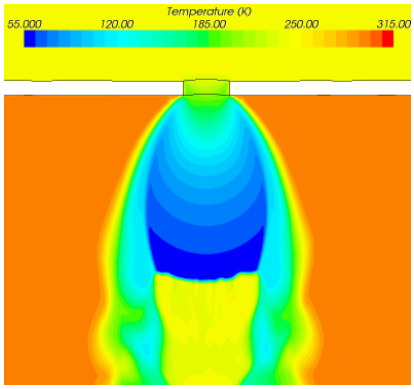

Fig.7: Temperature distribution in supersonic gas leak

In addition, multi-phase flow simulations have been used for decision support in cleaning offshore structures, in regular operation or in preparation for disposal, Fig.8. Simulations identify for example stagnant flow regions in tanks, required flow-through times or pipe dimensions to reach prescribed concentration levels of one fluid, or the effectiveness of cleaning procedures. Essentially the same simulations techniques are frequently used in Ballast Water Treatment problems on ships, Fig.9.

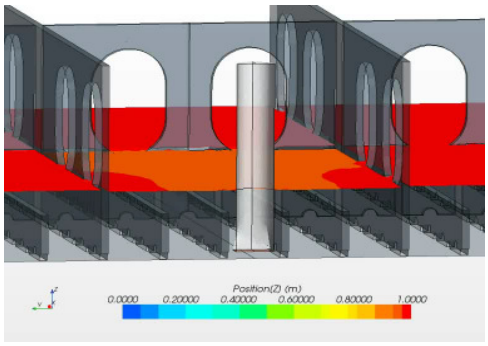

Fig.8: Simulation of stagnant or low-velocity regions in tank (sediment accumulation)

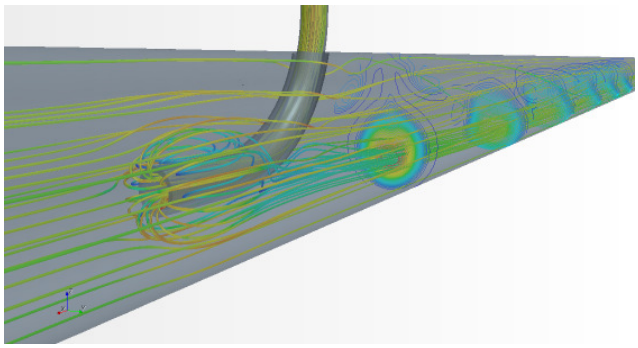

Fig.9: Pipe flow investigating turbulent mixing of two fluids

Offshore structures usually have much higher down-time costs than cargo ships. Consequently, much higher focus is placed on ensuring high availability of these structures. The role of CFD simulations in this context will be discussed in the following:

- Operational limits: Operational guidelines for risk mitigation contribute significantly to ensure high availability. A typical example is the specification of operational limits (sea states) for installation, maintenance and operation. The appropriate simulation tools depend on required accuracy, geometry of the object (slender monohull, catamaran, large displacement structure, hydrodynamically transparent jack-up structure, etc) and speed through water. For a jack-up installation ship, Fig.10, we computed the forces in waves just before touch-down of the jack-up legs. The simulations were performed using AQWA, a commercial Green function method seakeeping code. However, AQWA requires force coefficients for viscous force components. These can be specified using experience or semi-empirical formulae (where applicable), or (as in our case) using RANSE simulations in pre-processing once, before a wide parameter space is analysed using the fast potential-flow seakeeping code. For validation of the simplified potential-flow (frequency-domain) approach, we performed selective simulations with a free-surface RANSE method (in time domain). The results showed that AQWA (with viscous correction coefficients) gave similar results as the RANSE simulation, Fig.11. Such a hybrid approach combines thus accuracy with time and cost efficiency.

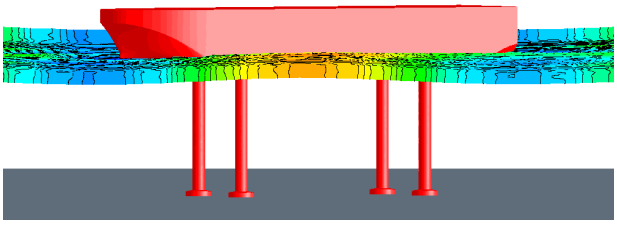

Fig.10: Jack-up platform in waves during touch-down

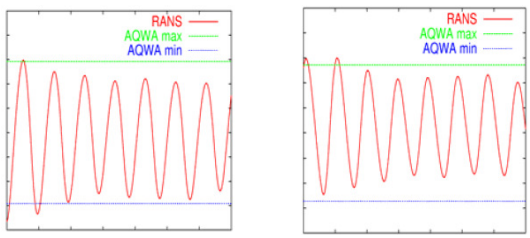

Fig.11: x-force (left) and y-force (right) over time for AQWA and Comet

- Vortex generation: For cylindrical structures, the vortex-induced vibrations can be investigated using simple, semi-empirical formulae. For complex systems like ships or FPSOs, there are many degrees of freedoms for local and global vibrations and these may be excited by vortex shedding at many local structures, typically at appendages or hull openings. The traditional trial-and-error approach to localise the source of vortex-induced vibrations may today be re-

placed by a more time and cost efficient search guided by CFD and vibration analyses, *Menzel et al. (2008)*. For a megayacht, vibrations in the owner's cabin had a distinct frequency that ruled out engine, propeller or sea waves as exciting source. Unsteady RANSE simulations gave then the time histories of pressures at all appendages. The frequency of the pressure fluctuations at the outer propeller shaft matched the frequency of the vibrations in the owner's cabin and had significant amplitude, Fig.12. The stern part was modified adding streamlined fairings between the propeller shafts and the underside of the hull, Fig.13. This resulted in a much smoother flow in this region, eliminating the vibrations completely.

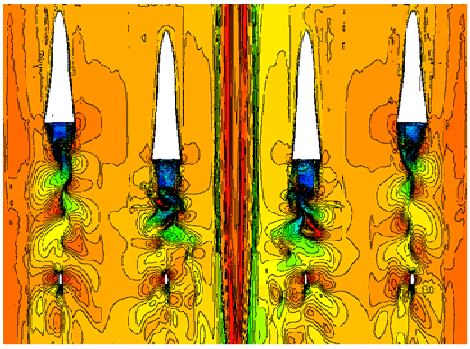

Fig.12: CFD simulation for vortex induced vibrations at propeller shafts

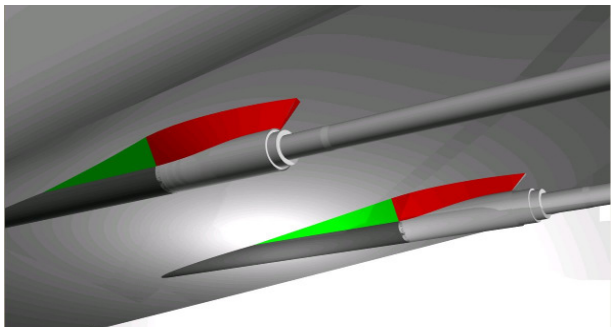

Fig.13: Redesign of problematic propeller shaft exit

In similar fashion, in a recent project, the focus was on the fatigue strength of bilge keels for an FPSO. The flows which induce the fatigue loads feature massive vortex generation, Fig.14, and are not properly captured at model scale. Hence the complete ship including bilge keels was modelled and simulated in waves.

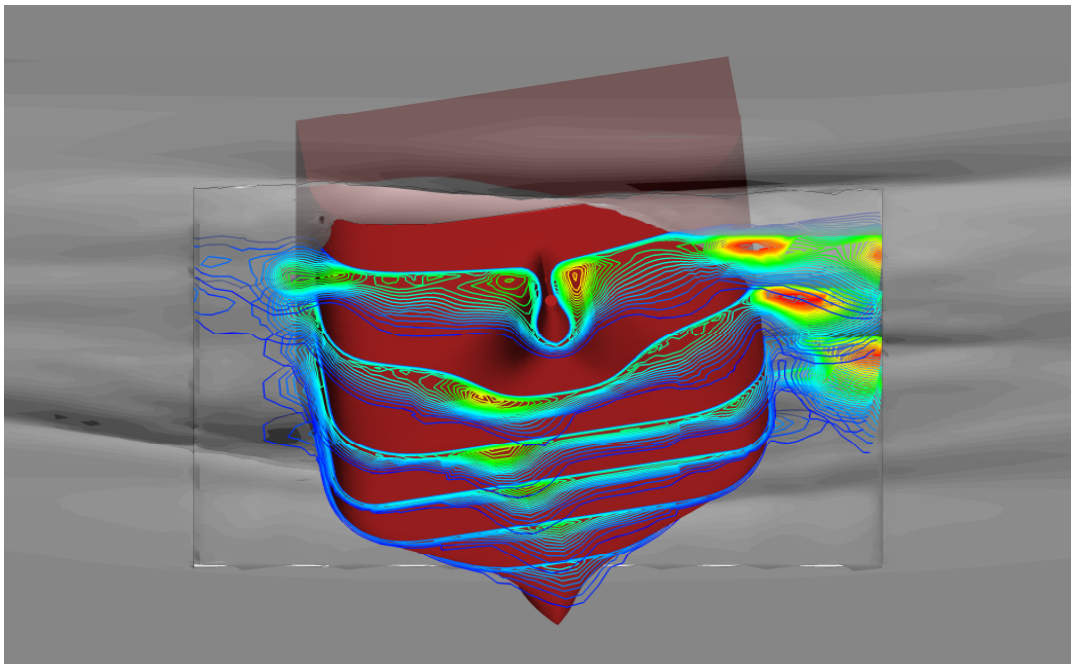

Fig.14: CFD simulations give load histories for fatigue strength analyses on bilge keels

Finally, modern design practice employs CFD and formal optimisation to derive optimum hull shapes, *Hochkirch und Bertram (2012)*. Similar applications can be envisioned for offshore platforms and supply vessels. OSV (offshore supply vessels) are good candidates for formal hull optimisation, but fuel efficiency, stability, and seakeeping must be reflected in the optimisation model to find good trade-offs. First such applications involving potential-flow seakeeping codes appear, Fig.15, *Harries et al. (2012)*. It is only a matter of time before we will see also RANSE codes applications.

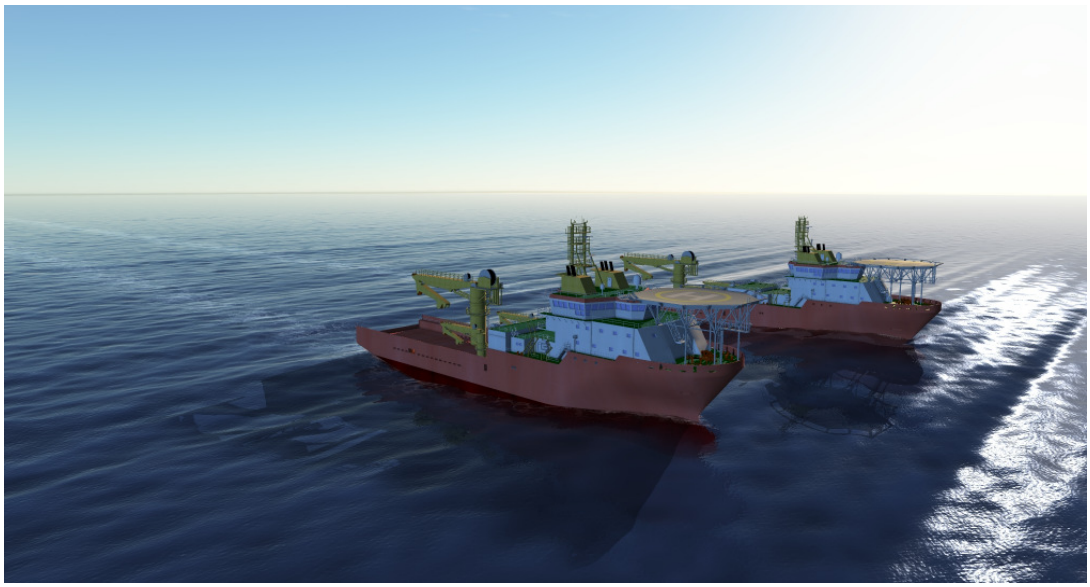

Fig.15: Comparison of two offshore supply vessels in virtual seaway, *Harries et al. (2012)*

References

EL MOCTAR, O.M.; SCHELLIN, T.E.; PERIC, M. (2007), *Wave load and structural analysis for a jack-up platform in freak waves*, 26th Int. Conf. Offshore Mechanics and Arctic Engineering (OMAE), San Diego

EL MOCTAR, O.; OBERHAGEMANN, J.; SCHELLIN, T. (2011), *Free-surface RANS method for hull girder springing and whipping*, SNAME Annual Meeting, Houston, pp.286-300

HARRIES, S.; LAND, J.; WEICKGENANNT, S.; QIU, W. (2012), *From analysis towards design in seakeeping,* 11th Conf. Computer and IT Applications in the Maritime Industries (COMPIT), Liege, pp.27-38

HOCHKIRCH, K.; BERTRAM, V. (2012), *Hull optimization for fuel efficiency – Past, present and future,* 11th Conf. Computer and IT Applications in the Maritime Industries (COMPIT), Liege, pp.39-49

MENZEL, W.; EL MOCTAR, O.; MUMM, H. (2008), *Advanced thinking on tricky excitations*, The Naval Architect, March, pp.64-69

OBERHAGEMANN, J.; EL MOCTAR, O.; HOLTMANN, M.; SCHELLIN, T.; BERTRAM, V.; KIM, D.W. (2008), *Numerical simulation of stern slamming and whipping*, 11th Numerical Towing Tank Symp. (NuTTS), Brest

PERIC, M.; BERTRAM, V. (2011), *Trends in industry applications of CFD for maritime flows*, 10th Conf. Computer and IT Applications in the Maritime Industries (COMPIT), Berlin, pp.8-18

PERIC, M.; ZORN, T.; EL MOCTAR, O.; SCHELLIN, T.; KIM, Y.S. (2007), *Simulation of sloshing in LNG-tanks*, 26th Conf. Offshore Mechanics and Arctic Engineering (OMAE), San Diego

VASCONCELLOS, J.M.; ALHO, A. (2012), *Computational fluid dynamics applied to a FPSO-tanker oil spill,* 11th Int. Conf. Computer and IT Applications in the Maritime Industries (COMPIT), Liege

WANG, J.; DERRADJI-AOUAT, A. (2011), *Numerical assessment for stationary structure (Kulluk) in moving broken ice*, 21st Conf. Port and Ocean Engineering under Arctic Conditions (POAC), Montréal

CFD Analysis of a U-shaped Water Tunnel Bilge Keel Experiment

Z. Boutanios (ziad.boutanios@sbmoffshore.com)
and
R. van 't Veer (riaan.vantveer@sbmoffshore.com)
SBM Offshore, Schiedam, The Netherlands

1 Introduction

This paper addresses the flow behaviour and normal force acting on a plate subject to oscillatory flow for KC numbers ranging from 1.4 to 105. For this purpose 3D CFD simulations were conducted on a U-shaped water tunnel configuration believe to be the same used by Sarpkaya and O'Keefe (1996) [4] in their experimental investigation. With each flow oscillation vortices are are shed from the tip of wall-mounted bilge keel plates installed at the middle of the water tunnel. The strength of such vortices is characterized by the KC number as first described by Keulegan and Carpenter (1958) [1]. The KC number is calculated as $KC = U_m T/h$ where U_m is the maximum velocity in the oscillating flow, T is the cycle period and h is the height of the plate. The normal force on the plate can be characterized by drag and inertia components associated with coefficients C_d and C_m respectively, the like of which were reported by Sarpkaya and O'Keefe (1996) [4] for their configuration. Such coefficients are used by Van 't Veer et al. (2012) [6] in a methodology to calculate the oscillatory loads on bilge keels of ships operating at zero forward speed in irregular sea states. In Van 't Veer et al. (2012) [6] 2D CFD simulations were used, similar to the approach of Kinnas et al. (1992) [2]. The 2D CFD results were in overall agreement with the experimental results of Sarpkaya and O'Keefe (1996) [4] but certain discrepancies were observed which initiated the present research.

2 Computational Setup

The water tunnel used in the 1996 experiment consists of a horizontal section that is $0.91m$ deep, $1.42m$ high and $10.67m$ long. The vertical legs on either side of the horizontal section are $0.91m$ deep, $1.83m$ wide and $7.62m$ high.The U-shaped water tunnel is designed so as to ensure a relatively homogeneous flow in the horizontal test section through the use of the varying section elbows. The general tunnel geometry is shown in Figure 1. The experimental setup includes an air supply system on one of the legs, where a butterfly valve mechanism oscillates at the natural frequency of the water in the tunnel. An additional fan and electronic feedback control mechanism allow maintaining the flow amplitude at the desired level indefinitely. A $102mm$-high and $6mm$-thick plate is located at the middle of the tunnel on its lower surface and spanning the entire depth of the tunnel of $91cm$. In the experiment the plate was fitted into a groove of about $8mm$ wide and $6mm$-deep but this detail was not included in the simulation. The top of the plate was beveled at 60° angles to minimize wall proximity effects. This configuration is referred to as a wall-bounded plate in the experiments. In comparison, plates suspended in the middle of the channel away from the lower and upper walls are referred to as free plates.

The 2D CFD simulations used by Van 't Veer et al. (2012) [6] to compute the drag coefficients were restricted to only the straight section of the tunnel, with inlet/outlet harmonic boundary conditions in time at both ends of the straight section with a preset time period. They were single-phase simulations with water as the working fluid and no free surface to compute. The present study is a full CFD reproduction of the experiment in that it includes the entire 3D configuration and computes the moving water free surface.

The computational mesh used is non-conformal and has 2.4M cells, mostly hexahedral. The solver used is interFoam, which is an OpenFOAM®solver based on the Volume of Fluid method. Turbulence is accounted for with the $k-\omega$ SST 2-equation model. The problem is initially set up by putting more water in one leg than the other and letting the water level oscillate under the effect of gravity. The initial setup and a zoom of the mesh around the plate are shown in Figures 1a and 1b. Unlike the 2D simulations no forcing was applied and the flow was allowed to gradually decay in an underdamped fashion. It is believed some forcing was applied in the experiment but not how much. Five simulations were performed, all with water up to height $3m$ in the left leg and $3.035m$, $3.25m$, $3.50m$, $4.00m$ and $7.00m$ in the right leg with KC numbers of roughly 1.4, 7, 15, 26 and 105 respectively. The corresponding KC numbers varied slightly from cycle to cycle for each case as the flow was being progressively damped by friction and the pressure drag of the plate. The free surface position in the right leg of the tunnel is plotted in Figure 2 against time for two cases, $3.25m$ and $4.00m$ initial water height, clearly showing the underdamped behaviour of the system.

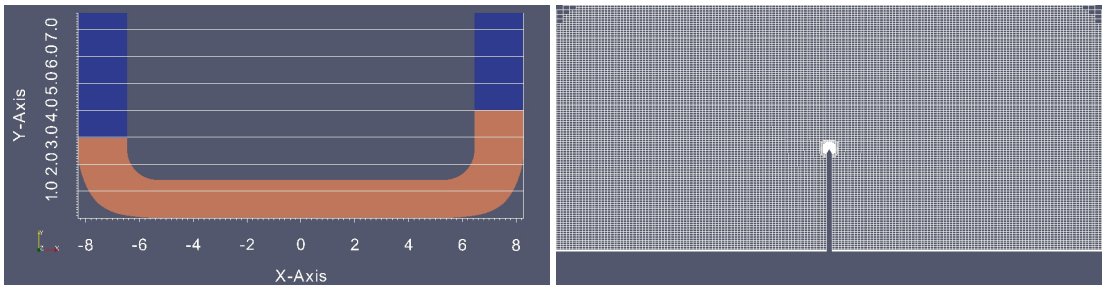

(a) Initial setup of the 3D CFD, water in orange. (b) Zoom of the CFD mesh around the plate.

Figure 1: Experimental and computational setups.

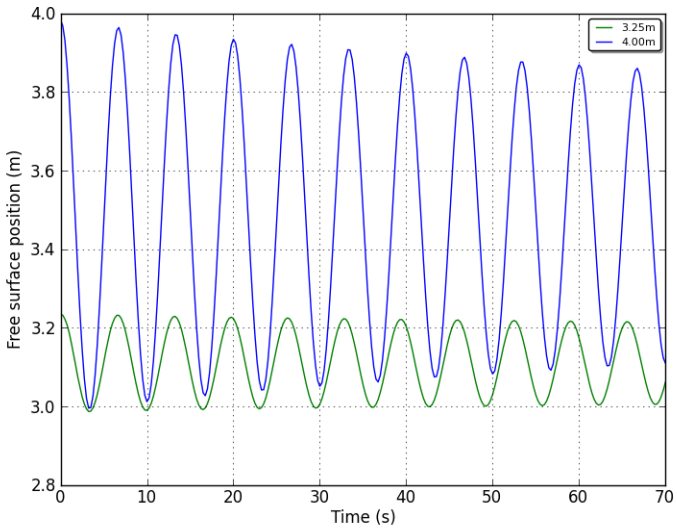

Figure 2: Variation of free surface position vs. time in the right leg of the tunnel for two initial water heights.

3 Plate Vortex Shedding

Sarpkaya and O'Keefe (1996) [4] included some flow visualizations for the different flow regimes encountered during their experiment. Sketches of the vortex shedding patterns were provided for three

different flow regimes: $KC < 3$, $3 < KC < 8$ and $KC > 8$. To compare flow velocity vectors were extracted on a plane section along the centre of the tunnel, parallel to the front and back faces.

The sketches of experimental vortex shedding at $KC < 3$ are shown in Figure 3a where we can see a general agreement with the numerical vortex shedding results of Figure 3b, corresponding to a $KC \approx 1.4$. The smaller vortices shed in steps 2 and 3 of Figure 3a are relatively smeared in Figure 3 but this is to be expected with the $k-\omega$ turbulence model. Another dissipative factor is the change of mesh size between the finer region around the plate and the rest of the mesh in the tunnel straight section. The shedding pattern seen results from the fact that a vortex shed by the plate during one half-cycle is still around by the time the flow reverses direction in the next half-cycle and another vortex is shed, since the average flow velocity is too low to dissipate it. Both vortices convect as a counter-rotating pair diagonally away from the plate. The flow is seen to retain the memory of past cycles throughout the present ones.

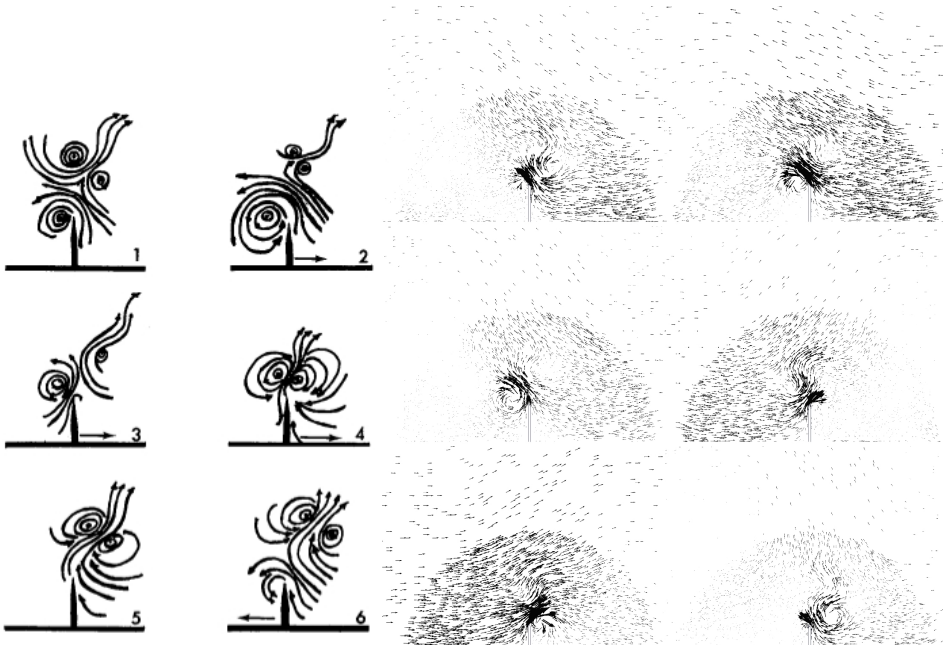

(a) Sketches of experimental vortex shedding for $KC < 3$ (Sarpkaya and O'Keefe, 1996).

(b) Numerical vortex shedding for $KC \approx 1.4$ on a plane section through the middle of the tunnel.

Figure 3: Experimental and numerical vortex shedding for $KC < 3$.

The same sketches at $3 < KC < 8$ are shown in Figure 4a where again we can see general agreement with the numerical vortex shedding results of Figure 4b, corresponding to a $KC \approx 6.8$. In this regime a vortex shed during a half-cycle has begun to decay by the time another vortex shed during the next half-cycle due to the higher average flow velocity. The weaker vortex then gravitates around the new stronger one. In the numerical case the weaker vortex decays faster due to the same reasons discussed for $KC < 3$. In general vortex decay is due to interaction with the average flow field so decay is faster for faster flows with higher average velocity which interact stronger with shedding vortices. In this regime the flow is seen to have a shorter memory of past half-cycles than the previous $KC < 3$ regime.

The sketches of experimental vortex shedding at $KC > 8$ are shown in Figure 5a where again we can see general agreement with the numerical vortex shedding results of Figure 5b, corresponding to a $KC \approx 26.2$. This flow regime has the highest average flow velocity so shed vortices can be seen to convect rather horizontally with the average flow direction and decay quite faster than the other two regimes. Vortices shed in successive half-cycles are too far apart for any meaningful interaction to result. Given the high average flow velocity a large vortex is shed by the plate and this is captured by the simulation. Additional smaller vortices are shed in the same direction in the experiments but these are completely smeared in the simulation for the same reasons stated above. In this regime the flow is seen to retain practically no memory of past half-cycles.

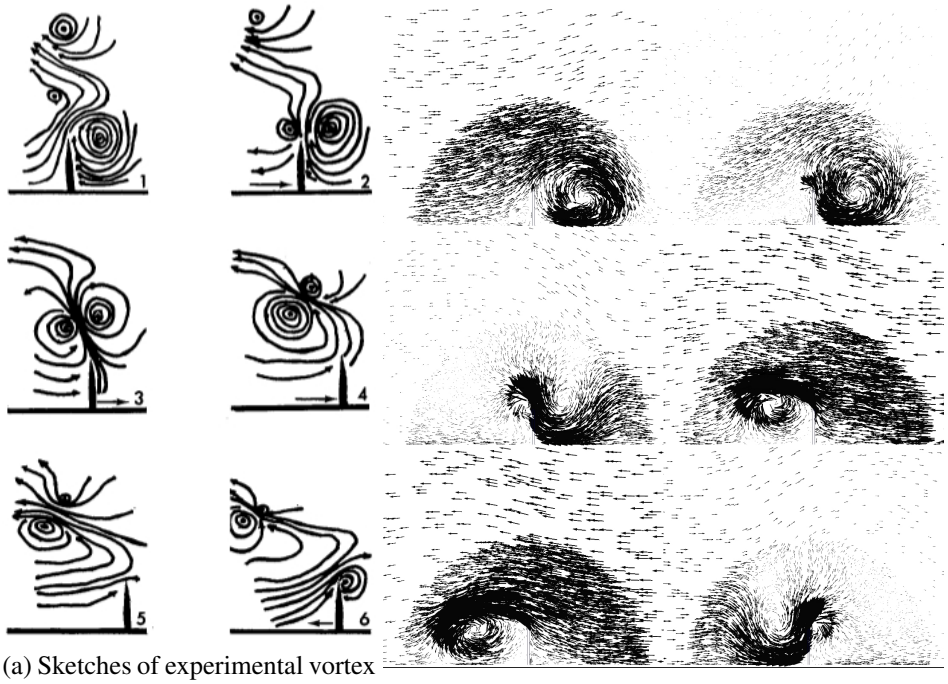

(a) Sketches of experimental vortex shedding for $3 < KC < 8$ (Sarpkaya and O'Keefe, 1996).

(b) Numerical vortex shedding for $KC \approx 6.8$ on a plane section through the middle of the tunnel.

Figure 4: Experimental and numerical vortex shedding for $3 < KC < 8$.

A good understanding of the flow pattern for different KC regimes and the vortex shedding memory effects are important for the development of a bilge keel force prediction model in both regular and irregular seas. In particular memory effects are important at low KC regimes which are associated with fatigue seastates. More work is planned in this regard and higher order turbulence models will be investigated to assess what would be required to better resolve the vortex shedding features of the flow and whether any improvements in the results can be obtained.

4 Plate Drag, Moment and Total Force Coefficients

Force measurements can be used to calculate C_d and C_m values using curve fits to the time traces of total force according to the Morison equation introduced by Morison et al. (1950) [3] and based on the work of Stokes (1851) [5],

$$F(t) = \frac{1}{2}\rho h w C_d \dot{x}(t)|\dot{x}(t)| + \frac{1}{4}\left(\pi h^2\right) w C_m \ddot{x}(t) \tag{1}$$

where $F(t)$ is the force on the plate of height h and width w. The reference area for the inertia coefficient is half the volume of a cylinder with radius h is considered the most meaningful for wall-mounted plates as discussed by Sarpkaya and O'Keefe (1996) [4]. However, they used the volume of a cylinder with diameter h to be consistent with the free-plate definition as used in this paper. Either Least-Squares fits or Fourier averaging can be used as reported by Keulegan and Carpenter (1958) [1] and Sarpkaya and O'Keefe (1996) [4]. Least-Squares fits were used here because they were found to approximate the data better than the Fourier averaging used for the experimental data. The simulations were run for $70s$, which was equivalent to about 10 cycles for all cases analysed. For the CFD simulations $\dot{x}(t)$ was taken as the free-surface average velocity in the right vertical leg of the tunnel and computed from the free surface position using a 2nd order central-difference scheme. It was found that $\dot{x}(t)$ varied a bit from cycle to cycle and C_d and C_m were calculated using the varying $\dot{x}(t)$ per cycle taken as U_m. The results are plotted in Figure 6 against the experimental data from Sarpkaya and O'Keefe, 1996 [4]. The red diamonds are 3D CFD values calculated with the variable U_m. The blue stars are for 2D CFD results from Van 't Veer

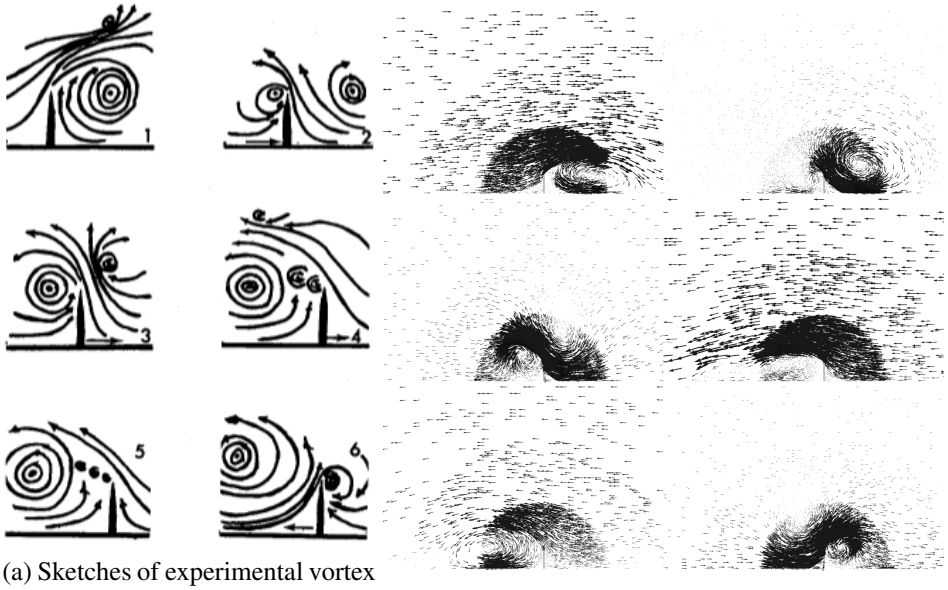

(a) Sketches of experimental vortex shedding for $KC > 8$ (Sarpkaya and O'Keefe, 1996).

(b) Numerical vortex shedding for $KC \approx 26.2$ on a plane section through the middle of the tunnel.

Figure 5: Experimental and numerical vortex shedding for $KC > 8$.

et al. (2012) [6] subject to the same Least-squares fit approach used for the 3D CFD data.

The computed C_d values show excellent agreement with the experimental data in Figure 6a. The KC numbers of the 1-cycle values vary a little bit owing to the underdamping of U_m but the trend still follows the experimental data. The KC number decreases with U_m and the largest variations and discrepancies are seen for the lowest KC number corresponding to the simulation with the largest memory effects in the flow, which produce longer vortex shedding cycles than at higher KC numbers. It is expected that longer simulation times are required in this case to obtain enough vortex shedding cycles and resolve this deviation. Indeed the lowest red diamond for this case which occurs latest in the simulation is much closer to the experimental data than its counterparts that occur earlier in the simulation. The 2D C_d results show an equally good agreement with the experimental data in the intermediate KC range. The largest discrepancy is at the lower KC numbers where the flow is mostly inertia dominated and the total force on the plate is expected to depend mostly on C_m. No experimental data was available for wall-bounded plates for $KC > 30$ but the trend of the experimental data seems to confirm the validity of the 3D result.

The computed C_m values also show good agreement with the experimental values shown in Figure 6b. The agreement is not as good as the C_d curves since the inertial coefficient depends on the flow details around the plate where the vortices are produced as was shown in Figures 3, 4 and 5. This is due to the inability of two-equation turbulence models to accurately reproduce the location and size of vortices in regions of high shear such as the immediate vicinity of the plate. Indeed the 2D simulations fair even worse since they are much less diffusive than the 3D simulations and typically produce larger and stronger vortices than what occurs in the tunnel. Comparing to the C_d curves of Figure 6a it is clear that the regions of better C_d match correspond to regions of better C_m match in the intermediate KC regions, where the 3D simulation did a relatively better job in reproducing the flow details near the plate as can be seen in Figure 4.

5 Conclusion

Five 3D simulations of the flow in a U-shaped water tunnel with a wall-bounded plate protruding in the middle were carried out spanning a KC range of $1.4 - 105$. Good agreement was observed in the vortex shedding pattern compared to sketches of the experimental shedding pattern with smearing of the smaller vortices that is attributed to the limitations of the $k - \omega$ turbulence model in regions of high shear.

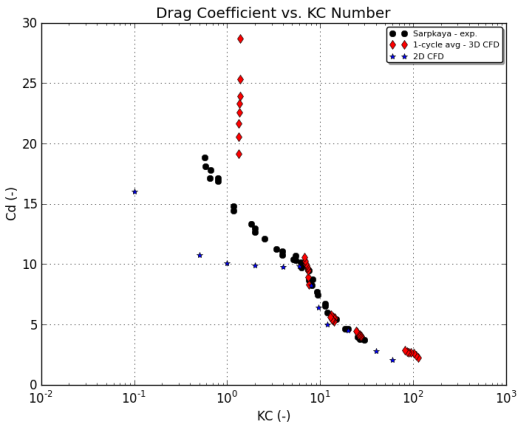

(a) Comparison of experimental and numerical C_d .

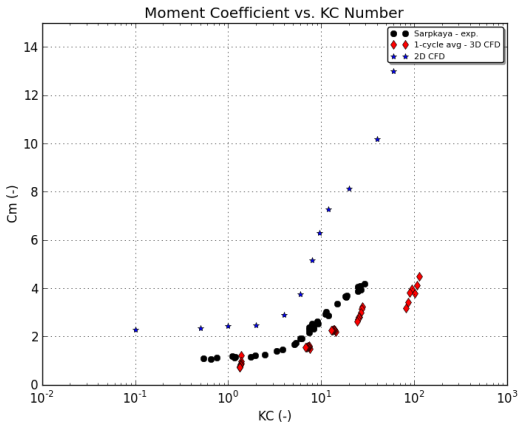

(b) Comparison of experimental and numerical C_m.

Figure 6: Comparison of experimental and numerical drag and moment coefficients.

More accurate comparison to the experiment cannot be done in the absence of true flow visualization as opposed to sketches of the vortex shedding. The 3D simulations showed notable improvements over the 2D simulations, especially for C_d coefficients at intermediate and high KC, and C_m coefficients for all KC. This is due to better representation of the flow around the plate by the 3D simulations. The largest differences to experiment were seen with C_d at the lowest KC where the flow retains much memory of its previous cycles. It is expected that the low KC simulation will need to be run for a longer time to obtain reliable statistics judging from the trend of the data points as flow time increases. More work is needed to investigate mesh resolution effects and obtain better resolved vortex shedding which will require a higher order turbulence model.

References

[1] G.H. Keulegan and L.H. Carpenter. Forces on cylinders and plates in an oscillating fluid. *Journal of Research of the National Bureau of Standards*, 60(5), 1958.

[2] S.A. Kinnas, Y.H. Yu, H. Lee, and K. Kakar. Modeling of oscillating flow past a vertical plate. In *Proceedings of the 13th International Ocean and Polar Engineering Conference*, Honolulu, Hawaii, May 2003. International Society of Offshore and Polar Engineers (ISOPE).

[3] J.R. Morison, M.P. O'Brien, J.W. Johnson, and S.A. Schaaf. The force exerted by surface waves on piles. *Petroleum Transactions*, 189:149–157, 1950.

[4] T. Sarpkaya and J.L. O'Keefe. Oscillating flow about two and three-dimensional bilge keels. *Journal of Offshore Mechanics and Arctic Engineering*, 118(1), 1996.

[5] G.G. Stokes. On the effect of the internal friction of fluids on the motion of pendulums. *Trans. Camb. Phil. Soc.*, 9:8–106, 1851.

[6] R. Van 't Veer, A. Pistidda, and A. Koop. Forces on bilge keels in regular and irregular oscillating flow. In *Proceedings of the 22nd International Ocean and Polar Engineering Conference*, Rhodes, Greece, June 2012. International Society of Offshore and Polar Engineers (ISOPE).

Numerical Study of Propeller Scale Effects

Tomasz Bugalski[1], Jan A. Szantyr[2]
[1]Ship Design and Research Centre CTO SA, Gdańsk, Poland
e-mail: Tomasz.Bugalski@cto.gda.pl
[2]Gdansk University of Technology. Gdansk, Poland
e-mail:jas@pg.gda.pl

Currently used scale effect corrections for open propellers have been developed about forty years ago. Since that time the geometry of propellers has changed significantly and the accuracy of model experiments and numerical methods employed for prediction of propeller open water characteristics has increased. In order to assess the adequacy of the classical scale effect corrections for contemporary propellers the following research plan was created at the Ship Design and Research Centre CTO SA:

- four different algorithms for calculation of propeller scale effect were included in the lifting surface programs, namely:
  - classical ITTC78 procedure (hereinafter Variant 1), based on the equivalent blade section at radius 0.75
  - ITTC78 formulae calculated locally for the respective blade sections and integrated along the blade radius (hereinafter Variant 2),
  - alternative formulae for blade section drag and lift integrated along the blade radius (hereinafter Variant 3),
  - alternative formula for blade section drag only, integrated along the blade radius (hereinafter Variant 4).
- reference CFD calculations were performed for the entire range of model and full scale Reynolds numbers.

Two propellers were selected: P9 with moderate skewback and CP6 with high skewback. The complete set of numerical calculations was performed for all propellers. The comparison and analysis of the computational results formed the basis for assessment of the accuracy and effectiveness of different methods for calculation of propeller scale effect corrections.

The classical ITTC78 method is based on the following corrections for propeller thrust and torque coefficients (as described in [3,4]):

$$\Delta K_T = K_{TS} - K_{TM} = \Delta C_D \cdot 0.3 \cdot \left(\frac{P}{D}\right)_{0.75} \cdot \left(\frac{c \cdot z}{D}\right)_{0.75} \tag{1}$$

$$\Delta K_Q = K_{QS} - K_{QM} = -\Delta C_D \cdot 0.25 \cdot \left(\frac{c \cdot z}{D}\right)_{0.75} \tag{2}$$

where the change of the equivalent blade section drag coefficient with scale is described by:

$$\Delta C_D = C_{DM} - C_{DS} \tag{3}$$

$$C_{DM} = 2\left[1 + 2\left(\frac{t}{c}\right)_{0.75}\right] \cdot \left[\frac{0.044}{\mathrm{Re}_M^{0.1667}} - \frac{5}{\mathrm{Re}_M^{0.6667}}\right] \qquad \text{model scale} \tag{4}$$

$$C_{DS} = 2\left[1 + 2\left(\frac{t}{c}\right)_{0.75}\right] \cdot \left(1.89 - 1.62 \log \frac{l}{k_s}\right) \qquad \text{full scale} \tag{5}$$

where: D - propeller diameter [m],
P - propeller pitch [m],
J - propeller advance coefficient [-]
z -number of blades [-],
c - blade section chord [m],
t - maximum blade section thickness [m],
Re - blade section Reynolds number [-],
k_s / l - relative roughness of the blade surface [-]
n - propeller rate of rotation [revs per second]

The above formulae are included in Variant 1 of the lifting surface calculations. In Variant 2 the Reynolds numbers together with drag coefficients (Formulae 4 and 5) are calculated separately for every blade section and then integrated along the blade radius, leading to the values of thrust and torque corrections for the required scale.
The alternative formula for blade section drag coefficient, in model and full scale alike, considered in this paper in Variants 3 and 4, has the following form (taken from [1]):

$$C_D = 0.05808\left(1-0.2\frac{t}{c}\right)\frac{1}{\mathrm{Re}^{0.1458}} \tag{6}$$

The formula for scale effect on blade section lift coefficient considered in this paper in Variant 3, has the following form (also taken from [1]):

$$C_{LV} = 2\pi\mu_1\left(\alpha+\mu_2\ \alpha_0\right) \tag{7}$$

where:

$$\mu_1 = 1-\exp\left(-0.0691+12.46\frac{t}{c}-0.1855\log\mathrm{Re}\right) \tag{8}$$

$$\mu_2 = 1+\frac{t}{c}\left(\frac{t}{c}-0{,}05\right)\frac{1}{(0.04664\log\mathrm{Re}-0.4378)^2} \tag{9}$$

where: α - angle of attack

α_0 - zero lift angle

μ_1, μ_2 - corrections for viscosity effects

The above formulae are the basis for computational options included in the calculations performed by the lifting surface methods described below.

A well-established and thoroughly validated lifting surface program UPCA92 for analysis of propeller operation in non-uniform velocity field [5] was used. The program was modified in such a way that it produced the complete open water diagram of propellers at the required scale. In the calculations usually the propeller rate of rotation was kept constant and the advance velocity was varied in order to produce the required values of the advance coefficient. Four different algorithms for prediction of scale effect corrections (Variants 1 to 4) were incorporated in both programs. The programs were used for calculations in model scale for 13, 20, 30, 40, 50 and 60 revolutions per second and for calculation of three different full scale situations, corresponding to propeller diameters of 3, 5 and 8 [m]. The full scale calculations were performed for standard propeller blade roughness of 30 microns.

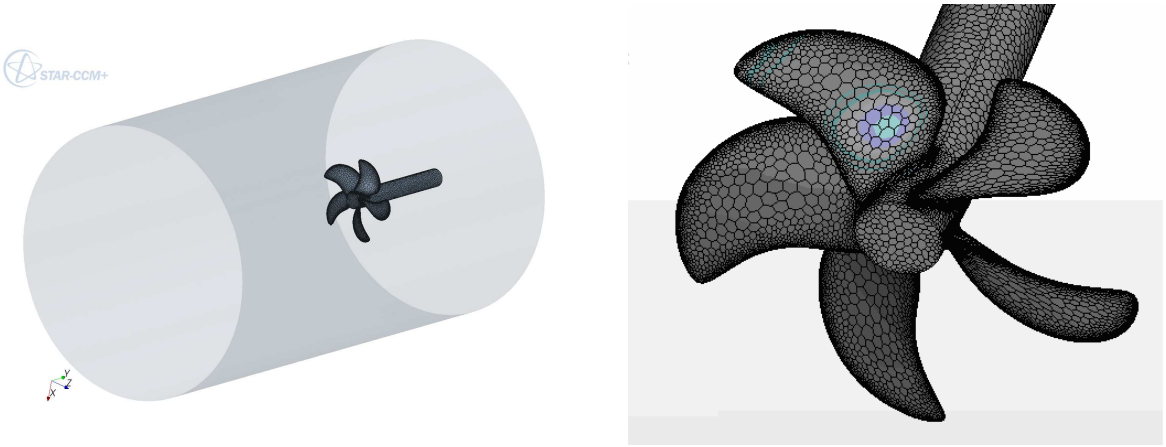

Figure 1 The CFD computational domain and grid used in calculation for propeller P9

Meshing and flow simulations are performed with the Reynolds Averaged Navier-Stokes (RANS) solver StarCCM+ from CD-Adapco. The code solves the RANS and continuity equations in integral form on a polyhedral mesh by means of the finite volume technique. The Reynolds stress problem is solved by means of "realizable" k-ε turbulence model. As in the open water situation the propeller inflow is uniform, the moving

reference frame approach is applied. The solution domain, shown in Fig. 1, was chosen to extend 10 propeller diameters in front of the propeller, 3 diameters in the radial direction and 5 diameters behind the propeller. The computational grid was constructed of about 900 000 polyhedral elements. The details of the calculations technique may be found in [2].

The calculations were carried out for advance coefficients in the range from J=0.0 to J=1.0. The computed thrust and torque on the propeller were converted into the dimensionless thrust coefficient, torque coefficient and the propeller open water efficiency was calculated. . The study of the flow field shows that the phenomena occurring in the flow (pressure distribution, tip vortices etc.) are typical for propeller flow and can be considered qualitatively correct. The examples of calculation results of the pressure distribution for propeller P9 are shown in Fig. 2.

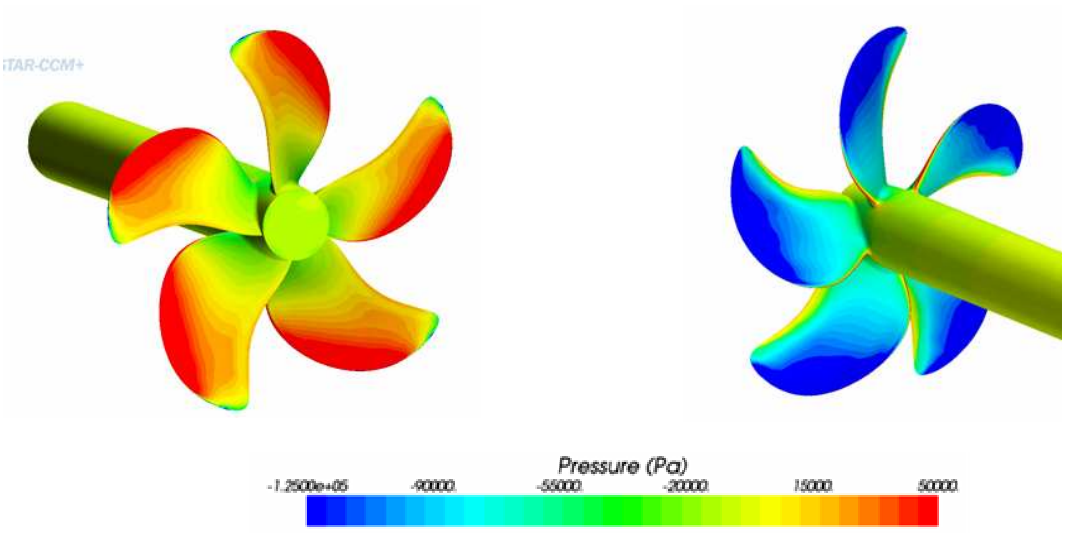

Figure 2 Calculated pressure distribution on the pressure and suction side of propeller P9 at 13 [rps]

The geometry of propeller P9 is shown in Fig. 3. This propeller may be regarded as a typical example of contemporary propeller designs for medium speed cargo vessels.

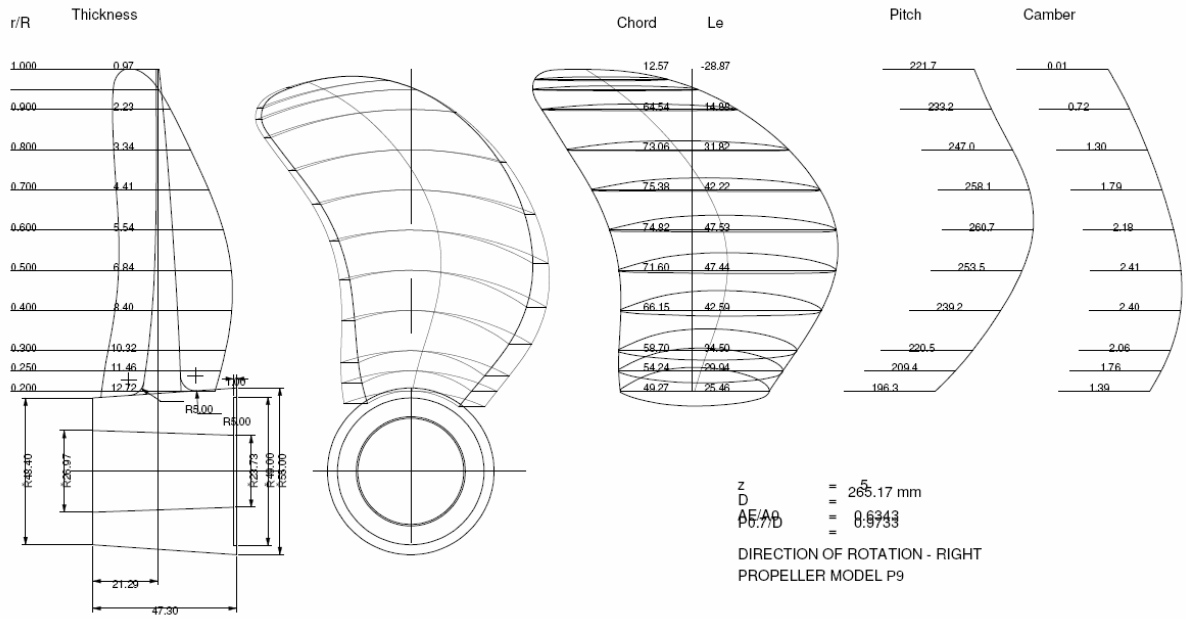

Figure 3 Geometry of the propeller P9

The results of computations are shown in consecutive Figures 4 and 5 in the form of scale effect corrections related to the model scale values of respective parameters at the lowest Reynolds number, i.e. at 13 revolutions per second. These scale effect corrections are shown for the design advance coefficient of the propeller P9 equal to J=0.6. Fig. 4 shows the corrections for propeller thrust coefficient, Fig. 5 - corrections for propeller torque coefficient.

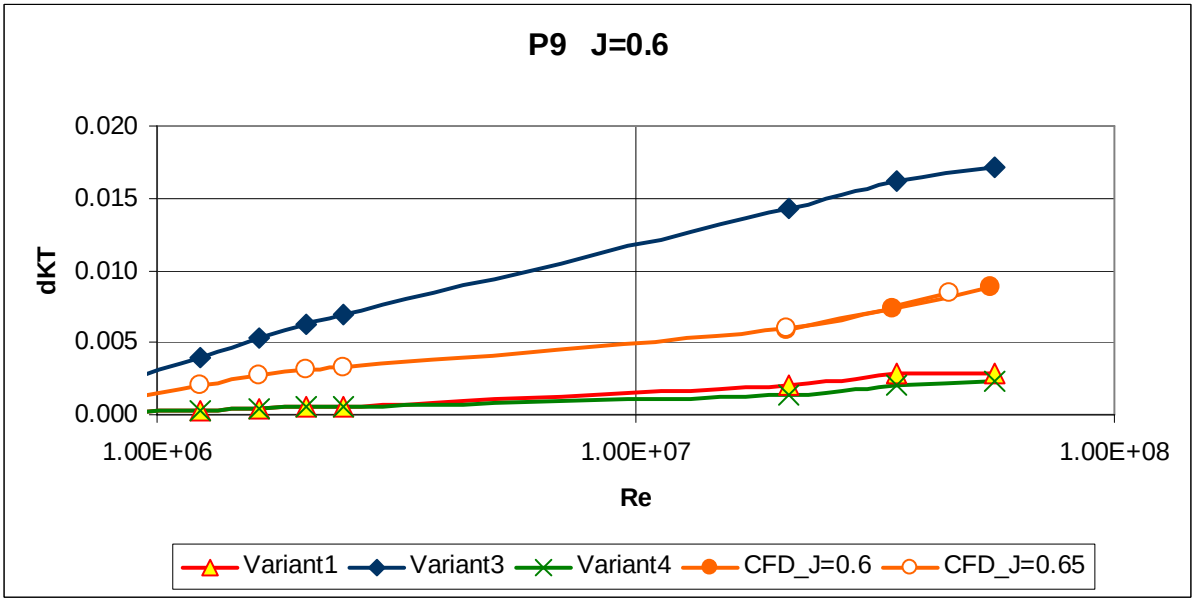

Figure 4 Results of calculations for the scale effect correction on the thrust coefficient of the P9 propeller

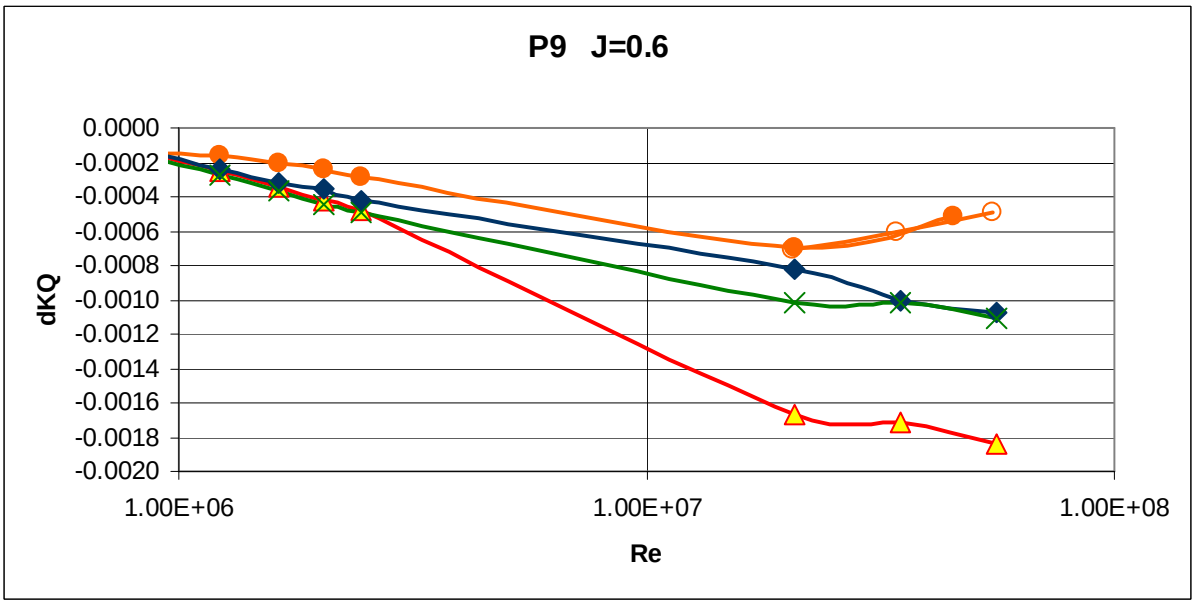

Figure 5 Results of calculations for the scale effect correction on the torque coefficient of the P9 propeller

The geometry of propeller CP6 is shown in Fig. 6. This propeller has a very high skewback, much higher than propeller CP2. The scope of calculations and the form of presentation of the results in Figs.7 and 8 is identical to those for propeller P9. The design advance coefficient is now J=0.9.

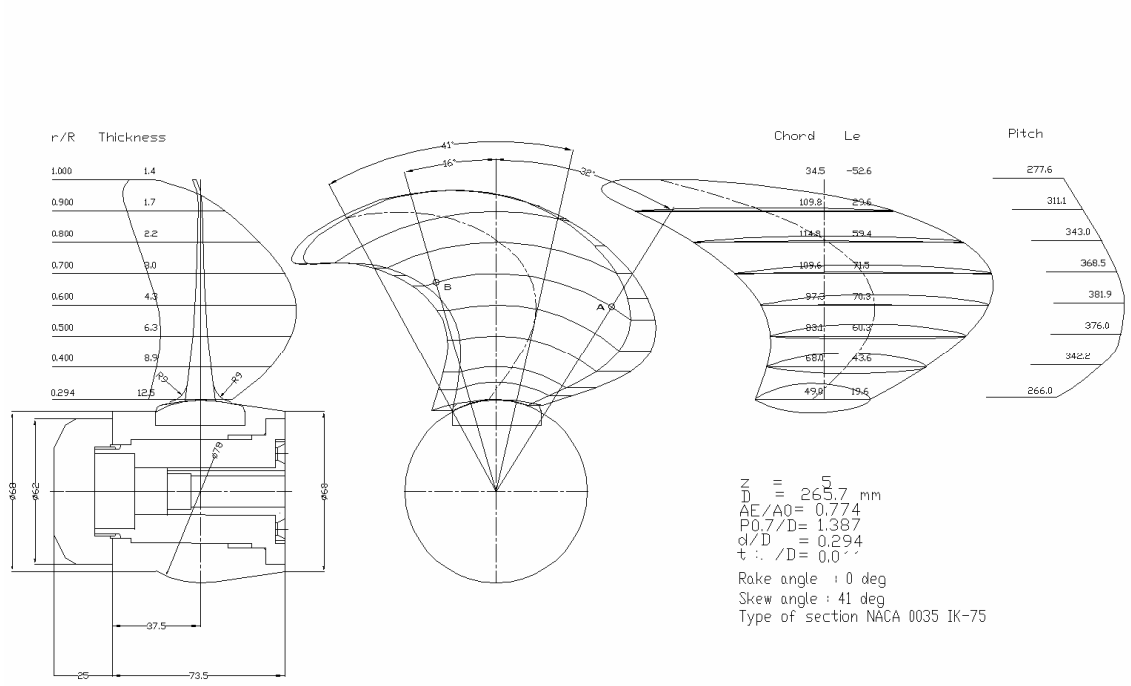

Figure 6 Geometry of the propeller CP6

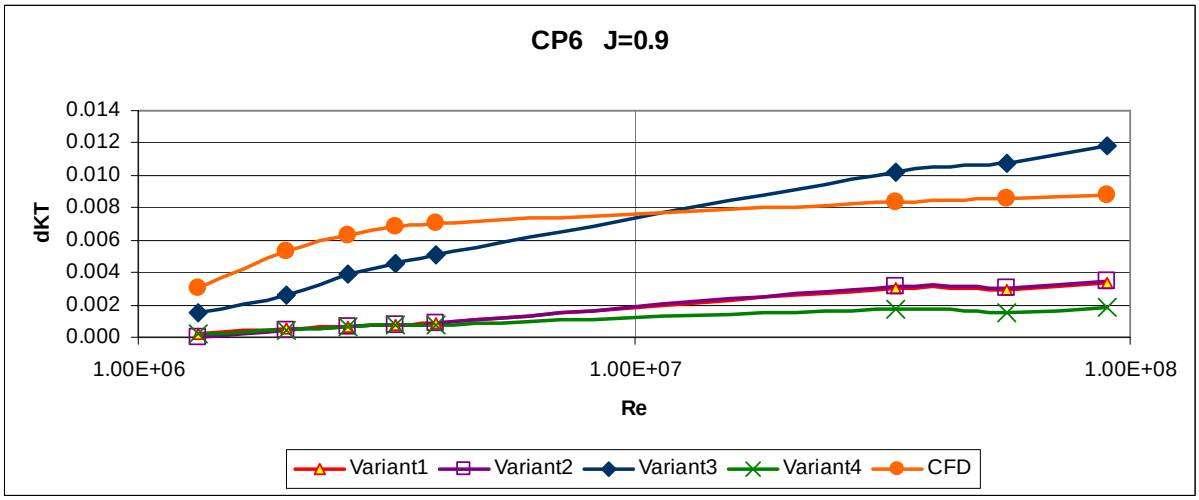

Figure 7 Results of calculations for the scale effect correction on the thrust coefficient of the CP6 (J=0.9)

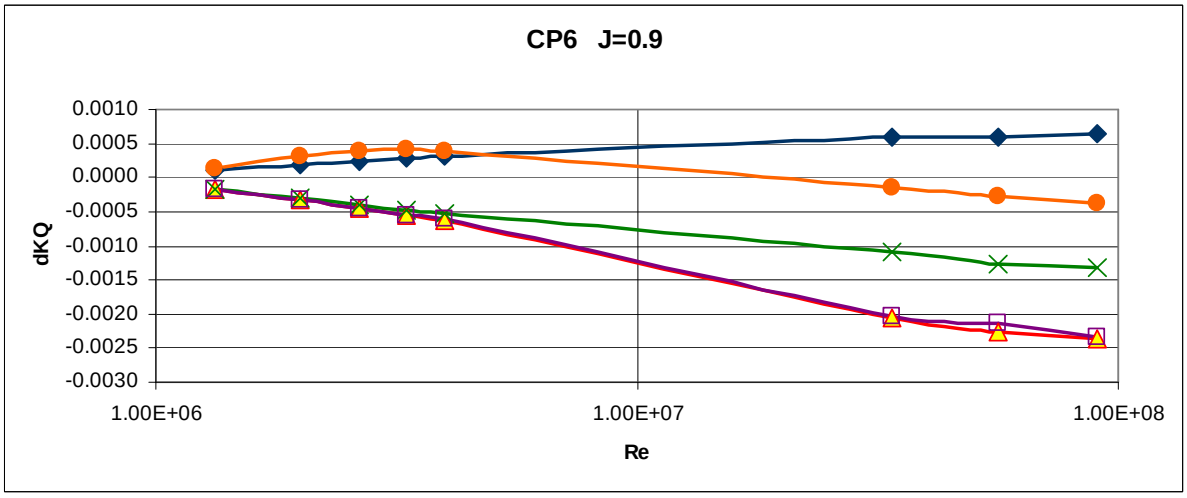

Figure 8 Results of calculations for the scale effect correction on the torque coefficient of the CP6 propeller (J=0.9)

The above presented research may be summarized with the following conclusions, assuming CFD results as the level of reference:

- classical ITTC78 formulae produce too small corrections for propeller thrust and too high corrections for propeller torque, effectively underestimating both these parameters in full scale; this may lead to the development of hydrodynamically "too heavy" propeller designs,
- classical ITTC78 procedure significantly overestimates the increase in propeller open water efficiency in full scale as compared with model scale; this may cause too optimistic predictions of ship powering performance,
- integration of ITTC78 corrections along the propeller radius does not produce visible changes in the results, even for highly skewed propellers; hence the original numerical coefficients included in Formulae 1 and 2 seem to be valid also for the highly skewed propellers,
- variant 3 based on alternative formulae for blade section lift and drag produces too high corrections for propeller thrust, but comparison with ITTC78 shows that some smaller scale effect on lift may need to be included in the scaling procedure in order to improve correlation of the thrust correction with CFD,
- alternative formula for blade section drag, employed in Variants 3 and 4, seems to predict scale effect corrections for torque much better than the original ITTC78 formula,
- the original formula (5), although formally not dependent on the Reynolds number, gives similar character of dependence of the scale effect corrections on propeller diameter in full scale as the alternative formula (6), which depends directly on Reynolds number; this is due to the relative blade surface roughness changing with scale.

Acknowledgements
The research presented in this paper was supported by the MARTEC II ERA-Network and the Polish National Centre for Research and Development (NCBiR)

References

[1] Bavin W.F. et al: Ship Propellers -Modern methods of calculations (in Russian), Izd. Sudostrojenije, Leningrad 1983
[2] Bugalski, T., Hoffmann, P. (2011): Numerical Simulation of the Interaction Between Ship Hull and Rotating Propeller. Proceedings of the Second International Symposium on Marine Propulsors, SMP'11, Hamburg, Germany, pp. 256-262
[3] Kuiper G.: The Wageningen Propeller Series MARIN Publ. No. 92-001, 1993
[4] Szantyr J.: Lift Based Propeller Scale Effect and its Influence on the Propulsive Characteristics of Ships, Trans. West Japan Society of Naval Architects, No. 84 (1992), str. 239-246
[5] Szantyr J., Centkowski J.: UPCA92 – the Lifting Surface Program for Hydrodynamic Analysis of Marine Propellers. Part II – Description of the Algorithm (in Polish), Raport IMP PAN Nr arch. 22/92

Resistance and Aerodynamic Performance Assessment for a Portuguese Indiaman of XVIth Century

Cosmin Ciortan, Det Norske Veritas, Veritasveien 1, 1322, Høvik, Norway, cosmin.ciortan@dnv.com
Nuno Fonseca, CENTEC, Instituto Superior Tecnico, Avenida Rovisco Pais, 1000-244, Lisbon, n.fonseca@mar.ist.utl.pt

Introduction The present work is focused on the hydrodynamics of the hull advancing with constant speed and it is the first step in a larger project whose intention is the better understanding of the sailing characteristics of ancient Portuguese ships. The focus of the present study is an early 17th century Portuguese Indiaman, a ship characterized by a very large beam to length ratio, a shallow keel that runs from bow to skeg and a relatively full underwater stern bodylines leading the flow to the rudder

1. THE INDIAMAN NOSSA SENHORA DOS MÁRTIRES

The East Indiaman *Nossa Senhora dos Mártires* (*NSM*) was probably built in the *Ribeira das Naus* shipyard, Lisbon, during the first years of the 17th century. The ship departed from Lisbon to India, on its maiden voyage, on the 21st of March 1605 and arrived at Goa on the 28th of September after a journey without incidents, for a short stay, and left for Cochim, to load the hold with peppercorns and other spices. On January 16th 1606, the loaded ship left Cochim to Lisbon. The voyage went without problems and it arrived near Lisbon in the middle of a severe Southwest storm on September the 13th. The ship dropped anchors outside the mouth of the Tagus River, but two days later the mooring cables broke and the captain decided to attempt entering the river. On the morning of September 15, *Nossa Senhora dos Mártires* touched the rocky bottom at the entrance of the Tagus Mouth in heavy following or stern quartering seas. The ship's hull was broken against the rocks in a matter of hours.

2. EXPERIMENTAL PROGRAM

2.1.Experimental set up and tested conditions

An experimental program was carried out at the El Pardo Model Basin (CEHIPAR) in Madrid, namely at the Still Water Tank, with the objective of assessing the hydrodynamic characteristics of the hull under steady sailing conditions. Regarding the model, it was wooden manufactured up to the main deck with a scale of 1:15 The model was tested with the rudder, as well as longitudinal strakes fixed to the hull sides and running from bow to stern (these strakes were installed on Portuguese Indiaman as part of the hull reinforcement. A moment has been imposed with a weight positioned forward of the center of floatation to simulate the longitudinal moment induced by the binary composed by the wind propulsion force and hydrodynamic resistance force.

3. NUMERICAL MODEL

3.1.Meshes for full scale simulations

The domain is discretized in control volumes using Star-CCM+' own grid generator. Trimmed meshes are used, with prism layers around the solid boundaries (in this case, the hull and rudder). Next to the bodies of interest, the mesh is finer, in order to assure an appropriate description of the free surface and avoid damping. On the other hand, in the far field, damping is desirable in order to avoid reflections from the boundaries, and therefore large cells are used.

The meshes have around 3 million cells, for full scale simulations. A symmetry boundary condition is used for the centreplane of the ship. The domain sizes are rather generous: 5L upstream, 6L downstream, 2L sideways and 1.5L depth. The mesh around the hull has about 250 cells/ship length in both model and full scale, which is deemed more than sufficient even for low Froude numbers. A fine discretization is also imposed in vertical direction. A detail of the mesh around the hull, for full scale model, is presented in Figure 1

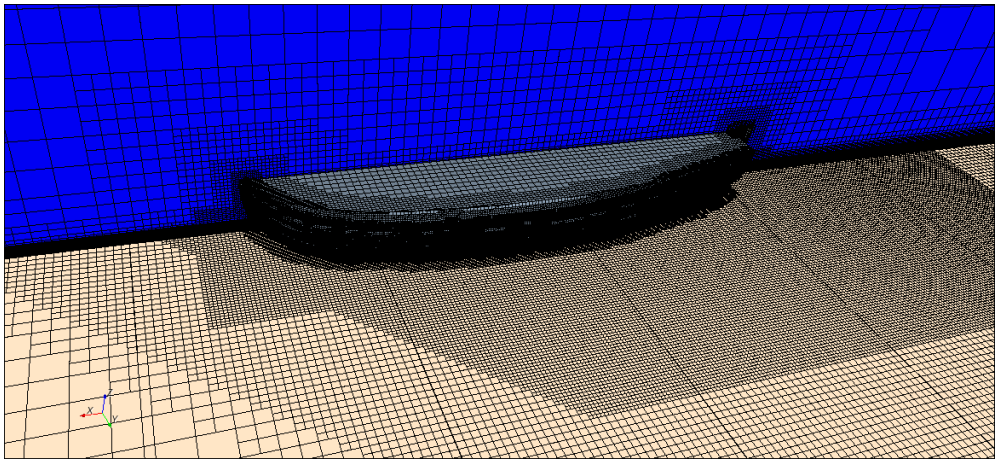

Figure 1 Mesh around the hull (detail)

For model scale simulations, the geometry of the boat is obtained by geometrically scaling the full scale geometry. In order to be as close as possible to the actual experiment, a trip wire is simulated, with the same dimensions as the one in the experiment (1 mm), but with a different shape (square as opposed to circular in the experiment, for practical purposes).
The number of cells for model scale simulations is about 1.1 millions. Again, the wall distance is tuned such as the y+ be about 50. A rough convergence study is performed, i.e., for one case, two other simulations, with wall distances of y+ ≈30 and y+ ≈100 were performed. The differences between the results were negligible.

4. RESISTANCE SIMULATIONS

The simulations carried out for assessing the resistance of the hull are split in two: full scale and model scale. In addition to the resistance curves, a sensitivity study on the influence of the rudder on the total resistance was performed with the captive model (i.e., no sinkage and trim allowed), for some of the speeds. The results are interesting in that the presence of the rudder is actually beneficial in terms of resistance, i.e., the improvement in wave resistance (due to the improvement of the wave profile in the aft part) is higher than the increase in viscous resistance. Only for 2 kn (where wave resistance is negligible, and therefore any improvement is negligible), and 10 kn (where the viscous resistance increases much more), the resistance respects the expect behavior. In Table 1, a comparison of the total resistance with and without rudder, for some of the velocities, is presented.

Speed [kn]	Without rudder	With rudder
2	1200	1230
4	4800	4600
6	10900	10760
8	20080	20160

Table 1. Hull resistance, with and without rudder

4.1 Full scale simulations

Full scale simulations, with the hull allowed to freely sink and trim, are performed for a range of speeds from 3 to 10 kn, in steps of 1 kn. The first step is to perform double body runs, in order to retrieve the form factor for extrapolating from model scale to full scale. In the model tests report, the value used is (1+k)=1.18. However, the results of the numerical simulations show much larger values (see Table 2), and these are the ones that will be used for calculations.

Speed [kn]	3	4	5	6	7	8	9	10
k	0,502	0,528	0,539	0,560	0,576	0,604	0,598	0,599

Table 2 Form factor as a function of hull speed

The full scale numerical simulations are obtained assuming a hydrodynamically smooth hull. Corrections must be made in order to account for hull roughness, appendages and air resistance. For consistency, the same procedure as the one described in the model tests report is applied. The extrapolated results from the model tests report are corrected with the difference between the form factor obtained using double body simulations and the one used in the towing tank's extrapolation. The results are presented in Table 3 and Figure 2.

Speed [kn]	3	4	5	6	7	8	9	10
Resistance 6DOF dynamometer [kN]	2,76	6,14	11,02	14,50	19,65	27,66	38,23	54,63
Resistance dynamometric bar [kN]	2,78	4,93	8,69	14,42	20,10	26,69	38,25	54,59
Numerical simulations [kN]	3,21	5,77	9,03	12,93	17,66	23,84	35,64	53,28

Table 3 Full scale resistance comparison, extrapolated model tests and numerical simulations

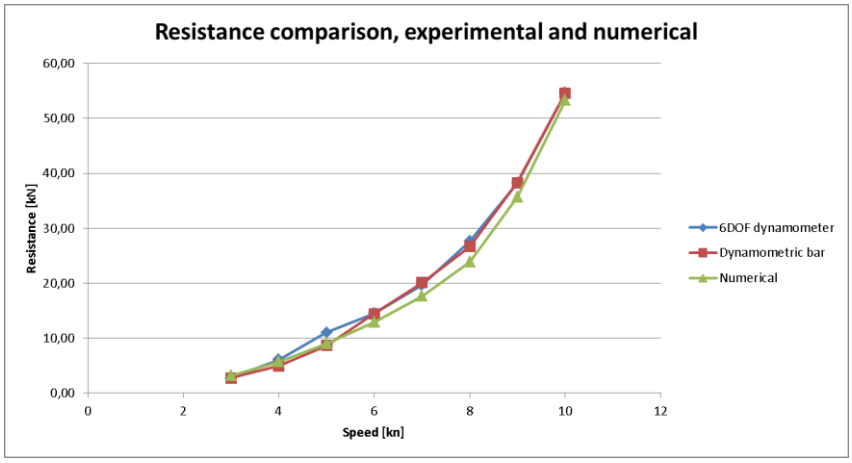

Figure 2. Full scale resistance comparison, experimental and numerical

The numerical results compare rather well against the experimental ones, especially given the complexity of the flow and the uncertainties in the geometrical correspondence between the numerical and the experimental hull. The most important differences refer to the position and size of the longitudinal strakes, and the size of the keel (though in this case, the differences are marginal).

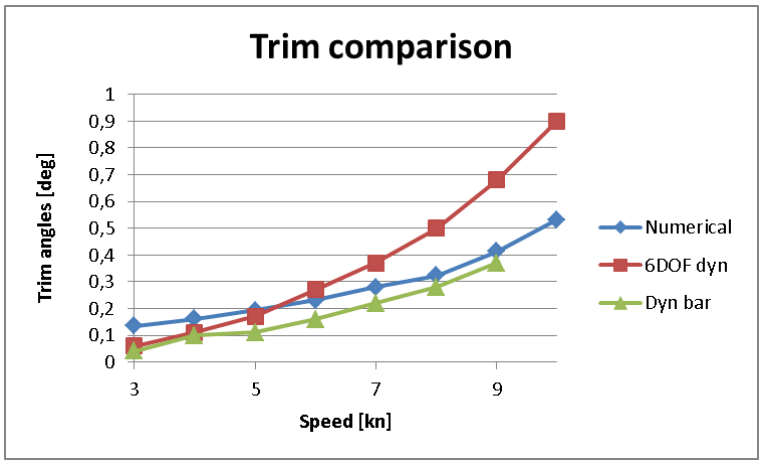

Figure 3 Trim comparison, numerical and experimental

In Figures 3 and 4, a comparison between the experimental and numerical sinkage and trim are presented. Again, the comparison is good. The numerical trim lays between the experimental data for most of the velocities, and close for the lower ones, while the sinkage values follow closely the experimental ones.

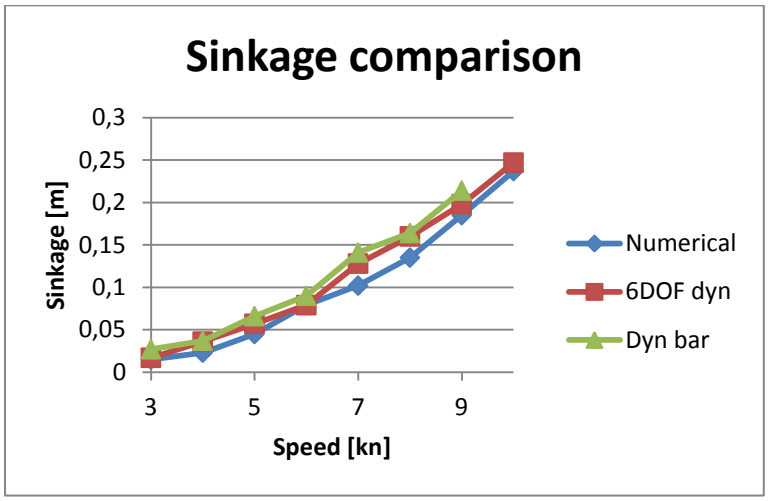

Figure 4 Sinkage comparison, numerical and experimental

4.2 Model scale simulations

Model scale simulations are performed using a somewhat simplified methodology, in that the model is fixed on the sinkage and trim retrieved from experiments. Thus, two sets of simulations, in steps of 2 kn, are performed for the results obtained with 6DOF dynamometer and with the dynamometric bar. The results are presented in Table 4 and Figures 5 and 6. Since the actual test conditions are reproduced, no other corrections are necessary.

Equivalent full scale speed [kn]	3	5	7	9	10
Resistance 6DOF dynamometer [N]	1.03	3.63	6.25		16.6
Numerical simulations 6DOF dynamometer [N]	1.3	3.66	7,16		17.86
Resistance dynamometric bar [N]	1.08	3.03	6.51	11.89	
Numerical simulations dynamometric bar [N]	1.44	3.76	7.14	13.24	

Table 4 Model scale resistance comparison, model tests and numerical simulations

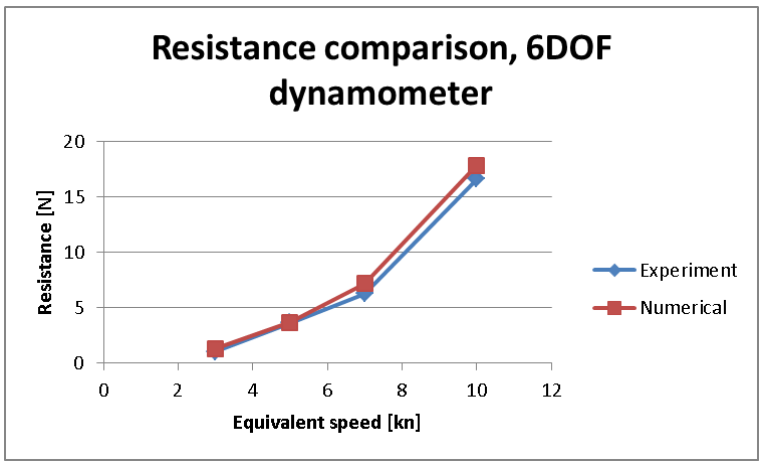

Figure 5. Model resistance comparison, experimental and numerical, 6DOF dynamometer

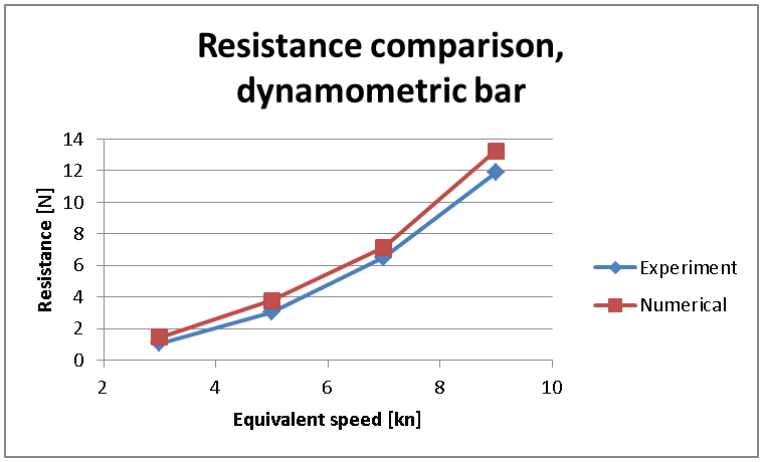

Figure 6. Model resistance comparison, experimental and numerical, dynamometric bar

The resistance comparison for model scale is good, more so for the 6DOF dynamometer than for the dynamometric bar. The reasons of the differences are unknown; the geometrical uncertainties should have the same relative effect in both cases. The meshes are almost identical, the only differences being the specific sinkage and trim.

5. AERODYNAMIC SIMULATIONS

The dimensions of the sails were determined from the lengths of the masts and yards, and are fairly consistent with the written sources. The total sail area is 1602 m^2. The speed of the wind is 15m/s

The free surface effects are neglected, i.e., a flat surface is used on the position of the free surface, which is common practice in the simulation of the around sails (more so if they are far enough from the free surface).

5.1 Aerodynamics results

The conditions for simulation (yards and wind angles) are presented in Table 5. Beta and Gamma represent the angles of the apparent wind and of the yards, respectively, with the longitudinal axis of the coordinates system.

Beta	50	60	70	80	100	120	180
Gamma	30	35	45	55	60	75	90

Table 5. Simulations conditions for aerodynamic study of the sails

The comparison in terms of drag and lift coefficients, with experimental results performed in the wind tunnel (Olsson, 2005), is presented in Figures 7 and 8

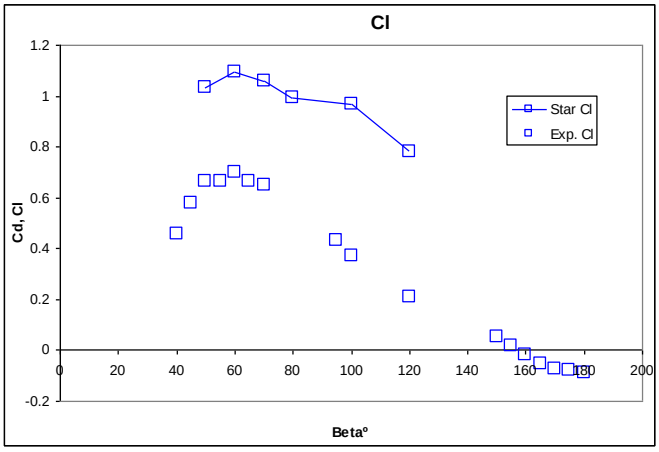

Figure 7. Lift coefficients for the nau, compared against Gothemburg results

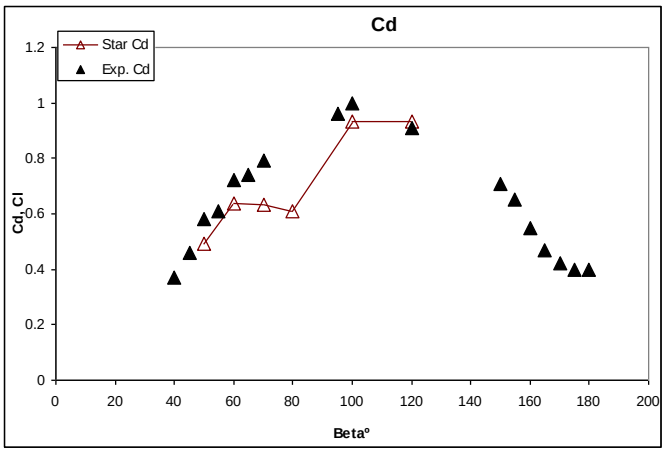

Figure 8. Drag coefficients for the nau, compared against Gothemburg results

6. CONCLUSIONS

In the present paper, a numerical study of the hydrodynamic characteristics with regard to resistance and sail plan of a 16th century Portuguese *nau* of the India Route is performed. The hull geometry is based on archaeological evidence from a wreck found in the Tagus River outside Lisbon and on naval architecture books of that period. The sail plan is reconstructed also from coeval documents. The shape of the sails is obtained using an empirical method.

The numerical study is performed using the commercial code Star-CCM+. Several preliminary studies of grid convergence, turbulence model sensitivity, and sails representation were performed in order to gain confidence in the quality of the results.

For the resistance comparison, a dedicated experimental tests programme was performed, and comparisons of the same conditions could be performed. The results agree well with the experiment, in both extrapolated full scale and model scale, in spite of the geometrical uncertainties. The dynamic sinkage and trim agree also well.

For the aerodynamic comparison, the results are consistent in the range of incidence angles that are studied and the values obtained for both lift and drag coefficients lie within the normal values for this kind of sails. A comparison with experimental data from wind tunnel tests with another historic ship is performed, with reasonable agreement; however, it is difficult to make a qualitative assessment of the results due to differences in the sail plan and above water hull, shape of the sails (in the numerical simulation, they are rigid) and the experimental setup (in the numerical simulations, no rigging or other ropes are present).

Prediction of hydrodynamic forces with and without transition model

Pierre-Luc Delafin, François Deniset, Jacques-André Astolfi
IRENav, Ecole navale, Lanveoc, CC-600, 29240 Brest cedex9, France
pierre-luc.delafin@ecole-navale.fr

Jean-Marc Laurens
ENSTA-Bretagne, 2 rue François Verny, 29806 Brest cedex9, France

1 Introduction

Sizing of ship appendixes such as rudders, propellers or stabilizers requires the accurate prediction of hydrodynamic forces and moments applied on these lifting bodies. Same requirements are needed in the domain of marine renewable energies. Correct prediction of marine current turbines performance is based on the accurate prediction of forces on the blades. One common problem encountered in the early stages of development of such devices is the difficulty to control the accuracy of the numerical prediction of forces for Reynolds close to the critical one. In these cases, laminar to turbulent transition can substantially influence the prediction. Laminar to turbulence transition occurs for Reynolds between 10^5 and 10^6. These transitional flows are frequently encountered on small appendixes encountered on ships at model scale or on full-scale small vehicles such as AUV's. Measurement of forces during model scale tests in towing tanks or hydrodynamic tunnels is often disturbed by transition inception and development which strongly modifies lift and drag values. In these cases, added rough stripes located on the ship bow or on the foil leading edge are commonly used, facilitating full-scale extrapolation procedure. However, consideration of transition in this critical Reynolds range still remains a problem for computational approaches, even if using recent versions of RANS CFD codes which propose different transition models based on the coupling between fully turbulent model and empirical transition correlations or transport equations [11], [10], [12].

The paper focuses on the influence of transition on prediction of forces on a NACA 66(mod)-312 hydrofoil at moderate Reynolds number Re = 7.5×10^5. The Menter $\gamma - Re_\theta$ two equations transition model is used [8]. The objective of this work is to identify when a laminar to turbulent transition model has to be activated to keep accurate forces predictions. First, a verification procedure is presented. Then, evolutions of global lift and drag coefficients and local pressure and friction coefficients are investigated. Finally, calculations and measurements obtained at constant angles of attack are compared to quasi-static and dynamic pitching results.

2 Experimental setup

The static foil calculations presented in this paper are validated by experiments carried out in the IRENav hydrodynamic tunnel. Dimensions of the test section are $1m \times 0.192m \times 0.192m$. The 0.15 m chord NACA 66(mod)-312 hydrofoil spans the entire width of the test section. Flow velocity is set as 5 $m.s^{-1}$ corresponding to Re = 7.5×10^5 and turbulence intensity has been measured to 3%. Lift and drag forces are measured by a 3 component hydrodynamic balance. Angles of attack range from 0° to 10° with an axis of rotation located at the quarter of the chord. Data acquisitions are led during 10s with a sample frequency of 1kHz.

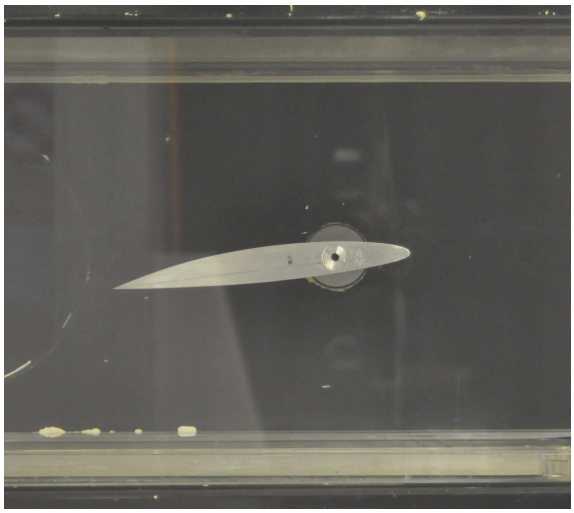

Figure 1: NACA 66(mod)-312 in the tunnel test section

3 Model and numerical methods

3.1 Geometry and mesh

The 2D computational domain has the height of the test section and extends 3 chords upstream and 6 chords downstream the 0.15m chord NACA 66(mod)-312 foil (Fig. 2). The O-4H grid is created and smoothed with ANSYS ICEM CFD. The foil is discretized by 742 nodes (Fig. 3) and the domain contains 160,000 quadrilateral elements. The mesh is voluntarily dense to capture accurately transition and detachment. Max y^+ is kept of the order of 1 during the simulations and the expansion ratios never exceed 1.2 in the region of the mesh close to the foil. The grid is extruded by one cell along the span direction to fit the 3D requirement of the solver.

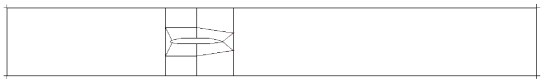

Figure 2: Mesh topology of the computational domain

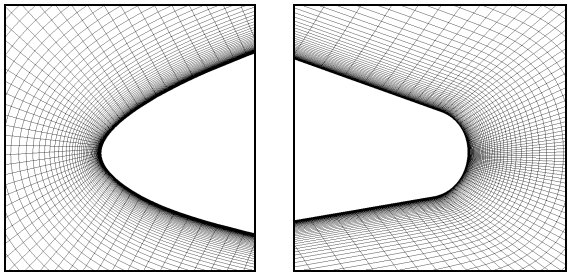

(a) (b)

Figure 3: High-density mesh (M2) close to the leading edge (a) and close to the trailing edge (b)

3.2 Model

The physical model is based on the mass and momentum conservation equations. The fluid is considered viscous and incompressible. The $k-\omega\ SST$ closure turbulence model used is known to predict better boundary layers submitted to adverse pressure gradients than other RANS turbulence models [9] [13]. The turbulence model is coupled with a two transport equations ($\gamma - Re_\theta$) transition model based on experimental correlations [8]. One equation is dedicated to intermittency (γ) which is used to turn on the production term of the turbulent kinetic energy downstream of the transition point.

$$\frac{\partial(\rho\gamma)}{\partial t} + \frac{\partial(\rho U_j\gamma)}{\partial x_j} = P_\gamma - E_\gamma + \frac{\partial}{\partial x_j}[(\mu + \frac{\mu_t}{\sigma_f})\frac{\partial\gamma}{\partial x_j}] \quad (1)$$

The second transport equation is for transition momentum thickness Reynolds number ($Re_{\theta t}$). This equation transforms non local empirical correlations into local quantities and allows the calculation of the transition length and the critical Reynolds number that are useful for the intermittency calculation.

$$\frac{\partial(\rho\overline{Re_{\theta t}})}{\partial t} + \frac{\partial(\rho U_j\overline{Re_{\theta t}})}{\partial x_j} = P_{\theta t} + \frac{\partial}{\partial x_j}[\sigma_{\theta t}(\mu + \mu_t)\frac{\partial\overline{Re_{\theta t}}}{\partial x_j}] \quad (2)$$

In the paper, calculations carried out with the fully turbulent $k-\omega\ SST$ model only will be referred as SST while those carried out with the $k-\omega\ SST$ model and the $\gamma - Re_\theta$ transition model will be referred as SST-TM.

3.3 Boundary conditions

Calculations are carried out in water (density ρ = 997 $kg.m^{-3}$, kinematic viscosity ν = 0.89 10^{-6} $m^2.s^{-1}$). The velocity inlet is set to 5 $m.s^{-1}$ so that the chord based Reynolds number equals 7.5 10^5 (c = 0.15 m). Inlet turbulence intensity is set to the experimental value of 3%. An *outlet* boundary condition with a 0 Pa static pressure is imposed on the outlet boundary. Lower and upper faces are set as *symmetry* since the hydrodynamic tunnel corresponding walls are slightly divergent to avoid a confinement effect due to the boundary layers development on these faces. Front and back faces are also set as *symmetry*. At last, a *wall* condition is imposed on the foil.

For pitching motion, the law defining the angular position of the foil is based on the characteristics of the electrical engine used in the corresponding experiments, presented in [3]. In this study, the foil executes a pitching motion between $\alpha = 0$ and $\alpha = 10°$ around an axis located at the quarter of its chord. The angular variation is linear excepted in the acceleration stage that last 0.08 s. Mesh deformation is performed so that small cells (i.e. near foil cells) are not distorted.

3.4 Numerical method

The problem is solved by the finite volumes method [5], using the CFD RANS based code CFX [1]. Continuity and momentum equations transient schemes are *Second order backward Euler* while the turbulent kinetic energy (k) and the turbulent eddy frequency (ω) transient schemes and all advection schemes are taken as *High Resolution*. *High Resolution* is a hybrid scheme between the first and the second order. A blending coefficient ensures a first order where convergence is difficult to provide robustness and a second order where convergence is easier to provide accuracy.

For pitching motion calculations with mesh deformation, conservation equations are resolved in an arbitrary referential with the ALE (Arbitrary Lagrangian Eulerian) formulation [7] [4].

4 Verification

The different meshes used to assess spatial convergence are displayed in table 1. Each of them have y^+_{max} close to 1 to agree with the $\gamma - Re_\theta$ transition model requirements [1].

Mesh	nb of cells	y^+_{max} (foil)	N_{foil}
M1	160,000	0.94	748
M2	102,000	0.67	424
M3	68,000	0.81	242
M4	31,500	1.75	230

Table 1: Grid resolutions and y^+_{max} values at AoA = 3°. N_{foil} is the number of nodes on the foil

4.1 Static calculations

4.1.1 Mesh refinement

Calculations are led with four different meshes at AoA=3° to evaluate spatial convergence. Table 2 displays lift and drag coefficients for mesh M1. C_L and C_D of meshes M2, M3 and M4 are expressed in percentage as the deviation from mesh M1.

	3°	
Mesh	C_L	C_D
M1	0.64875	0.007058
M2	-0.59%	+0.24%
M3	-1.86%	+1.26%
M4	-2.78%	+4.51%

Table 2: Mesh convergence for AoA = 3°

Table 2 shows that mesh M2 lead to less than 1% of deviation from mesh M1 while meshes M3 and M4 both lead to deviations higher than 1%. Spatial convergence is then considered reached for mesh M2.

4.1.2 Time step refinement

Three time steps are tested to assess the convergence. Table 3 shows that dt=10^{-3}s presents very little difference ($\ll$ 1%) with dt=5.10^{-4}s while dt=5.10^{-3}s leads to oscillations of C_L and C_D. dt=10^{-3}s is then chosen for the study.

	3°	
dt (s)	C_L	C_D
5.10^{-4}	0.64871	0.00706
10^{-3}	+0.006%	+0.001%
5.10^{-3}	$\pm$ 0.75%	$\pm$ 4.60%

Table 3: Time step convergence at AoA = 3°

4.2 Dynamic pitching calculations

Convergence and validation of calculation $\dot{\alpha} = 6°$/s have already been studied in [2]. The present dynamic pitching convergence study will then only focus on $\dot{\alpha} = 63°$/s.

Figure 4 shows the lift coefficient deviation between mesh M2 and mesh M1 (reference) expressed in percentage. Excepted an overshoot at the very beginning, both meshes lead to very similar results. Mesh M2 was then used in the dynamic study.

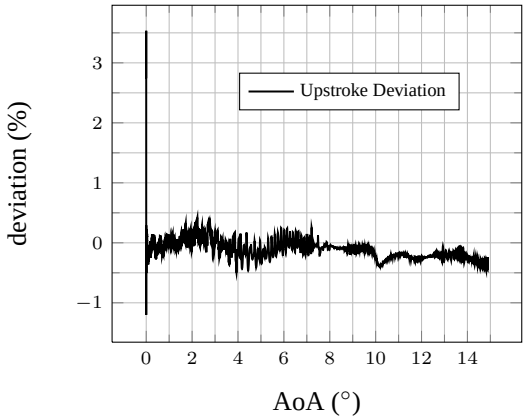

Figure 4: C_L deviation between M1 and M2

Time step convergence has been studied by Ducoin et al. [3] and a time step of 9.2×10^{-5}s was then adopted.

5 Results and discussion

5.1 Transition effect on C_L and C_D

Figure 5 (a) displays lift coefficients from 2D SST and SST-TM calculations, 3D SST-TM calculations and experiments. 2D SST-TM calculations follow the same trends as experiments, especially the plateau between 5° and 6° is well predicted. This plateau corresponds to the angle of attack when the laminar separation bubble (LSB), and then transition, moves from the trailing edge to the leading edge. However an offset exists between 2D-calculated and experimental C_L whereas 3D calculations correctly fit experimental values. 3D calculations take into account the 3D flow structures developing in the vicinity of the foil / side wall junction and that have a significant effect on forces because of the limited aspect ratio: $\frac{span}{chord} = \frac{0.192}{0.150} =$

1.28. 3D calculations carried out in this study assume a perfect junction between the foil and the side wall (i.e. no gap) and a horseshoe vortex then develops. 3D calculations meshes used a y^+ close to 1 for the side wall, as advised in [6] to accurately capture the horseshoe vortex. 2D SST calculations predict lower C_L than 2D SST-TM calculations from 0° to 6° and both predictions are then very similar.

Figure 5 (b) displays the corresponding drag coefficients of Figure 5 (a). Observations made for C_L are also true for C_D excepted that C_D predicted by the 2D SST calculations are higher than those predicted by the 2D SST-TM calculations from 0° to 6°. Then both C_D predictions are very similar. 3D calculations are in very good agreement with experiments.

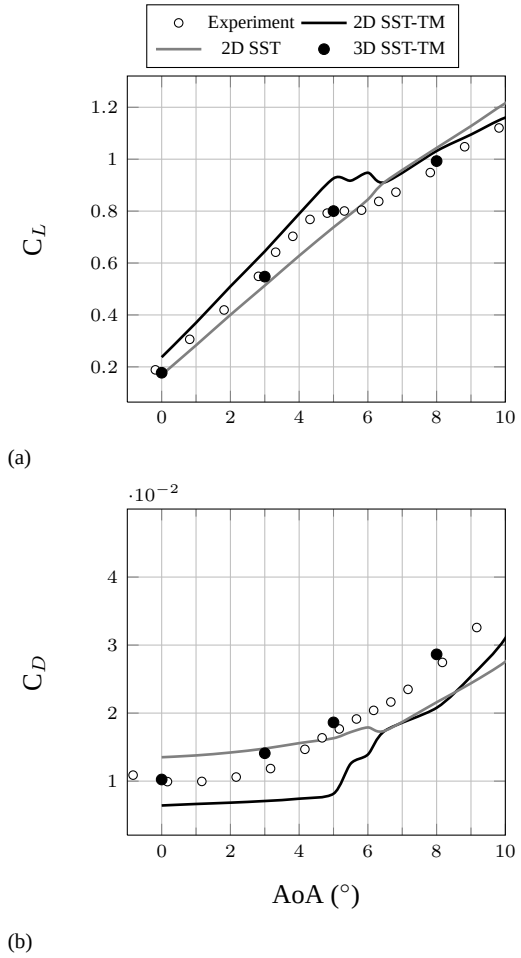

Figure 5: Experimental vs. numerical lift (a) and drag (b) coefficients, Re = 7.5×10^5

Differences observed on lift and drag coefficients between SST and SST-TM calculations from 0° to 6° come from the difference of boundary layer state prediction. SST turbulence model predicts a fully turbulent boundary layer whatever the angle of attack while SST-TM predicts the laminar separation bubble triggered transition and then takes into account the laminar part of the boundary layer. At an incidence of 3°, SST calculation predicts a C_L 20% lower and a C_D 110% higher than the SST-TM calculation. Figure 6 (a) displays the pressure coefficient distribution over the foil. The SST calculation leads to a lower inner area than the SST-TM calculation, what directly explains the difference of C_L. Low levels of friction coefficients (C_f) plotted on Figure 6 (b) corresponding to the SST-TM calculation indicate that the boundary layer remains laminar on a major part of the chord. Laminar separation bubbles are represented by the negative C_f close to the trailing edge. Considering the laminar to turbulent transition location as the closure of the LSB, transition occurs at x/c=0.8 on the suction side and the pressure side remains laminar. The LSB induces a pressure plateau right before x/c=0.8 on the SST-TM curve of Figure 6 (a). Beyond AoA=6°, the LSB moves from the trailing edge to the leading edge and the suction side boundary layer is turbulent over most of the chord. SST and SST-TM then lead to very similar C_L and C_D.

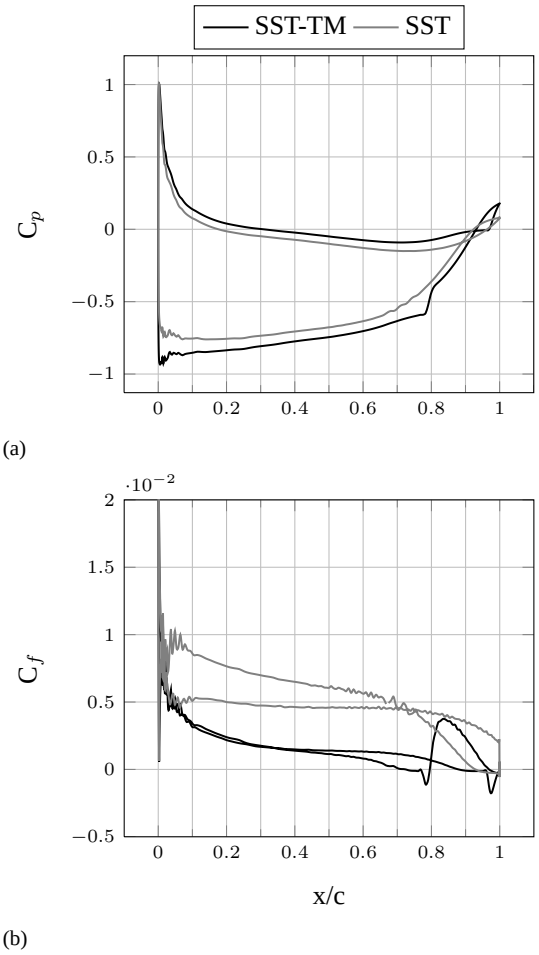

Figure 6: Pressure (a) and friction (b) coefficients at AoA = 3°

The differences observed on Figure 5 (a) are illustrated on Figure 7 as the C_L deviation from SST-TM calculation. Using a SST model instead of a SST-TM model leads to about 20 % of deviation from AoA=0° to AoA=5°. Deviation becomes close to 0 at AoA=6.5°. The SST-TM model is then relevant in this

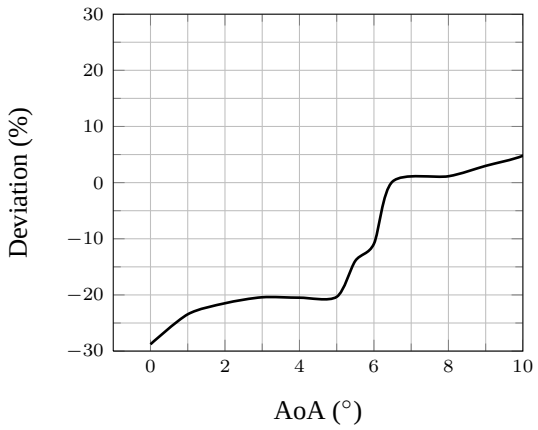

Figure 7: Deviation (%) of SST calculated values of C_L from SST-TM model, Re=7.5×10^5

range of incidences. From 6.5° to 10°, the deviation remains less than 5 % and SST calculation will be preferred because of its reduced CPU time requirement.

5.2 Dynamic pitching effect on C_L and C_D

In this section, previous calculations and experiments on a static foil are compared to pitching motion calculations. Two pitching velocities are studied: $\dot{\alpha}$ = 6 °/s corresponding to a reduced pitching velocity of $\dot{\alpha}^* = \frac{\dot{\alpha} \times c}{U_\infty} = 0.18$ and $\dot{\alpha}$ = 63 °/s corresponding to $\dot{\alpha}^* = 1.89$. Figure 8 shows the dynamic effects on lift and drag coefficients. The low pitching velocity ($\dot{\alpha}$ = 6 °/s) leads to C_L similar to static foil calculations excepted close to the angle of attack when the LSB moves from the trailing edge to the leading edge. Static calculations predict oscillating C_L at α = 5.5° and α = 6° and their averaged values form a plateau which is in good agreement with the experiment. However, pitching motion calculations predict a sudden move of the LSB from the trailing edge to the leading edge without intermediate oscillating states. Dynamic C_L remain higher than static ones until 1° after the beginning of the corresponding plateau and then rapidly decrease to reach static levels. High pitching velocity ($\dot{\alpha}$ = 63 °/s) delays the LSB upstream motion and C_L are then higher than static ones until 10°.

Drag coefficients plotted on Figure 8 (b) follow the same trends as lift coefficients. However, high pitching velocity drag coefficients are higher than static or low pitching velocity ones.

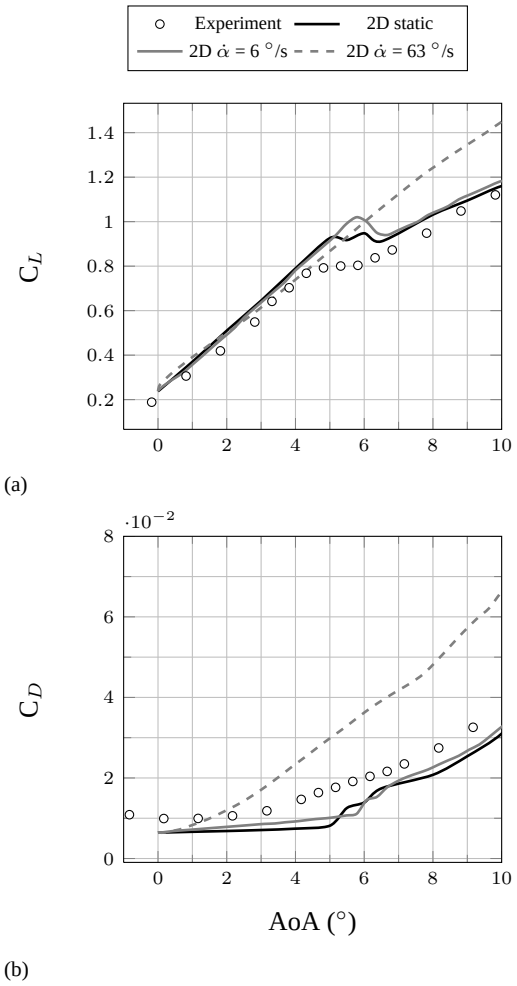

Figure 8: Experimental vs. numerical lift (a) and drag (b) coefficients with dynamic effect, Re = 7.5×10^5

6 Conclusion

Static and dynamic pitching calculations have been run on a NACA 66(mod)-312 at Re=7.5×10^5. $k-\omega$ SST turbulence model and $k-\omega$ SST $\gamma - Re_\theta$ transition model have been compared. Modeling the transition proved to be relevant for AoA $\in$ [0°,6°], or more generally for angles of attack with a laminar separation bubble located close to the trailing edge: SST calculations predict C_L 20% lower and C_D 110% higher than SST-TM calculations, which is in good agreement with the experiments carried out in the IRENav hydrodynamic tunnel. Beyond 6°, SST and SST-TM calculations predict very similar lift coefficients and SST is then sufficient. Pitching motion influence on lift and drag coefficients has been evaluated. A low pitching velocity leads to results very close to those of a static foil excepted the C_L plateau which is replaced by a decrease of C_L occurring 1° after the beginning of the static calculations plateau. A high pitching velocity generates a 15% higher C_L than low pitching velocity and static foil calculations between 6° and 10°.

References

[1] Ansys. *Ansys CFX Solver Modeling Guide*, volume 12. Ansys, 2009.

[2] P.L. Delafin, F. Deniset, and J.A. Astolfi. Influence of transition on hydrofoil fluctuating forces prediction. In *Proceedings of the 14th Numerical Towing Tank Symposium*, 2011.

[3] A. Ducoin, J.A. Astolfi, F. Deniset, and J.F. Sigrist. Computational and experimental investigation of flow over a transient pitching hydrofoil. *European Journal of Mechanics - B/Fluids*, 28(6):728–743, 2009.

[4] C. Farhat, M. Lesoinne, and P. Le Tallec. Load and motion transfer algorithms for fluid/structure interaction problems with non-matching discrete interfaces: Momentum and energy conservation, optimal discretization and application to aeroelasticity. *Computer Methods in Applied Mechanics and Engineering*, 157(1–2):95–114, 1998.

[5] J. Ferziger and M. Peric. *Computational methods for fluid dynamics*. Springer New York, 2002.

[6] A.M. Levchenya, E.M. Smirnov, and V.D. Goryachev. Rans-based numerical simulation and visualization of the horseshoe vortex system in the leading edge endwall region of a symmetric body. *International Journal of Heat and Fluid Flow*, 31:1107–1112, 2010.

[7] N. Maman and C. Farhat. Matching fluid and structure meshes for aeroelastic computations: A parallel approach. *Computers & Structures*, 54(4):779–785, 1995.

[8] F. Menter, R. Langtry, and S. Volker. Transition modelling for general purpose cfd codes. *Flow, Turbulence and Combustion*, 77:277–303, 2006.

[9] F. R. Menter, M. Kuntz, and R. Langtry. Ten years of industrial experience with the SST turbulence model. In K. Nagano Y Hankjalic and M. Tummers, editors, *Turbulence, Heat and Mass Transfer 4*, 2003.

[10] A. Shelton, J. Abras, B. Hathaway, M. Sanchez-Rocha, M.J. Smith, and S. Menon. An investigation of the numerical prediction of static and dynamic stall. In *61 American Helicopter Society Anual Forum*, 2005.

[11] M.J. Smith, T.C. Wong, M. Potsdam, J. Baeder, and S. Phanse. Evaluation of cfd to determine two-dimensional airfoil characteristics for rotorcraft applications. *American Helicopter Society*, 2004.

[12] D.K. Walters and D. Cokljat. A three-equation eddy-viscosity model for reynolds-averaged navier-stokes simulations of transitional flow. *Journal of Fluids Engineering*, 130:1–14, December 2008.

[13] S. Wang, D.B. Ingham, L.Ma, M. Pourkashanian, and Zhi Tao. Numerical investigations on dynamic stall of low reynolds number flow around oscillating airfoils. *Computers & Fluids*, 39(9):1529–1541, October 2010.

Geometric Modelling for Optimisation of Propeller Hub Caps

Markus Druckenbrod[1, 2], Lars Greitsch[3], Sven Bednarek[2], Stephan Berger[2], Moustafa Abdel-Maksoud[2]

[1]Markus.Druckenbrod@tu-harburg.de
[2]Hamburg University of Technology (TUHH), Hamburg, Germany
[3]Mecklenburger Metallguss GmbH (MMG)

INTRODUCTION

Increasing propulsion efficiency, especially for merchant ships, has been a central concern in the field of ship hydrodynamics over the last couple of decades. This development has been further motivated by the volatile oil market.

Additional concerns, such as vibration levels in passenger ships and noise emission in the oceanic environment, have become increasingly important.

For this reason, the maritime industry (including suppliers) is very interested in the detailed optimisation of propeller and rudder elements, which are known sources of vibration noise.

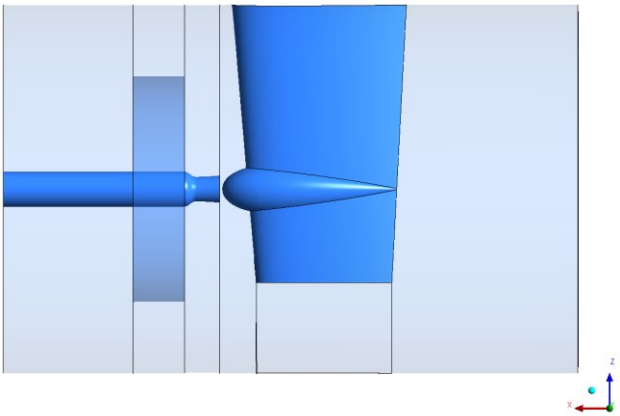

Figure 1: Optimisation domain

1 Overview

Hub caps have been investigated for a number of reasons: In some cases, an overview of the hub cap effects and its simulation by numerical methods has been given [1], and in other cases, the hub cap influence itself has been surveyed via numerical calculations [2].

The work presented in this paper is part of the project BossCEff, which aims to develop propeller hub caps under consideration of the whole propulsion system, including propeller, rudder and costa bulb, and is funded by the German Ministry of Economy and Technology (BMWi).

In order to find suitable hub cap geometries, we develop an optimisation process that includes the parametric definition and generation of the geometry, the mesh generation and the numerical calculation of the propulsor performance. An optimisation algorithm is applied to automatically vary the geometries. This means that all the steps mentioned also have to work automatically.

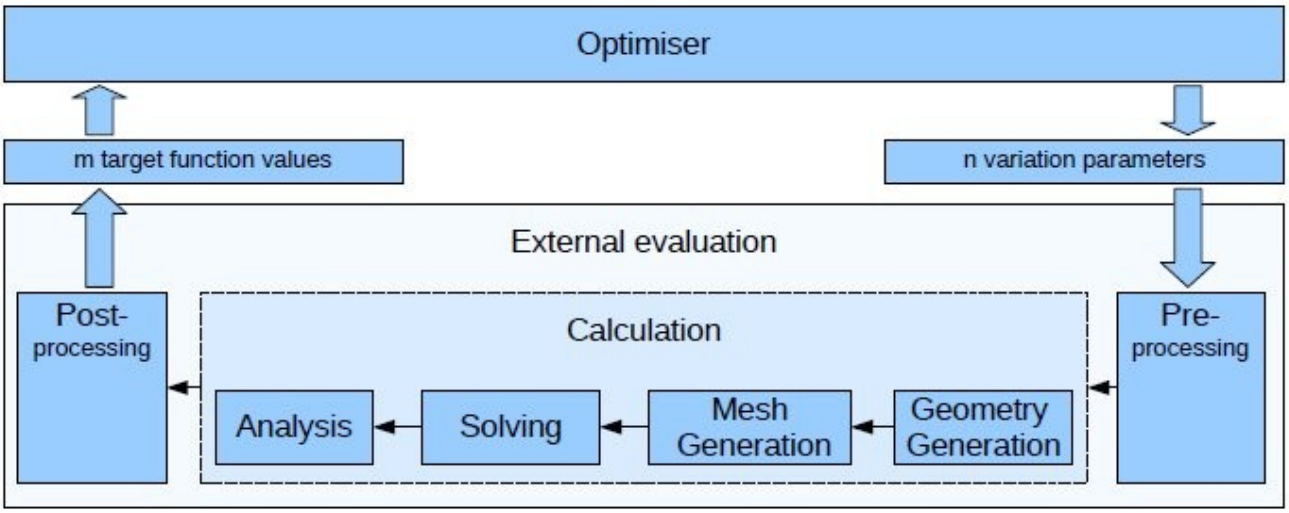

Figure 2: Optimisation Process

	one-piece		two-piece		one-piece		two-piece	
	1	2	3	4	5	6	7	8
$f(x=0)$	$=r_{shaft}$	$=r_{shaft}$	$=r_{shaft}$	$=r_{shaft}$	$=r_{shaft}$	$=r_{shaft}$	$=r_{shaft}$	$=r_{shaft}$
$f(x=x_I)$	$=r_{middle}$	$=r_{middle}$	$=r_{middle}$	$=r_{middle}$	$=r_{middle}$	$=r_{middle}$	$=r_{middle}$	$=r_{middle}$
$f'(x=0)$	$=0$	$=0$	$=0$	$=0$	$\neq 0$	$\neq 0$	$\neq 0$	$\neq 0$
$f'(x=x_I)$	$=0$	$\neq 0$	$=0$	$\neq 0$	$=0$	$\neq 0$	$=0$	$\neq 0$
$g(x=x_I)$	---	---	$=f(x_I)$	$=f(x_I)$	---	---	$=f(x_I)$	$=f(x_I)$
$g(x=x_E)$	---	---	$=r_{end}$	$=r_{end}$	---	---	$=r_{end}$	$=r_{end}$
$g'(x=x_I)$	---	---	$=f'(x_I)$	$=f'(x_I)$	---	---	$=f'(x_I)$	$=f'(I)$
$g'(x=x_E)$	---	---	$=0$	$\neq 0$	---	---	$=0$	$\neq 0$
Order $f(x)$	3rd	2nd	3rd	2nd	2nd	1st	2nd	1st
Order $g(x)$	---	---	3rd	2nd	---	---	3rd	2nd

Table 1: Detailed description of all geometry types

This paper presents an overview of the whole process while focussing on the following: 1) the reduction of the geometry model information for the numerical setup of the optimisation process, 2) the geometry definition and 3) the grid generation. Especially the two last aspects are a challenge if they are to work without manual intervention.

2 Optimisation

An overview of the entire optimisation process is given in Figure 2. The starting point is the optimiser. It enables the automatic and efficient variation of the geometry with the goal of improving its flow characteristics ([3] and [4]). Thus, all other steps mentioned, such as geometry and grid generation and calculation, need to perform automatically. An optimisation algorithm varies the free parameters (i.e. variation parameters), and via the calculation method, receives the calculated results of the

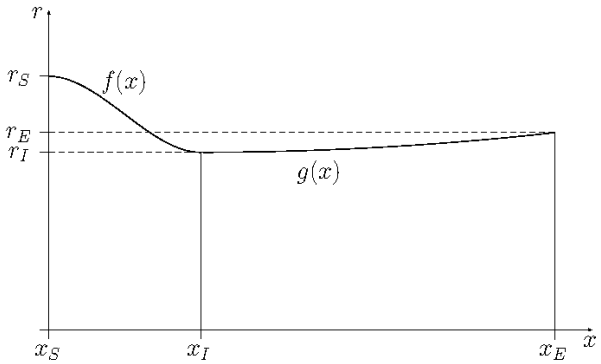

Figure 3: Parameters of two-piece geometry

geometries (i.e. target function values). In a first step in our attempt to optimise the efficiency of the whole propulsion system, the axial force on the hub cap surface is used as a target function value; however, an extension to other function values, such as the force on rudder geometry, can easily be integrated and, as such, is the next step.

The optimisation algorithm package DAKOTA (specifically, the Multi Objective Genetic Algorithm (MOGA)), from Sandia National Laboratories is used in the work presented [5]. A genetic algorithm (GA) uses the theory of natural evolution to find correlations between the variation of the free parameters and the results of the calculation method [6].

3 Parameterisation and geometry generation of the hub cap

In order to achieve an efficient optimisation, the number of free parameters needs to be minimized while the freedom of the geometry variation is simultaneously maximized. In regards to parametrical optimisation, analytic functions have been a consistent approach.

The current work is concerned with the optimisation of an axis-symmetric propeller hub cap geometry and aims to reproduce two major geometry types: 1) one-piece geometry and 2) two-piece geometry (see Figure 3).

The basic idea is, on the one hand, to use a single geometry description which is able to display all geometry categories and thus allow high flexibility; and on the other hand, to generate geometries that are feasible from a hydrodynamic point of view.

Thus, a two-piece description of the geometry consisting of two independent functions has been selected, both of which are up to third-order polynomials:

- $y_1 = f(x) = ax^3 + bx^2 + cx + d$
- $y_2 = g(x) = ex^3 + fx^2 + gx + h$

They enable enough geometries while being manageable without unacceptable geometry overshoot. As a third-order polynomial with four unknowns, four boundary conditions are needed. In the case of a one-piece geometry, the second polynomial is deactivated.

For parameterised boundary conditions, function values describing the radius of the boss cap at a given point x ($y_1 = f(x)$ and $y_2 = g(x)$) as well as their derivations

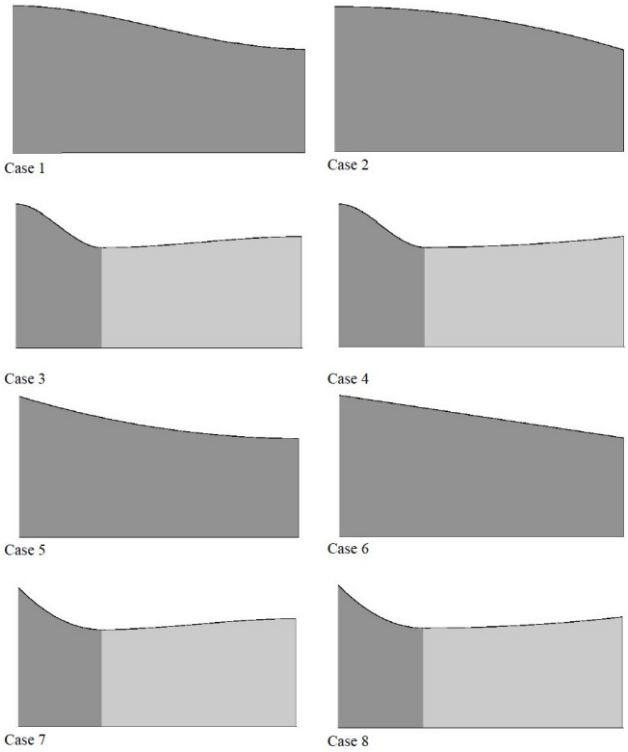

Figure 4: Examples for all eight geometry types (see Table 1)

($y'_1 = f'(x)$ and $y'_2 = g'(x)$) are available. Further, for the function value, there are three important x-positions:

- $x_S = x_{shaft}$
- $x_I = x_{intersection}$
- $x_E = x_{end}$

Up to five parameters are defined as free parameters:

- Type of geometry (see Table 1 and Figure 4)
- x_I
- x_E
- r_{middle}
- r_{end}

In addition to the major geometry types of one-piece and two-piece, there are two more type differences: $f'(x = 0)$ and $f'(x = x_I)$ equal or unequal to zero. The properties of all eight geometry types are summarized in Table 1 and Figure 4.

For each derivation unequal to zero, the order of the relative polynomial is reduced by one. The lack of boundary information can thereby be compensated for. This results in the fact that extreme values are only possible at the endings and not in between.

Thus, for two-piece geometries, the first polynomial can be of a 1st, 2nd or 3rd order, while the second polynomial, if existing, can only be of a 2nd or 3rd order. With the given order of the polynomials and a sufficient number of boundary conditions, the geometry of the axis-symmetric hub can be generated by inserting the polynomial coefficients at a given number of x-positions and hence be exported in discrete points. In order to represent the hub contour precisely, the distance dx, and therewith the spacing, is variable. Large changes in geometry have to induce fine spacing and thus dx is a function of $f'(x)$. Assuming a linear derivation, dx is calculated as follows:

$$dx_i = \sqrt{\frac{s^2}{f'(x_i)^2 + 1}} \qquad (1)$$

where i is the counter of the discrete points and s is a global variable which sets an average value for dx and is calculated as follows:

$$s = \frac{x_e}{m} \qquad (2)$$

where m is an approximated number of points.

The geometry is then exported by point data, and imported into the commercial cad and meshing program ANSYS ICEM 12.0 where it is generated. All ANSYS ICEM 12.0 operations are done with ICEM macro operations controlled by so-called replay scripts [7].

4 Calculation methods

The integration of computational fluid dynamics (CFD) into an optimisation process invariably leads to the question of required calculation time. In some cases, an optimisation process can require hundreds of calculated geometries. Seen from this perspective, the calculation time would need to be minimized by using a fast and reliable calculation method. However, the flow around a propeller boss cap is highly turbulent, meaning that highly detailed calculation tools are required. Therefore, a compromise approach which considers both aspects is

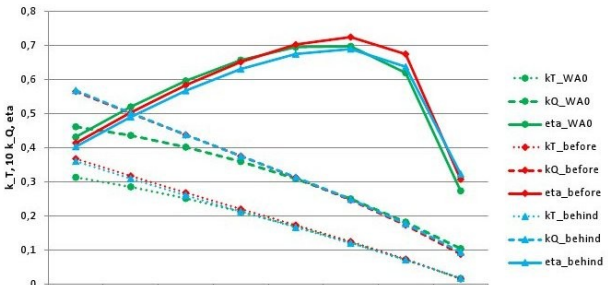

Figure 5: Propeller performance diagram

presented in the following.

4.1 Calculation Method for potential theory flows

The first calculation tool is the in-house panel code *pan*MARE (see [8]) of the Institute for Fluid Dynamics and Ship Theory at the Hamburg University of Technology. *pan*MARE has been specifically developed for the simulation of propeller flows and is based on potential theory. It is a boundary element method based on a three-dimensional low-order panel method.

4.2 Calculation Method for viscous flows

As the second calculation method, the commercial flow RANS solver ANSYS CFX (see [9]) for viscous flows is

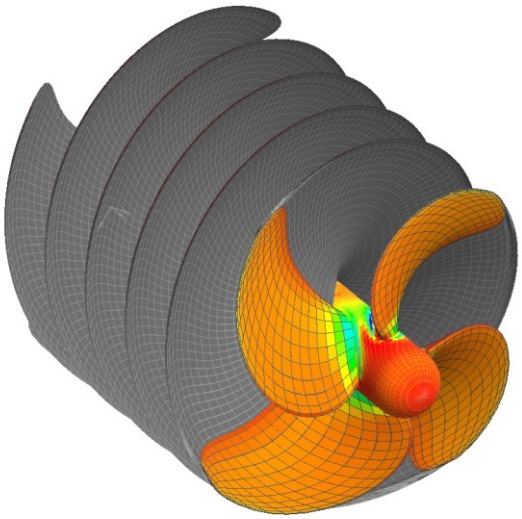

Figure 6: Surface grid of the propeller for *pan*MARE

used.

4.3 Propeller Model

Potential flow methods are able to calculate the flow characteristics on the propeller blade with acceptable accuracy, but it is not possible to calculate the flow behind the hub cap. Viscous flow methods deliver relatively more accurate numerical results than potential flow methods. For a concise yet sufficiently quick calculation it is necessary to combine the advantages of both methods. The potential flow method can be used to calculate the flow on the propeller blade and the viscous flow method can be applied to calculate the flow on the hub and the hub cap under consideration of the propeller thrust and torque.

As such, the basic idea of the propeller model is to

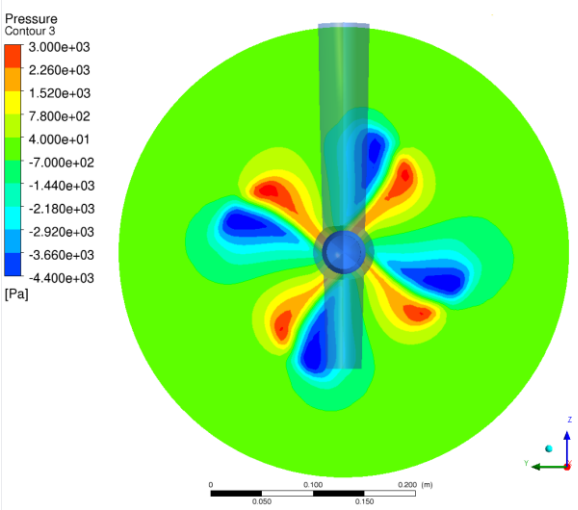

Figure 7: Body forces representing the propeller geometry visualised by a pressure plane

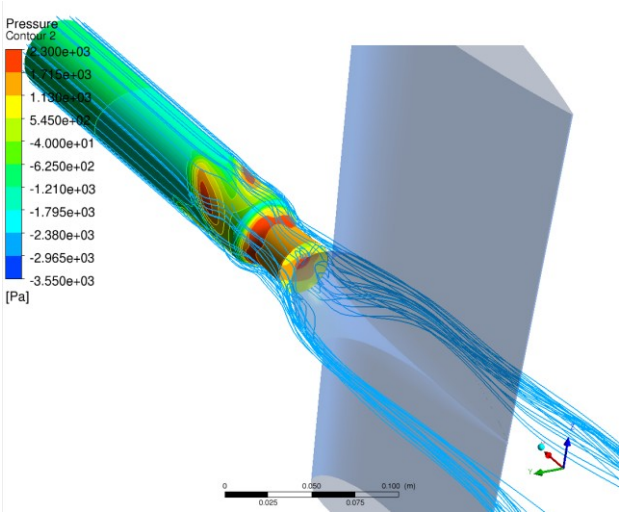

Figure 8: Influence of the propeller model on the flow

combine the methods mentioned above for viscous and for potential theory flows. The propeller is simulated with the calculation method for potential theory flow *pan*MARE. The results are sent to the calculation method for viscous flows. For this purpose, the pressure values on each panel are transformed into body forces and imported into ANSYS CFX by adding them to the source term of the time-averaged Navier-Stokes equations. Hence, the propeller geometry does not need to be reflected in the volume mesh for the calculation method for viscous flow, resulting in a marked reduction in grid size and therewith in calculation time. For more information on the coupling procedure see [10], [11] and [12].

5 Grid generation

The mesh generation process has to run automatically for an optimisation. The optimisation process presented here contains two different flow simulation theories which have their own requirements for the grid generation.

Calculation methods for potential theory need a surface grid, and in this work, the propeller and hub geometry meshes are also generated by the in-house code *pan*MARE. The propeller geometry mesh is visualised in Figure 7.

In contrast, the viscous flow solver ANSYS CFX requires a volume mesh, and hence the grid generation is carried out with ANSYS ICEM 12.0 [7] replay scripts.

A cylindrical domain is used for the optimisation, and consists of a number of single domains (shown in Figure 1). All domains are connected via interfaces with their neighbour domains. The interface between hub cap and rudder domain is located at the end position of the hub cap. As such, not only the variable geometry of the hub but also the constant geometry of the rudder has to be meshed automatically. The reason for this is that the dimension of the rudder grid domain is adjusted according to the hub cap length.

6 Case Study

The performance of propeller boss caps is strongly influenced by the presence of other propulsion elements such as the propeller and rudder. Therefore, this study considers propeller and rudder geometries in addition to that of the boss cap, although only the propeller boss cap geometry is varied. The optimisation domain, including the geometry of the propeller shaft, propeller hub cap and rudder, is shown in Figure 1.

6.1 Geometry of the propeller

The propeller geometry used here was developed for the KRISO Container Ship – KCS (Korean Research Institute of Ships and Ocean Engineering - KRISO). The main dimensions and characteristics of the propeller in model and full scale are summarized in the following table:

Dimension	Full scale	Model scale
Number of blades	4	
Diameter	8100 mm	265.3 mm
Hub radius	675 mm	21.4 mm
Pitch ratio r/R=0.7	1.04802	
Area ratio	0.69	
Scale factor	1	31.6

Table 2: Propeller characteristics and dimensions

6.2 Geometry of the rudder

Instead of the KCS standard rudder, a hanging rudder with a non-twisted geometry is used (see Figure 1 and Figure 8) in the optimisation. Further, the rudder geometry is equipped with a costa bulb positioned at the vertical height of the propeller shaft. The distance between the nose of the costa bulb and the end plane of the hub cap is restricted by the grid structure, resulting in a certain minimum distance.

6.3 Operation point

For validation reasons, all calculations are done in model-scale and will be carried out in full-scale. The operation point is at 24 kn and 90.42 number of revolutions. The calculations are carried out for a wake coefficient of 0.24.

It is important to validate the applied numerical methods with respect to the aim of the study before starting the optimisation. The BossCEff project also includes some model tests which are used for validation calculations. They are carried out by the project partner *Potsdam Model Basin* (SVA). Figure 4 Case 4 shows the hub geometry used for the model tests as well as for the validation calculations.

6.4 Application

As mentioned above, in addition to the hub cap, the propeller, the propeller shaft, and the rudder including costa bulb are considered. Propeller shaft, rudder and propeller hub cap are directly calculated in ANSYS CFX, while the propeller geometry is simulated in *pan*MARE and its data is transferred and imported into ANSYS CFX by the propeller model. Only validation calculations are presented in this paper.

In Figure 7, the effect of the propeller model is visualised by a pressure plot in the propeller plane. The upper images in Figure 9 and Figure 10 show the hub vortex induced by the propeller model without a rudder influence. Here the hub vortex is fully developed. The influence of the propeller-induced forces on the pressure on the hub and hub cap as well as on the progress of the stream lines is shown in Figure 5.

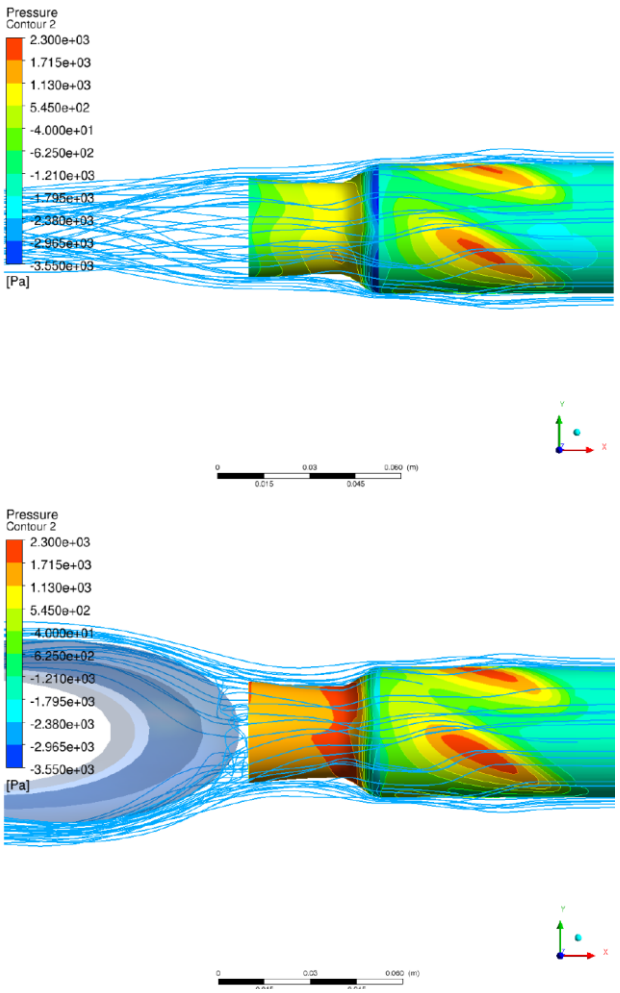

Figure 9: Influence of the costa bulb / rudder on the hub vortex (standard view incl. trailing edge of the rudder)

Figure 8 and the lower image of Figure 9 demonstrate the importance of taking rudder geometry into account.

The influence of the added forces imported by the propeller model is shown in Figure 8. In addition to the pressure on the propeller shaft and its hub cap, the streamlines near the hub cap are also visualised. The streamlines provide a clear image of the hub vortex. Figure 5 and Figure 9 show that the propeller model is able to represent the propeller in a sufficient way. Figure 9 illustrates the stream lines around the propeller hub. Especially the influence of the costa bulb on the hub vortex can be observed.

7 Conclusion and future work

Integrating CFD into an optimisation process is an effective approach for improving complex geometries with advanced flow conditions. Compared with the

conventional role of CFD, that is, recalculation, the optimisation process offers new challenges which have presented in the current work.

A next step would be to test all the elements of the optimisation process as a whole. In a further step, all the components of the optimisation process should be tested together. Subsequently, the various aspects of an

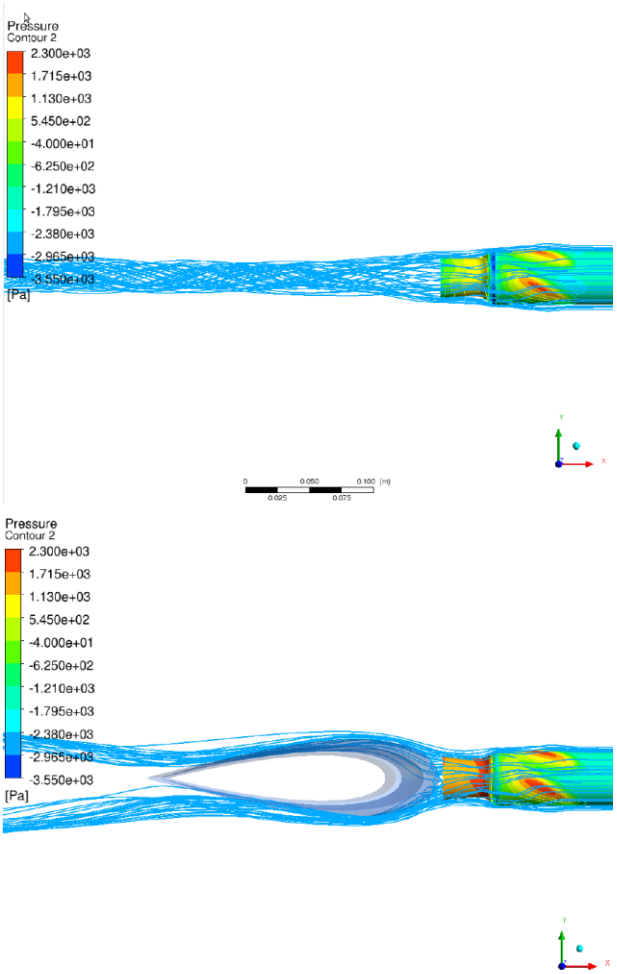

Figure 10: Influence of the costa bulb / rudder on the hub vortex (detailed view of the leading edge)

extension should also be targeted. In addition to the variation of the costa bulb geometry, the hub cap fins could be added to the propeller hub cap geometry.

REFERENCES

[1] Junglewitz, A., *Der Nabeneinfluss beim Schraubenpropeller*, Ph.D. thesis, The University of Rostock, Rostock, Germany, 1996.

[2] Abdel-Maksoud, M., et al., *Numerical and Experimental Investigation of the Hub Vortex Flow of a Marine Propeller*, 25th Symposium on Naval Hydrodynamics, St. John's, Newfoundland and Labrador, Canada, 2004.

[3] Abdel-Maksoud, M., et al., *Design of a Multi-Component Propulsor*, 28th Symposium on Naval Hydrodynamics, Pasadena, USA, 2010.

[4] Abdel-Maksoud, M., et al., *Optimisation of Single and Multi-Component Propulsors*, 9th International Conference on Computer Applications and Information Technology in the Maritime Industries (COMPIT '10), Gubbio, Italy, 2010.

[5] NN. Design Analysis Kit for Optimization and Terascale Applications - DAKOTA, *DAKOTA Documentation*, Sandia National Laboratories, Livermore, USA, 2012.

[6] Meyer, D., *Modellbasierte Mehrzieloptimierung mit Neuronalen Netzen und Evolutionsstrategien*, Ph.D. thesis, Ilmenau University of Technology, Ilmenau, Germany, 2004.

[7] NN. ANSYS ICEM 12.0, *ICEM Documentation*, ANSYS Inc., Canonsburg, USA, 2010.

[8] *pan*MARE project website, http://panmare.de.

[9] NN. ANSYS CFX 12.0, *CFX Documentation*, ANSYS Inc., Canonsburg, USA, 2010.

[10] Berger, S., Druckenbrod, M., Greve, M., Abdel-Maksoud, M., Greitsch, L., *An Efficient Method for the Investigation of Propeller Hub Interaction*, Proceedings of the 14th Numerical Towing Tank Symposium, Poole, U K, 2011

[11] Greve, M., Wöckner-Kluwe, K., Abdel-Maksoud, M., Rung, T., (2012). 'Viscous-Inviscid Coupling Methods for Advanced Marine Propeller Applications'.International Journal of Rotating Machinery.

[12] Abdel-Maksoud, M., et al., *Comparing a Propeller Model with a Rotating Propeller in a CFD Simulation of the Viscous Flow around a Ship*, Publication University of Duisburg-Essen, Duisburg, Germany, 2007.

The Turning-Circle Maneuver of a Twin-Screw Vessel with Different Stern Appendages Configuration

Danilo Durante*, Giulio Dubbioso, Riccardo Broglia
(INSEAN-CNR, National Research Council, Maritime Research Centre, Italy)
Andrea Di Mascio
(CNR-IAC, Istituto per le applicazioni del calcolo "Mauro Picone", Rome, Italy)

INTRODUCTION

The prediction of the dynamic stability and maneuverability behavior of a ship are among the most challenging problems in naval hydrodynamics; the main difficulties arise in the accurate evaluation of the hydrodynamic forces and moments which characterize the dynamic response of the vessels and its motion. Traditional approaches, like system based maneuvering model or potential based methods are extensively utilized, the negligible computational resource requirements being the key of their success. However, they cannot provide detailed information about the flow field around the hull and necessitate continuous verification and validation in case of novel hull forms [16][17].

It has been evidenced that the stern appendages region is a key aspect of the maneuverability of this kind of ships, and, if not properly represented in the mathematical model, rather misleading results can be obtained. This issue was remarkable in case of the tanker-like vessel, for both the twin rudder plus central skeg configuration and the single rudder one: indeed, it has been observed that all the regression models provided poor prediction of the maneuvering capabilities when applied to the single rudder configuration, in spite of the satisfactory predictions for the twin rudder configuration.

On the other hand, computational fluid dynamics has reached a noticeable level of accuracy in predicting ship performance in both straight ahead conditions and maneuverability. The availability of the flow details allows the complete analysis of the flow field around a ship maneuvering, which is characterized by large vortical structures shed from the hull and the appendages, as well as by flow separations, which can often be rather massive. The possibility to analyze the complex hull/appendages/propeller interaction makes this technique attractive, although its main drawbacks lies in the large computational resources requirements.

In this work, the unsteady Reynolds averaged Navier-Stokes solver *χnavis* coupled with the equations describing the 6DoF motion of a rigid body [3][4][5][2] is applied to the analysis of the turning behavior of the ship model equipped with both single and twin rudder configuration. The principal purpose of present work is to gain more insight into maneuverability of the tanker-like model, and in particular to explore the different dynamic behavior of the vessel when arranged with two different configuration for the stern appendages.

Another important aspect, which is also the matter of the present work, is to gain a deeper insight into the propeller contribution to the maneuvering properties of the vessel. Indeed, detailed measurements of hydrodynamic loads and flow features [1] around a twin screw frigate during a steady turn, have shown that the side forces generated by the propeller can be rather relevant (*15-20%* of the total lateral force) and therefore they noticeably contribute to its maneuvering behavior. A detailed analysis of the loads on the propellers, as well as on the individual appendages has been pursued also in [20].

The importance of the propeller behavior during a severe maneuver has been already assessed in a previous numerical study [9] on the same vessel under investigation here, in its single rudder configuration. In particular, it has been shown that, if the propeller side force is not taken into account, the turning quality of the ship provided by the numerical simulation is overestimated, i.e. comparing with the free running tests, a tighter turning circle is predicted. In the previous simulations, the propeller effects were taken into account by means of the Hough and Ordway model [11], which, in its original formulation, provides thrust and torque only, whereas transverse forces in the disk plane arising during oblique flow conditions are not accounted for. The addition of a "suitable" propeller lateral force, empirically determined, improved noticeably the results, both in terms of trajectory and kinematic parameters (speed drop, drift angle and yaw rate). In the present work, the generalized actuator disk model has been improved with the inclusion of a lateral force estimation based on the Ribner theory [14]. The proposed model has been used for the investigation of the turning ability of the considered vessel in both configurations; it has to be pointed out that the two configurations have a completely different dynamical behavior; in particular, the single rudder configuration is directionally unstable, whereas the twin rudder with skeg configuration is slight directionally stable. This makes the test rather challenging for both the numerical algorithm and the proposed propeller model.

NUMERICAL METHODS

The numerical solution of the governing equations is computed by means of the solver *χnavis*, which is a general purpose simulation code developed at CNR-INSEAN; the code yields the numerical solution of the unsteady Reynolds averaged Navier-Stokes (uRANS) equations for unsteady high Reynolds number

*e-mail: durante79@gmail.com

(turbulent) free surface flows around complex geometries (the interested reader is referred to [3][4][5][7][2] for details). The solver is based on a finite volume formulation with conservative variables co-located at cell center. The spatial discretization of the convective terms is done with a third order upwind based scheme, whereas the diffusive terms are discretized with second order centered scheme and the time integration is done by second order implicit scheme (three points backward). The solution at each time step is computed iteratively by a pseudo-time integration, that exploits an Euler implicit scheme with approximate factorization, local pseudo time step and multi-grid acceleration [10]. Although several turbulence models have been implemented in the code, in all the simulations reported the turbulent viscosity has been calculated by means of the one-equation model of Spalart and Allmaras [15]. Free surface effects are taken into account by a single phase level-set algorithm [4]. Complex geometries and multiple bodies in relative motion are handled by a dynamical overlapping grid approach [7]. High performance computing is achieved by an efficient shared and distributed memory parallelization [2].

PROPELLER MODEL

In marine CFD simulations the presence of the propeller is often taken into account by a simple model based on the actuator disk concept, according to which body forces are distributed on a disk of finite thickness. Such distributions are obtained by blade loads averaging in both time and space. Both axial and tangential body forces depend on the actual velocity field; this results in the sum of the nominal wake velocity and the propeller-hull interaction velocity, i.e. the effective wake. The body forces distribution and velocity field are mutually dependent; therefore, in order to take into account for the effective wake, an iterative procedure is required. In this work the propeller is modeled by means of an hybrid model: thrust and torque are evaluated by means of a modified Hough and Ordway model [11], whereas the in plane forces are computed by means of the semi-empirical method proposed by Ribner [14] (which is in turn derived from a blade element approach).

Following the idea proposed by Hough and Ordway [11], given the advance, thrust and torque coefficients (J, K_T, K_Q in the following), the axial, radial and tangential force distributions are computed under the assumption of an optimal distribution for the circulation along the blades. The original model was modified to take into account for the axial flow reduction at the propeller disk; in particular, at each time step the advance coefficient is estimated by keeping the number of the revolution constant and by using the instantaneous average axial velocity at the propeller disk inflow section. Then, new values of $K_T(J)$ and $K_Q(J)$ are estimated from the propeller characteristic curves; the resulting load (longitudinal and tangential) is then distributed over each cell of the propeller disk as volume forces in order to simulate the action of the propeller.

In order to capture the effects of the inflow lateral component, the semi-empirical method of Ribner [14] has been considered. Although the Ribner's model is very popular for the evaluation of stability qualities in aeronautics, its application to marine propeller is not documented to the authors' knowledge. The method was developed on the basis of the main flow characteristics around the propeller in oblique flow, and therefore is strongly related to the loads acting in the propeller plane and provides a reliable estimation of the propeller lateral force on the basis of theoretical considerations.

When the propeller works with an angle of yaw with respect to the incoming flow, it accelerates the flow behind the disk, therefore reducing the angle of attack with respect to the shaft. This results in a lateral momentum exerted on the flow by the propeller, and consequently, the propeller experiences a lateral force. This fact is accounted for in the Ribner's theory by means of an hybrid blade element approach (for the estimation of the loads acting on the propeller blades) and an actuator disk approach (for the evaluation of the effective angle of incidence due to the propeller induction effect). The interested reader is referred to [10] for the details of its derivation.

It should be emphasized that the addition of the side force model does not increase the computational burden; this makes the hybrid Hough and Ordway/Ribner model very attractive for those problems where the details of the flow field around the propeller are not required, but rather only the main effects of the propeller on the flow field are relevant for the simulation. Ship maneuvering is a typical framework, the key issue being the correct estimation of forces and moments on the hull, whose magnitude have effects of paramount importance for trajectory predictions.

GEOMETRY AND TEST CONDITIONS

A twin screw tanker-like model equipped with two different stern appendages configurations is considered for the numerical simulations (see Figure 1). The model is fully appended with bilge keels, struts, A-brackets and shafts for two propellers.

One configuration is characterized by a single central rudder, whereas the other one is a more classical twin rudder plus a central skeg arrangement. For this model an extensive free running test program has been carried out at the lake of Nemi [12][13]; this allow a comparison in terms of both trajectories and kinematic characteristics for both models. In the following, data

are shown only in non-dimensional form because of restrictions on distribution; all the quantities are made non dimensional by a reference length L_{PP} (the length between perpendicular of the model) and the approach velocity U_0 (the approaching speed at model scale). This gives a Reynolds number $Re=5\cdot10^6$ (at model scale) and a Froude number $Fn=0.217$. The turning circle maneuver test is carried out at fixed turning rate of the propeller; the propulsion point is chosen by means of an un-propelled steady state simulation at the given speed with fixed trim and sinkage.

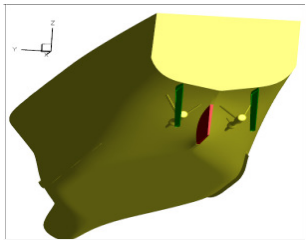

Figure 1: A ship model configuration: twin rudder plus skeg arrangement.

The simulation of the turning circle maneuver is carried out leaving all the six degree of freedom free; the turning rate of the rudder is *12.23* degrees per non dimensional time unit (at model scale); a turning circle with *35* degrees rudder deflection is considered. The maneuver is carried out at fixed turning rate of the propeller.

COMPUTATIONAL MESH

The physical domain is discretized by means of structured blocks with partial overlap; overlapping grid capabilities are exploited to attain a high quality mesh and for refinement purposes. The whole mesh consists of a total of about 6.2 million and about 7.8 million of computational volumes for the single and the twin rudder configuration, respectively. Grid distribution is such that the thickness of the first cell on the wall is always below 1 in terms of wall units ($y^+=O(1)$ i.e. $\Delta/L_{PP}=O(20/Re)$, Δ being the thickness of the cell). The use of overlapping grid capability allows to take into account all the details, in particular for the mesh around the rudder where both the fixed and the mobile parts are carefully discretized.
Moreover, it is to be pointed out that, instead of generating a fixed background mesh that covers the whole course of the hull, a relatively small background mesh that follows the hull during the motion translating in the horizontal plane and rotating around the vertical axis with the model has been generated.

RESULTS

In the following paragraphs numerical results for the two configurations will be presented; in particular the predicted turning qualities will be analyzed in terms of trajectory and kinematic parameters first; differences in maneuvering behavior among the two configurations will be also highlighted. The predicted turning parameters will be compared with experimental data from A complete verification and validation procedure has not been pursued yet. However, the accuracy of the solutions have been investigated by a grid dependency analysis on different meshes. A deep insight on the hydrodynamic loads acting on the horizontal plane is also provided in order to broaden their effects on the vessel manoeuvring capabilities. For the same reason the forces acting on the appendages will be also a matter of discussion. Moreover, in order to gain more insight into the propeller behaviour during an off-design condition (as the tight maneuver considered here), variation of propeller thrust and lateral force will be also investigated.

MANEUVER ANALYSIS

In Figure 3 and Figure 4 the predicted trajectories and the time histories of kinematic parameters (speed of advancement, drift angle and yaw rate) for the two configurations are presented and compared with free running experimental maneuvers. In the reported results, $t=0$ is the time at which the rudder starts its *35°* rotation, the origin of the earth fixed system of reference is taken as the position of the model at $t=0$ and the velocity of the ship is normalized with respect to the velocity at $t=0$, i.e. the nominal approach speed.

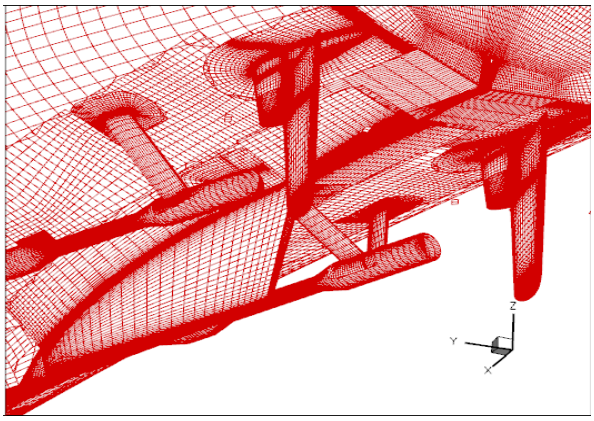

Figure 2: Computational mesh: twin rudder plus skeg configuration.

From Figure 3, it is evident that in the transient phase the course keeping ability of the single rudder configuration is slightly overestimated, i.e. form the numerical results the ship seems to be less reactive to the rudder deflection (i.e for heading angle up to 90°). After the initial transient phase, the maneuvering behavior is well reproduced. This is evidenced by comparison both the maximum transverse position and the diameter of the trajectory, as well as the kinematic parameters in the steady turning phase. Speed drop, drift angle and yaw rate are in fairly good agreement with respect to the measurements. In particular, the

attitude of the vessel with respect to the incoming flow, i.e. the drift angle, is in excellent agreement with experiments, whereas, speed drop and yaw rate are slightly underestimated. However, it should be pointed out that the effects of these two terms are opposite, i.e. the speed drop induces a destabilizing effect, which is counteracted by the higher resistance to rotation, which causes a lower yaw velocity; as a results, these effects cancels out and the final dynamic behavior is captured. The agreement during the steady phase clearly demonstrates that the main discrepancy with the experiments resides in a slight shift ahead of the trajectory, mainly due to the overestimation of the heading stability.

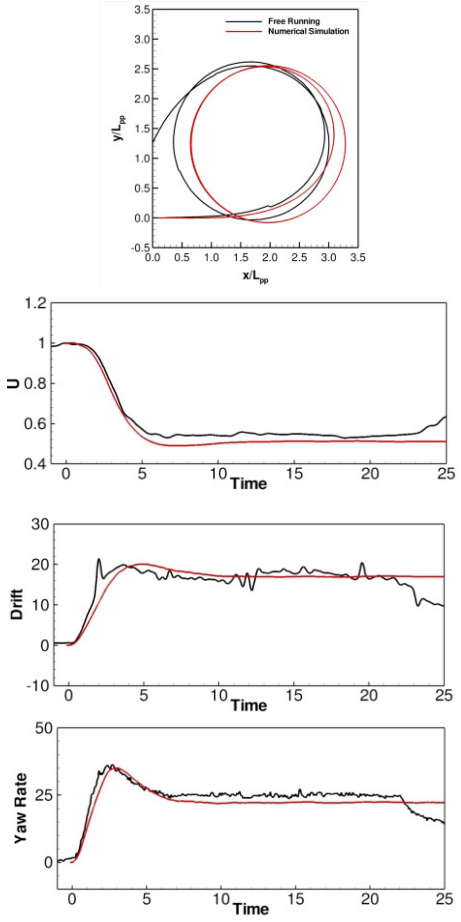

Figure 3: Single rudder configuration; predicted trajectory, and time histories for the speed of advancement, the drift angle and the yaw rate.

In Figure 4 analogous comparisons are shown for the twin rudder configuration; also in this case the dynamic behavior is very well captured, both in terms of trajectory and kinematic response.

In particular, for this arrangement, the transient phase seems to be well captured by the numerical simulation. In the stabilized phase the agreement with the experiments is rather good for the advancement speed and the yaw rate; large discrepancy can be observed for the drift angle. Anyhow, it has to point out that, this parameters is not directly measured during the experiments, and large uncertainty and or error can be introduced during the derivation process.

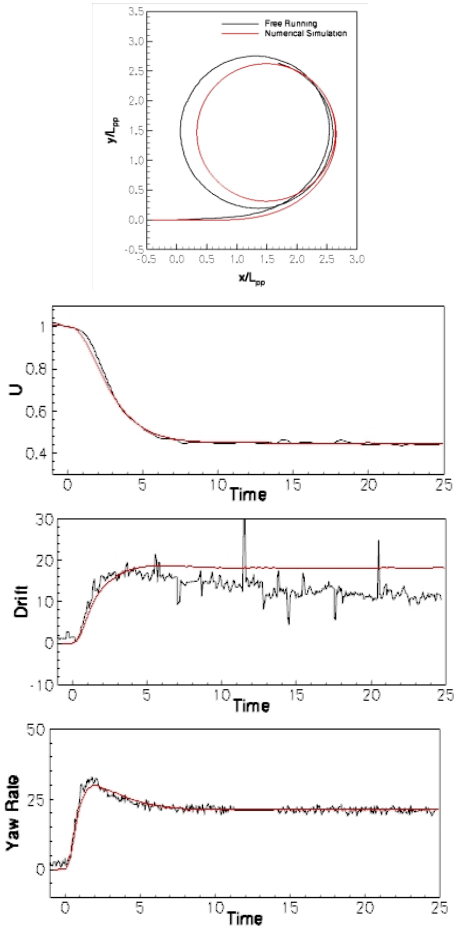

Figure 4: Twin rudders configuration; predicted trajectory, and time histories for the speed of advancement, the drift angle and the yaw rate.

To properly estimate both the turning ability of the two vessels and the quality of the numerical simulations, the predictions of the trajectory parameters (like transfer, advancing, tactical and turning diameters) and the kinematic parameters (speed drop, yaw rate and drift angle) are reported in Table 1 and Table 2, for the single and twin rudder arrangement, respectively; comparison error between numerical and experimental data are reported as well. In the same tables, for an estimation of the grid dependency, some values provided by computations of the medium mesh are also provided.

The considerations made in the previous paragraph are confirmed by the results summarized in the tables.

In particular for the single rudder arrangement (Table 1) the largest error is evidenced for the advance parameter, with a numerical prediction overestimation

for the advance of about *6%*, indicating a prediction of a ship with a slightly larger course keeping properties; nonetheless, the accuracy of the prediction is rather good, the error being very low, as well as the error for the time at which the 90° of heading angle is reached (less than *3%*). Transfer is also well captured, the difference with the experiments being only *2%*.

Table 1 Single rudder: trajectory parameters and comparison with experiments (values in red are the non dimensional times at which the position is reached).

		CFD		EFD
		Medium	Fine	
Transient	Advance	*3.33 (16.84%)*	*3.02 (5.96%)* *3.90 (2.98%)*	*2.85* *4.02*
	Transfer	*1.11 (10.00%)*	*1.02 (2.00%)*	*1.00*
	Yaw Rate		*35.04° (3.23°)*	*36.21°*
	Drift		*20.01°(0.60%)*	*19.89°*
Stabilized	Tactical	*2.67 (4.30%)*	*2.48 (3,13%)* *7.36 (0.27%)*	*2.56* *7.38*
	Turning	*2.89 (14.68%)*	*2.60 (2.44%)*	*2.52*
	Speed Drop		*0.510 (5.0%)*	*0.540*
	Yaw Rate		*22.0° (12%)*	*25.0°*
	Drift		*17.0° (5%)*	*16.2°*

Peak values for the yaw rate and the drift angle are also in very good agreement with experiments, with a comparison errors around *3%* and less than *1%*, respectively. Stabilized phase is also well captured, both tactical and turning diameter are in good agreement with free running tests (errors being around *3%*); similar agreement is observed for both speed drop and drift angle, whereas a larger discrepancy is noted for the yaw rate.

Finally, by the comparison between medium and fine computations and with experiments, a convergence toward experimental values refining the grid can be clearly inferred. From a preliminary verification assessment (i.e. including a coarse grid computation, not reported here), this trend has been confirmed; however, it has been also observed that convergence order is far from the theoretical value. This means that, the coarse grid is rather far from the asymptotic range.

For the twin rudder arrangement (Table 2), the agreement is generally less satisfactory. In the transient phase both the hydrodynamic loads due to the sway and yaw are slightly underestimated (advance and transfer are *4%* higher and *7%* lower than the experiments, respectively, with an error in time of about *7%*); peak values for the yaw rate and the drift angle show a discrepancy of similar amount. Also for this configuration, numerical simulations predict a vessel with a higher stability character

Moreover, the damping due to the yaw motion is more evident in the stabilized phase (tactical diameter and turning diameter are under predicted by 5% and 9%, respectively). Stabilized values for speed drop and yaw rate are in very good agreement with experiments, whereas a large discrepancy is observed for the drift angle.

It has to be pointed out, however, that discrepancies among trajectory and kinematic are probably affected by cancellation effects due to some inaccuracies in the evaluation of the forces distribution along the hull.

Table 2 Twin rudder: trajectory parameters and comparison with experiments (values in red are the non dimensional times at which the position is reached).

		CFD		EFD
		Medium	Fine	
Transient	Advance	*2.61 (4.98%)*	*2.59 (4.43%)* *3.89 (7.16%)*	*2.48* *3.63*
	Transfer	*1.04 (8.77%)*	*1.06 (7.02%)*	*1.14*
	Yaw Rate		*29.97°(7.50%)*	*32.40°*
	Drift		*18.66°(4.35%)*	*19.51°*
Stabilized	Tactical	*2.54 (5.92%)*	*2.56 (5,18%)* *7.75 (1.43%)*	*2.70* *7.64*
	Turning	*2.23 (12.55%)*	*2.31 (9.41%)*	*2.55*
	Speed Drop		*0.449 (1.0%)*	*0.445*
	Yaw Rate		*21.40° (2%)*	*21.00°*
	Drift		*18.15° (25%)*	*14.50°*

Table 3 Experimental tests: standard deviations.

	Single rudder	Twin rudder
Advance	*11.79%*	*7.54*
Transfer	*36.32%*	*6.84*
Tactical	*9.82%*	*3.88*
Turning	*1.92%*	*4.26*
Speed drop	*2.38%*	*3.13*

In the table, numerical predictions on both medium and fine grids are reported; also for this configuration a preliminary verification assessment has been performed; results similar to the single rudder computations have been observed, i.e. a reduction of the comparison error when the grid is refined, but with a convergence order far from the theoretical one. Investigations are still on going.

For the experimental tests, some repetitions are available. In the following table, a preliminary repeatability analysis (i.e. root mean square of the parameters) is presented.

A large scattered of the data can be observed for the transient phase of the single rudder configuration; this is clearly due to the poor stable properties of this configuration. Experimental uncertainty for the stabilized parameters is rather low. Comparing the errors for the fine mesh results and standard deviation of experimental data, it is clear that numerical results are nearly all validated, i.e. numerical error is generally lower than experimental uncertainty.

ACKNOWLEDGEMENTS

The work has been partially financed by the Italian Navy throughout the research project Submotion II, contracted through the European Defense Agency. Numerical computations presented here have been performed on the parallel machines of CASPUR Supercomputing Center (Rome); their support is gratefully acknowledged. The Authors acknowledge Dr. Salvatore Mauro for providing the experimental

data and useful suggestions during the writing of the present work.

REFERENCES

[1] Atsavapranee, P, Miller, R Dai, C, Klamo, J, Fry, D, 2010, "Steady-Turning Experiment and RANSE Simulations on a Surface Combatant Hull Form (Model #5617)", 28th ONR Symposium, Pasadena.

[2] Broglia R., Di Mascio A., Amati, G., 2007. "A Parallel Unsteady RANS Code for the Numerical Simulations of Free Surface Flows", Proc. of 2nd International Conference on Marine Research and Transportation, Ischia, Naples, Italy.

[3] Di Mascio A., Broglia R. Favini, B., 2001, "A second order Godunov-type scheme for naval hydrodynamics, in: Godunov Methods: Theory and Applications", Kluwer Academic/Plenum Publishers. pp. 253–261.

[4] Di Mascio A., Broglia R. and Muscari R., 2007, "On the application of the single-phase level set method to naval hydrodynamic flows", Computers & Fluids 36, 868–886.

[5] Di Mascio, A., Broglia, R., and Muscari, R. (2009). "Prediction of hydrodynamic coefficients of ship hulls by high-order Godunov-type methods". J. Marine Sci. Tech., Vol. 14, pag. 19-29.

[6] Di Mascio A., Dubbioso G., Notaro C., Viviani M., 2011, "Investigation of twin screw naval ships manoeuvring behaviour", Journal of Ship Research, accepted for publication.

[7] Di Mascio, A., Muscari, R., and Broglia, R. (2006). "An Overlapping Grids Approach for Moving Bodies Problems". 16th ISOPE, San Francisco, California (USA).

[8] Dubbioso, G., "Manoeuvrability Behaviour of twin screw vessels", PhD Thesis, Genova University, April 2011.

[9] Durante D., Broglia R., Muscari R. and Di Mascio A., "Numerical simulations of a turning circle maneuver or a fully appended hull", 28th Symposium on Naval Hydrodynamics, Pasadena (Ca), 12-17 September 2010.

[10] Favini, B., Broglia, R., and Di Mascio, A. (1996). "Multigrid Acceleration of Second Order ENO Schemes from Low Subsonic to High Supersonic Flows". Int. J. Num. Meth. Fluids, vol. 23, pag. 589-606.

[11] Hough G.R. and Ordway D.E., "The generalized actuator disk", Developments in Theoretical and Applied Mechanics, 2:, pag. 317-336, 1965.

[12] Mauro, S. (1998a). Prove di Manovrabilità su Modello di Unità Logistica. INSEAN Technical Report, N6/C 2280.

[13] Mauro, S. (1998b). Prove di Manovrabilità su Modello di Unità Logistica. INSEAN Technical Report, N8/C.2280.

[14] Ribner, H.S, "Propeller in yaw", NACA TECHNICAL REPORT 3L09, 1943.

[15] Spalart P.R. and Allmaras S.R., "A One-Equation Turbulence Model for Aerodynamic Flows", La Recherche Aerospatiale 1 (1994) 5-21.

[16] Stern, F. and Agdrup, K. (2008). Proceedings of Workshop on Verification and Validation of Ship Manoeuvering Simulation Methods, Copenhagen, Denmark.

[17] Stern F., Agdrup K., Kim S.Y., Cura-Hochbaum A., Rhee K.P., Quadvlieg F., Perdon P., Hino T., Broglia R., Gorski J., "Experience from SIMMAN 2008 - The first workshop on verification and validation of ship manoeuvring simulation methods", Journal of Ship Research, Vol. 55, No. 2, June 2011, pp. 135–147.

[18] Viviani M., Dubbioso G., Soave M., Notaro C., Depascale R., "Hydrodynamic coefficients regressions analysis and application to twin screw naval vessels", IMAM 2009, Istanbul.

[19] Crane, C. L., Eda, H., Landsburg, A., 1989, Controllability, In Principles of Naval Architecture, Vol. III, Chapter IX, ed. E. V. Lewis, Jersey City, N.J.: The Society of Naval Architects and Marine Engineers.

[20] Carrica, P.M., Sadat-Hosseini, H. and Stern, F., 2012, "CFD analysis of broaching for a model surface combatant with explicit simulation of moving rudders and rotating propellers", Computers & Fluids, 53, p. 117–132,

[21] Molland A.F., Turnock S.R., "Marine Rudders and Control Surfaces", Butterworth-Heinemann, 2006.

[22] Phillips A.B., Turnock S.R., Furlong M.E., "Accurate Capture of Rudder-Propeller Interactions using a coupled Blade Element–RANS Approach", 12th Numerical Towing Tank Conference, 2009.

Numerical modelling of moored floating structures using SPH. Preliminary results

Pawel Dymarski <pawdymar@pg.gda.pl>, Gdansk University of Technology

INTRODUCTION

This article presents partial results of the works carried out under the research project "The development of the method of modeling the dynamics of the floating (offshore) objects subjected to the environment influence", which aims at developing computational methods for modeling the dynamics of offshore structures.
The article contains the description of the method of modeling the hydrodynamic impacts using SPH method and the description of the computational model of the dynamic anchoring system (anchor chain model).

The elaborated mathematical model describes the motion of the chain as a result of the effect caused by the movement of the chain attachment points (on its both ends).
The model includes the following factors:
- mechanical properties of the chain: stiffness (*EA*), inertia,
- the presence of the hydrodynamic resistance of water
- the presence of the added mass of water
- the elasticity of the seabed
- gravitation force and buoyancy

THE DESCRIPTION OF THEORETICAL MODEL

The main assumptions of the model

The mechanical model of the chain has been presented in fig. 1. The chain consists of links, modeled as point masses connected together by weightless rods of a determined section area A, and elasticity module E. The rods are connected together with joints, and the position of the joints coincides with the location of the point masses.

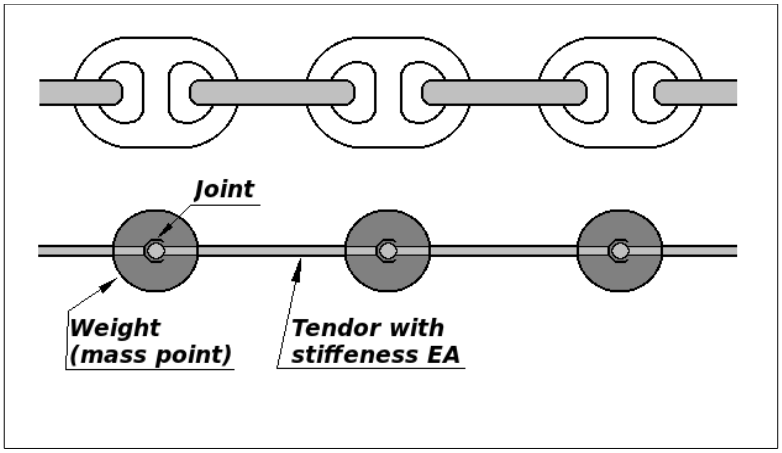

Fig. 1. Schematic model of the chain. The model shown in the figure had the actual chain fragments (consisting of two links) replaced with weights joined by ties with adjacent weights. In practice, the number of actual links modeled using one weight is much higher

The external forces acting on the chain are applied to point masses in the place of the occurrence of the joints and, therefore, the rods are only stretched or compressed. The chain has no practical ability to transfer compressive forces due to the presence of the a/m joints, however, with the dynamic loads of the chain, compressive forces may appear.
Basing on the original geometry of the chain, the diameter of the rods connecting the weights as well as the hydrodynamic resistance factors for the movement across and along the local direction of the chain are determined. The added masses coefficient, which are a measure of a additional hydrodynamic reaction in the accelerated motion of the chain links, are determined in a similar way. The hydrodynamic diameter is defined regardless of the section area *A* determining the stiffness of the chain.
The chain model also takes into account the impact of the seabed as a elastic substrate, the forces of the friction on the ground are omitted. The general formula for the acceleration of the *i*-th chain segment is formulated with Newton's third law:

$$m\ddot{\boldsymbol{x}}_i = \left(\sum_k \boldsymbol{F}_k\right)_i \quad , \tag{1}$$

where: $\boldsymbol{x}_i$ - the position of the centre of the chain link (point mass) $\boldsymbol{x}_i = (x_{i,1}, x_{i,2}, x_{i,3})$, $\ddot{\boldsymbol{x}}_i$ - the acceleration of the centre of the chain link, m - the mass of the chain segment, $\boldsymbol{F}_k$ - k-th an element of the force acting on the chain segment

The methods of calculating the components $\boldsymbol{F}_k$ of the force acting on the i-th chain link have been described later in the article.

Link-link interaction

The force acting between two adjacent chain links due to its extension (or compression) can be determined from the Hook's law:

$$\boldsymbol{F}_{Hook} = EA\frac{\left(L_{seg} - L_{seg0}\right)}{L_{seg0}}\boldsymbol{e}_i \quad , \tag{2}$$

where: EA - stiffness of the chain; E – Young's modulus, A – substitute cross sectional area, L_{seg} , L_{seg0} - the current and initial, $\boldsymbol{e}_i$ is a unit vector of the i-th link of a direction consistent with the direction of the segment joining two points of the chain and directed towards the link acting on the considered link

The length of the segment between two points of the indices i and $i+1$ can be expressed by the formula:

$$\left(L_{seg}\right)_i = \left(\boldsymbol{x}_{i+1} - \boldsymbol{x}_i\right)\cdot\boldsymbol{e}_i \tag{3}$$

Hence, the force acting on the i-th chain link from the link $i-1$ and the link $i+1$ is:
where:

$$\boldsymbol{F}_1 = EA\frac{\left[\left(\boldsymbol{x}_{i+1} - \boldsymbol{x}_i\right)\cdot\boldsymbol{e}_i - L_{seg0}\right]\boldsymbol{e}_i}{L_{seg0}} - EA\frac{\left[\left(\boldsymbol{x}_i - \boldsymbol{x}_{i-1}\right)\cdot\boldsymbol{e}_{i-1} - L_{seg0}\right]\boldsymbol{e}_{i-1}}{L_{seg0}} \quad , \tag{4}$$

Where: $\boldsymbol{e}_i = \frac{\boldsymbol{x}_{i+1} - \boldsymbol{x}_i}{|\boldsymbol{x}_{i+1} - \boldsymbol{x}_i|}$; $\boldsymbol{e}_{i-1} = \frac{\boldsymbol{x}_i - \boldsymbol{x}_{i-1}}{|\boldsymbol{x}_i - \boldsymbol{x}_{i-1}|}$ and $\boldsymbol{x}_{i-1}; \boldsymbol{x}_i; \boldsymbol{x}_{i+1}$ - the position coordinates of the successive weights of indices $i-1$; i; $i+1$.
Taking into account that:

$$\left[\left(\boldsymbol{x}_{i+1} - \boldsymbol{x}_i\right)\cdot\boldsymbol{e}_i\right]\boldsymbol{e}_i = \boldsymbol{x}_{i+1} - \boldsymbol{x}_i \quad \text{and} \quad \left[\left(\boldsymbol{x}_i - \boldsymbol{x}_{i-1}\right)\cdot\boldsymbol{e}_{i-1}\right]\boldsymbol{e}_{i-1} = \boldsymbol{x}_i - \boldsymbol{x}_{i-1} \quad , \tag{5}$$

we will receive:

$$\boldsymbol{F}_1 = \frac{EA}{L_{seg0}}\left[\boldsymbol{x}_{i+1} - 2\boldsymbol{x}_i + \boldsymbol{x}_{i-1} - L_{seg0}\left(\boldsymbol{e}_i - \boldsymbol{e}_{i-1}\right)\right] \quad . \tag{6}$$

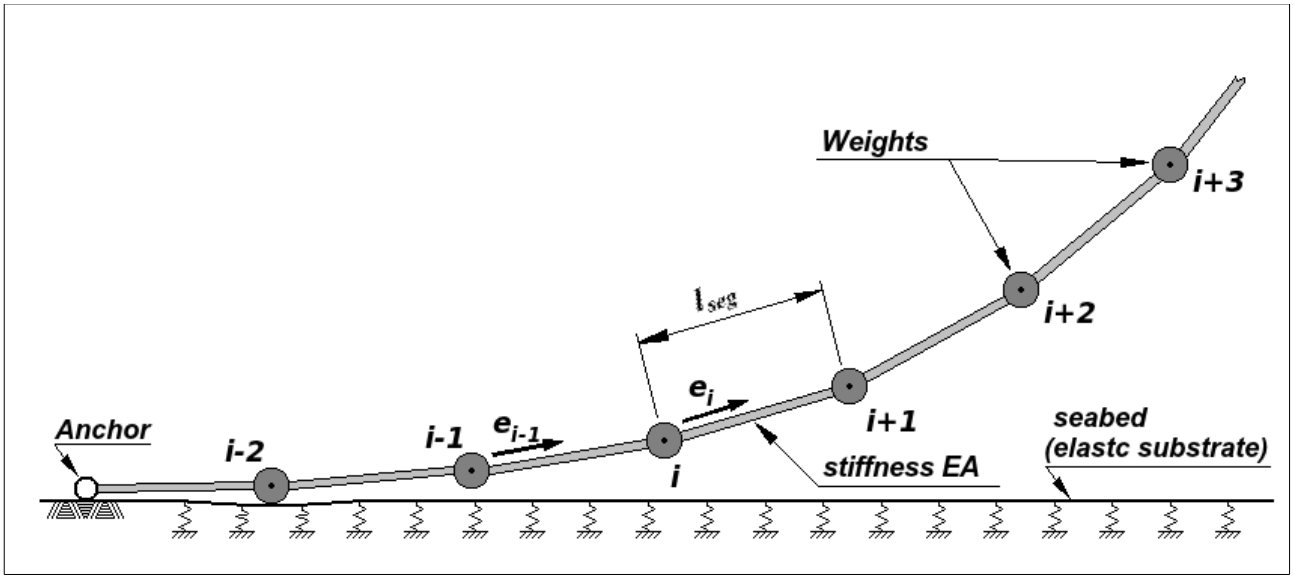

Fig. 2. Illustration of the main symbols

The impact of the substrate

The force of the impact of the substrate is calculated as a linear function of a 'depression' of the link in the substrate, the direction of the substrate reaction is vertical. In the chosen coordinate system, the vertical axis is the axis Oz, whereas, the ground level is indicated by a ordinate z_0 . Hence, the vector of the substrate reaction force is given by a formula:

$$\boldsymbol{F}_2=\begin{cases}\boldsymbol{0} & for\ \boldsymbol{x}\cdot\boldsymbol{e}_z\geq z_0\\ -k_G\left(\boldsymbol{x}_i\cdot\boldsymbol{e}_z-z_0\right)\cdot\boldsymbol{e}_z & for\ \boldsymbol{x}\cdot\boldsymbol{e}_z<z_0\end{cases}\quad , \tag{7}$$

Where: k_G - the coefficient of the elasticity of the substrate , $\boldsymbol{e}_z$ - unit direction vector of the axis *Oz*, z_0 - ordinate z determining the substrate level (bottom of the basin)

Hydrodynamic resistance

Hydrodynamic reaction is calculated on the basis of the coefficient of the resistance force, and this reaction has been divided into normal and tangential component. The general formula for drag force is usually given in the form below:

$$\boldsymbol{F}_{Hydro}=-\frac{1}{2}\rho|\dot{\boldsymbol{x}}|\dot{\boldsymbol{x}}\,c_R S\quad , \tag{8}$$

Where: ρ - the density of fluid, C_R - the dimensionless coefficient of the hydrodynamic resistance (determined empirically), S - the surface area of the projection of the chain segment on the direction of the inflow.
The segment of the chain has got clearly defined directions: normal and tangential to the local chain line, on which the resistance coefficients will significantly differ in value. Therefore, the hydro-mechanical reaction is also divided into two components:

$$\boldsymbol{F}_{Hydro}=-\frac{1}{2}\rho|\dot{\boldsymbol{x}}_n|\dot{\boldsymbol{x}}_n c_{Rn}S-\frac{1}{2}\rho|\dot{\boldsymbol{x}}_t|\dot{\boldsymbol{x}}_t c_{Rt}S \tag{9}$$

Where the normal and tangential component of the velocity of the chain segment is:

$$\dot{\boldsymbol{x}}_n=\dot{\boldsymbol{x}}-\left(\dot{\boldsymbol{x}}\cdot\boldsymbol{e}\right)\boldsymbol{e}\quad ;\quad \dot{\boldsymbol{x}}_t=\left(\dot{\boldsymbol{x}}\cdot\boldsymbol{e}\right)\boldsymbol{e}\quad . \tag{10}$$

The hydrodynamic reaction acting on the chain segment can be written in a slightly changed form, which will be useful while creating the equation system:

$$\boldsymbol{F}_3=-a_{Rn}\left[\dot{\boldsymbol{x}}_i-\left(\dot{\boldsymbol{x}}_i\cdot\boldsymbol{e}_i\right)\boldsymbol{e}_i\right]-a_{Rt}\left[\left(\dot{\boldsymbol{x}}_i\cdot\boldsymbol{e}_i\right)\boldsymbol{e}_i\right]\quad , \tag{11}$$

Where the coefficients a_{Rn} and a_{Rt} are defined by formulas:

$$a_{Rn}=\frac{1}{2}\rho|\dot{\boldsymbol{x}}_n|c_{Rn}S\quad ;\quad a_{Rt}=\frac{1}{2}\rho|\dot{\boldsymbol{x}}_t|c_{Rt}S \tag{12}$$

The added masses of the water

The reaction caused by the presence of the mass of the accompanying water is the sum of the products of accelerations multiplied by the coefficients of the added masses on the appropriate directions. The normal and tangential direction to the local chain line has been distinguished similarly as above:

$$\boldsymbol{F}_4=-a_{22}\left[\ddot{\boldsymbol{x}}_i-\left(\ddot{\boldsymbol{x}}_i\cdot\boldsymbol{e}_i\right)\boldsymbol{e}_i\right]-a_{11}\left[\left(\ddot{\boldsymbol{x}}_i\cdot\boldsymbol{e}_i\right)\boldsymbol{e}_i\right] \tag{13}$$

Where: a_{11} , a_{22} - the coefficient of the mass of the accompanying water on the direction tangential and normal to the chain line

Gravitation and buoyancy

The force of gravitation and the buoyancy is formulated below:

$$\boldsymbol{F}_5=(\rho_m-\rho)\,A\,L_{seg0}\,\boldsymbol{g} \tag{14}$$

The methods of solving non-stationary problems (integration in time)

Differential equation (1) can be solved using one of the many numerical methods.
From the stability point of view, it is important if the applied method is explicit or implicit as well as the precision of the method. The most stable are the low-order implicit methods, such as the implicit Euler's method, which scheme for solving ordinary differential equation (in time domain) can be formulated:

$$\phi^{n+1} = f\left(t_n, \phi^{n+1}\right)\Delta t \tag{15}$$

The modelling of fluid dynamics using the SPH model

The system of equations governing the inviscid fluid motion consists of the continuity equation and the momentum conservation Euler's equation [1],[2]:

$$\frac{d\rho}{dt} = -\rho \nabla \cdot \boldsymbol{v} \quad , \tag{16}$$

$$\frac{d\boldsymbol{v}}{dt} = -\frac{1}{\rho}\nabla P + \boldsymbol{g} \quad , \tag{17}$$

Where: $\boldsymbol{v}$ denoting the velocity, P – the pressure and $\boldsymbol{g}$ – external forces (gravity) .
The SPH [Smoothed Particle Hydrodynamics] method is based on the Lagrangian approach. The fluid is modeled using "fuzzy" particles. The continuous distributions of parameters such as density of the liquid are replaced with proper estimates with the assumed interpolation kernel described with function W. The calculations are performed for a discrete set of N particles of the liquid, which movement projects the fluid movement. The number of the particles in a given space has an effect on the density of the fluid, which is calculated on the basis of the kernel function described for each of the particles. The distribution function of the defined value A associated with a given particle of the fluid has a following form:

$$A(\boldsymbol{r}) = \sum_b m_b \frac{A_b}{\rho_b} W\left(\boldsymbol{r} - \boldsymbol{r_b}, h\right) \quad , \tag{18}$$

Continuity equation. The density of fluid at the point $\boldsymbol{r}_a$ is calculated on the basis of the distributions of the density functions of the neighboring particles:

$$\rho_a(\boldsymbol{r}) = \sum_b m_b W_{ab} \quad . \tag{19}$$

This equation results from the fact that the spatial distribution of mass is closely associated with the distribution of the particles. In the case of modeling the flows with a free surface, the density distribution in the area of the surface of the distribution is disrupted because of the absence of the particles outside the surface of the separation of the phases.
For this kind of issues for calculating the density, a different form of continuity equation is appropriate:

$$\frac{d\rho_a}{dt} = \sum_b m_b\left(\boldsymbol{v}_a - \boldsymbol{v}_b\right)\nabla_a W_{ab} \quad . \tag{20}$$

Momentum equation. In the SPH method the momentum conservation equation takes the following form:

$$\frac{d\boldsymbol{v}_a}{dt} = -\sum_b m_b\left(\frac{p_a}{\rho_a^2} + \frac{p_b}{\rho_b^2} + \Pi_{ab}\right)\nabla_a W_{ab} + \boldsymbol{g} + \boldsymbol{f}_{st} \quad , \tag{21}$$

gdzie: p_a , p_b – where: the pressure calculated for the particles a and b, the term Π_{ab} representing the effect of artificial viscosity (viscous "pressure"), $\boldsymbol{f}_{st}$ - surface tension.
Artificial viscosity. The so called viscous „pressure" is calculated using the following formula:

$$\Pi_{ab} = \begin{cases} \dfrac{-\alpha c_s \mu_{ab} + \beta \mu_{ab}^2}{\rho_{ab}}, & \boldsymbol{v}_{ab}\cdot\boldsymbol{r}_{ab} < 0; \\ 0, & \boldsymbol{v}_{ab}\cdot\boldsymbol{r}_{ab} \geq 0; \end{cases} \quad \text{and} \quad \mu_{ab} = \frac{h\,\boldsymbol{v}_{ab}\cdot\boldsymbol{r}_{ab}}{\boldsymbol{r}_{ab}^2 + \epsilon h^2} \quad , \tag{22}$$

where: $\bar{\rho}_{ab} = \frac{1}{2}(\rho_a + \rho_b)$, c_s is a speed of sound, α is viscosity constant, which takes a value from 0.08 to 0.5.
Surface tension. The force induced by a presence of the surface tension is calculated based on the approach proposed by M. Becker and M. Teschner [2]:

$$\frac{d\boldsymbol{v}_a}{dt} = -\frac{\kappa}{m_a}\sum_b m_b\left(\boldsymbol{r}_a - \boldsymbol{r}_b\right)W_{ab} \quad , \tag{23}$$

TEST CALCULATIONS OF CHAIN MODEL

The chain model shown above has been tested with regard to the behaviour in static and dynamic conditions. Two simple test cases will be presented below:
Testcase 1: .Determining the catenary curve and the value of the force with which the chain operates on the anchored object in the function of the value of a horizontal displacement of the object. Static test.

Testcase 2: Determining the trajectory of the movement of the chain links and the force N_1 for boundary conditions presented in fig. 3. Period of oscillations is 6 second.

The results of the calculations for the above mentioned test cases in the form of links trajectory chart are shown in fig. 6 and fig. 7. The charts of the reaction of the anchoring system for the static and dynamic tests (time function) are presented at fig. 4 and fig. 5.

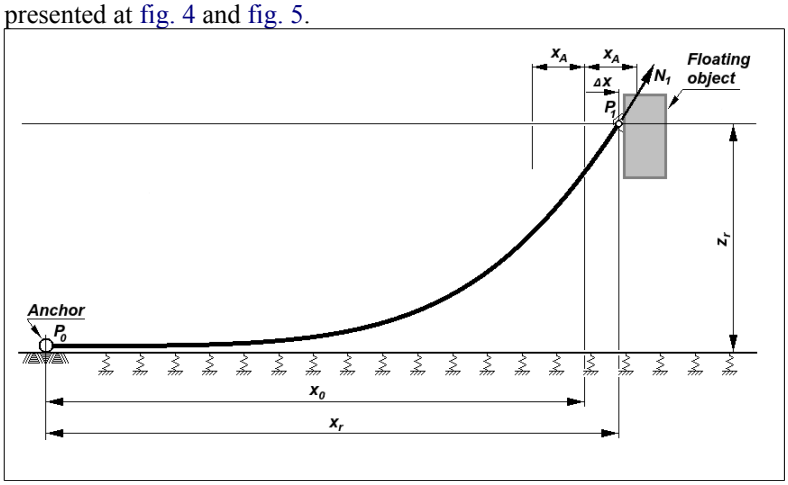

Fig. 3. Test configuration of chain model.

x_0 =30m; x_A = 3.0 m; z_r =10.0m; chain length: L_r =34.623 m; mass of the chain: m_L =7.657 kg/m; Stiffness EA=1.963e+8 N ; A_{Hydro} = 9.817e-4 N; drag coefficients: c_{Rn} =1.2; c_{Rt} =0.3;

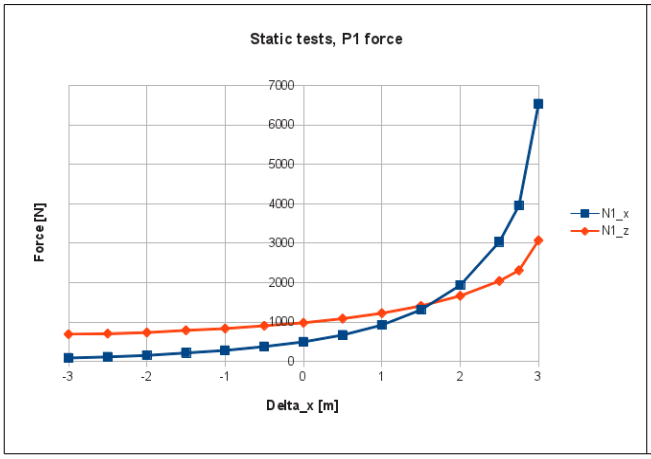

Fig. 4. Results of static test of the chain model: lateral and vertical force component in a function of Δx (position of floating object).

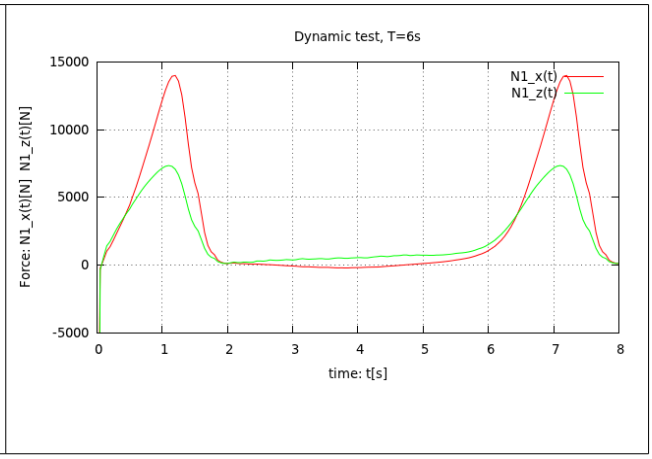

Fig. 5. Results of dynamic test of the chain model: lateral and vertical force component in a function of time.

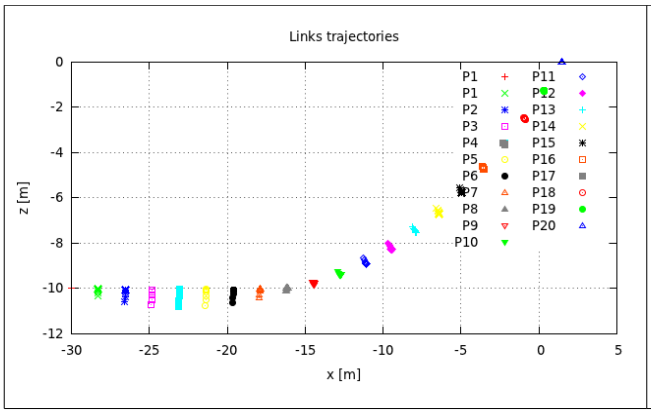

Fig. 6. Results of static test of the chain model: Trajectories of weights (links) of the chain model from initial position at t=0 to final (stable) position of links.

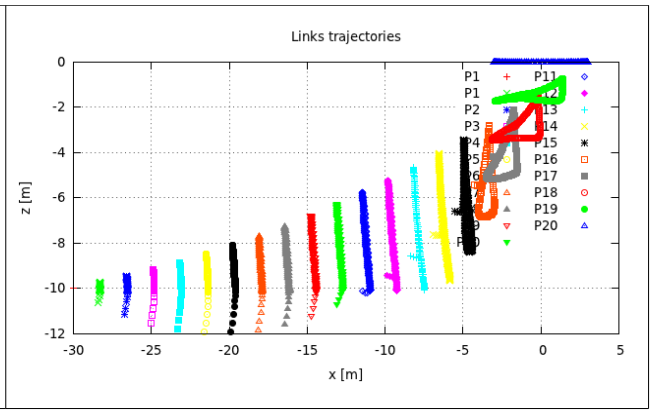

Fig. 7. Results of dynamic test of the chain model: Trajectories of subsequent links of chain forced by vertical oscillations of P_1 .

TEST OF SPH COMPUTATIONAL MODEL

The geometry of domain and configuration of boundary conditions for test of developed SPH model is presented at fig. 8a. The next pictures show the shape of the free surface in the subsequent time steps (fig 8 b-h).

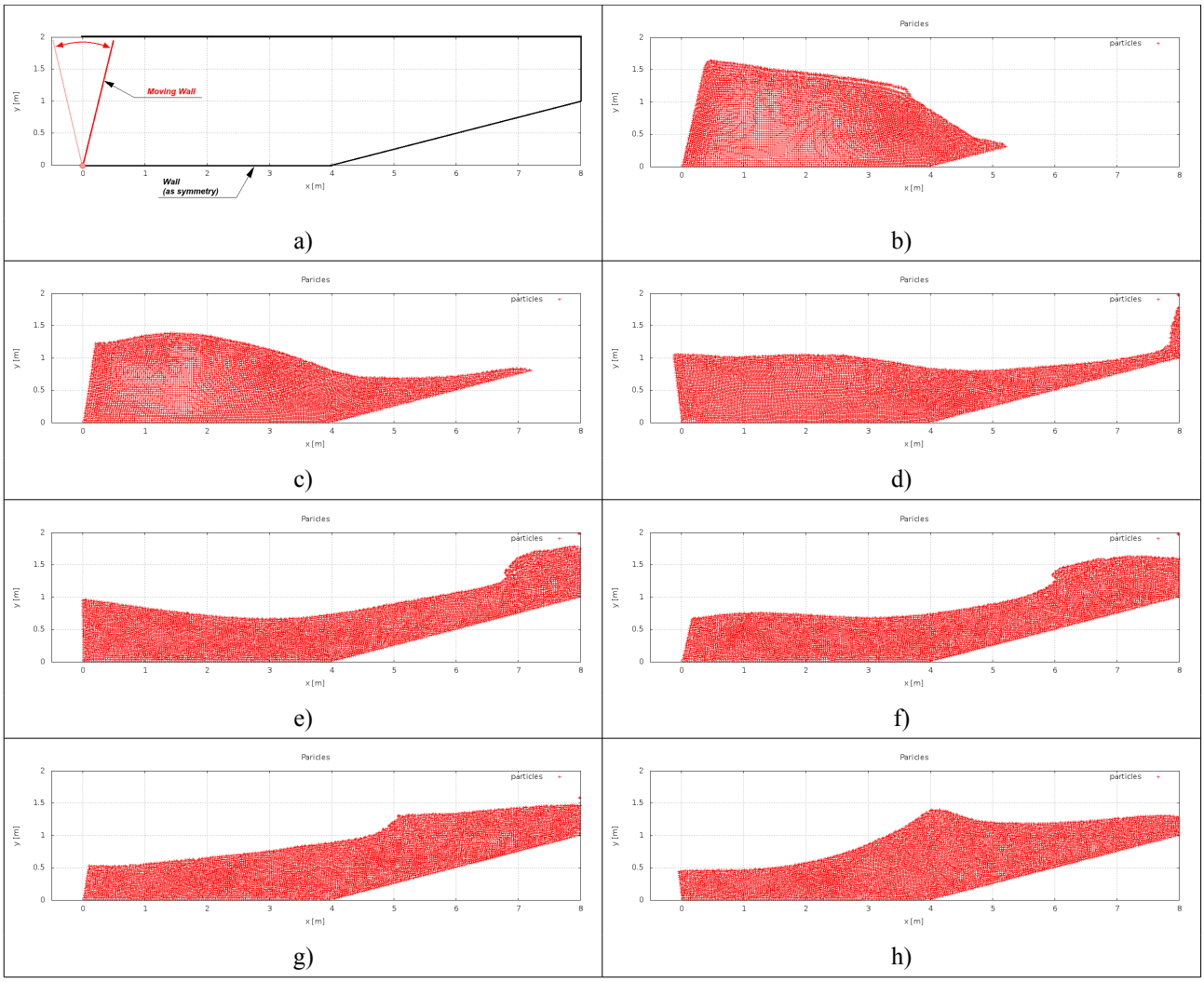

Fig. 8.. Results of test of SPH model. The particles of fluid in successive time steps.

CONCLUSIONS AND FUTURE WORK

- The testing computations of chain model give solutions which is similar to results which can be found in literature [3],[4].
- There is significant difference between maximum value of force N_1 obtained from stationary conditions and dynamic conditions (vertical oscillations of P_1), it means that the drag and inertia (including added masses) should be taken into account in resolving more complex issues.
- The simple test of SPH model gives results, which seems to be correct.
- As part of future work, it is planned to develop a 3D SPH model, and then develop procedures to simulate a movement of floating object. The next step will be the introduction of above presented chain model to calculate the movement of anchored objects.

REFERENCES:

[1] Morris J.P.: Analysis of Smoothed Particle Hydrodynamics with Applications. *Ph.D. Thesis*, Department of Mathematics, Monash University, July 1996

[2] Becker M.,Teschner M.: Weakly compressible SPH for free surface flows. *Eurographics/ ACM SIGGRAPH Symposium on Computer Animation* (2007), pp. 1–8

[3] Wilston J.F.: Dynamics of Offshore Structures, 2nd Edition. John Wiley & Sons, Inc.1984, 2003

[4] Chakrabarti Subrata K.:Offshore Structure Modeling. World Scientific Pub. Co. 1994

Critical evaluation of several LES and DES models for simulation of flow around a vertical surface-piercing cylinder

Grzegorz P. Filip[†1]**, Kevin J. Maki**[1] **and Sung-Eun Kim**[2]

[1]Department of Naval Architecture and Marine Engineering
University of Michigan, Ann Arbor, MI, 48109 USA
[gfilip, kjmaki]@umich.edu

[2]Naval Surface Warfare Center Carderock Division
West Bethesda, MD, 20817 USA
sungeun.kim@navy.mil

[†] Presenting Author

Introduction

The goal of this research is to simulate the flow around a vertical-oriented free-surface-piercing cylinder with high resolution in both the space and time coordinates. The spectrum of time-advancement and turbulence-modeling strategies to solve appropriate equations for this flow is broad. We utilize the OpenFOAM CFD toolkit as the platform for the development of our simulation tool. The freely available OpenFOAM library includes many commonly-used solution algorithms and turbulence modeling techniques, and provides the opportunity to implement custom solution methods. In this work we compare a fractional step (FSM) time advancement algorithm with the library-standard PISO-type method. Also, we examine several different sub-grid stress models, including a localized dynamic Smagorinsky model (locDynSmag) [10] and a localized dynamic kinetic energy transport model (LDKEM)[9].

Validation: Channel Flow

We begin with popular validation test case of fully-turbulent channel flow [7, 12]. The case corresponds to a Reynolds numbers based on the shear velocity of $Re_\tau = 395$. Results on a grid of 96^3 are shown here. Statistics are calculated over a time range of $100 < U_0 t/L < 200$.

Figure 1 shows the mean velocity profile compared to the DNS data of [12] and state-of-the-art LES simulations from the MPCUGLES code [1, 11]. In the left subfigure, the PISO time-advancement algorithm is used and the locDynSmag and LDKEM sub-grid stress models are compared. In the right subfigure, the locDynSmag sub-grid stress model is used and the PISO and FSM time-advancement strategies are compared. It can be seen that all of the presently computed solutions compare favorably with the DNS data of Moser et al.

Next, we turn to the prediction of the turbulent fluctuation. Figure 2 shows profiles of each component of the turbulent fluctuation. Here it is seen that the present LES simulations are close to those of Mattson [11], and slightly under predict the fluctuation when compared to the DNS data.

Validation: SUBOFF

A second validation case for the simulation of high-Reynolds number turbulent flow is the measurements made around the SUBOFF body [4]. Here we are concerned with the fully-appended configuration (AFF8) which includes a sail and four stern fins. Figure 3 shows the geometry and the solution where common features of the flow over a submarine can be seen. The fluid discretization is constructed using snappyHexMesh, an automated hexahedra-based mesh generator, which allows for significant time savings in the grid generation process. The extents of the domain are chosen to match the experimental setup inside of the DTRC Anechoic Flow Facility (AFF). The initial simulations of the SUBOFF geometry use grids containing approximately 11 million cells.

The Reynolds number is 1.2×10^7. The statistics are calculated over the time range $10 < U_0 t/L < 30$. The simulations used 100 computing cores and required approximately two hours of wall time per flow-over (defined as a characteristic length divided by the mean flow speed). In the results presented herein for this case, the PISO and PIMPLE time-advancement strategies are compared. PIMPLE is a method that permits large time steps to be taken, and in our practice maximum Courant numbers of 20 may be used. In PISO, the variable time-step

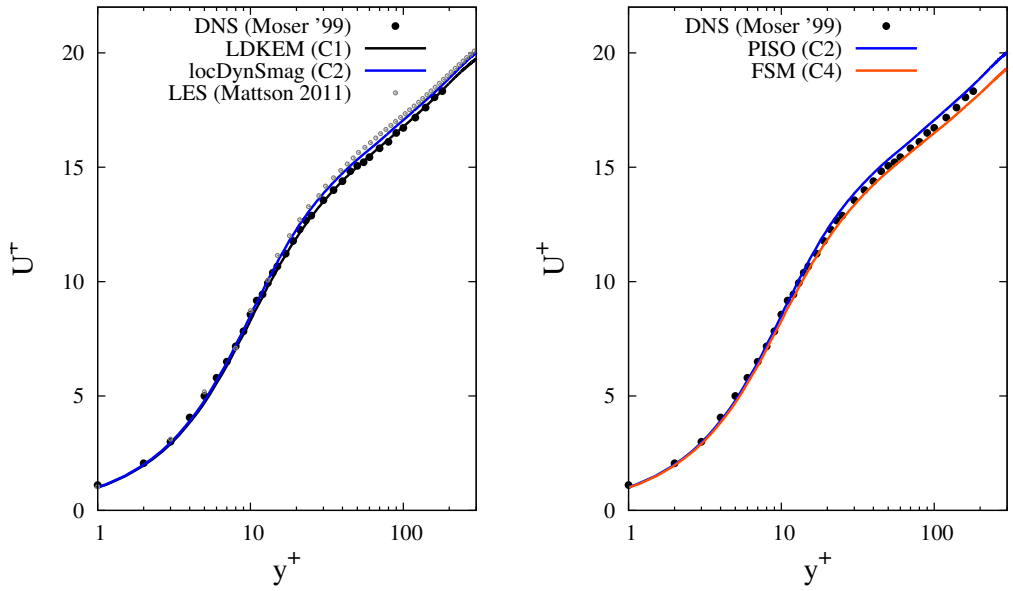

Figure 1: Mean velocity profile for channel flow $Re_\tau = 395$, on grid 96^3.

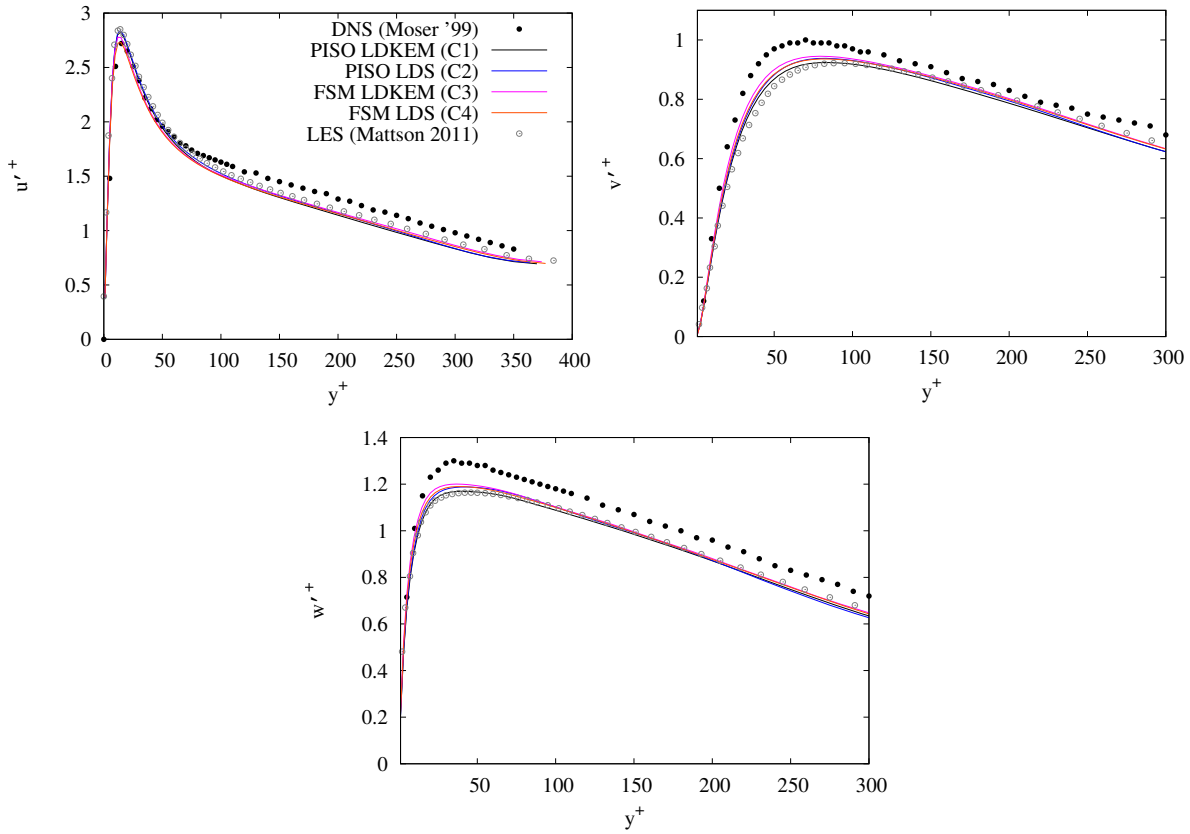

Figure 2: Turbulent fluctuation profile for channel flow $Re_\tau = 395$, on grid 96^3.

Table 1: Summary of SUBOFF case settings

Case	Turbulence Model	Solver
C1	LES+WF	PISO
C2	LES+WF	PIMPLE
C3	IDDES+WF	PISO
C4	IDDES+WF	PIMPLE

size is chosen so that the maximum Courant number is less than 0.4. Also, the local dynamic Smagorinsky LES solver is compared to results from a IDDES solver. In all cases, wall-functions are used. The four combinations of time-advancement and turbulence model are denoted C1-C4, and summarized in Table 1.

The mean-velocity profile in the propeller plane is shown in Figure 4. In the left subfigure, the two different turbulence modeling strategies are compared, each of which use the same PISO time-advancement algorithm. Comparison is also shown with the published LES data of [3] and the experiments of [4]. The present LES appear more regular than the IDDES, although both predictions compare well with the other data. The irregularity in the IDDES results could be due to a need for longer-time simulation for convergence of the statistics. Hybrid RANS/LES methods are also prone to switching problems which may cause the irregularity. In the right subfigure, the two time-advancement methods are compared, each of which employ the local dynamic Smagorinsky model. It appears that the larger time step size used in the PIMPLE algorithm has very little influence on the mean velocity profile.

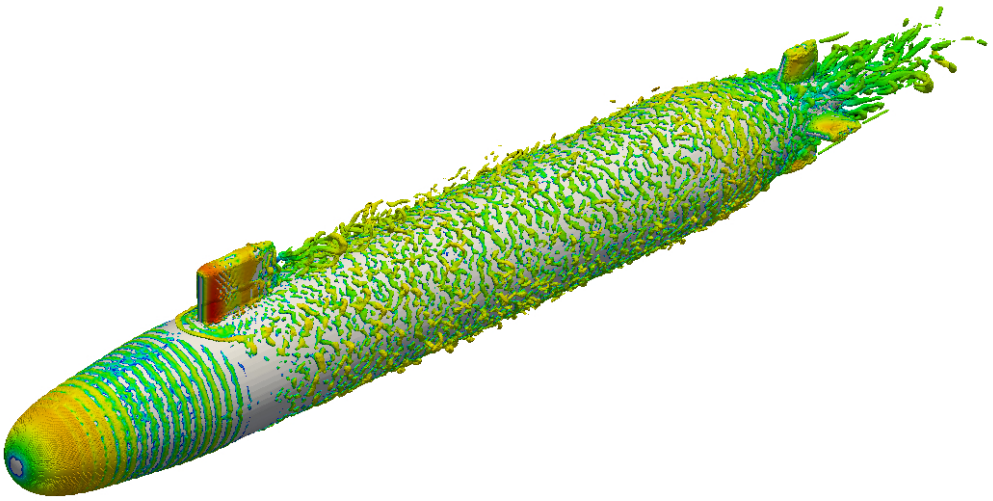

Figure 3: Turbulent structures colored by mean streamwise velocity - SUBOFF AFF8

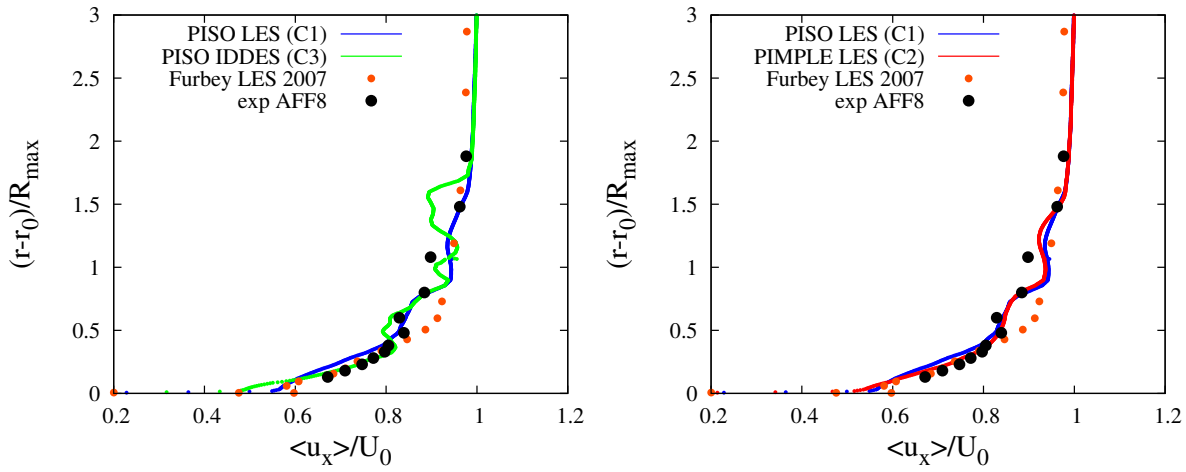

Figure 4: Mean velocity profile in propeller plane.

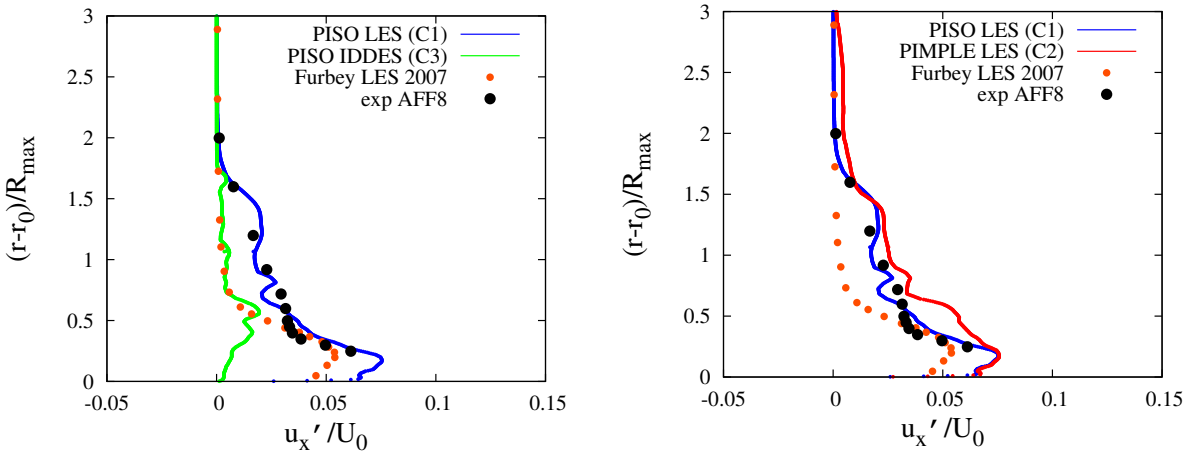

Figure 5: Fluctuating velocity profile in propeller plane.

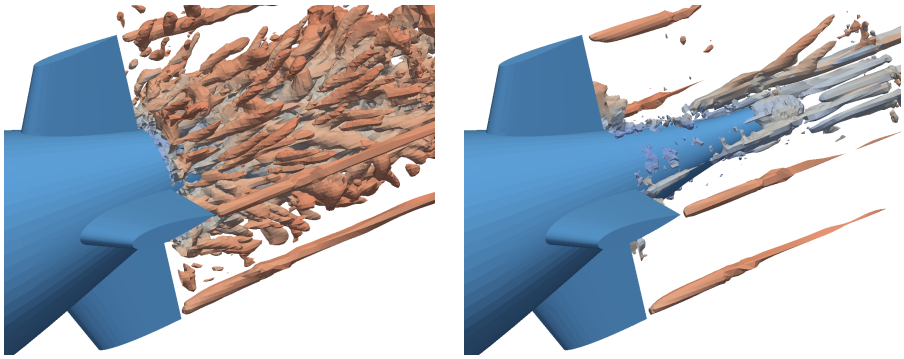

Figure 6: Turbulent structures in stern area. Left: LES, right: IDDES

Next, we examine the fluctuation of the velocity in the propeller plane, shown in Figure 5. In the left subfigure, the IDDES results show very little fluctuation compared to the experimental measurements. This is understandable because most of the fluctuation is in a region where the RANS-model is active, and hence should not accurately resolve the turbulent fluctuation. On the other hand, the LES results compare rather well with the experiments. Also, the current LES results appear to be better than the previously published simulation data [3]. In that work, a structured grid is used with stretching in the radial direction, whereas we employ a hex-dominant highly uniform discretization. This could explain the stronger agreement with our data and the experiments in the region near the edge of the boundary layer $(r - r_0)/R_{\max} \approx 1$.

The comparison of the two time-advancement methods is shown on the right of Figure 5. Here, the PIMPLE algorithm shows a slight over prediction in the velocity fluctuation.

To more easily visualize the performance of the different turbulence models in the wake, contours of the Q field are shown for each method in Figure 6. The LES results are shown on the left, and IDDES on the right. It is clear that the LES procedure allows for much finer structures to be resolved on the spatial grid. Also, in this figure the grid resolution of the tail-fins is easily observed.

Surface-Piercing Circular Cylinder

Loading on a vertically-oriented surface-piercing cylinder in the presence of a current are investigated next. We are interested in a high-fidelity numerical simulation of this problem because of the highly-nonlinear flow features present such as breaking waves and vortex shedding [2]. The results presented here utilize a discretized fluid domain composed of approximately 2.5 million hexehedral cells with an average non-dimensional near-wall spacing of 40. A universal wall-function is utilized to model the near-wall behavior (wall-resolved simulations are currently underway and will be included in our final presentation). The extents of the domain are similar to those of previously published numerical experiments [6, 13, 14].

The Reynolds number is 2.7×10^4 and the Froude number is 0.8 based on the free-stream velocity U_0 and the cylinder diameter D. The flow statistics are collected for 100 non-dimensional time periods (U_0t/D) after an initial 100 periods. The PISO algorithm is used with a maximum Courant number restricted to 0.4. The subgrid-scale terms are modeled using the localized dynamic one-equation eddy viscosity approach where a transport equation for the subgrid turbulent kinetic energy is solved.

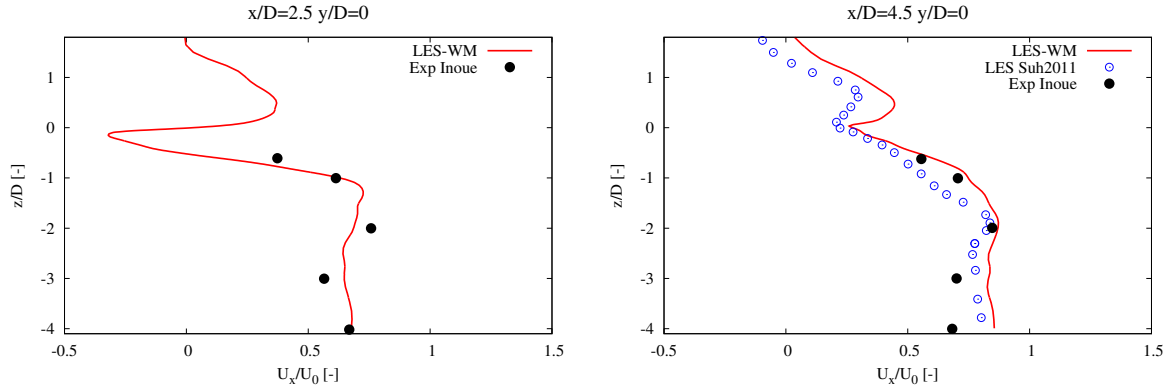

Figure 7: Vertical profiles of the mean streamwise velocity components with LES results of Suh et al [13] and experimental data of Inoue et al [5]

The vertical profiles of the mean streamwise velocity components at two locations in the wake of the cylinder are plotted in Figure 7 together with previously published LES results and experimental data points. The calm free-surface is located at $z/D = 0$. Our results on a relatively coarse, wall-modeled grid match the experimental results of [5] well and in some regions such as approximately one diameter below the calm free-surface, the present LES profiles match the experimental data better than those of Suh et al [13].

The time-averaged and the RMS free-surface elevations are shown in Figure 8. A well-defined wake pattern is clearly visible in the time-averaged contours but the magnitude and slope of the free-surface depression in the wake of the cylinder is under-predicted as also shown in Figure 9. The RMS free-surface fluctuations are estimated from the RMS of the vertical velocity component on the free-surface: $\eta' = w'^2/2g$ [8]. The near-body fluctuations compare favorably with the experimental data but the far-wake fluctuations are under-resolved.

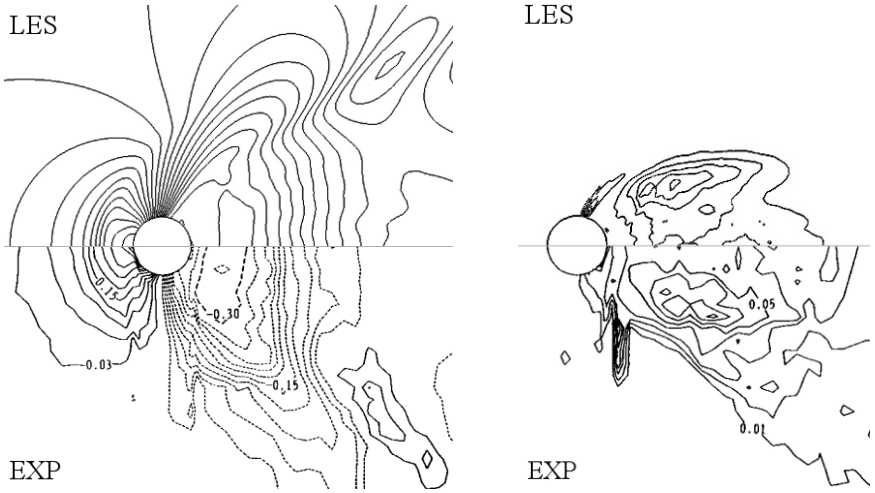

Figure 8: Time-averaged and RMS free-surface elevation contours compared to plots directly from [5]

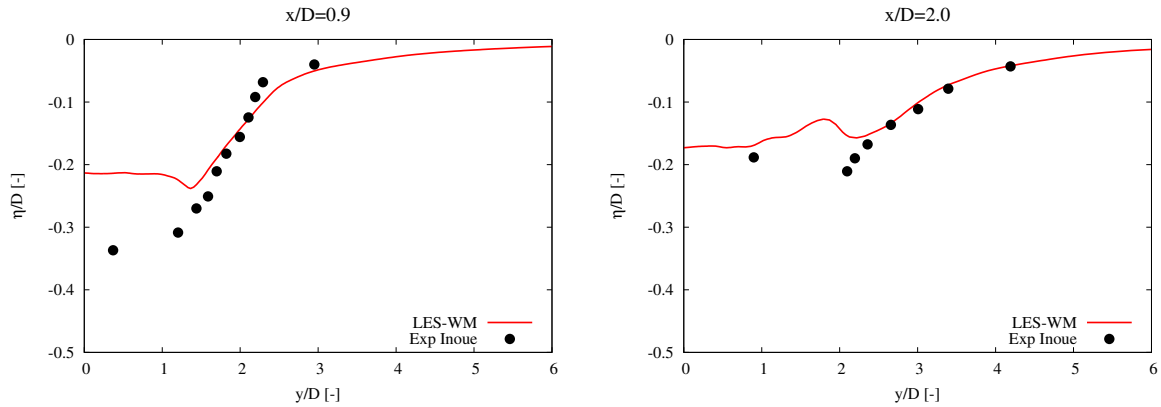

Figure 9: Time-average free-surface elevation slices at two locations in the wake of the cylinder

Bibliography

[1] Peter Chang, Minyee Jiang, Dory Lummer, and Krishnan Mahesh. Large-scale computations of unsteady forces on marine vehicles. In *2010 DoD High Performance Computing Modernization Program Users Group Conference*, 2010.

[2] J. R. Chaplin and P. Teigen. Steady flow past a vertical surface-piercing circular cylinder. *Journal of Fluids and Structures*, 18:271–285, 2003.

[3] C. Fureby. ILES and LES of complex engineering turbulent flows. *J. Fluids Eng.*, 129:1514–1523, December 2007.

[4] T. T. Huang, H-L. Liu, N. C. Groves, T. J. Forlini, J. Blanton, and S. Gowing. Measurements of flows over an axisymmetric body with various appendages (DARPA SUBOFF experiments). In *Proceedings of 19th Symposium on Naval Hydrodynamics*, Seoul, Korea, 1992.

[5] M. Inoue, N. Baba, and Y. J. Himeno. Experimental and numerical study of viscous flow field around an advancing vertical circular cylinder piercing a free-surface. *Journal of the Kansai Society of Naval Architects of Japan*, 220:57–64, 1993.

[6] T. Kawamura, S. Mayer, A. Garapon, and L. Sorensen. Largey eddy simulation of a flow past a free surface piercing circular cylinder. *Journal of Fluids Engineering*, 124:91–101, 2002.

[7] J. Kim, P. Moin, and R. Moser. Turbulence statistics in fully developed channel flow at low Reynolds number. *Journal of Fluid Mechanics*, 117:133–166, 1987.

[8] Sung-Eun Kim and Shin Hyung Rhee. Large eddy simulation of turbulent free surface flow around a surface-piercing hydrofoil. In *26th Symposium on Naval Hydrodynamics*, 2006.

[9] W. Kim and S. Menon. New dynamic one-equation subgrid-scale model for large eddy simulation. In *33rd Aerospace Sciences Meeting and Exhibit*, 1995.

[10] D. K. Lilly. A proposed modification of the Germano subgrid-scale closure method. *Physics of Fluids*, 4:633–635, 1992.

[11] M. D. Mattson. MPCUGLES: LES of turbulent channel flow. 2011.

[12] Robert D. Moser, John Kim, and Nagi N. Mansour. Direct numerical simulation of turbulent channel flow up to Re_τ=590. *Phys. Fluids*, 11(4):943–945, April 1999.

[13] Jungsoo Suh, Jianming Yang, and Frederick Stern. The effect of air-water interface on the vortex shedding from a vertical circular cylinder. *Journal of Fluids and Structures*, 27:1–22, 2011.

[14] G. Yu, E. J. Avital, and J. J. R. Williams. Large eddy simulation of flow past free surface piercing circular cylinders. *Journal of Fluids Engineering*, 130:1–9, 2008.

CFD Analysis of a Zero Speed Active Fin

A. Gattoronchieri – tel. +39 349 1259372 – mail a.gattoronchieri@gmail.com
S. Brizzolara – tel. +39 010 3532386 – fax +39 010 3532127 – mail brizzolara@dinav.unige.it
M. Viviani – tel. +39 010 3532547 – fax +39 010 3532127 – mail viviani@dinav.unige.it

Università degli Studi di Genova – Dipartimento di Ingegneria Navale e Tecnologie Marine (DINAV), Via Montallegro 1, 16145 Genova, Italy

INTRODUCTION

The reduction of the ship roll motions is a very important aim in the pleasure craft design because of its strong influence on the comfort onboard.
Fin stabilizers have been used to reduce the roll motion of ships in underway condition for years, since they generate the stabilizing moment working as a couple of foils with opposite angle of attack i.e. a symmetrical foil in an incoming flow generates a lift that is proportional to the square of the velocity and to its angle of attack, their effects at low and null speed are almost nil. For this reason anti-roll tanks have been adopted on many ships to reduce the roll at anchor but with serious drawbacks. The tanks have to be made quite large and have to be installed in a proper position to produce a considerable roll damping so it has a really strong influence on the internal arrangement.
In the last 15 years, pulled by the growing market of the pleasure craft and the request of higher comfort standards, different stabilizing systems have been studied.
The gyro stabilizers and the Zero Speed Fin are the most used, both of them are able to produce a stabilizing effect at zero speed and even in underway condition, the main differences between them are that the first one takes more time to be turned on and off, on the other hand the fins increase the hull resistance and can be damaged in collision with some floating object.
The working principle of the gyroscope is well known on the contrary the principle behind the zero speed stabilizers, explained as ‘‘paddle’’ Ooms 2002 [1], has not been deeply investigated yet. In literature it is possible to find analytical hydrodynamic models and 2D CFD simulations [2], and other works in which fins are compared with antiroll tanks and their use in anchored conditions is discussed [3,4] while CFD simulations of three dimensional model or model tests are not present. This research has the objective to find out the correct setting to realize an analysis of a zero speed fin with the commercial CFD code Star-CCM+, and later, using this model, to gain a deep understanding of the fluid dynamical behaviour.

WORKING PRINCIPLE

The active fin stabilizer systems belong to the group of the equilibrium stabilizer. These kinds of stabilizers generate a righting moment to counteract the disturbance moment from waves. Active fin stabilizer in underway condition produce the moment generating two lift forces in opposite direction, on the contrary when the ship is at a very low or null speed this system is disabled because the profile does not generate any lift force, in this condition Zero speed fins generate the force necessary to stabilize the ship rotating around their axis, producing the force by mainly two different contributions: a drag part that approximately scales with the square of the rotational speed and an inertial component related to the added mass and proportional to the rotational acceleration.
Considering this particular functioning principle the usual finite wing theory and the standard simplified design methods are not adequate to evaluate the fluid dynamic characteristics of a stabilizing fin working at zero speed. A CFD analysis has been carried out to investigate the fluid dynamic effects that characterize the problem. Some particular considerations are related to the design of these devices:

- The rotation axis is closer to the leading edge to limit the force reduction effect produced by the forward part.
- The aspect ratio is lower than a conventional stabilizing fin the chord being larger in order to have a higher rotational speed and flow acceleration at the trailing edge.
- The shaft is thicker than normal to withstand the torsional stresses.

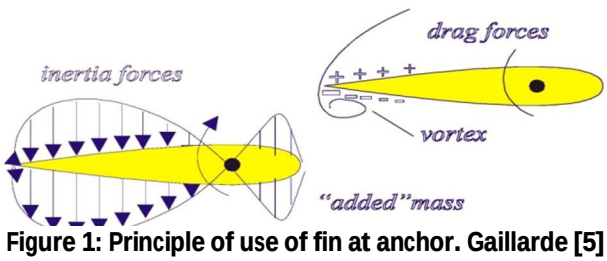

Figure 1: Principle of use of fin at anchor. Gaillarde [5]

CALCULATION SETUP AND RESULTS

A geometry of a typical commercial zero speed fin has been chosen as reference for the study. Its main dimensions are reported in Figure 2:

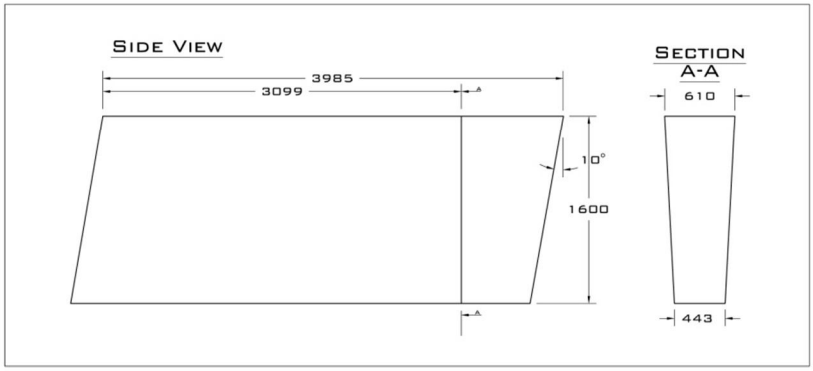

Figure 2: Sketch of Fin Geometry

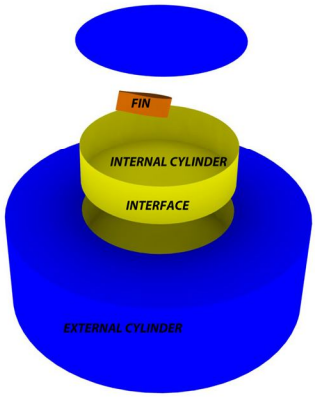

Figure 3 : Fin and fluid domain Geometry

In order to simplify the geometry of the problem the fin has been considered apart from the ship, placed in a cylindrical control volume split in two parts connected by an interface as can be seen in Figure 3. The inner region is characterized by a mesh finer than the outer one and rotates together with the fin; the external one is fixed and has an inlet boundary condition on the side surface which could allow in principle to set up an incoming flow in further analyses.

A preliminary sensitivity analysis on mesh resolution, time step and type of turbulence model has been carried out; the influence of these three parameters have been studied performing various simulations with different combinations of these factors, searching for the one that provides the more accurate description of the fluid with a reasonable computational cost. For the sake of shortness some details are provided for the mesh dependence analysis only.

Details of the dimensions of fin and cylinder adopted for the meshes in different cases are reported in table 1. The size on the outer boundary has been kept constant, because it has practically no effect on the flow-field around the fin; grid resolution close to the fin has been progressively increased to gain more accurate description of the various phenomena, among which the shed vortex. Details of the various meshes are reported in Figure 4, Figure 5 and Table 1, where the different meshes are named based on their target and minimum size on the fin surface: target is the length of the cell edge and minimum is the minimum length allowed where the target cannot be applied; these two parameters are used by Star-CCM+ mesher to produce the polyhedral mesh. All meshes have been tested in different conditions of constant speed and constant acceleration even higher than those reached by a real stabilizing fin (range 25-100 deg/s and 25-100 deg/s^2). A time step of about $2.5*10^{-3}$, small enough to satisfy the convective Courant condition for the smaller mesh with the highest speed, see Figure 6, has been used.

	Fin [cm]		Cylinder1 [cm]		Cylinder2 [cm]		
	target	min	target	min	target	min	Cells Num.:
mesh 1.2	2	1	8	4	100	25	1364723
mesh 2.4	4	2	16	8	100	25	219448
mesh 3.6	6	3	24	12	100	25	91393
mesh 4.8	8	4	24	12	100	25	43007

Table 1: Meshes dimensions

Considering the force and the moment, see figure 7 it is possible to observe only really small differences between the four mesh sizes while looking at the pressure contours shown in figure 8 it can be seen that the finest mesh allows to obtain a more accurate description of the vortices. Mesh1.2 has been adopted for the further simulations.

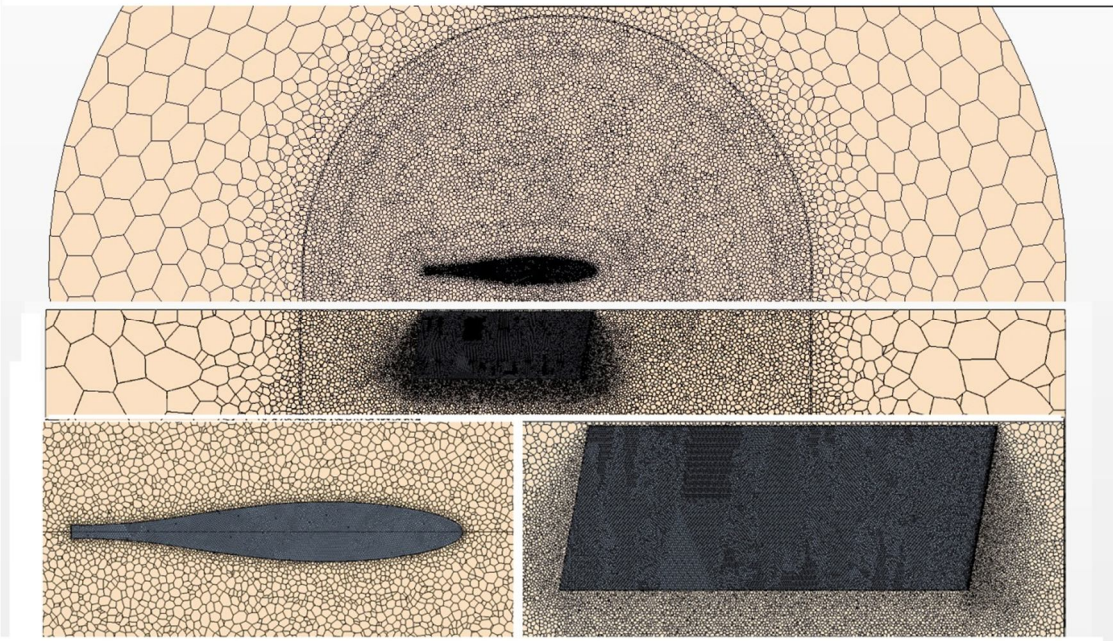

Figure 4: Mesh 1.2

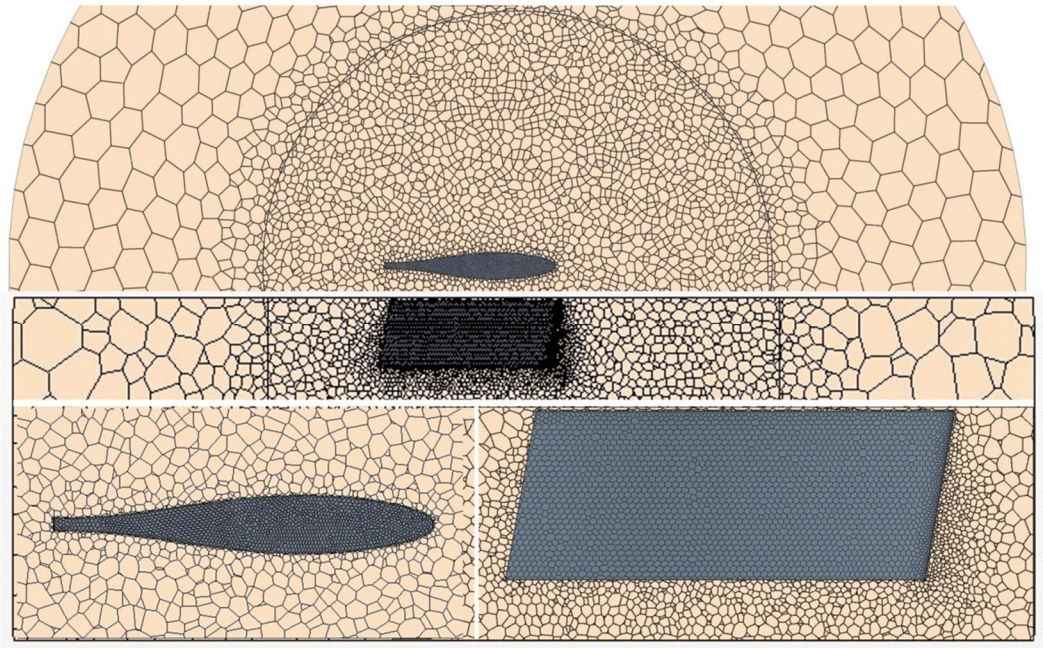

Figure 5: Mesh 3.6

In order to achieve a good convergence and reduce computational cost, the number of inner iterations was fixed to 10. As mentioned before, a similar sensitivity analyses have been carried out in order to choose the correct turbulence model and time step. The result obtained with LES, Reynolds Stress and K-ε models have been compared and no appreciable difference was observed, so the last one has been chosen for its higher simplicity. As regards the time step, it was found that the choice of an interval smaller than 0,0025s has no influence on the simulation except an obvious increase of the computational time, so this value has been used for all the simulations.

Using these settings several 2D and 3D tests have been made to evaluate how the three dimensional phenomena influence fin performance. First of all, some tests without the wall at the fin root were made paying attention to the spanwise flow and the change in the performance in order to get an approximated description of the effects of the hull proximity.

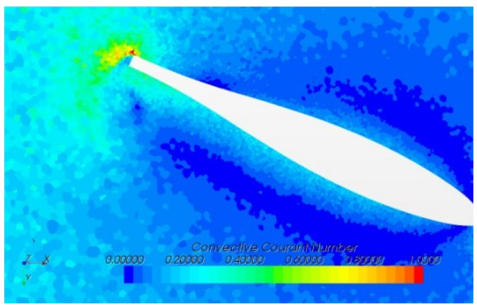

Figure 6: Courant Section -0.5m time 0.7s

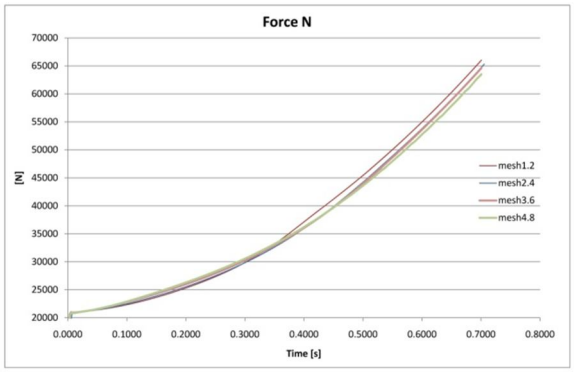

Figure 7: Force

The results corresponding to a rotation speed of 50°/s are reported in figure 9 as representative of the trends noted at different rotation speed. Pressure contours evidence that the tip vortex is wider and much more intense when the hull proximity effect is present; this is the reason why the normal force and the moment are higher in this configuration as shown in Figure 9.

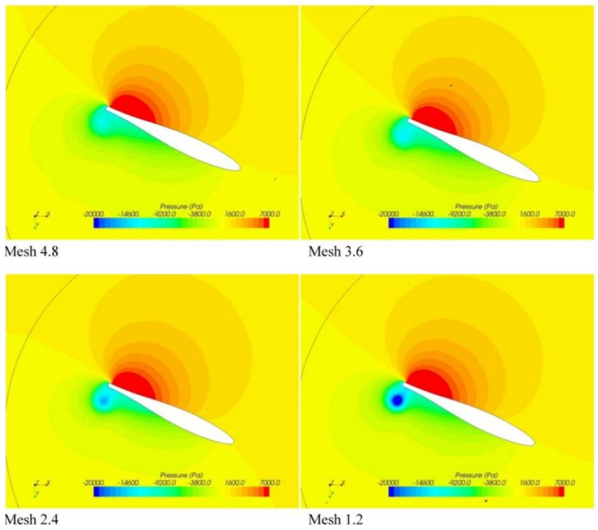

Figure 8: Pressure distribution section at z=1m from root

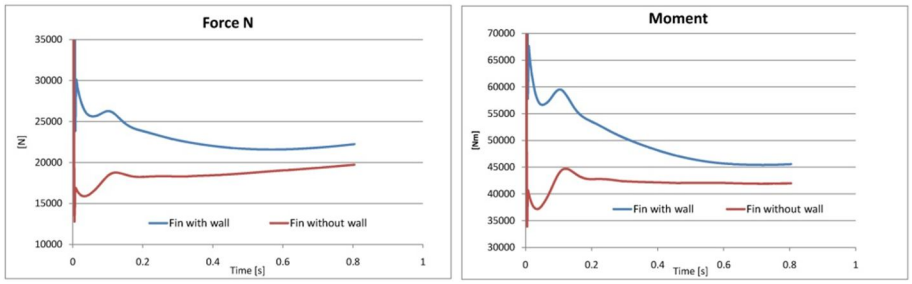

Figure 9: Force and momentum ω=50°/s

Figure 10 shows the pressure contour of an isolated fin (left) and the same fin with the wall close to the root (right). The blockage effect is clearly visible in the pressure contour: the cross flow region on the suction side (upper part of the image) is stronger and confined to the tip when the hull is present while it is distributed between the tip and the root in the other case; the iso-pressure (middle part of the image) on the pressure side of the fin without the wall shows a pressure drop close to the root due to the cross flow effects, in the middle; in the section at z=1m (lower part of the image) it can be seen that the vortex is larger and stronger when the wall is present. Figure 11 represent the generated vortex in three dimensions for the two cases through an iso-vorticity surface.

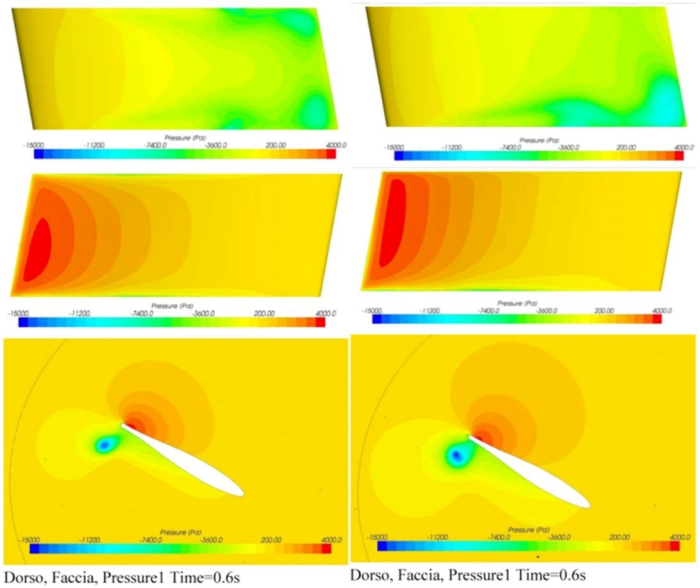

Figure 10 Pressure distribution at time 0.6 s suction side, pressure side, section at z=1m from root

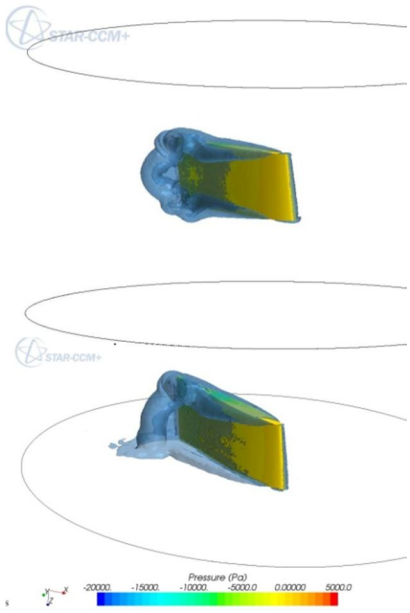

Figure 11 Iso-vorticity Time=0.6 s

These results confirm that zero speed fins show a relevant spanwise flow similarly to a wing in underway condition. The principal flow pattern induced by a moving fin is well captured by a 2D simulation where all the secondary three dimensional effects are neglected. Considering that analyzed fin is characterized by a down-sweep angle and has taper ratio equal to one the mid span profile has been used in the 2D simulation as representative of the entire fin. In this case the fin is actuated with a complete control law composed by three periods: constant acceleration of 50°/s^2 for 0.5s, constant speed of 25°/s for 1.9s and a constant acceleration opposite to the first one.
The time history of the force, represented in figure 12, can be divided in three parts: the first generated during the acceleration that is mainly due to the added mass effect, the second generated during the constant speed rotation due to the drag and the third part generated during the deceleration that is opposite to the first one and produce a destabilizing moment. Consequently the fin shape and the control law have to be developed in order to increase the performance during the constant speed period. The force produced by the 2D fin is 90% higher than the force of the 3D fin when it is moving with a constant speed and even higher during the acceleration; at the same time the Cp moves forward, due to a different evolution of the vortex generated at the trailing edge, resulting in a shorter lever arm. These results are plotted in figure 12. Overall, the 2D /infinite span profile is the best condition even at zero speed therefore it would be preferable to adopt geometries designed to reduce as much as possible the cross flow.

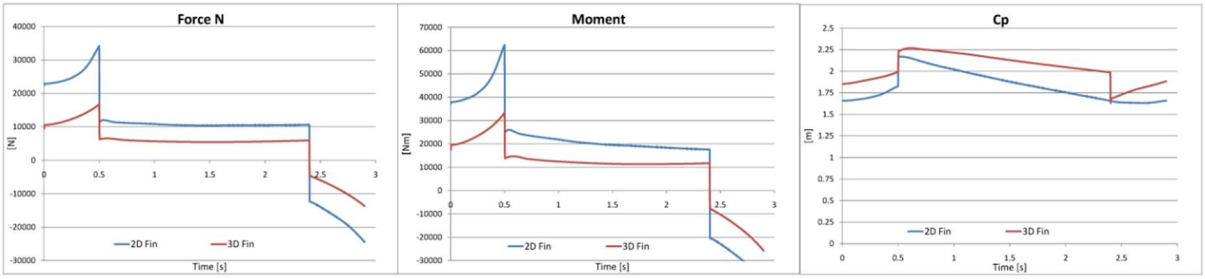

Figure 12: Force N, moment and Cp position 2D Fin and 3D Fin

Normally, in the case of a wing in an incoming flow the increase of the AR corresponds to an increase of the generated lift due to the reduction of the cross flow that tends to balance the pressure on the two sides of the fin. In the case of a zero speed fin an increase of the aspect ratio (keeping constant the fin area) produces two opposite effects: it reduces the cross flow but at the same time also the tangential velocity, which appears to have a quadratic influence on the generated force. For this reason an investigation about the influence of the aspect ratio has been carried out. Two different geometries with the same area of the original one and two different values of the aspect ratio, namely 0.25 (limit for a zero speed fin) and 1 (realistic for underway stabilizing fin) have been tested using the same control law. Two variables are used to compare the results of the different geometries: Cp/c is the ratio between the distance of the center of pressure from the rotation axis and the chord, the second one is the difference of the forces generated by the two geometries.

	Base	AR 0.25	AR 1
t/c	0.153	0.153	0.153
s/c	0.402	0.250	1.000
R.axis /c	0.223	0.223	0.223

Table 2: Fin characteristic with different aspect Ratio 0.4, 0.25, 1

For this analysis the results have been made dimensionless using the dimension of the original fin with aspect ratio equal to 0.4 to calculate the total pressure. As already discussed, increasing the aspect ratio of a wing operating underway an increment in the produced lift coefficient is obtained, on the contrary for a zero speed fin the lift coefficient increases at lower aspect ratio due to the larger chord.

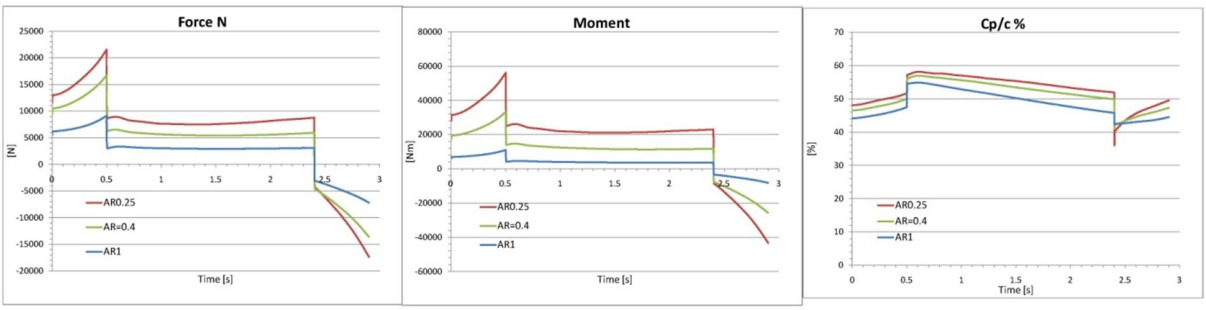

Figure 13: Force N, Moment, Cp for fin with AR 0.25, 0.4, 1

It is also interesting to compare the difference of the impulse of the force generated by the fin with the modified aspect ratio and the force generated by the fin with the standard geometry.
The comparison shows that the geometry with AR=0.25 produce an 80% increment of total force generated in a full run compared to the design with the AR=1. Cp/c % shows that the configuration with the AR=1 has the Cp closer to the leading edge due to the position of the trailing edge vortex closer to the rotation axis. This leads to a more efficient value of the moment per unit of stabilizing force.
The AR=1 presents also the more uniform pressure distribution (figure 14), in fact the important cross flow is less important compared to the case AR=0.25. However these two positive characteristic are less important with respect to the higher local velocities generated at the trailing edge by the AR=0.25. Hence if a high stabilizing force is required a fin design with a lower aspect ratio is eventually preferable.

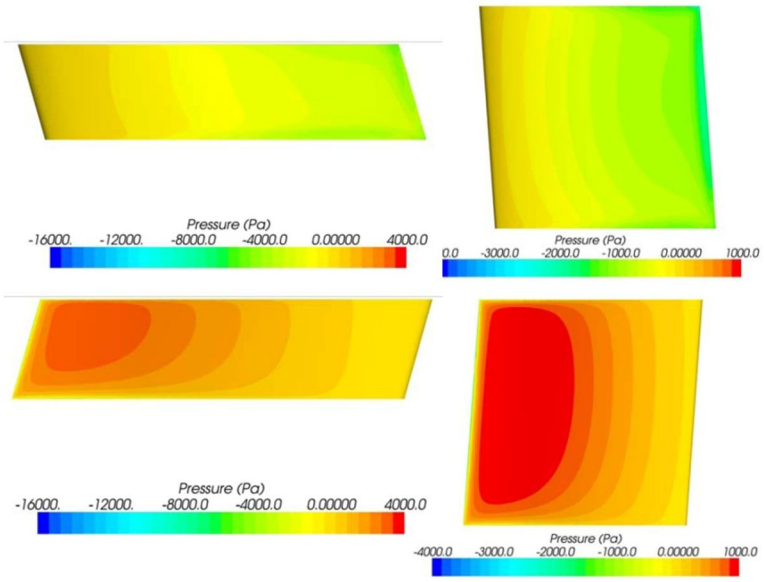

Figure 14: Pressure distribution at time 0.4 s AR=0.25 and AR=1

CONCLUSIONS

The setup for a CFD simulation of a zero speed fin has been defined with a sensitivity study for mesh size, time step and turbulence model. Using this model the three dimensional effects have been investigated and the importance of reducing the cross flow was underlined. The physics associated with the different phases of a complete fin flapping (pressure and inertial) have been discussed and finally the effects of the aspect ratio has been studied. It was proven that even if a fin with a low aspect ratio is more affected by cross flow phenomena, it is preferable in terms of stabilizing force due to the higher tangential velocity induced by its motions. Further analyses are still being performed to study a solution to reduce the cross flow and an analysis of influence of the ship roll motion on the fin performance is being carried out.

REFERENCES

1. J. Ooms:
   The Use of Roll Stabilizer Fins at Zero Speed, Project 2002, 18-20 Nov. 2002, Amsterdam

2. Wang Fan, JinHongzhang,QiZhigang:
   Modeling for active fin stabilizers at zero speed, Harbin University, Ocean engineering (36), 2009

3. Dallinga, R.P.:
   Roll Stabilization at Anchor: Hydrodynamic Aspects of the Comparison of Anti-Roll Tanks and Fins. Project 2002, Amsterdam, Nov. 2002

4. Dallinga, R.P.:
   Roll Stabilization of Motor Yachts: Use of Fin Stabilizers in anchored Conditions, Project 99, Amsterdam, Nov. 1999

5. G. Gaillarde, S.Toxopeus, T. Verwoest
   Hydrodynamics of large motor yachts: Past experience and future developments

6. A.Gattoronchieri
   Thesis: CFD Analysis of a Zero Speed Active Fin, University of Genova

Resistance Prediction of Medium-speed Catamarans Using Free-surface Viscous Flow Simulations

Max Haase, Jonathan Binns, Giles Thomas and Neil Bose
Australian Maritime College, University of Tasmania, Launceston, Australia
contact: mhaase@amc.edu.au

1 Introduction

High-speed catamarans have evolved in the last two decades as an efficient vessel class for fast sea transportation. To promote sustainable sea transportation and to meet raising ecological requirements to reduce the environmental impact, a new class of large fuel-efficient medium-speed catamaran ferries is under development. Rising fuel prices and the society's increasing awareness in environmental sustainability raise the demand for highly fuel-efficient vessels (Davidson et al., 2011a,b). As shown in earlier work (Haase et al., 2012), medium-speed catamarans will efficiently operate at Foude numbers of $Fr = 0.35$, but unfortunately resistance prediction tools lack for twin-hull craft in that particular speed range. Therefore, there is a demand for numerical tools to correctly determine the resistance of such craft independent of speed, hull form and scale.

Not only the resistance, rather the hydrodynamic phenomena occurring at this speed range between the displacement and planing regime are of interest to understand the flow to more efficiently design such craft. A viscous free-surface flow solver has been chosen to study the fluid-hull interaction for a variety of different hull forms which are free to heave and trim.

To validate the computational set up the results of the NPL catamaran series (Bailey, 1976; Molland et al., 1994) has been chosen, hull form particulars can be found in Table 1. They provide a broad variation of hull configurations and speeds, where total resistance, trim, sinkage and wave pattern resistance has been measured. Experimental results have to be carefully considered, as the median total uncertainty may go up to 10 % in resistance, 42 % in sinkage and even 52 % in trim depending on Froude number and model length, according to Gorski et al. (2011).

Table 1: Hull form parameters of catamaran utilised for this study.

NPL	$L[m]$	$L/\nabla^{1/3}$	s/L
6b	1.6	9.5	0.2

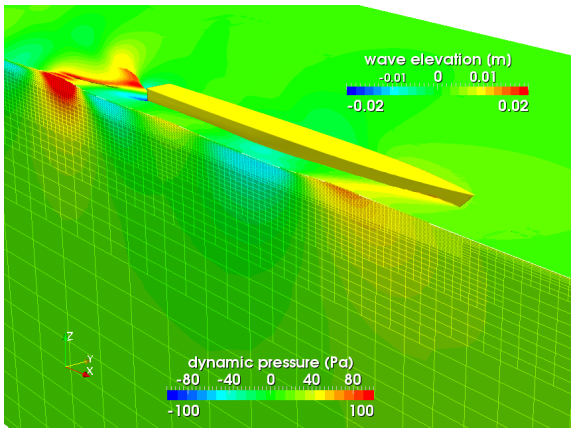

Figure 1: Wave elevation of NPL catamaran at $Fr = 0.35$ and the pressure distribution along the centre plane.

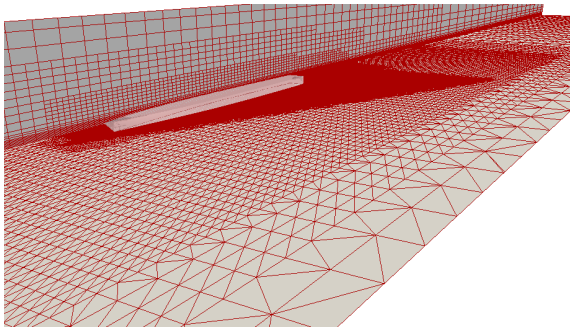

Figure 2: Structure of of hexagonal mesh for NPL 6b with $s/L = 0.2$ created using STAR-CCM+.

2 Computational Set-up

2.1 Viscous Flow Solver

In the framework of this research project, OpenFOAM has been chosen to simulate the flow around the vessel, which is much used within the community of computational fluid dynamics for marine applications, as by el Moctar et al. (2010); Maki (2011); Kornev et al. (2011); Haase et al. (2011).

The mesh to discretise the computational domain has been build using STAR-CCM+. Even though open source tools for mesh generation within OpenFOAM or third party contributors are available, it has been found convenient to use the meshing tools of STAR-CCM+.

In accordance with Marnet-CFD and ITTC (2011) the two-equation turbulence model $k - \omega$ SST (Menter, 1993, 1996) with wall functions has been applied.

2.2 Computational Mesh

It is expected that the flow phenomena around the ship needs to be well resolved to accurately predict the calm water resistance. Far away from the vessel, the resolution is chosen coarse as the influence on the resistance may be negligible and computational resources can be used more efficiently.

The hull is resolved with approximately 20,000 cells, whereas significant refinements have been made around the edge of the transom to resolve the large pressure gradients. The first cells in normal direction of the hull are logarithmically enlarged prism cells to capture the boundary layer flow. The use of wall functions allows relatively large cells with a $y^+ \approx 75$. The diverging waves are captured by a refinement of the area which is enclosed by the so called Kelvin angle. Further refinements can be found around and in between the demihulls and aft of the transom to resolve the rooster tail, pressure peaks around the hull (Figure 1) and potential and viscous wake effects. The boundaries have been chosen accordingly to the towing tank in which the experiments have been carried out. The mesh consists of around 1,300,000 cells and can be seen in Figure 2. A similar refinement strategy has been chosen by el Moctar et al. (2010).

2.3 y^+ Study

The flow close to the hull has been simulated using wall functions. Therefore, the first cell on the hull needs to be extended into the logarithmic region of the boundary layer where turbulent stresses are dominant. Closer to the wall, viscous stresses are of equal or major importance compared to turbulent stresses. The application of a wall function reduces the number of required cells, because it is not required to have a very fine resolution close to the hull in normal direction. Generally, the dimensionless cell height of the first cell is between $30 < y^+ < 100$ or

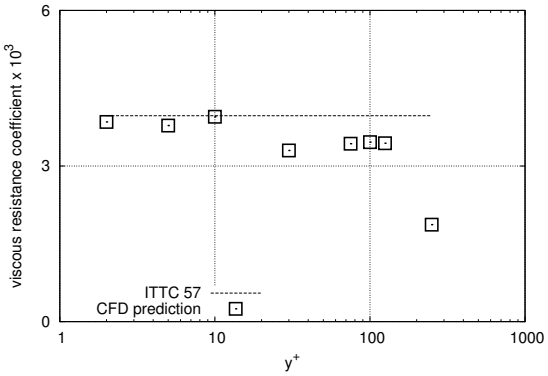

Figure 3: Force coefficient due to shear stress for different nominal values of y+.

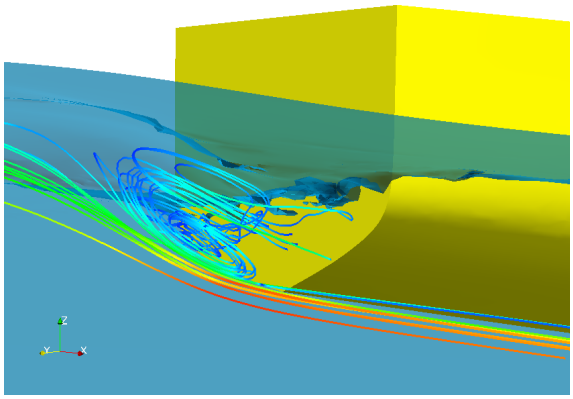

Figure 4: Flow Structure at the stern of NPL catamaran at $Fr = 0.20$.

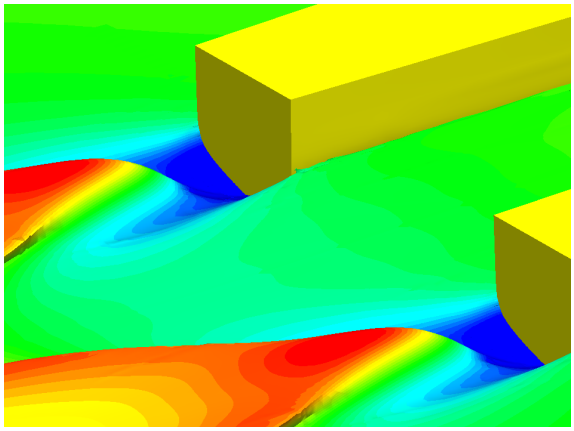

Figure 5: Dry transom and separated flow of NPL catamaran at $Fr = 0.35$.

larger values (Marnet-CFD; ITTC, 2011).

In Figure 3 the force coefficient due to tangential stresses on the hull has been plotted with respect to variations in y^+. The wetted hull has been considered in an unbounded fluid at a representative Reynolds number of $Re = 2.22 \cdot 10^6$, which corresponds to a Froude number of $Fr = 0.35$ at model scale. For values of $y^+ \leq 10$ the force is almost independent of y^+ and higher than for higher y^+. In the valid range $30 < y^+ < 125$ the force coefficient does not differ much, but decreases significantly when a certain limit of y^+ is exceeded.

3 Major Flow Phenomena

The forces on the hull can be simply subdivided into tangential and normal stresses, but a variety hydrodynamic phenomena occur around the demihulls of medium-speed catamarans, which need to be accurately predicted to correctly determine the overall calm water performance of such craft. So far, the following have been identified:

3.1 Transom Flow Separation

The flow separates at the transom stern after exceeding a certain speed. The simulations suggest a dry transom for $Fr \geq 0.30$, as can be seen in Figure 5. This causes ambient pressure at the separation point which leads to high pressure gradients around the edge of the transom. Compared to the pressure around the hull, a considerable low pressure region is induced which may have a significant effect on sinkage and trim of the boat, as can be seen in Figure 6. Furthermore, behind the dry transom a significant rooster tail builds up and interacts with the wake of the opposite demihull. Even though the transom is not dry, the fluid separates at the edge of the transom and forms a confused flow at the transom, as shown in Figure 4.

3.2 Sinkage and Trim

Due to a change in pressure distribution on the wetted hull surface, the floating position of the vessel changes dramatically around hump speed. Stagnation at the bow causes a high-pressure region, accelerated fluid around midship a low pressure and another small area of relatively high low-pressure directly at the transom edge, as shown in Figure 7. This results in a bow-up trim motion and an increase in draft. A change in trim causes an increase in wave resistance (Davidson et al., 2011b).

3.3 Demihull Interaction

The demihulls are in close proximity and influence the flow around each other. This can be seen through a asymmetric pressure distribution on the wetted hull as well as significant wave troughs and crests between the

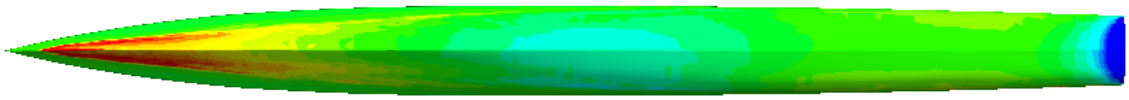

Figure 7: Distribution of dynamic pressure on the hull at $Fr = 0.35$.

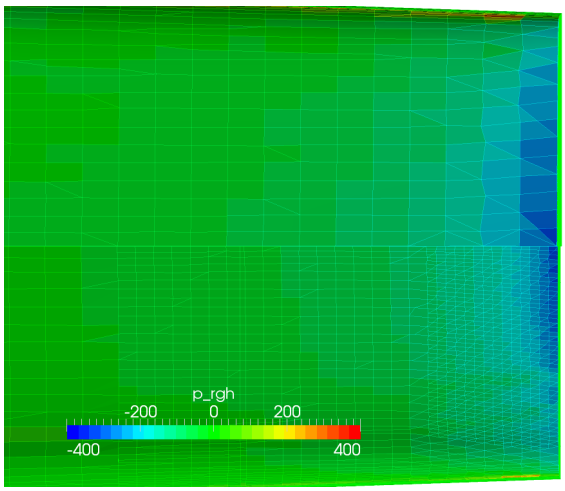

Figure 6: Dynamic pressure distribution at the stern. The upper part shows a coarse mesh resolution, the lower a finer one.

demihulls.

4 Calm Water Performance Prediction

The quality of the flow simulation around medium-speed catamarans is judged by different criteria. Most important the total resistance has to be predicted correctly, but also the correct ratio of tangential and normal pressures to which of major importance for extrapolating resistance data, i.e. being independent of Reynolds number. Secondly, the resistance is significantly influenced by the squat of the boat. Therefore, a correct resistance prediction can be achieved only when trim and sinkage are predicted correctly. Figure 1 shows the wave elevation and pressure distribution of a catamaran half model of the NPL series (Bailey, 1976) as used by Molland et al. (1994).

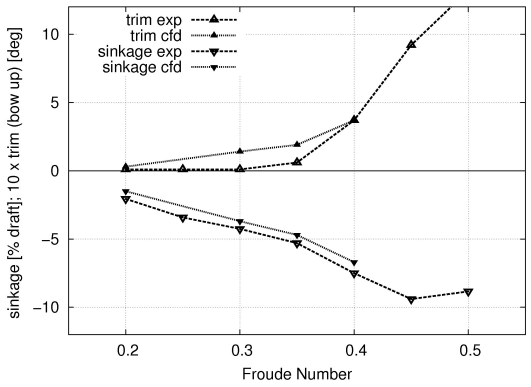

Figure 8: Trim (positive bow-up) and sinkage (increase in draft) of NPL 6b model with $s/L = 0.2$.

4.1 Sinkage and Trim

Figures 8 show the experimentally and numerically determined values for sinkage and trim. The value of sinkage rises almost by a linear rate for $0.20 < Fr \leq 0.45$ and the numerically derived values correlate well with the experimental values over a wide speed range of Froude numbers.

The trim of the model is negligible for $Fr \leq 0.35$ and increases significantly beyond that speed. However the increase for $Fr > 0.35$ is less pronounced in the simulation.

The values for trim and sinkage have been presented with respect to the numerically determined floating position at zero speed.

4.2 Total Resistance

The main goal of this research is to accurately predict drag force, expressed by the total resistance coefficient. As can be seen in Figure 9 the experimentally determined value is characterised by humps and hollows due to wave-making and demihull in-

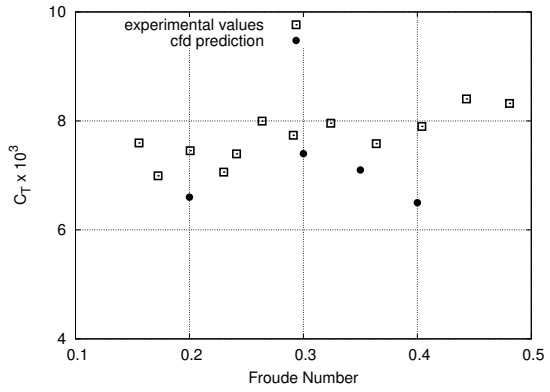

Figure 9: Total resistance coefficient of NPL 6b catamarans derived from experiments by Molland et al. (1994) and numerical simulations.

teraction. The simulations predicts values of the resistance coefficients which are under-predicted by 10 % referring to the experimental values for $Fr = 0.30, 0.35$ and under-predicted by 18 % at $Fr = 0.40$. An under-prediction by 10 % is in the range of measurement uncertainty Gorski et al. (2011).

At $Fr = 0.40$ the under-prediction of total resistance is in correlation with the under-estimated rise in trim. Catamarans are known to have significant demihull interference due to wave-making in that particular speed range which leads to an increased trim and wave-making, compared to a single demihull in isolation. The effect of interference influences the sinkage less significantly. Therefore, the under-prediction in trim and total resistance may be related to an insufficient resolution of the grid between the demihulls, where interference effects cannot fully develop.

5 Conclusions

First simulations of the resistance prediction using free-surface viscous flow simulations show promising results. Major flow phenomena have been resolved successfully and experimentally determined results could be reproduced. The code is able to predict values of sinkage and trim of a catamaran in a transitional speed range. Also, the total resistance coefficient can be obtained, even though the values is less accurate for speeds of $Fr = 0.40$ compared to experimental data. It can be concluded that an accurate value of total resistance is coupled to a satisfying prediction of the boat's squat.

In future research hull forms of wave-piercer catamarans will be investigated and hull form parameter varied towards a minimum resistance. The understanding of the flow phenomena at the medium-speed range is a major focus to efficiently design and optimise hull form for such craft. Another focus is the extrapolation the total model-scale resistance to full scale. Furthermore, effects of restricted water for the model ship and unbounded waterways for the full scale vessel will be taken into account.

Researchers have shown, that full-scale CFD can be a used to predict the full-scale performance including scaling effects due to a change in Reynolds number (Raven et al., 2008). Using CFD for model-ship extrapolation will take the viscous effects on the normal pressures into account and has the potential to be a fully non-linear tool to predict the full scale ship resistance independently of scale and hull form.

During this project, model scale experiments will be utilised to validate the resistance prediction in model scale for significantly restricted and less restricted waters data from full scale sea trials will be used to determine the required power of the vessel. Therefore the quality of the extrapolation can be evaluated.

6 Acknowledgements

This research has been conducted as part of a collaboration research project between Incat Tasmania Ltd Pty, Revolution Design Pty Ltd, MARIN, Wärtsilä, the University of Tasmania and the Australian Maritime College with funding from the Australian Research Council, project ID: LP110100080.

7 Bibliography

D. Bailey. *The NPL High-Speed Round Bilge Displacement Hull Series*, volume No. 4. Royal Institution of Naval Architects, 1976.

G. Davidson, T. R. Roberts, S. Friezer, M. R. Davis, N. Bose, G. Thomas, J. Binns, and R. Verbeek. Maximising Efficiency and Minimising Cost in High Speed Craft. In *International Conference on Fast Sea Transportation*, volume 11, 2011a.

G. Davidson, T. R. Roberts, S. Friezer, G. Thomas, N. Bose, M. R. Davis, and R. Verbeek. 130m Wave Piercer Catamaran: A New Energy Efficient Multihull Operating at Critical Speeds. In *Proceedings of International RINA Conference on High Speed Marine Vehicles*, pages 61–72, 2011b.

B. el Moctar, J. Kaufmann, J. Ley, J. Oberhagemann, V. Shigunov, and T. Zorn. Prediction of Ship Resistance and Ship Motions Using RANSE. In *Proceeding of Gothenburg Workshop*, 2010.

J. Gorski, S. R. Turnock, B. Alessandrini, H. Chun, U. Hollenbach, T. Mikkola, Y. Tahara, J. Valle, and L. Ying. The Resistance Committee - Final report and Recommendations to the 26th ITTC. In *Proceeding of 26th Iternational Towing Tank Conference*, 2011.

M. Haase, S. Winkler, N. Kornev, and R. Bronsart. Experimental Validation of Viscous Free Surface Flow Computation around Fast NPL Catamarans at Large Drift Angles. In *Proceedings of 1st International Symposium of Naval Architecture and Maritime*, 2011.

M. Haase, G. Davidson, S. Friezer, J. Binns, G. Thomas, and N. Bose. On the Macro Hydrodynamic Design of Highly Efficient Medium-Speed Catamarans with Minimum Resistance. *International Journal of Maritime Engineering*, 2012.

ITTC. Practical Guidelines for Ship CFD Applications. online, 2011.

N. Kornev, A. Taranov, E. Shchukin, and L. Kleinsorge. Development of Hybrid URANS-LES Methods for Flow Simulations in the Ship Stern Area. *Ocean Engineering*, 38: 1831–1838, 2011.

K. Maki. Ship Resistance Simulations with OpenFOAM. In *6th OpenFOAM Workshop*, 2011.

Marnet-CFD. Best Practice Guidelines for Marine Applications of Computatonal Fluid Dynamics. online.

F. R. Menter. Zonal Two Equation k-omega Turbulence Models for Aerodynamic Flows. *AIAA*, 1993.

F. R. Menter. A Cmparison of Some Recent Eddy-Viscosity Turbulence Models. *Transactions of SNAME*, 118:514–519, 1996.

A. F. Molland, J. F. Wellicome, and P. R. Couser. Resistance Experiments on a Series of High Speed Displacement Catamarans Forms: Variation of Length-Displacement Ratio and Breadth-Draught Ratio. Technical Report 71, University of Southampton, March 1994.

H. C. Raven, A. van der Ploeg, A. R. Starke, and L. Eça. Towards a CFD-based Prediction of Ship Performance - Progress in Predicting Fill-Scale Resistance and Scale Effects. In *Proceedings of RINA Marine CFD Conference*, 2008.

Database Fed Body Force Propulsor

Jens Höpken[*], Ould el Moctar[†]

1 Introduction

Assuring a ship's manoeuvrability is one of the most fundamental requirements for a safe and economic vessel operation. Considering the growth in overall shipping and demand for larger ships, the necessity of predicting the vessel's manoeuvrability more precisely arises.

Both the propulsion devices as well as the characteristics of the machinery do have an influence on the ship manoeuvrability and should be accounted for. Due to the different timescales between the motion of the ship and the rotation of the propulsor, a geometrical modelling of the latter forbids itself. This modelling would increase the required computational efforts even higher, rendering the entire model to be not feasible. Hence investigating the influence of the interaction between the propulsion devices and the hull on ship manoeuvring is a challenging task.

Choosing body force models as a compromise between accuracy and computational effort is a popular alternative. The aim of this study is to develop such a body force propulsor, but without a simple analytic model that distributes the thrust and torque over the propeller disk [2, 5]. Instead a database is filled with data gathered from various simulations of the desired propeller under diverse operational conditions, prior to the actual manoeuvring simulation. During the actual manoeuvring simulations, the volume forces can be calculated from the precomputed data and inserted as source terms to the momentum equation.

[*]jens.hoepken@uni-due.de, University of Duisburg-Essen, Duisburg, Germany

[†]ould.el-moctar@uni-due.de, University of Duisburg-Essen, Duisburg, Germany

Although no manoeuvring simulations can be shown, a validation of the current body force propulsor implementation is presented within this paper.

1.1 Database

The database should be accessible from any machine in the local network, regardless if it is a local workstation or the HPC Cluster. Gathering the desired data from the database must be possible with as less effort as possible. For this reason a MySQL database has been chosen.

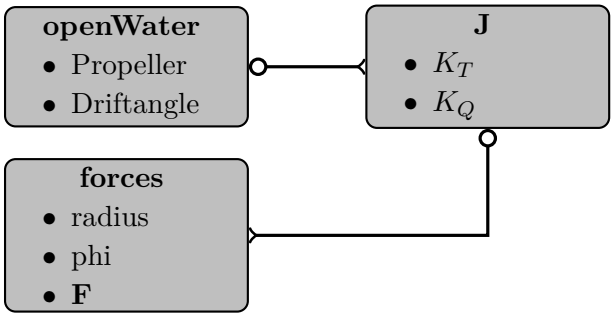

Figure 1: Database relation diagram

Besides the relevant data such as force distribution on the propeller blades and open water diagrams, additional data is stored in the database as well (see Figure 1). This additional data includes the geometries of both ship and propulsor, solver settings and a history the data. Depending on the solver used to generate the propeller forces, the data has to be structured differently (see section 3.1).

Using a fairly straightforward SQL syntax, the desired data can be selected almost instantly. The interpolation between different advance coefficients J and locations on the propeller blade

has to be done inside the body force model (see section 4).

All data that should be stored in the database is filled in during post-processing using various Python tools. This enables the database to be filled by results obtained by various solvers and codes.

2 Geometry

Being designed for validation purposes, the Duisburg Test Case (DTC) is a conventional single screw container vessel (cp. Figure 2 and Moctar, Shigunov, and Zorn [4]). With a length between perpendiculars of $L_{PP} = 355.0\,\mathrm{m}$, a breadth of $B = 51.0\,\mathrm{m}$ and a draught of $T = 14.5\,\mathrm{m}$, the DTC is a relatively large container ship.

Figure 2: Longitudinal view of the DTC

It's propulsor is a five bladed propeller with a diameter $D = 8.91\,\mathrm{m}$ and an area ratio of $\frac{A_E}{A_0} = 0.8$ and can be seen in Figure 3. Model tests at a scale of $\lambda = 59.407$ have been conducted at the Potsdam Model Basin (SVA) [6]. These investigations included ship resistance as well as open water tests in the circulation tank.

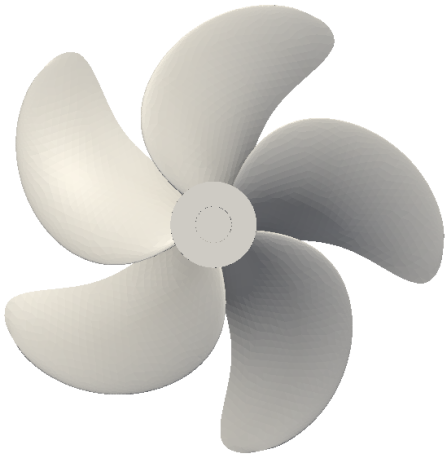

Figure 3: DTC Propller

3 Numerical Method

Three solvers are used within this study; two are used to generate input data for the database and the third one is utilised to test the output of the body force propulsor model.

To generate force input data for the database `MRFSimpleFoam` and `ISTHydro` are employed. The first one code solves the Navier-Stokes equations (1) for an incompressible and isothermal fluid in a steady-state formulation with multiple reference frames (MRF). Turbulence is modelled in a generic manner, that is common in OpenFOAM. This means that one can choose between a LES, RANS and laminar closure for the Reynolds stresses without having the need to switch between solvers. Pressure-velocity coupling is done with a SIMPLE algorithm.

$$\begin{aligned} \nabla \cdot \mathbf{u} &= 0 \qquad (1) \\ \nabla \cdot (\mathbf{uu}) - \nabla \cdot (\nu_{eff} \nabla \cdot \mathbf{u}) &= -\nabla p \end{aligned}$$

By taking advantage of the MRF method, certain regions of the mesh can be assumed to be rotating, though they are not doing so in a geometrical manner. The rotation is imposed by adding appropriate source terms to the right hand side of the momentum equation, accounting for additional Coriolis's forces. Such a region is employed around the propeller and the need to use a geometrically rotating propeller can be avoided by this.

Rather than being based upon the Navier-Stokes equations (1), `ISTHydro` is a boundary element method that solves Laplace's equation (2) on a discretised surface [3].

$$\nabla^2 \phi = 0 \qquad (2)$$

In the current implementation of `ISTHydro`, the surface has to be discretised solely using planar quads. The quads are generated from the PFF surface description in an automatic manner.

All tests of the body force propulsor implementation are performed by means of `simpleFoam`, that is similar to the previously described `MRFSimpleFoam`, but lacking the MRF feature.

3.1 Forces in ISTHydro

After an `ISTHydro` simulation is finished, a result file is written automatically. Among other data, the total force $\mathbf{F}$ on the propeller is stored as well as the average forces $\mathbf{f}$ acting upon discrete radii r_i. Adding all those forces gives the total force:

$$\mathbf{F} = \sum \mathbf{f}\left(r_i\right) \tag{3}$$

The output is thus assumed to be based on an infinite number of blades, as the forces solely depend on the radius and not on an angle.

3.2 Forces in OpenFOAM

In OpenFOAM the forces acting on a boundary patch can be calculated by using `libforces`. This gives one integral value for the forces and moments, respectively. To refine the spatial resolution of the force calculation, the above mentioned library is extended to calculate the forces for each boundary face separately and store that in a text file.

3.3 Mesh Generation

Mesh generation is done by utilising the standard OpenFOAM mesh generators `blockMesh` and `snappyHexMesh` are used, that are provided within the releases of OpenFOAM. The purpose of the first meshes is to evaluate the feasibility of `MRFSimpleFoam` for simulations of open water tests. Hence the propeller geometry must be modelled geometrically.

In order to compare the results of OpenFOAM with the ones obtained by `ISTHydro` on the basis of run times of same orders of magnitude, two major restrictions are applied for this kind of mesh:

1. Since the computed data will be stored in a database and a lot of interpolation will be necessary for their application in the body force propulsor, turbulence modelling as well as prismatic cells on the propeller are neglected.
2. Fairly coarse meshes are used to keep the required computational effort on a minimum.

All computational domains for the open water tests are generated using a very simple approach: A fully orthogonal mesh consisting of a single block (`blockMesh`) is used as a background mesh for `snappyHexMesh`.

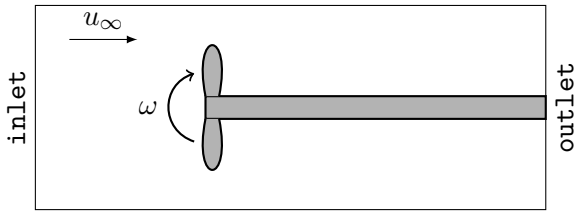

Figure 4: Sketch of longitudinal mesh layout

A shaft is included into the mesh, that reaches from the propulsor downstream until it penetrates the outer boundary, as shown in Figure 4. A halfsphere is used as a propeller hub cap.

To obtain an outer boundary of cylindrical shape, a `searchableCylinder` is introduced inside `snappyHexMesh` and all cells outside of this cylinder are deleted automatically. The outer diameter of the computational domain is $6D$ and the length of the domain is $15D$, with the propeller being located $5D$ downstream of the inlet. The meshing itself is done at model scale.

Table 1: Grids to generate input data for the database

Mesh	Cells
mesh1	$434 \cdot 10^3$
mesh2	$1425 \cdot 10^3$

The results of three different grids are presented in this paper and an overview of the mesh sizes is given in Table 1.

The second set of grids is used to test the body force propulsor, without any geometry. A fully orthogonal and purely hexahedral mesh is thus generated by means of `blockMesh`. In order to quantify the required mesh resolution in the area where the body force propulsor is applied, various mesh resolutions are applied (see Table 2).

All of the grids in Table 2 have a length of $13D$ and a width and height of $4D$. The body force propulsor is located in the centre of the domain. For all used meshes (cp. Table 2), the thickness of the propeller disk is kept constant.

Table 2: Grids to test the body force propulsor

Mesh	Cells	Cells in disk
mesh1	$250 \cdot 10^3$	960
mesh2	$432 \cdot 10^3$	1648
mesh3	$686 \cdot 10^3$	2480
mesh4	$1024 \cdot 10^3$	3792

4 Body Force Propulsor

To be able to use the body force propulsor with various solvers implemented in OpenFOAM-2.1.x without having to recompile the respective solvers, the existing list of `fieldSources` is adopted. All created models are at least derived from `basicSource` and compiled into a dynamic library that has to be linked to the solver during runtime.

The subset of cells where the volume must be applied are selected using a `cellSet`. Any interaction with the database described in Section 1.1 is handled by `libmysql++`, that is developed by Atkinson et al. [1].

The forces are only stored for discrete advance coefficients J in the database. To obtain force values for an arbitrary J, an interpolation between the two adjoining J must be performed. Whether or not a cell centre is located in the propeller disk is checked for all cells in the `cellSet`. A simplified overview of the employed interpolation method is shown in Algorithm 1.

Algorithm 1 Calculate volume forces

```
J ← interpolate forces between existing J_i
V_D ← calculate disk volume
for all cells in disk do
    r ← calculate radius for current cell
    f(r) ← interpolate forces between radii
    Apply volume weighting
end for
```

As the thrust has to be distributed over a certain volume, a volume weighting has to be applied on the interpolated force $\mathbf{f}(r_i)$ to calculate the volume force $\mathbf{f}_i$ for the current cell based on the contribution of the cell to the entire propeller disk:

$$\mathbf{f}_i = \frac{V_i}{V_D}\mathbf{f}(r_i) \tag{4}$$

with V_i being the i-th cell volume and V_D the total disk volume.

The current implementation is a static one. For the first tests, the user has to specify an advance coefficient that will be used for the entire simulation.

In the future this is planned to be selected automatically and on a cell to cell basis, depending on the local velocity. By doing that the code can be used to account for inhomogeneous inflow conditions, like they are present in the wake of an actual ship.

5 Results

Results for simulations of open water tests performed with both `ISTHydro` and `MRFSimpleFoam` are compared to each other. After this comparison some first tests of the body force propulsor are conducted.

5.1 Open Water Tests

The model tests were performed at three different revolutions to account for the influence of different Reynolds numbers on thrust and torque. For the numerical simulations only the revolution of $n = 15\,\mathrm{s}^{-1}$ was taken into account. Similar to the model tests a water density of $\rho = 998.49\,\mathrm{kg/m^2}$ is assumed and the simulations were performed in model scale.

An `inletOutlet` boundary condition is imposed on all outer boundaries. If there is an outflow at a face, a Neumann condition is used whereas at an inflow a Dirichlet condition is inserted. All velocity components are set to zero on the propeller surface and a Neumann condition is imposed on the remaining boundaries.

With the advance coefficient J given by

$$J = \frac{v}{nD} \tag{5}$$

the freestream velocity is varied to obtain 20 advance coefficients between 0 and 1.

Both thrust (K_T) and torque (K_Q) coefficients are calculated according to:

$$K_T = \frac{T}{\rho D^4 n^2} \qquad K_Q = \frac{Q}{\rho D^5 n^2} \tag{6}$$

Figure 5 compares both the thrust- and torque-coefficients obtained from the RANS simulations for the different grids.

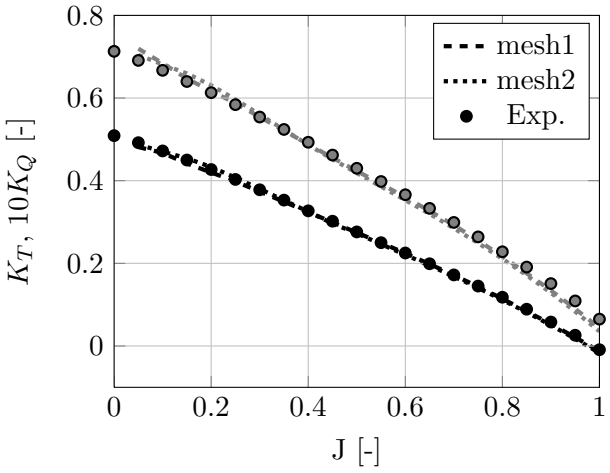

Figure 5: Open water test mesh study (black and gray indicate K_T and $10K_Q$, respectively)

For medium advance coefficients a good agreement between simulations and measurements can be found, independent of the grid resolution. The deviation for those advance coefficients is less than 3 %. Looking at the small advance coefficients and especially to the bollard pull, the deviation from the experimental data increases. The lack of grid resolution and negligence of turbulence modelling are most likely the reason for this.

Figure 6 shows a comparison of results from the RANS simulations and the ones gained from `ISTHydro` with experimental data. For large and small advance coefficients, the deviation of `ISTHydro` results from the experimental data is approximately an order of magnitude higher than the ones obtained with OpenFOAM. But as it is a potential flow solver, this discrepancy is expected and common for this type of solver.

In terms of required wall time for the execution of the particular solver, `ISTHydro` takes 10-20 min-

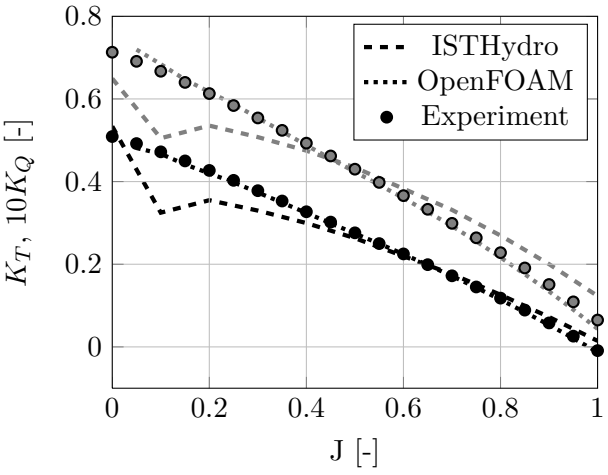

Figure 6: Comparison of open water tests between mesh1 and `ISTHydro` (black and gray indicate K_T and $10K_Q$, respectively)

utes for one simulation on a single core. OpenFOAM on the other hand needs 10 to 50 minutes for mesh1 and 80 to 180 minutes for mesh2. In both cases two cores on a single machine were used for the simulations. The higher wall times occurred for lower advance coefficients, due to the high unsteadiness of the flow.

5.2 Body Force Propulsor

As a first test of the current implementation of the body force propulsor, the interpolated force distribution is compared to the one of `ISTHydro`.

A notable dependency of the thrust distribution on the mesh resolution is indicated by Figure 7. With increasing resolution, the shape of the distribution calculated by the body force propulsor converges to the input data generated with `ISTHydro`. The volume forces actually applied are smaller than the ones showed in Figure 7, as the non volume weighted forces are displayed (cp. eq. (4)).

6 Conclusions

A simple implementation of a body force propulsor model is presented in this paper. The data generation for the database works fine, both with

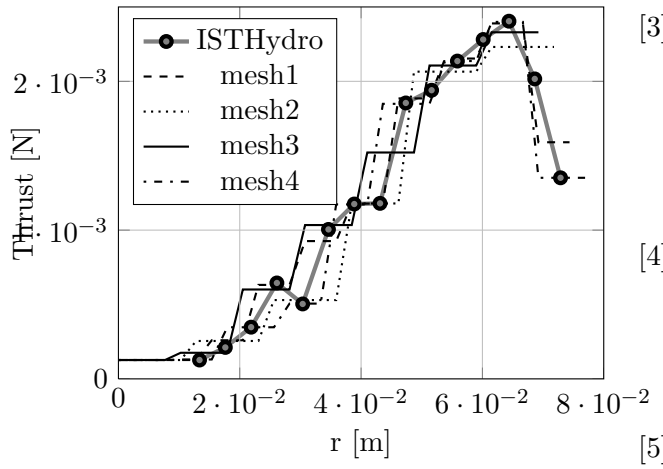

Figure 7: Thrust distribution over the radius for all meshes and `ISTHydro`

`ISTHydro` as well as OpenFOAM, though solely data generated by `ISTHydro` is currently used for the body force propulsor. With increasing mesh resolution, the thrust distribution converges towards the data in the database.

Future development steps include the use of cells that are partly inside the propeller disk area as well as to chose the local advance coefficient during runtime. An other important aspect is the use of different drift angles, as they are the rule in manoeuvring conditions.

Acknowledgements

This study is supported by the project PREMAN which is part of the BMWi development program "Schifffahrt und Meerestechnik für das 21. Jahrhundert".

References

[1] Kevin Atkinson et al. *MySQL++ v3.1.0 User Manual*. Tech. rep. Educational Technology Resources, 2010. URL: `tangentsoft.net/mysql++`.

[2] Andrés Cura Hochbaum. "Virtual PMM Tests for Manoeuvring Prediction". In: *26th Symposium on Naval Hydrodynamics*. 2006.

[3] Jochen Hundemer and Mustafa Abdel-Maksoud. "Prediction of tip vortex cavitation inception on marine propellers at an early design stage". In: *Proceedings of the 7th International Symposium on Cavitation*. 2009.

[4] Ould el Moctar, Vladimir Shigunov, and Tobias Zorn. "Duisburg Test Case: Post-Panamax Container Ship for Benchmarking". In: *Ship Technology and Research* 59 (2012), pp. 50–64.

[5] Claus D. Simonsen and Frederick Stern. "RANS Maneuvering Simulation of Esso Osaka With Rudder and a Body-Force Propeller". In: *Journal of Ship Research* 49 (2005), pp. 98–120.

[6] *Widerstands- und Propulsionsversuch für das Modell eines Containerschiffes*. Tech. rep. Potsdam Model Basin, 2011.

Design of retrofit devices using CFD, validated with wind tunnel tests

Marion C. James*, **Stephen R. Turnock, Dominic A. Hudson**

Fluid-Structure Interactions Research Group; University of Southampton, Southampton, UK. SO17 1BJ

1 Introduction

With the increase in fuel prices and growing pressure on the marine industry to reduce greenhouse gas emissions, there is a demand for ships in operation to develop novel ways to reduce both their fuel consumption and emissions. In 2009, the International Maritime Organisation (IMO) published methods on how both new and existing ships would be assessed on their emissions in the future via the Energy Efficiency Design Index (EEDI) and Energy Efficiency Operations Indicator (EEOI) respectively. As a conceptual idea, these indices may be expressed as the ratio between CO_2 emissions and the amount of transport work done for a ship.

This paper presents how the efficiency of an existing tanker hull form could be increased by 10% with the use of cost-effective retro-fit solutions. A method, involving CFD simulations performed using OpenFOAM® and validated with wind tunnel tests, is explained. An in-house code, based on the Blade-Element Momentum Theory (BEMT), is used to provide some propeller characteristics: efficiency, torque and thrust coefficients. Although, the efficiency output from the BEMT code is not the propulsive coefficient, η_D, the different appendage configurations may still be directly compared using this efficiency, denoted η_{BEMT} throughout this paper.

2 Wind Tunnel Testing

2.1 Benefits

Experiments were carried out in the Mitchell Wind Tunnel at the University of Southampton. These experiments are used to validate the CFD simulations and allow for an analysis of the existing naked hull form to be performed. The study of the naked hull is used as a benchmark to illustrate any flow changes observed in future investigations.

Using wind tunnel tests offers two main advantages. First, the model scale factor can be smaller when compared to towing tank tests,resulting in a Reynolds number high enough to model a steady turbulent flow as experienced by the full scale ship. Furthermore, in a wind tunnel, wake pressure measurements are not affected by free surface effects (wave pattern).

2.2 Model Dimensioning

In order to accurately model the effect of retro-fit devices on the flow around the hull, it is important to ensure that the turbulent flow condition around the full scale ship is replicated at model scale. The onset of turbulent flow will occur, even on smooth bodies, when the Reynolds number exceeds 0.5×10^6 (Molland and Turnock 2007).

The Reynolds number of the full scale ship is calculated to be 1.187×10^9, confirming the need for turbulent flow around the experimental model. The 3.5m x 2.1m closed return Mitchell Wind Tunnel was used to its limit with a working section accepting models of upto 4m long and with a wind speed of 30m/s. The maximum achievable Reynolds number is 7.648×10^6.

Since only the stern flow is of interest in this investigation, the parallel mid-body is truncated as shown in Figure 1. This modification is made providing the flow without the parallel middle body is sufficiently similar to that required. It is in the assessment of this that CFD provides considerable use. A 4m model with a much smaller scale factor may thus be tested, reducing the magnitudes of the experimental and scaling errors.

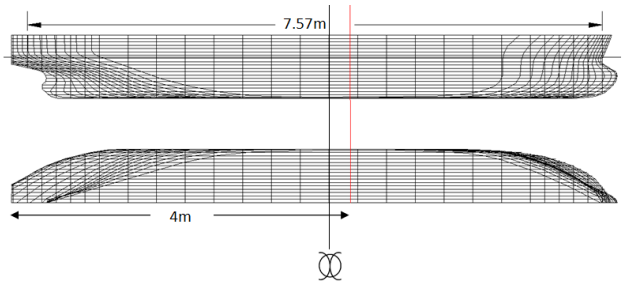

Figure 1: Truncated model length

The scale factor is calculated based on the assumption that at the propeller plane, the boundary layer thickness, δ (viscous wake), is approximately half of the propeller diameter. The boundary layer thickness is estimated, for the wrap around length of the 4m model, using the 1/7 power-law velocity distribution displayed in Equation 2.1 below:

$$\frac{\delta}{x} = 0.370 Re_x^{\frac{-1}{7}} \tag{2.1}$$

From these calculations the diameter of the propeller for the model is known and hence a scale of 1/23 is selected. For a 1/23 scale model, a blockage of 9.25% is created but still within the 10% limit where corrections may be applied. The dimensions of the wind tunnel model are summarised in Table 1.

Table 1: Wind tunnel model dimensions

		Ship	Model
Length, Over All	(m)	183.88	4.00
Breadth	(m)	32.2	1.40
Draught	(m)	12.416	0.54
C_B		0.8	-
Propeller Diameter	(m)	6.00	0.26
δ (at propeller plane)	(m)	1.40	0.14
% Blockage			9.25

*corresponding author's e-mail: mcj1g08@soton.ac.uk

2.3 Method of Wind Tunnel Testing

The wind tunnel experiments are aimed at recording pressures in the wake field and at the propeller plane of the truncated model. A traverse rig is used to move a Pitôt rake to the required locations. In addition, pressure tappings are employed to monitor that the flow reattached to the model at the stern despite the truncated bow. A schematic diagram of the set-up of the test may be seen in Figure 2.

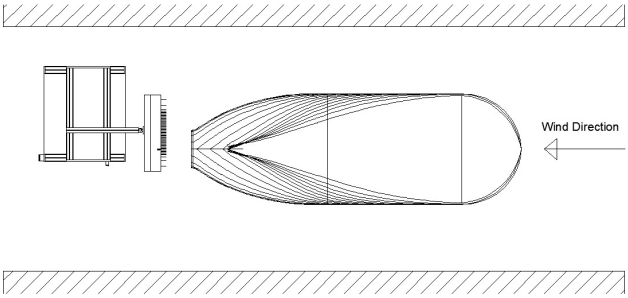

Figure 2: Wind tunnel test set-up with the wake traverse rig shown downstream of the model.

To qualitatively assess the flow pattern in the wind tunnel, tufts and an oil based paint are used. A matrix of x by y measurements is made at the desired plane using an automated traverse. The recorded pressures in Pascals are converted into velocities using the simplified form of the incompressible Bernoulli's equation. For each test, the velocities are non-dimensionalised with the free stream velocity, U. Velocity contour plots are then generated at different planes at the stern.

The different appendages are compared based on the propeller efficiency. The blade-element momentum theory (Phillips et al, 2009) requires the wake fraction at specific locations int the propeller plane. As a result, a wake analysis is conducted. The Taylor wake fraction w_T is a measure of how the hull influences the velocity of the flow in the propeller region, and it may be expressed as:

$$w_T = 1 - \frac{u}{U} \tag{2.2}$$

3 Numerical Set-Up: Computational Fluid Dynamics

3.1 Pre-processing

In order to effectively simulate the wind tunnel experiments and to investigate the design of the retrofit devices, the initial conditions of the CFD simulations are carefully chosen.

The domain size is based on the wind tunnel dimensions, such that the same blockage effect encountered by the model in the experiments is computationally modelled. However, due to the complexity of the wind tunnel, only the working section length is incorporated within the simulation (1.5L upstream and 3L downstream).

The boundary conditions applied to the domain and geometry are chosen in a similar manner to the domain size. The inlet and outlet boundary field types are defined as a fixed velocity inlet/outlet respectively (U = 30m/s). The hull form is defined as a non-slip wall, and the upper and side walls are given a slip condition. The effect of the slip condition is deemed to have a negligible effect on the flow around the model, when compared to the experimental results. The bottom wall is defined as a symmetry wall, as it may be used to simulate the free surface effect within the wind tunnel environment.

The mesh is generated using a hybrid technique, where a structured boundary layer mesh is surrounded by an unstructured domain mesh. Two refinement cylinders located on each bilge keel and one refinement box located at the aft section of the hull form are added. These regions are chosen as key areas to refine the mesh in order to correctly capture the flow around the bilges and the stern. The boundary layer mesh parameters are selected for a y^+ value of 30 and a minimum total thickness of 8mm (based on flat plate theory).

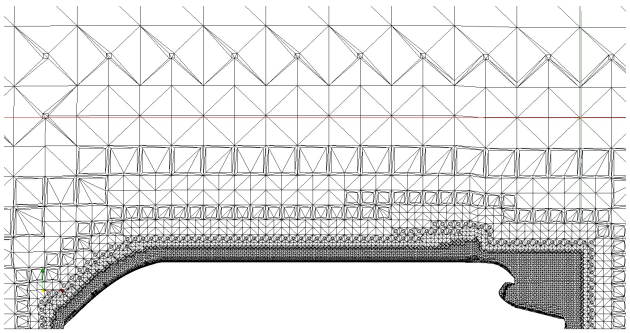

Figure 3: Final mesh along the x-direction

Overall, the quality of the mesh is reasonably good with just over one million elements. The parameters used to define the boundary layer mesh provide a 99.5% extrusion success. Figure 3 shows a smooth growth rate across the domain, allowing accurate interpolation of the field properties between elements. However, the thickness of the inner refinement level should ideally be reduced to limit the element counts without vastly compromising the accuracy of the solution. This could not be completed due to the inability to further refine the inner level with the available computational resources.

3.2 Simulation

Being a steady-state problem, the OpenFOAM® solver simpleFoam is chosen to simulate the flow around the hull form (single phase). This solver is based on a Semi-Implicit Method for Pressure-Linked Equation (SIMPLE) and uses a pressure correction. The flow properties are solved until the predefined convergence criteria are met (10^{-6} - Good convergence).

Since this study is based on a RANS simulation, the SIMPLE algorithm requires a turbulence model. The $k-\omega$ SST model is chosen to be the most appropriate.

3.3 Verification and Validation Studies

In order to verify CFD simulations, several analyses may be performed: y^+ value, domain analysis, mesh dependency study and turbulence model analysis. Initially, the y^+ value is checked to ensure compatibility with the chosen

turbulence model, $k-\omega$ SST. As required, y^+ lies between 30 and 250.

In addition, a domain analysis is conducted. Since the width and height of the domain are restricted (wind tunnel cross-section), only the effect of the domain length is assessed. The lengths upstream and downstream are increased; but the efficiency differences prove to be negligible.

The next step in the validation process is to undertake a mesh dependency study. The refinement process is completed using a systematic approach. The base size is multiplied by a factor of $2\sqrt{2}$ repetitively until a desired mesh resolution is achieved (greater than 10 million) without modifying the boundary layer mesh. The efficiencies obtained from the BEMT code for each mesh are within the error band of the wind tunnel experiments. This proves that the mesh used has a a sufficient resolution to achieve convergence of the results. Further details of this process and of the experiment may be found in Collison et al, (2012).

4 Naked Hull Results and Analysis

The flow pattern is initially analysed using streamlines. To quantify the results, the local axial velocities from CFD are extracted at the propeller plane to form the wake matrix used in the BEMT code. Moreover, velocity components are probed over the entire propeller plane and further aft in the wake field. Using the visualisation tool 'Paraview', contour plots may then be generated allowing a direct comparison with the wind tunnel test results (Section 4.2).

4.1 Effects of Truncation

The effect of the truncation is studied based on the radial distribution of the wake obtained from the CFD simulations. The radial wake fraction may be expressed as:

$$w_T{}' = \frac{1}{2\pi}\int_0^{2\pi} w_T{}'' \, d\theta \tag{4.1}$$

A comparison between the wind tunnel model (truncated L=4m) and the non-truncated model (L=8m) for identical Reynolds number is undertaken. In addition, a simulation of the non-truncated model with a matching Reynolds number to the full scale ship is completed.

Table 2 shows that the effect of truncation on the flow field is negligible. However, a model scale simulation where the Reynolds number is matched to the full scale ship still induces scaling errors, as the boundary layer thickness does not vary linearly with Reynolds number. The use of oversized devices is therefore required to counteract this effect.

Table 2: Effect of truncation: nominal mean wake

	w_T
Truncated model - U = 30m/s	0.3987
Non-truncated model - U = 15m/s	0.4386
Non-truncated model - U = 2186m/s	0.2773

As well as affecting the boundary layer thickness, truncation of the model is likely to affect the flow separation around the model. Similarity of the flow around the truncated model and the full size ship is essential to ensure the validity of the study. Although a certain amount of separation ahead of the point where the devices are to be fitted is tolerable, it is important that the flow reattaches by the time the vanes are reached.

Separation (areas of lower pressure, shown in blue in Figure 4) does occur just aft of the truncated bow but only for a small area before the flow reattaches. Indeed, a slowly increasing pressure with distance towards the stern verifies that the flow is being affected by the presence of the curved hull, suggesting it is attached to the hull. Figure 4 confirms the suitability of using a truncated model. As a validation, pressure tappings are placed on the hull and a similar trend as the CFD predictions is obtained.

Figure 4: Pressure distribution on hull as predicted by CFD

4.2 Flow and Wake Fields

The flow pattern is identified using streamlines in CFD and an attempt is made to validate the CFD results in the wind tunnel using oil based paint and tufts, as shown in Figures 5 and 6.

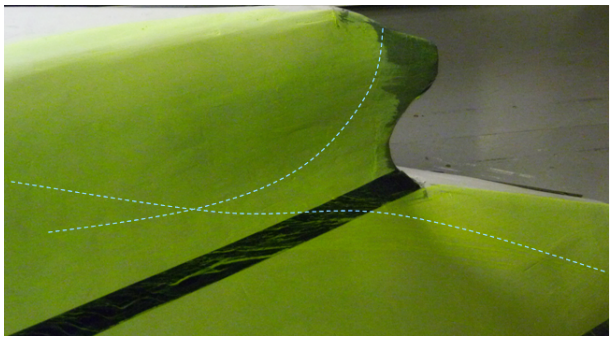

Figure 5: Flow streamlines on the wind tunnel model captured using paraffin oil. Lines are added to highlight different zones.

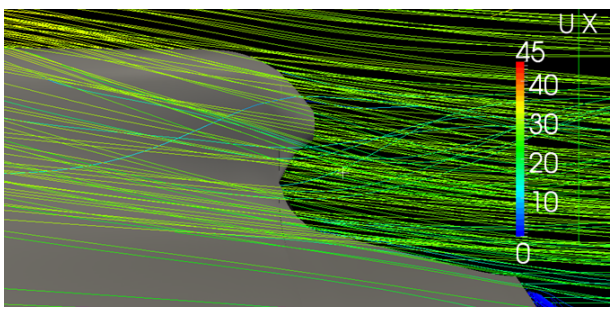

Figure 6: Flow streamlines generated by CFD

A clear similarity between the flow patterns may be observed, suggesting that the flow is diverted away from the propeller plane. Indeed, this first impression may be confirmed upon examination of the contour plots shown in Figure 7. The propeller operates in the region where the flow is slowest, whereas for increased efficiency, it is desirable for the flow into the propeller to have a higher velocity. The figures also confirm that the CFD and wind tunnel wake plots are similar, although the mid-wake obtained in the wind tunnel does seem to be wider and higher than that predicted by CFD. Furthermore, the CFD does not seem to predict the small gradual changes in velocity which can be seen in the experimental wake both in the Y direction (at the propeller plane) and in the Z direction (at the mid-wake).

These differences are likely to explain the discrepancies in efficiency values shown in Table 3. Indeed, when operating in the CFD generated wake, a much greater proportion of the propeller blade is located in the lighter grey region of faster flow, whereas when operating in the experimental wake, the propeller operates in a region of slower flow which gradually increases to the velocity predicted by CFD.

Considering the likely sources of experimental error, combined with the percentage tolerances of the CFD, a difference in efficiency of just over 9% is judged to be acceptable when comparing predictions obtained from computational and experimental methods. This, together with the similar general trends obtained both in wake and hull flow fields, suggests that the CFD simulation provides a reasonable prediction of the wind tunnel results. The CFD simulation may therefore be used to analyse the effect of various devices on the wake field and propeller efficiency.

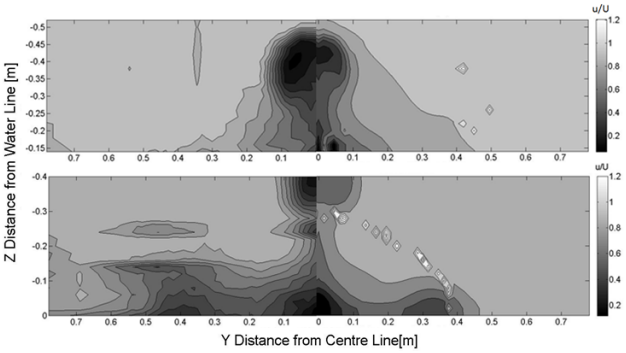

Figure 7: Propeller plane (top) and mid-wake (bottom) contour plots of wind tunnel test 1 (left) and CFD (right)

Table 3: Naked hull results - comparisons of wind tunnel efficiencies against CFD predictions. Test 1 was the initial wind tunnel test session and Test 2 the final refined test process.

	K_T	K_Q	η_{BEMT}	$\Delta\,\eta_{BEMT}$ (%)
CFD	0.1920	0.0229	0.6821	-
Test 1	0.1167	0.0153	0.6188	9.28
Test 2	0.1055	0.0146	0.7033	-3.11

5 Investigation of Devices

5.1 CFD Analysis

Based on the initial study of the flow pattern around the naked hull and the research on current retro-fit devices, two main types of devices are retained: vortex generating fins and flow channelling ducts. Since the flow appears to be diverging away from the propeller plane, it is decided to position a vortex generator upstream (see Section 4) to redirect the flow with an increased velocity. Vanes with varying parameters of location, angle and shape are designed and tested in CFD to analyse their effects on the flow field. Moreover, two types of duct are studied: Mewis and Wake Equalising Ducts (WED). The duct design is based on Mewis (2009) and a NACA 0006 section is assumed. Different ratios between inlet and outlet diameter are tested. The devices' dimensions are clearly too large to be realistically fitted onto a ship, but are for research purpose only.

Table 4: Comparison of potential retro-fit devices

	K_T	K_Q	η_{BEMT}	w_T
CFD naked hull	0.1920	0.0229	0.6821	0.3987
Test 1	0.1167	0.0153	0.6188	-
Vane	0.1879	0.0225	0.6892	0.3854
Duct	0.2063	0.0245	0.6919	0.4588
WED	0.2032	0.0241	0.6501	0.4404

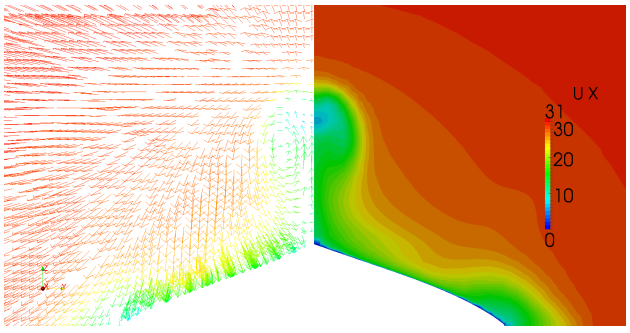

Figure 8: Naked hull wake at propeller plane: velocity vectors and contour plot

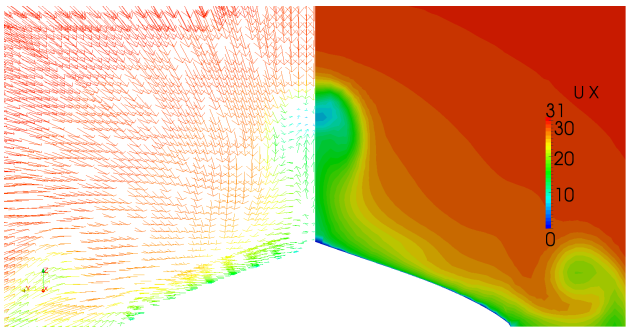

Figure 9: Effect of vane on wake at propeller plane: velocity vectors and contour plot

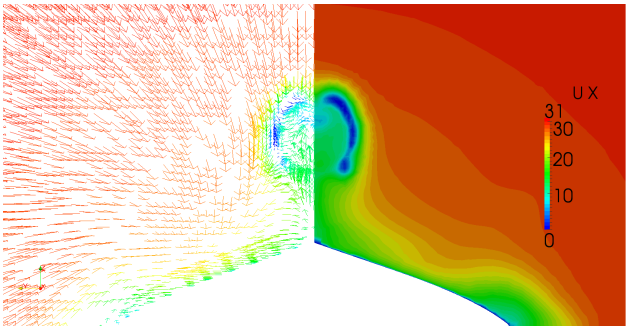

Figure 10: Effect of duct on wake at propeller plane: velocity vectors and contour plot

Qualitative data are extracted from CFD to obtain an initial idea of the impact of adding a device on the flow. Figures 8-10 show contour plots of the axial velocity, where each shade represents a variation of $1m/s$. Table 4 shows a comparison of some devices tested in CFD in preparation of the wind tunnel test 2. Moreover, the nominal wake is calculated from the local wake matrix derived at the propeller plane.

A vane is first tested to obtain an initial estimate of its influence on the flow field. When comparing the velocity plots for the naked hull and with device (Figures 8-9), it may be observed that thanks to the addition of the vane, the flow speed increases at top dead centre. Out of all the vane configuration tested, the best gain in efficiency is found to be 1%. As a result, this vane configuration is suggested to be used as an initial set-up for the wind tunnel test 2. However, since the vane is located too close to the floor the tip vortex and associated flow are reflected. This phenomenon may improve the propeller flow field, hence the increase in efficiency. The introduction of a free-surface in CFD would eradicate this unrealistic flow behaviour.

The initial duct design is modified to an inlet-outlet diameter ratio of 1.3 in order to increase the flow speed into the propeller plane (Figure 10- 'Bernoulli Effect'). This gives an increase of 1.42% in efficiency. Due to the time and manufacturing constraints, it was decided to focus on the development of further vane designs in the wind tunnel; while a duct is tested later on in the towing tank. The attempt of testing a wake equalising duct in order to create a more uniform flow into the propeller plane is not as successful and it shows a slight decrease in efficiency.

Although the addition of retro-fit devices shows overall gains in efficiency, the accuracy of the results still needs to be assessed. The differences in efficiency are minimal (below 2%) and may therefore be considered to be within the 'noise'of CFD.

5.2 Wind Tunnel Analysis

Following the CFD analysis, the most promising vane location is tested in the wind tunnel, using variations on the geometry and size of the suggested fin.

The variation in propeller efficiencies across the tested devices is minimal when compared to the naked hull efficiency. However, the greatest recorded change in efficiency is just under 0.02, which equates to a percentage change of around 3%. This is a significant change in efficiency, suggesting the experimental procedure used is successful in measuring the effect of different devices on the wake field.

Despite the high repeatability observed for repeat runs, no general pattern is obtained when relating efficiency to angle of attack and vane size. This suggests many more repeat runs and tests, with a greater range of angles of attack, device sizes and geometries should be undertaken before drawing any conclusions with acceptable confidence.

Although general trends for device design cannot be obtained, the results provide interesting and encouraging evidence that vanes may indeed be effective retro-fit devices. The largest improvement measured is just under 3%.

The result of this slight change in flow around the stern of the hull results in the flow into the propeller being accelerated, as may be seen from Figure 11. This slight acceleration in the flow explains the increase in propeller efficiency obtained.

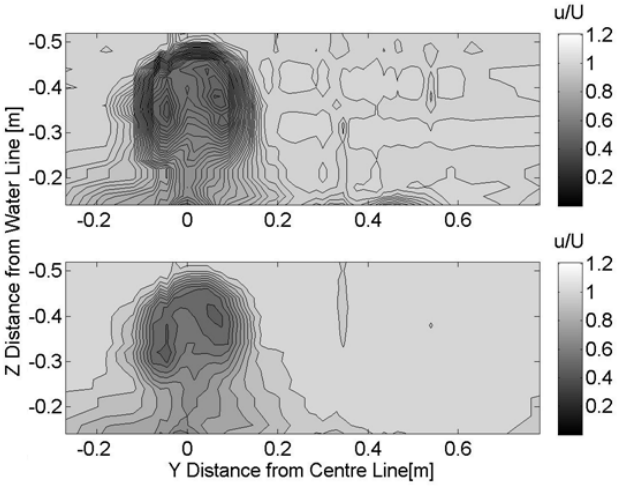

Figure 11: Wake velocities for vane (top) and the naked hull (bottom)

Figure 11 highlights the fact that changes are minimal and very difficult to observe at this scale. Moreover, the magnitude of the changes is such that any experimental error will create a large percentage error in the efficiency value obtained, leading to a high uncertainty value for the obtained results. The considerable increase in efficiency observed on some vanes during this project does however suggest that further work and research in vane development is worthwhile.

6 Towing Tank Tests

Further investigations were conducted in the Solent University Towing Tank. A series of naked hull resistance and self-propulsion tests were undertaken using a 1/60 scale geosim ship model. The resistance discrepancy between the naked and appended hull was negligible. Although the normal limits of the towing tank are exceeded (high displacement), definite trends are observed from the variation of device configurations. The decrease in RPM at self-propulsion point after the addition of appendages shows an improvement in performance. The use of the duct, gives a 9.6% gain in the propulsive efficiency. This gain shows the same trend as the results from CFD simulations but these

results are suspected to be unrealistically high. In order to obtain more accurate results, a larger scale towing tank would be required and several load conditions should be tested.

A CFD simulation including a free-surface was completed to increase the physical reality of further investigations of retro-fit devices. However, a high discrepancy between the CFD and towing tank naked hull resistance is observed due to an inaccurate viscous resistance component. An initial verification study is performed in an attempt to understand the source of error, by using different means of obtaining forces and by investigating the effect of the boundary layer mesh. Even though results obtained from this investigation do not determine the source error associated with the viscous resistance, a thorough verification process should be completed.

7 Conclusions

Wind tunnel and towing tank experiments are used, in conjunction with open-source computational fluid dynamics modelling, to analyse the wake field changes induced by retro-fit devices. These changes are assessed using the propeller efficiency obtained from blade element momentum theory. A testing procedure is developed, explained in terms of methodology, with justifications for improvements. This procedure successfully detects changes in propeller efficiency at model scale due to devices and thus provides a route to investigate a wide variety of devices.

A cost analysis model was developed to assess the viability of fitting devices on a ship during a routine drydocking period. Results, based on voyage data provided by the ship operator and European shipyard rates, suggest that a 1% reduction in required delivered power could lead to a payback period of 25 days for devices as simple as a triangular vane. Preliminary results highlight that efficiency gains up to 3% could be obtained with vanes and up to 9% with flow increasing ducts.

8 Further Work

To validate the current result and further the initial investigations, testing of devices with a greater range of geometries, angles of attack and locations should be carried out. Moreover, the effect of the devices on the wake in several load conditions should be tested. This analysis would provide a clearer understanding of the relationships between the device parameters and the propeller efficiency gains.

Furthermore, a finite element analysis should be used to calculate the structural loading on each device during service. The feasibility of the chosen retro-fit solution could therefore be determined. Such findings would allow further investigations to determine an optimum retro-fit device for the hull form studied.

Acknowledgements

The group would like to acknowledge the following people:

The project supervisors, Professor Stephen Turnock and Dr Dominic Hudson, for their continued help and advice during the year.

The project sponsors without whom this project would not have been possible.

All the Ship Science and Faculty staff and research fellows for their support and time throughout the year in towing tank supervision and general availability for consultation and advice.

Nomenclature

C_B	Block coefficient	
K_Q	Propeller torque coefficient	
K_T	Propeller thrust coefficient	
U	Free stream velocity	$[m/s]$
$w_T{}'$	Taylor wake fraction	
$w_T{}''$	Radial distribution of the wake	
$w_T{}''$	Axial wake component	
y^+	Non-dimensional wall distance	
δ	Boundary layer thickness	$[m]$
η_{BEMT}	Efficiency from the BEMT code	
η_D	Propulsive efficiency	

References

Collison, R., James, M., Mathieson, S., Rident, C., Scott, C., Unwin, E. (2012) Retro-fit Solutions for Energy Efficient Shipping, Ship Science MEng Group Design Project Report No 41.

IMO (2011) Reduction of GHG Emissions from Ships *MEPC 62/5/17*

Lee, S.J., Kim, H.R., Kim, W.J., Van, S.H. Wind Tunnel Tests on Flow Characteristics of the KRISO 3,600 TEU Containership and 300K VLCC Double-Deck Ship Models. (2003) *Journal of Ship Research*, 47 (1), 24-38

Mewis, F., Guiard, T. (2011) Mewis Duct - New Developments, Solutions and Conclusions *Second International Symposium on Marine Propulsors*

Molland, A.F., Turnock S.R., Hudson D.A. (2011) *Ship Resistance and Propulsion. Practical Estimation of Ship Propulsive Power* New York: Cambridge University Press

Molland, A.F., Turnock S.R.,(2007) *Marine Rudders and Control Surfaces; Principles, Data, Design and Applications* Oxford: Elsevier

Phillips, A.B., Furlong, M.E, Turnock, S.R. (2009) Accurate capture of rudder-propeller interaction using a coupled blade element momentum-RANS approach, 12th Numerical Towing Tank Symposium, Cortona, Italy

Wilcox, D.C. (2006) *Turbulence Modelling for CFD*, 3rd edn., California: Birmingham Press

Evaluation of RANS turbulence models for the flow around an axisymmetric streamlined body

Mattias Johansson* and Mattias Liefvendahl†

September 25, 2012

1 Introduction

Flow around streamlined bodies at high Reynolds (Re-)number is an important class of model problems for ship hydrodynamics in general, and submarine hydrodynamics in particular. With an axisymmetric body on a straight course, as studied here, the flow is dominated by; (i) the development of the turbulent boundary layer, affected by the pressure gradients caused by the shape of the body; (ii) the low-velocity region over the stern, with possible unsteady flow separation and; (iii) the wake flow. In this study, we use RANS-models implemented in the open-source CFD software `OpenFOAM` to investigate the flow around a baseline submarine hull, the design of which is described in, [4]. We refer to it as the Joubert model after the author of the design report. The shape of this model is shown in figure 1. In the recent paper, [1], extensive data, obtained both with measurements and large-eddy simulation (LES), was published, both for baseline hull and the appended configuration with sail and rudders. In the present study a systematic simulation campaign is carried out in order to evaluate RANS turbulence models, for this problem, by comparison with the data from experiments and LES. The main objective being to make method recommendations for this class of problems.

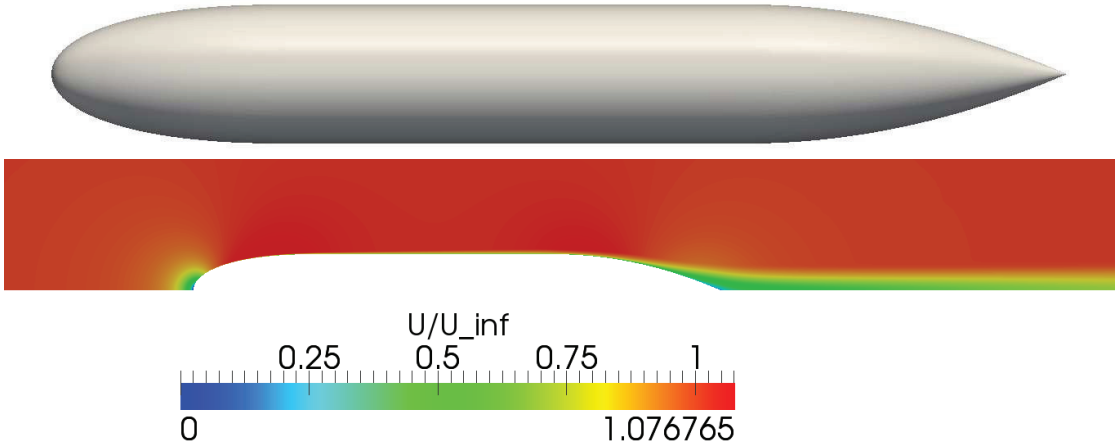

Figure 1: Above: The streamlined body (Joubert model). Below: The mean axial velocity distribution around the body, in the top half-plane, obtained with the $k-\varepsilon$ model.

Three different categories of turbulence models are studied; linear eddy viscosity models, non-linear eddy viscosity models and stress-transport models. The stress-transport models include the solution of the transport equation for the Reynolds stresses. Generally, the employed RANS-models introduce additional transport equations for different sets of turbulence quantities used in the modeling. These quantities include the turbulent kinetic eneryg, k, the dissipation of turbulent kinetic energy, ε, the quantity, $\omega = k/\varepsilon$, and the Reynolds stresses. We refer to [8, 6, 7] and the references therein for a description of the models. In table 1, we list the turbulence models which are included in our study.

*Swedish Defence Research Agency, FOI, Stockholm, Sweden. 147 25 Tumba. `mattias.johansson@foi.se`
†Swedish Defence Research Agency, FOI, Stockholm, Sweden. 147 25 Tumba. Tel: +46 8 5550 4170. Fax: +46 8 5550 4144. `mattias.liefvendahl@foi.se`

Table 1: List of turbulence models which are evaluated.

Turbulence model	`OpenFOAM` keyword
$k-\varepsilon$	`kEpsilon`
Realizable $k-\varepsilon$	`realizableKE`
RNG (Re-Normalization Group) $k-\varepsilon$	`RNGkEpsilon`
Lien cubic $k-\varepsilon$	`LienCubicKE`
Non-linear Shih $k-\varepsilon$	`NonlinearKEShih`
$k-\omega$	`kOmega`
$k-\omega$ SST (Shear Stress Transport)	`kOmegaSST`
LRR Reynolds stress transport	`LRR`

The numerical method implemented in `OpenFOAM`, for the solution of the RANS equations, relies on a cell-centered finite volume discretisation, and the pressure-velocity coupling is handled by the SIMPLE-algorithm, [2]. The computational grid is treated as unstructured and general polyhedral cells are supported.

2 Simulation campaign and setup

The geometry of the problem, and the mean flow (but not the instantaneous flow) are axisymmetric, hence the RANS-problem is reduced to 2D. The simulations are set-up at the conditions of the wind tunnel experiments described in [1], with a model length, $L = 1.35$m, and a length-based Reynolds number, $\mathrm{Re} = 5.4 \cdot 10^6$, based on the free-stream velocity, $V_\infty = 60$m/s, and the kinematic viscosity, $\nu = 1.5 \cdot 10^{-5}\mathrm{m}^2/\mathrm{s}$.

The boundary conditions employed are the following. For the velocity, we prescribe the free-stream velocity on the inflow patch, we use the no-slip condition on the surface of the body, and we set the normal gradient of the velocity to zero at the outflow and far-field boundaries. The pressure is set to zero at the outflow boundary, whereas it has zero normal gradient at all other boundaries. For all models using, k, it is prescribed to the value,

$$k = \frac{3}{2}(0.03V_\infty)^2, \tag{1}$$

on the inflow patch. This is based on the assumption that the turbulence in the inflow is homogeneous and isotropic, and that the level of fluctuations is at 3%, which is the estimated value, in [1], of the turbulence level in the wind tunnel. The same value is also used for calculating the initial value of, k, in the wall function used at the body surface. At all other boundaries, we set zero normal gradient for, k. To obtain an estimate of the inlet value of, ε, is it assumed that the ratio of turbulent viscosity to the laminar viscosity, ν, is five. Then ε can be calculated as,

$$\varepsilon = C_\mu \frac{k^2}{5\nu}, \tag{2}$$

where $C_\mu = 0.09$. The same value is used as initial data in the wall function for ε. The outlet and far-field boundary conditions for ε is set to zero normal gradient. Using the relation, $\omega \equiv \varepsilon/k$, the inlet, and initial value for the wall function of ω, can be calculated as,

$$\omega = \frac{\varepsilon}{k} = \frac{C_\mu k}{5\nu}. \tag{3}$$

The above explains the boundary conditions for all turbulence models except the LRR model. In order to set up the LRR-simulation, we started from the converged solution obtained with the $k-\varepsilon$ model. The we used a standard `OpenFOAM` utility to create a Reynolds stress field, in the domain and on the boundaries. The boundary conditions in the azimuthal directions are set to the boundary condition with `OpenFOAM`-keyword, `wedge`, which acts as a cyclic boundary condition for axisymmetric problems.

The main grid used in the simulation consists of so-called wedge-cells (with 5^o wedge angle) of hexahedral shape. The grid consists of approximately $8 \cdot 10^4$ cells. Wall functions are employed, and, $y^+ \approx 40$, is a representative value for the cell-center of the first layer of cells along the body. The grid was constructed using the `OpenFOAM` pre-processing program `blockMesh`, which implements a block-structured approach to mesh generation.

3 Experimental and LES based validation data

The experimental validation data are described in [1], and for the results comparison we use both; (i) distribution of pressure and wall shear stress along the body and; (ii) the mean axial velocity distribution,

obtained by Particle Image Velocimetry (PIV), around the stern and the near wake. The number of image pairs used in the PIV were 1000, which is adequate in establishing convergence considered to be sufficient for the statistical analysis. The pressure distribution was measured with 21 static pressure taps along the centerline at the top of the model. The reference free-stream static and total pressure were also measured and the pressure coefficient is calculated as

$$C_p = \frac{p_{tap} - p_s}{p_T - p_s} \tag{4}$$

where p_{tap} is the static pressure measured at the taps, p_T is the free-stream total pressure and p_s is the free-stream static pressure. The friction coefficient C_f was measured using the Preston tube method. the experiments were conducted in the DSTO low speed wind tunnel in Melbourne, Australia. For a more complete description of the experiments we refer to [1].

The LES validation data are also described in [1]. The LES data were obtained with near-wall modeled LES, of which three types have been used; the Localized Dynamic Kinetic energy Model (LDKM), the One Equation Eddy Viscosity Model (OEEVM), and the Mixed Model Spalart Allmaras here referred to as MMSA. The simulations were carried out on a computational grid with $18{\cdot}10^6$ cells. For a fuller description of this near-wall modeled LES-approach and its implementation and validation for naval hydrodynamics, we refer to [5], and the references therein.

4 Results

In figure 1, we show the mean axial velocity distribution around the body obtained with the $k-\varepsilon$ model. We see the stagnation point at the bow, at the end of the forebody and the beginning of the stern we see the two high velocity zones, and the main low velocity zone is located at the stern and behind the body in the wake. In figures 2 and 3, we show results obtained with RANS, LES and measurements. The axial coordinate, x, has the origin at the bow and increases downstream.

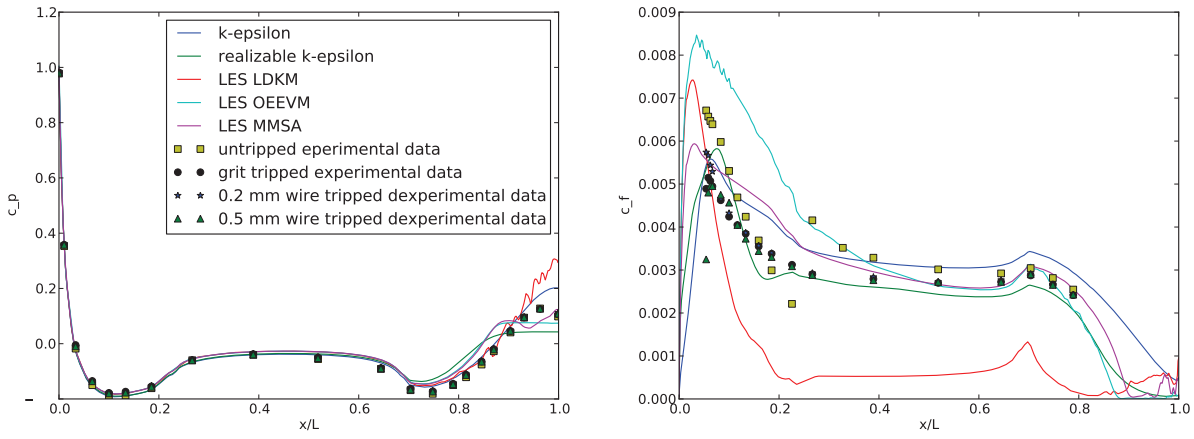

Figure 2: In the left graph, the pressure coefficient, C_p, is plotted and in the right graph, the friction coefficient, C_f. On the horizontal axis we have the normalized axial coordinate, x/L. Results from two RANS-simulations, three LES and four measurement set-ups are included. The lines and symbols have the same meaning in both graphs.

Generally, the pressure distribution is well predicted by all models, except possibly near the stern, where the shape of the low velocity region has an important influence as seen in figure 2. The $k-\varepsilon$ model does not predict the small separation suggested by the experiments whereas the realizable $k-\varepsilon$ model over-predicts the separation. The other RANS models, not included in figure 2, all give C_p-distributions close to what $k-\varepsilon$ predicts. The wall shear is more difficult to predict and the results display a larger scatter, but are generally close to the experimental data, within 20% in the interval, $0.2 < x/L < 0.8$, for all models except the LRR Reynolds stress model.

The comparison with the PIV-data, in figure 3, shows that most of the models provide a good prediction of the mean flow in the stern region. The exceptions are the realizable $k-\varepsilon$ model and the non-linear Shih $k-\varepsilon$ model. The realizable $k-\varepsilon$ model gives a very significant overprediction of the size of the low velocity region, while Non-linear Shih $k-\varepsilon$ underpredicts it. The top four profiles in figure 3 clearly shows how the

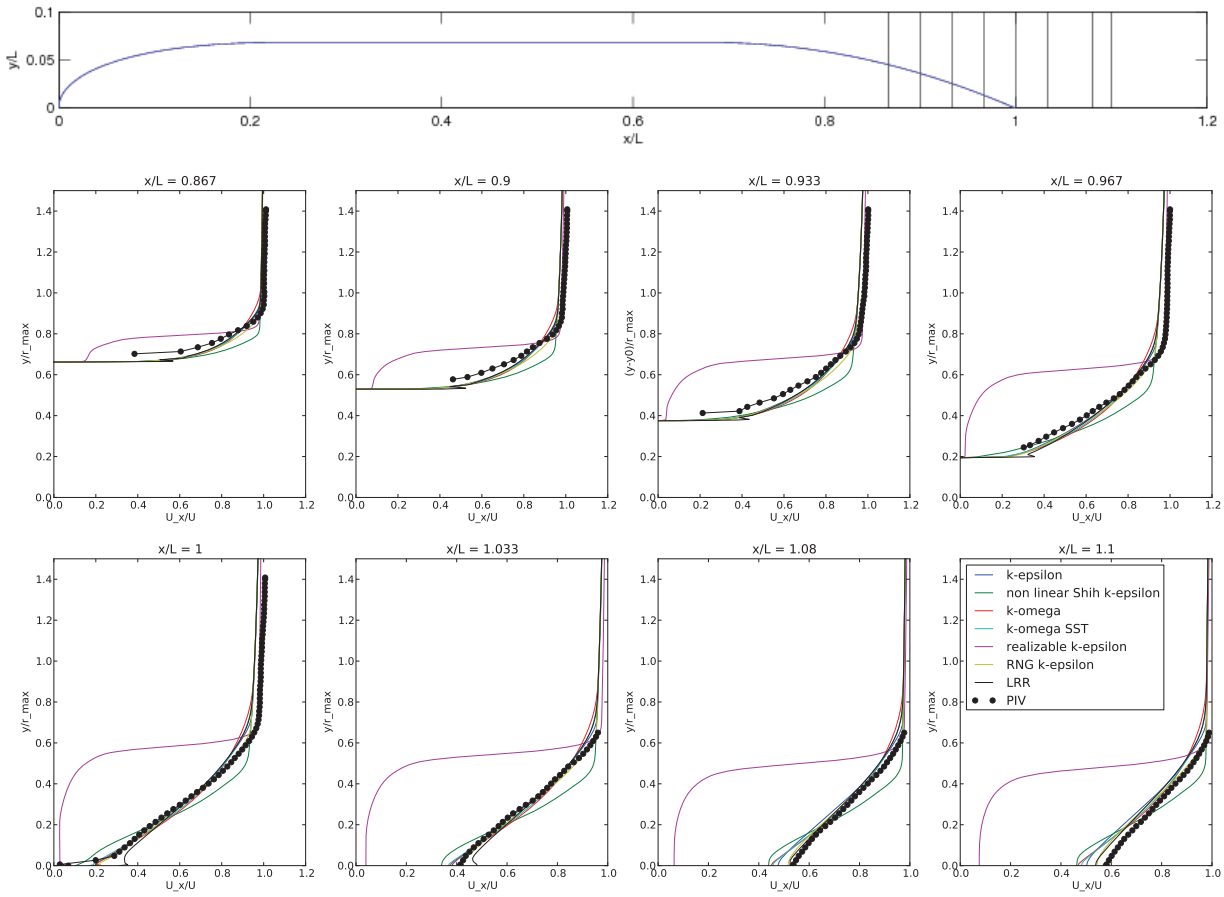

Figure 3: Mean normalized axial velocity profiles, $\langle u_x \rangle / V_\infty$, at different stations along the body. In the top graph, the lines along which profiles are plotted are shown relative to the body. Results from seven RANS-simulations and from PIV-measurements are included. The lines and symbols have the same meaning in all eight profile plots in this figure.

low velocity zone is getting thicker down-stream along the stern. The small difference in the free-stream velocity between the simulations and the PIV data indicates that there are some effects of blockage in either the simulations or the experiments, or in both. We mainly use the velocity distribution around the stern to rank the RANS-methods and in particular the following four models give a good prediction of the mean flow in the stern region.

- The $k - \varepsilon$ model.
- The RNG (Re-Normalisation Group) $k - \varepsilon$ model.
- The $k - \omega$ model.
- The $k - \omega$ SST (Shear Stress Transport) model.

These models differs little from each other and are in very close agreement with the PIV data. Especially in the wake, where the difference in, $\langle u_x \rangle / V_\infty$, between these models and the PIV data generally is less than a few percent, and they do not differ more than 20% from the PIV data, and 12% from the each other.

5 Conclusions and discussion

A systematic simulation campaign has been carried out in order to evaluate eight of the turbulence models implemented in `OpenFOAM`, with respect to flows around streamlined bodies. The results from the campaign show that the four turbulence models, $k - \varepsilon$, RNG $k - \varepsilon$, $k - \omega$ and $k - \omega$ SST, are agreeing well with the experimental data. For these models, the predicted pressure distribution is very close to the experiments,

except near the very end of the stern where they do not predict the small separation suggested by the experiments. The predicted wall shear stresses differ between the models, but are relatively close to the experiments for the four models which perform best. The conclusion is that the models $k-\varepsilon$, RNG $k-\varepsilon$, $k-\omega$ and $k-\omega$ SST, are suited for simulating this class of flows, while the study indicates that the rest of the models give relatively large prediction errors.

A comparison of the convergence between the well performing models shows a faster convergence for the $k-\varepsilon$ and RNG $k-\varepsilon$ models, as compared to $k-\omega$ and $k-\omega$ SST. However, the residuals at convergence, for $k-\omega$ and $k-\omega$ SST, are smaller, and they perform fewer inner iterations for each outer iteration. Hence, we recommend the use of either one of the turbulence models, $k-\varepsilon$, RNG $k-\varepsilon$, $k-\omega$ or $k-\omega$ SST.

Another similar study for the evaluation of RANS-turbulence models, [3], recommends the realizable $k-\varepsilon$ model for flow problems with significant impact of boundary layers. That recommendation is directly contradicting this study, where the realizable $k-\varepsilon$ model was one of the worst performing models. The case studied in [3] consists of a relatively thick boundary layer over an axi-symmetric smooth hill. Thus, there are significant differences from the geometry in this study, but both problems have a large impact from the boundary layer, so the differences in model performance are somewhat surprising.

Further development of this work could be to perform a mesh convergence study in order to resolve the boundary layer, instead of employing wall functions. This was attempted, but no convergence was reached in those simulations. Furthermore, other turbulence models could be included, and the implementation of all the turbulence models in `OpenFOAM` should be investigated. Finally, a parametric study of how the geometry, in particular the stern design, affects the low velocity region at the stern, would be of great interest.

References

[1] B. Anderson, M. Chapuis, L. Erm, C. Fureby, M. Giacobello, S. Henbest, D. Jones, M. Jones, C. Kumar, M. Liefvendahl, P. Manovski, D. Norrison, H. Quick, A. Snowden, A. Valiyff, R. Widjaja, and B. Woodyatt. Experimental and computational investigation of a generic conventional submarine hull form. In *29th Symposium on Naval Hydrodynamics*, Göteborg, Sweden, August 2012.

[2] J.H. Ferziger and M. Perić. *Computational Methods for Fluid Dynamics*. Springer, 2002.

[3] Eric Furbo. Evaluation of RANS turbulence models for flow problems with significant impact of boundary layers. Technical Report FOI-R-3134–SE, FOI, Swedish Defence Research Agency, 2010.

[4] P. N. Joubert. Some Aspects of Submarine Design. Part 2, Shape of a Submarine 2026. Technical Report DSTO-TR-1920, Defence Science and Technology Organisation, Australia, 2006.

[5] M. Liefvendahl, N. Alin, M. Chapuis, C. Fureby, U. Svennberg, and C. Troëng. Ship and propulsor hydrodynamics. In *V European Conference on Computational Fluid Dynamics, ECCOMAS CFD2010*, Lissabon, Portugal, 2010.

[6] S. B. Pope. *Turbulent flows*. Cambridge, 2000.

[7] Tsan-Hsing Shih, William W. Liou, Aamir Shabbir, Zhigang Yang, and Jiang Zhu. A new k-epsilon eddy viscosity model for high reynolds number turbulent flows. *Computers Fluids*, 24(3):227–238, 1995.

[8] D. C. Wilcox. *Turbulence Modeling for CFD, 3rd edition*. DCW Industries, Inc., 2006.

Real-time computation of interactive waves using the GPU

Martijn de Jong, m.d.jong@marin.nl
Auke van der Ploeg, a.v.d.ploeg@marin.nl
Auke Ditzel, a.ditzel@marin.nl
Kees Vuik, c.vuik@tudelft.nl

1 Introduction

The Maritime Research Institute Netherlands (MARIN) supplies innovative products for the offshore industry and shipping companies. Among their products are highly realistic, real-time bridge simulators [2], see Figure 1.

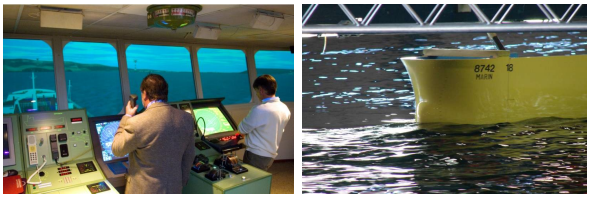

Figure 1: Left: full-scale bridge simulator. Right: towing tank.

Currently, the waves are deterministic and are not affected by ships, moles, breakwaters, piers, or any other object. To bring the simulators to the next level, a new interactive wave model is being developed. This is the so-called Variational Boussinesq model (VBM) as proposed by Gert Klopman [3]. The main improvement will be that the waves and ships really interact, i.e., the movements of the ship are influenced by the waves and the waves in their turn are influenced by the ship. However, one pays for the higher realism: the new model is much more computational intensive and therefore a really fast solver is needed to fulfill the requirements of real-time simulation.

In this paper we present how a very efficient iterative solver can be combined with a very efficient implementation on the graphical processing unit (GPU). In this way speed up factors of more than 30 can be obtained compared to sequential code on the CPU for realistic problems. With the new solver interactive waves can be computed in real-time for large domains.

2 Model equations and discretization method

The governing linearized VBM equations are given by:

$$\frac{\partial \zeta}{\partial t} + \nabla \cdot (\zeta \mathbf{U} + h\nabla\varphi - h\mathcal{D}\nabla\psi) = 0, \tag{1a}$$

$$\frac{\partial \varphi}{\partial t} + \mathbf{U} \cdot \nabla\varphi + g\zeta = -P_s, \tag{1b}$$

$$\mathcal{M}\psi + \nabla \cdot (h\mathcal{D}\nabla\varphi - \mathcal{N}\nabla\psi) = 0, \tag{1c}$$

Equations (1a) and (1b) are the mass conservation equation and the Bernoulli equation. They describe the evolution in time of the free surface elevation $\zeta(x_1, x_2, t)$ and free-surface velocity potential $\varphi(x_1, x_2, t)$, respectively, where (x_1, x_2) are the Cartesian horizontal coordinates and t is the time. The third equation is an elliptic equation for the free-surface vertical velocity $\psi(x_1, x_2, t)$, and has to be solved at each time frame for given $\zeta(x_1, x_2, t)$ and $\varphi(x_1, x_2, t)$. The other symbols in (1a-c) are:

$\mathbf{U}$	horizontal flow-velocity
h	water depth
g	gravitational acceleration
P_s	"pressure pulse" ship
$\mathcal{D}, \mathcal{M}, \mathcal{N}$	model parameters

The VBM equations are discretized with the finite volume method (FVM) on a Cartesian grid. Discretization leads to:

$$\frac{\mathrm{d}\mathbf{q}}{\mathrm{d}t} = L\mathbf{q} + \mathbf{f}, \tag{2}$$

$$S\vec{\psi} = \mathbf{b}. \tag{3}$$

Equation (2) is solved using the Leapfrog integration scheme, a second order explicit integration method. System (3) is a linear system that has to be solved. In this system the matrix S is real-valued, sparse (5-point, pentadiagonal), diagonally dominant (not very strong for small mesh sizes), symmetric positive definite (SPD), and large (in the order of millions by millions).

3 The RRB-solver

For a system with a matrix as described above a Preconditioned Conjugated Gradient (PCG) type solver is most proficient. The PCG-algorithm is given by Algorithm 1 (cf. [4]; Algorithm 9.1).

Rather than solving system (3) we solve a preconditioned system

$$M^{-1}S\psi = M^{-1}\mathbf{b}, \tag{4}$$

Algorithm 1 The PCG algorithm.

$\mathbf{r} = \mathbf{b} - S\vec{\psi}$, solve $M\mathbf{z} = \mathbf{r}$ for $\mathbf{z}$,
$\rho_1 = \langle \mathbf{r}, \mathbf{z} \rangle$, set $\mathbf{p} = \mathbf{z}$.
While (not converged)

$\rho_0 = \rho_1$	
$\mathbf{q} = S\mathbf{p}$	Matrix-vector product
$\sigma = \langle \mathbf{p}, \mathbf{q} \rangle$	Inner product
$\alpha = \rho_0 / \sigma$	
$\vec{\psi} = \vec{\psi} + \alpha\mathbf{p}$	Vector update
$\mathbf{r} = \mathbf{r} - \alpha\mathbf{q}$	Vector update
Solve $M\mathbf{z} = \mathbf{r}$	Preconditioner step
$\rho_1 = \langle \mathbf{r}, \mathbf{z} \rangle$	Inner product
$\beta = \rho_1 / \rho_0$	
$\mathbf{p} = \mathbf{z} + \beta\mathbf{p}$	Vector update

End while

where the preconditioning matrix M^{-1} is chosen such that the location of the of eigenvalues of $M^{-1}S$ are more favorable than those of S leading to faster convergence, i.e., fewer CG-iterations.

The RRB-solver is such a PCG solver with the RRB-method [1] as preconditioner. RRB stands for "Repeated Red-Black" which refers to how nodes in a 2D grid are colored and numbered. The RRB-method makes an incomplete factorization

$$S = LDL^T + R, \tag{5}$$

where L is a lower triangular matrix, D a block diagonal matrix, and R a matrix of adjustments resulting from so-called lumping procedures. As preconditioner for CG the matrix

$$M = LDL^T \approx S$$

is taken.

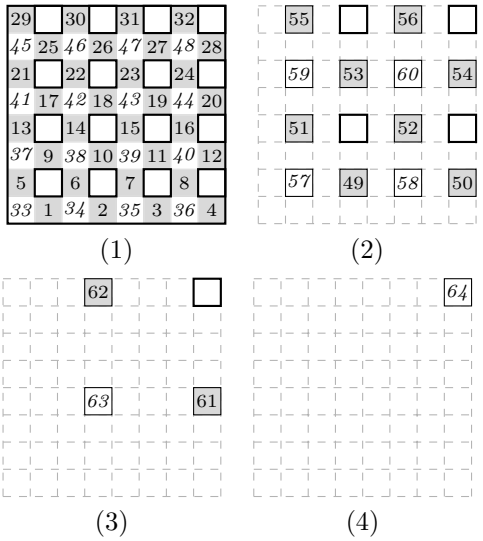

Figure 2: RRB-numbering for an 8×8-grid. The black nodes are represented by gray squares, red nodes by white squares.

Let us now explain the RRB-numbering using an 8×8-example, see Figure 2. The nodes in the first level (1) are divided into two groups: the nodes (i, j) with $\mathrm{mod}(i+j, 2) = 0$ are red nodes, the nodes with $\mathrm{mod}(i + j, 2) = 1$ are black nodes. Then all black nodes are numbered sequentially (1-32), and half of the red nodes are numbered (33-48) in the way as indicated. The remaining 16 nodes form the next level (2). For level (2) the numbering procedure is repeated. Ultimately this procedure leads to 4 levels for an 8×8-grid. For grids with "not so perfect" dimensions, i.e., N_x and N_y are not powers of 2, things are a little more complicated, but the same procedure can be applied. For general N_x and N_y the maximal number of levels is given by:

$$k_{\max} = 1 + \lfloor (\log_2(\max\{N_x, N_y\})) \rfloor. \tag{6}$$

We do not have to go all the way down; we can stop at any level k and make a complete Cholesky factorization on that level. The corresponding method is called RRB-k. In Figure 3 the sparsity pattern of S is shown for RRB-1 and RRB-4 for the 8×8-example.

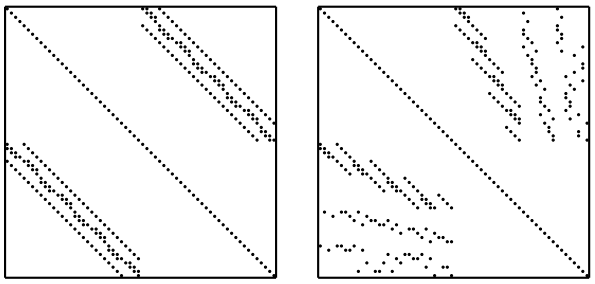

Figure 3: Left: Sparsity pattern of $S \in \mathbb{R}^{64 \times 64}$ when the basic Red-Black numbering is applied (RRB-1). Right: sparsity pattern after the RRB-4 numbering.

By applying a basic Red-Black numbering we can write system (3) as

$$\begin{bmatrix} D_b & S_{br} \\ S_{rb} & D_r \end{bmatrix} \begin{bmatrix} \vec{\psi}_b \\ \vec{\psi}_r \end{bmatrix} = \begin{bmatrix} \mathbf{b}_b \\ \mathbf{b}_r \end{bmatrix}, \tag{7}$$

where the red nodes are indicated by "r" and the black nodes by "b". Herein D_r and D_b are diagonal matrices and $S_{rb} = S_{br}^T$ are matrices with 4 diagonals, see Figure 3. Applying Gaussian elimination yields

$$\begin{bmatrix} D_b & S_{br} \\ 0 & S_1 \end{bmatrix} \begin{bmatrix} \vec{\psi}_b \\ \vec{\psi}_r \end{bmatrix} = \begin{bmatrix} \mathbf{b}_b \\ \mathbf{b}_1 \end{bmatrix}, \tag{8}$$

where $S_1 := D_r - S_{rb}D_b^{-1}S_{br}$ is called the *1st Schur complement* (given by a 9-point stencil) and $\mathbf{b}_1 := \mathbf{b}_r - S_{rb}D_b^{-1}\mathbf{b}_b$ is the corresponding right-hand side. Hence the original system (3) can be solved as follows:

1. Compute $\mathbf{b}_1$;

2. Apply CG to the system $S_1\vec{\psi}_r = \mathbf{b}_1$;

3. Compute $\vec{\psi}_b$ via $\vec{\psi}_b = D_b^{-1}(\mathbf{b}_b - S_{br}\vec{\psi}_r)$.

This is beneficial for the amount of computational work as for the vector updates and inner products in CG the work is reduced by a factor two. Note that the matrix-vector product in CG becomes $\mathbf{q} = S_1\mathbf{p}$, with S_1 given by a 9-point stencil and not by a 5-point stencil, and hence the work is not reduced by a factor two for this operation.

3.1 Construction of the preconditioner

The RRB-method makes an incomplete factorization (5) as follows. In each level Gaussian elimination is applied. Elimination of nodes leads to fill-in: a 5-point stencil becomes a 9-point stencil. By using graph representation, see Figure 4, the occurence of fill-in can be explained nicely. A *lumping* procedure is then used to simplify the 9-point stencil to a 5-point stencil: the four outermost coefficients are added to the center coefficient, which leads to a rotated 5-point stencil after elimination of black nodes, see Figure 4.

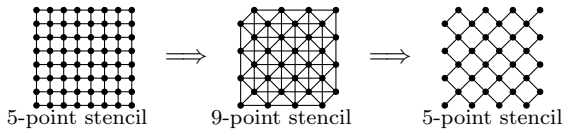

Figure 4: Elimination of the black nodes leads to fill-in and a 9-point stencil. A lumping procedure is used to obtain a (rotated) 5-point stencil again.

In Figure 5 the sparsity pattern of $L + D + L^T$ is shown when the RRB-method is applied to matrix $S \in \mathbb{R}^{64\times 64}$.

The RRB-solver offers good parallelization options. The basic operations in the CG-algorithm, see Algorithm 1, such as matrix-vector products, vector updates and inner products parallelize very well on shared memory machines. Further, from Figure 5 we see that within a block (the gray shaded areas) the nodes do not depend on each other. Therefore, within such a block the elimination described above can be performed fully in parallel. As we shall see this is the key in parallelizing the application of the preconditioner as well.

3.2 Application of the preconditioner

At each CG-iteration the preconditioning step $M\mathbf{z} = \mathbf{r}$ needs to be solved for $\mathbf{z}$. The preconditioner matrix M can be written as $M = LDL^T$ so that solving $M\mathbf{z} = \mathbf{r}$ can be done in three steps as follows. Set $\mathbf{y} := L^T\mathbf{z}$ and $\mathbf{x} := DL^T\mathbf{z} = D\mathbf{y}$, then:

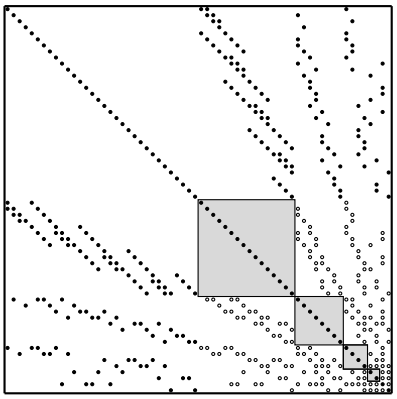

Figure 5: Sparsity pattern of $L + D + L^T$. The gray areas indicate where fill-in has been lumped.

1. Solve $L\mathbf{x} = \mathbf{r}$ using forward substitution;

2. Compute $\mathbf{y} = D^{-1}\mathbf{x}$;

3. Solve $L^T\mathbf{z} = \mathbf{y}$ using backward substitution.

If we have a closer look at the structure of matrix L, see Figure 6, we see that Step 1 can be done level-wise in parallel as follows.

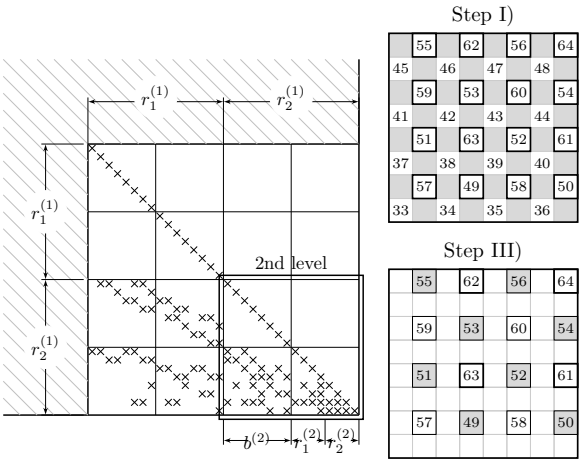

Figure 6: Forward and backward substitution can be done level-wise in parallel.

Solving $L\mathbf{x} = \mathbf{r}$ using forward substitution:

I) *Do in parallel*: Update $\mathbf{x}$-values corresponding to r_2-nodes using the $\mathbf{x}$-values of the r_1-nodes from the same level (according to a rotated 5-point stencil);

II) Go to the next level if there is any; otherwise: *stop*;

III) *Do in parallel*: Update $\mathbf{x}$-values corresponding to r_1- and r_2-nodes using the $\mathbf{x}$-values of the b_1- and b_2-nodes from the same level (according to a straight 5-point stencil);

IV) Repeat I).

Step 3, solving $L^T\mathbf{z} = \mathbf{y}$, can be done level-wise in parallel by a similar procedure (but in the reverse order). Step 2 is trivially parallelized as it comes down to elementwise division.

3.3 Convergence behaviour

Because of the multiple levels the RRB-solver shows "Multigrid-like" behaviour: the required number of CG-iterations grows only very slowly with increasing problem size N. In Figure 7 the required number of CG-iterations is shown when Poisson's equation on the unit square with Dirichlet boundary conditions, i.e.,

$$\begin{aligned} -\Delta u &= f(x,y) \quad \text{on} \quad \Omega = (0,1)\times(0,1), \\ u(x,y) &= 0 \qquad\quad \text{on} \quad \partial\Omega, \end{aligned} \tag{9}$$

is discretized on an $N \times N$ (internal) nodes grid, and solved with the RRB-solver. The right-hand side f is taken such that $u(x,y) = x(x-1)y(y-1)\exp(xy)$ (cf. [1]; model problem (2)). As termination criterium we have taken: $\|r_i\|_{M^{-1}}/\|r_0\|_{M^{-1}} \leq 10^{-5}$ and as initial guess the zero-vector.

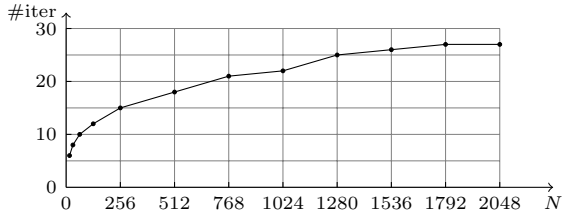

Figure 7: Number of CG-iterations versus problem size for model problem (9).

4 A parallel implementation on the GPU using CUDA

We have implemented the RRB-solver on the GPU using CUDA C. CUDA stands for "Compute Unified Device Architecture". It is NVIDIA's parallel programming environment to program the GPU.

A program on the GPU is divided over kernels which are invoked by the CPU. A kernel basically is a C function that is executed as many times in parallel as there are different CUDA threads. Threads are organized by the programmer by defining a grid and making a division of the grid in thread blocks. The GPU follows the SIMD (single instruction multiple data) programming model. The thread blocks are divided among the physical processors of the GPU. The physical processors are divided among several streaming multiprocessors (SMs), each having many cores; e.g., the GeForce GTX 580 has 16 SMs each having 32 cores, a total of 512 cores, hence a massively parallel architecture.

The GPU has different layers of memory including (cached) global memory, texture memory, shared memory and registers. The global memory is the largest in size (up to 6 GB) but it is also the slowest (400-800 cycles latency). Shared memory is very fast but also very limited in amount. Threads within the same SM communicate through this shared memory.

Programming on the GPU comes with a rich set of rules. One of the most important rules is related to the notion of coalesced memory. The global memory bandwidth is highest when the global memory accesses can be coalesced within a half-warp, e.g., for 16 threads in a half-warp the consecutive 4-byte words must fall within 64-byte memory boundaries, and the 16 threads must access the words in sequence: the kth thread in the half-warp must access the kth word. The penalty for non-coalesced memory transactions varies according to the actual size of the data type and architecture of the device. However, in any case performance is degraded when memory transfers are non-coalesced.

For modern architectures (Fermi, Kepler) the penalty for reading or writing data with a shift is small. However, when reading or writing data with a stride, the effective bandwidth is strongly reduced, see Figure 8 and Figure 9.

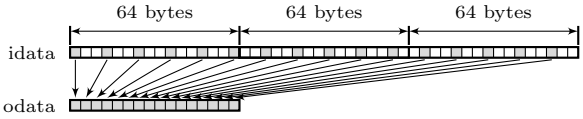

Figure 8: Copying data with a stride. Each thread handles 1 output. On the GPU data is read and written using 32-, 64-, and 128-byte memory transactions only (related to half-warps).

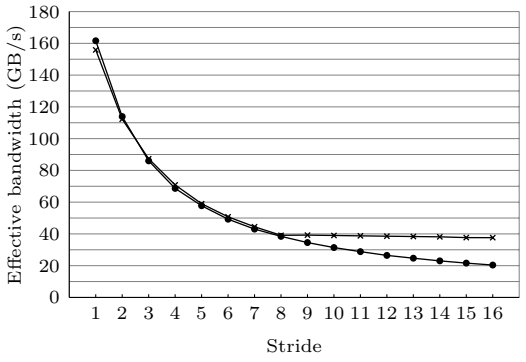

Figure 9: Throughput versus stride for GeForce GTX 580 with (×) and without (•) textures.

This small example already nicely illustrates the main problem we had to deal with when implementing the RRB-solver with CUDA on the GPU: with a naive storage format the required data for each of the operations in CG would not be located next

to each other in the global memory. As we mentioned earlier, the CG-algorithm operates on the first level red nodes only. This means that if we were to perform, say, a vector update, we would have to read data with stride 2 (red/black), and hence we would loose 1/3th bandwidth according to Figure 9. Even worse, when solving the preconditioner step $Mz = r$ for z we would access data with stride $2, 4, 8, 16, 32, \ldots$.

To overcome this problem we have introduced a new storage format: the so-called $r_1/r_2/b_1/b_2$ storage format, see Figure 10.

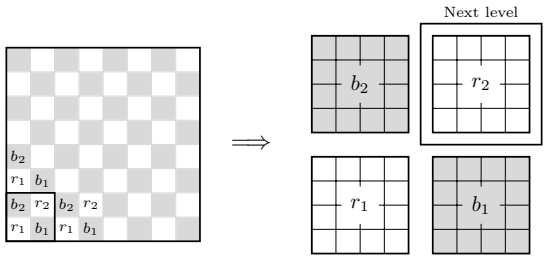

Figure 10: The nodes are divided into four groups: r_1-, r_2-, b_1- and b_2-nodes. Note that all the r_2-nodes together form the next level. On the next level the grouping procedure can be reapplied.

Every vector (and the matrix S) occuring in the CG-algorithm is only stored in this new format, except from $\mathbf{b}$ and $\vec{\psi}$ which are stored in both formats. This is necessary as in a real-time simulator each time frame we have to communicate $\mathbf{b}$ and $\vec{\psi}$. The overhead that comes with $r_1/r_2/b_1/b_2$ is thus restoring 2 vectors. The overhead is very little and worth it by realizing how much throughput we gain every CG-iteration: all operations can be performed fully coalesced. To ensure coalesced memory transactions throughout the preconditioner step, the $r_1/r_2/b_1/b_2$ storage format is recursively applied for all levels. Notice how using the new format comes for free for the preconditioner step.

5 Test problems and testing method

To test our solver we have used a collection of various test problems, including Poisson's problem (9) (for throughput analysis) and several realistic domains from MARIN's extensive database such as the Gelderse IJssel, a small river in the Netherlands, Plymouth Sound, a bay located in the South Shore region of England, see Figure 11, and Port Presto, a fictional region that shows great similarities with Barcelona. Port Presto is used frequently as a reference harbour in real-time simulator studies and assesments of mariners. The realistic domains were discretized on Cartesian grids varying from 100k to 1.5M nodes.

Figure 11: Left: the Gelderse IJssel. Right: Plymouth Sound.

All experiments were performed using single-precision numbers (floats). The experiments were performed on a Dell T3500 workstation equipped with a Xeon W3520 processor (@2.67 GHz), 6GB RAM and a GeForce GTX 580 graphics card (CUDA dedicated). The operating system is Ubuntu 10.04.3 LTS (2.6.32-34-generic x86_64) with CUDA version 4.0 (driver 270.41.19).

We have compared an optimized C++ RRB-solver (without the $r_1/r_2/b_1/b_2$ format) on 1 core of the Xeon W3520 with the CUDA RRB-solver on all cores of the GTX 580. Speed ups were computed at the hand of wall-clock timings on the host. For throughput analysis of the CUDA RRB-solver NVIDIA's profiler was used.

6 Results

In Figure 12 we have plotted the speed up that we obtain when we use the CUDA RRB-solver instead of the C++ RRB-solver.

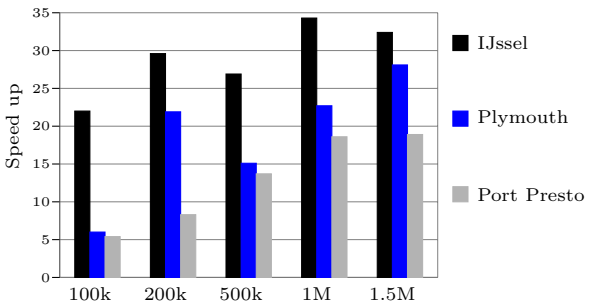

Figure 12: Speed up numbers for the realistic test problems.

For the largest test problems we find a speed up around a factor 25. The 1.5M IJssel, Plymouth and Port Presto problems were respectively solved within 10.7, 10.6 and 11.6 milliseconds, hence the 1.5M test problems can be solved in real-time. Depending on the specific problem it is to be expected that realistic domains consisting of up to 4 million nodes can be solved in real-time.

The RRB-solver is very efficient in itself as we can see from the required number of CG-iterations, see Table 1. All test problems were solved within 7 CG-iterations.

Problem	IJssel	Plymouth	Port Presto
100k	5.814	5.804	5.924
200k	5.832	5.892	5.962
500k	5.836	5.964	5.986
1M	5.859	5.976	6.362
1.5M	5.766	5.984	6.921

Table 1: Average number of CG-iterations over 1000 time frames.

To see how well the CUDA RRB-solver has been parallelized we have listed in Table 2 the performance for each of the routines that are part of the CG-algorithm, recall Algorithm 1. All routines are expected to be bandwidth bound as they are level 1 and level 2 BLAS routines. From the table this is clear as the achieved effective throughput is close to the device's peak bandwidth: the GTX 580 has a peak bandwidth of 193 GB/s. We have to remark that the listed throughput number for the preconditioner step is an average over the throughput number of the kernels on the 1st level; on coarser levels the throughput is lower due to overhead. The table shows that the time is well divided amongst the routines as there are 3 vector updates and 2 inner products in the CG-algorithm, hence there is no bottleneck.

Operation	Time (μs)	Gflop/s	Throughput (GB/s)
Matrix-vector	732	48.7	184
Vector update	160	13.1	164
Inner product	139	15.1	148
RRB solve step	1092	32.9	188

Table 2: Performance of the separate routines of the CUDA RRB-solver on the GTX 580 for a 2048×2048 *domain.*

In Table 3 it is shown how the time in the preconditioner step is distributed over the various levels. According to Equation (6) the maximal number of levels is $k_{\max} = 1+\lfloor(\log_2(\max\{1024, 1024\}))\rfloor = 11$. However, the coarsest 6 levels fit in the cache of the GPU and are therefore handled by 1 SM at once on the 6th level. As we can see only a small fraction of the time is taken by the coarsest levels. So, the typical "Multigrid-issues" such as idle threads on the coarsest levels are not really an issue for the CUDA RRB-solver.

Finally, in Figure 13 an example of the solution of Equation (1) is shown.

7 Conclusions and discussion

To solve the systems of linear equations we have used a solver which is very efficient in itself. In combination with a very efficient implementation

Level	$\frac{1}{2}$#Nodes	Time (μs)	Percentage
1	1024×1024	428	39.2
2	512×512	405	37.1
3	256×256	130	11.9
4	128×128	50	4.6
5	64×64	25	2.3
6-11	32×32	54	4.9
Total		1092	100

Table 3: Time spent per level for a domain of 2048×2048 *nodes.*

Figure 13: A ship sailing through the Gelderse IJssel.

on the GPU, the solver allows real-time simulation of interactive waves using up to 4 million nodes.

ILU preconditioners tend to parallelize very poorly as the operations usually are inherently sequential. However, we have demonstrated that the RRB-solver allows an efficient parallelization for both the construction and the application of the preconditioner. With the $r_1/r_2/b_1/b_2$ storage format we were able to implement the RRB-solver efficiently on the GPU. By doing so we found speed up factors of more than 30 compared to a sequential implemention on the CPU.

In our experiments we used equidistant Cartesian meshes, but this is not mandatory. With non-equidistant and curvilinear meshes one should be able to simulate even much larger domains in real-time.

Acknowledgement

The authors gratefully acknowledge the contributions of Gert Klopman and Anneke Sicherer-Roetman to the research project.

References

[1] C.W. Brand, An Incomplete-factorization Preconditioning using Repeated Red-Black Ordering, *Numerische Mathematik*, pp. 433–454, 1992.

[2] A. Ditzel, N. Leith, Deep Water Anchor Handling Simulation. MARSIM, Singapore, 2012.

[3] G. Klopman, Variational Boussinesq Modelling of Surface Gravity Waves over Bathymetry, PhD Thesis, University of Twente, Twente, 2010.

[4] Y. Saad, *Iterative Methods for Sparse Linear Systems*, SIAM, 2nd edition, Philadelphia, 2003.

Implementation of Anisotropic Mesh Refinement in OpenFOAM®

J. Karlsson, A. Feymark, C. Eskilsson

Department of Shipping and Marine Technology
Chalmers University of Technology
SE-412 96 Gothenburg, Sweden

karjonas@student.chalmers.se
andreas.feymark@chalmers.se
claes.eskilsson@chalmers.se

1 Introduction

Researchers and engineers practicing Computational Fluid Dynamics (CFD) have over the years gained a lot of experience on how to design good computational meshes. Nevertheless, for a general hull shape it is impossible to a priori know the resolution and exact design of the coarsest mesh required to obtain a certain computational accuracy. Here, the use of self-adapting schemes becomes vital. There are several methods to design self-adapting schemes. By far the most popular method is Adaptive Mesh Refinement (AMR) where the mesh is refined by adding cell points in order to split cells and reduce cell size.

There is an important distinction between isotropic and anisotropic (sometimes referred to as directional) AMR. In isotropic mesh refinement the aspect ratios of the original mesh cells are saved since all cell edges (faces in 3D) are split, e.g. one triangle is split into four triangles and one hexahedron is split into eight hexahedra. This approach guarantees that the mesh quality is not degraded and that the resulting matrices stay well conditioned. However, often there is a pronounced directional behaviour in the flow field investigated. Two examples are boundary layers and shocks waves, where the flow varies dramatically only in the normal direction of the boundary layer or shock. For such cases it is computationally more efficient to use highly stretched cells with high aspect ratios. Such cells can be obtained from a coarse initial mesh undergoing anisotropic refinement, splitting only some of an element's edges. Typically, the number of cells given by an anisotropic refinement constitutes only a fraction of the number of cells given by an isotropic refinement. Within Naval Hydrodynamics anisotropic AMR is well established. Examples of this is the ISIS-CFD code [7, 8] and the ongoing development of anisotropic mesh refinement in the ReFRESCO code [10].

A code with growing popularity within the ship CFD community is OpenFOAM [9, 6], an open-source finite volume framework. In the last Gothenburg workshop in 2010 several contributions using OpenFOAM were presented [1, 5, 4]. OpenFOAM supports multiphase flow, moving meshes and parallel execution. Notably the vanilla version of OpenFOAM also supports AMR. The original implementation of AMR in OpenFOAM is described in the PhD thesis of Jasak [3]. Jasak describes an implementation of directional refinement. However, neither the vanilla version of OpenFOAM as maintained by OpenCFD (release 2.1.1) nor the extend-project (release 1.6-ext) supports anisotropic mesh refinement (albeit the extend version do support dynamic re-meshing of tetrahedra). With regard to AMR there is no difference between the two versions of the code: they both support an isotropic 1-8 split of hexahedra only. Further, the vanilla version does not support dynamic load-balancing which effectively limits the use of AMR for general cases.

This paper will outline the implementation of anisotropic mesh refinement in OpenFOAM[1]. As

[1]This development is not approved, endorsed or supported by OpenCFD Limited, the producer of the OpenFOAM software and owner of the OpenFOAM® and OpenCFD® trade marks.

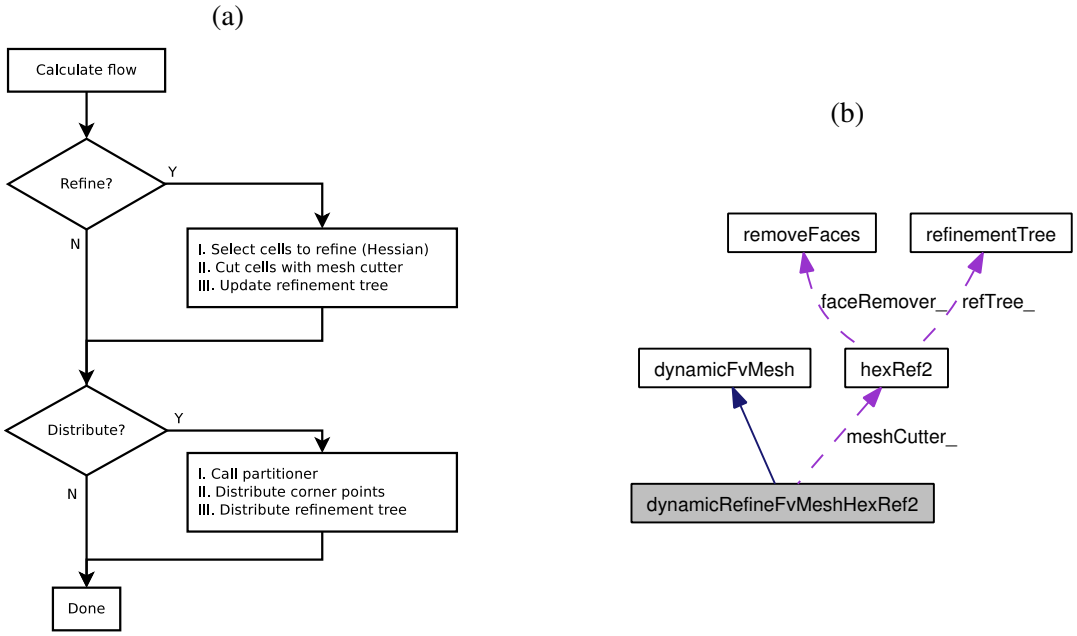

Figure 1: Key concepts for the anisotropic AMR. (a): The high level flow graph of the application (the flow graph is executed for every time-step (or iteration step). (b) The collaboration diagram of the class `dynamicRefineFvMeshHexRef2`. `dynamicRefineFvMeshHexRef2` contains a variable `meshCutter_` of class `hexRef2` and is a subclass of `dynamicFvMesh`.

of now the we restrict to hexahedra, but the design has been done with the intention of also being able to support tetrahedra mesh refinement in the future. The development described in this paper has been made using a version of OpenFOAM-2.1.x with added support for dynamic load-balancing.

2 Implementation of AMR

The implementation of AMR in OpenFOAM depend upon three key components; refinement-engine, mesh-cutter and refinement-tree. The implementation for isotropic AMR in OpenFOAM does provide these parts although the mesh-cutter and the refinement-tree only works for octasectal refinement so to handle anisotropic refinement they need to be replaced with anisotropic counterparts. Figure 2a shows a high-level overview of how the anisotropic implementation works. Figure 2b shows the collaboration diagram for the class `dynamicRefineFvMeshHexRef2` which is the name of the refinement-engine. In the figure the mesh-cutter is the class `hexRef2`, from hexahedron refinement into two cells, and `refinementTree` is the name of the refinement-tree class.

The main task of the refinement-engine is to select the cells to refine (and direction based upon the hessian), call the mesh-cutter to cut them and also redistribute the mesh when needed. The redistribution is achieved by using functions provided through OpenFOAM which in turn uses external libraries like metis and scotch. The redistribution function gives a list that for every cell in the mesh contains the processor number of the processor it should be sent to.

To be able to refine a cell some scheme for orienting the cell is needed, without an orientation it is impossible to know how to execute a split in the wanted direction. The created scheme makes use of corner points as its underlying framework where each cell has a list of its corner points. The corner points are used to make sure that a split is done properly by splitting between pre-determined pairs of corner points. The corner points are defined as the corners of a hexahedron which means that every cell will always have eight corner points. When the mesh is created, or rather read, the corner points will need to be calculated. Naturally just knowing the corner points will not tell you between which pair of points a split is done, therefore a uniform way of indexing the corner points is needed. The corner points are indexed according to Figure 2. Note that the numbering can be arbitrary as long as we keep track of how the split will be done, that is knowing between which pair of points the splits are to be inserted. If

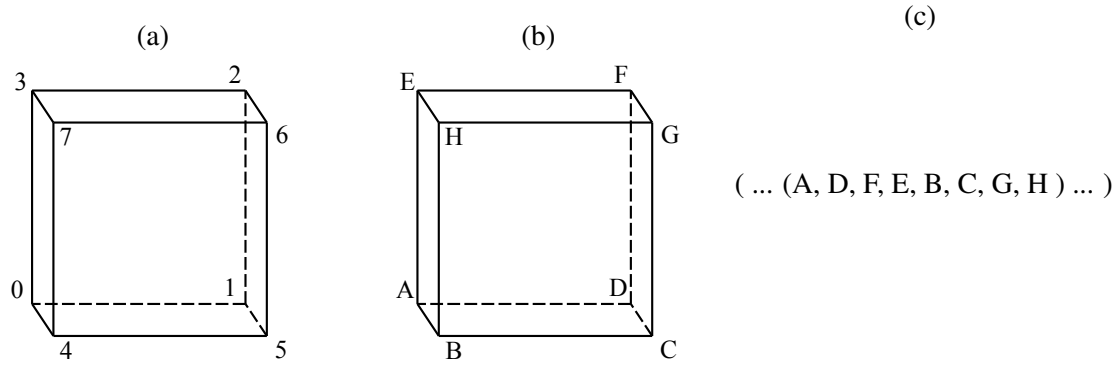

Figure 2: An example of a cells corner points. (a) shows the index numbering of the corner points used for all cells, (b) the labels of a cell and (c) illustrates how the cell in (a) is stored in the list of corner points.

we look at figure 2 the edge $A \rightarrow D$ will be one axis, the edge $A \rightarrow E$ another axis and the edge between $A \rightarrow B$ the last axis. Because of this the direction of a split is stored relative to the corner points and not the axis.

The mesh-cutter had to be rewritten to handle anisotropic refinement. When doing cell splitting we need to make sure the mesh is consistent and satisfies the "two-to-one" rule which means that every side of a hexahedron should be composed of at most two faces. If we look at figure 3 we can see the three different ways the side of a hexahedral can be split and one case where splitting is not allowed. Note that these different cases assume the mesh is consistent, any consideration for inconsistent meshes is not taken. From these cases we can see that for a face to be splittable it needs to contain four corner points from its neighbour. The neighbour is in this setting defined as the neighbouring cell to the cell marked for refinement. From this we can formulate a simple constraint for keeping a mesh consistent: let c be a cell marked for refinement and $F : \{f_0, ..., f_n\}$ the set of faces f_i on c needed to be split for a certain anisotropic refinement direction d of c. For every face $f \in F$ we define the set N of neighbour corner points:

$$N(f) = \begin{cases} \text{Corner points of f:s face neighbour} & \text{if neighbour exist} \\ \emptyset & \text{otherwise} \end{cases}$$

We say that a cell is consistently refinable if all faces with a neighbouring cell contain exactly four corner points on it or the neighbour is nonexistent. More formally, c is consistently refinable in direction d if:

$$\forall f \in F, N(f) = \{\emptyset\} \vee |N(f)| = 4$$

The class `hexRef2` provides the functionality of consistent refinement in the function `consistentRefinement`. This function takes a list of cell labels and their split direction as input, then unmarks the cells that are not splittable and returns a new list of cells to split.

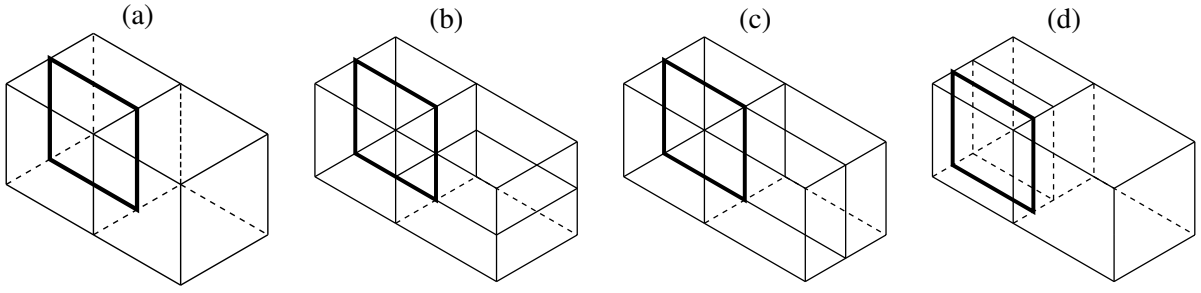

Figure 3: Anisotropic refinement of a hexahedron. The thick lines represent the edges the cell split aims to create. Three allowed types of splits of a hexahedron: (a) splitting a regular side between two cells, (b) splitting a side with an edge perpendicular to the split and (c) a side already split where no new split is needed. (d) shows a disallowed split due to consistency constraints.

The actual refinement commands will be executed when calling `setRefinement`. The function `setRefinement` takes as input a list of cells for refinement and an object of `polyTopoChange`. The class `polyTopoChange` contains functions for changing the mesh (adding/removing points, faces and cells) and also holds the new mesh that is updated whenever any mesh-changing function is called. The function `setRefinement` works by first calculating for all faces by which points or edges the face will be split. The faces are then synchronized between the processor boundaries to know how faces on the other processes will be split. Then for the edges that will get split their midpoints are computed and synchronized. Next the faces that are in some way affected by any change are collected. For instance a change can come from a split, new points or a change of owner and neighbour. Now the new cells for the refinement are created. The cell refinement is achieved by creating one new cell and modifying the old. Now the faces gets split, new points gets added and the neighbours and owners for every face gets updated. Lastly the middle face between the old and new cell is created. For each modified and added cell the corner points gets updated and lastly the split is added to the refinement-tree.

The refinement-tree is used for keeping track of the history of the refined cells as to enable unrefinement. It is based upon REFTREE [11] and does not make any assumptions about which type of refinement is done. Because of this the tree can handle both isotropic and anisotropic refinement which means that it can be used for all types of refinements in OpenFOAM. Mitchell describe a way of distributing the refinement-tree across multiple processes where every child can be sent to any process leaving its siblings on another process. This is done by keeping a lightweight substitute data structure of the sibling on the processor it was moved from. This feature was not implemented due to time limit and complexity, however the problem of distribution is solved by another method. This method forces the distribution-method to only distribute children of the root node and with them all their children. It is then up to the application computing the distribution to put the weights on the initial mesh based on the size of the tree for these cells i.e. their number of children. However redistributing the mesh will make the calculated corner points and the refinement-tree invalid since they depend upon cells that may be distributed. To counteract this problem the refinement-tree contains a function to redistribute itself, likewise the mesh-cutter also contains a function to redistribute the corner-points.

3 CFD Modelling

While the AMR implementation descried above is general and not equation or solver dependent, we will here initially only use the steady-state incompressible RANS solver `simpleFoam`, a segregated solver using the SIMPLE algorithm. As the AMR is encapsulated is in the OpenFOAM libraries that are linked to the solvers, the solvers themselves needs only minor alteration to incorporate AMR – typically only a few lines needs to be changed.

OpenFOAM supports a wide array of discretization schemes but we restrict ourselves to use only one convection scheme: `limitedLinear` which is a second-order TVD scheme. All other operators, the gradient, the Laplacian, interpolation, etc, are all employing second-order central differencing.

With regard to AMR we use a very simple error indicator, based on the jump in pressure over the cell faces see e.g. [2, 10], for both isotropic and anisotropic mesh refinement. For the anisotropic refinement we use the Hessian of pressure to determine the direction of the split. Please note that a present restriction of the AMR implementation is that we do not allow any refinement of wall boundary cells – the y^+ is set manually and the cells are not to be modified during the simulations.

4 Preliminary Results

4.1 Backward facing step

The classical backward facing step in the ERCOFTAC C-30 database is initially used for testing the AMR. The Reynolds number based on step height, H m is 50 000 and the tunnel extends is $40H$ downstream of the step and $4H$ upstream. The height of the tunnel is $9H$. We use the Spalart-Allmaras RANS model with a continuous wall function and a y^+ of roughly 10. The inflow conditions are the same as developed for the Lisbon Uncertainty Workshops.

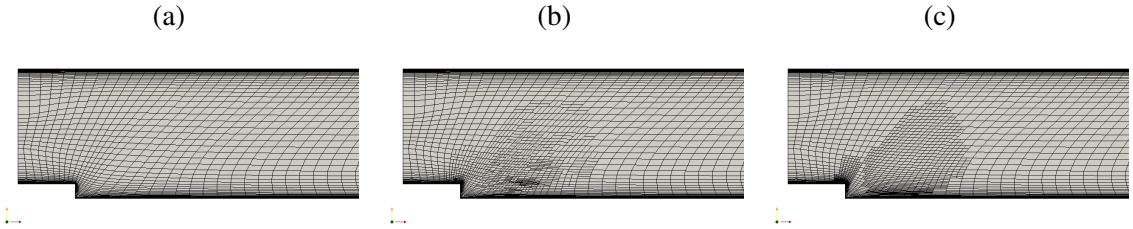

Figure 4: Meshes for the backward facing step: (a) initial mesh, (b) anisotropic mesh and (c) isotropic mesh.

We use the pressure jump error indicator with a tolerance of 1×10^{-3}. Figure 4 shows the resulting meshes using anisotropic and isotropic refinement, respectively. The initial mesh was made up of 3300 hexahedrals (as computations in OpenFOAM always is 3D). The used tolerance is rather lax and the isotropic refinement needs just one refinement step to fulfil the tolerance, ending up with a mesh of 5000 cells while the anisotropic mesh is just short of 4000 cells. Both simulations show similar results with a reattachment length of roughly 6.

4.2 NACA0012 wing

Next we apply the AMR to resolve the tip-vortex of a NACA0012 with a rounded wing tip at 10 degrees angle of attack. The chord based Reynolds number is 4.35×10^6. We compute this with anisotropic and isotropic refinement using a tolerance of the error indicator of 1×10^{-4}. Here we also turn off the spreading in isotropic refinement.

In Figure 5a is the refinement shown. The bulk of the refinement occurs in the downstream tip vortex and some at the leading edge of the wing. The areas are virtually identical for the three AMR approaches but the isotropically refined mesh is denser (0.90M cells) compared to isotropic with no spreading (0.89M) and anisotropic (0.78M). The pressure in the vortex core (defined as the position of minimum pressure) is presented in Figure 5b. Here we also compare to two static meshes (gridA has 0.75M and gridC 2.98M cells). It is interesting to note that it is only the standard isotropic AMR that picks up the low pressure at $x/c \approx 0.7$, indicating that the only a few restrictions of cells that should be refined can be devastating. We also believe that the lack of spreading gives a lot of unnecessary hanging nodes that are responsible for the rapid damping of the core pressure (as this does not happen for the static coarse mesh) .

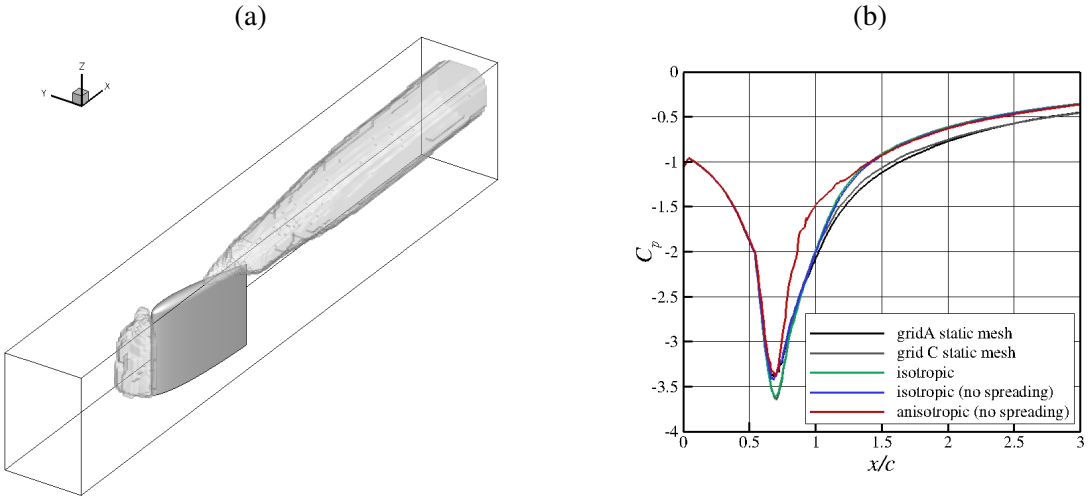

Figure 5: NACA0012 wing. (a) areas of refinement and (b) pressure in the vortex core.

5 Concluding Remarks

We presented the initial work made on anisotropic AMR in OpenFOAM. While the fundamental 1:2 splitting of the hexahedrals work we stress that this is work in progress and that the implementation still suffer from a number of shortcomings. Most notably is that spreading of refinement due to requirement from a neighbour is not functioning. This is we believe the cause of the unfavourable comparison to the isotropic refinement. Although refinement of wall cells is not included yet we mention that this feature is available in OpenFOAM as a stand alone utility which should be incorporated in the dynamic AMR.

Acknowledgements

The initial hexahedra grids for the NACA0012 case were kindly provided by MARIN. The computations were performed on C3SE computing resources.

References

[1] Fureby, C., Alin, N. and Liefvendahl, M. (2010): Large eddy simulation of the flow past the DTMB 5415 surface combat hull. In *Proceedings Gothenburg 2010 - a Workshop on Numerical Ship Hydrodynamics*, Vol. II, pp. 476–472.

[2] Eskilsson, C. and Bensow, R.E. (2011): A mesh adaptive compressible Euler model for the simulation of cavitating flow. In *Proceedinggs of the IV International Conference on Computational Methods in Marine Engineering*.

[3] Jasak, H. (1996): *Error Analysis and Estimation for the Finite Volume Method with Applications to Fluid Flows* PhD thesis, Imperial College of Science, Technology and Medicine, U.K.

[4] Kim, S.-E., Rhee, B.J., Shan, H., Gorski, J., Paterson, E.G. and Maki, K. (2010): A scalable multiphase RANSE capability based on object-orientated programming and its application to ship hydrodynamics. In *Proceedings Gothenburg 2010 - a Workshop on Numerical Ship Hydrodynamics*, Vol. II, pp. 569–574.

[5] el Moctar, B., Kaufmann, J., Ley, J., Oberhagemann, J., Shigunov, V. and Zorn, T. (2010): Prediction of ship resistance and ship motions using RANSE. In *Proceedings Gothenburg 2010 - a Workshop on Numerical Ship Hydrodynamics*, Vol. II, pp. 495–505.

[6] OpenFOAM Foundation (2012): Available from `http://www.openfoam.org`.

[7] Wackers, J., Ait Said, K., Deng, G.B., Mizine, I., Queutey, P. and Visonneau, M. (2010a), Adaptive grid refinement applied to RANS ship flow computation, In *Proceedings of the 28th ONR Workshop on Naval Hydrodynamics*.

[8] Wackers, J., Deng, G.B., Leroyer, A., Queutey, P. and Visonneau, M. (2012): Adaptive grid refinement for hydrodynamics flows. *Computers and Fluids*, Vol. 55, pp. 85–100.

[9] Weller, H.G., Tabor, G., Jasak, H. and Fureby, C. (1998): A tensorial approach to CFD using object oriented techniques, *Computers in Physics*, Vol. 12, pp. 620.

[10] Windt, J. and Klaij, C.M. (2011): Adaptive mesh refinement in MARIN's viscous flow solver ReFRESCO: Implementation and application to steady flow. In *Proceedinggs of the IV International Conference on Computational Methods in Marine Engineering*.

[11] W. F. Mitchell, A refinement-tree based partitioning method for dynamic load balancing with adaptively refined grids, J. Parallel Distrib. Comput. 67 (4) (2007) 417–429.

A Study of CFD Modelling Variations for Numerical Underwater Noise Prediction

Paula Kellett, Osman Turan, Atilla Incecik,
Department of Naval Architecture and Marine Engineering, University of Strathclyde, Glasgow, UK

Email: paula.kellett@strath.ac.uk

The maritime industry sector has a significant impact on the marine environment, with the potential to cause a considerable damage. However, only in recent years has underwater noise begun to be recognised as a potentially serious threat to wildlife, in particular marine mammals and fish, with conservation groups and government departments highlighting the issues, and calling for further research into relevant fields. Little research has so far been carried out focussing on the more passive form of noise pollution known as ship underwater radiated noise; most attention has been turned on the more deliberate noise impacts associated with sonar and airgun arrays. These intermittent impulse noises are believed to have a significant impact on some marine animal species in the very short term, however the potential short and long term impacts of the lower intensity, lower frequency, more continual ship radiated operational noises are less clear.

Empirical prediction models for ship underwater noise do exist; however the true noise "signature" is dependent on many factors and the different source levels for specific frequency bands is only accurately known through full-scale measurements. Unfortunately, delaying the investigation of a vessel's acoustic characteristics until the ship is fully designed and built leaves very little room for alteration and improvement, suggesting that more accurate models need to be developed, based on a better understanding of the composition of ship noise spectra at different ship speeds and loading conditions. The nature and mechanics of noise propagation has been the most researched area in this field, and some theoretical models do exist for noise transmission, attenuation and spreading mechanisms in a variety of conditions.

Numerical approaches to hydroacoustic modelling is a relatively new area of research, and different techniques are still being developed. This study forms a part of a larger project aiming to design a numerical noise prediction model which can be used to predict the noise of a new build vessel to a suitable degree of accuracy, in the design stages. The investigations discussed below will inform how the final model will work, and what will be incorporated in it, and also the levels of error to be expected when using alternative approaches. The resulting model should be reliable and provide suitably accurate results, whilst minimising computational time and complexity, and hence cost.

This work is carried out using CD-Adapco's StarCCM+ CFD package, which has a built-in acoustic model, in the form of the Ffowcs-Williams Hawkings (F-WH) equation. The Ffowcs-Williams Hawkings equation uses generalized functions to extend the application of Lighthill's Acoustic Analogy, which is originally used to predict the aerodynamic noise generated by rotating bodies such as helicopter rotors and fan blades. More recently this equation has also been applied to operations in other fluids, namely water, for the noise generated by marine propellers. In situations where detailed data on the turbulent phenomena in the near-field can be obtained, the Ffowcs-Williams Hawkings equation can also be used for broadband noise prediction. The equation in its best-known form can be seen below:

$$\overline{\square}^2 p' = \frac{\partial}{\partial t}[\rho_0 v_n \delta(f)] - \frac{\partial}{\partial x_i}[l_i \delta(f)] + \frac{\bar{\partial}^2}{\partial x_i \partial x_j}\left[T_{ij} H(f)\right]$$

Where: $\overline{\square}^2$ *is the D'Alembert, or wave operator as defined above*
p' *is the acoustic pressure in the undisturbed medium, in this case* $p' = p - p_0 = c^2 \rho'$
ρ_0 *is the density of the quiescent medium, or fluid static density*

v_n is the local normal velocity of the source surface
l_i is the local force per unit area of the fluid in the i-direction
$\delta(f)$ is the Dirac delta function, where

$$\delta(f) = 0 \; for \; f \neq 0$$
$$\delta(f) = +\infty \; for \; f = 0$$

T_{ij} is the Lighthill stress tensor as defined above
$H(f)$ is the Heaviside Function, where

$$H(f) = 0 \; for \; f < 0$$
$$H(f) = 1 \; for \; f > 0$$

The three terms on the right-hand side of the equation are then the thickness, loading and quadrupole source terms respectively. Most of the analogy is now linear, with all non-linearity being collected in the Lighthill Stress Tensor. As the Ffowcs-Williams Hawkings equation is valid in the whole 3D space, it is common to use the Green's Function of the wave equation, to turn the equation into an integral form, allowing it to be solved numerically.

Mesh generation was carried out using the automatic meshing tool, resulting in a computation mesh of approximately 6.4 million cells in total; a typical medium density grid. The frequency range from 0 - 500 Hz is modelled, and in order to ensure that results up to this value are obtained accurately, a time-step size of 0.001 seconds is used throughout, with a maximum run-time of 5 seconds. The Realizable k-Epsilon Two-Layer turbulence model is used.

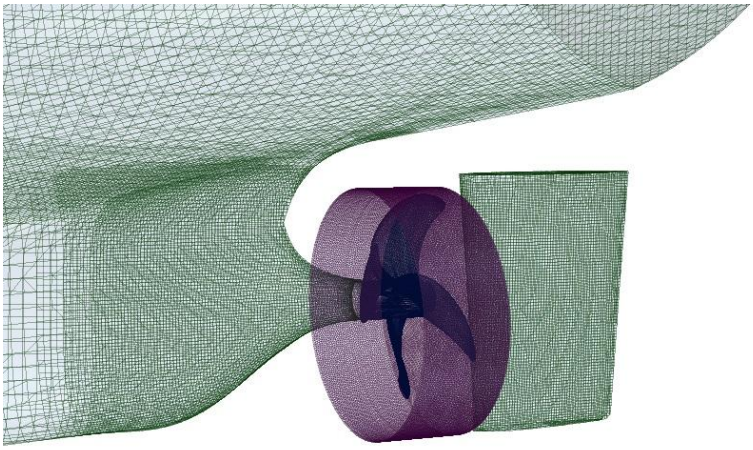

Figure 1 - Aft section showing stationary and rotating parts, and interfaces

Full scale measured hydroacoustic data for an LNG Carrier travelling at 19 and 9 knots is used to validate the predicted values. The full scale data was measured in calm, shallow water (approx. 45m depth) in the area east of Singapore, with a hydrophone suspended at 30m depth. This area was selected for its relatively low levels of background noise, as well as the calm water conditions. The virtual receivers included in the CFD model are located to correspond with the Closest Point of Approach (CPA) seen in each of the full scale runs. Once the model has run, the frequency domain data from each receiver is transformed into time series data using a Fast Fourier Transform (FFT).

The first investigation looks briefly at the effects of the free surface on the predicted results. In order to model the free surface, or rather the assumed flat calm waters surface, a Volume of Fluid (VoF)

flat wave is used. This is used together with the Eulerian Multiphase model, to account for the two different fluid domains present, i.e. water and air.

The graph below shows the results from this comparison at the port receiver; those for the starboard receiver are very similar. It can be seen that at the lower frequencies, up to around 200Hz, the model with no free surface over-predicts the sound pressure level. This may be due to the fact that the low frequencies are not being partially absorbed by the free surface as they would be in reality. However, it can also be observed from the results that above 200Hz, the results with and without a free surface present show good agreement, suggesting little impact from the free surface at these frequencies. These findings suggest that, depending on the requirements of the designer carrying out the modelling, there are instances in which neglecting the free surface to speed up computation and reduce costs could be justified.

It should be noted that there is a significant discrepancy in lift, drag and thrust values predicted in the two models. This is assumed to be due to the fact that the entire ship is effectively under water and therefore will be seriously increasing the wetted surface area and underwater volume of the ship. This will increase the resistance and therefore the drag value, as well as affecting the lift and thrust values.

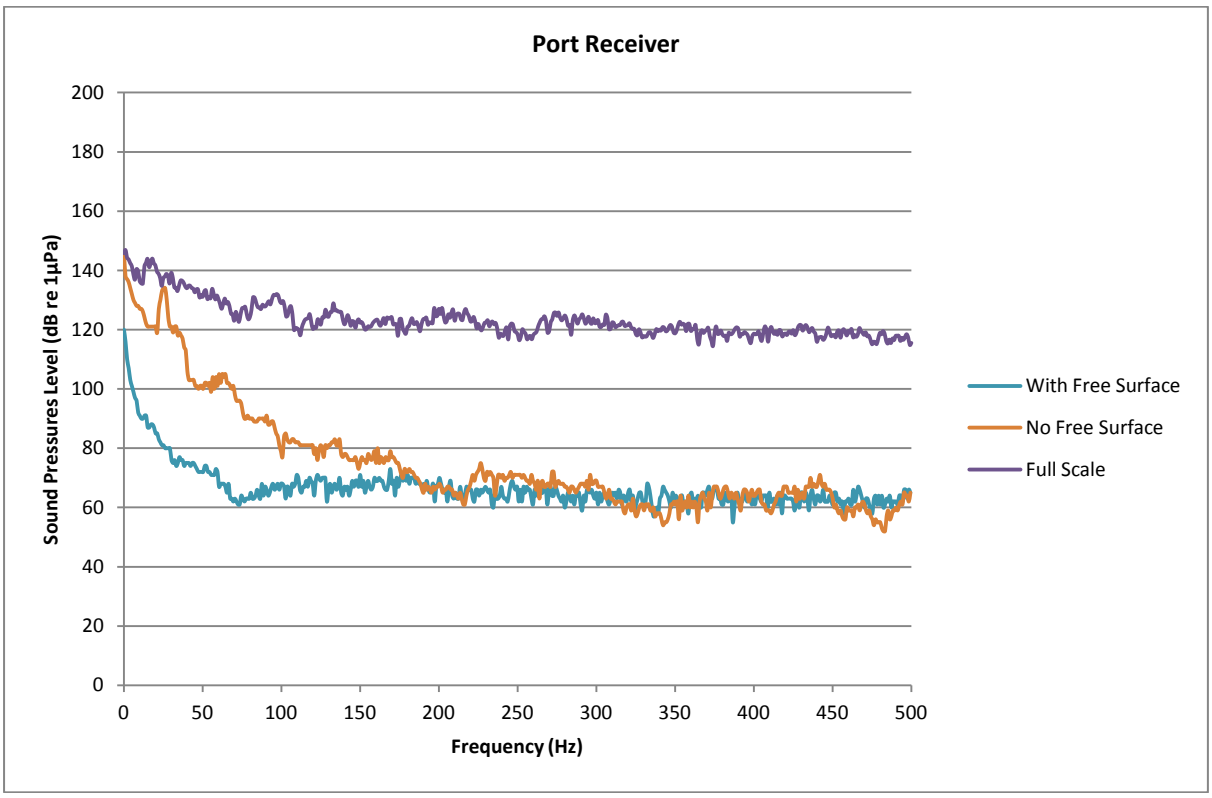

Figure 2 - Comparison of Results With and Without Free Surface, Port Receiver

The next investigation looked at a comparison between different propeller modelling methods. Those included in this investigation are a static propeller geometry, a moving frame of reference associated with a static propeller geometry, and a fully rotating propeller geometry and associated mesh, with a sliding interface.

In the rotating propeller approach, the propeller geometry is meshed as a separate region, and a purely rotational motion is applied to the entire propeller mesh. This results in a transient calculation, which will provide time-accurate results; the closest representation of reality of the three methods presented here. The interface between the rotating and stationary mesh

components is known as a sliding interface, and it is important that the interface is properly defined, to allow flow properties and calculation variables to be properly propagated through the simulation domain.

The moving frame of reference approach assigns a frame of reference to a static mesh region incorporating an accurate propeller geometry, and the frame of reference itself moves in a purely rotational motion with respect to the global co-ordinate system. The simulation will calculate the variations in flow and pressure distributions at each time-step according to the relative location of the rotating frame of reference. A source term is added to the momentum equation, to account for the added Coriolis forces which occur due to the rotating reference frame.

In the static propeller approach, the propeller geometry is present in the simulation, however no rotation of any nature is applied to it. This is an overly simplified approach, and is therefore representing a baseline option, as the run time associated with this option is significantly less than for the more complex approaches outlined above.

The results of this comparison at 19 knots, with the free surface modelled in all simulations, is shown below:

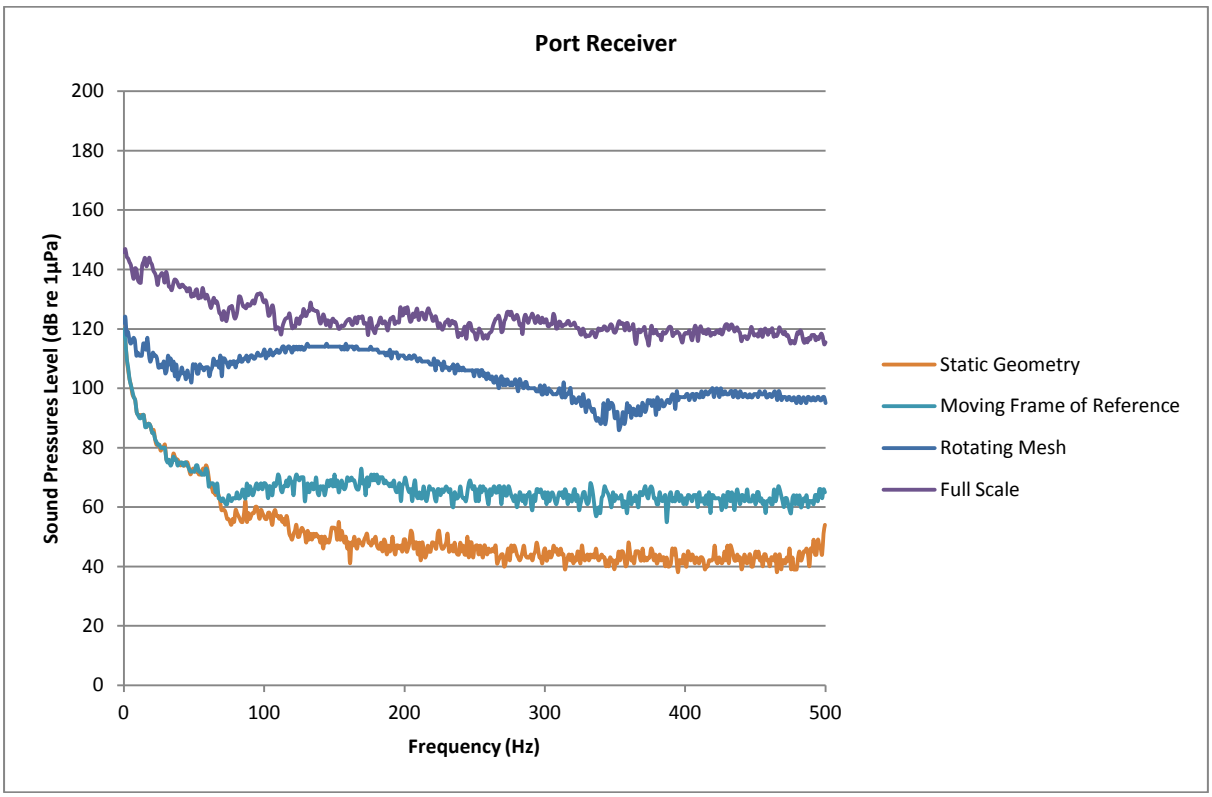

Figure 3 - Comparison of Propeller Representation Methods, Port Receiver

The results above show that in terms of overall sound pressure level, the rotating mesh, as expected, appears most accurate. However in terms of spectral shape, the moving frame of reference approach gives more realistic results. Further investigation is required into the rotating mesh simulation to ascertain whether these inaccuracies are caused by user error or are in fact a consequence of the method itself. The static geometry approach is the least accurate and is therefore not considered to be suitable for hydroacoustic problems.

It should be noted that the rotating propeller approach has a much longer run time that the other two approaches, and also has higher computational memory requirements.

The third investigation looks at the effects of including a permeable source surface in the flow region to account for quadrupole sources. In aeroacoustic application, the quadrupole source term is assumed to be negligible at low rotational mach numbers, and is usually only considered when the rotational speed approaches Mach 1; in such applications this is a reasonable assumption. However, as discussed in (Ianniello, 2012), and contrary to popular opinion, the quadrupole noise sources present within the fluid are not negligible in hydroacoustics as they are in aeroacoustic applications, and they should be suitably accounted for. Quadrupole noise sources arise from the unsteady shear stress and vorticity content of a highly turbulent flow domain such as that observed in the wake of the hull and propeller. However as with most CFD packages, these are neglected within StarCCM+ and only the contributions from the thickness and loading terms are calculated. The most appropriate method for incorporating the quadrupole term back into a CFD simulation is to use the Porous Formulation developed by (Farassat, 2007). In this approach, a permeable source surface, which encloses the vessel, is placed within the flow and is used as the radiating surface for the acoustic model. This surface will then allow for the monopole and dipole sources from the hull and propeller surfaces to be captured, as well as the quadrupole sources within the flow, such as those arising from turbulence.

In this investigation, the results from a model with no permeable source surface, and with semi-cylindrical source surfaces of two different radii are compared.

Overall it can be seen that the results using the porous formulation are higher than the standard simulation. The discrepancy of 25-30dB between the porous formulation simulation results in a non-cavitating condition and full scale results agrees well with results presented in (Hallander, Li, Allenstrom, Valdenazzi, & Barras, 2012) which quotes a 20-25dB gap. This gap in results between full scale and modelled data can be attributed to lack of representation for cavitation and machinery noise, as well as difficulties in recreating an accurate representation of real conditions in a mathematical model. The variation in predicted results between these results and those referenced can be attributed to the use of a different CFD Code and turbulence model, lack of free surface in the referenced data, and other modelling dissimilarities.

Looking more specifically at the variations in results for the two different permeable source surface locations, it can be seen that although the dB levels for the Sound Pressure Level re 1µPa are slightly higher with the more distant surface at lower frequencies, this difference disappears for higher frequencies, especially in the case of the further placed starboard receiver. It can also be seen that although the tonal peaks agree fairly well, the general broadband noise level results with the further surface are less well defined, and do not replicate the spectra seen in full scale measurements as accurately. The simulation with permeable source surface of half-cylinder with a smaller radius appears to be more generally accurate and reliable. However it is suggested that further study is conducted in this area, as well as into the possible reasons for large tonals appearing in the numerical results, where none are observed in the full scale results.

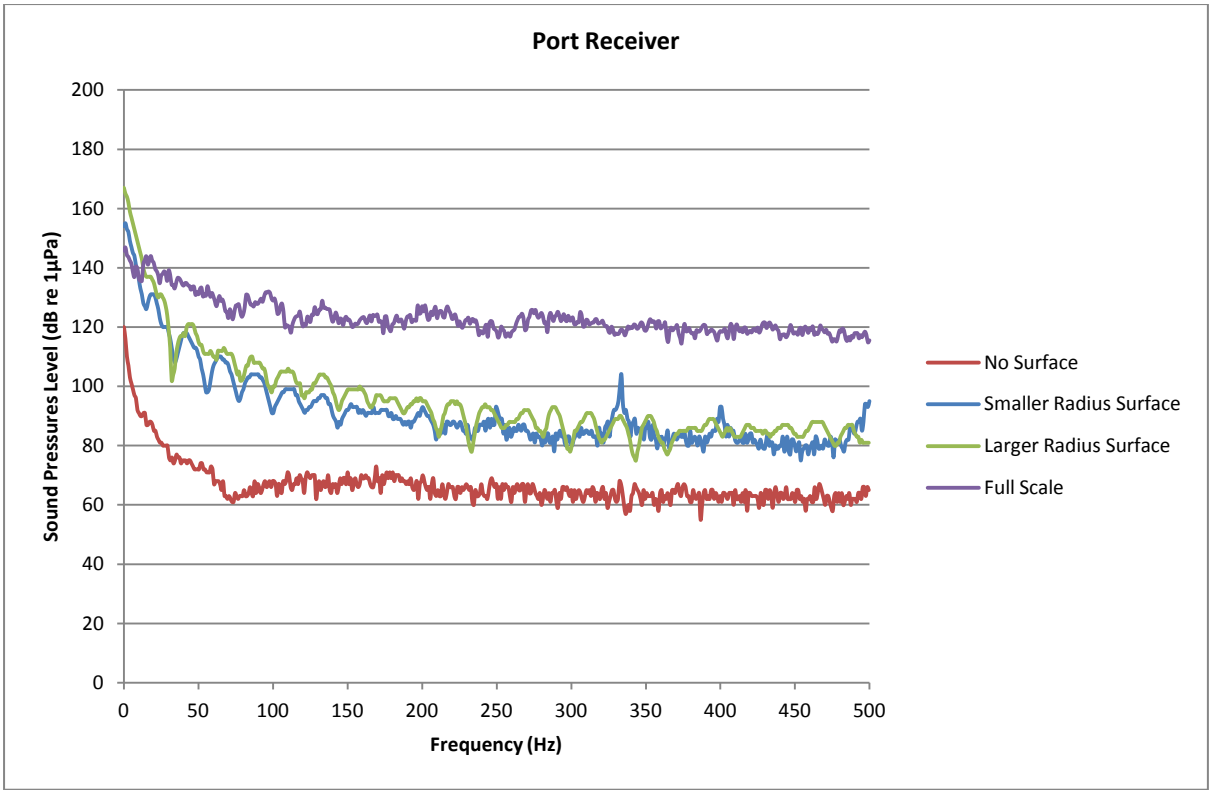

Figure 4 - Comparison of Results with Porous Formulation Model, Port Receiver

Given the inaccuracies observed in the spectral form prediction by the rotating mesh approach, the added computational costs associated with this methods, and the relative accuracy of the moving reference frame method with permeable source surface, initial results could point to the latter being a more suitable modelling technique for hydroacoustic problems.

References

Farassat, F. (2007). *Derivation of Formulations 1 and 1A of Farassat*.

Hallander, J., Li, D.-Q., Allenstrom, B., Valdenazzi, F., & Barras, C. (2012). Predicting underwater radiated noise due to a cavitating propeller in a ship wake. *Proceedings of the 8th International Symposium on Cavitation - CAV2012* (pp. 1–7). Singapore.

Ianniello, S. (2012). Ship Underwater Noise Prediction Through the Acoustic Analogy. In University of Strathclyde (Ed.), *International Conference on Advances and Challenges in Marine Noise and Vibration, MARNAV 2012* (pp. 109–121). Glasgow.

Acknowledgements

This work is carried out at the University of Strathclyde, Glasgow with support from Shell Shipping and the University of Strathclyde. It has been carried out using the University of Strathclyde High Performance Computer (HPC) Facility.

About the Effect of Discretisation Schemes on the Results of Numerical Calculations of Ship Flow

Lutz Kleinsorge, University of Rostock, Germany, lutz.kleinsorge@uni-rostock.de
Robert Bronsart, University of Rostock, Germany, robert.bronsart@uni-rostock.de
Katja Hartig, Neptun Ship Design, Germany, k.hartig@neptun-germany.com

Introduction:

Reynolds-Average-Navier-Stokes-Equations (RANSE) are state-of-the-art in today's Computational Fluid Dynamics (CFD). Thereby the accuracy of simulations with RANSE depends on the numerics and meshes to be used. To insure a good agreement and stability of the numerical solutions it is important to investigate how the different discretisation schemes are influencing the result. A simple example for the motivation of this paper is presented in Figure 1: depending on the scheme used in the simulation the results for the mixing of a fluid with two velocities look different. Therefore the effect of these schemes on the numerical results for ships will be investigated. This helps to improve the trustworthiness of the solutions, especially in cases where experimental results are not available.
In the following a parameter study is presented where various discretisation schemes are used for double body simulations of the well-known KVLCC2 ship model. The numerical results are compared with experimental measurements described in Kim *et al.* (2001) and Stern *et al.* (2003).

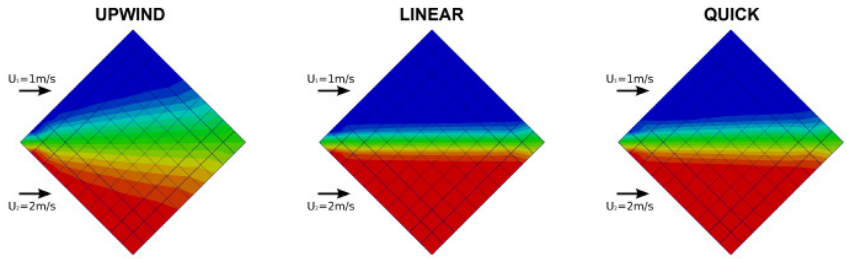

Figure 1: Motivation of this study: Simple example that shows the influence of different discretisation schemes on the numerical solution.

Computational Set-Up

Mesh Generation

The ship and its domain are meshed according to two different approaches:

- Unstructured hexahedral meshes (US) created with the Software *Numeca Hexpress*.
- Block-structured hexahedral meshes (BS) created with the Software *Ansys ICEM*.

Both tools and their meshing strategies are in more detail discussed in Bronsart and Kleinsorge (2011).
Using two different meshing techniques makes it possible to analyse also the influence of the mesh on the results of different schemes. To minimize the errors between the meshing strategies, the domain, the size of the cells near the ship and the average dimensionless wall distance y+=30 are tried to be kept constant. Additionally a grid refinement study is performed to be aware of the numerical error and to check for a converging solution. Therefore three different grids have been created for each meshing approach. The size of the meshes varies between 200,000 and 4,000,000 cells. The size of each created mesh for the study is shown in Table 1. Due to the structured meshing the blockstructured approach needs more cells for getting the same refinement at the hull as the unstructured approach. For each mesh it is checked, that the quality of the meshes fulfills the needs of the solver (skewness, orthogonal cells, etc.). In total six different meshes are generated. Figure 2 shows a part of the meshed domain for the medium grids.

Table 1: Mesh size of used meshes in this study

		Mesh Size in Cells
Unstructured (US)	Coarse Mesh	$0.61 \cdot 10^6$
	Medium Mesh	$0.85 \cdot 10^6$
	Fine Mesh	$3.80 \cdot 10^6$
Blockstructured (BS)	Coarse Mesh	$0.29 \cdot 10^6$
	Medium Mesh	$0.90 \cdot 10^6$
	Fine Mesh	$4.20 \cdot 10^6$

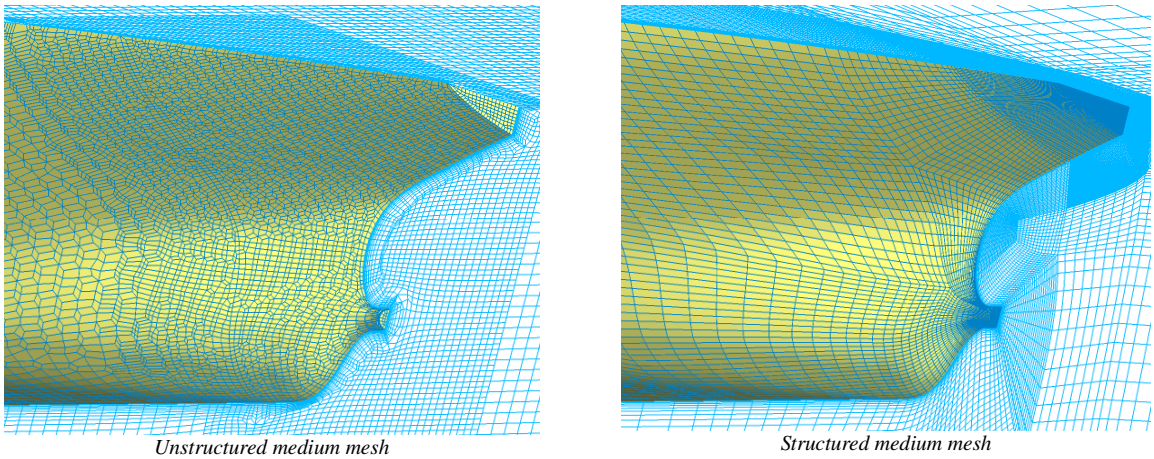

Unstructured medium mesh *Structured medium mesh*

Figure 2: Meshed stern of KVLCC2

Simulation Set-Up

The KVLCC2 is simulated in model scale at Fn=0.142, Re=$1.4 \cdot 10^7$ with the same parameters as in the towing tank test done by Kim *et al.* (2001), except that due to the low Froude number the influence of waves is neglected and the ship is simulated as a double body in this study.

The computation itself is performed with the open source CFD-Toolkit *OpenFoam.* For solving the RANS equations the incompressible, steady-state solver for turbulent flows *simpleFoam* has been used. The turbulence is modeled with the kOmegaSST-model, which is a standard in the CFD-community.

To solve the general transport equation in all *OpenFOAM* solvers it is possible to choose between different discretisation schemes for the divergence theorem of diffusive and convective flux terms. As the flow around a ship hull can be seen as almost convective driven, only the scheme for the approximation of this term is changed during this study. For the diffusive flow the discretisation scheme *linear* is chosen and kept constant for all simulations.

For each generated mesh seven double body simulations are performed with the following discretisation schemes for the convective flow:

- *Upwind*
- *Linear*
- *Linear Upwind Differencing Scheme (LUDS)*
- *Quadratic Upwind Interpolation for Convective Kinematics (QUICK)*
- *Total Variation Diminishing (TVD) Scheme: limitedLinear*

The different schemes represent a wide field of approaches for the approximation, from simple *upwind* schemes to nonlinear *QUICK* and more complex *TVD*-Schemes. A more detailed description of these schemes can be found in Versteeg and Malalasekera (2007). For the TVD scheme the additional parameter $0 < \psi < 1$ has to be defined to control the flux-limiter-function. Therefore three additional simulations have been performed with ψ=0.1;0.5;1. While a small ψ tends to give the most accurate solution, a higher value of ψ helps stabilizing the simulation run.

Results

Simulating the KVLCC2 with six different meshes and vary each with seven different schemes for the divergence in the convective flux terms results in total 42 simulations to be performed. It is obvious that therefore only a brief discussion of the results can be presented here. More detailed results are given in Hartig (2012).

Resistance

For analysing the influence of the schemes on the total resistance the simulations are compared to the experimental values given in Kim *et al.* (2001). For each of the meshes the results for the total resistance coefficient are shown for the applied discretisation scheme in Figure 3 and 4. The results of numerical calculation would perfectly match the experimental values, if the total resistance coefficient of the simulations is a bit lower than the experimental value due to neglecting the water surface and therefore the wave resistance component.

In Figure 3 and 4 the experimental values are divided into frictional and residuary resistance according to ITTC. The coefficient of the simulations are divided into the viscous resistance and the pressure resistance, calculated with the shear stress and the pressure normal to the hulls surface. Even though the components of the total

coefficient cannot be compared exactly, their value should be in the same range between simulation and experimental results. The difference in total resistance between simulation and experiment is also given in percent.
Comparing both figures it can be noticed, that for all schemes, the results differ only in a small percentage when using different meshing approaches. For the blockstructured meshes the total resistance coefficient is slightly lower, than for the unstructured meshes. It can be also seen that the *linear* and *limitedLinear* schemes overall show the best result in total resistance. These schemes differ only in a small percentage to the experimental result. The *linear* scheme shows a more fluctuating solution over the iterations during the simulation, while the *limitedlinear* scheme shows good convergence over the iterations of each simulation.
Simulations with high order *QUICK* schemes work very unstable with all kind of investigated meshes. In this study it is only possible to perform the convergence study for total resistance with the structured mesh. Contrary to this are the simulations with the *upwind*-scheme, which unfortunately insufficiently calculates the pressure component.

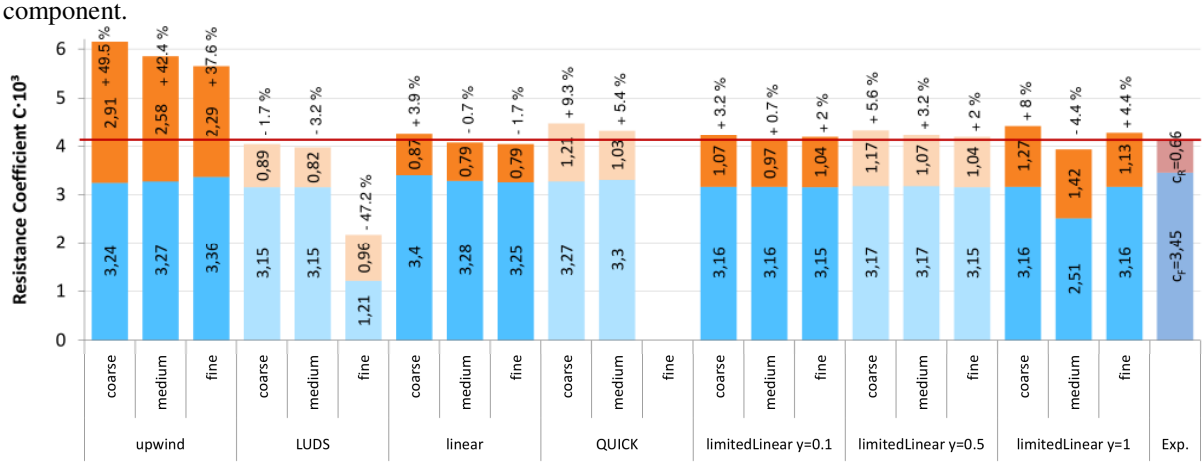

Figure 3: Total resistance coefficient and components (blue – viscous; orange – pressure) of simulations with unstructured mesh

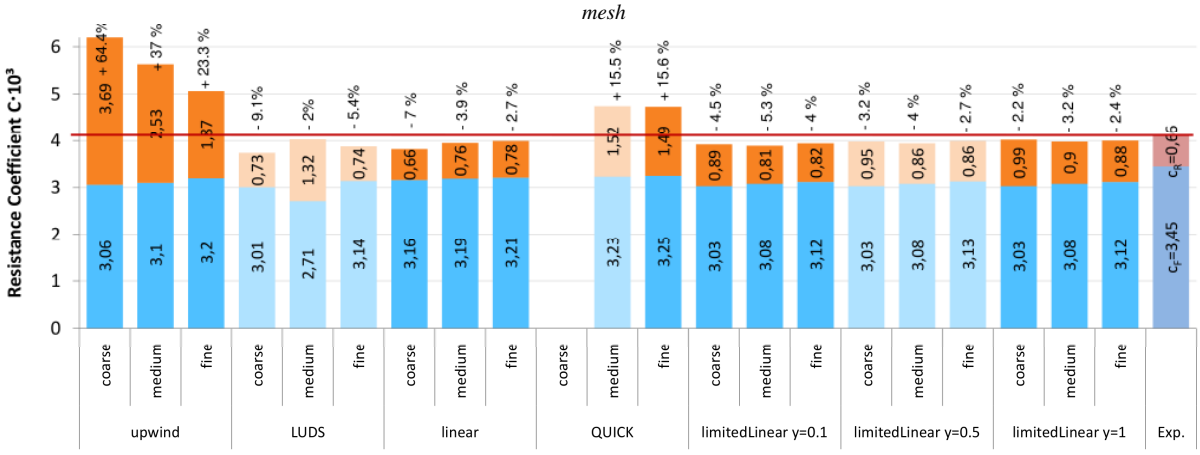

Figure 4: Total resistance coefficient and components (blue – viscous; orange – pressure) of simulations with structured mesh

Looking in more detail on the results of *limitedLinear* it can be seen, that with increasing ψ the accuracy of the resistance decreases. This is expected because of the shift of the flux-limiter to a more convective flow solution. For the *limitedLinear* schemes it has to be noticed that there is only a small difference in resistance between the coarse and fine meshes. The result is almost converged with the coarse meshes.

Nominal Wake in Propeller Plane

For CFD analyses of ship hull forms it is of great interest to determine a sufficient nominal wake field in the propeller plane. Thus also the wake field is compared with measured values. Due to the problems with convergence of the simulations of *QUICK* and *linear* schemes (see above) the results for these schemes will not be discussed.
Figure 5, 6 and 7 show the results for the wake field of the structured and unstructured meshes compared to the measurements in the towing tank. The simulation is plotted on the left side of the propeller plane, while the measurements are shown on the right side. The dimensionless axial velocity is shown by contour lines. The flow in the propeller plane is plotted as vectors.
Figure 5 shows the results for the *upwind* scheme. It can be seen, that for both meshes the agreement with the

measurement is insufficient. The vortex below the stern tube is not resolved in the upwind calculations with the blockstructured mesh. Furthermore the contour lines of the axial velocities do not agree with the experimental velocities. The same can be identified for the unstructured mesh, the axial wake lines are too smooth compared the experiment.

Figure 6 shows the propeller plane for calculations with the *LUDS* scheme. The profile of the axial velocity predicted by the blockstructured mesh is too thick in the region below the stern tube. Also the vectors of velocity components point into the wrong direction. The unstructured result does not fit in any case with the measured one. Looking at the different mesh refinements, it is interesting to note that there is no consistency between the results.

Figure 7 shows the most appropriate result for the *limitedLinear* scheme, derived with $\psi = 1$. The numerical results for both meshes predict the boundary thickness quite well, especially in case of the unstructured mesh. The profile of the contour lines for the axial velocity is under predicted in the upper part of the wake. However the vortices below and above the stern tube are represented by the simulation.

Due to the complexity of the wake it is difficult to finally evaluate the quality of simulation results. Even integral parameters like wake number cannot quantify the agreement with the measurements.

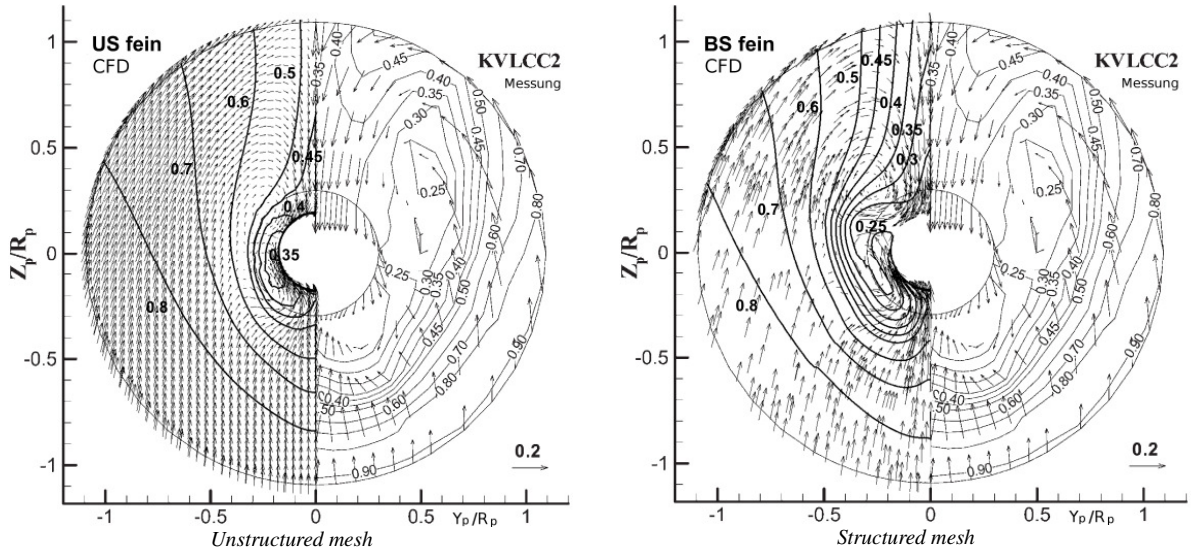

Figure 5: Wake field in propeller plane calculated with upwind scheme

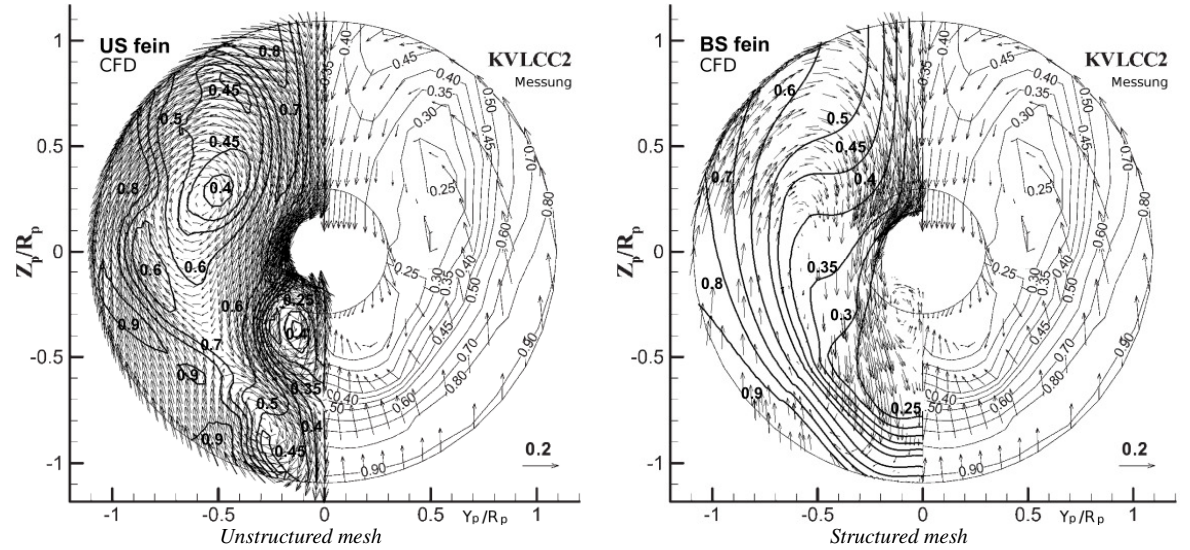

Figure 6: Wake field in propeller plane calculated with LUDS scheme

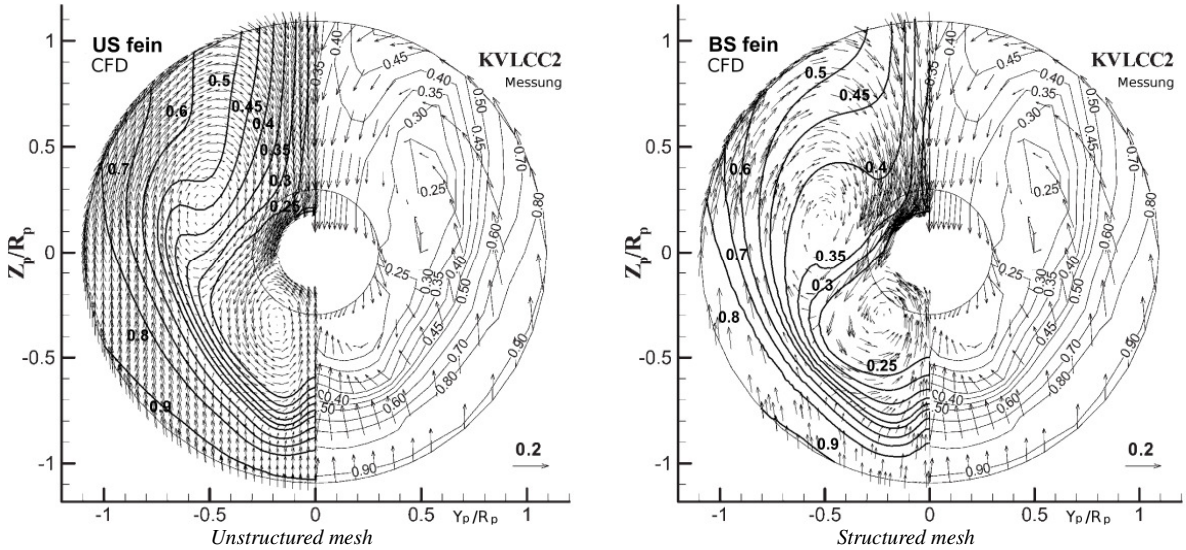

Figure 7: Wake field in propeller plane calculated with limitedLinear scheme

Conclusion and Future Work

In this paper a study on the effect of different discretisation schemes has been given. Different blockstructured and unstructured meshes have been investigated. During the numerical simulations all parameters have been kept constant, except of the scheme for the approximation of the convective flux term. The effect of the *upwind, linear, LUDS, QUICK and limitedLinear* schemes on the result of total resistance and the propeller wake field has been evaluated. Convergence studies have been performed to identify the numerical error.

For the calculation of the total resistance the *limitedLinear* and *linear* schemes have shown good agreement with the experimental values for both meshes. The *upwind* scheme does not give appropriate agreement. Higher order schemes like *QUICK* have shown to be too unstable to predict reasonable results. Concerning the wake field prediction the only calculated field that corresponds approximately with the measurement is the one of the *limitedLinear* scheme. Due to this fact it can be said, that *limitedLinear* seems to be a sound scheme for calculating the ship flow. One additional reason for this is that convergence in the solution is found already with the coarse mesh.

Additional simulations have to be carried out to support the discussed results. The parameter study should be expanded to different kind of ship hulls, to see if the results can be transferred to other cases. Also it might be helpful to develop more sophisticated procedures to quantify the results of the wake prediction.

References

Bronsart, R. and Kleinsorge, L. (2011) Integration of CFD Grid Generation Tools into the Ship Design Process, *Proceedings of 1st International Symposium on Naval Architecture and Maritime*, Istanbul, Turkey

Hartig, K. (2012) Einfluss der Interpolationsverfahren auf die Ergebnisse numerischer Berechnungen der Schiffsumströmung. *Diplomarbeit*, in german

Kim, W.J., Van, S.H. and Kim, D.H. (2001) Measurement of flows around modern commercial ship models, *Experiments in Fluids*, pp. 567-578, Springer-Verlag

Larsson, L., Stern, F. and Bertram, V. (2003) Benchmarking of Computational Fluid Dynamics for Ship Flows: The Gothenburg 2000 Workshop, *Journal of Ship Research, Vol. 47, No.1, pp. 63-81*

Versteeg, H.K. and Malalasekera, W. (2007) *An introduction to Computational Fluid Dynamics, The Finite Volume Method*, second edition, Pearson Education Limited

Wave Reconstruction for Deterministic Prediction of Nonlinear Wave-field

Hiroshi KOBAYASHI National Maritime Research Institute, Japan, hiroshi@nmri.go.jp
Claudio LUGNI CNR-INSEAN, Italy, c.lugni@insean.it

1. Introduction

Statistics-based spectral wave model are used to predict the evolution of the ocean wave-field. In spite of the progress and success of spectral wave models in past years, further developments of the models have been limited due to the inherent homogeneous and stationary assumptions, the linear transportation equation, and the approximate source formulations. In addition, though they accurately predicte the evolution of the wave spectrum, they are intrinsically unable to give a phase-resolved evolution of the wave elevation in the ocean sea. The latter aspect is of concern when deterministic wave propagation needs to be calculated, e.g. the wave-body interaction during the violent transient phenomena or to forecast quiescent period of a ship in rough sea.

Recently, with the growth of computing power, phase-resolved direct simulations such as second-order irregular wave model and High Order Spectral(HOS) method[1)2)3)] are feasible alternatives to spectral wave models. There simulation can properly capture the nonlinear mechanisms of the wave interactions, at least until wave overturning occurs.

The accuracy in the prescription of the initial condition becomes a critical issue on the use of the phase-resolved approach and is then the focus of the present study. A more accurate initial condition gives a more accurate simulation of free-surface elevation related with the influence of the initial conditions on the energy transfer mechanisms during the wave-wave interactions.

G. Wu[4)] and D.K.P. Yue[5)] used the HOS method in the wave reconstruction. They focused on multidirectional irregular wave-field using a second order Stokes model to generate the initial conditions for the HOS method. Blondel et. al. [6)] also applied the HOS method for the wave-field reconstruction. They states the second order surface potential is of significance and cannot be neglected, however, they did not investigate the influence of the third-order contributes.

The initial conditions can be assumed as a series expansion of M_0 higher-order terms. To this purpose, the minimum value of M_0 that gives a satisfactory approximation of the initial solution is still an issue, especially for moderate steepness of the wave system. The present study aims to investigate the role of the higher-order terms the initial conditions, as well as their influence in the accuracy of the reconstructed wave field.

Some works concerning the wave reconstruction for the irregular wave field have been conducted[4)6)7)8)9)]. They involved phase-resolved simulation such as the HOS method, however none of them starts from the initial conditions including third order term.

In the studies of Wu[4)] and Blondel[6)], the frequency not the wave number was chosen for one of free components. This is because the measured wave is the time-series data and simple analysis can give frequency components. However, for the HOS method, the required initial condition is a spatial wave configuration. It has an advantage that it does not use of the nonlinear dispersion relation to adopt the wave number as the free component. Our future aim is enhancing the wave reconstruction to deal with a multi-directional wave field by using time instantaneous spatial data, such as a wave configuration taken by an on-board RADAR, as the initial condition of the HOS method. In this case, since both of the given data and the initial condition to be generated are spatial, the free components which represents periodicity should be the wave number. Thus, we adopt the wave number as the free component in the current study.

In this paper, the definition of the reconstruction and two wave models are described first. Then optimization scheme and predictable region are explained followed by the comparison between the reconstructed results and the measured data discussing their accuracy. Firstly we verify the initial conditions for the HOS method to get an accurate estimation of the error, we use a reference solution corresponding to the analytical solution of the fully nonlinear unidirectional Stokes wave (Schwartz[10)]), then perform reconstruction for the irregular wave field.

2. Procedures

2. 1 Definition of reconstruction

The Problem of deterministic reconstruction of a wave-field can be stated as follows: a reference data of free-surface elevation such as wave measurements in a specified space-time subset $\mathcal{P}(\boldsymbol{x}, t)$ of an original wave-field $\tilde{\eta}(\boldsymbol{x}, t)$ is used to reconstruct a wave-field $\eta^R(\boldsymbol{x}, t)$ in another space-time subset $\mathcal{Q}, \mathcal{Q} \supset \mathcal{P}$ which satisfies the conditions:

$$\eta^R(\boldsymbol{x}, t) = \tilde{\eta}(\boldsymbol{x}, t), \quad \text{for } (\boldsymbol{x}, t) \in \mathcal{Q} \tag{1}$$

where $\boldsymbol{x} \equiv (x, y)$ is the horizontal coordinates of a Cartesian coordinate system with its origin on the mean free surface and $z-$axis positive upwards. Two fundamental goals consist in achieving $\mathcal{Q}$ for a given $\mathcal{P}$, and in reconstructing $\eta^R(\boldsymbol{x}, t)$ in $\mathcal{Q}$ based on measured reference data in $\mathcal{P}$.

A possible reconstruction strategy consists in the prediction of the exact wave-field which satisfies Equation(1). However, the exact solution is generally unknown, implying the use of an optimal fitting of the reference data by minimizing the misfit error, is more feasible way. For example, in case of wave elevation measured at a single or multiple probe locations for a limited period of time, that is, $\mathcal{P}(\boldsymbol{x}, t) \equiv \{\boldsymbol{x} = \boldsymbol{x}_p, p = 1, 2, \cdots, N_p; t \in [t_0, t_0 + T]\}$, Wu[4] defined the misfit error as

$$\mathcal{E} \equiv \frac{\left\{ \sum_{p=1}^{N_p} \int_{t_0}^{t_0+T} W(\boldsymbol{x}_p, t) \left[\eta^R(\boldsymbol{x}_p, t) - \tilde{\eta}(\boldsymbol{x}_p, t) \right]^2 dt \right\}^{\frac{1}{2}}}{\left\{ \sum_{p=1}^{N_p} \int_{t_0}^{t_0+T} \left[\tilde{\eta}(\boldsymbol{x}_p, t) \right]^2 dt \right\}^{\frac{1}{2}}} \tag{2}$$

where $W(\boldsymbol{x}_p, t)$ is a weighting function, which emphasize the misfit error in certain regions of the time-space domain. One effectual way is to accentuate the error near the wave crests and troughs to estimate the amplitude more correctly.

$$W(\boldsymbol{x}_p, t) = \frac{\left[\tilde{\eta}(\boldsymbol{x}_p, t) - < \tilde{\eta}(\boldsymbol{x}_p) > \right]^2 T}{\int_{t_0}^{t_0+T} \left[\tilde{\eta}(\boldsymbol{x}_p, t) - < \tilde{\eta}(\boldsymbol{x}_p) > \right]^2 dt} \tag{3}$$

where the mean wave elevation $< \tilde{\eta}(\boldsymbol{x}_p) >$ is:

$$< \tilde{\eta}(\boldsymbol{x}_p) > = \frac{1}{T} \int_{t_0}^{t_0+T} \tilde{\eta}(\boldsymbol{x}, t) dt \tag{4}$$

The objective of wave reconstruction is to obtain the wave-field η^R which satisfies boundary conditions of wave dynamics and minimizes the misfit error $\mathcal{E}$ in Equation(2). We compared two wave models for calculating the propagation of the wave.

2. 2 Wave models

2. 2. 1 Second order irregular wave model

The surface elevation of second order irregular wave model is described with as follows.

$$\begin{aligned} \eta(\boldsymbol{x}, 0) = \eta^{(0)} &+ \sum_{n=1}^{N_s} A_n \cos(\psi_n) \\ &+ \sum_{n=1}^{N_s} {A_n}^2 \left[G_n^+ \cos(2\psi_n) - G_n^- \right] \\ &+ \sum_{m=1}^{N_s-1} \sum_{n=m+1}^{N_s} A_m A_n \left[H_{mn}^+ \cos(\psi_m + \psi_n) \right. \\ &\left. + H_{mn}^- \cos(\psi_m - \psi_n) \right] \end{aligned} \tag{5}$$

$$\text{where} \quad \psi_n = \boldsymbol{k}_n \cdot \boldsymbol{x} - \omega_n t + \alpha_n \tag{6}$$

Here, $\eta^{(0)}, A_n, \boldsymbol{k}_n, \alpha_n, \omega_n, N_s$ are a mean free surface, an amplitude, a wave number vector, a phase delay and a number of free waves, respectively. And the coefficients are defined as following:

$$\begin{aligned} G_n^+ &= \frac{|\boldsymbol{k}_n|}{4 \tanh(|\boldsymbol{k}_n h|)} \left[2 + \frac{3}{\sinh^2(|\boldsymbol{k}_n h|)} \right] \\ G_n^- &= -\frac{|\boldsymbol{k}_n|}{2 \sinh(2|\boldsymbol{k}_n h|)} \end{aligned} \tag{7}$$

$$\begin{aligned} H_{mn}^{\pm} = &\frac{{\omega_m}^2 + {\omega_n}^2}{2g} \mp \frac{\omega_m \omega_n}{2g} \left[1 \mp \frac{g^2 (\boldsymbol{k}_m \cdot \boldsymbol{k}_n)}{{\omega_m}^2 {\omega_n}^2} \right] \\ &\times \left[\frac{(\omega_m \pm \omega_n)^2 + g|\boldsymbol{k}_m \pm \boldsymbol{k}_n| \tanh(|\boldsymbol{k}_m \pm \boldsymbol{k}_n| h)}{(\omega_m \pm \omega_n)^2 - g|\boldsymbol{k}_m \pm \boldsymbol{k}_n| \tanh(|\boldsymbol{k}_m \pm \boldsymbol{k}_n| h)} \right] \\ &+ \frac{\omega_m \pm \omega_n}{2g} \\ &\times \left[\frac{1}{(\omega_m \pm \omega_n)^2 - g|\boldsymbol{k}_m \pm \boldsymbol{k}_n| \tanh(|\boldsymbol{k}_m \pm \boldsymbol{k}_n| h)} \right] \\ &\times \left[\frac{{\omega_m}^3}{\sinh^2(|\boldsymbol{k}_m|)} \pm \frac{{\omega_n}^3}{\sinh^2(|\boldsymbol{k}_n|)} \right] \end{aligned} \tag{8}$$

For a nonlinear wave with given wave number, its frequency is a function of both the wave number and the amplitude of all wave components. For a unidirectional wave, the nonlinear dispersion relation is described as follows:

$$\begin{aligned} \omega_n = \sqrt{g k_n} \left[1 + \frac{1}{2} (k_n A_n)^2 + \sum_{m=1}^{n-1} \left(\frac{k_n}{k_m} \right)^{\frac{1}{2}} (k_m A_m)^2 \right. \\ \left. + \sum_{m=n+1}^{N_s} \left(\frac{k_n}{k_m} \right)^{\frac{3}{2}} (k_m A_m)^2 \right\} \end{aligned} \tag{9}$$

Free components to be optimized in the reconstruction scheme for unidirectional wave are $(A_n, k_n, \alpha_n), n = 1, 2, \cdots, N_s$.

2. 2. 2 HOS method

The HOS method[1)2)3)] is a pseudo-spectral method and based on Zakharov equation. The evolution of a certain number of wave modes N are followed and their nonlinear interactions are taken into account up to arbitrary order in wave steepness.

In the HOS method, the flow can be described by a velocity potential $\Phi(\boldsymbol{x}, z, t)$, which satisfies Laplace's equation within the water. Following Zakharov[11)], we define the surface potential

$$\Phi^S(\boldsymbol{x}, t) = \Phi(\boldsymbol{x}, \eta(\boldsymbol{x}, t), t) \tag{10}$$

where $z = \eta(\boldsymbol{x}, t)$ denotes the free surface, assumed to be continuous and single-valued. In terms of Φ^S, the kinematic and dynamic boundary conditions can be written as

$$\eta_t + \nabla_{\boldsymbol{x}} \Phi^S \cdot \nabla_{\boldsymbol{x}} \eta - (1 + \nabla_{\boldsymbol{x}} \eta \cdot \nabla_{\boldsymbol{x}} \eta) \Phi_z(\boldsymbol{x}, \eta, t) = 0 \tag{11a}$$

$$\Phi_t^S + \eta + \frac{1}{2} \nabla_{\boldsymbol{x}} \Phi^S \cdot \nabla_{\boldsymbol{x}} \Phi^S - \frac{1}{2} (1 + \nabla_{\boldsymbol{x}} \eta \cdot \nabla_{\boldsymbol{x}} \eta) {\Phi_z}^2(\boldsymbol{x}, \eta, t) = -P_a \tag{11b}$$

where $\nabla_{\boldsymbol{x}} = \left(\frac{\partial}{\partial x} \frac{\partial}{\partial y} \right)$ denotes the horizontal gradient, and P_a is the atmospheric pressure respectively.

Given the surface potential $\Phi^S(\boldsymbol{x}, 0)$ and elevation $\eta(\boldsymbol{x}, 0)$ for initial conditions, the only remaining non-surface quantity is the vertical velocity Φ_z, which is evaluated as Taylor series with using a perturbation series in wave steepness.

As described above, the values of the surface elevation $\eta(\boldsymbol{x},0)$ and the velocity potential $\Phi^S(\boldsymbol{x},0)$ in space domain are required as the initial conditions to calculate wave propagation by the HOS method. Conceivable wave models to generate initial conditions are described below.

2. 3 Models for the initial condition of the HOS method

2. 3. 1 Second order Stokes model

The wave elevation and the velocity potential in deep water are as follows.

$$\eta(\boldsymbol{x},0) = \eta^{(0)} + \sum_{n=1}^{N_s}\left\{A_n\cos(\psi_n) + \frac{1}{2}|\boldsymbol{\kappa}_n|{A_n}^2\cos(2\psi_n)\right\}$$

$$\Phi(\boldsymbol{x},0) = \sum_{n=1}^{N_s}\frac{gA_n}{\omega_n}e^{|\boldsymbol{\kappa}_n|z}\sin(\psi_n), \quad z\le 0 \tag{12}$$

$$\text{where} \quad \psi_n = \boldsymbol{\kappa}_n\cdot\boldsymbol{x} + \alpha_n \tag{13}$$

where $\eta^{(0)}, A_n, \boldsymbol{\kappa}_n, \alpha_n$ are a mean free surface, an amplitude, a wave number vector and a phase delay, respectively.The parameters which determines the initial condition are $(A_n, \boldsymbol{\kappa}_n, \alpha_n)$.

2. 3. 2 Model with higher order terms

$$\eta(\boldsymbol{x},0) = \eta^{(0)} + \sum_{n=1}^{N_s}\sum_{m}^{M_0}A_{m,n}\cos(m\psi_n) \tag{14a}$$

$$\Phi^S(\boldsymbol{x},0) = \sqrt{\frac{g}{|k|}}e^{|k|z}\sum_{n=1}^{N_s}\sum_{m}^{M_0}A_{m,n}\sin(m\psi_n) \tag{14b}$$

$$\text{where} \quad \psi_n = \boldsymbol{k}_n\cdot\boldsymbol{x} + \alpha_n$$

Here, $A_{m,n}, m = 1,2,\cdots,M_0, n = 1,2,\cdots,N_s$ are the amplitude of each order of each free wave.

2. 4 Optimization Scheme

An iterative optimization algorithm is required in order to solve nonlinear wave reconstruction and forecasting problem. The iterative optimization is composed of following steps

(1) gauge the surface elevation at $\boldsymbol{x}_p$ to obtain the reference data $\tilde{\eta}(\boldsymbol{x}_p,t), t\in[t_0,t_0+T]$

(2) for given wave model, generate the initial conditions in terms of the parameters

- the second order irregular wave model: $A, \boldsymbol{k}, \alpha$
- HOS: the initial conditions of η and ϕ
  - $A, \boldsymbol{k}, \alpha$ for Second order Stokes model
  - $A_m\,(m = 1,2,\cdots,M_0), \boldsymbol{k}, \alpha, \eta^{(0)}$ for the model with higher order terms

(3) simulate numerically the reconstructed wave-field to obtain the reconstructed wave records η^R.

(4) adjust the parameters and go back to (2)

At step (4), an optimization algorithm has to be employed. In this study, Rosenbrock method[12] was adopted.

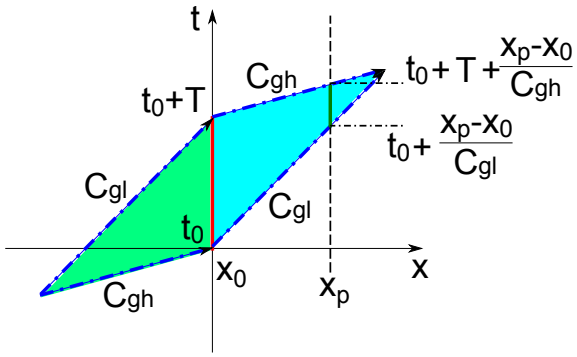

Fig. 1 Predictable region of a unidirectional wave field

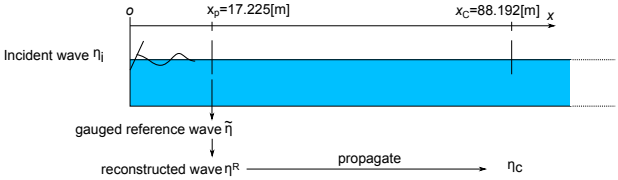

Fig. 2 The schematic view of a numerical wave tank for regular wave case

2. 5 Predictable region of the irregular wave field

The prediction of wave based on the reconstructed wave can only be considered in a specific time-space region. Wu[4] discussed the predictable region introducing the slowest and fastest group velocities C_{gl} and C_{gh} of the measured wave-field, respectively. Assuming the linear dispersion relation, the group velocity can be calculated as $C_g = \frac{g}{2\omega}$. Given measured data $\eta(x_0,t)$, the predictable time range at $x = x_p$ should be determined as follows:

$$\begin{cases} t_0 + \dfrac{x_p - x_0}{C_{gl}} \le t \le t_0 + T + \dfrac{x_p - x_0}{C_{gh}} & \text{if } x_0 \le x_p \\ t_0 + \dfrac{x_p - x_0}{C_{gh}} \le t \le t_0 + T + \dfrac{x_p - x_0}{C_{gl}} & \text{if } x_p < x_0 \end{cases} \tag{15}$$

The group velocities C_{gl} and C_{gh} are calculated by the highest and lowest frequency ω_h and ω_l in the measured wave-field. The range $[\omega_l,\omega_h]$ is decided in order to contain 95% of wave energy in the range.

$$0.95 \le \frac{\int_{\omega_l}^{\omega_h} S(\omega)d\omega}{\int_0^{\infty} S(\omega)d\omega} \tag{16}$$

Fig. 1 shows the region determined by Equation(15).

3. Results and Discussions

3. 1 verifying the initial conditions for the HOS method with regular wave

The schematic view of a numerical wave tank is shown in Fig. 2. Numerical probes are located in the same positions of the physical wave gauges used in an experimental campaign recently performed at the CNR-INSEAN wave tank. These data will be useful for a verification activity of the proposed algorithm to be done as a next step of the present research investigation.

The incident wave η_i is given as 'exact' solution of the fully nonlinear Stokes theory proposed in Schwartz[10]. A more accurate and efficient Newton-Raphson iteration method is used to solve the nonlinear equations associated with the mapping functions (ensuring a convergence of the solution with 14 significant figures), rather than a higher order perturbation method as proposed by Schwartz. $\boldsymbol{x}_p$ is a position of a target probe at which the reconstructed wave η^R should be fitted to the gauged reference surface elevation $\tilde{\eta}$ of the incident wave. Sampling interval Δt is 0.02. $\boldsymbol{x}_c$ is a position of a probe at which the propagated wave η_c based on the reconstructed wave field η^R is compared with the incident wave.

Fig. 3 shows the reconstructed waves with different initial conditions at the target probe located at $\boldsymbol{x}_p$. The steepness and the wave number of the incident wave are $\varepsilon = 0.25$ and $|\boldsymbol{\kappa}| = 2$, respectively. A number of periods is $8(t_0 = 0$ and $T = 11.0$[sec]) and the order of the HOS method is 3. Top and Bottom figures of Fig. 3 are the waves in whole time region and closeup for $[1, 4]$ of $\mathcal{Q}[0, T]$, respectively. Square symbols of the reference wave are plotted in every four points for visibility. Fig. 4 shows the difference between reconstructed waves and the reference wave $\eta^R - \tilde{\eta}$. In Figs. 3, 4, the initial condition by second order Stokes model gives large discrepancy to the reference wave, while the present models with higher order terms show good agreement. The values of misfit error $\mathcal{E}$ defined Equation(2) are shown in Table 1. The present model with third order terms ($M_0 = 3$) gives smaller errors than others.

Fig. 5 shows the vertical velocity at free surface $\frac{\partial \Phi^S}{\partial z}$ of the theoretical wave and the reconstructed waves. The-

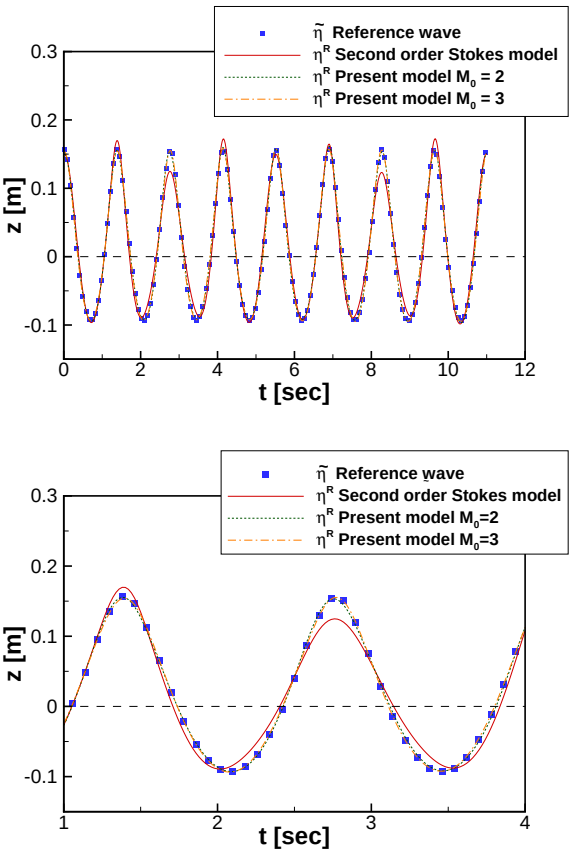

Fig. 3 The reference wave and the reconstructed waves, top: for a whole time region $\mathcal{Q}[t_0, t_0 + T]$, bottom: closeup to $[1, 4]$.

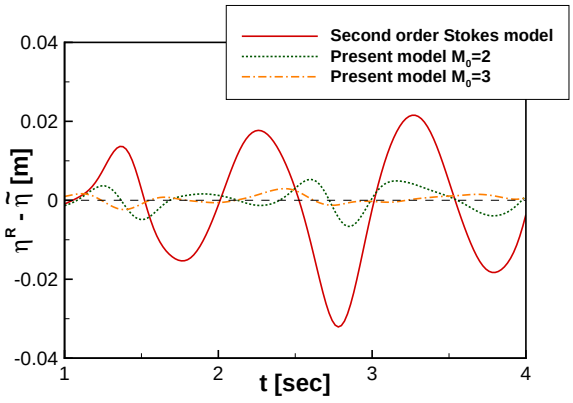

Fig. 4 Difference between reconstructed waves and the reference wave $\eta^R - \tilde{\eta}$.

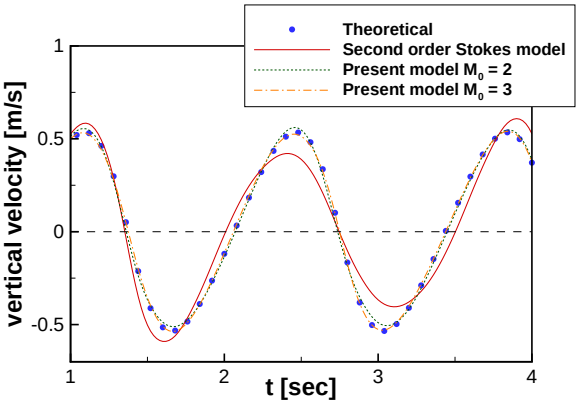

Fig. 5 The vertical velocity at free surface $\frac{\partial \Phi^S}{\partial z}$ of the theoretical wave and the reconstructed waves.

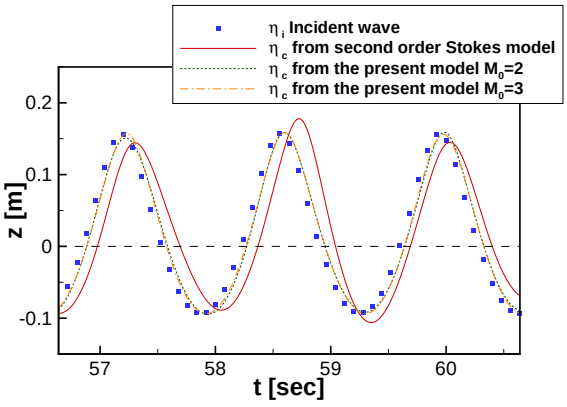

Fig. 6 Propagated waves and incident wave.

Table 1 The values of misfit error function

Model for initialization	Second order Stokes model	Present study ($M_0 = 2$)	Present study ($M_0 = 3$)
HOS order = 2	1.511×10^{-1}	3.649×10^{-2}	2.167×10^{-2}
HOS order = 3	1.483×10^{-1}	3.259×10^{-2}	1.298×10^{-2}
HOS order = 4	1.541×10^{-1}	3.523×10^{-2}	1.299×10^{-2}

oretical wave is generated by fully nonlinear Stokes wave model[10]. Second order Stokes model does not estimate the vertical velocity correctly. Both of the present models give good agreement with the theoretical value, and the present model with third order term ($M_0 = 3$) is slightly better than the model with up to second order term ($M_0 = 2$). It is considered that the difference of the vertical velocity causes the discrepancy of the surface elevation in HOS simulation.

Table 1 also shows the results with different order of HOS simulation($M = 2$ and $M = 4$). The larger number of the order in HOS simulation than the order in the initial conditions does not decrease the errors, hence it is considered that the order in the initial conditions crucially important to achieve better results.

The calculation of wave propagation can be performed by using the reconstructed wave field η^R as the new initial condition. The time region $\mathcal{Q}[0,T]$ at $\boldsymbol{x}_p$ moves to $\mathcal{Q}_c[\frac{|\boldsymbol{x}_c-\boldsymbol{x}_p|}{|c_g|}, \frac{|\boldsymbol{x}_c-\boldsymbol{x}_p|}{|c_g|} + T] \sim [55.64, 66.64]$, where c_g is a group velocity of the incident wave($c_g = \frac{1}{2}\sqrt{\frac{g}{|\kappa|}}\frac{(1+3\varepsilon^2)}{\sqrt{1+\varepsilon^2}} \sim 1.276$[m/s]).

Fig. 6 shows the propagated free surface elevations η_c at $\boldsymbol{x}_c$ compared to the incident wave.

A propagated wave η_c from the reconstructed wave based on the initial condition with the second order Stokes model shows oscillation of amplitude and retardation in phase, while the wave with both of present study($M_0 = 2$ and $M_0 = 3$) improve discrepancy between η_c and η_i.

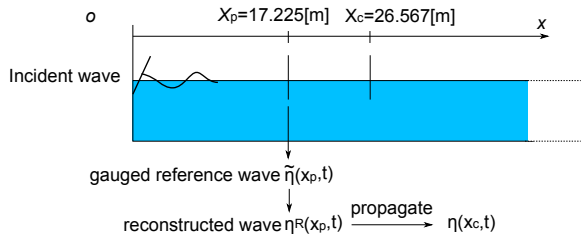

Fig. 7 The schematic view of the wave tank for irregular wave case

Table 2 The values of misfit error function $\mathcal{E}$

with second order irregular model	0.218
with HOS method	0.065

3. 2 the reconstruction for irregular wave

The wave reconstruction was performed by using the experimental data measured at the CNR-INSEAN wave tank. The irregular wave was generated by using Pierson and Moskowitz spectrum to represent Sea State 4. The nominal setting of a significant wave height $H_{1/3}$ is 9.4×10^{-2}[m].

The schematic view of the wave tank is shown in Fig. 7. The reference record of the surface elevation is gauged at $\boldsymbol{x}_p$. We clipped a period $[t_0, t_0 + T(= 20.48)]$ [sec] of data from the gauged record to obtain the reference data $\tilde{\eta}(\boldsymbol{x}_p, t), t \in [t_0, t_0 + T]$. We applied Fourier transform to $\tilde{\eta}$ in order to calculate a spectrum, then determine the frequency band $[\omega_l, \omega_h] = [2.0, 7.0]$[rad/s], and the corresponding group velocities C_{gh} and C_{gl} are 2.45[m/s] and 0.70[m/s] respectively. The predictable region at $\boldsymbol{x}_c$ can be obtained by Equation(15).

The reconstruction was performed with both the second order irregular wave model and the HOS method. The number of free waves N_s is 18 which is the same value as the

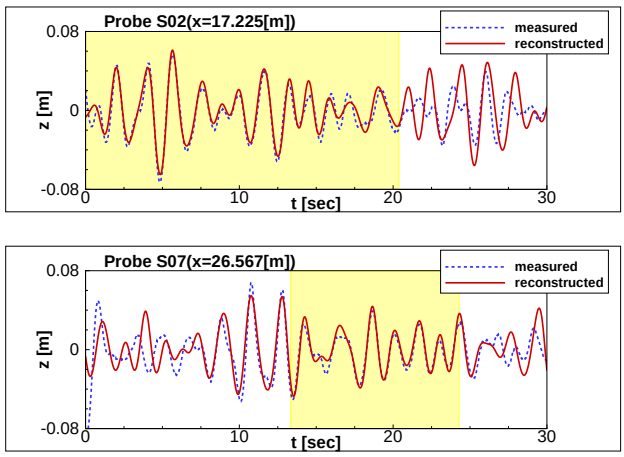

Fig. 8 The measured wave and the reconstructed wave with second order irregular wave model, top: at $\boldsymbol{x}_p$, bottom: at $\boldsymbol{x}_c$.

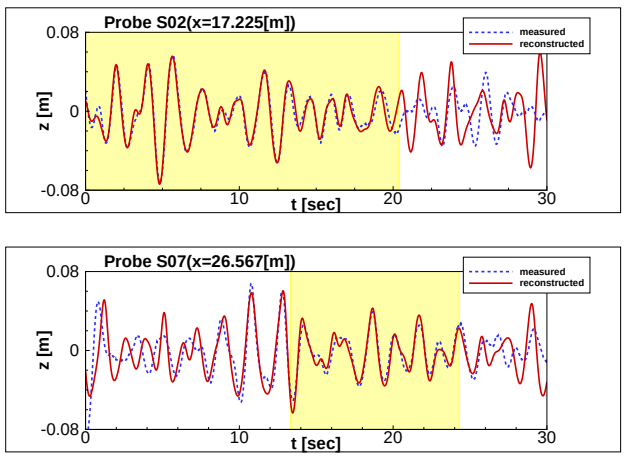

Fig. 9 The measured wave and the reconstructed wave with HOS method, top: at $\boldsymbol{x}_p$, bottom: at $\boldsymbol{x}_c$.

number of free waves within the frequency band $[\omega_l, \omega_h]$ in the results of Fourier transform of $\tilde{\eta}$. Once the wave reconstruction at $\boldsymbol{x}_p$ was performed, the surface elevation at $\boldsymbol{x}_c$ can be calculated with each wave models respectively by using the results of the reconstruction as the initial condition for the calculation of propagation.

Fig. 8 and Fig. 9 show the results of the reconstruction with second order irregular wave model and the HOS method respectively. Top of each figures compares the reconstructed wave with the measured reference data at $\boldsymbol{x}_p$ and bottom of each figures compares propagated wave at $\boldsymbol{x}_c$ calculated from the reconstructed results with the measured data. The shaded areas of both figures, $t \in [0, 20.48]$ at $\boldsymbol{x}_p$ and $t \in [13.35, 24.93]$ at $\boldsymbol{x}_c$, denote the predictable region defined by Equation(15). Both second order irregular wave model and the HOS method give good agreement with the measured reference data to be fit to.

Table 2 shows the value of misfit error function $\mathcal{E}$ in Equation(2). The reconstruction with the HOS method show smaller value of $\mathcal{E}$ than the one with the second order irregular wave model. The HOS method has better accuracy of data assimilation than the second order irregular wave model as the wave model built into the reconstruction.

4. Concluding Remarks

We performed the wave reconstruction with the HOS method, using different models for generating the initial conditions for the HOS method. While the initial condition with second order Stokes model causes the oscillation of the reconstructed wave, the reconstructed wave by using the present model with higher order terms as the initial condition shows good agreement with the reference wave. The present model with third order term($M_0 = 3$) gives better agreement of the surface elevation than the model with up to second order term($M_0 = 2$). The initial conditions with the present model results in good estimation of predicted waves in the further probe from the target probe at which the reconstructed wave is fitted, however, the results initiated from the second order Stokes model gives oscillation of amplitude and retardation in phase. These results show the present model for the initial condition can enhance the capability of the wave reconstruction for nonlinear waves.

The approach which use the wave number not the frequency as the the free component were introduced to this study to reconstruct unidirectional irregular wave field with phase-resolved direct simulations. It was shown that the approach can reconstruct the irregular wave field with both second order irregular wave model and HOS method. And the initial conditions for the HOS method configured by the model including third order term gave better agreement than the second order irregular wave model. It is confirmed that the wave reconstruction using the wave number as the free component with the HOS method whose initial conditions are configured by the model including third order term, has capability to predict a unidirectional irregular wave. In light of the results, we will enhance the approach of the present study to cope with a multi-directional wave field with spatial data such as a wave configuration taken by an on-board RADAR as the future work.

References

1) Doublas G. Dommermuth and Dick K. P. Yue, A high-order spectral method for the study of nonlinear gravity waves, Journal of Fluid Mechanics, Vol. 184, pp. 267-288, 1987

2) Bruce J. West and Keith A. Brueckner, et al., A New Numerical Method for Surface Hydrodynamics, Journal of Geophysical Research, Vol. 92, No. C11, pp. 11,803-11,824, 1987

3) Xi-zeng Zhao, Zhao-chen Sun and Chang-hong Hu, A NUMERICAL METHOD FOR NONLINEAR WATER WAVES, Journal of Hydrodynamics, Vol. 21, pp. 401-407, 2009

4) G. Wu, Direct Simulation and Deterministic Prediction of Large-scale Nonlinear Ocean Wave-field, Ph.D Thesis, M.I.T., 2004

5) Dick K.P. Yue, Nonlinear Wave Environments for Ship Motion Analysis, Proceedings of 27th Symposium on Naval Hydrodynamics, 2008

6) E. Blondel, F. Bonnefoy and P. Ferrant, Deterministic non-linear wave prediction using probe data, Ocean Engineering, Vol. 30, p.p. 913-926, 2010

7) J. Zhang and J. Yang, et. al., Deterministic wave model for short-crested ocean waves: Part I. Theory and numerical scheme, Applied Ocean Research, Vol. 21, pp. 167-188, 1999

8) J. Zhang and I. Prislin, et. al., Deterministic wave model for short-crested ocean waves: Part II. Comparison with laboratory and field measurement, Applied Ocean Research, Vol. 21, pp. 189-206, 1999

9) S. Aragh, O. Nwogu, Assimilating Synthetic Radar Data into Pseudo-Spectral Surface Wave Model, Journal of Coastal Research, SI-52

10) L.W. Schwartz, Computer extension and analytic continuation of stokes' expansion for gravity waves, Journal of Fluid Mechanics, Vol. 62, pp. 553-578, 1974

11) V. E. Zakharov, Stability of periodic waves of finite amplitude on the surface of a deep fluid, Journal of Applied Mechanics and Technical Physics, Vol. 9, No. 2, pp. 190-194, 1968

12) H. H. Rosenbrock, An Automatic Method for finding the Greatest or Least Value of a Function, The Computer Journal, Vol. 3, Issue 3, pp. 175-184, 1960

Influence of Roughened Propeller Tip Surface on Tip Vortex Structures

Christian Krüger, Nikolai Kornev, Mathias Paschen, Christian Semlow

University of Rostock, Chair of Modelling and Simulation
Albert-Einstein-Str. 2
D-18055 Rostock

christian.krueger@uni-rostock.de

Introduction

Modern shipbuilding and development shows a strong demand for highly efficient and powerful propulsion systems. Moreover, tendencies of maximizing the cargo hold leads to decreasing space provided for the propulsion system. On the downside of this progression are highly tip-loaded propellers. This can lead to prominent tip vortex structures and subsequently forwarding to frequent tip vortex cavitation, hull excitation and rudder erosion.

Within a joint research project of MMG Waren GmbH and the University of Rostock an innovative approach has been investigated claiming the possibility of pertubating propeller tip vortices by a roughened propeller tip region.

Theoretical Background

In marine propulsion tip vortices come to mind especially when showing up in its extreme occurrence, forming a cavitating vortex helix. Even though erosion, induced by tip vortex cavitation, in general does not impact on the propeller itself, the harmful effects on installations placed downstream like rudders are quite remarkable [3]. Furthermore, the comfort conditions are affected as well. Hull excitation and underwater noise [9], arising from increased 2^{nd} order pressure fluctuations, are challenges of modern propeller design.

The approach, for delaying or modifying tip vortex structures and cavitation for wing configurations by technical solutions is fairly old. Besides the familiar aspects of classic propeller design, one may know for instance the propeller tip vane by Vatanabe [7], ducted tips or bulbous tips [6], to name but a few. With each solution having its individual benefits, it is obvious that application for retrofit becomes difficult, if cavitation characteristics and customers expectations does not comply.

In lights of this, the investigations of Katz and Galdo [4] pointed out a distinct relation between surface roughness and tip vortex roll-up for a rectangular hydrofoil, demonstrating a shift in detachment point and a substantial reduction in tip vortex strength due to increasing surface roughness. Based on these results, Johnsson and Ruttgerson [1] studied the influence of leading edge roughness on the tip vortex roll-up for different angles of attack. It was shown, that application of roughness on the pressure side near the leading edge has a delaying effect on tip vortex cavitation. On the downside of these results was an increase in drag up to 10% due to the highly exposed roughened area causing a total decrease in efficiency by 2%.

Philipp and Ninnemann [5] suggested, that small scale turbulence pertubation within the boundary layer, caused by surface roughness, may result in a destabilizing of the tip vortex structure. They claimed the back on the suction side of the propeller tip to be the most efficient application area. Cavitation tunnel experiments proved a scattered cavitating vortex structure and a decrease of 2^{nd} order pressure fluctuations of 35% accompanied by a lowering of open water efficiency of 2.5%.

An evidence for the connection between turbulence of the outer flowfield and vortex core dynamics was given by the work of Hussain and Pradeep [2], pointing out that the eigenmodes of the evolving vortex allow resonance effects with the relatively week outer turbulence leading to pertubation amplification by several orders of magnitude.

Numerical Setup

A blade model based on the P1380 benchmark propeller was designed, providing an equal thrust distribution within translational flow as its rotational counterpart. Using the chord-, skew- and thickness distribution of the original P1380, the blade sections were straightening into horizontal plane. Using symmetric sections, the original camber distribution was reset. The pitch distribution was found impressing the calculated thrust distribution $F_{A,des}$ of the original P1380 propeller to the translational model using a panel code for solving the equations

$$\Delta F_{A,j} = \left[F_{A,des,j} - \sum_{i=1}^{N} \left(\frac{\partial F_{A,j}}{\partial \alpha_i} \alpha_i \right) \right] \rightarrow 0$$

$$\frac{\partial F_{A,i}}{\partial \alpha_i} = \frac{F_{A,i}\left(\alpha_{init} + \Delta\alpha_i\right) - F_{A,i}\left(\alpha_{init}\right)}{\Delta\alpha_i}$$

For optimal validation the blade model was scaled by a factor of 1:7.5, leading to a total span of b=445.5mm and a chord length of c(r/R=0.7)=412.7mm with a maximum thickness of t(r/R=0.7)=17.9mm.

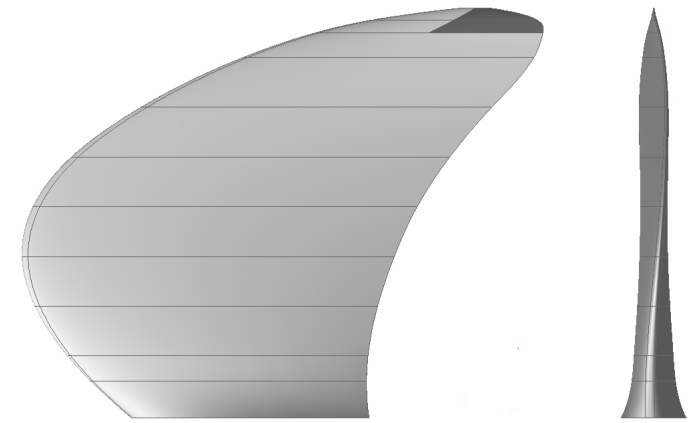

Figure 1: P1380 blade model for translational inflow with tip roughness (dark grey)

The computational domain consists of a block-structured ICEM grid using 19 Mio. hexahedron cells. To ensure grid independent vortex development, the downstream section of the tip was set up with an equally spaced cartesian grid, resolving the vortex cross section by 56 x 56 cells. Calculating the flowfield with the OpenFoam steady state RANS Solver SimpleFoam and a SST turbulence model, the wall function implementation of Tapia [8] was used to model different sizes of sand grain roughness $h_s^+ = h_s u_\tau / \nu$ in the transitional and the fully rough regime. Within the logarithmic profile

$$u^+ = \frac{1}{\kappa} \ln\left(y^+\right) + B - \Delta B$$

the velocity shift for the roughened wall reads

$$\Delta B = \frac{1}{\kappa} \ln\left[\frac{h_s^+ - 2.25}{87.75} + C_s h_s^+ \right]^{\sin\left(0.4258\left(\ln h_s^+ - 0.811\right)\right)} \text{ for } 2.5 \leqslant h_s^+ \leqslant 90$$

$$\Delta B = \frac{1}{\kappa} \ln\left(1 + C_s h_s^+\right) \text{ for } h_s^+ \geqslant 90$$

The constant Cs, denoting the roughness type, was found in a series of calculation of the Nikuradse wall friction factor for turbulent pipe flows at Re=10^6, showing best overall prediction for Cs=0.35 (fig. 2).

According to [5] sand grain roughness elements of h_s=(0.5, 0.6, 1.0, 2.0)mm has been considered for suction sided (SS), pressure sided (PS) and suction + pressure sided (SSPS) application areas of $0.95 \leqslant r/R \leqslant 1$ and $0.5 \leqslant c_L \leqslant 1$. The Reynolds-Number was set to Re=10^6 leading to an inlet velocity v_{inlet}=42.3m/s.

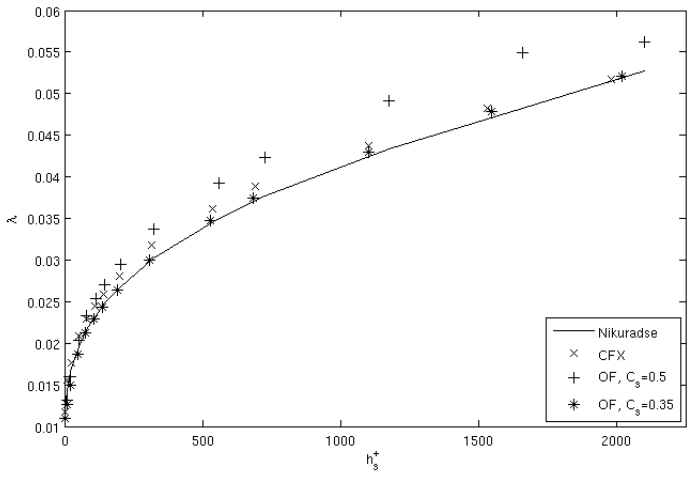

Figure 2: Wall function calculations for wall friction factor in turbulent pipe flows Re=10^6

Experimental Setup

For validation purpose the pressure and the velocity field within the tip vortex for a smooth and a roughened wing were measured, showing the same dimensions as in the numerical setup. By a single layer of corundum with a mean diameter of D_C=0.6mm in an adhesive matrix the roughness structures were applied on the suction side of the tip region.

The measurement series was carried out at a Goettingen type subsonic wind tunnel, providing a quadratic measurement cross-section of $2m^2$. Integral forces and momentum on the blade model have been measured by a six-component measurement system. To ensure matching of experimental and simulation data angle of attack and lift of the wing was selected representing the numerical data.

Within a vertical cross section perpendicular to the main inflow direction 0.5m downstream from the generator line with its center at 0.427 m vertical height 3D Hot-Wire as well as Prandtl Tube measurements were performed. The cross section extended 165 mm x 165 mm being resolved as in the numerical setup by 56 x 56 measurement points.

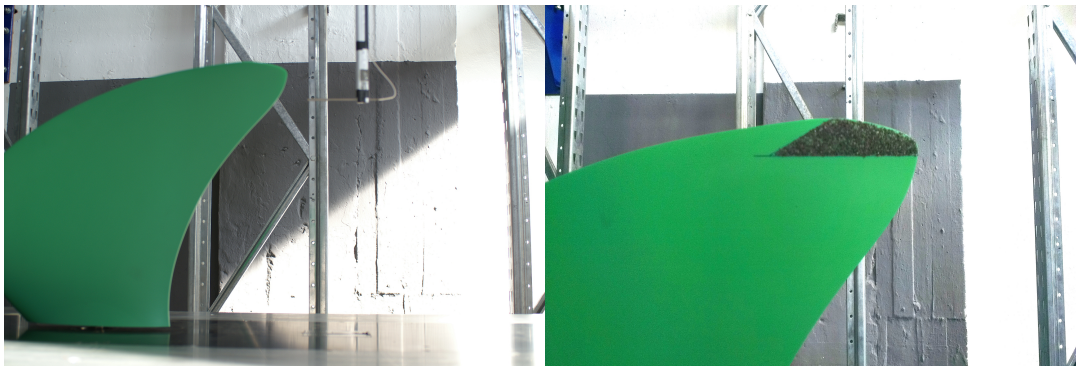

Figure 3: Center of the measurement section for 3D Hot Wire and Prandtl Tube measurements (left); Suction side sand grain roughness on the wing model (right)

Numerical Results

The simulations showed a distinct relation between type and area of the applied tip roughness and specific tip vortex parameters just as vortex core pressure. For suction sided tip roughness all investigated heights leaded to an increased vortex core pressure compared to the smooth configuration. Due to additional viscous stresses the overall drag of the blade body rises, while the lift decreases.

Applying sand grain roughness to the pressure side, the tip vortex pressure decreases further compared to the smooth wing, tending to increase while traveling downstream. Acting on the boundary layer, the roughened region virtually thickens the blade section in the tip area, increasing the lift slightly. The drag of this configuration is larger than for the smooth wing and for the suction sided roughened wing as well.

Suction and pressure sided tip covered with sand grain roughness show a comparable impact on the tip vortex pressure as for the suction sided configuration. Drag and lift nearly superposition from the single sided types, leading to the highest drag of all investigated configurations and lift decreasing slightly compared to the smooth wing.

Calculating the inverse of the glide ratio ε one can obtain a decrease in wing efficiency for all setups. These effects become stronger for all configurations as the roughness height increases (fig. 4).

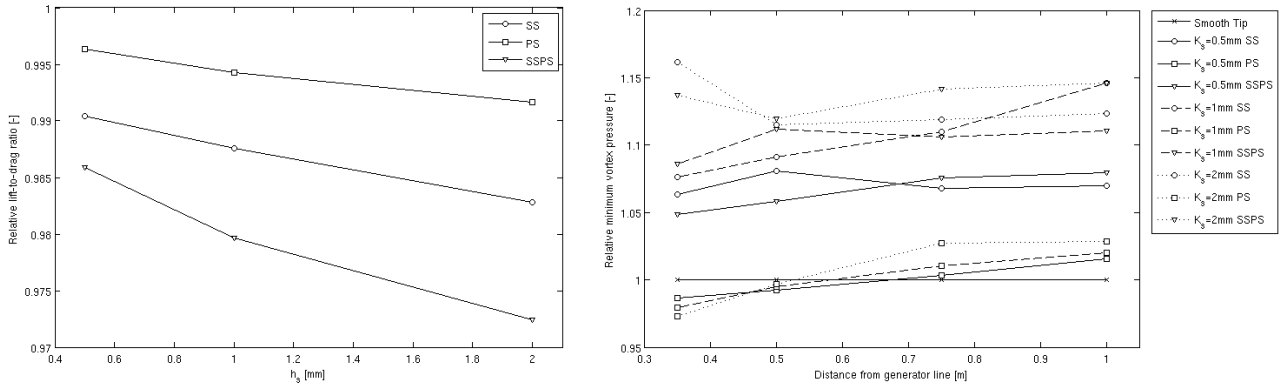

Figure 4: Calculated blade efficiency (left) and tip vortex pressure (right) relative to a smooth wing depending on type and application area of propeller tip roughness

Experimental Results

For validation purposes the calculations were assisted by a series of wind tunnel measurements, proving the low-pressure region of the tip vortex being effected by the applied tip roughness. For the roughened tip an increase of about 19% is measured compared to the smooth tip configuration, whereas the vortex core thickens slightly. The dynamic vortex core pressure being effected by the roughened tip region as well (Prandtl tube: +11.1%; 3D Hot Wire: +8.6%), implies a significant drop in axial vortex velocities by 10%.

Comparing the second order moments a diffusion of the turbulent kinetic energy for the roughened wing configuration, thickening of the turbulent vortex core (fig. 5) is also observed. By a closer look at the diagonal Reynolds stresses, an amplification of the axial vortex stresses can be noticed, whereas the radial stresses seem to be diminished. Taking into account that for the given configuration the axial stresses averaging at 1/3 of the radial stresses, the vortex diffusion can be divided into two fractions: First, a thickening of the vortex core by an amplification of the axial stresses, and second, the lowering of the total kinetic energy within the core by damping the radial stresses (fig. 6).

The shifting relation between axial and radial core stresses is also reflected by the experimental data for the cross-correlations, showing an amplification of the correlations between axial and radial fluctuations in opposite to the damping of the correlations between both components of the radial fluctuations.

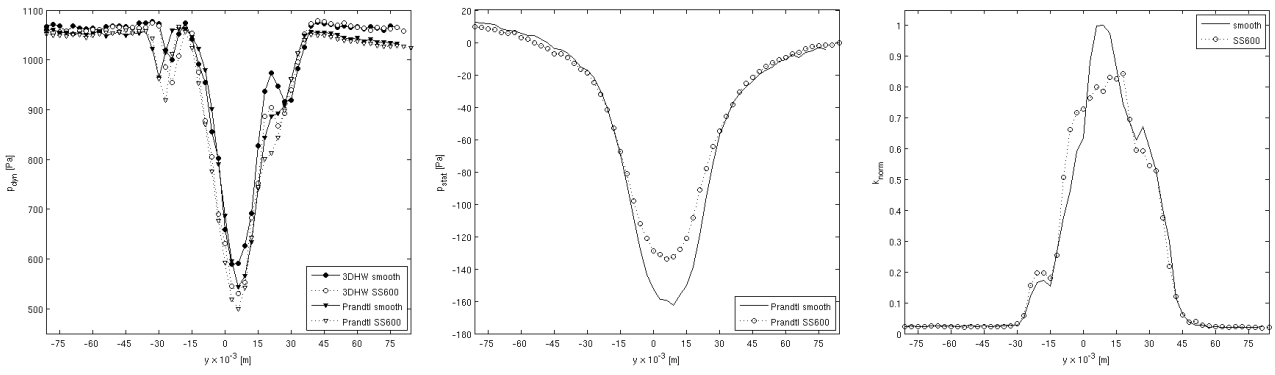

Figure 5: Dynamic pressure (left), static pressure (center) and turbulent kinetic energy (right) for a smooth and a suction side roughened wing ($h_s{}^+$=600μm) on a horizontal line through the vortex core (distance from generator line x=0.35m, z=0.427m)

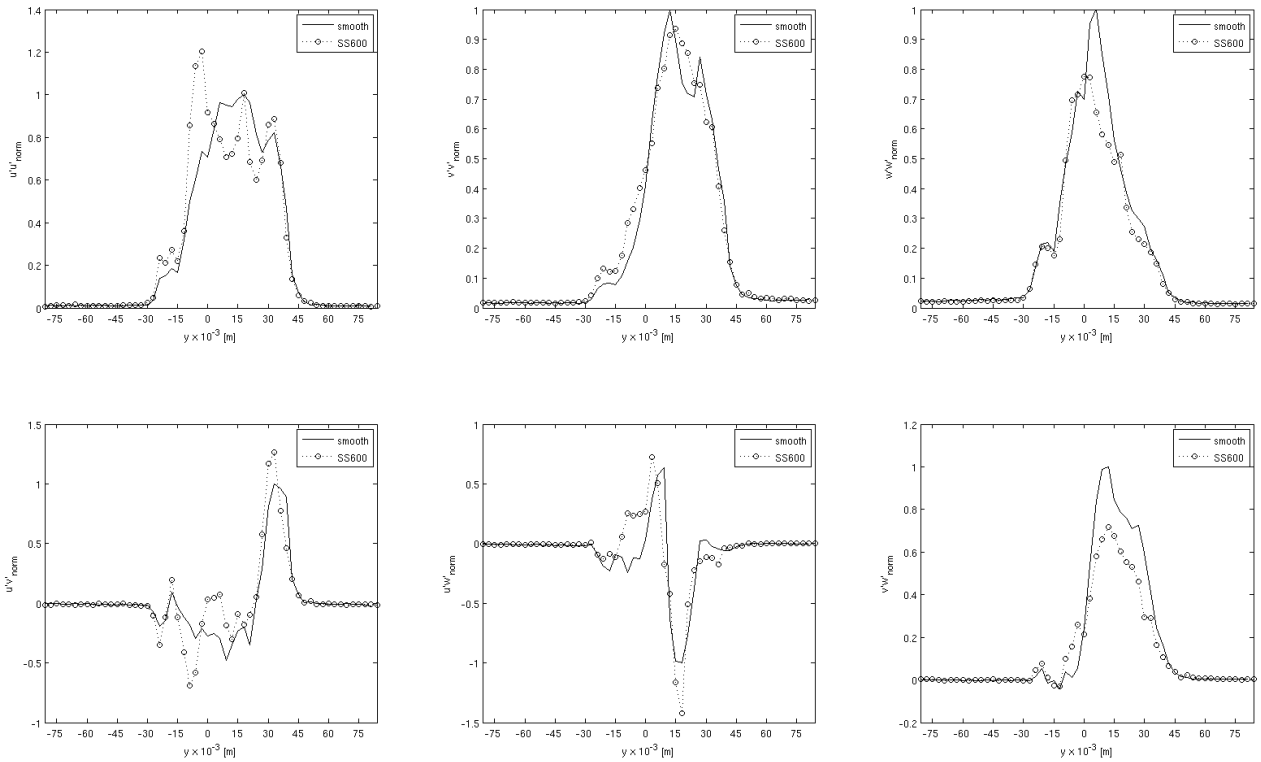

Figure 6: Components of the Reynolds stress tensor for a smooth and a suction side roughened wing ($h_s{}^+$=600μm) on a horizontal line through the vortex core (distance from generator line x=0.35m, z=0.427m)

Conclusion

By showing qualitatively good agreement between the different measurement techniques and the simulation results for the resolved vortex structures and the propeller wake, giving a good estimation about peaks and inflection points, a noticeable over estimation of the axial core velocity within the calculations for the smooth as well as the roughened blade can be observed. Examining the resolved pressure field for the smooth configuration a fairly well prediction of the minimum vortex core pressure is presented. Although the pressure increase was suggested by the calculations, an even stronger influence of the roughened tip region on the low-pressure region of the tip vortex was measured. Considering the suction sided tip roughness to be the most effective solution within this investigation, it can be estimated that by minimized reduction of the open water efficiency due to friction induced losses, cavitation safety in the tip vortex can be improved by nearly 14%.

At the present state of the investigation it can be expected, that the specific application of discrete roughness structures near the propeller tips offers potential to efficient propulsion systems that meets highest industries demands for cavitation-free operation.

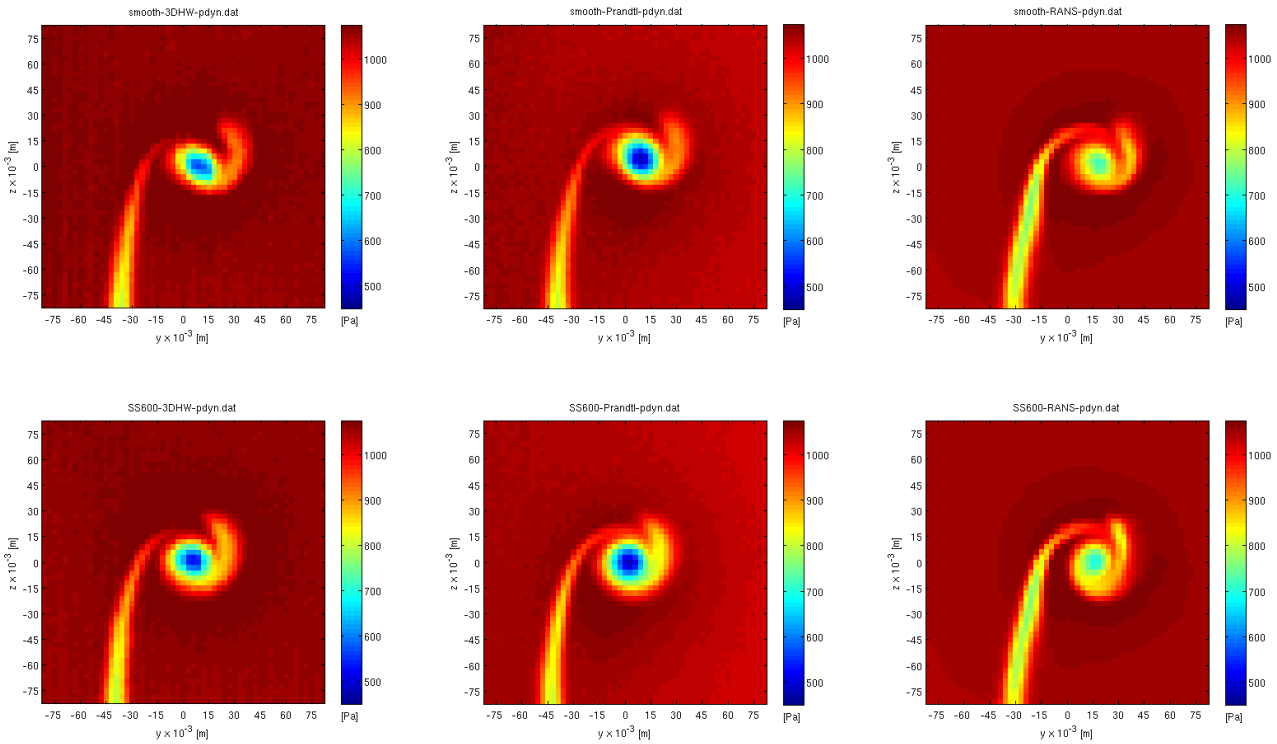

Figure 7: Dynamic pressure from 3D Hot Wire (left), Prandtl Tube (middle) and RANS (right) behind a smooth (top) and a roughened (bottom) propeller tip

References

[1] O. Rutgerson C. A. Johnsson. Leading edge roughness - a way to improve propeller tip vortex cavitation. *Propellers and Shafting Symposium*, 1991.

[2] D. S. Pradeep F. Hussain. Mechanism of core pertubation growth in vortex-turbulence interaction. *12^{th} Asian Congress of Fluid Mechanic*, 2008.

[3] A. Junglewitz J. Friesch. Erocav - improved test methods based on full scale investigations and new theoretical approaches for the prediction of erosion damages. *Summer Meeting STG*, 2003.

[4] J. Galdo J. Katz. Effect of roughness on rollup of tip vortices on a rectangular hydrofoil. *Journal of Aircraft*, 26, 1989.

[5] P. Ninnemann O. Philipp. Wirkung von flÃ¼gelrauigkeiten auf kavitation und erregung. 2007.

[6] S. Z. Duan S. I. Green. The ducted tip - a hydrofoil tip geometry with superior cavitation performance. *Journal of Fluids Engineering*, 117, 1995.

[7] H. S. Koyama T. Watanabe, H. H. Nigim. The effects of propellertip vane on flow-field behavior. *Experiments in Fluids*, 23, 1997.

[8] X. P. Tapia. Modelling wind flow over complex terrain using openfoam. 2009.

[9] D. Wittekind. Current status of underwater noise from shipping and the contribution of the propeller. 2011.

OpenFOAM Simulation of Regular Wave and Wave Load on Cylinder

Linghan Li, Mingyi Tan, James Blake

Fluid Structure Interactions Research Group,
School of Engineering Sciences,
University of Southampton, UK.
Email: ll18g11@soton.ac.uk

1. Introduction

Ocean wave energy is a resource with relatively high energy density and large global capacity and the potential to extract this energy from waves is considerable. The research in this area has been very active since 1970s. The aim of this project is to address the fluid structure interaction (FSI) problem on soft bodied wave energy converter (WEC) by developing a numerical method. Initially, a fixed and rigid cylinder is used as simplified WEC to predict the wave-induced load on it and the results are validated against physical experiment data and other simulation results. The research process is divided into several procedures:

1. Regular wave theory
2. Wave tank modeling
3. Wave-induced load validation

In reality, the ocean waves are disperse and random. For ocean wave modeling, in linear theory, the irregular wave motion can be described by the superposition of a series of first-order linear waves. In deep water, Ochi (1998) adopted Gaussian distribution to represent ocean wave elevation at any moment. Additionally, JONSWAP and Pierson-Moskowitz ocean wave spectrum model offer an alternative solution for ocean wave modeling.

The structure of wave energy device will experience various types of loads when in operation. In the initial stage, only wave-induced load, which is the dominant load on structure especially for the floating type of WEC, is taken into consideration. In order to predict the behaviour of the interaction of the body of WEC and waves accurately, correct wave models and forces prediction are needed. In this paper, the interaction between wave and WEC structure is simulated by using a fixed semi-submerged cylinder column which is placed vertically and horizontally respectively in the wave tank. It is chosen since it is comparatively simple to setup and there are a large number of previous researches offering the relevant results. The drag and viscous force can be estimated through a semi-empirical formulation: Morison equation which is shown below.

$$F = C_m \rho V \frac{\partial U_h}{\partial t} + \frac{1}{2} C_D \rho A |U_h| U_h \qquad (1)$$

Where, F is the total inline force on the structure, ρ is the water density, V is the volume, C_m and C_D are the inertia and drag coefficient respectively, U_h is the horizontal fluid velocity and A is the project area. While, the forces estimated through Morison equation are correct only if the object body is compact which means the diameter of the cylinder column is much smaller than the wave length, and the accuracy is affected by Keulegan-Carpenter number as well (Sarpkaya and Issacson, 1981).

This paper adopts a numerical method to calculate the wave-induced effect in an open-source CFD code OpenFOAM which based on the finite volume method (FVM). The free surface between air and water are modeled through volume of Fluid (VOF) scheme, and the pressure and velocity fields are coupled by semi-implicit method for pressure-linked equations (SIMPLE).

In order to test the performance of OpenFOAM simulation, a series of wave with different wave parameters are modeled firstly and validated by linear and nonlinear wave theory, then the results of wave-induced load on cylinder are compared with physical experimental data provided by Westphalen et al. (2012).

2. Problem Specification

The domain is three dimensional and consists of a rectangular domain with a cylinder located two wavelengths away from the inlet boundary. The wave tank dimensions are set to be the same as the ones used by Westphalen et al. (2012). The cylinder and the bottom of basin are modeled as non-slip wall, and the tank vertical wall boundaries are slip one. The boundary condition at the top of wave tank is pressure inlet/outlet open to the atmosphere. The pressure field at inlet is zero gradient, and the velocity boundary condition is specified.

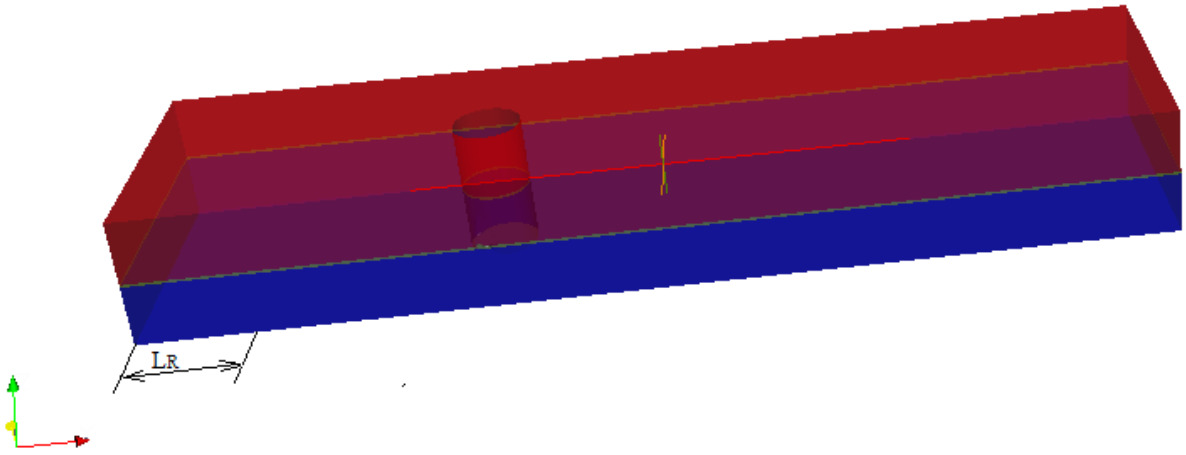

Figure 1Wave tank with a vertical cylinder

Table 1 wave tank with vertical cylinder parameters

Tank length, T_L (m) = 12	Cylinder diameter, D (m) = 0.325
Tank width, T_W (m) = 0.9	Cylinder horizontal displacement (m) = 3.77
Tank height, T_H (m) = 0.8	Still water level, d (m) = 0.45

Waves are generated and modified using the custom code, waveFoam, with relaxation zone technology which is developed based on interFoam (Jacobsen et al., 2012). The relaxation technology is used to modify the computational results by analytical solution after each time step during the numerical calculation. It is employed before the momentum equation is solved. The relaxation zone (L_R) solution is implemented according to the following relationships (waves2Foam. [online] Available at http://openfoamwiki.net/index.php/Contrib/waves2Foam):

$$\begin{aligned} \mathrm{U} &= (1-\mathrm{w})U_{analytical} + wU_{computational} \\ \mathrm{P} &= (1-\mathrm{w})P_{analytical} + wP_{computational} \\ \alpha &= (1-\mathrm{w})\alpha_{analytical} + w\alpha_{computational} \\ \mathrm{w} &\in [0,1] \end{aligned} \tag{2}$$

Where U is velocity, P is the field pressure, α is phase fraction value in VOF and w is weighting function. The length of relaxation zone in this study is set to be one wavelength.

The relaxation zone is also employed at the end of wave tank for water waves damping.

3. Mesh generation

3.1 BlockMesh

The meshes are set respectively due to different wavelength in each case. The cell size in wave propagation direction equals to 1/40~1/20 of wave length and this should be sufficient to resolve wave information. The number of cells in vertical direction needs to be not less than the one in horizontal direction. A layout of the grid around the cylinder is shown in Figure 2; the meshes are finest at the boundary of cylinder and gradually stretched outwards in the radial direction.

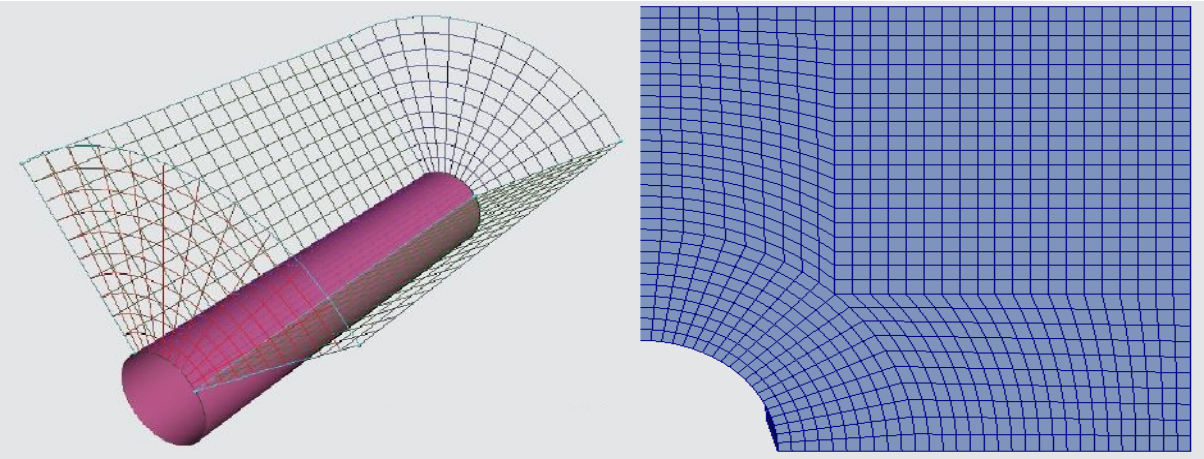

Figure 2 Mesh generation around cylinder

3.2 SnappyHexMesh (SHM)

The cylinder surface data in STL format is generated in Blender software and then imported into SnappyHexMesh dictionary. There is a major drawback of SHM for this study is that SHM is weak in respecting sharp edge as shown in the left picture of Figure 3, the following methods can be used to avoid jagged edges:

1. The cylinder height described by STL is larger than the height of background hex mesh; therefore the sharp edge will be created and restrained by the background mesh.
2. The sharp edge is replaced by curved edge.
3. The jagged edges can be fixed by a custom SnapEdge utility by Niklas (Contrib snapEdge, [online] Availabe at http://openfoamwiki.net/index.php/Contrib_snapEdge).

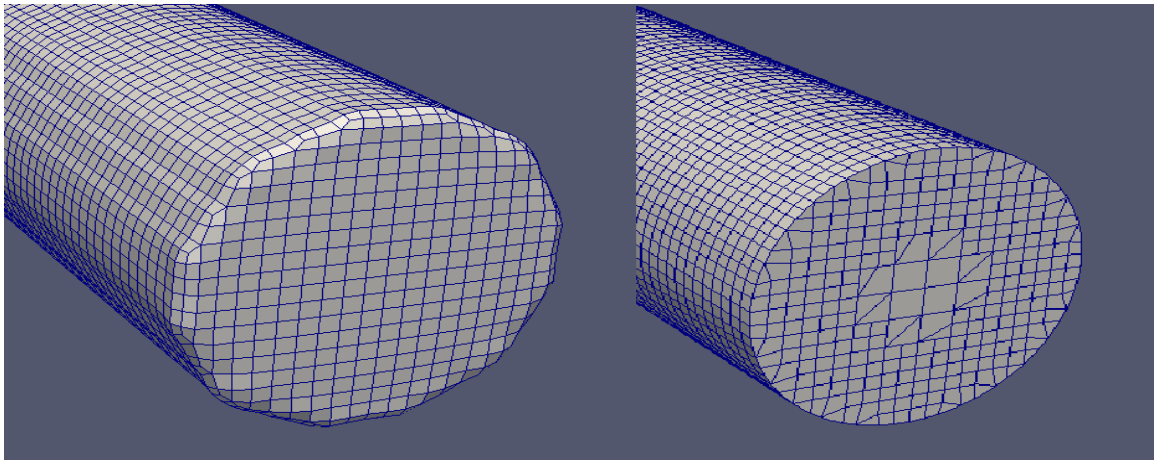

Figure 3 Cylinder mesh generated by SnappyHexMesh

4. Simulation

Firstly, the regular wave models are generated in OpenFOAM, and then validated by comparing the results with the wave theory. The wave tank depth used is predicted through linear wave theory (McCormick, 1987):

$$h \geq \frac{gT^2}{4\pi} \text{ (Deep water)} \tag{3}$$

Where, h is water depth and T is wave period.

In experiment, the wave generated consists of progressive wave and standing wave, and the standing wave can be neglected after a distance of 3h away from the wavemaker. Therefore, the optimum measure point in a wave tank is at this distance (Finnegan and Goggins, 2012).

The wave elevations, where α(volume fraction in VOF) equals 0.5, can be calculated through the linear interpolation equation. The recording data of α is obtained by adding the probe function into the controlDict under case file.

The vertical and horizontal forces are calculated in the simulation of wave-induced load on horizontal cylinder and vertical cylinder respectively.

To compare the numerical results of wave-induced load, the forces used are non-dimensional using the following expression:

$$\begin{cases} F_v{}' = \frac{F_v}{\rho g(\frac{\pi D^2 l}{4})} \\ F_h{}' = \frac{F_h}{\frac{\rho g a H h \tanh kh}{kh}} \end{cases} \tag{4}$$

Where F_v and F_h are measured vertical and horizontal force respectively, D is the cylinder diameter, l is the length of cylinder, a is the radius of the cylinder, H is the wave height, h is the water depth.

In order to obtain vertical and horizontal force in OpenFOAM, a force function is added into the program. The default force function only works for forces in single phase, since the original force function cannot simply read global coefficient “nu” or “rho” from transportProperties file since there are several “nu” and “rho” in multiphase. The following summarize the key points in new compiled force function file

```
scalar pDyn = 0.5*rhoRef_*magUInf_*magUInf_;
vector totForce = fm.first().first() + fm.first().second();
vector totMoment = fm.second().first() + fm.second().second();
scalar liftForce = totForce & liftDir_;
scalar dragForce = totForce & dragDir_;
scalar pitchMoment = totMoment & pitchAxis_;
scalar Cl = liftForce/(Aref_*pDyn);
scalar Cd = dragForce/(Aref_*pDyn);
scalar Cm = pitchMoment/(Aref_*lRef_*pDyn);
```

Where, fm.first().first() is pressure forces in phase 1, fm.second().first() is pressure forces in phase 2, fm.first().second() is viscous forces in phase 1 and fm.second().second() is viscous force in phase 2 .

5. Results

The results of the calculated wave elevation are shown below:

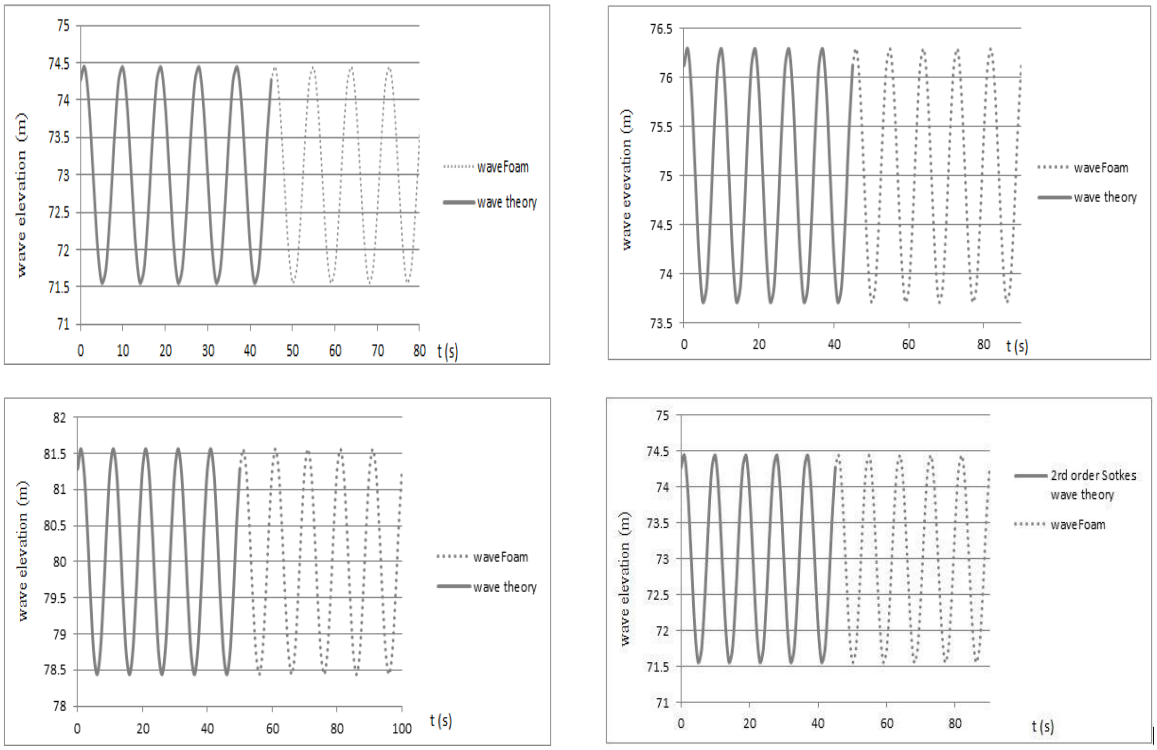

Figure 4 Comparisons of calculated results and wave theory

The first three graphs in Figure 3 show that the results from waveFoam simulation match perfectly with 1st order wave theory for water waves with periods of 8s, 9s and 10s, and wave height of 2.92m, 2.62m and 3.12m respectively. The 4th one proves that waveFoam can also be used to generate higher order waves.

The figures below show the comparisons of calculated non-dimensional forces and physical experimental data:

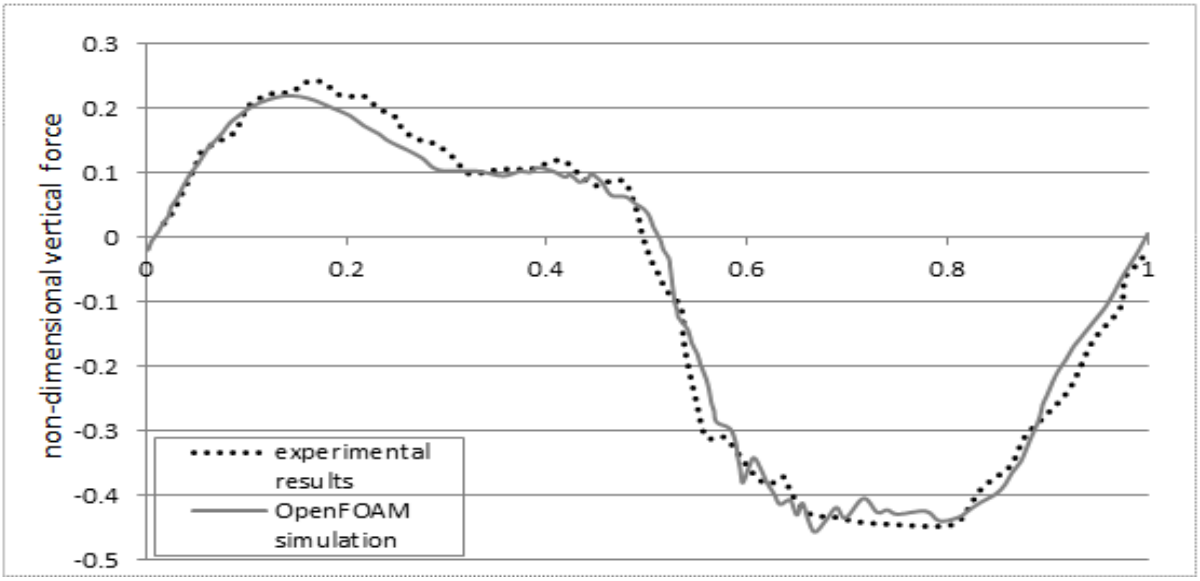

Figure 5 Comparison of experimental data (Westphalen et al., 2012) and simulation results of non-dimensional vertical force

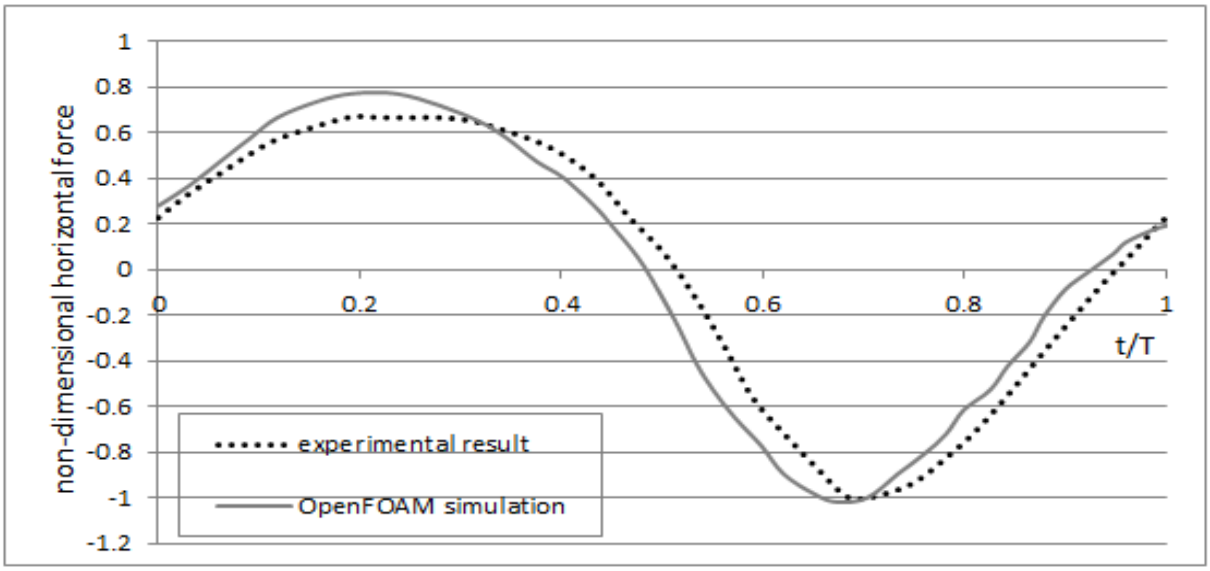

Figure 6 Comparison of experimental data (Westphalen et al., 2012) and simulation results of non-dimensional horizontal force

The comparison results show that the numerical results match well with the experimental results except the slightly phase shift in the horizontal force comparison.

6. Conclusions and Future work

The calculated vertical and horizontal forces are compared with physical experiments and the results show a good agreement. The waveFoam solver offers a reasonable solution to simulate wave motion and wave-structure interactive problem, and this will be used for further research. More simulations of wave-induced load are conducted on floating cylinder with 3DOF and 6DOF motion, and spring and damping effects are also taken into consideration.

7. References

Contrib snapEdge, [online] Availabe at http://openfoamwiki.net/index.php/Contrib_snapEdge

Finnegan, W. and Goggins J. (2012). "Numerical simulation of linear water waves and wave–structure interaction." Ocean Engineering **43**: 23-31.

Jacobsen N. G. Fuhrman D. R. and Freds E. J. (2011). "A wave generation toolbox for the Open-Source CFD Library: OpenFOAM" DOI: 10.1002/fld.2726.

McCormick M. E. (1987). "Ocean wave energy conversion" Wiley&Sons, New York.

Ochi M. K. (1998). "Probability distribution of wave height in finite water Depth".

Sarpkaya T. and Issacson M. (1981). "Mechanics of Wave Forces on Offshore Structures" Van Nostrand Reinhole (1981).

Waves2Foam. [online] Availabe at http://openfoamwiki.net/index.php/Contrib/waves2Foam.

Westphalen, J., Greaves D. M. et al. (2012). "Focused waves and wave–structure interaction in a numerical wave tank." Ocean Engineering **45**: 9-21.

Simulation of inflow turbulence noise

Thomas P. Lloyd[a,b*], Mathieu Gruber[c], Stephen R. Turnock[a] and Victor F. Humphrey[b]

[a]Fluid-Structure Interactions Research Group; [b]Institute of Sound and Vibration Research, University of Southampton, Southampton, UK. SO17 1BJ; [c]Department of Acoustic, Snecma Villaroche, Rond point rene Ravaud, REAU, 77550 Moissy-Cramayel, FRANCE.

1 Introduction

Broadband noise of turbomachines has become an important design consideration in numerous applications, including axial fans, marine propulsors and wind turbines. *Leading edge* (or *inflow turbulence*) noise has been shown to dominate when the flow into the rotor is turbulent (Carolus et al., 2007). In case of a submarine propeller, this occurs when the turbulent boundary layer of the hull enters the propulsor. For wind turbines, the inflow turbulence may be due to the atmospheric boundary layer or wakes from upstream turbines.

Amiet (1975) derived an analytical model showing that the far field acoustic pressure is proportional to the integral length scale ($\mathcal{L}$) and square of the turbulence intensity (I^2). As such, the measurement or specification of these quantities is important in the investigation of inflow turbulence (IT) noise. Measurements have also focussed on the leading edge noise of fixed aerofoils (e.g. see Devenport et al. (2010)). The inflow turbulence in most cases is generated using grids placed in the flow of wind tunnels, thus generating approximately homogeneous, isotropic turbulence.

This noise source can also be studied numerically using synthetic turbulence. Christophe et al. (2007) used such a method implemented inside FLUENT to simulate a jet impinging on an aerofoil. The low Reynolds number of $36,000$ allowed a large eddy simulation (LES) to be performed. Curle's analogy (Curle, 1955) is used to compute the low-frequency noise. Since the compact formulation of this method is only valid at lower frequencies (when the aerofoil chord $c << \lambda$), Amiet's model is used for the high frequency part of the spectrum to account for diffraction effects, with the *rms* velocities predicted by LES used as input to the model.

2 Simulation Details

2.1 Numerical method

In this study, we employ the Improved Delayed DES (IDDES) technique of Shur et al. (2008). The IDDES extension reformulates the length scale used to switch between the RANS and LES regions so as to resolve part of the boundary layer in the unsteady mode; it has been described as a form of wall modelled LES when inflow turbulence is present (Shur et al., 2008). For the simulation of inflow turbulence noise this seems a natural choice, since the unsteadiness seen by the wall will increase compared with DES due to the presence of eddies inside the boundary layer.

IDDES re-formulates both the DES length scale and grid filter definitions. The grid filter is given as

$$\Delta = min(max[C_w d_w, C_w h_{max}, h_{wn}], h_{max}) \tag{1}$$

where C_w is a constant, d_w the wall distance, $h_{max} = max(\Delta_x, \Delta_y, \Delta_z)$ and h_{wn} the wall-normal grid spacing. The DES length scale becomes

$$L_{IDDES} = f_B(1 + f_e)L_{RANS} + (1 - f_B)L_{LES} \tag{2}$$

where L_{LES} includes the DDES functions. A full description of the model functions f_B and f_e is given by Shur et al. (2008). Turbulence modelling is handled by the $k-\omega$ SST model, which has been shown to provide improved predictions of broadband noise sources over the Spalart-Allmaras turbulence model (Greschner et al., 2008).

The governing equations are solved using the open-source, finite-volume code OpenFOAM. The equations are discretised in their integral form, and solved on multi-block structured grids, using co-located variables. The solution method is based on the PISO algorithm and Rhie-Chow interpolation.

2.2 Case description

The simulations presented are based on measurements of leading edge noise of a NACA 65(12)10 aerofoil made by Gruber (2012) in the DARP open-jet aeroacoustic wind tunnel at the University of Southampton.

* *corresponding author's e-mail*: T.P.Lloyd@soton.ac.uk

Turbulence is generated inside the nozzle contraction using two grids, placed $50mm$ upstream of the nozzle exit. Results are presented for a jet velocity corresponding to a Mach number of ~ 0.06.

Two sets of measurements are used for validation. The first consists of hot-wire probe data, which is used to estimate the integral length scale and turbulence intensity of the inflow turbulence. A second set is made up of far field noise measurements at $1.22m$ of a NACA 65(12)10 aerofoil of $0.15m$ chord and $0.45m$ span, held in the flow by end plates attached to the nozzle. The chord-based Reynolds number is approximately 2.9×10^5. The co-ordinate system is depicted in Figure 1.

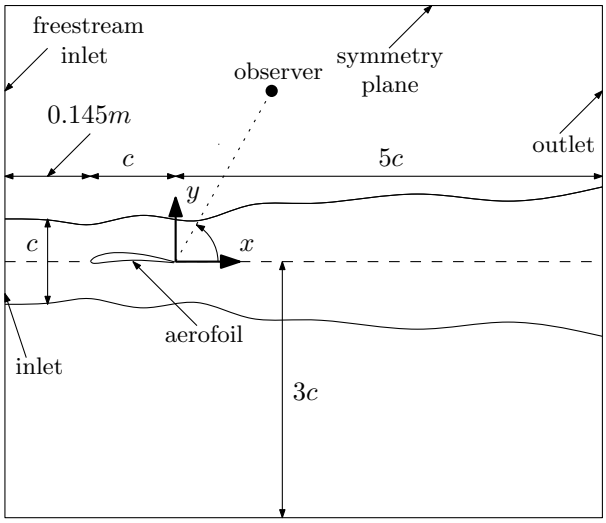

Figure 1: Schematic of simulation coordinate system and grid design.

2.3 Grid design

A structured gridding approach has been adopted. Grid design is influenced by the smallest size of eddy that can be resolved within the desired limit of computational expense. For the case considered here, the jet velocity, $U_\infty = 27.34ms^{-1}$, the mean streamwise turbulence intensity, $I = u'_{x,rms}/U_\infty$, is equal to 2.06% and the integral length scale is approximately $\mathcal{L} = 0.005m$. An ideal grid will contain cell sizes much smaller than the integral length scale; for example, Michel et al. (2009) recommend using 4 grid points per convection length scale $L_c = U_c/f$, where U_c is the convection velocity. We estimate the grid cutoff frequency, following Ask and Davidson (2006), to be $f_{max,i} = |u'_{i,rms}|/2\Delta_i$ where Δ_i is the grid spacing in the direction. Hence, the smallest cell size must be half the highest resolvable eddy length. The resulting grid has dimensions of $L_x \times L_y \times L_z = 7c \times 6c \times 0.1c$. To further reduce the number grid cells required, the nozzle walls are not included, with the jet exit placed at the simulation inlet, at $x = -0.295m$ (see Figure 1).

The cells upstream of the aerofoil are approximately isotropic, and of size $0.001m$. The aerofoil is meshed using a C-grid, with 250 points on the suction side and 200 points on the pressure side. The cells are clustered at the leading and trailing edges in order to better resolve the sound source regions. A wall-normal first cell height of $y_1^+ \approx 1.6$ is achieved, with ≈ 35 cells used to resolve the boundary layer at the trailing edge. Spanwise slices through the grid at the leading and trailing edges are shown in Figure 2.

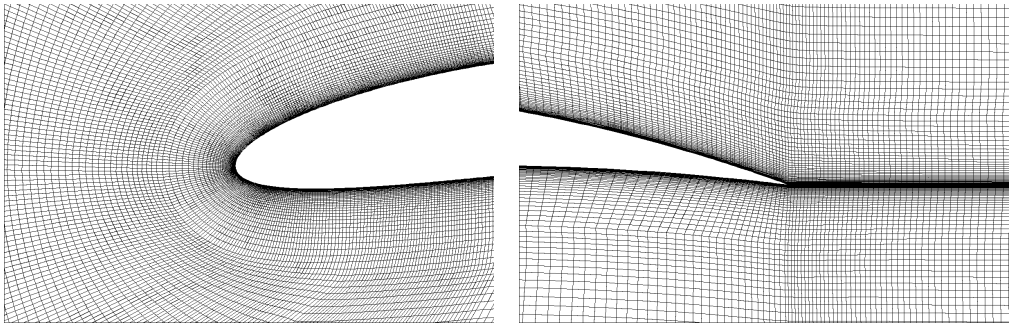

(a) Leading edge (b) Trailing edge

Figure 2: Leading and trailing edge grids for NACA65(12)10 at $Re_c = 2.9 \times 10^5$.

2.4 Computational setup

The turbulent jet is generated using the 'vorton' method of Kornev et al. (2007), which has been implemented into OpenFOAM and made freely available. The turbulence is modelled as homogeneous and *almost* isotropic - since only the streamwise turbulence intensity is known from the experimental measurements, the v' and w' components are estimated as $0.9u'$, based on Comte-Bellot and Corrsin (1966). For the parameters specified, the turbulence generated is divergence free. In order to maintain the stability of the jet shear layer, a small freestream inlet velocity is used, equal to $0.15U_\infty$.

Pressure is set to *zero gradient* (ZG) at the inlet and aerofoil surface, with *fixed value* (FV) at the outlet. Velocity and turbulent kinetic energy are FV zero on the aerofoil, and mixed FV/ZG on the outlet, preventing hydrodynamic reflections. Symmetry planes are used at the top and bottom far field boundarys, while the spanwise sides are periodic. The simulation is initialised from a Reynolds-averaged Navier-Stokes solution, where the residuals for velocity and pressure have reduced to 1×10^{-5}.

A time step $\Delta t = 2 \times 10^{-6} s$ is used, which results in a maximum Courant number, $Co = \Delta t u_i / \Delta x_i \sim 0.65$. The flow is allowed to develop for $\Delta T U_\infty / c = 28$ flow throughs of the domain, after which flow field statistics and acoustic sources are sampled for a further $\Delta T U_\infty / c = 28$ at $\Delta t_{sample} = 1 \times 10^{-5} s$. The simulation duration is approximately 300 hours on 72 23GB processors.

3 Results and Discussion

3.1 Inflow turbulence

The mean velocity and turbulence intensity components are presented in Figure 3, sampled across the jet height at the location $x = -0.2m$, $z = 0.0075m$. The profiles are all approximately uniform across the jet, although the mean velocity does show a $\sim -3\%$ reduction from U_∞ at $y = 0$. The intensities all have similar values, which is surprising considering the v'_{rms} and w'_{rms} components were specified to be smaller than u'_{rms} at the inlet. The mean values between $y = -0.05m$ and $y = 0.05m$ are 2.94% for I_x, and 2.85% for I_y and I_z. Hence all the intensities upstream of the aerofoil are slightly higher that desired. Despite this they do exhibit the characteristics of homogeneous isotropic turbulence.

The power spectra are also seen to be fairly consistent between the three fluctuating components, as shown in Figure 4. The power spectral density (PSD) has been normalised by U_∞^2, with Strouhal number plotted on the abscissa, where $St = fc/U_\infty$. The $-5/3$ power law is included in the Figure to provide an indication of the mesh cut-off frequency. This confirms that the grid is resolving small enough length scales, since a Strouhal number of ~ 11 corresponds to the desired cut-off of $\sim 2\ kHz$.

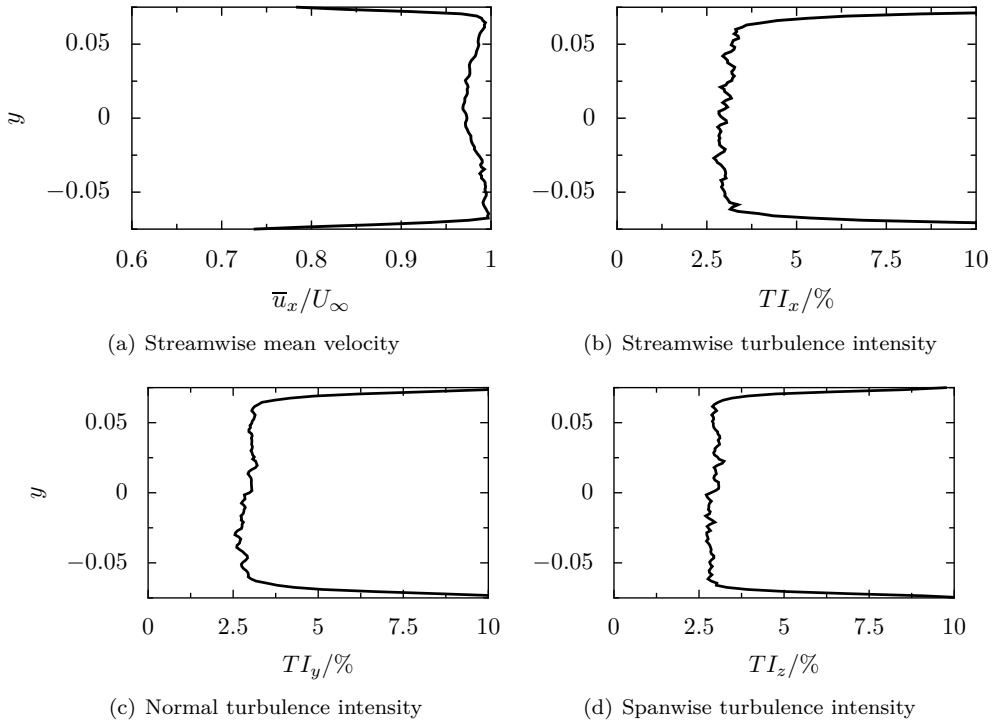

(a) Streamwise mean velocity

(b) Streamwise turbulence intensity

(c) Normal turbulence intensity

(d) Spanwise turbulence intensity

Figure 3: Non-dimensionalised velocity profiles in the jet, sampled across the height of the jet centreline, at $x = -0.2m$.

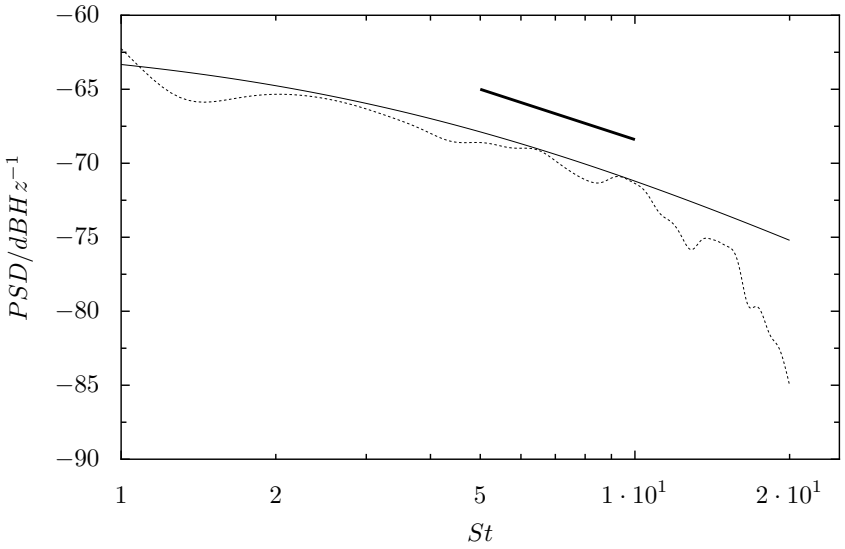

Figure 4: Power spectral density of streamwise velocity fluctuation u', upstream of NACA 651210 leading edge, at $x = -0.2m$: dashed - streamwise; solid - 1-D von Kármán; thick solid - power law with slope $-5/3$.

3.2 Aerodynamic results

The turbulent structures close to the aerofoil surface are visualised in Figure 5 using an iso-surface of $\lambda_2 = 10^7$, coloured by the normalised streamwise velocity. Figure 5 reveals turbulent structures at both the leading and trailing edges, as well as along much of the pressure side of the chord. This has been attributed to a leading edge separation bubble for the 0° angle of attack case (Gruber, 2012). This is corroborated by the chordwise distribution of the pressure coefficent, $C_p = p/0.5\rho U_\infty^2$ where ρ is the fluid density, shown in Figure 6. Figure 6(b) reveals the effect of the pressure side separation bubble on the *rms* surface pressure at approxiamtely $x/c = -0.8$. The unsteady boundary layer structures which lead to trailing edge noise are also noticable for $x/c = -0.4 \to 0$.

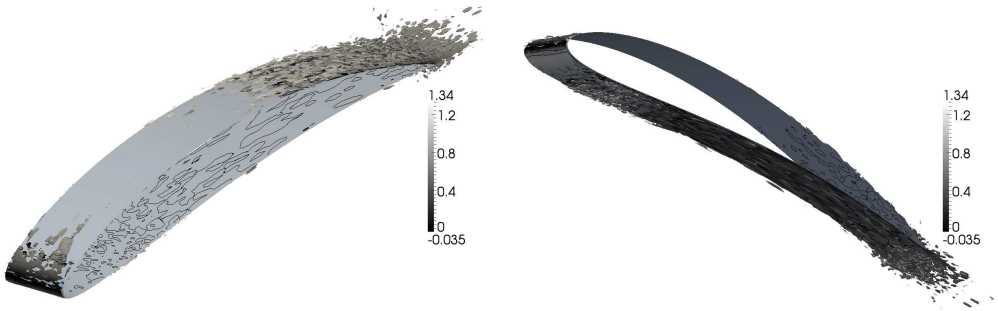

(a) Suction side (b) Pressure side

Figure 5: Iso-surface of $\lambda_2 = 10^7$ coloured by the mean streamwise velocity.

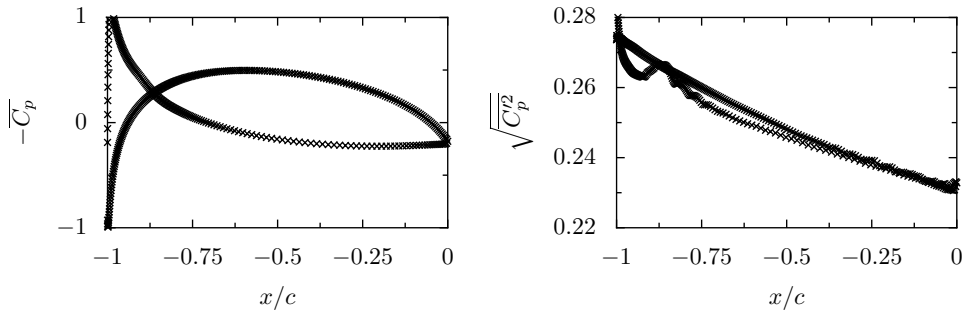

(a) Mean surface pressure coefficient (b) *rms* surface pressure coefficient

Figure 6: Mean and *rms* surface pressure coefficient distribution on NACA65(12)10, sampled at $z/L_z = 0.5$.

3.3 Aeroacoustic results

Figure 7 compares the simulation sound pressure level (SPL) to the experimental data, and the inflow turbulence model of Amiet (1975). This predicts the third-octave SPL based on a von Kármán spectrum for isotropic turbulence as

$$SPL = 10log_{10}\left[\frac{\mathcal{L}sM^5}{2r^2}TI_x^2\frac{\hat{k}_x^3}{(1+\hat{k}_x^2)^{7/3}}\right] + 181.3 \tag{3}$$

where s is the aerofoil span, M the Mach number, r the receiver distance and $\hat{k}_x$ the modified streamwise turbulence wavenumber. This is given by $-\hat{\omega}/u_x$ where $\hat{\omega} = \omega c/2u_x$ and ω is the circular frequency $2\pi f$. The SPL is defined as

$$SPL = 10log_{10}\left(\frac{PSD(f)}{p_{ref}^2}\right) \tag{4}$$

where $p_{ref} = 2 \times 10^{-5}Pa$. In the numerical simulation, the data used to calculate the PSD is the acoustic pressure at the receiver location equivalent to a polar angle of 90°. This has been calculated using the acoustic analogy of Curle (1955), which has been implemented into OpenFOAM by the authors.

The SPL predictions derived from the simulation are corrected for the limited spanwise domain width. To achieve this, the method of Kato et al. (1993) is used, which requires the spanwise coherence length to be estimated. This is given by $L_\gamma = C_c U_c/f$. C_c is a constant determined from the data of Corcos (1963), equal to 0.69 for the 0° angle of attack case presented here. For the frequency range plotted in Figure 7, a correction of $20log(L_\gamma/L_{sim}) + 10log(L_{exp}/L_\gamma)$ is applied to the simulation data.

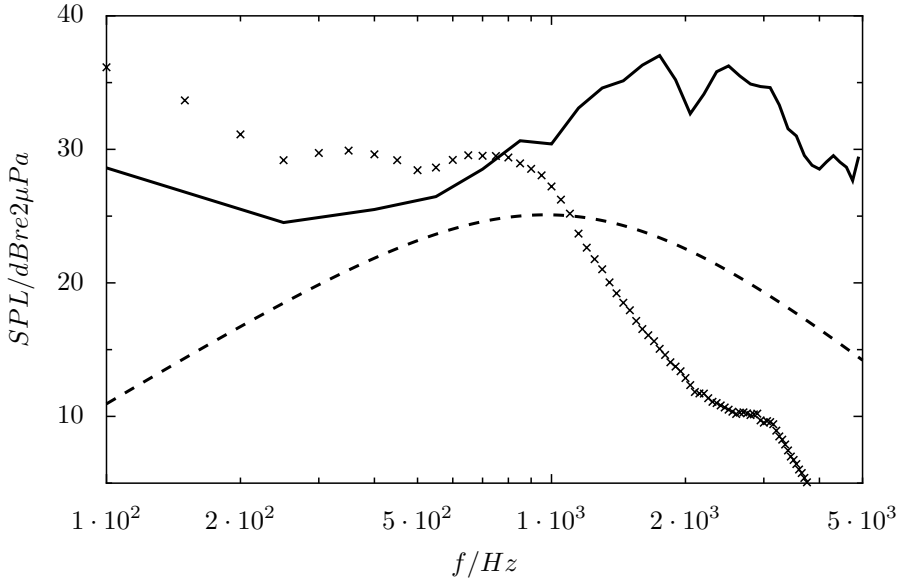

Figure 7: Sound pressure level for NACA 651210 at receiver location $1.22m$ above trailing edge: solid - non-compact Curle's equation; dotted - comapct Curle's equation; dashed - leading edge noise model of Amiet (1975); crosses - experimental data of Gruber (2012).

Figure 7 reveals that the simulation predicts the SPL reasonably well in the range $\sim 400Hz - 1kHz$. However, at higher frequencies the discrepancy between the experimental and simulation result is of the order of 25 dB. This has been attributed to vorticity in the pressure side boundary layer causing a large trailing edge noise source (Deniau et al., 2011). Further work will focus on separating these sources so as to estimate the leading edge noise more accurately. One key observation is the large difference between the experimental and numerical results below $500Hz$. Although the frequencies of the spectral peaks and troughs are correct, the low frequency noise is underpredicted. This suggests that the simulation is not representing the correct range of scales (scales larger than $\mathcal{L}$).

4 Conclusions

The subject of inflow turbulence noise for a fixed aerofoil has been addressed using a viscous flow solver, and the results compared to experimental and empirical predictions. An acoustic analogy approach has been implemented into the code OpenFOAM, thus significantly reducing data post-processing effort when predicting noise.

The IDDES methodology has been shown to provide reasonable prediction of the unsteady aerodynamics that must be captured in order to predict acoustic sources. Use of an inflow turbulence generator has allowed accurate representation of a homogeneous isotropic turbulent inflow. Despite this, the predicted SPL does not closely match experimental data.

Future work will focus on tuning the inflow generator to allow improved noise predictions, and address the problem of inhomogeneous inflow, whereby the turbulence and thus acoustic source strength takes on a spanwise dependency.

5 Acknowledgements

The experimental data was collected by Dr. Gruber as part of the FLOCON project. Gratitude is also expressed to Dr. Richard Sandberg for providing the $k - \omega$ *SST* implementation of IDDES, as well as Evgeny Shchukin for the inflow generator. The authors acknowledge the use of the IRIDIS High Performance Computing Facility, and associated support services at the University of Southampton. Mr Lloyd wishes to acknowledge the financial support of a University of Southampton Postgraduate Scholarship, dstl and QinetiQ.

References

Amiet, R. (1975), 'Acoustic radiation from an airfoil in a turbulent stream', *Journal of Sound and Vibration* **41**(4), 407–420.

Ask, J. and Davidson, L. (2006), The sub-critical flow past a generic side mirror and its impact on sound generation and propagation, number May, pp. 1–20.

Carolus, T. H., Schneider, M. and Reese, H. (2007), 'Axial flow fan broad-band noise and prediction', *Journal of Sound and Vibration* **300**(1-2), 50–70.

Christophe, J., Anthoine, J., Rambaud, P., Schram, C. and Moreau, S. (2007), Prediction of incoming turbulent noise using a combined numerical/semi-empirical method and experimental validation, *in* 'Proceedings of the West-East High Speed Flow Field Conference', 19th-22nd, Moscow.

Comte-Bellot, G. and Corrsin, S. (1966), 'The use of a contraction to improve the isotropy of grid-generated turbulence', *Journal of Fluid Mechanics* **25**(4), 657–682.

Corcos, G. M. (1963), 'The structure of the turbulent pressure field in boundary-layer flows', *Journal of Fluid Mechanics* **18**(03), 353–378.

Curle, N. (1955), 'The influence of solid boundaries upon aerodynamic sound', *Proceedings of the Royal Society A: Mathematical, Physical and Engineering Sciences* **231**(1187), 505–514.

Deniau, H., Dufour, G., Boussuge, J.-F., Polacsek, C. and Moreau, S. (2011), Affordable compressible LES of airfoil-turbulence interaction in a free jet, *in* 'Proceedings of the 17th AIAA/CEAS Aeroacoustics Conference', number June, 5th-8th June, Portland, pp. 1–17.

Devenport, W. J., Staubs, J. K. and Glegg, S. A. (2010), 'Sound radiation from real airfoils in turbulence', *Journal of Sound and Vibration* **329**(17), 3470–3483.

Greschner, B., Thiele, F., Jacob, M. C. and Casalino, D. (2008), 'Prediction of sound generated by a rod-airfoil configuration using EASM DES and the generalised Lighthill/FW-H analogy', *Computers & Fluids* **37**(4), 402–413.

Gruber, M. (2012), Airfoil noise reduction by edge treatments, Ph.D. thesis, University of Southampton.

Kato, C., Iida, A., Takano, Y., Fujita, H. and Ikegawa, M. (1993), Numerical prediction of aerodynamic noise radiated from low Mach number turbulent wake, *in* 'Proceedings of the 31st Aerospace Sciences Meeting and Exhibit', 11th-14th January, Reno, NV.

Kornev, N. V., Kröger, H., Turnow, J. and Hassel, E. (2007), 'Synthesis of artificial turbulent fields with prescribed second-order statistics by the random spots method', *Proceedings in Applied Mathematics and Mechanics* **7**(1), 2100047–2100048.

Michel, U., Eschricht, D., Greschner, B., Knacke, T., Mockett, C. and Thiele, F. (2009), Advanced DES methods and their application to aeroacoustics, *in* S.-H. Peng, P. Doerffer and W. Haase, eds, 'Progress in Hybrid RANS-LES Modelling', Springer-Verlag, pp. 59–76.

Shur, M., Spalart, P. R., Strelets, M. and Travin, A. (2008), 'A hybrid RANS-LES approach with delayed-DES and wall-modelled LES capabilities', *International Journal of Heat and Fluid Flow* **29**(6), 1638–1649.

Introducing Non-condensable Gas in Unsteady Sheet Cavitation Modelling

Nai-Xian Lu*, Göran Bark , Rickard Bensow
Department of Shipping and Marine Technology, Chalmers University of Technology
SE-412 96, Gothenburg, Sweden
*Email: naixian.lu@chalmers.se

1. Introduction

Previous work carried out by the authors [1] using an incompressible mixture approach reveals that except for a compression rebound, which is considered as an indication of erosion risk and has its origin in the compression of cavity content, a rebound can also be generated through collapse asymmetry and defined as "vortex rebound," which may actually reduce the erosion potential. However due to the lack of compressibility in the modelling approach, it has not been possible to reproduce the compression rebound. Therefore we want at this stage to introduce non-condensable gas in the simulation technique to see if this is sufficient to include effects of compressibility, at least of the gas, and try acquiring the correct balance between the rebound components and achieving a more reliable erosion analysis.

In Franc [2] it states that when a bubble holds non-condensable gas, it will be compressed during collapse and will partly resist the inward liquid motion. The collapse will be damped and the bubble may rebound, often splitting into smaller structures. Numerical methods that solve the incompressible Navier-Stokes equation with the effect of non-condensable gas included have been previously developed and studied by various authors, *e.g.* Kunz *et al.* [3], Singhal *et al.* [4] and Qin *et al.* [5] etc., but then with different objectives, e.g. to study ventilated cavities.

This paper deals with the introduction of non-condensable gas into the Sauer's mass transfer model. A NACA15 hydrofoil at 8 degrees angle of attack and cavitation number 1.1 is chosen for demonstration. Although this hydrofoil under the simulated condition is not suitable for erosion study, it still, at this preliminary stage, offers a clue of the influence of gas by comparing with the results in [1,6] of the same computational configurations.

2. Simulating cavitating flows

For the simulations described in this paper, an incompressible implicit LES approach is used in combination with a single fluid mixture assumption based on a Volume Of Fluid (VOF) implementation. A mass transfer model based on Sauer's model [7] with a modification to take into account the effect of non-condensable gas is introduced and used to capture vaporization and condensation processes. The solution procedure is based on a segregated PISO algorithm, implemented using the OpenFOAM libraries (Weller *et al.* [8]). For the general governing equations and numerical methodology, see Lu [6] for details.

2.1. Introducing non-condensable gas to the Sauer's mass transfer model

Sauer's model considers cavities as a distribution of bubbles that grow or collapse as they travel through varying pressure field. The dynamic of the bubbles is governed by the Rayleigh equation (Rayleigh, 1917), when used by Sauer is simplified by neglecting the second-order derivative. Solving for the derivative of the bubble radius gives the growth rate as

$$\dot{R} = \sqrt{\frac{2}{3}\frac{p(R)-p_\infty}{\rho_l}}\,. \tag{1}$$

The original Sauer's model connects the bubble radius and the vapour volume fraction through

$$\alpha_v = \frac{\left(4\pi R^3/3\right)n_0}{1+\left(4\pi R^3/3\right)n_0}\,. \tag{2}$$

We now introduce a third phase, the non-condensable gas, assuming that this certain amount of gas is dissolved in the fluid with mass fraction f_g. A parameter study carried out by Berchiche and Bark [9] shows that the value of f_g has an influence on the thickness and length of the predicted cavity. In this paper a suggested initial value of 7 ppm by Li [10] has been used. The corresponding gas volume fraction α_g can be deducted from f_g as

$$\alpha_g = f_g \frac{\rho}{\rho_g} . \tag{3}$$

where ρ_g is the density of non-condensable gas and ρ is the mixture density. The gaseous phase is assumed to follow the ideal gas law, therefore

$$\rho_g = \frac{p}{R_{specific} T} . \tag{4}$$

The temperature is assumed to be 300K, and the specific gas constant takes the value of 287 J/kg*K of air. The vapour/liquid/gas mixture density ρ reads:

$$\rho = \alpha_v \rho_v + \left(1 - \alpha_v - \alpha_g\right)\rho_l + \alpha_g \rho_g , \tag{5}$$

and the material derivative of the mixture density becomes

$$\frac{\mathrm{D}\rho}{\mathrm{D}t} = \left(\rho_v - \rho_l\right)\frac{\mathrm{D}\alpha_v}{\mathrm{D}t} + \left(\rho_g - \rho_l\right)\frac{\mathrm{D}\alpha_g}{\mathrm{D}t} . \tag{6}$$

Now we consider that the bubbles are composed of a gas/vapour mixture, and equation (2) becomes

$$\alpha_v + \alpha_g = \frac{\left(4\pi R^3/3\right)n_0}{1 + \left(4\pi R^3/3\right)n_0} . \tag{7}$$

The material derivative of the vapour/gas mixture volume fraction can be derived as

$$\frac{\mathrm{D}\left(\alpha_v + \alpha_g\right)}{\mathrm{D}t} = \left(1 - \alpha_v - \alpha_g\right)\left(\alpha_v - \alpha_g\right)\frac{3\dot{R}}{R} . \tag{8}$$

As the pressure in the flow falls below the vaporization pressure, the liquid that vaporizes is assumed to release its portion of non-condensable gas. When the pressure rises above the critical pressure, the portion of vaporized water is assumed again to follow the reversible process and condenses to water. However the non-condensable gas will remain gaseous. Moreover, the non-condensable gas must also satisfy the equation of continuity

$$\frac{\partial \alpha_g \rho_g}{\partial t} + \nabla \cdot \left(\alpha_g \rho_g \mathbf{U}\right) = 0 . \tag{9}$$

The transport equation of the vapour volume fraction remains

$$\frac{\partial \alpha_v}{\partial t} + \nabla \cdot \left(\alpha_v \mathbf{U}\right) = -\frac{\dot{m}}{\rho_v} = \mathrm{S} . \tag{10}$$

The mass transfer rate can be expressed by the addition of equation (9) and (10)

$$\mathrm{S} = -\frac{\dot{m}}{\rho_v} = \frac{\mathrm{D}\left(\alpha_v + \alpha_g\right)}{\mathrm{D}t} + \left(\alpha_v + \alpha_g\right)\nabla \cdot \mathbf{U} . \tag{11}$$

From the continuity equation and equation (6) the velocity divergence can be derived as

$$\nabla \cdot \mathbf{U} = -\frac{1}{\rho}\frac{\mathrm{D}\rho}{\mathrm{D}t} = \frac{\rho_l - \rho_v}{\rho}\frac{\mathrm{D}\alpha_v}{\mathrm{D}t} + \frac{\rho_l - \rho_g}{\rho}\frac{\mathrm{D}\alpha_g}{\mathrm{D}t}, \tag{12}$$

therefore equation (11) becomes

$$\mathrm{S} = \frac{\mathrm{D}\left(\alpha_v + \alpha_g\right)}{\mathrm{D}t} + \left(\alpha_v + \alpha_g\right)\frac{\rho_l - \rho_v}{\rho}\frac{\mathrm{D}\alpha_v}{\mathrm{D}t} + \left(\alpha_v + \alpha_g\right)\frac{\rho_l - \rho_g}{\rho}\frac{\mathrm{D}\alpha_g}{\mathrm{D}t}. \tag{13}$$

Approximating that $\frac{\rho_l - \rho_v}{\rho} = 1$ and $\frac{\rho_l - \rho_g}{\rho} = 1$, equation (13) reads

$$\mathrm{S} = \left(1 + \left(\alpha_v + \alpha_g\right)\right)\frac{\mathrm{D}\left(\alpha_v + \alpha_g\right)}{\mathrm{D}t} = \left(2 - \alpha_l\right)\left(1 - \alpha_v - \alpha_g\right)\left(\alpha_v + \alpha_g\right)\frac{3\dot{R}}{R}. \tag{15}$$

The final expression of the mass transfer rate is

$$\dot{m} = \rho_v\left(2 - \alpha_l\right)\left(1 - \alpha_v - \alpha_g\right)\left(\alpha_v + \alpha_g\right)\frac{3}{R}\mathrm{sgn}\left(p_v - p\right)\sqrt{\frac{2}{3}\frac{|p_v - p|}{\rho_l}}. \tag{16}$$

where $R = \sqrt[3]{\dfrac{\alpha_v + \alpha_g}{n_0 \dfrac{4}{3}\pi\left(1 - \alpha_v - \alpha_g\right)}}$.

3. Computational Configurations

A NACA15 profile with chord length 81 mm is mounted at an angle of attack of 8° with a free stream velocity $\mathbf{V}_\infty$ =7.1 m/s. The Reynolds number, $\mathrm{Re} = \mathbf{v}L/\nu$, for this flow is Re = 5.75e5 and the simulated cavitation number, $\sigma = \left(p - p_v\right)/\left(0.5\rho\mathbf{V}_\infty^2\right)$, is 1.1. The computational domain extends two chord lengths upstream of the leading edge and ends four chord lengths behind the trailing edge, with a vertical extent 0.19m, see Fig. 2(a). The simulation is kept two-dimensional (2D) to facilitate a clear visualization on the simulated mechanisms. The wall resolution around the foil is y^+ = 34, see Fig. 2(b). For the detailed specifications, see Table 1.

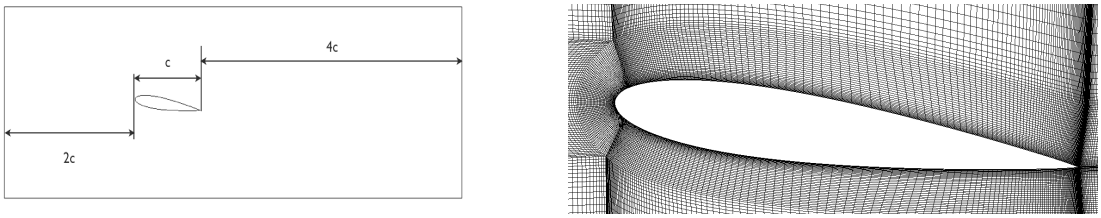

(a) (b)

Figure 1: The computational domain (a) and a close-up view of the grid around the foil (b).

Table 1. Computational configurations

Inlet Velocity	7.1	m/s
Outlet Pressure	101325	Pa
Vaporisation Pressure	73655	Pa
Liquid Density	998	kg/m^3
Gas Density	According to Ideal Gas Law	
Vapour Density	0.023	kg/m^3

4. Results

Compared with previous work in [1,6,11] on the same foil without the effect of non-condensable gas taken into account, the basic mechanisms that dominate the shedding remain unaltered – being the upstream moving collapse with the current resolution of the mesh. However,

in most shedding cycles, the simulations with gas content predict a more stratified sheet cavity while without gas the sheet is more unified and mostly of pure vapour. Moreover, there is noticeable variation in the thickness and extent of the cavity, demonstrated by Fig. 2 where the full extent of the cavity during its third shedding cycle is plotted for simulation without gas, with 1 ppm, 7 ppm and 13 ppm gas respectively. The simulation without any gas content predicts a slightly thicker cavity than the ones with gas, and when comparing only the simulations with gas, the higher the gas amount the longer the cavity extent. The finding that a higher gas content will likely result in a larger void fraction is supported and discussed in [12]. The following discussion will focus on the simulation with 7 ppm of gas.

The sheet is under an upstream moving collapse in Fig. 3, where the vapour volume fraction is plotted with contour lines and the gas volume fraction is plotted in the background. Compared with a commonly used approach plotting the void fraction, this plotting approach is adopted to best visualize the behaviour of the vapour and gas separately and still not losing the indication of interaction between the two phases. It should be pointed out that the vapour fraction is still the main indicator of the cavity shape.

Inside the cavities – the major sheet and the shed cavities in Fig. 3(a), the gas volume fraction is low as the liquid that vaporizes releases its portion of gas. One can also consider that in reality a certain amount of gas expands in the low-pressure region inside the cavity and its volume fraction does drop. As the sheet is moving in the upstream direction, two cavitating vortices are generated at the "tail" of the sheet, Fig. 3(b) to 3(d), where a high gas concentration is present. These two cavities are both shed from the main sheet, for some time almost looks like they are going to disappear, e.g. Fig. 3(d) the circled cavity is with a very low vapour fraction and finally starts to grow again, in Figs. 3(e) and 3(f). The author believes that the creation and growth of these cavities is still due to the strong shear flow between the free stream and the back flow. However, if the presence of gas influences the strength of these cavities and how much is still a task to be investigated carefully. In the circled cavity in Fig. 3(f), the gas volume fraction drops again as the cavity grows.

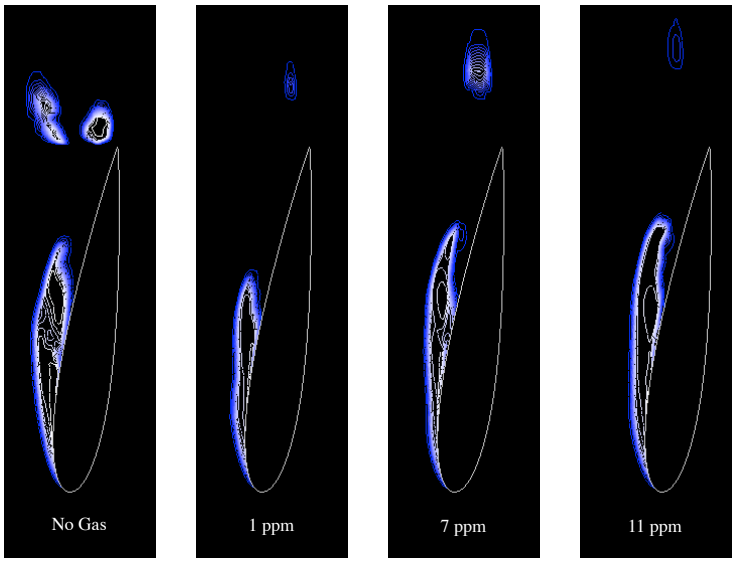

(a) (b) (c)

Figure 2: Full extent of cavity during its third shedding cycle predicted by simulation without gas (a), 1 ppm gas (b), 7 ppm gas(c) and 13 ppm gas (d). The plotted contours are vapour volume fraction, blue indicates pure liquid and white indicates pure vapour.

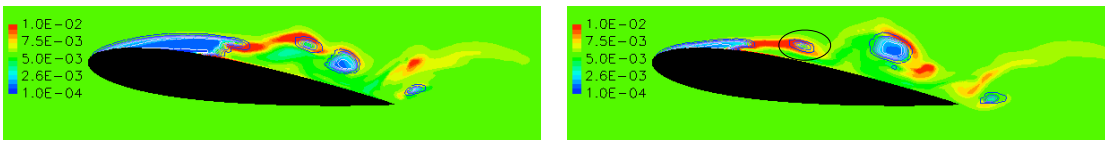

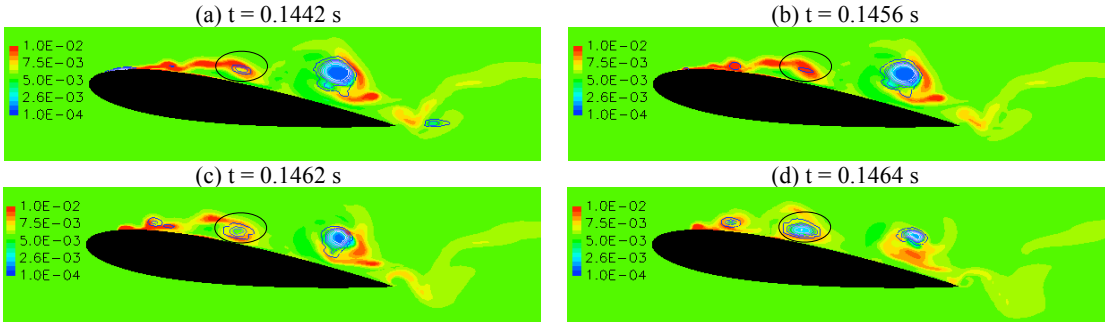

(a) t = 0.1442 s (b) t = 0.1456 s

(c) t = 0.1462 s (d) t = 0.1464 s

(e) t = 0.1470 s (f) t = 0.1478 s

Figure 3: Upstream moving collapse. Background indicates the gas volume fraction, with its colour scale illustrated by the legend. Contour lines indicate vapour volume fraction, where blue indicates pure liquid and white pure vapour.

The group of cavitating vortices generated from the upstream moving collapse eventually merge into a large cloudy structure and has been convected downstream close to the trailing edge in Fig. 4. At the same time at the trailing edge a cavity has grown from a vortex and later shed off from the surface. During the collapse of the cloud, i.e. Fig. 4(a) to Fig. 4(d), the trace of the fast condensation of vapour can be visualized through the gas volume fraction, until vapour completely disappears in Fig. 4(d). This increase in the gas fraction is in correspondence to physical observations when the violent cavitating flow can collect gas nuclei in its surrounding and release gas when vapour collapses. In the next two frames (e) and (f), vapour appears from the high concentration of gas and starts growing again. Whether this indicates a compression rebound should be further investigated.

After some collapsing and merging, the remnants of the cloudy structure is being further transported downstream in Fig. 5(a), and eventually disappears in frame (b). The “collected” gas released from the collapses remains as gas being mixed with the freestream liquid and transported to the far downstream. Qin et al. [5] has shown that the turbulent wake can be visualized through the evolution of gas in the far downstream. Due to the limited grid resolution in this region, this effect has not been captured in this work.

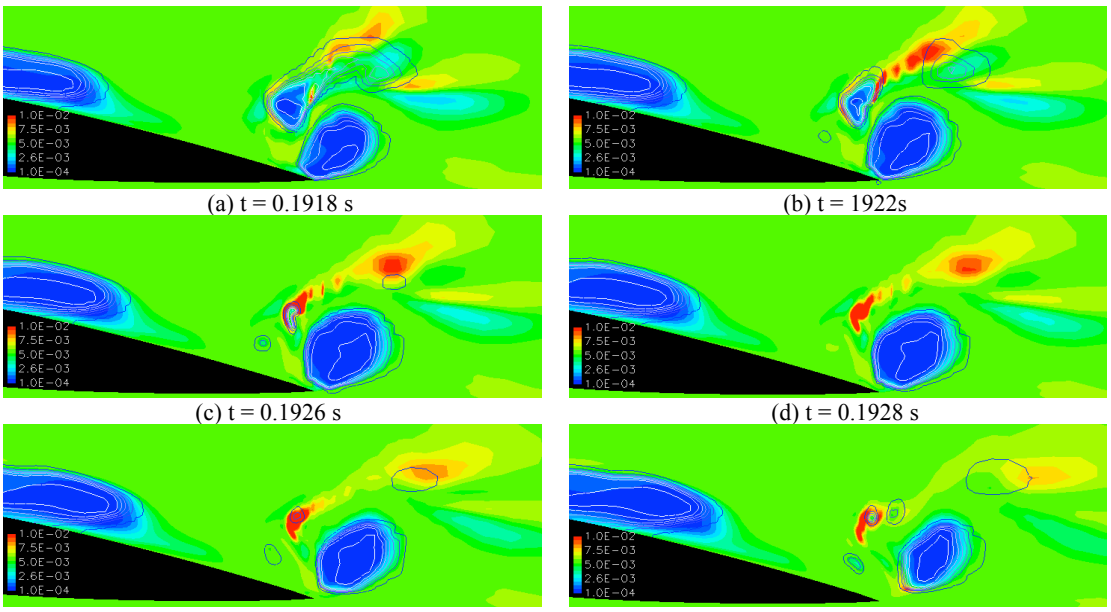

(a) t = 0.1918 s (b) t = 1922s

(c) t = 0.1926 s (d) t = 0.1928 s

(e) t = 0.1932 s (h) t = 0.1938 s

Figure 4: (a)-(d) collapse of the cloud; (e)-(f) rebound appears at almost the centre of high gas concentration.

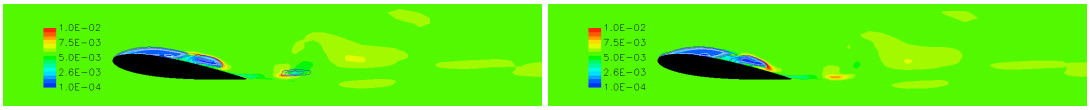

(a) t = 0.1698 s (b) t = 0.1796 s

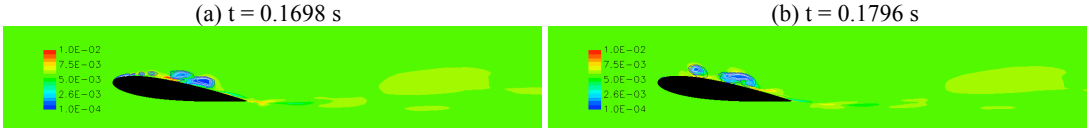

(c) t = 0.1758 s (d) t = 0.1782 s

Figure 5: Illustration of the gas "collected" by the collapses transporting downstream.

5. Concluding Remarks and Future Work

The non-condensable gas has been introduced to the Sauer's mass transfer model and some reasonable, although preliminary, results have been demonstrated on a 2D NACA15 hydrofoil. Simulations indicate firstly that the existence and amount of gas have an impact on the cavity length and thickness. Secondly the expanding behaviour of the gas inside cavity, and the possible interaction between gas and vapour seem to be realistic. At this stage it is still pre-mature to make the conclusion of whether the current simulation captures the compression rebound. It shall be carefully checked against the simulation without gas content, together with correctly plotted vector fields to identify the origin of the rebound. The impact of the initial gas mass fraction should also be studied as it clearly plays a role, at least in deciding the shape of the cavity, which can later affect the collapse strength and the erosion analysis.

6. Acknowledgement

This work is supported by Rolls Royce AB through the University Technology Center at Chalmers University of Technology. The computations were performed on C3SE computing resources.

7. References

[1] Lu N.-X., Bensow R.E., Bark G., 2011: Indicators of erosive cavitation in numerical simulations, *The 7th Internationl Workshop on Ship Hydrodynamics*, Shanghai, China.

[2] Franc J.-P., 2006 : Physics and Control of Cavitation. In Design and Analysis of High Seed Pumps (pp. 2-1 – 2-36). Educational Notes ROT-EN-AVT-142. Paper 2. Neuilly-sur-Seine, France.

[3] Kunz R., Boger F., Stinebring D.R., Chyczewski T.S., Lindau J.W., Gibeling H.J., Venkateswaran S., Govindan T.R., 2000 : A preconditioned Navier-Stokes method for two-phase flows with application to cavitation, *Computers and Fluids*, 29(8), pp. 849-875.

[4] Singhal A.K., Athavale M.M., Li H., Jiang Y., 2002: Mathematical basis and validation of the full cavitation model, *Journal of Fluids Engineering*, 124, pp. 617-624.

[5] Qin Q., Song C. C. S., Arndt R. E. A., 2003 : Incondensable gas effect on turbulent wake behind a cavitating hydrofoil, The 5th International Symposium on Cavitation, Osaka, Japan.

[6] LU Nai-xian, 2010 : Large Eddy Simulation of Cavitating Flow on Hydrofoils. Licentiate thesis, Chalmers University of Technology, Gothenburg, Sweden.

[7] Sauer J., Schnerr G. H., 2000 : Unsteady cavitating flow – a new cavitation model based on a modified front capturing method and bubble dynamics. *Fluids Engineering Summer Conference*, *Proceedings of FEDSM'00*.

[8] Weller H., Tabor G., Jasak H., Fureby C., 1998 : A tensorial approach to computational continuum mechanics using object-oriented techniques. *Computers in Physics*, **12**: 620-631.

[9] Berchiche, N., Bark, G., 2006: Numerical studies of cavitating flows around 2D foils, Chalmers University of Technology, VIRTUE Deliverable D4.4.3b.

[10] Li D-Q, Grekula M., 2008 : Prediction of dynamic shedding of cloud cavitation on a 3D twisted foil and comparison with experiments, *The 27th Symposium of Naval Hydrodynamics*, Seoul, Korea.

[11] Bensow R. E., 2011: Capturing Secondary Cavitation - A Step Towards Numerical Assessment of Cavitation Nuisance. Ship Technology Research, 58(2): 70-81.

[12] Arndt R. E. A., 2006: From Wageningen to Minnesota and back: Perspectives on cavitation research, *The 6th International Symposium on Cavitation*, Wageningen, The Netherlands.

The influence of phase difference and pitch axis position on the performance of heaving and pitching hydrofoils

J. Mattheijssens[1], J.-P. Marcel[1], W. Bosschaerts[1], D. Lefeber[2]
[1]Royal Military Academy, Department MECA
Renaissancelaan 30-1050 Brussel
[2]Vrije Universiteit Brussel, Robotics and Multibody Mechanics Group
Pleinlaan 2-1050 Brussel
email: joris.mattheijssens@rma.ac.be

1 Introduction

1.1 Literature review

Biologists and fluid dynamicists have applied a wide range of experimental and computational methods on various natural and artificial fish-inspired propulsive mechanisms. Below, an overview of the most important contributions is given. Since the carangiform mode, the swimming mode of tuna fish, is our main interest, the review of literature concerning other swimming modes is limited.

Lighthill [9] fomulated an elongated-body theory for the calculation of hydrodynamic forces on fish swimming in carangiform mode. One of the conclusions is that a long, slender tail fin, flapping with a small amplitude, guarantees high efficiency at high speeds because the tip vortex losses are limited.

Early panel method computations by Blake [3] of the pectoral fins of the angelfish showed already that for labriform swimming most of the power and thrust are generated by the outer part of the pectoral fins. A distinction can be made between a power stroke and a recovery stroke. During short periods of the flapping cycle, a small amount of negative thrust is generated.

Static foils at high angle of attack suffer from the *stall* phenomenon: a suddden decrease in lift due to separation of the leading edge vortex [1]. When a foil is oscillating, the stall is largely delayed: the separated leading edge vortex temporarily reattaches to the foil surface. This phenomenon is called *delayed* or *dynamic* stall [5]. Under optimal motion parameters, a reverse von Kármán street can be seen in the wake. The difference with a normal von Kármán street is that the vortices are inversely oriented, and that a central jet is generated. The body (the foil) experiences thrust instead of drag. Under less optimal conditions, secondary vortices are also shed, partly destroying the reverse von Kármán street and reducing the thrust force and the efficiency.

A series of linked elliptical vortex rings was observed during PIV experiments by Nauen and Lauder [11] on a mackerel, a caudal fin swimmer. This is the three-dimensional version of the reverse von Kármán street [15]. The heigth of the vortex rings was approximately equal to the fin span, while the length of the rings was dependent on the swimming speed. Between the rings, a strong jet was generated. Forces were calculated from the observed circulation in the wake. The lateral forces were approximately the double of the thrust force, and the pitching moment due to these was probably balaced by the pectoral fins in steady forward swimming. The inclination of the vortex rings with respect to the vertical symmetry plane of the fish differs significantly between different carangiform swimmers. The higher the inclination angle, the higher the ratio of the maximal lateral force to the maximal thrust force. Even labriform swimmers, with a completely different morphology and swimming motion, have a similar wake structure [8].

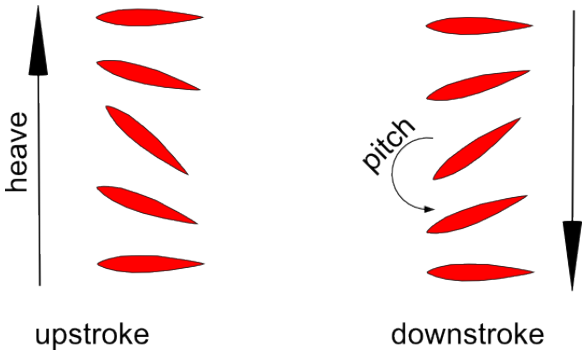

Figure 1: A foil in combined heaving and pitching motion

1.2 Current research

The motion of the hydrofoil in this study is a combination of heaving and pitching. The heaving motion is a sinusoidally varying sideward displacement of the foil. The pitching motion is a sinusoidally varying rotational angle of the foil around a spanwise axis. Between the two motions, there is a phase difference ϕ. Figure 1 illustrates these motions.

The heave motion can be described as

$$h(t) = h_0 \sin(2\pi f t) \tag{1}$$

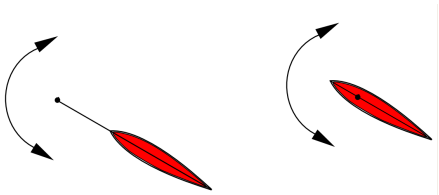

(a) Upstream of LE, $\frac{x_p}{c} > 1$ (b) Downstream of LE, $\frac{x_p}{c} < 1$

Figure 2: Pitching point position

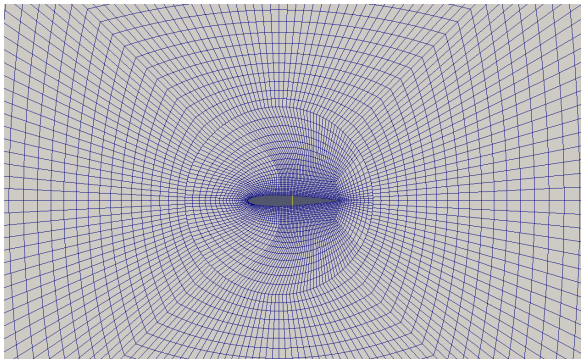

Figure 3: The mesh for the validation case

and the pitch motion as

$$\theta(t) = \theta_0 \sin(2\pi f t - \phi) \tag{2}$$

with h_0 the heave amplitude, f the frequency of both motions, θ_0 the pitch amplitude and ϕ the phase difference. The fin is an unflexible foil. An overview of fish swimming speeds by Bainbridge [2] shows that this motion yields excellent swimming speeds and efficiencies.

Most researchers focus on the frequency and the amplitudes of the heave and the pitch motion. The current research investigates the influence of two other important motion parameteres: the position of the pitch axis on the foil and the phase difference between the heave and pitch motion. The position of the pitch axis is nondimensionalized as $\frac{x_p}{c}$, with x_p the distance of the leading edge to the pitch point, postitive in the direction of the thrust, and c the chord length, see Figure 2.

The hydrodynamics, and more specifically the generated forces on these oscillating foils are studied using Computational Fluid Dynamics.

2 Computational Fluid Dynamics methodology applied to flapping foils

In order to have a better understanding of the complex wake and force generation of oscillating foils, Computational Fluid Dynamics (CFD) simulations have been made.

The main difficulties in the simulations are the moving foil and the complex flow characteristics. The motion of the foil was captured by a moving mesh method that allows large linear and rotational displacements, while conserving a good mesh quality. The complexity of the flow requires an advanced turbulence model.

2.1 Computational setup

The open-source CFD software OpenFOAM-1.6-ext was used for the simulations [12] [16]. Gradients and divergences were linearly discretized, time discretization is implicit Euler. The time step is adapted at run time, limiting the Courant flow number to 0.25. The cases were run for six motion cycles, to completely eliminate transient behaviour. The PIMPLE algorithm, which is a blend of PISO and SIMPLE, was used.

The simulation has a Reynolds chord number of $40,000$. Locally, the flow will have much higher velocities than the incoming velocity, since the foil is oscillating fast. A complex vortex-shedding pattern has been observed for even slightly oscillating foils.

Common turbulence models (algebraic models, kε, and kω) are not capable of tracking boundary layer detachment [17]. Several authors have used Menter's kω_{SST} model for pitching foils [14] [10]. Kim et al [7] compared six different two-equation models for turbulence of a typical detachment flow, the backwards facing step, for a Reyolds number of about $38,000$. The skin friction and pressure coefficient, our main interests since they determine the forces on the foil, were best captured by the standard kω and the kω_{SST} model. The latter proved to generate a more realistic flow field. In the boundary layer a wall function, conform the theory of Wilcox [17] was applied. A Large Eddy Simulation (LES) would be a good choice as well, but requires more computational time and power, and is not strictly applicable to a two-dimensional mesh.

2.2 Mesh

The foil's motion is rather wide and consists of a rotational and a translational component. A new class was written in order to keep a good mesh quality at all foil position. The foil is surrounded by a cylindrical inner part of the mesh. The cylinder fits in a hole in a rectangular outer mesh. Between the two parts of the mesh, a mapping of the variables is done using Generalized Grid Interface (GGI) [4]. The mesh of the cylinder moves as one block, while the outer mesh deforms as the cylinder moves inside. Figure 3 shows a detail of this mesh.

Four different mesh sizes were tested for the validation case: 3k, 6k, 12k and 24k cells. The local continuity errors for these runs were calculated. The coarsest mesh did not converge; the second coarsest mesh has very low errors; the errors of the two finest meshes cannot be distinguished anymore. Figure 4 shows the time history of the residuals of the continuity equation for the different mesh sizes. Hence, the mesh with only

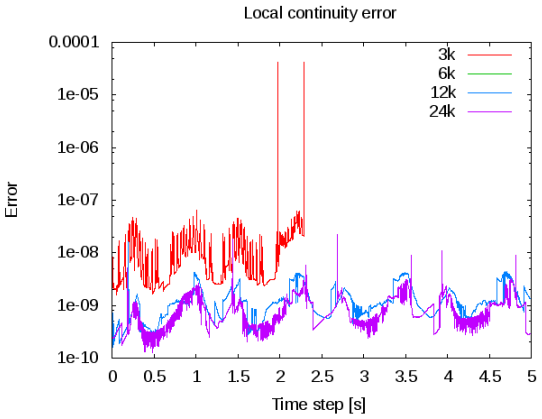

Figure 4: Residuals for the validation case

12k cells is optimally refined.

2.3 Performance parameters

Since the oscillating foil is to be used for the propulsion of ships, the most important performance parameters are the thrust and the efficiency. The average thrust coefficient is defined as

$$c_T = \frac{-\overline{F_x}}{0.5\rho U_0^2 cs} \tag{3}$$

where averaging is done over the last three motion cycles. The efficiency is

$$\eta = \frac{-\overline{F_x} U_0}{\overline{F_y \dot{h}} + \overline{M_z \dot{\theta}}} \tag{4}$$

with F_x and F_y the force on the foil in the direction of the main flow and perpendicular to it, respectively, M_z the pitching moment acting on the foil and around the pitch axis, ρ the density of the fluid and U_0 the inflow speed.

2.4 Validation Case

Read et al. [13] performed force measurements on a stiff heaving and pitching NACA0012 with chord length 100 mm and span 600 mm. Since the tips were covered with large end plates, which moved along with the foil, the flow field is almost two-dimensional. The pitch axis is 1/3 chord length behind the leading edge. The heave amplitude is one chord length, the pitch amplitude 26°, the frequency 0.8 Hz and the phase difference between both motions is 90°. Between the inflow speed and the average pitch position of the foil there is a bias angle of 10°. The inflow speed is 0.4 m/s. The Strouhal number, defined as $St = \frac{2fh_0}{U_0}$ is equal to 0.4. Further details can be found in [13].

Figures 5 and 6 show the good comparison of the thrust and lift coefficients.

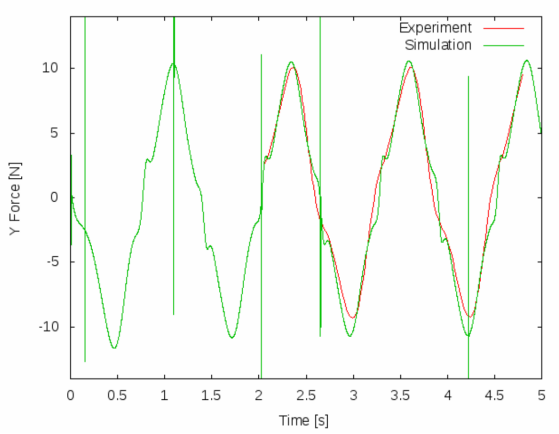

Figure 5: Time history of the lift coefficient for the validation case

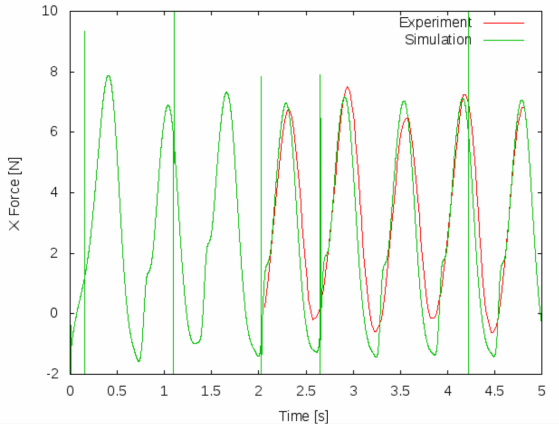

Figure 6: Time history of the thrust coefficient for the validation case

3 Results

Heaving and pitching foils were simulated for a range of phase differences and pitch axis locations. For all cases, the Reynolds number was 40,000, the Strouhal number was equal to 0.4, the heave amplitude was one chord length and the pitch amplitude was 40.11°. From [13], this combination is known to have high efficiency when the phase difference is 90° and the pitch point is at $1/3$ chord length behind the leading edge.

The phase difference range is

$$\phi = \{60^\circ, 75^\circ, 90^\circ, 105^\circ, 120^\circ\}$$

while the pitch axis position range is

$$\frac{x_p}{c} = \{-1.0, -0.5, 0.0, 0.5, 1.0\}$$

Contourplots of the thrust coefficient and efficiency for these ranges are shown is Figures 7 and 8. The highest thrust force is obtained for low phase difference and high x_p/c, i.e. for a pitching motion that lags less than 90° and a pitching axis that is far upstream of the leading edge. However, the efficiency is very low in this zone. The isolines of efficiency are almost straight, diagonal lines. This means that changing the phase difference or the pitch axis position, has a similar effect on the efficiency (but not on the thrust!).

There is a clear relationship between the flow field and the performance parameters. The central jet generated by the oscillating hydrofoil is visualized in Figure 9, by plotting the x-component of the flow field, u, for the extremes of the parameter ranges. The vorticity of the flow, $\omega_z = \frac{\partial u}{\partial y} - \frac{\partial v}{\partial x}$, is plotted in Figure 10. The strongest jet is found for low phase difference and high x_p/c, i.e. Figure 9(a). This corresponds to the highest thrust coefficient. The largest vortices with the largest lateral spacing are found in the corresponding Figure 10(a).

Figures 9(b) and 9(c) have a moderate u in the central jet. The vortices are still very large in Figure 10(b), but their lateral spacing is small. This is a so called neutral wake. Figure 10(c) yields only small vortices, but with reasonable lateral spacing. Both combinations b and c result in moderate thrust, but relatively high efficiency.

The flow field in Figure 9(d) is seriously distorted, with secondary vortices, visible in 10(d). A negative thrust coefficient (drag) and low efficiency are the results of this unfavourable combination of a pitch axis that is far downstream and a high phase difference.

4 Conclusions

The performance of heaving and pitching hydrofoils has been studied using CFD. The good comparison between our results and experiments found in the literature show our capability to calculate the forces accurately. The large influence of the phase difference and the pitch axis position, two parameters that have received little attention so far, on the thrust and efficiency, is demonstrated.

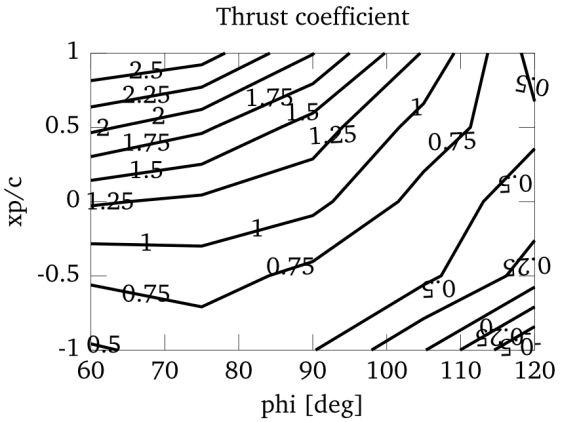

Figure 7: Thrust coefficient

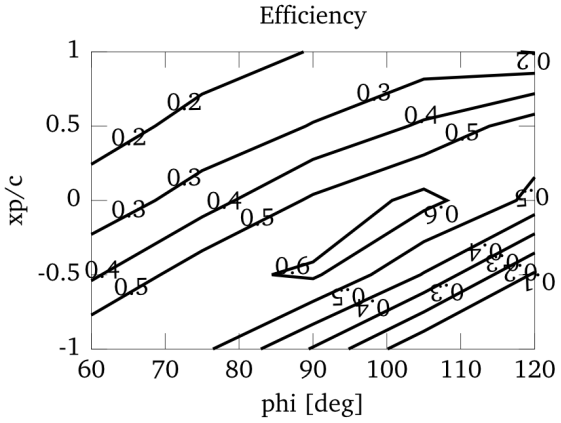

Figure 8: Efficiency

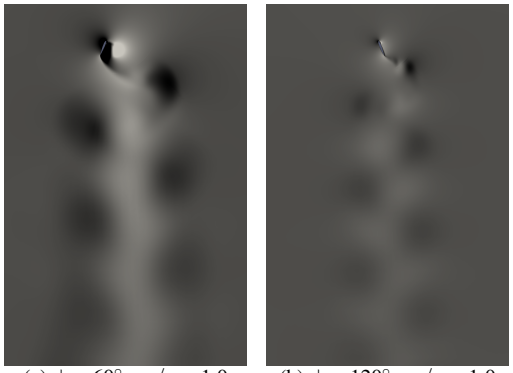

(a) $\phi = 60°; x_p/c = 1.0$ (b) $\phi = 120°; x_p/c = 1.0$

(c) $\phi = 60°; x_p/c = -1.0$ (d) $\phi = 120°; x_p/c = -1.0$

Figure 9: X-component of velocity u, black ≤ 0 ms^{-1}, white ≥ 1 ms^{-1}

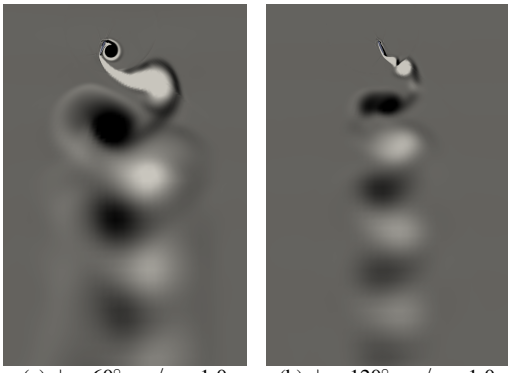

(a) $\phi = 60°; x_p/c = 1.0$ (b) $\phi = 120°; x_p/c = 1.0$

(c) $\phi = 60°; x_p/c = -1.0$ (d) $\phi = 120°; x_p/c = -1.0$

Figure 10: Vorticity ω_z, black $= -5$ s^{-1} (clockwise), white $= +5$ s^{-1} (counterclockwise)

References

[1] Abbott, I. H., and Von Doenhoff, A. E., 1959, *Theory of Wing Sections* Dover Publications Inc.

[2] Bainbridge, R., 1958, *The Speed of Swimming of Fish as related to Size and to the Frequency and Amplitude of the Tail Beat*, Journal of Experimental Biology, vol. 35, no. pp 109–133.

[3] Blake, R. W., 1979, *The mechanics of Labriform locomotion*, Journal of Experimental Biology, vol. 82, pp. 255–271.

[4] Beaudoin, M., Jasak, H., 2008, *Development of a Generalized Grid Interface for Turbomachinery Simulations with OpenFOAM*, Open Source CFD International Conference 2008, Berlin, Germany.

[5] Dickinson, M., 1996, *Unsteady mechanisms of force generation in aquatic and aerial locomotion*, American Zoologist, vol. 36, pp. 537–554.

[6] Jasak, H., 1996, *Error Analysis and Estimation for the finite Volume Method with Application to Fluid Flows*, PhD thesis, London Imperial College.

[7] Kim, J.-Y., Ghajar, A. J., Tang, C., Foutch, G. L., 2005, *Comparison of near-wall treatment methods for high Reynolds number backward-facing step flow*, International Journal of Computational Fluid Dynamics, vol. 19, no. 7, pp. 493-500.

[8] Lauder, G. V., Drucker, E. G., Nauen, J. C. & Wilga, C. D., 2003, *Experimental hydrodynamics and evolution: caudal fin locomotion in fishes*, Vertebrae Biomechanics and Evolution, (ed. Bles, L. V., Gasc, J.-P., & Casinos, A.), pp. 117–135.

[9] Lighthill, M. J., 1971, *Large-amplitude elongated-body theory of fish locomotion*, Proceeding of the Royal Society of London, Series B. Biologocal Sciences vol. 179, pp. 125–138.

[10] Menter, F. R., 1993, *Zonal Two Equation k- Turbulence Models for Aerodynamic Flows*, AIAA Paper 93-2906.

[11] Nauen, J. C. & Lauder, G. V., 2002, *Hydrodynamics of caudal fin locomotion by chub mackerel, Scomber japonicus (Scombridae)*, Journal of Experimental Biology, vol. 205, pp. 1709–1724.

[12] *OpenFOAM User Guide Version 1.6*, 2009, Free Software Foundation Inc., OpenCFD Ltd.

[13] Read, D. A., Hover, F. S., Triantafyllou, M. S., 2003, *Forces on oscillating foils for propulsion and maneuvering*, Journal of Fluids and Structures, vol. 17, pp. 163-183, Elsevier Science Ltd.

[14] Spentzos A. et al., 2005, *CFD Investigation of 2D and 3D Dynamic Stall*, AIAA Journal, vol. 34 no. 5, 1023-1033.

[15] Tyell, E. D., Standen, E. M. & Lauder, G. V., 2008, *Escaping Flatland: three-dimensional kinematics and hydrodynamics of median fins in fishes*, Journal of Experimental Biology, vol. 211, pp. 187–195.

[16] Weller, H. G., Tabor, G., Jasak, H., Fureby, C., 1998, *A tensorial approach to computational continuum mechanics using object-oriented techniques*, Computers in Physics, vol. 12, no. 6, American Institute of Physics.

[17] Wilcox, D.C., 1994, *Turbulence Modeling for CFD*, DCW Industries, Inc.

Simulation of Extreme Motion of Floating Bodies Using Overlapping Grids

Milovan Perić and Eberhard Schreck, CD-adapco, Nürnberg Office, Germany
Milovan.Peric@cd-adapco.com, Eberhard.Schreck@cd-adapco.com

Introduction

Overlapping (or Chimera) grids have been used in the past by various authors, but the application was usually limited to structured grids and a weakly coupled solution approach was used. Thereby the computation is performed sequentially on each grid, and the coupling between the grids is achieved via a combination of inlet (where flow enters solution domain) and pressure (where flow leaves solution domain) boundary conditions at overlapping grid boundaries.

Recently, CD-adapco developed an improved overlapping grid approach, which has the following features:

- Any number of overlapping grids can be used;
- Each grid can be of any type (arbitrary polyhedra);
- Individual grids can fall partly outside solution domain;
- The solution is obtained on all grids simultaneously (a tight coupling of all equations through the coefficient matrix is achieved).

This method has substantial advantages over the currently available approaches in several important application areas:

- In the case of steady flow around bodies at various relative positions, one needs to generate the individual grids only once and can then compute the flow for many combinations of relative body positions by simply moving grids around (no need to generate new grids or change boundary conditions).
- Unsteady flow around bodies moving relative to each other are easier handled than by using sliding or deforming grids (e.g. for vessels passing each other, vessels entering harbor, lifeboat launching from a platform etc.).
- Flow around and motion of flying or floating bodies can be simulated for an arbitrary motion by moving the grid attached to each body with it (with little or no deformation), while the background grid can be adapted to arbitrarily shaped surroundings and environmental conditions (wind and waves).

In the the following sections, the solution method is briefly described and a number of application examples from the above mentioned areas are shown to demonstrate the versatility and applicability of the new method.

Solution Method

The solution method using overlapping grids was implemented into STAR-CCM+ code. The basic numerical method is of finite-volume (FV) type and will not be described here; details can be found in literature [1-5]. Here only the method of solution on overlapping grids is described.

One grid is adapted to environment without the body and is called *background grid*. One of more grids are attached to moving bodies; they extend to some distance from the body and are called *overset grids*. The method analyzes the relations between all grids involved and classifies the cells as either *active* or *passive*. In active cells, regular discretized equations are solved. Passive cells are temporarily (for unsteady flows with moving grids) or permanently (for steady-state flows) deactivated; no equation is solved in these cells, but they are (in the case of temporary deactivation) kept in the grid system as they may become active at later times.

The first layer of active cells next to passive cells requires special treatment, since some of its neighbors are deactivated. Variable values at passive cells which are referenced by active cells are expressed through variable values at active cells from another grid. This is best explained with reference to Fig. 1, which shows schematically computational molecules for one last active cell on both overset and background mesh.

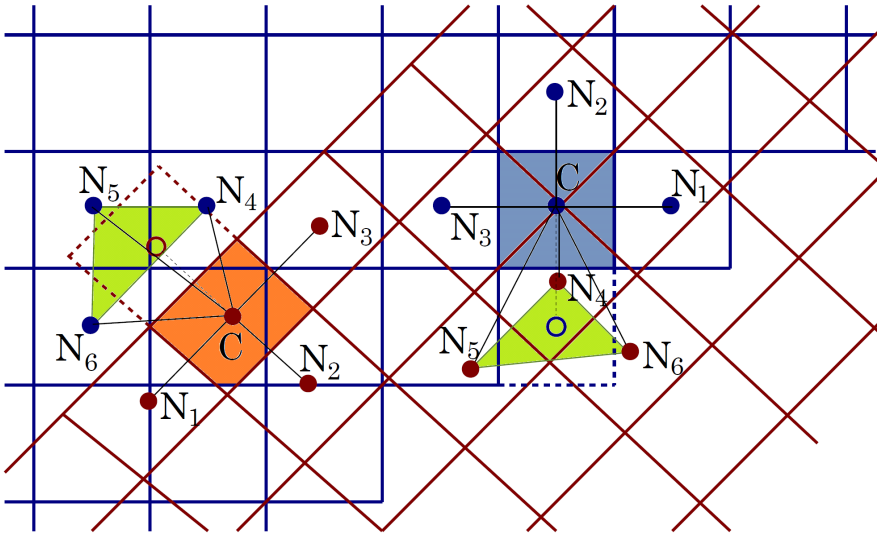

Fig. 1: Computational molecules for one active cell next to passive cells in both background (blue) and overset (red) grid in two dimensions.

The cell around node C has three active neighbors on the same grid and it has one passive neighbor cell (here called *acceptor cell*). The variable value at the center of acceptor cell is expressed through values at three active cells (donors) in the grid which overlaps the passive cell via an interpolation function (e.g. linear interpolation). In three dimensions, one needs at least 4 donors (a tetrahedron as interpolation element). Higher order interpolations involving more donors are also possible – the linear interpolation is only an example.

The fluxes through the face common to the active and passive cell are thus expressed in terms of value at cell center C and three neighbors from another grid, N_4, N_5 and N_6. The coefficient matrix of the linear equation system contains thus three coefficients pointing to neighbors N_1, N_2 and N_3 on the same grid and three nodes on the overlapping grid. Therefore, all grids are implicitly coupled within the linearized coefficient matrix of every equation solved – there are no internal boundaries and the solution is, at each iteration level, computed simultaneously on all grids. This ensures that the iterative solution method can be converged down to the round-off level of residuals, and that the convergence rate is similar to what would be obtained for the same problem on a single grid. More details about several options related to grid coupling can be found in PhD thesis of H. Hadžić [5].

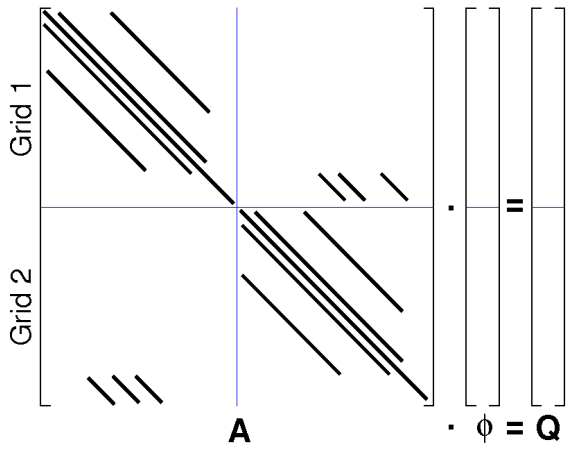

Fig. 2: A schematic representation of resulting coefficient matrix for a system of one background and one overset grid.

Figure 2 shows an example of what the coefficient matrix for one background and one overset grid might look like: in addition to block matrices containing coefficients that multiply variable values from the same grid, there are also coupling matrices that contain coefficients multiplying variable values at donor cells from the other grid.

There are, however, some requirements that should be taken into account when computing flows using overlapping grids. If grid overlapping takes place in small gaps between solid walls belonging to different grids, any such gap has to be discretized by at least four cells. This is necessary in order to ensure that there are enough donors for each acceptor cell in each grid.

The cell size in the overlapping region should be similar on all grids that overlap, at least in the direction normal to the overlap interface (i.e. the surface between active and passive cells). This is desirable for accuracy reasons, especially if the overlap zone is in the region of significant variation of variables (e.g. near walls, in shear layers or in recirculation zones). If there are no constraining walls, the method will work even if cells sizes are different, but the accuracy of interpolation on the coarser grid will determine the accuracy of grid coupling.

The next section describes some examples of application, which emphasize the advantages of overlapping grids compared to other alternatives.

Simulation of Lifeboat Launching

Lifeboats are launched from a position high above water; they fly through the air subject to wind and initial conditions, impact water surface whose shape depends on current and waves, and upon re-surfacing switch on their own propulsion system to move away from danger. Simulation of this process is important for many reasons, an important one being that some conditions cannot be realized in an experiment (drop height, wind, current and waves). On one hand, structural integrity of the boat is important, but on the other hand, people inside it must not be subjected to too high decelerations over a too long period. Also, the boat should not dive too deep into water (which would be one way of minimizing decelerations) but should re-surface as soon as possible and move away under all conditions. Taking into account that current and wind can come from any direction, that waves can propagate in any direction, have any amplitude and period within expected range, and that the boat can impact water at any location relative to wave crest make it obvious that the number of parameters to investigate is huge.

The use of overlapping (also called “overset”) grids makes the simulation of this kind of problems much simpler than with any alternative approach. One defines the background region such that it accommodates the environment: if regular, long-crested waves are assumed, one can have a rectangular domain with inlet conditions (water level and velocity specified with the help of wave theory, e.g. Stokes 5th-order wave) on one side, symmetry conditions on two sides parallel to wave propagation direction, and a damping zone towards outlet opposite to inlet. Top boundary can usually be modeled as a slip wall, while bottom boundary can be either sea bed (shallow water), inlet with conditions from wave theory (long wavelengths) or slip wall (deep water). The grid needs to satisfy the requirements for accurate wave propagation (e.g. 80 cells per wavelength and 20 cells per wave height) with gradual coarsening in vertical direction, while it can be coarse in the lateral direction. Only in the impact zone one needs to refine the grid also in the lateral zone. The overset region can be a box, cylinder or any other regular shape from which the lifeboat has been substracted. The boat surface would be a no-slip wall boundary, and the outer surface is not a physical boundary since it will be embedded in the background mesh.

One can now easily simulate the process for various drop heights, orientations of the lifeboat and impact position on the wave without changing grids or boundary conditions – just moving the initial position of the overset region around. This can be easily automated, allowing automatic and parallel execution of simulations for many parameters (akin to parametric studies in shape optimization).

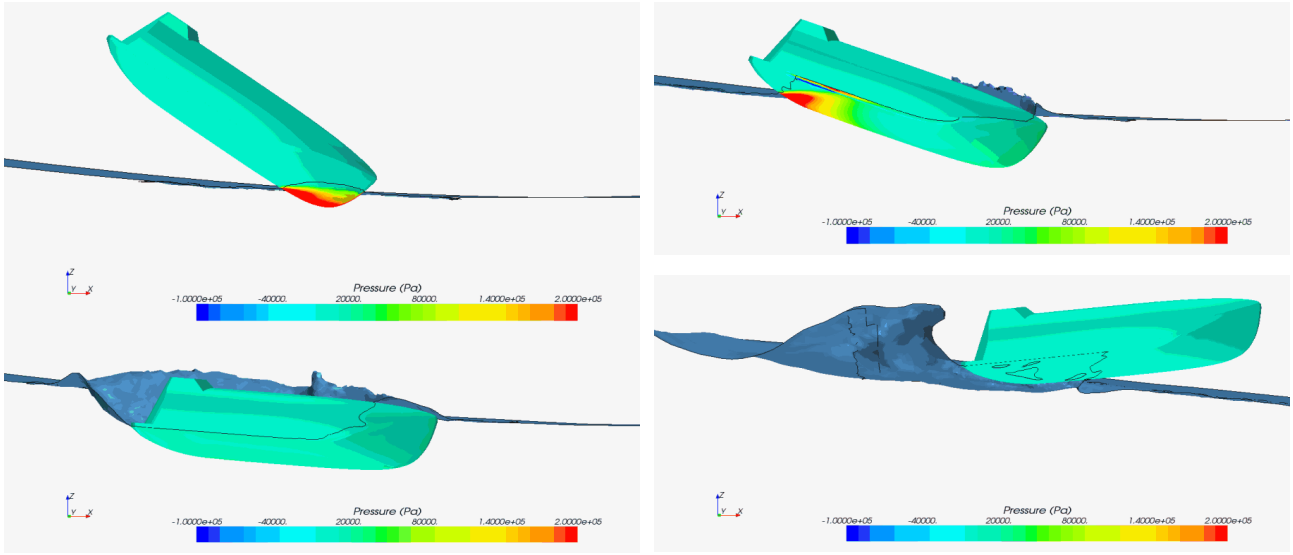

Fig. 3: Lifeboat falling into a Stokes wave propagating from left to right: pressure distribution shortly after impact (top left) and shortly before stern is submerged (top right), at deepest submergence, with a large air cavity behind stern (bottom left) and after resurfacing and the collapse of the air cavity (bottom right).

Figure 3 shows an example of a lifeboat in model scale falling into a Stokes wave (propagating from left to right) close to the troth. Within red zone pressures are above 2 bar. Note the rotation of the boat after the bow hits water, due to a relatively low impact angle. This causes the boat not to dive deeply into water, but at the same time leads to much higher decelerations at the stern than at the bow. A large air cavity is formed behind the boat as it dives into water. The large amount of water displaced by the boat finally comes back to fill the air cavity, creating a big splash. In this final stage compressibility of air needs to be taken into account in order to correctly predict pressures at the stern

region. Mørch et al [6] presented effects of geometry modifications on lifeboat motion during water entry; effects of impact point on a wave were investigated in another work by Mørch et al [7].

Simulation of Vessel Motion in Oblique Waves

Another application for which overlapping grids are predestined is the simulation of vessel motion in oblique waves. Again, the background grid is adapted to waves, while the overset grid is attached to the vessel. One can easily set up a simulation for another angle between vessel and wave propagation by simply repositioning the overset grid, without changing grids or boundary conditions. This facilitates automation of simulation process.

Figure 4 shows a vessel (KRISO container ship) without forward speed exposed to Stokes 5th-order waves with -30° and +30° incidence. Simulation is performed with STAR-CCM+ using the same set of grids in both cases; for one simulation, the overset region has been rotates by 30° clockwise and for the other by 30° counter-clockwise. This allows one to simulate the stability of a vessel whose engine is not running and e.g. assess the effectiveness of bilge keels.

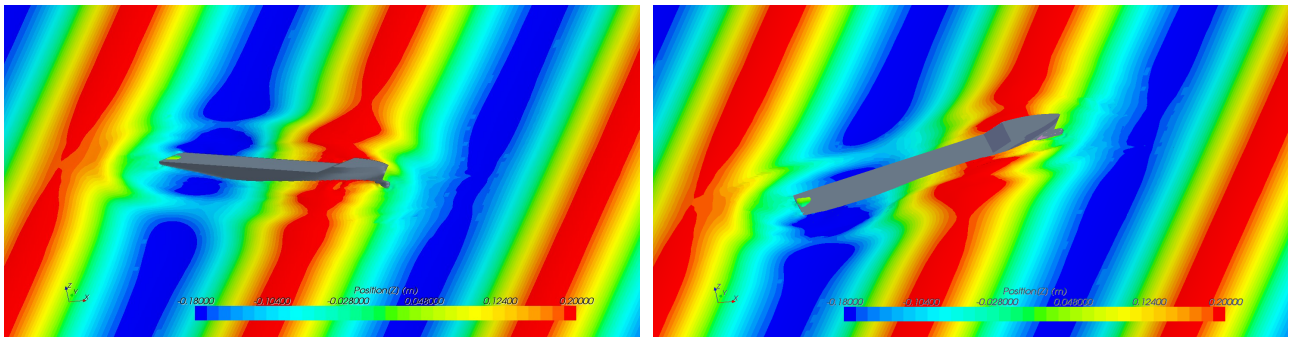

Fig. 4: Simulation of motion of a container ship in Stokes waves propagating from right to left: initial vessel orientation 30° (left) and -30° (right) relative to the direction of wave propagation .

Simulation of Relative Motion of two Vessels with Crossing Paths

When a smaller vessel crosses the wake of a larger one, it can experience severe roll motion, leading in extreme cases to capsizing. Simulation of motion of two vessels whose paths are crossing is relatively simple when overlapping grids are used, while it would be very difficult otherwise. The alternative is a combination of mesh morphing accounting for the motion of both vessels, and regridding when the mesh quality becomes poor. Such a simulation is more difficult to set up and control, requires many events of mesh generation and data mapping from one grid to another, and suffers from the poor mesh quality in the critical zone near vessels over a large portion of simulation. With overlapping grids, the grid remains always the same and interpolation of data takes place only in the overlap zone which is far from the critical regions near vessels.

Figure 5 shows an example of a simulation of relative motion of one large and one small vessel. The background region is a simple block with a Cartesian grid which is only adapted to free surface. The large vessel moves from left to right, while the small vessel crosses its wake at right angle. Each vessel is embedded in an overset grid region that moves with it as a rigid body. The large vessel is free to trim and sink, while the small vessel has all six degrees of motion. The small vessel undergoes severe roll motion and barely remains afloat as it crosses oblique waves generated by the passing large vessel.

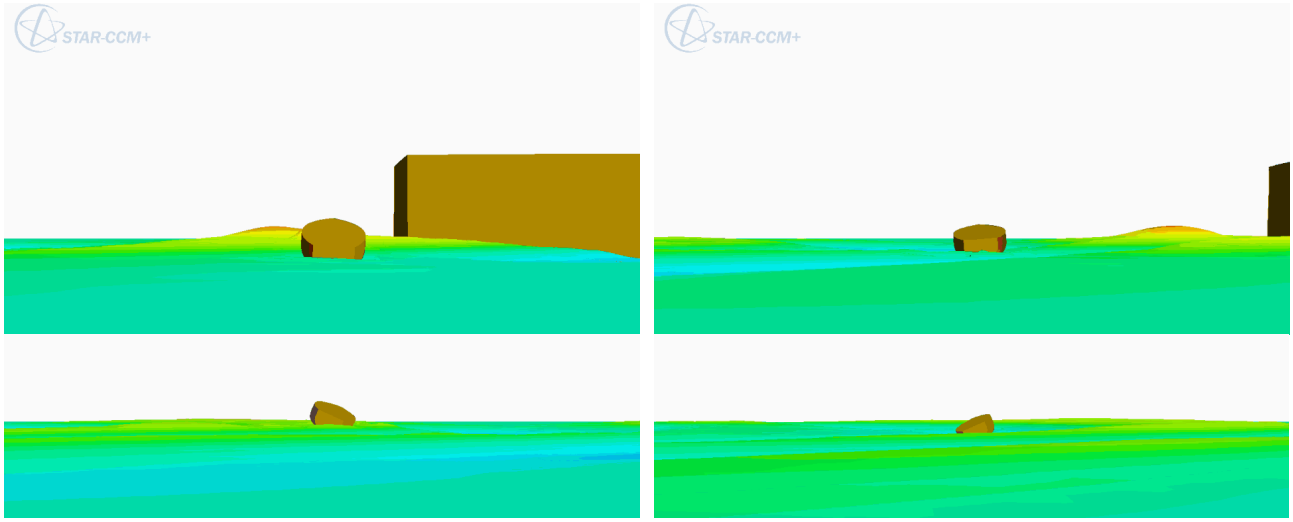

Fig. 5: Simulation of relative motion of two vessels crossing each others path: small vessel approaching the wake of the large vessel (top left); large vessel leaving the scene, small vessel entering the wake (top right); small vessel struggling not to capsize while crossing the waves generated by the large vessel (bottom left and bottom right).

Overlapping grids are especially suitable for simulation of relative motion of vessels in shallow water, like in rivers and channels. There it can happen that a smaller vessel is attracted towards the larger vessel due to asymmetric pressure distribution as the larger vessel moves close by and simulation can help predict forces and required countermeasures to prevent an accident.

References

1. Demirdžić, I., Muzaferija S.: Numerical method for coupled fluid flow, heat transfer and stress analysis using unstructured moving meshes with cells of arbitrary topology, *Comput. Methods Appl. Mech. Engrg.*, Vol. **125**, pp. 235-255 (1995).
2. Ferziger, J.H., Perić, M., *Computational Methods for Fluid Dynamics*, 3rd ed., Springer, Berlin, 2003.
3. Muzaferija, S., Perić, M.: Computation of free surface flows using interface-tracking and interface-capturing methods, chap. 2 in O. Mahrenholtz and M. Markiewicz (eds.), *Nonlinear Water Wave Interaction*, pp. 59-100,WIT Press, Southampton, 1999.
4. Xing-Kaeding, Y., Unified approach to ship seakeeping and maneuvering by a RANSE method, Dissertation, TU Hamburg-Harburg, 2005.
5. Hadžić, H.: Development and application of a finite-volume method for the computation of flows around moving bodies on unstructured, overlapping grids, Dissertation, TU Hamburg-Harburg, 2005.
6. Mørch, H.J., Enger, S., Perić, M., Schreck, E.: Simulation of lifeboat launching under storm conditions, *Proc. 6th Int. Conf. on CFD in Oil & Gas, Metalurgical and Process Industries*, SINTEF/NTNU, Trondheim, Norway, June 10-12, 2008.
7. Mørch, H.J., Perić, M., Schreck, E., El Moctar, O., Zorn, T.: Simulation of flow and motion of lifeboats, *Paper OMAE2009-79608*, 2009.

Numerical modelling and error estimation of the flow behind marine propellers

Robert Pfannenschmidt, Lars Greitsch, Martin Greve

pfannenschmidt@mmg-propeller.de
Mecklenburger Metallguss GmbH, Germany

Introduction

The open water characteristic is a key element in evaluating the design of marine propellers as the prediction procedure of the propulsive performance is still based on conventional model tests including the open water test. Numerical simulations of the propeller open water performance show good agreement with these experiments in terms of the integral values thrust and torque. Typically, propeller open water tests (POT) are carried out with the propeller ahead of the dynamometer. Studying flow details like partially detached flow in the region past the propeller hub requires to reverse the POT set-up. Reverse POTs conducted by Heinke [3] show that the cap shape influence on the thrust of the propeller–cap system is on the order of one per cent. In view of significantly increased fuel costs and the government driven requirements as the Energy Efficiency Design Index (EEDI), even this small difference in efficiency becomes important.

Propulsion improving devices (PIDs) which focus on hub near vortex losses are of special interest in case of newbuildings as well as in case of retrofits, because of low installation costs and reliable saving effects. An important precondition for the design of these PIDs is the proper numerical consideration of dominant flow properties. Therefore, the paper deals with a study of the capability of capturing flow details like dead water areas behind propeller caps by using systematically optimised grids.

The investigation is based on three different cap shapes and different grid refinement criteria. Coming from more globally optimised grids based on a global criterion the study also includes local grid optimisation under consideration of local grid refinement criteria. All calculations are carried out as open water set-ups using the grid convergence index (GCI) method as recommended by the Journal of Fluids Engineering [1] in order to obtain grid indepedent solutions. Thus, the work has to be seen as a groundwork for further investigations of hub near flow characteristics with and without propulsion improving devices.

The work presented in this paper is part of the project BossCEff, which is funded by the German Ministry of Economy and Technology (BMWi). Aim of the project is to develop design methods for propeller cap configurations with special focus on the energy saving potential.

Methods

The computations were conducted using the commercial solver ANSYS CFX 14, a finite volume (U)RANS-method. The convective term is discretized using a second order upwind scheme and a high-resolution advection scheme is applied. The continuity and momentum equations are fully coupled using an implicit algorithm. For solving the linear equation system an algebraic multigrid (AMG) accelerated incomplete lower-upper (ILU) factorization technique is used.

For modeling the turbulence the SST model is employed, which blends the k-ω model in the inner part and a k-ε model in the outer part of the boundary layer. The simulations were carried out in steady state using a frozen rotor interface between rotating and stationary parts of the domain.

To determine grid independence of the calculation results we followed the grid convergence index (GCI) method as described by Celik [2] which is based on the Richardson Extrapolation (see e.g. [6]). When applying the GCI method to unstructured grids in a domain having constant flow volume the defini-

tion of an effective refinement ratio r_{cf} is

$$r_{cf} = \left(\frac{N_f}{N_c}\right)^{1/d}, \tag{1}$$

where N is the number of nodes of consecutive grids and the subscripts c and f denote for the coarse and the fine grid. The factor d accounts for the number of dimensions of the flow problem. The value of r_{cf} should be around 1.3. According to [2] three structurally refined grids should be used. When the variable of interest ϕ is a global quantity the grid refinement is also to be globally and should be performed in structural manner even if the grid topology is unstructured.

The apparent order of the method p can be determined by.

$$p = \frac{1}{ln(r_{21})}|ln|\varepsilon_{32}/\varepsilon_{21}| + q(p)| \tag{2a}$$

$$q(p) = ln\left(\frac{r_{21}^p - s}{r_{32}^p - s}\right) \tag{2b}$$

$$s = 1 \cdot sgn(\varepsilon_{32}/\varepsilon_{21}) \tag{2c}$$

using the subscripts 3, 2 and 1 for the coarse, medium and fine grid respectively. The value of ε is determined by $\varepsilon_{ji} = \phi_j - \phi_i$ with ϕ_i beeing the solution of ϕ on the i-th grid.

Using the refinement ratio and the values of ϕ of the medium and the fine grid, the value of ϕ_1 can be extrapolated to ϕ_{ext}^{21}.

$$\phi_{ext}^{21} = (r_{21}^p \phi_1 - \phi_2)/(r_{21}^p - 1) \tag{3}$$

Then the extrapolated relative error e_{ext}^{21} can be determined using

$$e_{ext}^{21} = |\frac{\phi_{ext}^{21} - \phi_2}{\phi_{ext}^{21}}| \tag{4}$$

The second error estimate is the approximate relative error e_a^{ji}, for example

$$e_a^{21} = |\frac{\phi_1 - \phi_2}{\phi_1}| \tag{5}$$

The final result of the grid study is the grid convergence index GCI_{ji}, which is for the fine grid

$$GCI_{21} = \frac{1.25 e_a^{21}}{r_{21}^p - 1} \tag{6}$$

Setup

The present study focuses on the performance prediction of a reference propeller in combination with varying boss cap shapes. The investigated case is based on the research object KRISO CV 3600 TEU. Special attention is paid to resolving the dead water region behind the propeller cap. The propeller main particulars are listed in Table 1.

We chose three different boss cap shapes for the study. Cap one has a converging cone contour, cap two also has a cone contour, but diverging and cap three is converging in the front part and cylindrical in the aft part. The shapes of the investigated caps are depicted in Figure 1.

Table 1: P1380 propeller main particulars

Diameter	D	(m)	8.1
Hub diameter ratio	d_N/D	(-)	0.175
Chord at $r/R = 0.7$	$C_{0.7}$	(mm)	3095
Design pitch ratio	$P_{0.7}/D$	(-)	1.048
Expanded area ratio	A_E/A_0	(-)	0.69
Skew angle	Θ	(°)	36.996
scale factor	λ	(-)	31.6
Number of blades	z	(-)	4

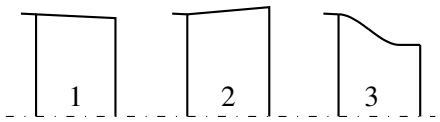

Figure 1: Boss cap contours

Further we simplified the test set-up by replacing the open water dynamometer in front of the propeller by a semi-infinite cylindrical shaft. The flow domain used in the computations consists of two parts, an inner, rotating and an outer, stationary subdomain. The inner subdomain spans $0.6D$ in axial direction with a diameter of $1.5D$. The inflow length of the outer subdomain stretches $7.5D$ and $15D$ upstream and downstream, respectively. The outer domain diameter amounts to $5D$.

Assuming rotational periodicity we split the flow domain along the rotation axis to obtain a single blade passage. On the rotational periodic boundaries between the blades a 1:1 grid was realized. For the grid generation we used the ANSYS workbench Meshing software. The inner subdomain grids consist of tetrahedral elements with prism layers on the wall boundaries.

The outer subdomain grids are structured with hexahedral elements. In order to get a converged solution for the forces and moments acting on the system, an in-house convergence criterion was used monitoring K_Q. The requirement of a steady solution is achieved when the value of K_Q does not change more than $1e^{-5}$ over the last 40 Iterations.

Results

Grid Uncertainity

The grid convergence analysis was performed on the grids of the inner subdomain in two stages. In stage one the grid was refined globally. Therefore the maximum cell size was adjusted, so the three grids for the rotor domain contain $435k$, $1.03m$ and $2.25m$ nodes as shown in Table 3. The effective refinement ratio between the grids is 1.33 and 1.30, respectively.

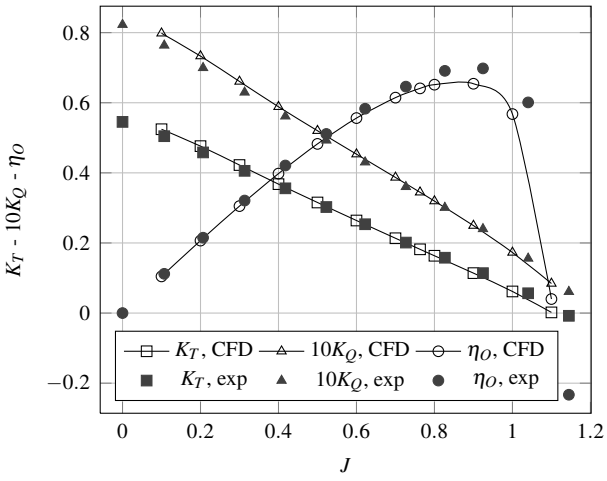

Figure 2: Open water performance

The variables of interest are thrust and torque of the propeller blade and cap and the derived ratios K_T, K_Q and η, which are determined on the whole geometry containing blade, hub and cap. For the first part of the grid study (see Table 3) a medium grid convergence index GCI_{32} below 0.5% for the blade thrust and torque could be obtained. So, already the medium grid predicts the open water performance with a high level of accuracy. The result is shown in Figure 2.

However, the thrust and torque fraction produced by the cap does not converge even for the fine grid and the value of GCI_{21} is around 10%. Because the efficiency gain resulting from a PID is expected to be about 1% a second grid study was essential. Since the pressure distribution on the boss cap is strongly influenced by the hub vortex, the aim was to capture the vorticity and the minimum pressure in the vortex. In stage two a cylindrical region downstream of the propeller, which starts at the boss cap flange and reaches to the rear end of the domain, was refined based on the medium grid of stage one. The diameter of this cylinder is $0.25D$. The grid inside this cylinder contains $64k$, $127k$ and $223k$ nodes. Because the sizes of the cells surrounding the refinement area are also adjusted, the finest grid contains $1.58m$ nodes in total. The global quantities are analyzed similar to the above in Table 4. It can be found that the thrust fraction of the hub converges well and the values of the medium and the fine grid are nearly identical. The torque fraction of the hub has a fine grid convergence index GCI_{21} of 2.66% and an approximate relative error of 4%. Because the torque produced by the hub is extremely small when compared to the total torque, the fine grid could be chosen for further investigations.

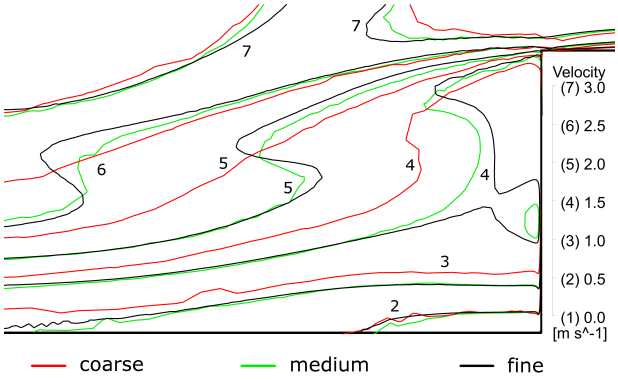

Figure 3: Velocity profile aft of hub cap (right end of figure) shown in a longitudinal plane passing through the rotation axis. Apicted are the differences between the three grids of the second part of the grid study.

In order to visualize the results of the second stage of the grid study a velocity profile is given in a contour plot in Figure 3. Here the velocities in a plane tangential to the advance velocity are given as a comparison between the coarse, medium and fine grid. The significant characteristics of the velocity distribution cannot be found for the coarse grid solution, especially for the contour lines 5 and 6. The discrepancies between the medium and the fine grid solu-

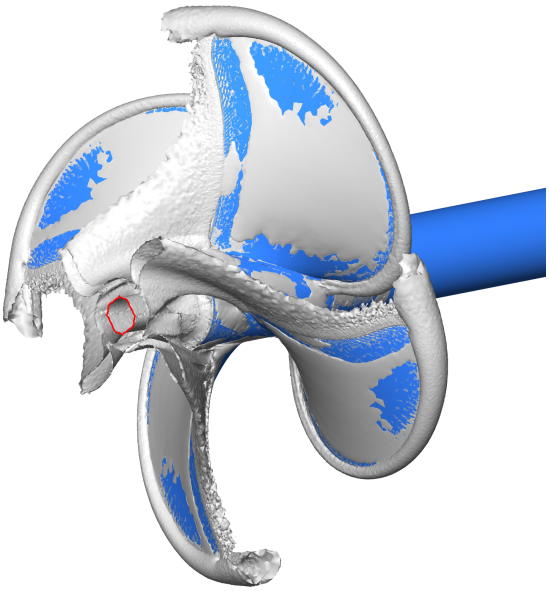

Figure 4: Visualisation of vorticity in the flow around the propeller using the lambda-2 criterion.

tion are small, so the relevant flow features are most likely captured by both computations, whereas the result for the fine grid is more smooth.

When looking at the vorticity of the flow, the lambda-2 criterion is used (see [5] for a detailed description). The surfaces of equal vorticity in the trailing flow of the propeller are depicted in Figure 4 for the fine grid solution. The leading edge vortex and the trailing wake sheet of the propeller blades can be clearly identificated. The surface is cut off at a certain position behind the boss cap for a better visualisation. Aft of the hub two circular vortex sheets are visible. The mean diameter of the inner one (marked with red color) is used as a criterion for the convergence of the flow structures in that region. The diameter is 7.73*mm*, 8.20*mm* and 8.22*mm* for the coarse, medium and fine grid, so the value is nearly the same between the medium and the fine grid.

Results for Boss Caps

In this section the calculated results for the three different boss caps shall be presented and compared to measurements conducted by Heinke (see [3] and [4]). In reference [3] the open water performance of the P1380 Propeller with different boss caps is determined using the reverse POT setup as described above. Reference [4] refers to velocity measurements for the same setup using an LDV (Laser Doppler Velocimetry) system. The advance velocity is adjusted, so that the three variants generate the same thrust. The computed thrust and the measured values can be found in Table 2. The advance ratio is slightly different than the one used for the grid study, therefore the values are not compareable to Table 3.

Table 2: Open water coefficients; calculated with grid obtained from GCI (CFD), measured in towing tank (EFD)

	cap	1	2	3
J		0.739	0.739	0.737
K_T	CFD	0.190	0.192	0.194
	EFD	0.189	0.189	0.189

The velocity profiles aft of the hub cap in a plane

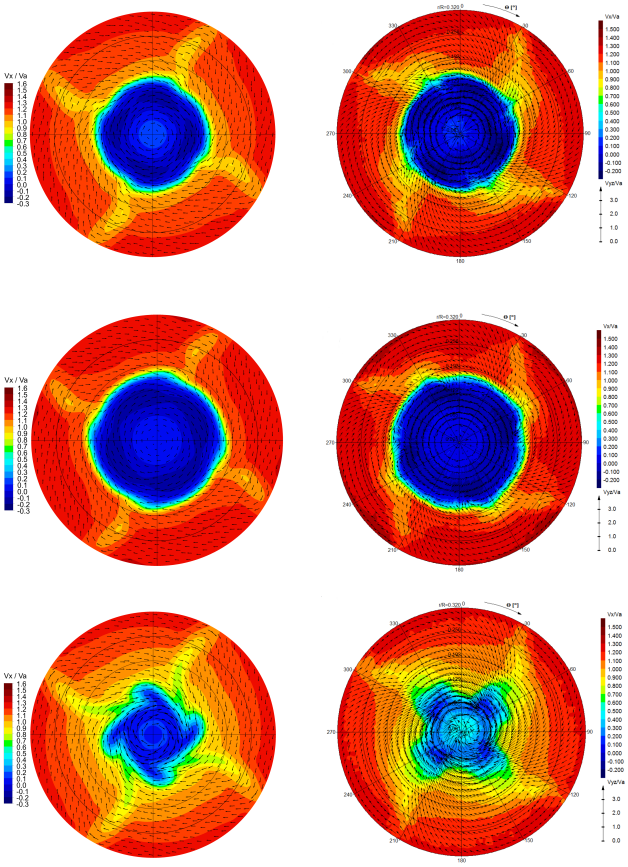

Figure 5: Comparison of velocity profiles for the investigated hub cap 1 (top), 2 (middle) and 3 (bottom) between CFD (left) and EFD (right) in a plane normal to the advance velocity.

normal to the advance velocity are shown in Figure 5 for the simulations and the LDV measurements of the investigated variants. It is obvious that the dominant flow properties are found by the CFD simulations. The dimension of the dead water area is captured quite well, although some of the details are not identical when compared to EFD. The dead water area of hub cap 1 is smaller than the one of hub cap 2 due to the converging shape (hub cap 2 is diverging) but the velocitiy distribution is comparable with values approx. zero. The zone of reduced velocities is much smaller in the case of hub cap 3 and the values are in the order of 20% of the advance velocity. The characteristics of the trailing flow of the propeller blade show some differences between CFD and EFD.

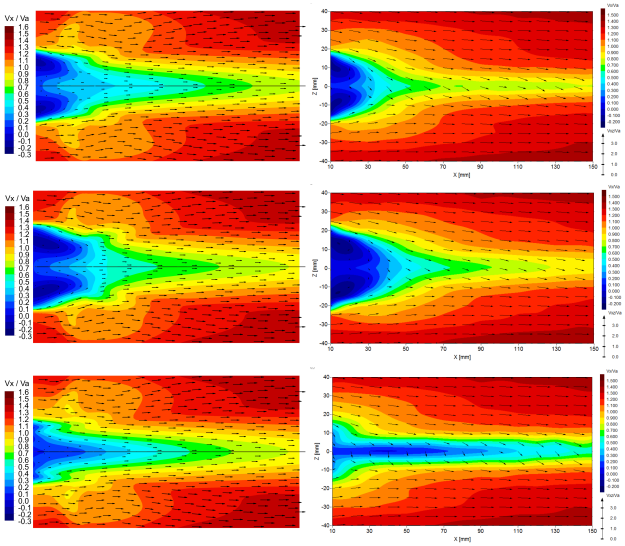

Figure 6: Comparison of velocity profiles for the investigated hub cap 1 (top), 2 (middle) and 3 (bottom) between CFD (left) and EFD (right) in a plane tangential to the advance velocity.

When comparing the velocity profiles in a plane tangential to the advance velocity the results are similar to the above mentioned. The CFD results are slightly different when compared to EFD but the differences between the hub caps are clearly apicted. Because of the smaller diameter at the aft end the area of reduced velocities is a lot smaller for hub cap 3 when compared to the others. As a result of that the hub vortex is stronger. This in general unfavorable behaviour can be clearly observed when looking at the velocity vectors accounting for the in plane velocities of Figure 5. They show a strong rotational component for hub cap 3 and much less for the others.

Discussion

In the present paper a grid study for propeller open water calculations was conducted. The focus of this investigation was to capture the dominant flow properties aft of the propeller in the region of the hub cap and behind of it. The two-staged grid study showed a good convergence behaviour of the examined variables for the investigated grids. Using the final grid from the grid study simulations were conducted showing a good agreement with measurements. The differences in the trailing flow of the propeller blade may be due to unsteady behaviour in that region. The approach shown here is an excellent basis for optimising the shape of hub caps.

References

[1] ASME. *Journal of Fluids Engineering Editorial Policy Statement on the Control of Numerical Accuracy*.

[2] I.B. Celik, U. Ghia, P.J. Roache, and Freitas C.J. Procedure for Estimation and Reporting of Uncertainity Due to Discretisation in CFD Applications, Editorial. *ASME Journal of Fluids Engineering*, 2008.

[3] Hans-Juergen Heinke. Freifahrtversuche mit dem Propeller P1380 mit unterschiedlichen Ablaufhauben. Technical Report 3845, SVA Potsdam, October 2011.

[4] Hans-Juergen Heinke. Geschwindigkeitsmessungen in Nabenbereich des Propellers P1380 mit unterschiedlichen Ablaufhauben. Technical Report 3848, SVA Potsdam, October 2011.

[5] J Jeong and F. Hussain. On the Identification of a Vortex. *Journal of Fluid Mechanics*, pages 69–94, 1995.

[6] Resistance Committee of 25th ITTC. Uncertainty Analysis in CFD, Verification and Validation: Methodology and Procedures. Technical report, International Towing Tank Conference, 2008.

Table 3: Results of grid convergence index analysis stage 1

	Thrust T [N]		Torque Q [Nm]		$K_T[-]$	$K_Q[-]$	$\eta_O[-]$
location	blade	cap	blade	cap		total	
N_1			2250835				
N_2			1028902				
N_3			434571				
r_{21}			1.30				
r_{32}			1.33				
ϕ_1	176530	−2520.6	8572870	478.2	0.179	0.0345	0.629
ϕ_2	175627	−2315.6	8549030	549.2	0.178	0.0344	0.629
ϕ_3	175590	−2182.5	8692110	576.2	0.178	0.0350	0.619
$p[-]$	21.29	2.14	6.32	4.33	8.90	6.04	9.56
$e_{21}^{ext}[\%]$	0.0	9.8	0.1	7.6	0.0	0.1	0.0
$e_{21}^{a}[\%]$	0.5	8.1	0.3	14.8	0.4	0.3	0.1
$e_{32}^{a}[\%]$	0.0	5.7	1.7	4.9	0.0	1.7	1.6
$GCI_{21}[\%]$	0.02	13.56	0.08	8.87	0.05	0.10	0.01
$GCI_{32}[\%]$	0.00	8.44	0.41	2.5	0.01	0.45	0.14

Table 4: Results of grid convergence index analysis stage 2

	Thrust T [N]		Torque Q [Nm]	
location	blade	cap	blade	cap
N_1		223416		
N_2		126776		
N_3		64130		
r_{21}		1.21		
r_{32}		1.26		
ϕ_1	176092	−2551.8	8580000	459.6
ϕ_2	176157	−2551.7	8585000	477.9
ϕ_3	175627	−2315.6	8549030	549.2
$p[-]$	9.43	–	8.89	5.57
$e_{21}^{ext}[\%]$	0.0	0.0	0.0	2.2
$e_{21}^{a}[\%]$	0.0	0.0	0.1	4.0
$e_{32}^{a}[\%]$	0.3	9.3	0.4	14.9
$GCI_{21}[\%]$	0.01	–	0.02	2.66
$GCI_{32}[\%]$	0.05	–	0.08	7.32

Using CFD to Assess Fluid Structure Interaction in a Moonpool

Alessio Pistidda, Harald Ottens, Heerema Marine Contractors, Leiden/NL,
apistidda@hmc-heerema.com, hottens@hmc-heerema.com

INTRODUCTION

Heerema Marine Contractors (HMC) is a marine contractor that operates in the offshore Oil and Gas industry. HMC transports, installs and removes all type of offshore facilities with three of the four largest construction vessels in the world. A new deep water construction vessel, Aegir (Figure 1), now under construction, will start working in 2013. Aegir will have a crane capacity of 4000mT and can install pipelines in deep and ultra-deep water with J-lay and reeling mode. Structures will be lowered through a moonpool.

Figure 1: DCV vessel Aegir

Vessels equipped with a moonpool are frequently used in the offshore oil and gas industry. They are used to lay pipelines, risers, structures cables and for drilling. These operations are generally possible if the water motion inside the moonpool remains within workable limits.

Water oscillations are generated by waves, related to vessel motion and forward speed. The water motion in the moonpool is characterized by two dominant modes, sloshing (lateral motion) and pumping (vertical motion). Both modes are usually present during sailing, while during installation phase, where the vessel is keeping a fix position, the pumping mode is dominant and sloshing is negligible.

If the resonant condition is reached, large water level oscillations are observed; such condition requires an accurate investigation in order to properly assess material stress of the structures in the moonpool which are going to be lowered. Depending on the structure location respect to the water level, slamming and/or drag forces and buoyancy variation can affect the structural integrity of the structure during installation; possible fatigue damage has to be assessed. Figure 2 illustrates two typical examples of structure lowering, a startup structure (top) and a inline structure (bottom). The startup structure, which is the first structure of a pipeline, generally stays few hours in the moonpool before the lowering due to installation procedure, therefore possible fatigue damage as to be assessed. On the other hand, the lowering of a inline structure is a continuous process, which means fatigue is not an issue, but since this kind of structures are installed with a certain angle, forces are larger than startup structure and their magnitude needs to be assessed.

The behavior of the water column in the moonpool and the interaction with the structure can be potentially predicted with model test and numerically. The experimental data publically available typically focuses on the behavior of the moonpool for a certain seastate/sailing condition or focuses on slamming forces for a specific type of structure during water entry [2]. Also in CFD the simulation of the behavior of the moonpool is generally split from the simulation of the interaction between water column and structure.

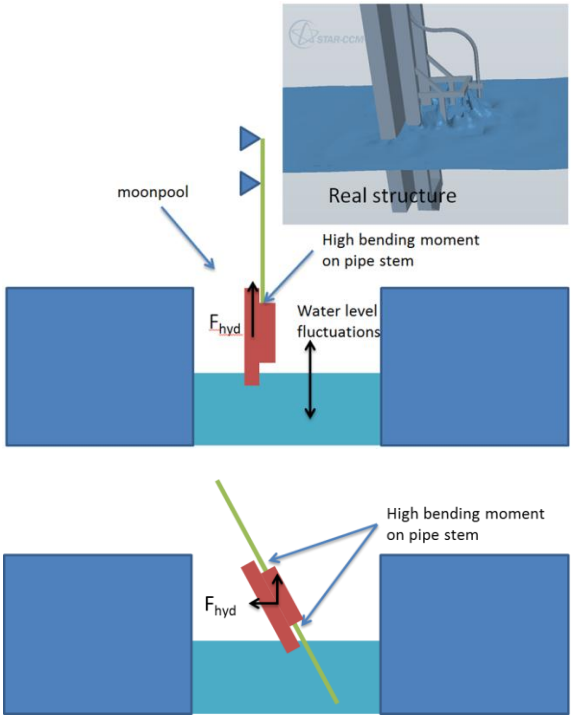

Figure 2: structure lowering with moonpool, startup structure (top) and inline structure (bottom)

In this work, a hybrid approach will be used. The motion of the water column in the moonpool will be derived from model test data while the interaction water-structure will be reproduced in CFD using the water level fluctuation from model test as input. Analyses will be performed with STAR-CCM+ [3].

CFD plays an important role in the evaluation of the fluid structure interaction. CFD is considered as a cost-effective tool complementary to model tests to obtain hydrodynamic coefficients. For this reason, it is important not only to understand the possibilities, but also the limitations of CFD. In order to assess how CFD can predict slamming forces a validation study is also presented; it refers to a water entry of a V-shaped section with 30 degrees dead-rise angle, which is considered representative for this application. After the validation the results for a typical structure subject to slamming in a moonpool will be presented.

CFD VALIDATION

The experiment of Zhao and Faltinsen [2] is used for validation. The experiment consisted in a drop test where a wedge impacts on water during free falling; velocity, impact vertical force and pressure on the wedge were measured. Here, the force and the pressure will be used for the validation. A sketch of the wedge used for the drop test is shown in Figure 3; main dimensions are reported in Table 1.

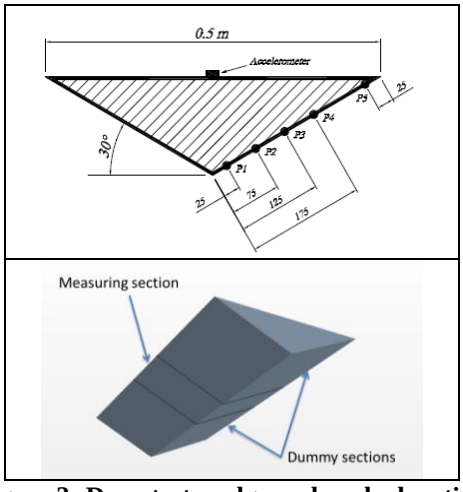

Figure 3: Drop test wedge and probe location

Table 1: Main data of the test section

Breadth of the section	0.5 m
Length of measuring section	0.2 m
Length of each dummy section	0.4 m
Total length	1.0 m

The drop velocity is shown in Figure 4; t = 0 [s] corresponds to the impact of the wedge with the free surface.

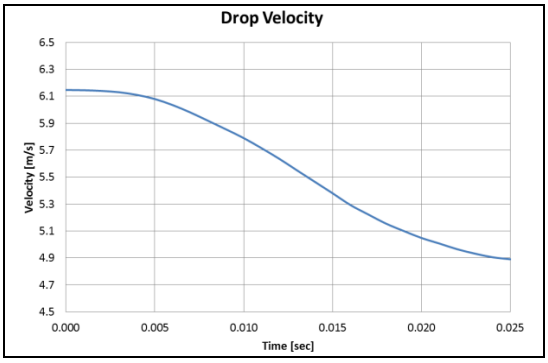

Figure 4: Drop velocity

The drop test can be reproduced in several ways in CFD. In this work three approaches have been investigated:

- Dynamic mesh - translation: the whole mesh is translating with the wedge while the water level is constant
- Dynamic mesh - overset [3]: the mesh of the wedge slides within the background mesh (domain) which is fix
- Static mesh: the relative velocity between water and wedge is obtained changing the water level according to drop velocity.

Boundary conditions for all methods are shown in Figure 5. The liquid and gas phase have been modeled with VOF approach [3].Results show that using a static mesh a larger diffusion of the interface was present compared to the dynamic mesh for large time step as shown in Figure 6; this is probably because the free surface is continuously moving in order to follow the velocity inlet BC. If the time step is small enough, no differences are observed from the interface diffusion point of view. Two-dimensional and three-dimensional analyses have been performed, a summary of the setting is reported in Table 2 (values are reported for the final simulations).

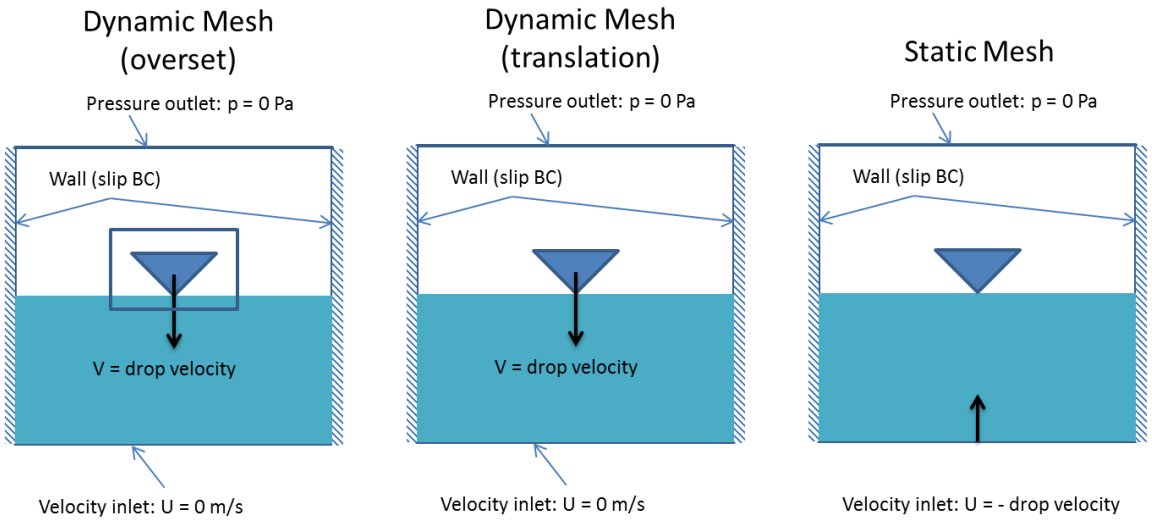

Figure 5: Boundary conditions

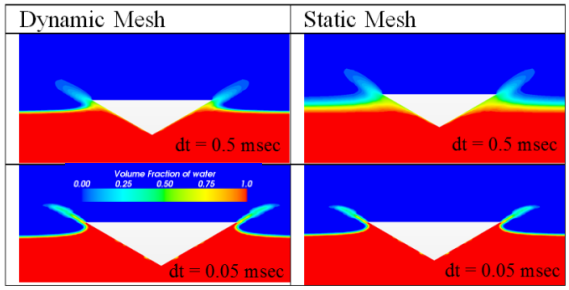

Figure 6: Volume fraction diffusion at interface at t = 16 ms

Table 2: CFD analyses settings

	2D	3D – A	3D – B	3D – C
Mesh type	Hexahedral	Hexahedral	Hexahedral + Prism. Layer	Hexahedral
Motion approach	Dynamic translation	Dynamic translation	Dynamic translation	Dynamic overset
Mesh size	15k	6M	1M	3M
Multiphase approach	VOF	VOF	VOF	VOF
Turbulence model	SST	SST	SST	SST
Time step	0.05msec	0.05msec	0.05msec	0.05msec
Simulation Time	25msec	25msec	25msec	25msec

Some snapshots of the grids used are reported in Figure 7. Three three-dimensional grids have been tested; one fully hexahedral (6M cells) and one hexahedral with prismatic layer around the wedge (1M cells) for dynamic mesh translation; the mesh used for the overset mesh was hexahedral without prismatic layer around the wedge (3M cells).

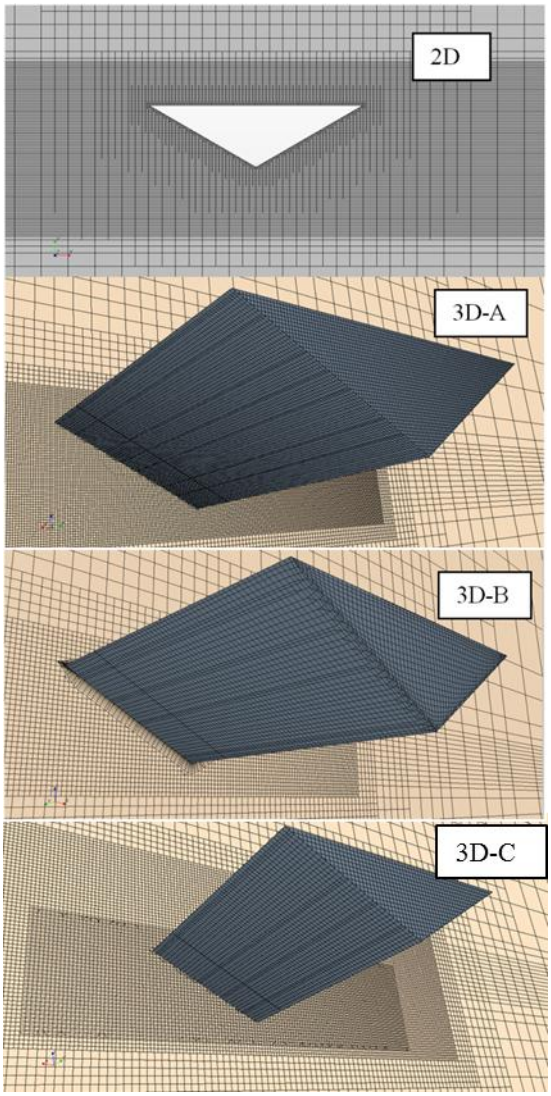

Figure 7: Grids snapshots for 2D, 3D-A, 3D-B and 3D-C models.

The force measured for the 2D and 3D analysis are shown in Figure 8. The 2D model does not give an accurate force trend while 3D models do. As expected the two-dimensional approach gives a force which is larger than the one from the experiment because three-dimensional effects observed during the drop test are not taken into account; this is in line with observation from [2]

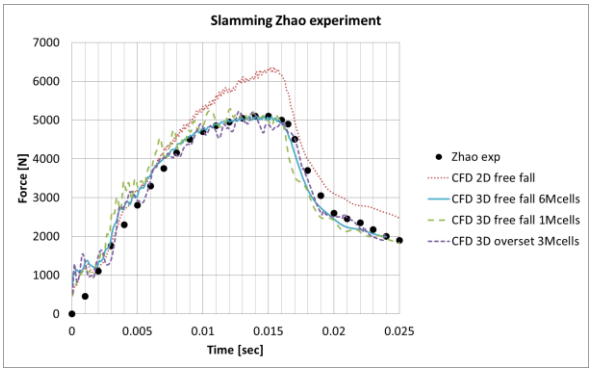

Figure 8: Slamming load

Using 3D grids, even with a relatively small grid size, results remain reasonably accurate, at least from an engineering perspective.

The pressure measured for the 3D simulations is plot in Figure 9. Each experimental point represents the value measured with the probes shown in Figure 3; *x* denotes the horizontal distance from the wedge center. Results show that the pressure coefficient is well predicted. This is in line with the measured force.

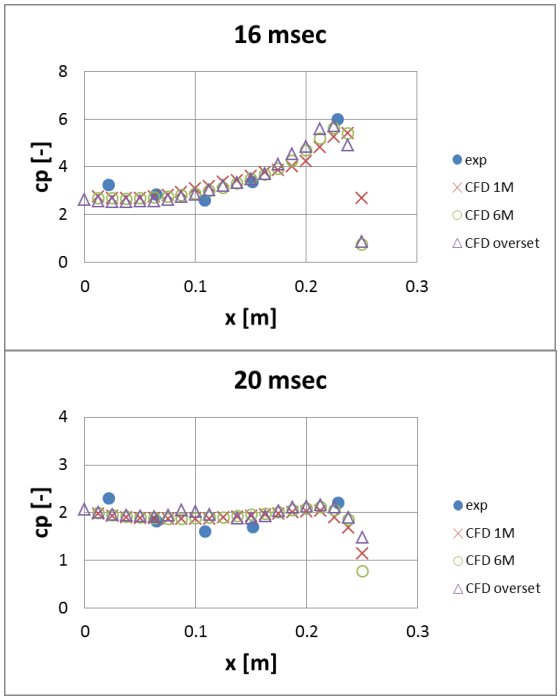

Figure 9: pressure for two simulation time

The previous results build some confidence in performing slamming calculation with CFD. In the next section, calculation of the slamming forces for a structure in the moonpool will be presented. The preferred method for the simulation with real structure will be "dynamic mesh with translation" because it is less sensitive to the time step size and also it is faster than "dynamic mesh with overset".

STRUCTURE IN MOONPOOL – CFD SIMULATION

During 2010-2011 Heerema Marine Contractors performed several model tests for her new deep-water construction vessel Aegir. Part of the test campaign was dedicated to the evaluation of the water level fluctuation in the moonpool with predefined sea-state at zero sailing speed, which represent the typical condition during operation.

Three probes (Figure 10) were used to measure the water level. During the tests, the signals measured show that the water level was basically the same at all locations, which means the dominant mode in the water motion is pumping only; no sloshing was observed.

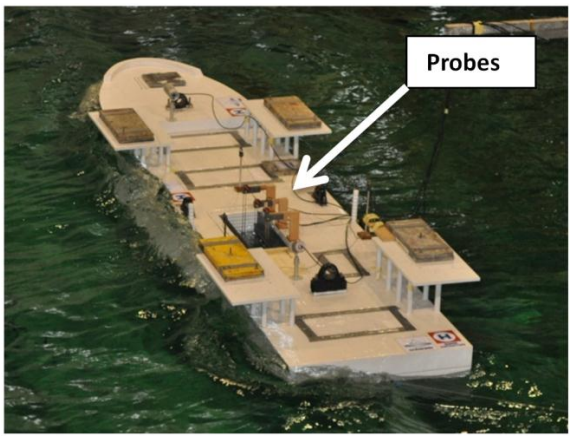

Figure 10: Probes locations at moonpool

Since the flow motion in the moonpool is unidirectional, it is possible to study the interaction between water column and structure simply simulating the structure to be installed in a fluctuating water level.

The workflow which connects the model test to the CFD simulation is as follow:

1. Measure water level for a certain sea-state during model test
2. Evaluate moonpool RAO from model test data
3. Simulate a certain level fluctuation via CFD
4. Correlate forces on structure with sea-state and water level fluctuation and/or water level velocity

5. Use those forces as input for pipe installation software, where hydrodynamic forces are combined to the pipe stress of different origin (static and dynamic).

Figure 11 shows a snapshot of the simulations performed. Several simulations have been performed; in Figure 12 the correlation between the maximum forces measured and water level amplitude is shown. It is noted that the forces include not only slamming but also drag and buoyancy. Since the moonpool RAO is known, those forces can be correlated to the seastate and therefore to the vessel motion in order to be implemented in installation software. The correlation reported in Figure 12 is valid for a specific case and needs to be generalized; for that reason more simulations have to be performed for different structures and different mean water levels.

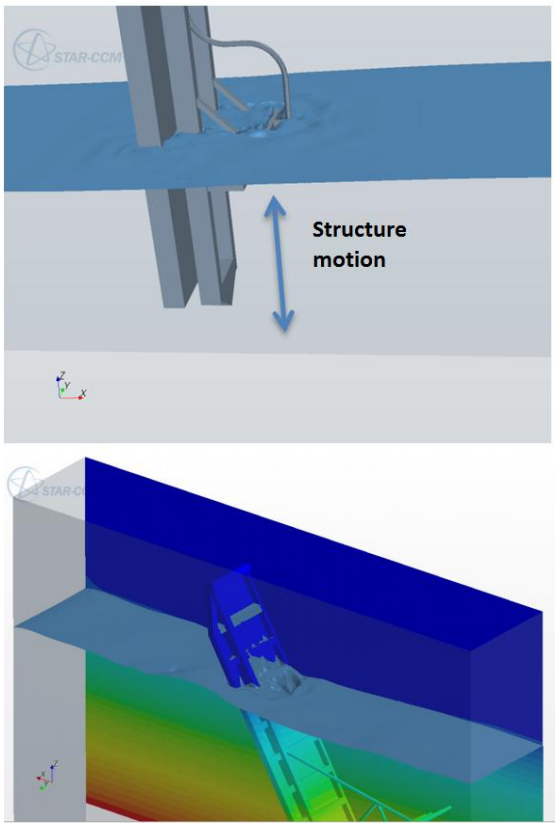

Figure 11: Domain for water-structure interaction in the moonpool, startup structure and inline structure

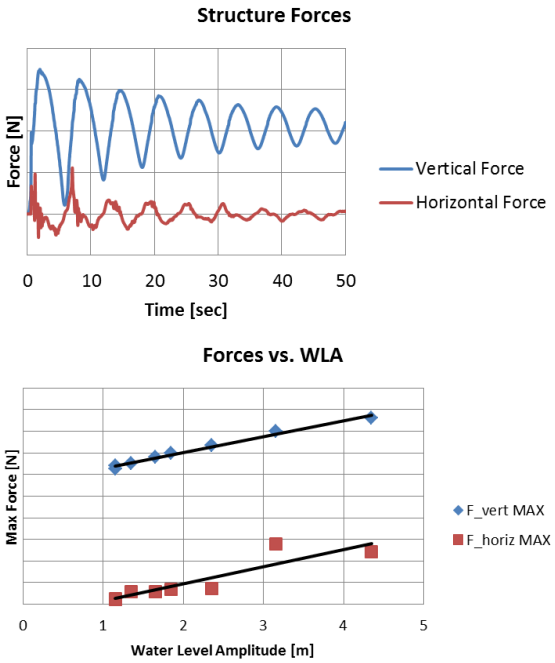

Figure 12: Forces on structure vs. water level fluctuation for startup structure

CONCLUSIONS

Slamming forces on structures have to be properly assessed when they are in the moonpool during installation. CFD can be a powerful tool to evaluate the magnitude of the forces involved.

In this work, the VOF multiphase method has been validated for slamming using the experiment of [2] which is considered representative for the application discussed in this work.

Validation has been performed using a two-dimensional and three-dimensional approach. Two-dimensional approach generally overestimates the slamming forces, as expected; three-dimensional approach can provide accurate results.

Three methods have been used to reproduce the relative motions between structure and water, which are “dynamic mesh with translation”, “dynamic mesh with overset” and “fluctuating flow”. All methods give similar results provided that the time step used in the computations is small enough. The dynamic mesh approach is nonetheless preferred for the lower diffusion of the interface air-water.

Simulation with a real structure in the moonpool has been presented. A correlation between water oscillation amplitude and maximum vertical and horizontal forces has been derived. Those forces can be used as input for other pipe installation software.

More analyses are required in order to better characterize different structures in different seastate conditions.

REFERENCES

[1] Marcer, R., Berhault, C., de Jouëtte, C., Moirod, N., Shen, L. (2010), *Validation of CFD Codes for Slamming*, ECCOMAS CFD 2010

[2] Zhao, R., Faltinsen, O., Aarsnes, J. (1997), *Water Entry of Arbitrary Two-Dimensional Sections With and Without Flow Separation*, 21st Symposium on Naval Hydrodynamics

[3] CD-Adapco, *User Guide STAR-CCM+*, version 7.02.011, London

Radiation moment on a vertical bottom-hinged flap

Otto Puolakka*, Tommi Mikkola†
Aalto University, School of Engineering, Department of Applied Mechanics

Vertical bottom-hinged flaps have been suggested for power absorption out of the waves, both for purposes of energy production and coastal protection (Scher, 1985). Solution of the radiation problem is central in linear analysis of the wave–flap interaction. Havelock (1929) presented a general solution of the problem for small horizontal oscillations using linear wave theory. In two dimensions, both sides of an oscillating flap in the sea can be treated as a hinged wavemaker in the end of a channel, if flap thickness is ignored. Much research has been conducted on the wave-making properties of such wavemakers (Biésel, 1951; Biésel & Suquet, 1951; Gilbert *et al.*, 1971; Hyun, 1976; Patel & Ionnaou, 1980; Hudspeth & Chen, 1981; Hudspeth *et al.*, 1981; Hudspeth & Sulisz, 1991; Sulisz & Hudspeth, 1993*a*,*b*). Focus of the studies has been on the progressing wave and resistive moment. There seems to be more uncertainty in evanescent wave modes related to added inertia. This property is of great importance in the tuning of a wave-absorbing flap.

In this article, the radiation problem of a vertical bottom-hinged flap is studied by solving the Euler equations in a channel of intermediate depth using the finite volume method. In contrast to the linear wavemaker theory, the method fulfils the exact (nonlinear) boundary conditions on the flap and free surfaces. Despite the discretization error, the method is considered more accurate than the linear theory. Results of the linear theory, derived for flaps hinged above channel base by Hyun (1976), will be compared against the numerical results for the radiation moment at various oscillation amplitudes. The radiation moment is expressed using the concepts of added mass and damping for clearer relevance to the roll response problem.

The solution domain is illustrated in Fig. 1. A vertical flap is hinged at a depth $h = 9.5$ m in the end

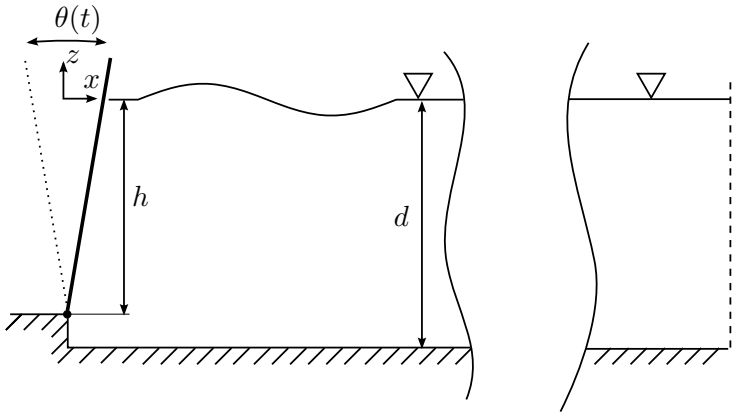

Figure 1: A hinged wavemaker in the end of a channel of depth d.

of a channel of depth $d = 12$ m and infinite length. The backside of the flap is assumed dry. The flap performs harmonic oscillations in roll

$$\theta(t) = \Re[-i\theta_0\, e^{i\omega t}], \tag{1}$$

where θ_0 is the oscillation amplitude, at a phase frequency ω. The frequency range of interest in this study is one corresponding to wave periods $T = 5$–15 s, where most of the wave energy to be absorbed

*email: otto.puolakka@aalto.fi
†email: tommi.mikkola@aalto.fi

lies at ocean coastlines. Oscillations and resulting waves of periods $T = 5$ s and 15 s were simulated using the numerical method and the radiation moment studied at these frequencies.

The finite volume method of this study is applied in a Euler solver YAFFA (Mikkola, 2007, 2009). Co-located grid and SIMPLEC algorithm are applied in pressure correction. Dual time-stepping is used to achieve time-accuracy. The free surface is treated by surface tracking. Inviscid "slip" condition is set at the flap and stem surfaces as well as at the channel bottom. At the far end of the channel, free-stream boundary conditions are set. Length of the computational domain was chosen 1000 m for 5-second waves and 2000 m for 15-second waves (see Table 1).

Table 1: Properties of simulation cases.

wave period	5 s			15 s		
grid density	coarse	medium	fine	coarse	medium	fine
domain length (m)		1000			2000	
development area (m)		200			800	
near-flap area (m)		24			18	
simulation time (s)		50			150	
oscillation amplitudes (°)		5, 10			5, 10, 15, 20, 30	
timestep (s)	0.2	0.1	0.05	0.2	0.1	0.05
cell side at flap (m)	0.25	0.125	0.0625	0.25	0.125	0.0625
——— at 24 (18) m	2.0	1.0	0.5	2.0	1.0	0.5
——— at 200 (800) m	2.0	1.0	0.5	4.0	2.0	1.0
——— at 1000 (2000) m	4.0	4.0	4.0	4.0	4.0	4.0

Unstructured grids consisting of triangles were created for the channel using Frontal Delaunay method (Frod) (Müller, 1996). The grids were deformed by stretching them as linear spring systems to match the moving boundaries during computation. In addition, Laplacian grid smoothing was performed after the stretching.

In the beginning of the simulation, the oscillation amplitude of the flap was increased to full within two periods using a cosine ramp. The moments were evaluated at roll amplitudes $\theta_0 = \{5°, 10°\}$ for 5-second oscillations and $\theta_0 = \{5°, 10°, 15°, 20°, 30°\}$ for 15-second oscillations. The flow was simulated for 10 periods, but practically full development in the moment was observed already at 4th period. The radiation moments to be analyzed were averaged from the interval 3–6 T.

The grid density and timestep for the 5-second oscillations were decided to give approximately 50 steps per period and cells per wavelength of the progressive wave solution predicted by the linear wave theory. This resolution was given for the length of channel, which the advancing wavegroup would travel in simulation time $10\ T$ (named "development area" in Table 1). Near the wavemaker, the cell size was linearly decreased to enable more accurate modelling of the evanescent wave solutions (Havelock, 1929) related to added inertia. Far from the wavemaker the grid was gradually coarsened to consist of only a few cells in the vertical direction.

Similar tactics were employed with 15-second waves with a few exceptions. The use of only 50 timesteps per period produced difficulties in computation and bad results. Consequently, short timesteps equal to those with 5-second waves were used. The evanescent wave solutions decay faster with distance from flap x for 15-second oscillations than for 5-second. For this reason, equal grid density at flap was used for both waves despite the greater length of the progressive wave with $T = 15$ s. Also in the development area, a requirement of sensible vertical resolution (6 cells for channel depth) set the lateral resolution relatively higher than with 5-second waves. The development area was set shorter relative to group velocity as with 5-second oscillations, since the 15-second wave was only slightly damped even in the damping zone. Properties of the simulation cases are more accurately described in Table 1.

Density of the original grids and length of timesteps were doubled and halved to reveal the effect of spatial and temporal resolution on the radiation moment. Development of the moment was mostly

uniform and differences were rather small. Differences in radiation moment amplitude were (usually considerably) less than 1 % and in phase less than 0.3°. However, monotonically converging results were not always obtained and practical issues prevented adjustment of the grids for improved convergence. For this reason, no extrapolation of results to infinite grid density is carried out. Results of the finest grid are used in analysis.

In the situation of interest for wave-absorbing vertical flap in sea, water occupies also the back-side of the flap. In this study, the one-sided wavemaker solution was mirrored to the other side of the flap 180° shifted in phase for the total radiation moment:

$$M_{\mathrm{R}}(t) = M_r(t) + M_l(t) = M_r(t) - M_r(t - T/2), \tag{2}$$

where M_r is radiation moment due to the right side and M_l due to the left.

For analysis, a sine signal $\hat{M}_{\mathrm{R}} = \Re[-iM_0 e^{i(\omega t+\alpha)}]$ was least-square fitted for amplitude M_0 and phase α to the simulated radiation moments $M_{\mathrm{R}}(t)$ at the interval 3–6 T. The moments and fitted signals are illustrated in Fig. 2. The radiation moment in 5-second oscillation was quite closely harmonic for both amplitudes 5° and 10°. The studied amplitude range in 15-second oscillation was wider. At amplitudes 5° and 10°, the fit was very good. At higher amplitudes, the peaks of the moment signal started to flatten and the weight to shift to the left, making the rise of the moment steeper than the descent. At oscillations with amplitude 30°, a clear double peak started to form.

In simulation of roll response of a wave-absorbing flap, it is convenient to express the radiation moment using the concepts of added mass and damping. Within linear wavemaker theory (Havelock, 1929) this expression is exact. The added masses and dampings for the flap of this study were derived from linear wavemaker theory based on Hyun (1976), and are illustrated in Fig. 3. The sine fits $\hat{M}_{\mathrm{R}}$ of the radiation moments were transformed into added masses m and added dampings c for quantitative comparison with linear wavemaker theory:

$$\hat{M}_{\mathrm{R}} = -m\ddot{\theta} - c\dot{\theta} \tag{3}$$

$$\Rightarrow \quad m := \Re\left[\frac{-\hat{M}_{\mathrm{R}}}{\ddot{\theta}}\right] \quad \text{and} \quad c := \Re\left[\frac{-\hat{M}_{\mathrm{R}}}{\dot{\theta}}\right]. \tag{4}$$

The added masses and dampings from these fits are plotted for relevant frequencies in Fig. 3.

From the results it can be seen, that when the assumptions of linear wavemaker theory hold (small oscillation and wave amplitude), its results are very consistent with those of the current finite volume method. With oscillations of amplitude 5°, the linear estimates of both added mass and damping are within a few per cent of simulation results. With 10°, the difference is no more than 10 %, with the largest relative difference in m at $T = 5$ s. At the largest amplitude in practical operation 20°, the difference in added mass is 15 % and in added damping 8 % for $T = 15$ s, which can be still considered moderate. Compared to simulation results, the linear theory underestimates the added damping at both frequencies and the added mass at $T = 15$ s. The same can be stated compared to the experimental results of Hudspeth *et al.* (1981), although the scatter in their results is wide. Interestingly, the difference in added mass estimates changes sign between $T = 15$ s and $T = 5$ s. The agreement in added damping is in general better than in added mass, as discovered experimentally by Hudspeth *et al.* (1981).

Concludingly, radiation moments by the applied finite volume method are in close agreement with the linear wavemaker theory at small oscillation amplitudes (less than 10°). At larger amplitudes, the radiation moment is no longer harmonic in time, and equivalent added masses and dampings start to differ from the linear wavemaker theory.

The simulations should be validated and extended to intermediate frequencies as well as larger amplitudes. More efficient grids should be constructed to yield monotonic convergence at practical levels of refinement. The results could be compared with analytical second-order solutions (Sulisz & Hudspeth, 1993*b*). The effect of exclusion of friction should be investigated. More results will be presented at the symposium.

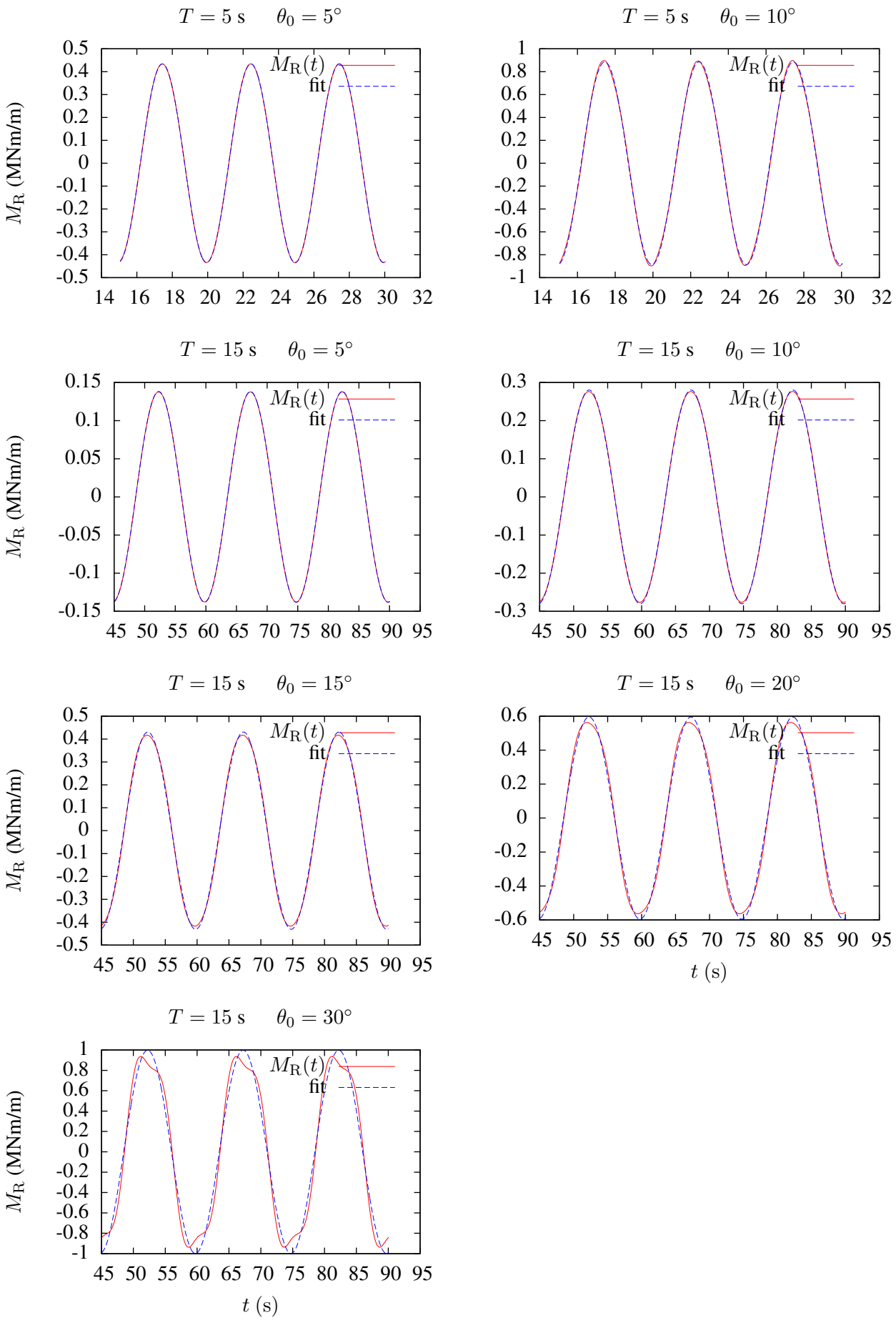

Figure 2: Radiation moments from simulations and least-square fitted sine signal in the interval 3–6 T for oscillations with period $T = 5$ s at amplitudes 5° and 10°, as well as for o. w. period $T = 15$ s at amplitudes 5°, 10°, 15°, 20°, 30°.

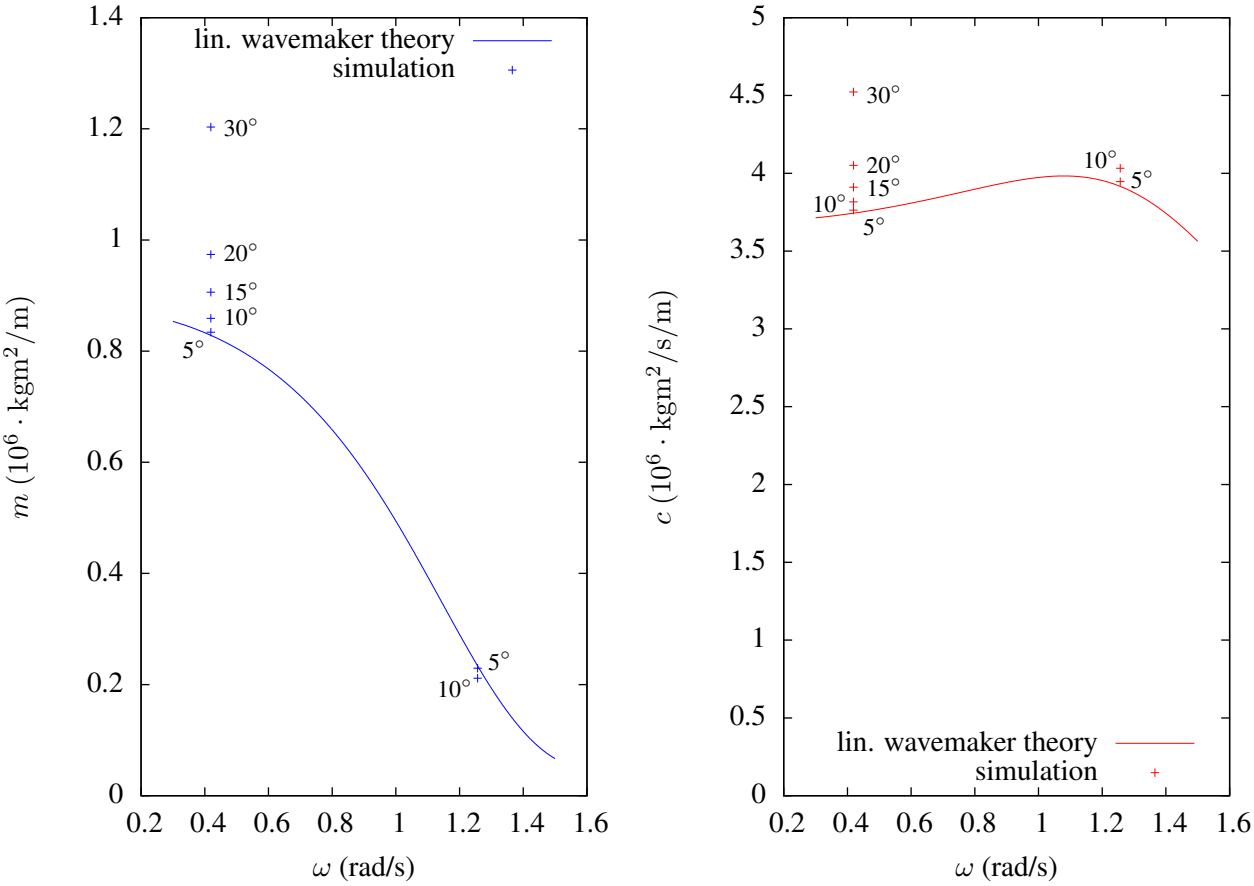

Figure 3: Added mass and damping estimated by linear wavemaker theory and equivalent added mass and damping from current simulations at frequencies corresponding to oscillation periods $T = 15$ or 5 s and at various oscillation amplitudes (θ_0 indicated at points).

References

BIÉSEL, F. 1951 Étude théorique d'un certain type d'appareil a houle. *La Houille Blanche* (2), 156–165.

BIÉSEL, F. & SUQUET, F. 1951 Les appareils générateurs de houle en laboratoire. *La Houille Blanche* (4-), 475–,723–,779–.

GILBERT, G., THOMPSON, D. M. & BREWER, A. J. 1971 Design curves for regular and random wave generators. *Journal of Hydraulic Research* **9** (2), 163–196.

HAVELOCK, T. H. 1929 Forced surface-waves on water. *Philosophical Magazine* **viii**.

HUDSPETH, R. T. & CHEN, M-C. 1981 Design curves for hinged wavemakers: Theory. *Journal of the Hydraulics Division, ASCE* **107** (HY5), 533–552.

HUDSPETH, R. T., LEONARD, J. W. & CHEN, M-C. 1981 Design curves for hinged wavemakers: Experiments. *Journal of the Hydraulics Division, ASCE* **107** (HY5), 553–574.

HUDSPETH, R. T. & SULISZ, W. 1991 Stokes drift in two-dimensional wave flumes. *Journal of Fluid Mechanics* **230**, 209–229.

HYUN, J. M. 1976 Theory for hinged wavemakers of finite draft in water of constant depth. *Journal of Hydronautics* **10** (1), 2–7.

MIKKOLA, T. 2007 Verification of a free surface code with method of manufactured solutions. In *10th Numerical Towing Tank Symposium*.

MIKKOLA, T. 2009 Simulation of unsteady free surface flows – code verification and discretization error. PhD thesis, Helsinki University of Technology.

MÜLLER, J.-D. 1996 On triangles and flow. PhD thesis, University of Michigan.

PATEL, M. H. & IONNAOU, P. A. 1980 Comparative performance study of paddle- and wedge-type wave generators. *Journal of Hydronautics* **14** (1), 5–9.

SCHER, R. M. 1985 A study of flap-type wave absorbing devices (energy). PhD thesis, University of Michigan.

SULISZ, W. & HUDSPETH, R. T. 1993*a* Complete second-order solution for water waves generated in wave flumes. *Journal of Fluids and Structures* **7**, 253–268.

SULISZ, W. & HUDSPETH, R. T. 1993*b* Second-order wave loads on planar wavemakers. *Journal of Waterway, Port, Coastal, and Ocean Engineering* **119** (5), 521–536.

Investigations of Design Criteria for Ships with Split-Stern by RANS

Nobuaki SAKAMOTO[†], Yasutaka KAWANAMI[†] and Shotaro UTO[†]
[†]National Maritime Research Institute (NMRI), Tokyo 181-0004 JAPAN
sakamoto@nmri.go.jp; kawanami@nmri.go.jp; uto@nmri.go.jp

1. Introduction

National Maritime Research Institute (NMRI) has been investigating twin-skeg ships (Sasaki 2010, 2011) which can contribute to meet the regulation of Energy Efficiency Design Index (EEDI, IMO 2011) by reducing emissions of Green House Gas (GHG). One representative hull form is MS791, a 4,000 twenty-foot equivalent unit (TEU) twin-skeg container ship with an electrical propulsion system supported by two off-centered podded propulsors. Such configuration makes it possible to search optimal location of the propeller to minimize effective wake coefficient $1\text{-}w_T$ and delivered power P_D as well as to maximize hull efficiency η_H (Sasaki 2010). In terms of hull design, podded propulsors make skegs free from propeller shaft which means that their geometrical design would be much more flexible than those of conventional twin-skeg ships. In order to take this advantage, understanding relationship between skeg geometry and resistance/self-propulsion/local flow characteristics of the ship would be quite important for better design of a hull (Van et al. 2004).

The objective of the current study is to analyze resistance and self-propulsion characteristics of MS791 depending on different skeg geometries and to obtain useful information for further investigation of twin-skeg ships with podded propulsors. Viscous Computational Fluid Dynamics (CFD) simulations for towed and self-propelled conditions of MS791 are performed using Reynolds Averaged Navier-Stokes (RANS) solver SURF ver.6.44 (Hino 1997) developed by CFD research group in NMRI.

2. Computational Method

All the simulations presented in this manuscript are carried out by SURF ver6.44, a finite-volume unstructured grid based RANS solver with Spalart-Allmaras (SA) one-equation turbulence model (Spalart and Allmaras 1994) and body-force propeller model (Ohashi et al. 2003) based on simplified propeller theory (Moriyama 1979). Inviscid fluxes in momentum and turbulence transport equations are evaluated by the 2nd-order upwinding scheme based on the flux-difference splitting of Roe, and 1st-order upwinding scheme, respectively. Viscous fluxes appeared in momentum and turbulence transport equations are evaluated by the 2nd-order central differencing scheme. Temporal discretization is accomplished using 1st-order Euler backward differencing scheme with fully implicit manner.

The computational grid is generated by Gridgen® and consists of hexahedra cells without hanging node. The smallest grid spacing normal to the wall non-dimensionalized by the ship length between perpendiculars (L_{pp}) is approximately 2.5E-06 which maintains y^+ value smaller than 1 at target Reynolds number (Rn), a requirement for turbulence models with low-Rn without wall function. Total number of cells is approximately 0.9M for half-side (starboard) of the hull for which solutions are mostly in the asymptotic range as was quantified by Sakamoto et al. (2011) using Verification and Validation (V&V) method.

3. Simulation Design

3.1 Geometry and flow condition

The portion of MS791 subjected to the modification is its skeg, in particular, it is below the waterline at full-load condition ($z/L_{pp} \leq 0.0$) and is from square station (S.S.) 3 to near aft-perpendicular (AP), therefore the wave making resistance coefficient C_w is assumed to be constant among all the modifications. This motivates to perform double-model flow simulations in the current study for which Rn based on L_{pp} ($Rn = U_0 L_{pp} / \nu$ where U_0 is ship speed and ν is fluid kinematic viscosity) is set to Rn=7.48E+06. In estimating P_D, the C_w at Froude number based on L_{pp} $\left(Fn = U_0 / \sqrt{g L_{pp}}\right)$ 0.235 corresponding to the navigation speed (20.0knots) of MS791 is taken from

the computational result by Sakamoto et al. (2011). The ship is non-dimensionalized by L_{pp} and its fore-perpendicular (FP) and AP is located at x/L_{pp}=0.0 and 1.0, respectively, in the computational domain with right-handed coordinate, i.e. positive x-direction from FP to AP, positive y-direction from port to starboard, and positive z-direction from keel to deck. The optimal propeller location for MS791 found by Sasaki (2010) is systematically rotated or translated depending on the parametric deformation of skeg geometry described in the next section. Notice that the rotating direction of the propeller is inward.

3.2 Parametric deformation of skeg geometry

Geometrical handling of the skeg is done by HullDes® which is a Computer Aided Design (CAD) and grid generation interface developed by collaborative works between ACT Co., Ltd. and NMRI. HullDes® defines hull surface via Non-Uniform Rational B-Spline (NURBS) and several pre-defined modification functions for hull surface have been prepared. These features allow users to deform hull geometry as parametric as possible without missing the smoothness, i.e. the 2nd-order continuity, of hull surface.

In the present study, three design parameters have been investigated: 1) rake of skeg in yz-plane (termed vertical rake) from -20.0deg to +20.0deg, 2) rake of skeg in xy-plane (termed horizontal rake) from -1.8deg to 2.8deg, and 3) stern "UV" shape. Constraint condition for these deformations is that the displacement of modified hull is the same as the original hull, and it is accomplished throughout Lackenby's criteria (Lackenby 1950). Since the computational results of current study are quite extensive, outcomes from 1) and 2) are presented herein and 3) will be presented on-site. Figures 1a and 1b show the schematic definition for vertical and horizontal rake of skeg, respectively. For the vertical rake, the center of rotation (CoR) is located at (y/L_{pp}, z/L_{pp})=(-4.5454E-02, -1.8181E-02) along x-direction, and body plan within $0.70 \le x/L_{pp} \le 0.981$ are subjected to the rotation in yz-plane. In order to avoid unintended collapse of NURBS patches, weight for the rotation linearly varies from 0.0 to 1.0 along x/L_{pp}=0.7 to 0.981, and z/L_{pp}=0.0 (design waterline) to -5.4545E-02 (bottom of the skeg), respectively. For the horizontal rake, the maximum displacement in y-direction is given to the longitudinal cusp of the skeg, and the waterlines within $0.70 \le x/L_{pp} \le 0.981$ and $-5.4545E\text{-}02 \le z/L_{pp} \le -1.8181E\text{-}02$ linearly move with the weight varying from 0.0 to 1.0 along x/L_{pp}=0.7 to 0.981. The angle of horizontal rake can be defined by the arc-tangent of the maximum displacement in y-direction at longitudinal cusp of the skeg divided by the distance between the root (x/L_{pp}=0.7) and longitudinal cusp (x/L_{pp}=0.981) of the skeg.

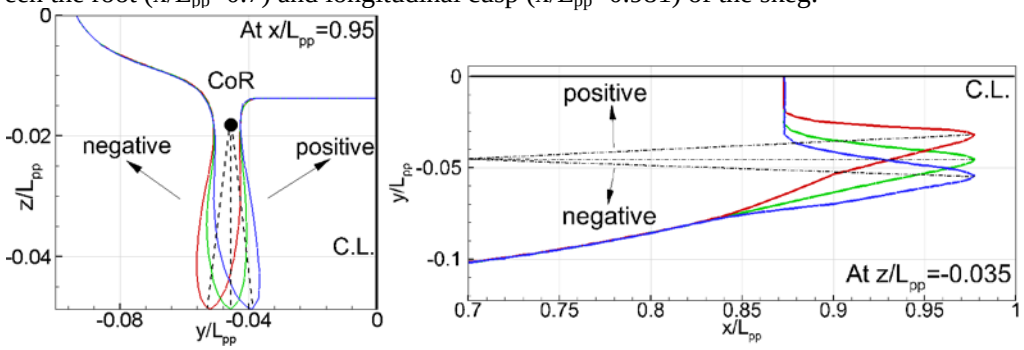

Fig. 1 Schematic definition for geometrical variations of skeg at port side:
a) vertical rake observing from AP, b) horizontal rake observing from deck

3.3 Physical quantities subjected to the analysis

Physical quantities appeared in the three-dimensional viscous resistance formulation (Lewis Ed., 1988), with the exception of C_w, are subjected to the analysis. Resistance simulation provides total resistance coefficient C_{tm}, form factor 1+k computed by adopting Schoenherr's skin-friction formula, and nominal wake coefficient $1\text{-}w_n$. Self-propulsion simulation at ship-point (with model-ship correlation allowance $\Delta C_f = 2.0E-04$) provides thrust deduction coefficient 1-t, effective wake coefficient $1\text{-}w_T$ at model-scale, propeller open-water efficiency η_o at model scale, relative rotative efficiency η_R calculated by thrust-identity method, hull efficiency η_H, propulsive

efficiency η_D and tank delivered power P_D computed using L_{pp}=110.0m.

4. Results and Discussions

4.1 Vertical rake

Figure 2 shows the computational results of resistance and self-propulsion factors as well as estimated P_D depending on the variation of vertical rake. Most of the physical quantities except η_D change in accordance with quadratic or higher order polynomial. Maximum vertical rake in negative direction minimizes C_{tm} and k up to 2.6%original, yet the maximum vertical rake in positive direction maximizes η_D by 2.7%original. This opposite trend results in P_D minimized at zero vertical rake, i.e. original geometry. Figure 3 shows the computational results of pressure distribution on the hull for variation of vertical rake. The low pressure region inside the tunnel stern becomes smaller as the vertical rake becomes larger in negative direction which contributes to decrease pressure resistance by 13.4%original. This phenomenon is caused by 'diffuser' effect. As the vertical rake becomes larger in negative direction, width of the tunnel becomes wider which enhances low velocity and the pressure becomes higher accordingly. It explains the trends of C_{tm} and k shown in Fig. 2. Figure 4 shows the computational results of axial velocity distribution with cross-flow vector at propeller plane for variation of vertical rake. Strong axial velocity region becomes wider at outside of the skeg on the propeller plane as the vertical rake becomes larger in negative direction which increases 1-w_n up to 2%original. As shown in Fig. 2, the trend of 1-w_n resembles to 1-w_T, in the meantime, η_H and η_D become maximum when 1-w_T is minimum which indicates that the improvement of 1-w_T is the key to earn better η_D for variation of vertical rake.

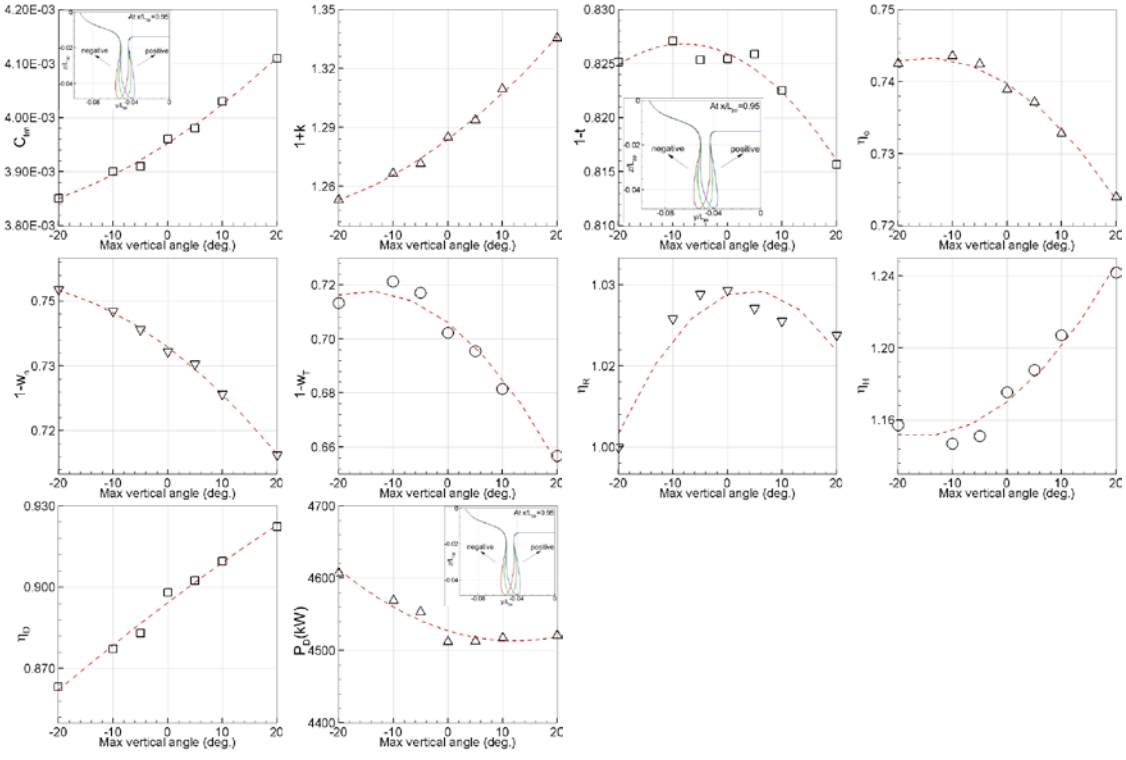

Fig. 2 Computational results of resistance/self-propulsion factors and P_D for variation of vertical rake. Symbols represent the computational result and lines depict fitting curve with 2nd-order.

4.2 Horizontal rake

Figure 5 shows the computational results of resistance and self-propulsion factors as well as estimated P_D depending on the variation of horizontal rake. All the physical quantities change in accordance with linear or quadratic polynomial. Maximum horizontal rake in positive direction

minimizes the resistance by 3.6%original, yet the variation of horizontal rake has relatively minor influence on η_D by 1.0%original.

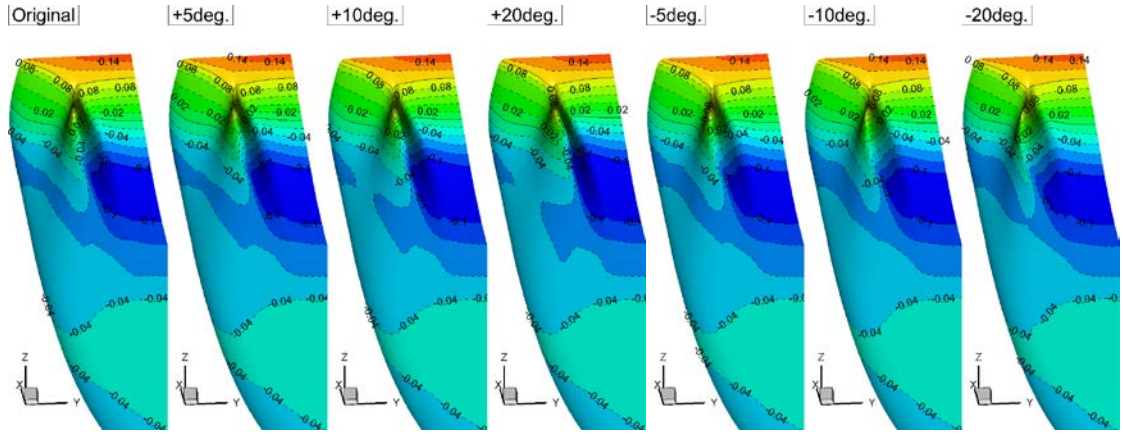

Fig. 3 Computational results of pressure distribution on the hull for variation of vertical rake

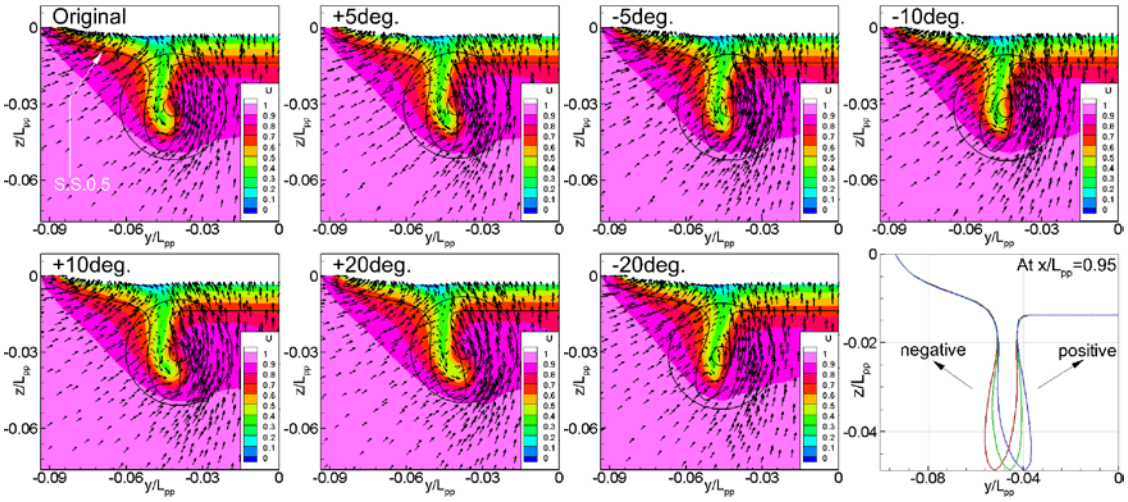

Fig. 4 Computational results of axial velocity distribution with cross-flow vector at propeller plane for variation of vertical rake

This trend results in P_D minimized by 1.4%original at largest horizontal rake in positive direction. Figure 6 shows the computational results of pressure distribution on the hull for variation of horizontal rake. As the horizontal rake becomes larger in positive direction, the low pressure region inside the tunnel stern becomes smaller and it slightly becomes larger at outside the tunnel stern. This phenomenon can be explained by assuming the skeg as an airfoil with attack angle (leading edge is x/L_{pp}=0.7 and trailing edge is a longitudinal cusp of the skeg). Positive horizontal rake makes outside skeg suction side, and inside the skeg pressure side, which contributes to decrease pressure resistance inside the skeg and k can be minimized by 18% and 3.5%, respectively. Opposite trend can be observed for negative horizontal rake since the suction side and pressure side is inverted. Figure 6 shows the computational results of axial velocity distribution with cross-flow vector at propeller plane for variation of horizontal rake. The distribution of circumferential mean velocity (CMV) along radial direction is presented as well. The less momentum defect in axial direction can be observed as the horizontal rake becomes larger in negative direction which increases $1\text{-}w_n$. As shown in Fig. 5, the trend of $1\text{-}w_n$ is opposite to $1\text{-}w_T$ which is different from what observed in the vertical rake series. This is most likely due to the increase of CMV along radial direction up to 1.5 times stronger than original as the horizontal rake becomes larger in negative direction. Stronger

counter rotating flow relative to the propeller rotating direction increases apparent rotation speed of the propeller, and then the advancing coefficient J becomes smaller which contributes to improve $1\text{-}w_T$.

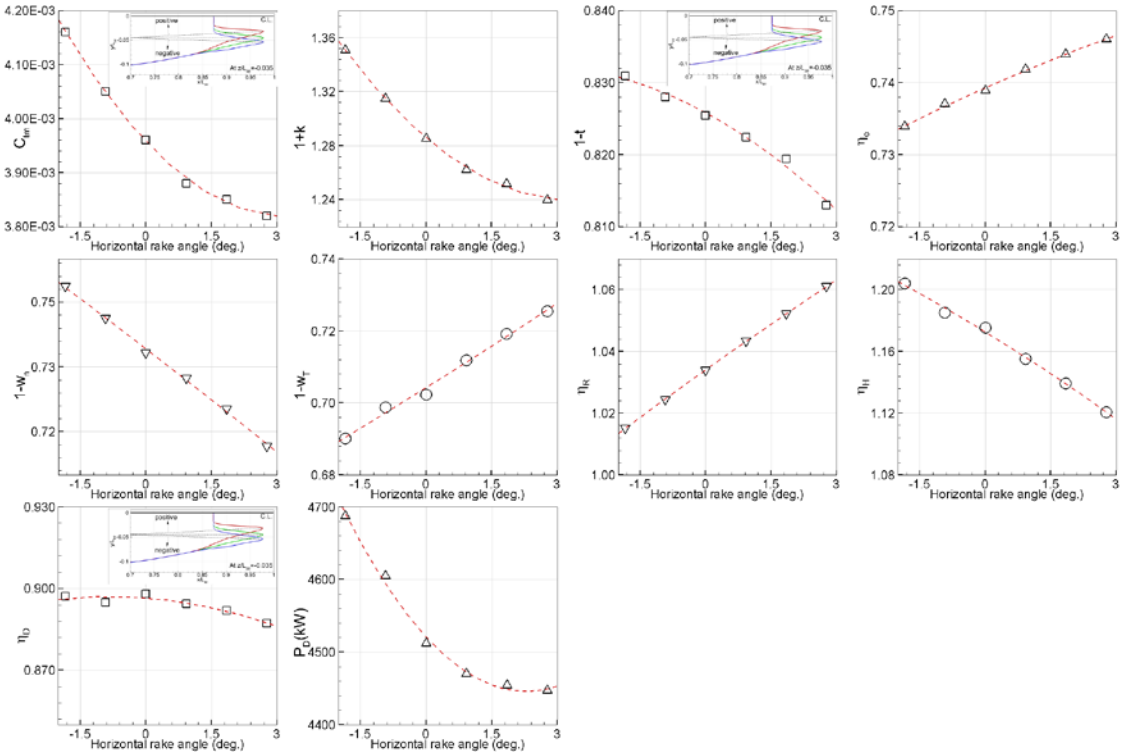

Fig. 5 Computational results of resistance/self-propulsion factors and P_D for variation of horizontal rake. Symbols represent the computational result and lines depict fitting curve with 2nd-order.

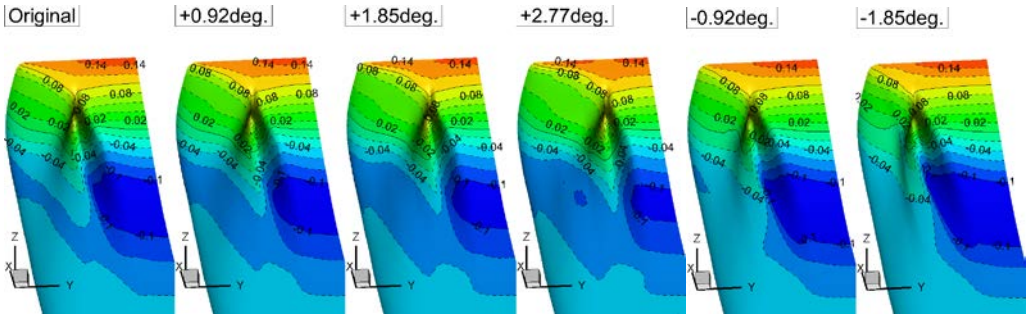

Fig. 6 Computational results of surface pressure distribution for variation of horizontal rake

5. Conclusion and Future Works

Relationship between skeg geometry of twin-skeg container ship and resistance/self-propulsion characteristics are investigated using viscous CFD approach. Three design parameters are considered and two representative results, vertical and horizontal rake of the skeg, are presented. For vertical rake, k and η_D show trade-off trend which makes minimizing P_D difficult with non-zero vertical rake. For horizontal rake, the skeg behaves as an airfoil with angle of attack which contributes for active variation in k with less influence on η_D, and resultant P_D becomes minimum when the horizontal rake becomes maximum in positive direction.

Based on the current results, several future works to be accomplished are; 1) confirm whether the influence of current deformation of the hull on C_w is really negligible or not by viscous or inviscid CFD; 2) expand the range of geometrical change above the waterline especially at

aft-part of the ship in view of minimizing C_w; 3) come up with innovative (but feasible) design parameters for skeg modification; 4) confirm whether the current criteria are valid for different type of twin-skeg ship, e.g. bulk carrier; and 5) complementary study with towing tank experiments.

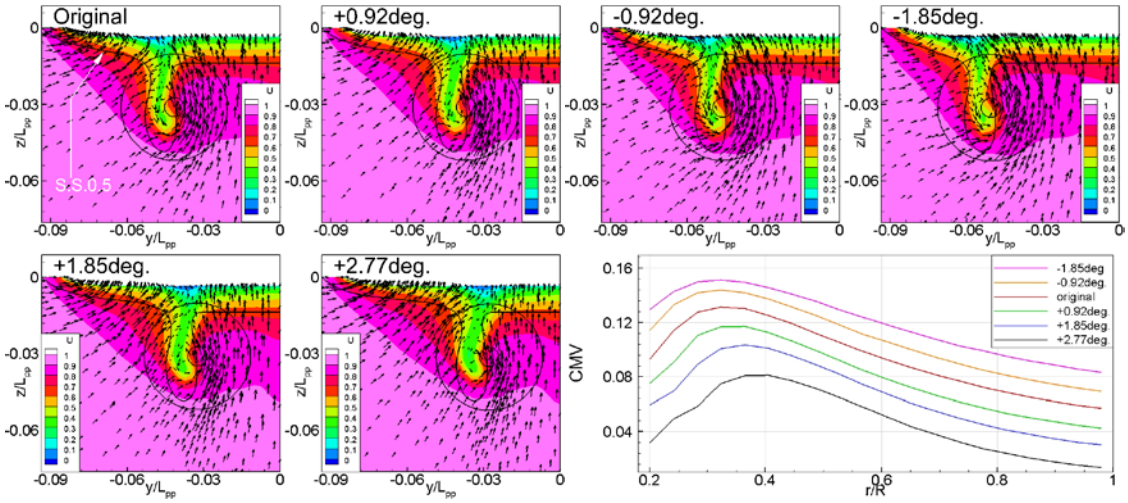

Fig. 7 Computational results of velocity distributions at propeller plane for variation of horizontal rake. Line figure describes the distribution of circumferential mean velocity (CMV) along radial direction at propeller plane.

Acknowledgements

This work is partially supported by MEXT Grant-in-Aid for Young Scientist (B) #24760680. Active and useful discussions from Mr. Kishimoto, Dr. Hirata and Dr. Ohashi, senior research associates at NMRI, are greatly appreciated.

References

1. Sasaki, N., 2010, What is the best propeller for ZEUS?, Proceedings, International Propulsion Symposium, 116-123, Okayama, Japan.
2. Sasaki, N., 2011, Boundary layer control of twin-skeg hull form with reaction podded propulsion, Proceedings, The 2nd International Conference on Marine Propulsors, 244-249, Hamburg, Germany.
3. International Maritime Organization, Resolution MEPC.203 (62), 2011, MEPC 62/24/Add.1.
4. Van, S-H., Park I-R., Kim, J., Lee, Y-Y., Park, N-J. and Kim Y-S., 2004, Hydrodynamic performance analysis of a twin-skeg container ship using CFD simulation, Proceedings, 4th Conference for New Ship and Maritime Technology, Shanghai, China.
5. Hino, T., 1997, A 3D unstructured grid method for incompressible viscous flows, Journal of the Society of Naval Architects of Japan, 182, 9-15.
6. Spalart, P.R. and Allmaras S.R., 1994, A one-equation turbulence model for aerodynamic flows, La Reschereche Aerospatiale, 1, 5-21.
7. Ohashi, K., Hirata, N., and Hino, T., 2003, A comparative study of body force models representing effects of contrarotating propellers, Proceedings, 105th Meeting of the West-Japan Society of Naval Architects, 55-64.
8. Moriyama, F., 1979, On an approximate numerical method for estimating the performance of marine propellers (in Japanese), Annual Report of Ship Research Institute, 16, 5, 361-376.
9. Sakamoto, N., Kawanami, Y., and Uto, S., 2011, Estimation of resistance and self-propulsion characteristics for low L/B twin-skeg container ship by unstructured-grid based RANS solver, revised, Journal of Ship Research.
10. HullDes Ver6.0 User's manual, ACT Co.,Ltd., http://www.actechnology.co.jp/english/index.html
11. Lackenby, H., 1950, On the systematic geometrical variation of ship forms, Transactions of the Institute of Naval Architects, vol.92, 289-316.
12. Lewis, E.V., Editor. 1988, Principle of Naval Architecture Second Revision Volume II Resistance, Propulsion and Vibration, SNAME, ISBN No. 0-939773-01-5.

Numerical simulation of a ship wake in shallow water using hybrid URANS-LES method

I. Shevchuk* and N. Kornev

Chair of Modelling and Simulation, University of Rostock, 18057 Rostock, Germany

1 INTRODUCTION Ship performance in shallow water conditions is a classical problem considered in ship theory and it has been studied by marine engineers for a long time. The influence of the depth restriction on ship performance is a complex matter, including a lot of significant phenomena: the increase of wave and viscous resistance, squat-effect, change in the manoeuvring behavior [1], the intensification of unsteady effects in the stern area and high velocity oscillations in the propeller plane [2], etc.. The latter effect combined with the pressure oscillations on the hull leads to the arise of high vibration at the stern.

The effects mentioned above are closely interconnected to each other. This connection is the reason for the complexity of ship behavior prediction in shallow water. For instance, the usual assumption of ship hydrodynamics that the wave pattern has insignificant influence on the viscous resistance and the breakdown into independent resistance parts are not quite correct in shallow water. The change of the pressure distribution due to the intensified wave generation is high and may lead to considerable boundary layer separations. This phenomenon causes a dramatic change in the viscous pressure resistance. For instance, it may become equal and even higher than the frictional resistance at the critical moving mode ($Fr_H \sim 1$) [3].

Due to these problems it is difficult to develop a reliable method to extrapolate the resistance forces from the model to the full scale at shallow water conditions. Even the experimental study of a ship behaviour in such conditions is complicated.

On this account the significance of computational methods for the study of the bottom influence is very high. The accuracy of the numerical simulations of squat-effect carried out so far using the potential flow theory and RANS is not yet satisfactory [4]. The analysis of the unsteady effects in the ship wake in shallow water has not been carried out yet. The reason of this consists in the poor URANS capability predicting the small-scale flow instabilities due to the high diffusivity of Reynolds' stress closure models. Indeed, URANS approach reproduces the large scale unsteady effects well, but it can't capture all vortex structures appearing in such conditions in the ship wake. LES method, capable to model this phenomenon is impractical due to enormous computational resources needed. So there is a need for an alternative.

This alternative is hybrid turbulence modeling, which is the combination of URANS and LES approaches. This class of methods has the main advantages of URANS and LES

*ivan.shevchuk@uni-rostock.de

and resolves the small-scale flow oscillations satisfactory with the reasonable computational effort. The main idea of the hybrid method is the use of URANS approaches in the region near the body and LES away from the body.

The present study is the continuation of the work being done at the Chair of Modelling and Simulation of the Rostock University [5]. While the previous study was dealing with the deep water conditions, the present study focuses on the study of capability of hybrid methods to model the unsteady effects in the ship wake behind full bottomed ships at the shallow water.

2 HYBRID METHOD The hybrid model used was developed in [5] on the base of a series of works done by swedish LES group (Peng et al.). It is based on the fact that the basic equations for LES and RANS methods have the same form:

$$\frac{\partial}{\partial t}(\rho\bar{u}_i) + \frac{\partial}{\partial x_j}(\rho\bar{u}_i\bar{u}_j) = \frac{\partial}{\partial x_j}[\rho\nu\frac{\partial\bar{u}_i}{\partial x_j} - \rho\tau_{ij}] - \frac{\partial\bar{p}}{\partial x_i} + \rho g_i \tag{1}$$

$$\frac{\partial}{\partial t}(\rho\bar{u}_i) + \frac{\partial}{\partial x_j}(\rho\bar{u}_i\bar{u}_j) = \frac{\partial}{\partial x_j}[\rho\nu\frac{\partial\bar{u}_i}{\partial x_j} - \rho\tau_{ij}^{SGS}] - \frac{\partial\bar{p}}{\partial x_i} + \rho g_i \tag{2}$$

The difference between (1) and (2) is the interpretation of the overline and the way of τ_{ij} modelling. The overline means filtering in LES and Reynolds averaging in RANS. τ_{ij} is a Reynolds' stress in the first equation and a subgrid scale stress in the second.

The computational domain is dynamically divided into LES and RANS regions according to the relation between the integral lenth scale L and the extended LES filter Δ :

$$\begin{aligned} &\text{if} \quad L > \Delta \quad \text{the cell is in LES region} \\ &\text{if} \quad L < \Delta \quad \text{the cell is in URANS region} \end{aligned} \tag{3}$$

L is calculated from the well-known formula of Kolmogorov and Prandtl with the correction factor 0.168 [6]:

$$L = 0.168\frac{k^{3/2}}{\epsilon}$$

Here k is the turbulent kinetic energy and ϵ is the dissipation rate. Both for LES and URANS domains the turbulent stresses are calculated from the Boussinesq approximation. The only difference between these regions is the definition of the turbulent viscosity, for LES the subgrid scale model is used and for URANS it is determined from the corresponding closure model.

This hybrid approach with a lot of different combinations of URANS and LES methods was implemented in OpenFOAM CFD software package (version 1.6-ext).

3 VALIDATION The described above method was validated on a few test cases and compared to the results of URANS simulation and EFD data.The validations were performed by two groups of CFD experts - one from the University of Rostock, and another one from the Voith company [7].

The tests of resistance prediction were carried out for two well known ship benchmark tests - KCS (2-phase) and KVLCC2 (1-phase). For the both cases hybrid models gave perfect results. The discrepancy with EFD was less than 5 % even for the coarsest meshes used (900k for the full body). For the KCS the mesh containing 1.7 million cells created

using snappyHexMesh gave the discrepancy less than 0.1 %. So one can conclude that the simulation of the integral flow parameters is very well performed by hybrid model.

The tests of the mean axial velocity in the propeller plane prediction gave also satisfactory results. The isolines obtained with the hybrid model were compared to these from EFD. Unlike the standard URANS models, hybrid method reproduces the experimental curves with a satisfactory accuracy both qualitatively and quantitatively. OpenFOAM with the implemented hybrid approach showed one of the best results compared to other CFD codes. For the wave pattern modelling one can draw the same conclusion [7].

On the analysis of the validation data one can conclude that the best results were obtained using the combination of $k-\omega$ SST for URANS and Dynamic Smagorinsky (DSM) LES models [5].

4 RESULTS OF UNSTEADY EFFECTS PREDICTION The computations have been performed for the generic ship with the form and dimensions similar to these of a real inland cruise ships: $L = 135\,m$, $B = 12\,m$, $T = 2\,m$. Fig. 1 illustrates the form of the generic hull. The probable locations of the propellers on one side are shown by red spheres. Such ships usually have four propellers.

Two depths were considered: $H = 1.5\,T$, $H = 1.25\,T$. For the both cases the inflow velocity was 6 m/s. These conditions correspond to $Fn = 0.15$ and $Fn_H = 1.1, 1.2$.

Although this moving mode is critical concerning the Froude number Fn_H, the influence of the free surface was neglected, since the main objective of the work was to capture the unsteadiness in the stern area. It is believed that these effects in the two phase flow are intensified or remain unchanged. Thus the doubled body approach was used.

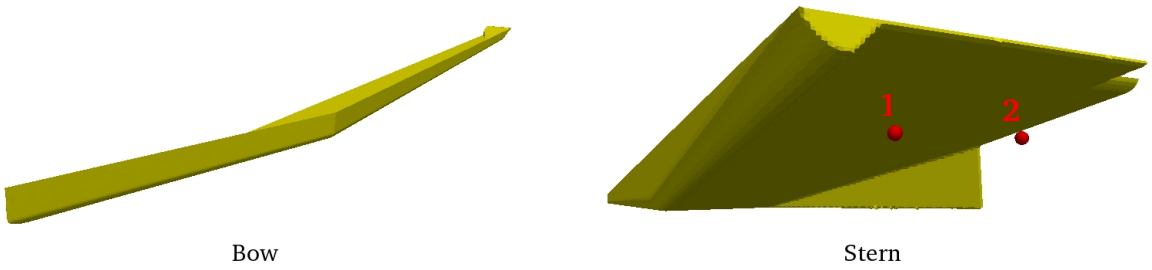

Figure 1: The form of generic hull

All simulations were carried out using OpenFOAM 1.6-ext on unstructured mesh of 2.2 million cells created with snappyHexMesh generator. The computational grid had $y^+ = 30$ in the bow area and $y^+ = 15$ at the stern. The used hybrid method combines dynamic Smagorinsky SGS model (DSM) with $k-\omega$ SST approach which also uses the wall functions at the ship boundary. All test cases were also computed with URANS approach to compare the results with these from hybrid method. The vortex structures in the flow were identified using λ_2 criterion developed by Jeong and Hussain [8].

4.1 COMPARISON OF URANS AND HYBRID The comparison of vortex structures in the stern area predicted with URANS and hybrid models is shown in the Fig. 2, and 3. Both methods predict two large longitudinal vortices which are generated in the stern area - one bilge vortex - and one near the skeg. The intensity of these structures predicted by URANS is much lower than these predicted by the hybrid approach. Since the grid is the same for both methods the only reason is that the URANS approach is

more dissipative. A large number of small vortices making the serious contribution to the unsteady velocity field is not captured by URANS. The vortex field gained from the hybrid method is more complicated and rich of vortex structures of different scales. As shown below, these structures are of a high importance for the propeller performance.

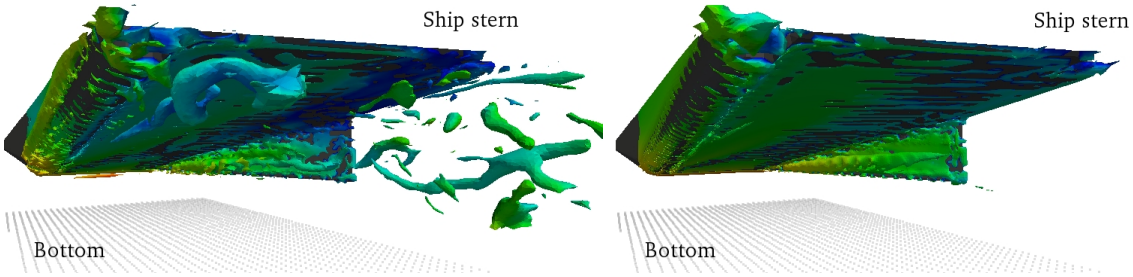

(a) Hybrid $k-\omega$ SST (b) URANS $k-\omega$ SST

Figure 2: Comparison of the vortex structures from URANS and hybrid model for $H = 1.5, T$ ($\lambda_2 = -7$)

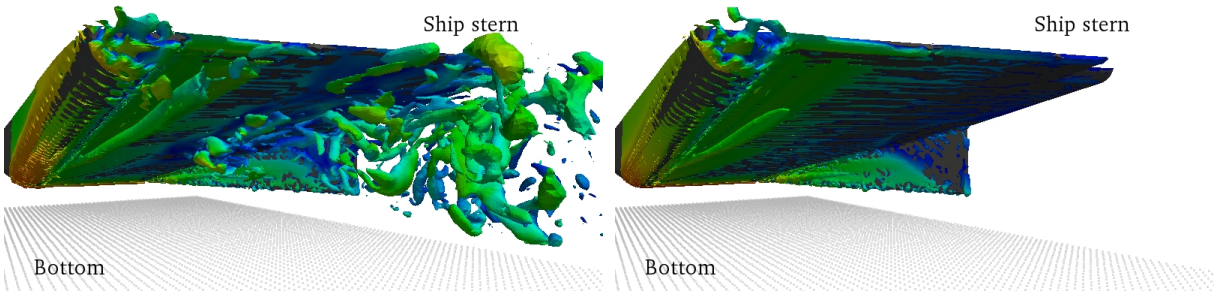

(a) Hybrid $k-\omega$ SST (b) URANS $k-\omega$ SST

Figure 3: Comparison of the vortex structures from URANS and hybrid model for $H = 1.25\,T$($\lambda_2 = -15$)

As seen from Fig. 2a,3a the change of the water depth leads to the increase of vortex sizes and intensification of instability in the wake flow which is not captured by URANS.

4.2 SEPARATION OF A BOUNDARY LAYER Another effect, which was also captured only by hybrid model is the intensification of the boundary layer separation observed at $H = 1.25T$ on the skeg. The reproduction of this phenomenon is very significant due to the sudden increase of the viscous pressure resistance. In our computations we observed that the difference in pressure force between URANS and hybrid model is about $+12\%$. Of course it is hard to say if it is due to the separation or not, because there is no experimental data available.

4.3 VELOCITY OSCILLATIONS IN PROPELLER PLANE The flow instability influences the propeller performance due to strong oscillations of the axial velocity. The probes of U_x in propeller working area are presented in Fig. 4.

P1 and P2 are the expected propeller axis locations (see Fig. 1). As can be seen the oscillations predicted by the hybrid method at point P1 are not significant and their

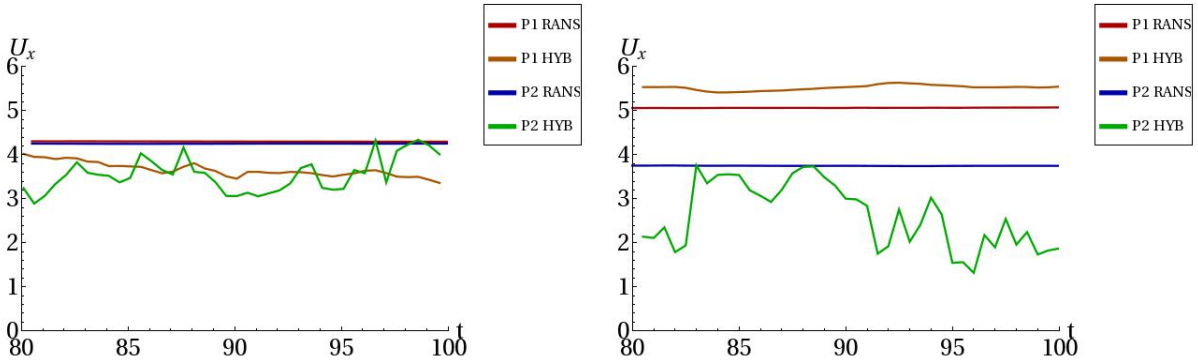

(a) H = 1.5 T (b) H = 1.25 T

Figure 4: U_x at propeller working area

intensity almost doesn't depend on H/T ratio. But as for the prediction at P2, the results obtained using URANS and hybrid method are qualitatively different. The flow oscillations arising close to the skeg cause high unsteadiness of the velocity field. At $H = 1.5T$ the fluctuations of U_x are within a 15% range from the average value. When the hull gets closer to the bottom the vortices detaching from the flow separation area interact with the skeg vortex and it leads to 30% fluctuations. The interesting result is that even the mean velocity predicted by hybrid and URANS approaches considerably differ from each other. This effect is to be studied further.

CONCLUSION In the scope of this work the capability of the hybrid turbulence modelling method to predict the unsteady effects in the wake flow behind a generic inland ship at shallow water conditions was tested. The analysis of the results shows, that the vortex structures predicted using this approach are much more intense than these predicted by URANS method. The significant achievement is the reproduction of the intense boundary layer separation, whereas the URANS model gave poor resolution. It is shown that appearance of these phenomena leads to the sharp change in the velocity field at the propeller location, and it is apparent that the forces acting on the propeller will also oscillate more strongly than it is predicted by URANS. Since the EFD data for the generic ship are not available, the validation has not been carried out. Thus, so far it is not possible to draw conclusions on the prediction accuracy. However, qualitatively, the effects modelled (such as the flow separation) are in complete agreement with the practical observations.

References

[1] Schoop-Zipfel, J., Abdel-Maksoud, M., Rung, T., Investigation of the Influence of Water Depth on Ship Manoeuvring Behaviour, 13th Numerical Towing Tank Symposium. Duisburg, Germany, October 2010.

[2] Basin, A., Velednicky, I., Ship hydrodynamics in shallow water, Leningrad, Sudostroenie, 1976.

[3] Ship Theory Handbook, In 3 Volumes. Vol I. Hydromechanics, Resistance of Ship, Ship Propulsion Devices, Ed.by Y.I.Voitkounski., Leningrad, Sudostroenie, 1985, 768 p.

[4] A. von Graefe, B. O. el Moctar, V. Shigunov, H. Söding, T. Zorn, Squat computations for containerships in restricted waterways, Proceedings of the 2nd International Conference on Manoeuvring in Shallow & Coastal Waters, Trondheim, Norway 2011.

[5] Kornev, N., Taranov, A., Shchukin, E., Kleinsorge, L., Development of hybrid URANS-LES methods for flow simulation in the ship stern area, Ocean Engineering, Vol. 38, 2011, pp. 1831–1838.

[6] Schlichting, H., Boundary layer theory, Springer, 2000.

[7] N. Kornev, A. Taranov, E. Shchukin, J. Springer, M. Palm, Yu. Batrak, Development, application and validation of hybrid URANS-LES methods for flow simulation in the ship stern area, 29th Symposium on Naval Hydrodynamics, Gothenburg, Sweden, 26-31 August 2012.

[8] Jeong, J. and Hussain, F., On the Identification of a Vortex, J. Fluid Mech., Vol. 285, pp. 69-94.

Computing Added Resistance in Waves – Rankine Panel Method vs RANSE Method

Heinrich Söding, TU Hamburg-Harburg, Hamburg/Germany, h.soeding@tu-harburg.de
Vladimir Shigunov, Germanischer Lloyd, Hamburg/Germany,
vladimir.shigunov@gl-group.com
Thomas E. Schellin, Germanischer Lloyd, Hamburg/Germany,
thomas.schellin@gl-group.com
Ould el Moctar, Germanischer Lloyd, Hamburg/Germany, moct@gl-group.com
Sebastian Walter, Universität Duisburg, Duisburg/Germany, presently Meyer Werft GmbH,
Papenburg/Germany, sebastian.walter@meyerwerft.de

1 Introduction

Ship design is usually performed on the basis of powering requirements in calm water without detailed consideration of the actual operating conditions. The effect of seaway is included using an experience-based allowance on the required power called the sea margin. This practice can lead to either unnecessary excessive power reserves, or to underpowered ships. Reliable prediction of the propulsion power increase in waves is important for both ship designers (selection of the propulsion system) and operators (establishing time schedules, estimation of service speed and fuel consumption, optimising speed and course).

2 Model tests

Model tests for added resistance in waves use either self-propelled or towed models. Self-propelled models eliminate the influence of the towing equipment on model motions; however, the influence of motions and waves on the thrust deduction factor (required to estimate the added resistance) remains a factor of uncertainty. Towed models have either restrained surge motion, or they are connected by soft springs to the towing carriage. Restraining the surge motion may influence the added resistance, especially if it interferes with the pitch and heave motions; thus the arrangement with springs appears more appropriate. The model set-up should ensure that springs do not influence ship motions; for instance, the natural frequency of the springs must differ from the encounter frequency as much as possible.

Another difficulty with experiments for added resistance in waves is the fact that the added resistance (average longitudinal force over time) is small compared to the amplitude of the force variations. Thus, errors in measuring these forces might be comparable to or even exceed the average force itself. Further, the added resistance is sensitive to the quality of wave generation and wave measurement, especially in short waves, because, unlike linear reactions, added resistance depends on wave amplitude squared.

3 RANSE solvers

CFD methods might, in principle, directly address the problem of power increase in irregular waves (if combined with an engine model). However, both long waves (leading to large ship motions) and short waves (which contribute to the added resistance by wave diffraction) have to be resolved simultaneously, which would increase significantly the required grid size, number of cells and computational time. Therefore, CFD methods have so far been applied only to the problem of added resistance in regular head waves in a restricted range of wave frequencies.

CFD methods provide the total resistance, i.e. calm water resistance and added resistance in waves. The calm-water contribution has to be calculated separately on the same grid as used for the prediction of the total resistance, and subtracted from the total resistance. To accurately

compute the calm-water resistance, fine grids are required to resolve the turbulent boundary layer on the hull and the steady wave system. Much coarser grids suffice for the resolution of (medium and longer) incoming, radiated and diffracted waves that are relevant for added resistance. Predictions of ship motions and added resistance in medium and long waves agree well between fine and coarse grids (Fig. 1). This suggests that added resistance in medium and longer waves can be computed on grids which resolve the waves, but not the boundary layer. To obtain the total resistance, an additional calculation on a fine grid is necessary.

4 Potential flow codes

Because CFD methods require too much computer resources to study the influence of the various parameters on added resistance, potential flow methods are applied predominantly. Linear seakeeping analysis describes ship response (motions, sectional forces and moments, hull pressures, etc.) as time-periodic sinusoids, neglecting effects that depend nonlinearly on wave height. Time averages of linear responses are zero. However, waves generate also forces and moments that are non-zero when averaged over a wave encounter period. The lowest non-zero order of these forces and moments is two, i.e., they are proportional to the wave amplitude squared.

In a regular wave of encounter frequency ω_e, any second-order effect consists of a part which oscillates with frequency $2\omega_e$ and has the average zero, and of a stationary part. Only the latter is of interest here. It can be determined without knowing the second-order oscillating flow potential; that simplifies the solution very much. But even the remaining potential flow problem is so complicated that certain terms (e.g. those containing third-order space derivatives of the stationary potential) have to be neglected. Within the second-order framework, effects like wave breaking or the hull shape above the stationary waterline cannot be accounted for. (Model tests and numerical simulations showed that the bow sharpness above the calm-water waterline has influence on added resistance.)

When considering the energy balance, the increased resistance in waves is caused by (a) wave radiation due to ship motions, and (b) diffraction of incident waves by the ship hull. The radiation-induced added resistance is large when ship motions are large, i.e., in longer waves. The diffraction of incident waves produces a diffraction-induced component of added resistance, which depends weakly on the wave frequency and thus becomes the dominant component in shorter waves, where ship motions are small. In short waves, say for waves shorter than 1/4 to 1/3 of the ship length, added resistance is difficult to predict accurately by any method.

Instead of considering this energy balance, for computing the added resistance we prefer to use the pressure distribution on the hull. The second-order stationary force follows from the expression

$$\overline{\vec{F}_2} = \sum_{all\ panels} \overline{\left(\underline{p}_0 \vec{f}_2 + \underline{p}_1 \vec{f}_1 + \underline{p}_2 \vec{f}_0\right)} + \sum_{waterline\ panels} \frac{|\underline{\hat{p}}|^2 \vec{\underline{s}} \times (\vec{f}_0 \times \vec{\underline{s}})}{4\rho g\ (\vec{f}_0 \times \vec{\underline{s}})_3}. \tag{1}$$

Indices 0 to 2 indicate the order (with respect to wave amplitude), whereas index 3 designates the vertical component. $\underline{p}$ is pressure at a hull-fixed location, ρg the statical downward pressure gradient, $\vec{f}$ is the panel area vector (inward normal direction in inertial coordinates), and $\vec{s}$ is a vector along the stationary waterline contour. An overbar designates a time average, and the hat symbol indicates the amplitude. The first sum designates the second-order force on the hull up to the stationary waterline; the last term takes account of the variable hull immersion including dynamic swell-up.

5 Potential flow code *GL Rankine*

Here a new panel method is applied to compute added resistance in waves. The code *GL*

Table I: Main particulars of WILS containership

L_{pp}	321.00 m	KG	21.296 m
B	48.40 m	GM	2.000 m
T	15.00 m	k_{xx}	19.073 m
C_B	0.6016	$k_{yy} = k_{zz}$	77.228 m

Rankine is based on the theory described in Söding (2011). Söding et al. (2012a,b) give more *GL Rankine* applications for other ships (Wigley hull and KVLCC2 tanker). The frequency-domain panel method is based on Rankine sources. Like in other Rankine source seakeeping codes, the flow potential is taken as the sum of the parallel flow due to forward speed, the steady disturbance potential ϕ_0, and the time harmonic flow potential due to the incoming wave, its diffraction at the hull, and due to ship motions:

$$\phi = -ux + \phi_0(\underline{\vec{x}}) + \mathrm{Re}(\hat{\phi} \mathrm{e}^{\mathrm{i}\omega_e \mathrm{t}}). \tag{2}$$

One distinctive feature of our code is the steady disturbance potential: It is taken to be constant in the ship-fixed coordinate system, not in the inertial system as usual. Both assumptions are physically correct, but they lead to different boundary conditions for $\hat{\phi}$ and thus to different amplitudes $\hat{\phi}$. The so-called m terms, which are difficult to determine accurately, appear in our formulation not in the hull boundary condition, but in the free surface boundary condition, where they can be determined more accurately, and where inaccuracies have less influence on the pressure force on the hull.

Other features in which our method differs from other Rankine source methods are:

- No second derivatives of the steady potential appear in determining the first-order hull pressure. (These terms should be present in the usual Rankine source method, but are mostly ignored.)
- A transom condition is satisfied, which states that, at an immersed transom, the water surface hight oscillates just as that of the transom.
- The term involving $\vec{f}_2$ in (1) is ignored in other methods; the same holds for some terms in the complicated expression for $\underline{p}_2$.

6 Test case

As a test case, the WILS containership designed by the Maritime and Ocean Engineering Research Institute (MOERI) is used. The model was tested in two wave directions at two Froude numbers in a scale of 1/60 under the Joint Industry Project WILS II. Table I lists main particulars of the ship. Two experimental techniques provided the average longitudinal force in waves. One technique relied on the sum of the spring forces, the other on the relative surge displacement of the model with respect to the carriage. The resistance in calm water was subtracted from the post-processed resistance to obtain the added resistance in waves.

Here, the test in head waves at the Froude number 0.183 is used for validation.

Both *GL Rankine* and the RANSE code *Comet* were used to compute added resistance for the full-scale ship. The RANSE simulations were performed on two different grids. The fine grid resolved the turbulent boundary layer and the steady ship wave system. The coarse grid was chosen to just resolve incoming waves and wave-induced ship motions, but it did not accurately resolve the calm-water ship wave system and the calm-water resistance. On both grids, separate simulations in calm water obtained the calm-water contribution to the resistance, which was then subtracted from the time-averaged value of the total resistance in waves, computed on the same grid, to obtain the value of the added resistance.

Figure 1 plots the non-dimensional added resistance coefficient

$$C_{aw} = \frac{R_{aw}}{\rho g \zeta_a^2 B_{WL}^2 / L_{pp}} \tag{3}$$

as a function of the non-dimensional wave frequency

$$\tilde{\omega} = \omega \sqrt{L_{pp}/(2\pi g)} = \sqrt{L_{pp}/\lambda}. \tag{4}$$

Results of *GL Rankine* (curve) are compared with experimental data (filled markers) and with results of *Comet* on fine and coarse grids (light markers). Note the large difference between the results of the two test evaluations, especially in short waves. The two RANSE predictions are quite similar to each other and to the results of the potential code in medium and long waves, whereas they show gross relative errors in the high-frequency region. This demonstrates the inherent difficulty to obtain reliable estimates of added resistance in short waves. The results of *GL Rankine* end at about $\tilde{\omega} = 1.4$ because for higher frequencies more than the upper limit of about 22000 panels (due to the hardware used) would have been required.

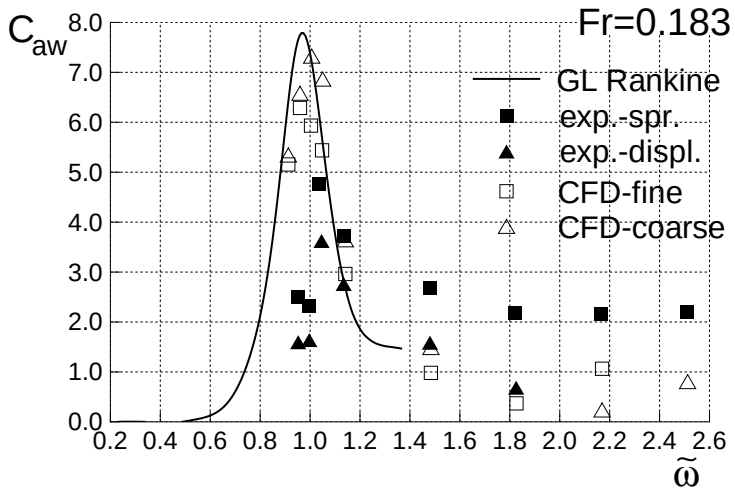

Figure 1: WILS containerschip. GL Rankine results (curve) compared to measurements based on different evaluation techniques, and to computations with *Comet* on a fine and a coarse grid.

7 Conclusion

Because of the good agreement between results of RANSE calculations and of the potential flow code *GL Rankine* at medium and large wave lengths, we conclude that both methods can give accurate results for added resistance in this frequency range. The experimental results deviate substantially from the computed ones and appear less reliable.

In the high-frequency range, on the other hand, neither computational nor experimental results appear both feasible and correct. For large ships, these relatively short waves are most interesting because they are generated by moderate and, thus, more frequently occuring wind speeds. Formulae given in the relevant literature for the added resistance at the high frequency limit appear also not correct, at least not in the practically important frequency range between about $\tilde{\omega} = 1.4$ and 2. Own attempts to establish better approximations for this case were unsuccessful.

Thus, for higher frequencies than about $\tilde{\omega} = 1.4$ (depending a little on Froude number and wave heading) we use a simple extrapolation of C_{aw}: Beyond the highest ω for which reliable calculations are possible, C_{aw} is increased by a factor depending on the ratio of ship draft (for head waves: in the forebody) to incident wave length. That is motivated by the fact that only waves of a length shorter than about twice the draft are fully reflected by a long obstacle.

8 References

SÖDING, H. (2011), Recent progress in potential flow calculations, Proc. 1st Int. Symp. on Naval Architecture and Maritime, Istanbul, Turkey

SÖDING, H.; GRAEFE, A. von; EL MOCTAR, O.; SHIGUNOV, V. (2012a), Rankine source method for seakeeping predictions, 31st Int. Conf. on Ocean, Offshore and Arctic Eng. OMAE, Rio de Janeiro

SÖDING, H.; SHIGUNOV, V.; SCHELLIN, T.; EL MOCTAR, O. (2012b), A Rankine panel method for added resistance of ships in waves, 31st Int. Conf. on Ocean, Offshore and Arctic Eng. (OMAE), Rio de Janeiro

Towards goal-oriented simulation in ship hydrodynamics

Jeroen Wackers, Ganbo Deng and Michel Visonneau
Laboratoire de recherche en Hydrodynamique, Energétique et Environnement Atmosphérique,
Ecole Centrale de Nantes, CNRS-UMR 6598, 44321 Nantes Cedex 3, France
Jeroen.Wackers@ec-nantes.fr

1 Introduction

Goal-oriented flow simulation, for the purpose of this article, denotes simulation methods where numerical or physical parameters and techniques can be automatically adjusted by the solver in order to provide accurate and efficient computation of a given single output parameter. The concept originates from the idea that flow computations are often performed to answer a specific question and that computational resources should therefore be applied for answering this question, and for nothing else. And also, if non-expert users are to base crucial design decisions only on the results of CFD computations, they need simulation software which provides reliable results at least partially in an automatic way. Thus, goal-oriented simulation has two key aspects: the simulation has to be adaptive to provide efficient results and the precision of these results must be estimated to guarantee reliability.

Solutions to the adjoint equations of the Navier-Stokes system are often at the heart of goal-adaptive techniques. The adjoint solution gives the relative influence of the local solution anywhere in the flow domain on a given flow output parameter. It can be used in two different ways. First, a weighting of the local truncation errors with the adjoint solution provides an error estimator for the output parameter. And second, this local weighted error indicates the zones which have the greatest importance for the accurate computation of this parameter and can thus be used as a criterion to pilot automatic grid refinement.

While adjoint-based error estimation and mesh refinement is common for the simulation of structures [1] and has been successfully applied to compressible Euler flow [4], its use for incompressible Reynolds-averaged Navier-Stokes flows at high Reynolds numbers is not straightforward and few results have been reported. Notably, Stück and Rung [7] use the adjoint solution for hull form optimisation. Particular difficulties for these flows are:

- The RANS equations contain turbulence models which are in general not taken into account for the computation of the adjoint solution. This may have an influence on the quality of the error estimation.
- To model turbulent boundary layers, meshes are used with very high aspect-ratio cells near the walls. The adjoint equations and especially the estimation of the local truncation error are sensible to these meshes.
- The flow is incompressible, which is very hard for grid refinement. In fact, there are no obvious local zones which require great precision (such as shock waves and contact discontinuities in compressible flow); to get accuracy, the flow needs to be more or less well resolved everywhere. Finding the resulting optimum grid sizes requires a delicate balance which puts strong requirements on the quality of the refinement criterion.

The goal of this article is to provide an initial investigation of the possibilities for adjoint-based error estimation and grid refinement for ship flows. A continuous adjoint solver is under development for ISIS-CFD, the unstructured Navier-Stokes solver developed by ECN-CNRS. This solver is combined with local truncation error estimation by high-order integration of the RANS equations over the grid cells [3] for error estimation. Grid refinement for the flows of interest and the unstructured hexahedral meshes that we use, is necessarily anisotropic [9]: grid cells to be refined can be divided in only one direction, as well as in several. For goal-oriented anisotropic refinement, we adapted the technique proposed by [4] where the criterion is based on the Hessians (second-derivative matrices) of the fluxes. In the light of the difficulties outlined above, these techniques are investigated critically.

Section 2 briefly describes the ISIS-CFD flow solver. Then section 3 introduces the continuous adjoint equations and very briefly describes their discretisation. Sections 4 and 5 give, respectively, an overview of the error estimation and grid refinement techniques. Finally, section 6 shows initial tests on laminar and turbulent flows which shed some light on the possible efficiency of these methods.

2 The ISIS-CFD flow solver

ISIS-CFD, available as a part of the FINE^{TM}/Marine computing suite, is an incompressible unsteady Reynolds-averaged Navier-Stokes (RANS) method [2, 6]. The solver is based on the finite volume method to build the spatial discretisation of the transport equations. Pressure-velocity coupling is obtained through a Rhie & Chow SIMPLE-type method: in each time step, the velocity updates come from the momentum equations and the pressure is given by the mass conservation law, transformed into a pressure equation.

The discretisation is face-based. While all unknown state variables are cell-centered, the systems of equations used in the implicit time stepping procedure are constructed face by face. Fluxes are computed in a loop over the faces and the contribution of each face is then added to the two cells next to the face. This technique poses no

specific requirements on the topology of the cells. Therefore, the grids can be completely unstructured, cells with an arbitrary number of arbitrarily-shaped faces are accepted. The code is fully parallel using the MPI (Message Passing Interface) protocol.

An automatic adaptive grid refinement technique is included in the solver ISIS-CFD [8, 9]. The method supports the isotropic and anisotropic refinement of unstructured hexahedral meshes. Earlier refinements can be undone in order to adapt the grid to unsteady problems. The refinement criterion, which indicates where the grid must be refined, can be modified very easily; different refinement criteria have already been tested. And finally, the grid refinement is performed in parallel and includes an automatic dynamic load balancing in order to redistribute the refined grid over the processors when some partitions have been refined more than the others.

3 Adjoint equations and discretisation

This section shows very briefly how the adjoint to the RANS equations follows from the estimation of the error in a global quantity. The RANS system of equations itself, $\mathcal{N}(\mathbf{U}) = 0$ can be expressed as follows:

$$\left[u_i u_j + p\delta_{i,j} - \mu\left((u_i)_j + (u_j)_i\right)\right]_j = 0, \tag{1a}$$

$$(u_j)_j = 0, \tag{1b}$$

with u_i the velocity components, p the pressure, μ the (variable) viscosity coming from a turbulence model, and δ the Kronecker delta function. The Einstein summation convention is used, indices outside brackets denote differentiation. $\mathbf{U} = [u_1, u_2, u_3, p]^T$ is the exact solution of this system. Finally, $\mathbf{U}_h$ denotes an approximate (numerical) solution of (1).

We consider an output functional on the solution $J(\mathbf{U})$, i.e. a scalar parameter computed from $\mathbf{U}$. This can be for example a force on the boundary such as lift or drag, or a volume integral over a part of the interior, e.g. a propeller plane flow quality function. We are interested in the error in J when it is computed from $\mathbf{U}_h$ instead of $\mathbf{U}$. If this error is small, we can linearise:

$$J(\mathbf{U}_h) - J(\mathbf{U}) \approx (\mathbf{g}, \mathbf{U}_h - \mathbf{U})_\Omega. \tag{2}$$

The field quantity $\mathbf{g}$ is the linearisation of J around $\mathbf{U}$, $\mathbf{g} = [\frac{\partial J}{\partial u_1}, \frac{\partial J}{\partial u_2}, \frac{\partial J}{\partial u_3}, \frac{\partial J}{\partial p}]$. $(\cdot,\cdot)_\Omega$ denotes an inner product, integrated over the flow domain.

In practice, it is not easy to evaluate the error in J using (2), because $\mathbf{U}$ is unknown and difficult to estimate. It would be much easier to compute the error in J from the local residuals, as it is possible to estimate these. Therefore, we shall try to find a field $\mathbf{z}$ which gives the same results as $\mathbf{g}$ in (2), but working on the residuals:

$$(\mathbf{z}, \mathcal{N}(\mathbf{U}_h) - \mathcal{N}(\mathbf{U}))_\Omega = (\mathbf{g}, \mathbf{U}_h - \mathbf{U})_\Omega. \tag{3}$$

If a $\mathbf{z}$ dependent on $\mathbf{U}$ but independent of $\mathbf{U}_h - \mathbf{U}$ can be found such that (3) holds $\forall(\mathbf{U}_h - \mathbf{U})$, then we call $\mathbf{z}$ the adjoint solution.

A system of equations for the adjoint solution can be found as follows:

- Construct a linearisation L of $\mathcal{N}$ and substitute it in the left-hand side of (3): $(\mathbf{z}, \mathcal{N}(\mathbf{U}_h) - \mathcal{N}(\mathbf{U}))_\Omega \approx (\mathbf{z}, L(\mathbf{U}_h - \mathbf{U}))_\Omega$.
- Reorder and rework this expression using integration by parts, such that all the linear operators work on $\mathbf{z}$ and $\mathbf{U}_h - \mathbf{U}$ becomes isolated. This leads to a new linear system L^* such that $(\mathbf{z}, L(\mathbf{U}_h - \mathbf{U}))_\Omega = (L^*\mathbf{z}, \mathbf{U}_h - \mathbf{U})_\Omega$ plus boundary integral terms.
- Given this expression, (3) holds iff $L^*\mathbf{z} = \mathbf{g}$. This is the adjoint system of equations, which is solved for $\mathbf{z}$.

For the RANS equations, the adjoint system reads:

$$-u_i(z_j)_i - u_i(z_i)_j + (z_p)_j - \mu\left((z_i)_j + (z_j)_i\right)_j = g_j, \tag{4a}$$

$$(z_j)_j = g_p, \tag{4b}$$

where $\mathbf{z} = [z_1, z_2, z_3, z_p]^T$.

Like the primal system, the adjoint equations are discretised with a finite-volume technique and a segregated Rhie & Chow method; this is possible because the continuity equation (4b) is the same as in the primal system. Space is lacking here to describe the discretisation in full, but a few remarks are given:

- The velocities in the convective operators are the velocities u_i coming from the primal system. However, due to the minus signs in (4a), the adjoint 'flow' is backwards! This must be taken into account in the upwind discretisations.

- The term $-u_i(z_i)_j$ makes these equations non-conservative and impossible to write in conservative form. The system can be written in different ways, we chose the fully convective form (4a) because it is the simplest expression. To construct a finite-volume discretisation, we use constant cell-centred values for the velocities u_i when integrating over a cell. Thus, for all convective terms, the fluxes over a face are different for the left and right cells, since the u_i on the two sides of the face are different.

- The term $-u_i(z_j)_i$ is discretised with upwind reconstruction. However, the term $-u_i(z_i)_j$ originates from the linearisation of the mass fluxes which have central discretisations in the primal system. We found that, for the adjoint system to be stable, also the adjoint terms $-u_i(z_i)_j$ require a central discretisation. Despite this discretisation, the current formulation lacks robustness for high-Reynolds flows in regions of very low velocity. This is a problem on which we are working.

As for the primal system, the z_i-equations are solved with Gauss-Seidel while PGCStab is used for the z_p-equation. The z_i-corrections are underrelaxed, but not the the z_p-correction.

4 Estimating residuals

Equation (3) can be used directly to estimate the error in $J(\mathbf{U}_h)$ or even to obtain an improved approximation by subtracting the error estimation from the computed value of J. For this, besides the adjoint solution, we need to compute the residuals $\mathcal{N}(\mathbf{U}_h)$, the result of applying the exact RANS equations to the approximate numerical solution (the term $\mathcal{N}(\mathbf{U})$ is zero, of course). Since we cannot evaluate these exact equations, the residuals are approximated with a higher-order finite-volume discretisation, similar to [3]. This approximation is performed as follows:

- Flux vectors in the face centres and in the nodes of the faces are computed with least-squares polynomials. For each node, third-order polynomials for each component of U_h are fitted through the values in the neighbour cells of the nodes and the neighbours' neighbours. For the faces, the two cells next to the face are used as well as their neighbours and neighbours' neighbours. From these fitted polynomials, we get the state vector and derivatives in the nodes and face centres, which are used to compute fluxes.

- Then, third-order accurate quadrature integration of the flux over the faces is performed with the face centre and nodal values. In 2D, third-order accuracy is obtained by assigning a weight of $\frac{2}{3}$ to the face and $\frac{1}{6}$ to each of the two face nodes. Weighting coefficients for arbitrary faces in 3D are under study.

Since the least-squares polynomials are fourth-order accurate, the resulting finite-volume approximation of $\mathcal{N}(\mathbf{U}_h)$ is at least third-order accurate for the convection (which involves one differentiation) and second-order for the diffusion (which requires two differentiations). This is an order more than the standard discretisation, so it is sufficient.

5 Goal-oriented refinement

Apart from error estimation, the adjoint solution can be used for grid refinement. A straightforward way to do this would be to use the local integrand $\mathbf{z} \cdot \mathcal{N}(\mathbf{U}_h) - \mathcal{N}(\mathbf{U})$ from equation (3) as a refinement criterion. However, this experssion is a scalar so it cannot be used for anisotropic grid refinement, as it cannot specify different cell sizes in different directions.

A method for anisotropic grid refinement which is suitable for our metric-tensor refinement criteria [9] is presented by Loseille et al. [4]. They express the local residuals in terms of projection errors for the fluxes, i.e. the errors coming from the impossibility to represent a continuous function on a finite mesh. Using this, they show that these projection tensors can be minimised if a refined mesh is based on metric tensors that are the Hessian matrices of second spatial derivatives of the flux components. The optimum mesh for computing J is obtained by weighting these Hessians with the gradients of the adjoint solution.

Loseille et al. show excellent results for their method applied to compressible Euler flow. We have made an approximate implementation of this method for RANS flows: the viscous terms are added to the fluxes without further analysis, also we do not use the limited class of finite-element discretisations for which the paradigm is theoretically valid. Some initial tests for RANS will be presented in the next section.

6 Numerical tests

6.1 Error estimation for 2D profiles

The quality of the adjoint error estimation is tested with two 2D wing section test cases. The first, laminar case is the NACA0012 profile at 4° angle of attack and $Re = 1000$. Turbulent flow is computed around the Nakayama B profile [5] at 4° angle of attack and $Re = 1.2 \cdot 10^6$. Adjoints are computed for two functionals: the drag force and the integral of u_1 over a rectangle in the wake, which resembles the evaluation of the propeller plane flow.

The rectangle is centred at $[0.9, -0.02]$ and has dimensions 0.02×0.04 for the NACA wing and 0.01×0.02 for Nakayama. The computed functionals are corrected with the estimated error in order to improve the estimate.

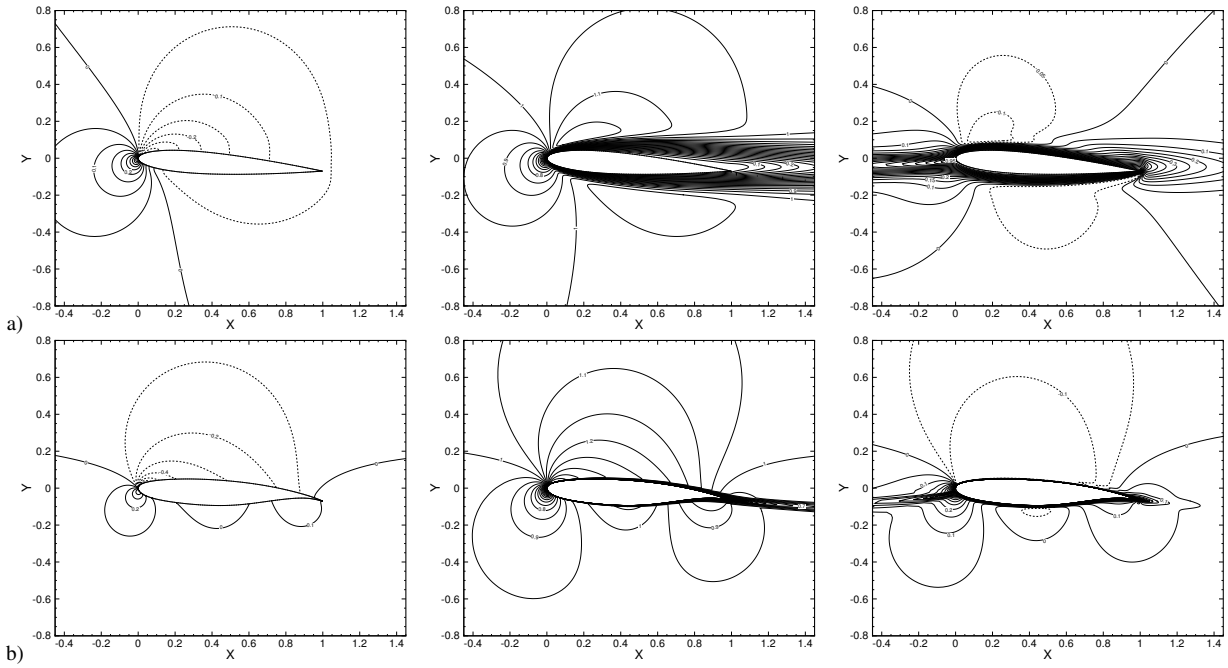

Figure 1: Flow around the NACA0012 (a) and Nakayama B (b) airfoil: pressure, horizontal velocity, and z_1 for the drag functional.

For both cases, computations have been performed on structured C-topology and unstructured HEXPRESS grids with low-Reynolds boundary layers. Figure 1 gives an impression of the solutions. While the boundary layer is of course much thinner for the turbulent case, both flows are similar. No particular problems were encountered for the computation of the primal and the adjoint solutions. However, the computations of the residuals are prone to errors in the high aspect-ratio cells near the wall, especially in the cells on the surface since these are missing the neighbours' neighbour cells in the wall direction. Also, the evaluation of the disk integral is complicated because the meshes are not specially refined in the disk zone, so on the coarser structured grids there were too few cells in the disk to perform the integration.

Computed and corrected functional values are given in figure 2. The adjoint error estimation is based on linearisation (section3) so it is only valid near the asymptotic range. True asymptotic convergence is only reached for the NACA0012 drag functional on structured meshes; here the correction seems to improve the solution on the finer meshes even though the influence of near-wall errors in the residuals is non-negligible. Also for the turbulent Nakayama case, improvement may be obtained on the two finest meshes despite the catastrophic failure on the coarser meshes. On unstructured meshes in the laminar case, the error is systematically overestimated by a factor two. And while the solution is not improved for the turbulent case, the estimation is of the same order as the numerical error.

For the rectangle integral, the solutions are not in the asymptotic range so it is difficult to say whether the solutions are improved by the correction or not. However, also here the magnitude of the corrections is the same as the difference between the solutions.

In conclusion, it seems unrealistic to improve functional computations by error correction. However, the adjoint technique can be used as an error estimator, certainly if the reliability of the residual computation is further improved.

6.2 Goal-oriented grid refinement for the KVLCC2

To show how adjoint-based refinement works, we shall compute the double-model flow around the KVLCC2 tanker at model scale, $Re = 6.4 \cdot 10^6$. The refinement criterion is EASM without rotation correction. The refinement criterion consists of the flux Hessians, weighted by the gradients of the adjoint solution (section 5). To improve robustness, the adjoint solution is computed on the original coarse grid (265k cells), based on the converged primal solution for this grid. Automatic refinement is then performed in several steps until the solution and the mesh are converged; for these steps the flux Hessians are computed on the refined grid but the original adjoint solution is kept. In the future, we plan to compute also the adjoint solution on the refined mesh. The final mesh has about 1M cells, an automatic procedure in the solver was used to adjust the threshold for the criterion in order to obtain this

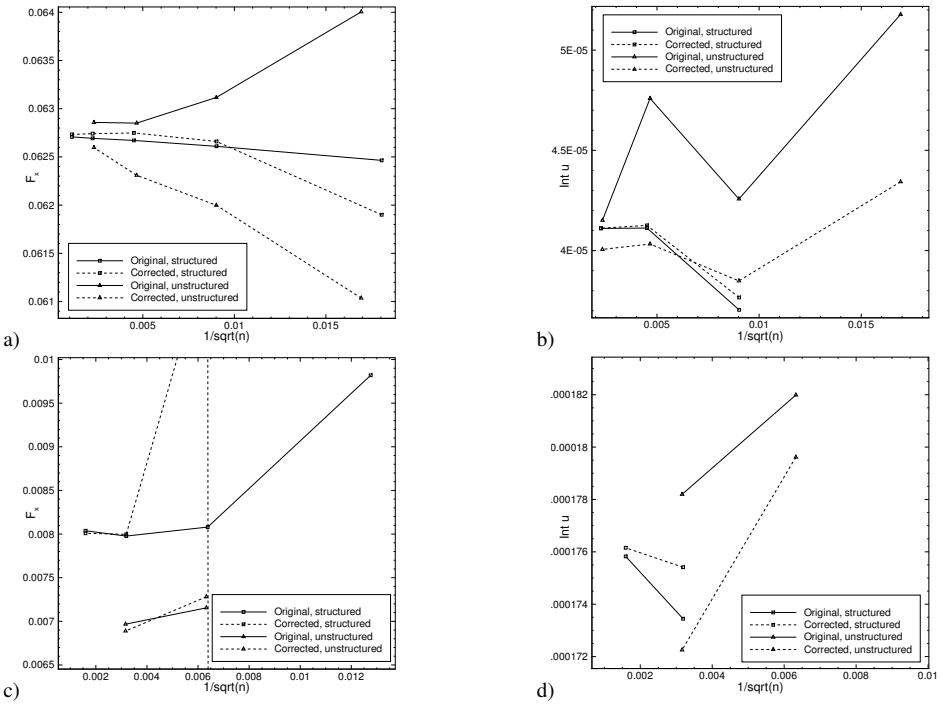

Figure 2: Original and corrected functionals for the NACA0012 airfoil: drag (a) and rectangle integral (b); for the Nakayama B airfoil: drag (c) and rectangle integral (d).

number of cells.

The functional is the integral of the axial velocity over the propeller disk with (non-dimensional) radius 0.01541 and thickness 0.01, centered at x/L=0.0175 and z/L=-0.04688. This functional is chosen due to its importance for propeller design, however it does not guarantee that all flow details in the propeller plane are well captured: only the integral value has to be right!

In the solution (figure 3) we see how the adjoint is non-uniform in the propeller plane, then gets high values around the skeg and continues upstream at the ship's side. Near the bow it has diminished but it is still noticeable. This is reflected in the refined grid, which has fine cells mainly in the boundary layer region. We also see the formation of the hook shape in the mesh of figure 3b. Compared with refined grids created using a pressure Hessian criterion (see [8, 9]) the refinement is concentrated very close to the ship. Also, of course, there is much less refinement at the front of the ship, although some refinement below the hull is visible in figure 3d. The velocity contains the familiar hook shape. Note that, according to the adjoint solution, the flow near the hub has a bigger influence on the integral than the hook.

7 Conclusion

This paper investigates the use of goal-oriented error estimation and adaptive grid refinement for high-Reynolds incompressible RANS flows. Error estimates and corrections for a functional are obtained by weighing the local residuals with an adjoint solution to the RANS equations. Tests on 2D airfoils show that it is probably unrealistic to improve computed functionals by adding the error estimate, but that the estimations are of the same order as the actual errors and could thus be used as error estimators. Notable difficulties are the evaluation of the residuals near walls and the correction of functionals that are far away from asymptotic convergence.

An example is shown of anisotropic grid refinement based on the weighing of flux Hessians with the gradient of the solution. Whether this is the optimal choice for goal-oriented refinement and whether significant gains in efficiency can be made with respect to non goal-oriented grid refinement, remains to be investigated.

References

[1] D. Aubry, P. Díez, B. Tie, and N. Parés. *Proceedings of the V International Conference on Adaptive Modelling and Simulation (ADMOS 2011)*, Paris, France (2011).

[2] R. Duvigneau, M. Visonneau, and G.B. Deng. On the role played by turbulence closures in hull shape optimization at model and full scale. *J. Mar Sci Techn*, **8**(1), 1–25 (2003).

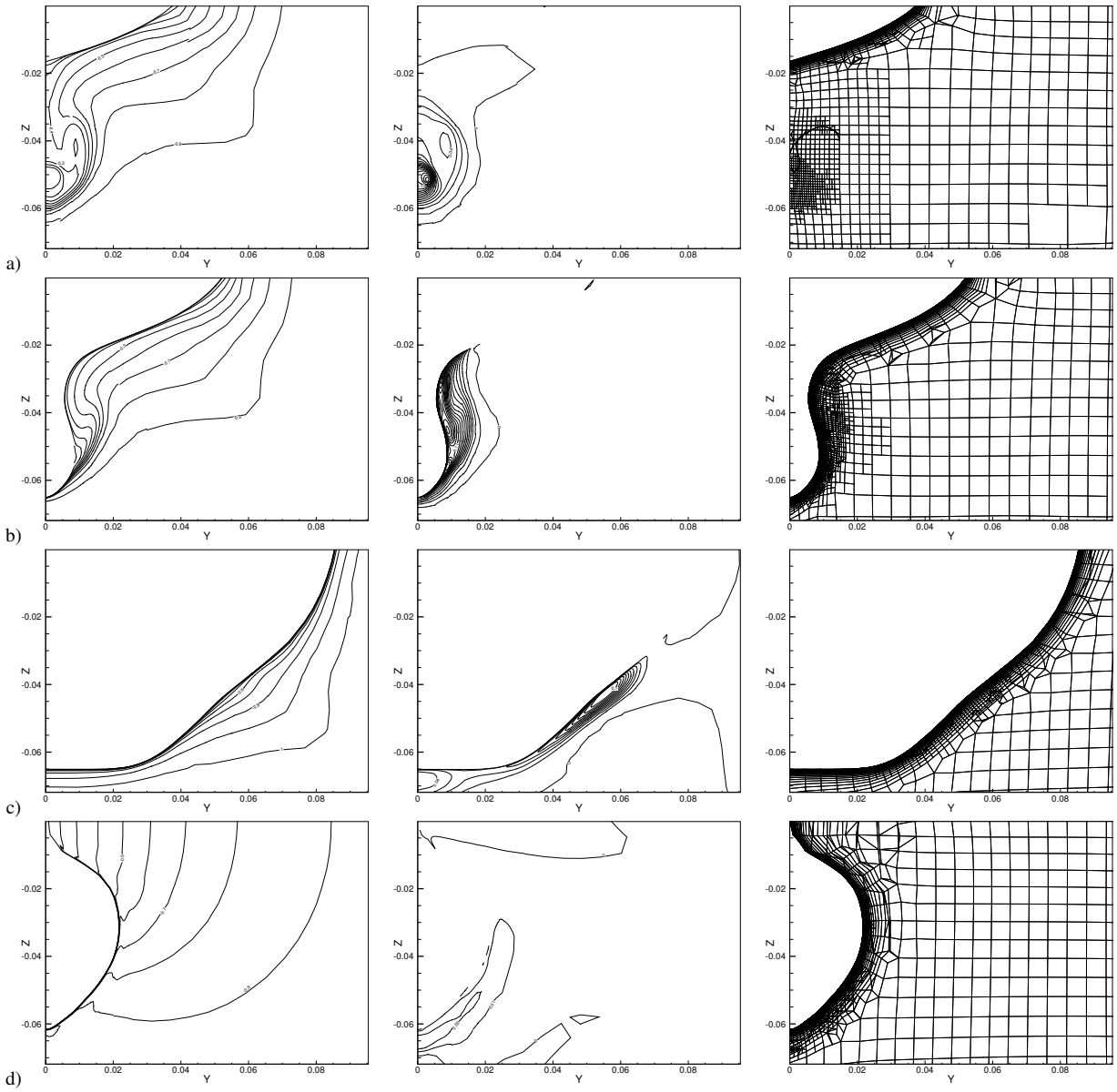

Figure 3: Goal-adaptive refinement for the KVLCC2: axial velocity, z_1 for the propeller plane functional, and the refined mesh in x-cross sections at $x/L = 0.0175$ (a), $x/L = 0.05$ (b), $x/L = 0.17$ (c), and $x/L = 1.0$ (d).

[3] A. Hay and M. Visonneau. Error estimation using the error transport equation for finite-volume methods and arbitrary meshes. *Int J Comput Fluid Dyn*, **20**(7), 463–479 (2006).

[4] A. Loseille, A. Dervieux, and F. Alauzet. Fully anisotropic goal-oriented mesh adaptation for 3D steady Euler equations. *J Comput Phys*, **229**, 2866–2897 (2010).

[5] A. Nakayama. Characteristics of the flow around conventional and supercritical airfoils. *J Fluid Mech*, **160**, 155–179 (1985).

[6] P. Queutey and M. Visonneau. An interface capturing method for free-surface hydrodynamic flows. *Comput Fluids*, **36**(9), 1481–1510 (2007).

[7] A. Stück, T. Rung. Adjoint RANS with filtered shape derivatives for hydrodynamic optimisation. *Comput Fluids*, **47**(1), 22–32 (2011).

[8] J. Wackers, G.B. Deng and M. Visonneau. Tensor-based grid refinement criteria for ship flow simulation. In *Proceedings of the 12th Numerical Towing Tank Symposium (NuTTS '10)*, Duisburg, Germany (2010).

[9] J. Wackers, G.B. Deng, A. Leroyer, P. Queutey, and M. Visonneau. Adaptive grid refinement for hydrodynamic flows. *Comput Fluids*, **55**, 85–100 (2012).

Validating Force Calculations using OpenFOAM© on a Fixed Wigley Hull in Waves

Björn Windén[1]*, Stephen R. Turnock[1] and Dominic Hudson[1]

[1]Fluid-Structure Interactions Research Group University of Southampton, Southampton, UK. SO17 1BJ

1 Introduction

The prediction of the fuel consumption of a ship on its desired route is interesting for many reasons, most important of which are the environmental impact and the cost of the fuel itself. Such a prediction can either be made based on experience, data from similar hulls on similar routes or; through *a priori* predictions based on fluid dynamic modelling and experiments. In a world where the allowed margins of error on the predictions of cost- and environmental impact grows smaller, the later is more suitable since it allows for optimisation and corrections to be made earlier in the design spiral.

Numerical predictions of the added resistance of a ship in waves have historically been made using the assumption that viscosity has no impact in such methods as Maruo (1957), Gerritsma and Beukelman (1972) and Faltinsen et al. (1980). The problem with using potential flow is that it is too mathematically complicated to arrive at a solution accounting for all phenomena involved. The solution therefore, comes with a long list of assumptions, linearisations and simplifications. In most cases when this is shown to influence the results, it can be adjusted for using empirical corrections but no method has been show to work for all types of hulls in all sea states. It is therefore hard to tell if the weakness of potential flow for the purpose of describing a ship in waves lies in the original assumptions or if it is due to the many assumptions used to make the problem mathematically approachable. Furthermore, using potential flow does not allow for detailed coupling between the flow around the hull and the performance of the propeller. These are the two main causes of decreased performance in waves and should be considered together in any prediction of said performance(Prpić-Oršić and Faltinsen, 2012).

2 Aim

A RANS based prediction allows for phenomena such as the behaviour of the boundary layer under the waves and other viscous effects to be modelled. Even though a prediction based on RANS modelling comes with much fewer assumptions, the complexity of the problem means that it is very sensitive to meshing, selected schemes, boundary conditions etc. For example; to accurately predict the forces on the hull, the correct motions are needed, this in turn requires accurate force prediction which can lead to large discrepancies if the exciting force had a small discrepancy to begin with. Incorrect predictions of the phase of the hydrodynamic forces is something that has been highlighted in previous CFD workshops as one of the weaknesses of using RANS (Larsson, 2010).

For this reason this paper concerns a fixed hull in waves. Previous studies have shown that using a fixed hull can give a good insight into the force distribution on the hull and, using a body force model for the propeller, predict the self propelled performance of a ship with good accuracy (Turnock et al., 2010). Using a fixed hull also eliminates any progressive expansion of errors due to phasing problems which allows for more detailed studies of phenomena such as boundary layer disturbances due to the waves and how this affects the propeller inflow.

To thoroughly validate the performance of OpenFOAM for predicting the forces on a fixed hull in waves, a comparative study with several wavelengths was conducted. The experimental data is provided from a study of fixed Wigley hulls in waves by Journée (1992). For further comparison, predictions made using a non-linear Boundary Element Method (BEM)are also included (Kjellberg, 2011).

3 Setup

Waves were generated and dissipated using the relaxation-based wave generation toolbox waves2Foam (Jacobsen et al., 2012). The length of the relaxation zones used in the wave generation were chosen to match the wavelength of the longest wave in the validation case (6m.) For all cases in this paper, the speed was corresponding to $Fn = 0.2$.

The geometry and boundary conditions were set up to match the conditions of the experiments. Forward speed was achieved by imposing a steady current and wind velocity in the domain and thus all boundary

* *corresponding author's e-mail*: b.winden@soton.ac.uk

conditions on walls were set to a slip-type. The outlet was set to vary between a Neumann type boundary condition (zero gradient) for the velocity if the velocity vector points into the domain and a Dirichlet type (with a fixed value on the flux representative of the freestream) if the velocity vector points out of the domain. This was done to increase the stability of the outlet. The inlet boundary condition was set so that the volume fraction and velocity follows those of the waves being generated in the adjacent relaxation region ensuring that the all gradients over the inlet boundary equals zero.

For turbulence modelling, the $k-\omega$ SST model(Menter, 1994) was used with small initial values of k to represent some initial turbulence present in the tank.

3.1 Validation hull

The used hull was the one labelled "Wigley III" by Journée (1992), the particulars of which are shown in Table 1.

Table 1: Particulars of validation hull

L_m	=	3 m	B_m	=	0.3 m	a_2	=	0.2
T_m	=	0.1875 m	∇_m	=	0.0780 m^2			
C_{33}	=	6119	C_{55}	=	2874			

L_m, B_m and T_m are the length, width and draught of the hull. C_{33} and C_{55} are the stiffness terms in the equations of motion for heave and pitch respectively given by the geometry and ∇_m is the volume displacement of the hull. a_2 gives the shape of the hull as:

$$z_m = \frac{B}{2}\left(1-\frac{{y_m}^2}{{T_m}}\right)\left(1-\frac{2{x_m}^2}{L_m}\right)\left(1+\frac{2a_2{x_m}^2}{L_m}\right) \tag{1}$$

with x_m,y_m,z_m being a hull-fixed system originating amidships, on the waterplane and on the centreline with the same orientation as in Figure 1. Above the waterline, the cross section was fixed at the one when $y_m = 0$.

3.2 Geometry

The basin has the same principal dimensions as the Delft University of Technology towing tank where the experiments were conducted. Only a section of the tank before and after the hull just enough to capture the relevant flow features and waves was used. Furthermore two relaxation zones were allowed before and after the measurement region for generating and dissipating waves.

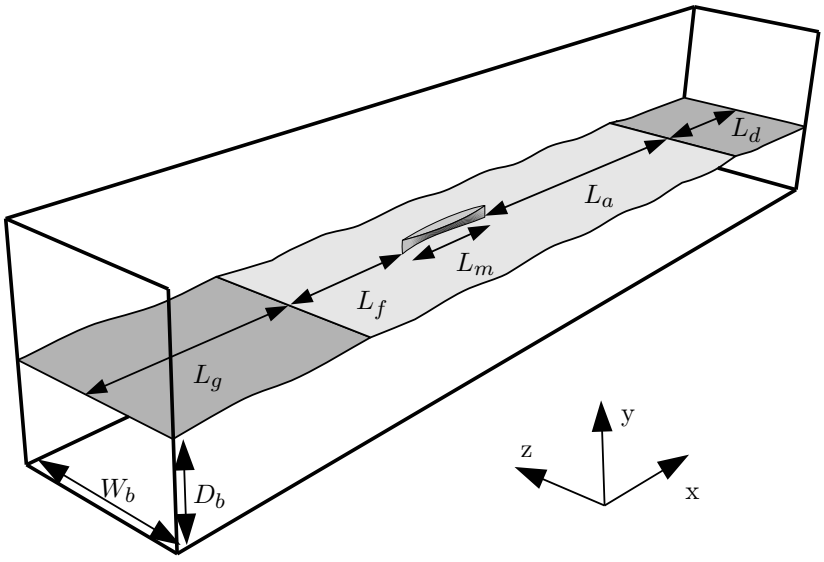

Figure 1: Geometry

Table 2: Domain particulars

D_b	=	2.5 m	W_b	=	4.22 m
L_g	=	6 m	L_d	=	6 m
L_f	=	L_m	L_a	=	$3L_m$

3.3 Meshing

When simulating a ship travelling in waves, there are several requirements of the mesh. Away from the hull, the main requirement is that it should allow for the undisturbed propagation of incoming and ship-generated waves. Close to the hull and in the wake, the mesh should be as uniform (aspect ratio 1) as possible to more accurately capture detailed flow features.

The impact of the mesh density in the free surface region on the quality of the propagating regular waves was investigated prior to generating the final mesh. As a measure of quality, the reduction in the height of the wave at a point four hull-lengths downstream of its generation was used. This was done for varying numbers of cells in the horizontal and vertical directions and for varying wavelengths. The amplitude was kept constant at $\zeta = 0.023m$ which is close to all the amplitudes in the validation case.

Because the impact typically varies with wave elevation and -steepness, there will be an optimal mesh for each wave in the testcase. However, in the interest of simplicity, one mesh was used here for all cases. Because of this, the lowest performance across the range of wavelengths was chosen as representative. This is shown in Figure 2.

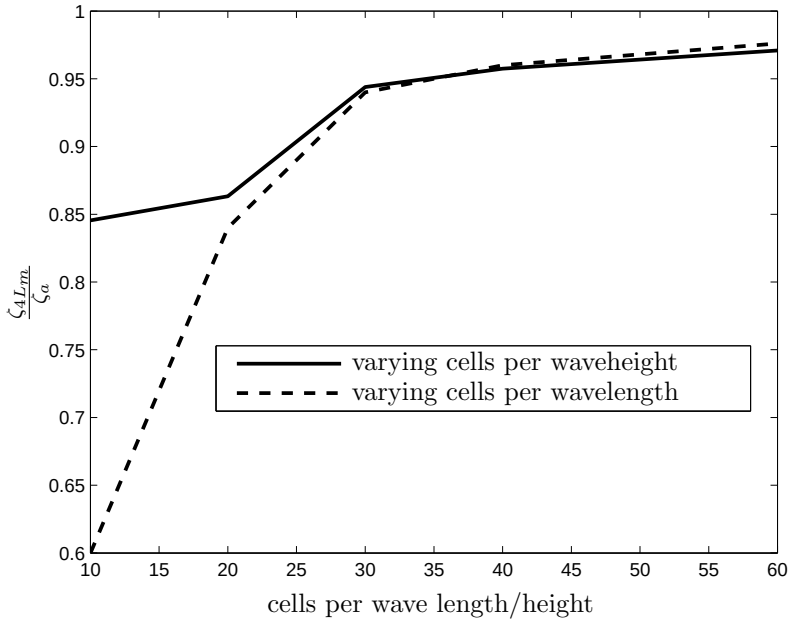

Figure 2: Results of mesh independence study for wave propagation

From Figure 2, it can be concluded that 30 cells per waveheight and 30 cells per wavelength should be enough to ensure undisturbed propagation. Because one mesh is used for all cases, the spacing is based on the shortest wavelength in the series. Because the wavelength is much greater than the waveheight in this case, this means that relatively high aspect ratio cells are needed in the free surface region. Since this is not desireable close to the hull, a way of blending the mesh refinement between these two different regions is needed.

This is achieved by selecting and refining cells based on distance from the body and the region of the free surface. The procedure is illustrated in Figure 3 and can be described as follows:

(a). If more body refinement is needed, select cells with a distance d_b from the body. If more vertical free surface refinement is needed select cells where $|y| < \zeta$.

→ Refine vertically

(b). If more body refinement is needed, Select cells with a distance d_b from the body. If more horizontal free surface refinement is needed select cells where $|y| < \zeta$.

→ Refine horizontally

(c). Shrink the distance d_b and repeat step (a)

(d). Repeat step (b)

(e). When all refinement levels have been reached, snap to body and grow boundary layer mesh.

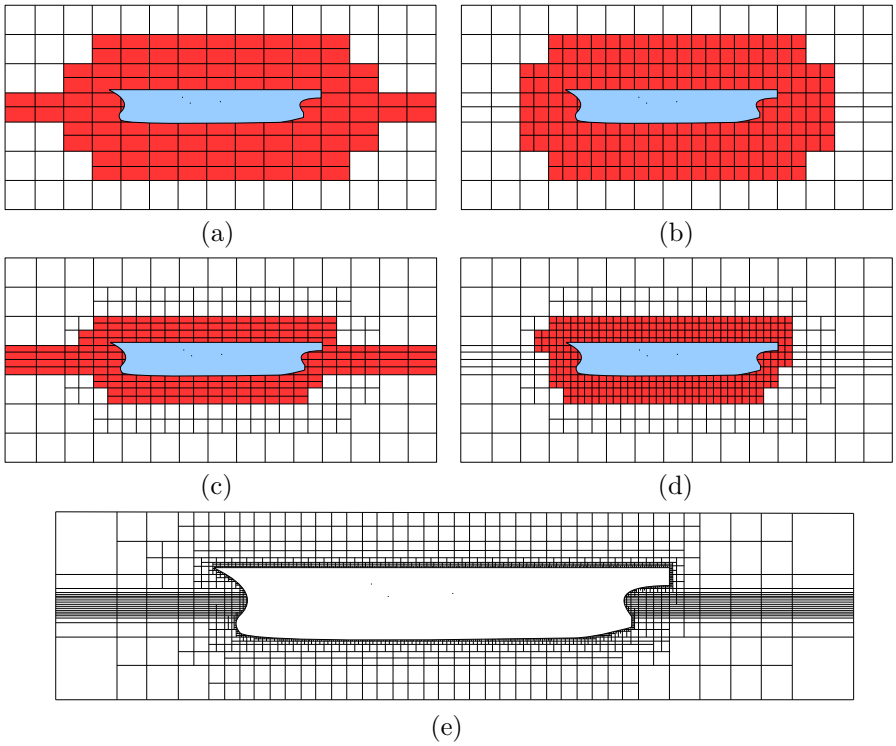

Figure 3: Mesh generation strategy

Steps (a)-(d) are achieved using the native OpenFOAM-tools for cell selection and splitting (cellSet and refineMesh) using an automated script while snapping to the surface and boundary layer mesh generation are done using the standard meshing tool snappyHexMesh. The boundary layer mesh was added to achieve a y^+-value of 50-60 for the hull. The final mesh contains 7M cells.

3.4 Solving and data recording

The used solver was the standard OpenFOAM VOF solver interFoam with modifications applied to incorporate the relaxation zones. Wave elevations were measured by probing the volume fraction α across the free surface region. Two adjacent points (i and $i-1$): one where $\alpha < 0.5$ and one where $\alpha > 0.5$ were found and the point where $\alpha = 0.5$ calculated as

$$\zeta = y_{i-1} + \frac{\alpha_{i-1} - 0.5}{\alpha_{i-1} - \alpha_i} (y_i - y_{i-1}) \tag{2}$$

from which the amplitude ζ_a could be extracted by averaging over several wave periods. The forces on the hull were calculated using the OpenFOAM force library which is based on wall shear stress and pressure distribution. These were calculated for each face and summed over the hull to give total forces and moments.

4 Results

The results of the validation study are presented as amplitudes of the surge force F_{xa}, heave force F_{ya} and pitch moment M_{za} and their phases $\varepsilon_{1,3,5}$ relative to the wave elevation amidships.

The amplitudes are nondimensionalised as

$$F''_{xa} = \frac{F_{xa}}{k\zeta_a \rho g \nabla_m} \tag{3}$$

$$F''_{ya} = \frac{F_{ya}}{\zeta_a C_{33}} \tag{4}$$

$$M''_{za} = \frac{M_{za}}{k\zeta_a C_{55}} \tag{5}$$

where k and ζ_a are the wave number and -amplitude of the incident waves.

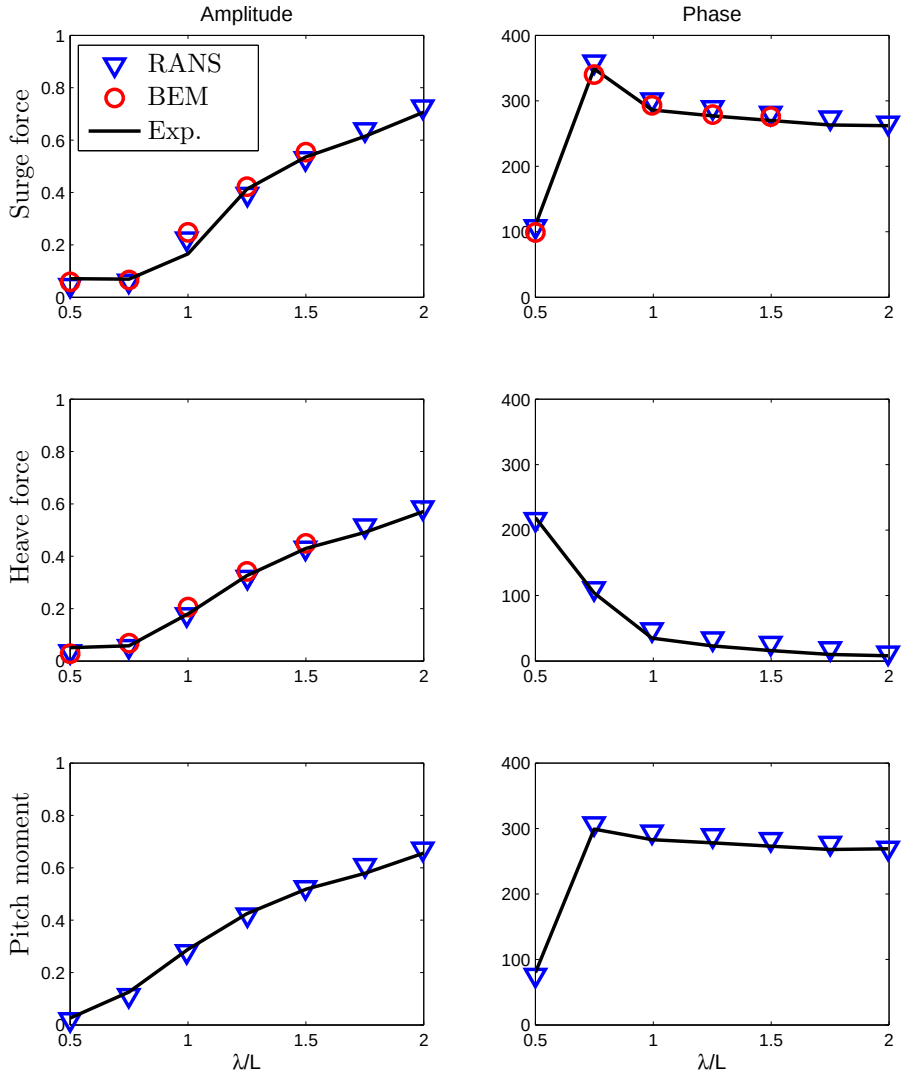

Figure 4: Results of validation case

5 Conclusions

Both the RANS and the BEM show good correlation with experimental results in terms of amplitude with RANS having the best performance. The RANS prediction of the phases is slightly worse than that from the BEM with a discrepancy of around 10^o across the range of wavelengths. This shows that, for a fixed hull, the viscous contribution to the amplitude of the force variation is minimal. There is however an effect on the mean values of force when viscosity is considered. This is shown in Figure 5. This does not say much about the actual viscous effect on a moving hull since motions would greatly increase the pressure contribution as

well as move the hull to other positions relative to the waves. It is however interesting when considering self propulsion since a change in the viscous force means a disturbance of the boundary layer which means an altered inflow to the propeller. This has implications for bow design since the flow at the bow has been shown to be very influential for the character of the boundary layer further aft (Landweber and Patel, 1979).

This study has shown that forces on a fixed hull can be accurately predicted using the described setup. The next step in this study will be to use this setup to investigate what changes in the shape (especially above the waterline) at the bow does to the viscous force distribution on the hull.

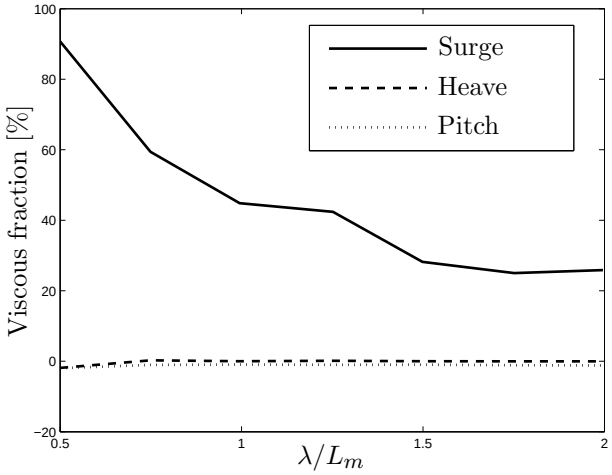

Figure 5: Viscous contribution to the increase in mean values of force/moment

References

Faltinsen, O., Minsås, K., Liapis, N. and Skjørdal, S. (1980), Prediction of Resistance and Propulsion of a Ship in a Seaway, *in* 'Proceedings of the 13th Symposium of Naval Hydrodynamics'.

Gerritsma, J. and Beukelman, W. (1972), 'Analysis of the Resistance Increase in Waves of a Fast Cargo Ship', *International Shipbuilding Progress* **19, no. 20**.

Jacobsen, N. G., Fuhrman, D. R. and Fredsøe, J. (2012), 'A Wave Generation Toolbox for the Open-Source CFD Library: OpenFoam®', *Int. J. Numerl. Meth. Fluids* **In print**.

Journée, J. (1992), 'Experiments and calculations on 4 Wigley hull forms in head waves'.

Kjellberg, M. (2011), 'Fully Nonlinear Unsteady Three-Dimensional Boundary Element Method for Force Predictions on a Restrained Hull in Waves'.

Landweber, L. and Patel, V. (1979), 'Ship Boundary Layers', *Annual Review of Fluid Mechanics* **11**, 173–205.

Larsson, L. (2010), Proceedings of the Gothenburg 2010 CFD Workshop.

Maruo, H. (1957), 'The Excess Resistance of a Ship in Rough Seas', *International Shipbuilding Progress* **4, no 35**.

Menter, F. (1994), 'Two-equation eddy-viscosity turbulence models for engineering applications', *AIAA Journal* **32**(8), 269–289.

Prpić-Oršić, J. and Faltinsen, O. (2012), 'Estimation of ship speed loss and associated CO_2 emissions in a seaway', *Ocean Engineering* **44**, 1–10.

Turnock, S., Lewis, S., Philips, A., Banks, J., Winden, B., Hudson, D. and Molland, A. (2010), Evaluating the self-propulsion of a container ship in a seastate using computational fluid dynamics, *in* 'William Froude Conference: Advances in Theoretical and Applied Hydrodynamics - Past and Future', p. 12.

CALL FOR PAPERS

16th Numerical Towing Tank Symposium (NuTTS'13)

Mülheim, Germany, 2-4th September 2013

Topics:

- Nonlinear flows around marine structures (LES, RANSE, Euler with or w/o free surface)
- Free-surface flows around marine structures (3-d ship seakeeping, free-surface viscous flows)
- Related topics (validation experiments, numerical techniques, grid generation, etc)

Deadlines:

Early feedback (optional):	15 March 2013
Extended Abstracts received:	15 June 2013
Payment received:	15 July 2013

You are invited to participate in the above event. The objective of the event is to provide a forum for informal discussions among experts in the field and to disseminate latest results. Younger workers and Ph.D. students are especially encouraged to participate. The event will be held at the Wolfsburg hotel in Mülheim (near Düsseldorf). All participants stay and have meals together to maximize interaction and discussion.

The extended abstracts of the proposed talk will be directly reproduced in pdf proceedings. Work in progress, encountered problems, etc. should be discussed in an open, informal atmosphere (no ties!) among colleagues. The first page of the extended abstract should be headed with the title and authors' names, affiliation and email address in a compact form to economize on space. Academic titles and page numbers shall be omitted. The extended abstract shall neither contain an abstract of the abstract, nor keywords, nor further headers. Font size shall not be less than 10pt Times New Roman. Extended abstracts should be limited to 6 pages in A4 format with 2.5 cm margin. An early reply will help us in organizing the event better. For the early feedback, a tentative title or topic will suffice.

Following the tradition of previous NuTTS events, the fees will be kept low to allow a maximum number of scientists to attend. The fees including accommodation (2 nights) and all meals during the symposium will be:

250 Euro PhD candidates and students
350 Euro authors
400 Euro other participants

Contact: Volker Bertram
Volker.bertram@GL-group.com

Sponsors: CD-adapco**,** further sponsors to be announced